

Lecture Notes in Mechanical Engineering

Chandan Pandey  
Vikas Goyat  
Sunkulp Goel *Editors*

# Advances in Materials and Mechanical Engineering

Select Proceedings of ICFTMME 2020

 Springer

# Lecture Notes in Mechanical Engineering

## Series Editors

Francisco Cavas-Martínez, Departamento de Estructuras, Universidad Politécnica de Cartagena, Cartagena, Murcia, Spain

Fakher Chaari, National School of Engineers, University of Sfax, Sfax, Tunisia

Francesco Gherardini, Dipartimento di Ingegneria, Università di Modena e Reggio Emilia, Modena, Italy

Mohamed Haddar, National School of Engineers of Sfax (ENIS), Sfax, Tunisia

Vitalii Ivanov, Department of Manufacturing Engineering Machine and Tools, Sumy State University, Sumy, Ukraine

Young W. Kwon, Department of Manufacturing Engineering and Aerospace Engineering, Graduate School of Engineering and Applied Science, Monterey, CA, USA

Justyna Trojanowska, Poznan University of Technology, Poznan, Poland

Francesca di Mare, Inst of Energy Tech, Building IC-2/63, Ruhr-Universität Bochum, Bochum, Nordrhein-Westfalen, Germany

**Lecture Notes in Mechanical Engineering (LNME)** publishes the latest developments in Mechanical Engineering—quickly, informally and with high quality. Original research reported in proceedings and post-proceedings represents the core of LNME. Volumes published in LNME embrace all aspects, subfields and new challenges of mechanical engineering. Topics in the series include:

- Engineering Design
- Machinery and Machine Elements
- Mechanical Structures and Stress Analysis
- Automotive Engineering
- Engine Technology
- Aerospace Technology and Astronautics
- Nanotechnology and Microengineering
- Control, Robotics, Mechatronics
- MEMS
- Theoretical and Applied Mechanics
- Dynamical Systems, Control
- Fluid Mechanics
- Engineering Thermodynamics, Heat and Mass Transfer
- Manufacturing
- Precision Engineering, Instrumentation, Measurement
- Materials Engineering
- Tribology and Surface Technology

To submit a proposal or request further information, please contact the Springer Editor of your location:

**China:** Ms. Ella Zhang at [ella.zhang@springer.com](mailto:ella.zhang@springer.com)

**India:** Priya Vyas at [priya.vyas@springer.com](mailto:priya.vyas@springer.com)

**Rest of Asia, Australia, New Zealand:** Swati Meherishi at [swati.meherishi@springer.com](mailto:swati.meherishi@springer.com)

**All other countries:** Dr. Leontina Di Cecco at [Leontina.dicecco@springer.com](mailto:Leontina.dicecco@springer.com)

To submit a proposal for a monograph, please check our Springer Tracts in Mechanical Engineering at <http://www.springer.com/series/11693> or contact [Leontina.dicecco@springer.com](mailto:Leontina.dicecco@springer.com)

**Indexed by SCOPUS. All books published in the series are submitted for consideration in Web of Science.**

More information about this series at <http://www.springer.com/series/11236>

Chandan Pandey · Vikas Goyat · Sunkulp Goel  
Editors

# Advances in Materials and Mechanical Engineering

Select Proceedings of ICFTMME 2020

 Springer

*Editors*

Chandan Pandey  
Indian Institute of Technology Jodhpur  
Karwar, Rajasthan, India

Vikas Goyat  
SRM Institute of Science and Technology  
Ghaziabad, Uttar Pradesh, India

Sunkulp Goel  
Herbert Gleiter Institute of Nanoscience  
Nanjing, China

ISSN 2195-4356

ISSN 2195-4364 (electronic)

Lecture Notes in Mechanical Engineering

ISBN 978-981-16-0672-4

ISBN 978-981-16-0673-1 (eBook)

<https://doi.org/10.1007/978-981-16-0673-1>

© The Editor(s) (if applicable) and The Author(s), under exclusive license to Springer Nature Singapore Pte Ltd. 2021

This work is subject to copyright. All rights are solely and exclusively licensed by the Publisher, whether the whole or part of the material is concerned, specifically the rights of translation, reprinting, reuse of illustrations, recitation, broadcasting, reproduction on microfilms or in any other physical way, and transmission or information storage and retrieval, electronic adaptation, computer software, or by similar or dissimilar methodology now known or hereafter developed.

The use of general descriptive names, registered names, trademarks, service marks, etc. in this publication does not imply, even in the absence of a specific statement, that such names are exempt from the relevant protective laws and regulations and therefore free for general use.

The publisher, the authors and the editors are safe to assume that the advice and information in this book are believed to be true and accurate at the date of publication. Neither the publisher nor the authors or the editors give a warranty, expressed or implied, with respect to the material contained herein or for any errors or omissions that may have been made. The publisher remains neutral with regard to jurisdictional claims in published maps and institutional affiliations.

This Springer imprint is published by the registered company Springer Nature Singapore Pte Ltd. The registered company address is: 152 Beach Road, #21-01/04 Gateway East, Singapore 189721, Singapore

# About This Book

This book presents the proceedings of the 1st International Conference on Future Trends in Materials and Mechanical Engineering (ICFTMME-2020), organised by the Department of Mechanical Engineering, SRM Institute of Science and Technology (formerly known as SRM University), Delhi NCR Campus, Ghaziabad, Uttar Pradesh, India. The aim of this book is to provide a deep insight of future trends in the advancement of materials and mechanical engineering. A broad range of topics and issues in material development and modern mechanical engineering are covered including polymers, nanomaterials, magnetic materials, fibre composites, stress analysis, design of mechanical components, theoretical and applied mechanics, tribology, solar and additive manufacturing and many more. This book will prove its worth to a broad readership of engineering students, researchers and professionals.

# Contents

## Future Trends in Materials

<b>Synthesis and Stability of Al<sub>2</sub>O<sub>3</sub>/Water Nanofluids</b> .....	3
Vinay Singh, Ajay Kumar, Kaushal Kumar, and Munish Gupta	
<b>Enhanced Electrocatalytic Activity of Poly (Trans-2,3-Dimethylacrylic Acid) Modified Electrode for Hydrazine Sensing</b> .....	13
Rajasree G. Krishnan, Beena Saraswathyamma, S. Gopika, P. Vibhooshann, Anjitha Aravind, and M. G. Gopika	
<b>Effect of Temperature on the Sliding Wear Behavior of HVOF Sprayed Al<sub>2</sub>O<sub>3</sub> Composite Coating</b> .....	23
Ankit Tyagi, S. M. Pandey, R. S. Walia, Qasim Murtaza, and Ajay Kumar	
<b>Engine Friction Reduction Using Cu Nanofluid as Lubricant</b> .....	29
Amar Kumar Jain, Manoj Kumar, and Gananath D. Thakre	
<b>Review of Transformer Core and Winding Design with Material Used</b> .....	39
Sumit Saroha, Vineet Shekher, Pankaj Kumar, and Suvir Kumar	
<b>Develop an Al-Alloy for High-Pressure–High-Temperature Applications by Enhancing Thermo-Mechanical Properties</b> .....	51
J. Joy Mathavan, A. Kunaraj, and N. Sakthivelnathan	
<b>A Review on Mechanical Properties of Bamboo Fiber-Based Composites</b> .....	61
Jagdeep Kumar, Shivaji Chaudhary, Vikas Goyat, and Amit Goyal	
<b>Review of the Approaches and Modeling Methodology for Lithium-Ion Battery Thermal Management Systems in Electric Vehicles</b> .....	75
Indraneel Naik and Milankumar Nandgaonkar	

## **Future Trends in Mechanical Engineering**

<b>Failure Criteria for Composite Blades with Wavy Edge in Aerospace Applications</b> .....	113
Prakash Jadhav	
<b>Stress and Deformation Analysis of Hip Joint for Design of Hip Prosthesis</b> .....	123
Amiya Kumar Dash, K. Sai Vishwak, and Vaibhav Pahuja	
<b>Stress and Displacement Propagation Analysis of Lumbar L4 Vertebrae for Prosthesis Design</b> .....	133
Amiya Dash and Vaibhav Pahuja	
<b>Design Optimization of Torque Link of an Aircraft Landing Gear Assembly</b> .....	145
Srishti Singh, Rishabh Chaudhary, Vaibhav Kumar Pathak, and Vipul Saxena	
<b>System Modeling, Simulation, and Analysis of Electrohydrostatic Actuator for Armoured Recovery Vehicles</b> .....	155
Manish Kumar and Shweta Singh	
<b>An Improved Hydro-mechanical Braking System to Maintain a Constant Pedal Feel During Deceleration of Electric Vehicle</b> .....	171
Sutapa Mondal and Arup Kumar Nandi	
<b>Design of Sandwich Panel Using Taguchi Analysis</b> .....	179
Prashank Sharma, Chandan Singh Mehra, Utkarsh Jha, Sachin, and Anil Kumar	
<b>A Review on Solar Desalination Still Designs</b> .....	193
Rajat G. Kawalkar, Samish M. Fale, and Satish P. Lokhande	
<b>Design and Fabrication Errors of Foil Bearings: A Review</b> .....	205
Vishal Mourya and Skylab P. Bhore	
<b>Computational Investigation on Dynamics of Drop Formation: Effect of Viscosity</b> .....	221
Pardeep Bishnoi, Mukesh Kumar Sahu, and M. K. Sinha	
<b>Viscous Oscillatory Exponentially Stratified Flow Through Parallel Plates</b> .....	233
L. Prasanna Venkatesh	
<b>A Review of Various Kinds of Cascade Refrigeration Cycle and Application of Ejector Mechanism</b> .....	245
Sachin Kumar and Virender Chahal	



**Microstructure and Mechanical Properties of Rapid Solidified Hypereutectic AlSi24Cu3.8Mg0.8 Alloys by UV-Assisted Stir-Squeeze Casting Method Under T-6 Condition** ..... 267  
 M. Peeru Naik and K. T. Balaram Padal

**A Complete Study on Various Area Filling Strategies Used in Weld Deposition-Based Additive Manufacturing** ..... 279  
 Kishore Kumar Panchagnula and Jayaprakash Sharma Panchagnula

**Characterization and Optimization of Machining Parameters for High-Strength Steel** ..... 297  
 Gagandeep Garg, Bhaskar Thakur, and Satish Kumar Sharma

**An Alternative Approach for Turning of Inconel 825: Feasibility Analysis of Process Parameters** ..... 309  
 Neel Sanghvi, Dhairya Vora, Jash Patel, and K. N. Vijayakumar

**Analysis of PMEDM Parameters for the Machining of Inconel-800 Material Using Taguchi Methodology** ..... 321  
 Satish Kumar, Sanjeev Kumar, Rajdeep Singh, Pardeep Bishnoi, and Virender Chahal

**Influence of Wall Angle, Feed Rate, and Sheet Thickness on Forming Force in SPIF** ..... 329  
 Ajay Kumar, Parveen Kumar, and Hari Singh

**Laser Polishing of Laser Additive Manufactured Hastelloy-X: Parametric Dependence and Process Optimization** ..... 339  
 Poonam Deshmukh, Ambar Choubey, A. N. Jinoop, C. P. Paul, S. S. Mohite, and K. S. Bindra

**Elucidating Corrosion Behavior of Hastelloy-X Built Using Laser Directed Energy Deposition-Based Additive Manufacturing in Acidic Environments** ..... 347  
 P. K. Diljith, A. N. Jinoop, C. P. Paul, P. Krishna, S. Bontha, and K. S. Bindra

**3-D Printing Technology: Inclusive Study and Applicability in Different Sectors** ..... 357  
 Mohd. Yunus Khan, P. Sudhakar Rao, and B. S. Pabla

**Advanced Finishing Processes for External Cylindrical Surfaces—A Review** ..... 367  
 Manpreet Singh, Gagandeep Singh, and Maninder Singh

**A Study of Ceramic Core for Investment Casting** ..... 379  
 Ganesh Vidyarthee, Nandita Gupta, and Himanshu Khandelwal

**Resilient and Robust Strategies for Process-Line Supply Chain in Textile Industry** ..... 391  
Dhairya Vora, Jash Patel, Omkar Chandhere, and Satish Takalikar

**Assessing Cognitive Behavior of Subjects Using Learning Effect and NASA-TLX in a Manual Pen Assembly** ..... 401  
M. P. Giridhar and Vinay V. Panicker

**Ranking of Lean Critical Success Factors in Manufacturing Industry: AHP Approach** ..... 411  
Virender Chahal, M. S. Narwal, and Sachin Kumar

**Evaluation of the Barriers in the Adoption of Automated Technology by the Manufacturing Sector: A Case from India** ..... 421  
Koppiahraj Karuppiah, Bathrinath Sankaranarayanan, and Saravanasankar Subramaniam

## About the Editors

**Dr. Chandan Pandey** is currently working as an Assistant Professor at the Department of Mechanical Engineering, Indian Institute of Technology Jodhpur, Rajasthan, India. He has completed his Master of Technology and Doctor of Philosophy in Mechanical Engineering from Indian Institute of Technology Roorkee, India, in 2012 and 2018, respectively. His major areas of research interest include welding, processing of nuclear grade steel, material characterization and heat treatments. He has published more than 70 papers in reputed international journals.

**Dr. Vikas Goyat** is working as an Assistant Professor in Mechanical Engineering Department of SRM Institute of Science and Technology, Ghaziabad, Uttar Pradesh, India. He obtained Doctorate of Philosophy in Mechanical Engineering and Master of Technology in Mechanical Engineering (CAD) with a gold medal from Deenbandhu Chhotu Ram University of Science and Technology, Murthal, Haryana, India in 2018 and 2012, respectively. He obtained Bachelor of Technology with Honours in Mechanical Engineering from Kurukshetra University, Kurukshetra, Haryana, India, in 2009. He has published 10 papers in reputed international journals/conferences. His areas of research include mechanical engineering design, fracture mechanics, functionally graded materials and finite element method.

**Dr. Sunkulp Goel** is currently working as Assistant Professor in Herbert Gleiter Institute of Nanoscience, Nanjing University of Science and Technology, Nanjing, Jiangsu, China. He obtained his Bachelor of Technology in Mechanical Engineering from Uttar Pradesh Technical University, Lucknow, India, and Master of Technology in Applied Mechanics from National Institute of Technology Allahabad, India. He completed his Doctorate of Philosophy from Department of Metallurgical and Materials Engineering, Indian Institute of Technology, Roorkee, India in 2015. He has published 28 papers in reputed international journals. He has expertise in the field of severe plastic deformation, mechanical behaviour of materials and characterisation of materials.

# **Future Trends in Materials**

# Synthesis and Stability of Al<sub>2</sub>O<sub>3</sub>/Water Nanofluids



Vinay Singh , Ajay Kumar, Kaushal Kumar, and Munish Gupta

**Abstract** The nanofluids may be considered as multifaceted fluids, generally employed to improve the effectiveness of thermal systems, though poor stability due to sedimentation and agglomeration has limited their applications in practical use. In this work, commercial Al<sub>2</sub>O<sub>3</sub> nanopowders were dispersed in distilled water using CTAB as surfactant. Stable Al<sub>2</sub>O<sub>3</sub>/water nanofluids with weight concentrations ranging from 0.02–0.5 wt% were synthesized using bath and probe ultrasonication. Nanopowders were characterized using high-resolution TEM micrography. UV–Vis spectroscopy and zeta potential tests were also conducted to check stability of the nanofluids.

**Keywords** Al<sub>2</sub>O<sub>3</sub>/water nanofluid · Characterization · Aggregate · UV–Vis · Zeta potential

## 1 Introduction

Recent developments in the nanotechnology have helped the researchers to carry out research on nanofluids in vigorous manner. Ever since the introduction of nanofluids [1–4], continuous research to study their thermophysical properties is in progress. Some studies [5, 6] reported 100% enhancements in thermal conductivity with nanoparticles addition to base fluids. However, due to increase in density

---

V. Singh (✉)

Department of Mechanical Engineering, Jagan Nath University, Bahadurgarh, Haryana, India

A. Kumar

Department of Mechanical Engineering, FET, Shree Guru Gobind Singh Tricentenary University, Gurugram, Haryana, India

K. Kumar

Department of Mechanical Engineering, K.R. Mangalam University, Gurugram, Haryana, India

M. Gupta

Department of Mechanical Engineering, GJUS&T, Hisar, Haryana, India

© The Author(s), under exclusive license to Springer Nature Singapore Pte Ltd. 2021

C. Pandey et al. (eds.), *Advances in Materials and Mechanical Engineering*,

Lecture Notes in Mechanical Engineering,

[https://doi.org/10.1007/978-981-16-0673-1\\_1](https://doi.org/10.1007/978-981-16-0673-1_1)

and viscosity because of nanoparticle concentration, which in turn, it increases power consumption and hence becomes a barrier to use nanofluids [7].

One of the key issues in the field of nanofluids is preparing stable nanofluids, because surface forces acting between particles are mainly responsible for stability [8]. Agglomeration in nanofluids occurs because of interaction between attractive and repulsive forces. So, to overcome this problem, stabilization techniques are performed after the dispersion technique for obtaining long-term stable nanofluids [9]. The above literature concludes that the stability of nanofluids depends upon pH value and surface concentration. Zeta potential helps in identifying surface charge of nanoparticles and associates it with stability of nanofluids. Zeta potential values having +30 mV or -30 mV determine that nanoparticles remain dispersed over a time.

In this research paper, zeta potential values were determined for different weight concentrations of Al<sub>2</sub>O<sub>3</sub>/water nanofluids, and the stability of Al<sub>2</sub>O<sub>3</sub> nanofluids was evaluated.

## 2 Materials and Methods

### 2.1 Materials

Al<sub>2</sub>O<sub>3</sub> nanopowders were purchased by order from High Purity Chemicals Limited (HPCL), and no purification methods were used.

### 2.2 Methods

#### 2.2.1 Characterization of Nanoparticles

The morphological characteristics of Al<sub>2</sub>O<sub>3</sub> nanoparticles were studied using high-resolution transmission electron microscope (*FEI, Technai G2 instrument at NIPER, Mohali*).

#### 2.2.2 Formulation of Nanofluid

Al<sub>2</sub>O<sub>3</sub>/water nanofluids were formulated using two-step method. Samples with five different concentrations, i.e., 0.02, 0.05, 0.1, 0.2 and 0.5 wt% were prepared by adding appropriate amount of nanopowders in distilled water. Cetyl trimethyl ammonium bromide (CTAB) was used as a surfactant. For ensuring the proper mixing of nanofluids, (POWERSONIC 410) bath sonicator and (BANDELIN SONO PLUS) probe sonicator were used for 3–4 h.

### 2.2.3 Characterization of Nanofluids

UV–Vis–NIR spectrophotometer, *Varian Cary 5000* (at Central instrumentation Laboratory, GJUST, Hisar), was used for spectroscopy of nanofluids. It works upon the principle that molecules possessing non-bonding electrons absorb energy in the form of visible light or ultraviolet in order to excite the electrons to a higher anti-bonding molecular orbitals. Higher the excitement between the electrons, longer will be the wavelength of the light it can absorb. Zeta potential of the nanofluids was measured for determining the stability of nanofluids using *Malvern Zetasizer Nano ZS 90*. This Zetasizer works upon the principle of electrophoretic light scattering in the measurement range of 3.8 nm–100 μm \* (diameter) with 150 μL as minimum sample volume. For aqueous systems, accuracy of the device is 0.12 μm cm/V s and sensitivity is 10 mg/mL.

### 2.3 Nanofluids Stability

Stability in nanofluids is quite important as it can alter the thermophysical properties of the nanofluid. Heat transfer abilities may be lost because of agglomeration of the nanoparticles. For stability evaluation of nanofluids, zeta potential is best method. Zeta potential is the potential that develops between fluid medium and charged nanoparticles. It shows the degree of repulsive forces between the particles in the fluid [10]. For stable colloids, zeta potential must be higher (either positive or negative). Low zeta colloids tend to lumps. Zeta potential is calculated by the electrophoretic movement of the charged particles under the influence of electric field. Zeta potential tests were performed at Bio and Nano Technology Department, GJUST, Hisar, using Malvern Zetasizer at temperature of 25 °C.

## 3 Results and Discussions

### 3.1 Morphology and Crystalline Structure of Particles

TEM images are shown in Fig. 1. TEM micrograph of Al<sub>2</sub>O<sub>3</sub> nanopowders showed that particles are oval-shaped. The particle size as observed under TEM was found less than 100 nm. Few particles of 0.2 μm were also observed/traced in the TEM micrographs. The reason for this can be explained that some particles have seemed to be agglomerated.

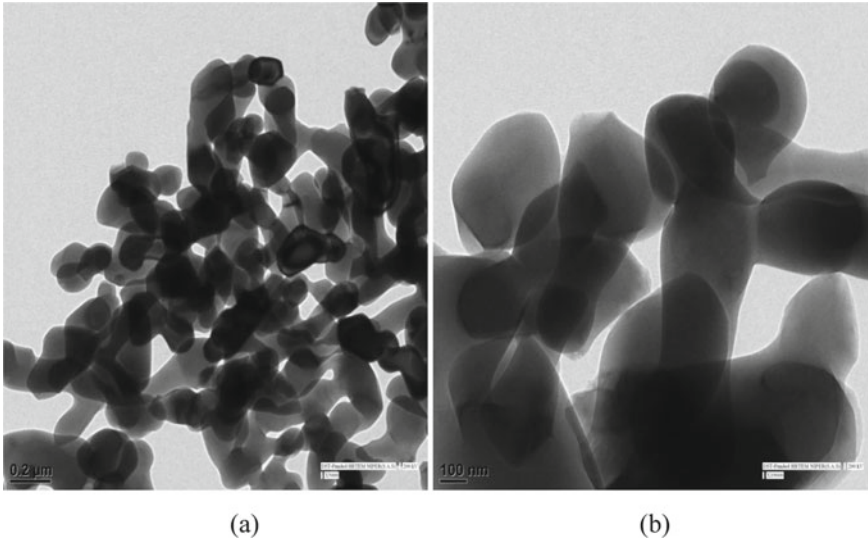


**Fig. 1** TEM micrograph of  $\text{Al}_2\text{O}_3$  nanopowders

### 3.2 *UV-Vis-NIR*

The UV spectroscopy of all the five weight concentrations of  $\text{Al}_2\text{O}_3$ /water nanofluid samples was performed in the wavelength range from 400 to 200 nm. In Fig. 2a–e, absorbance vs. wavelength graph was plotted for five different concentrations of the nanofluid. Maximum value of absorbance in all nanofluid samples was observed with 0.5 wt% concentration at wavelength 304 was 3.569. At same wavelength, minimum value of 1.614 was achieved using nanofluids with 0.02 wt% concentration. However, least value of absorbance, i.e., 0.311 was observed by  $\text{Al}_2\text{O}_3$  nanopowder at wavelength 204.

### 3.3 *Zeta Potential*

According to electrophoresis theory, zeta potential ( $\zeta$ ) is the measure of the repulsive force between the two particles and increments or decrements in zeta potential can be done by pH control. Solutions possessing a zeta potential value exceeding 60 mV are highly stable. Physically stable solutions possess values above 30 mV. Fluids having 20 mV values are limiting stable, and below this, solutions agglomerate. Highest value of zeta potential was observed in 0.1 wt % nanofluids having value of 44.9 ensuring the best stability of nanofluids, whereas in 0.5 wt% nanofluids, zeta potential of 36 was observed pointing towards less stability because of agglomeration



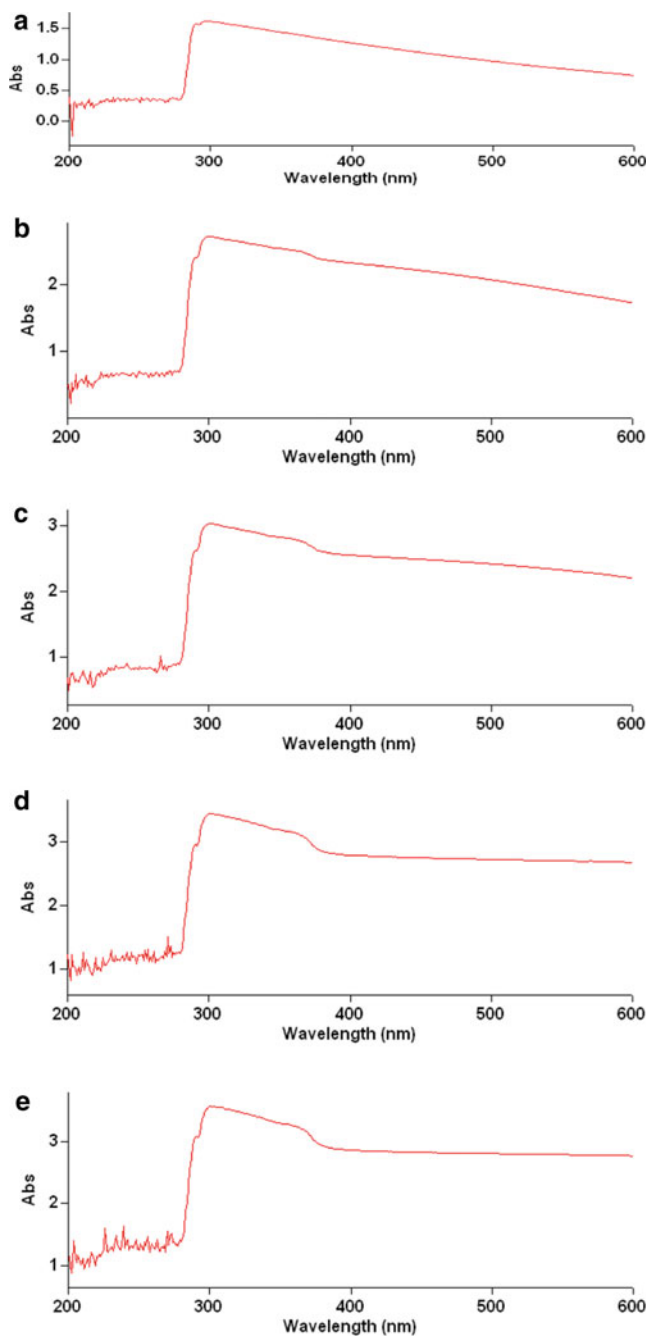
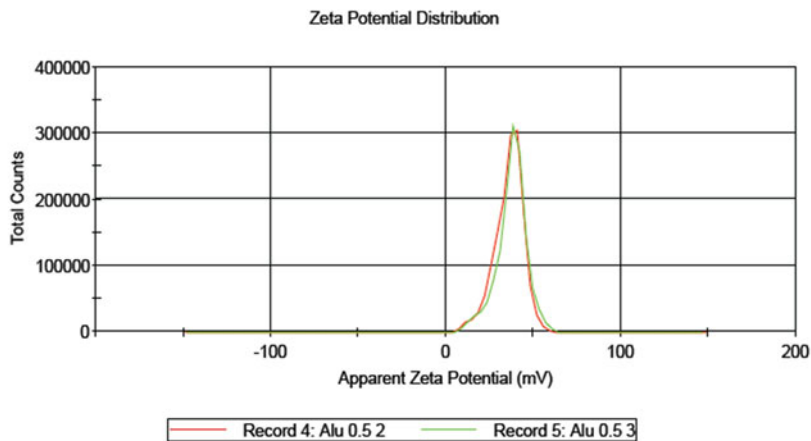
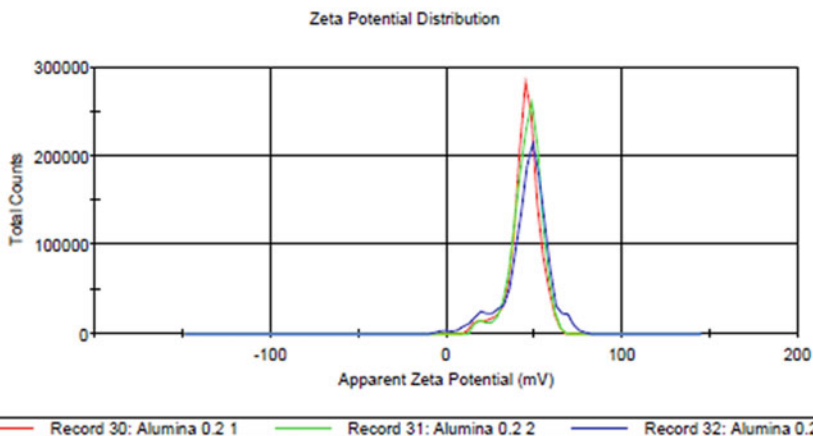


Fig. 2 a–e UV–visible spectra of aluminium oxide nanofluids

	Mean (mV)	Area (%)	St Dev (mV)
<b>a</b>			
Zeta Potential (mV): 36.0	Peak 1: 36.0	100.0	8.34
Zeta Deviation (mV): 8.34	Peak 2: 0.00	0.0	0.00
Conductivity (mS/cm): 0.245	Peak 3: 0.00	0.0	0.00
Result quality : Good			

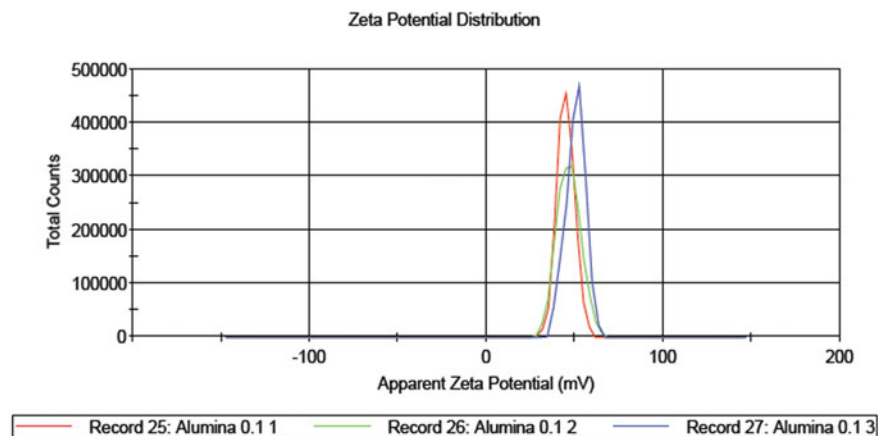


	Mean (mV)	Area (%)	St Dev (mV)
<b>b</b>			
Zeta Potential (mV): 44.5	Peak 1: 45.2	96.5	7.48
Zeta Deviation (mV): 8.63	Peak 2: 18.0	3.5	3.20
Conductivity (mS/cm): 0.0909	Peak 3: 0.00	0.0	0.00
Result quality : Good			



**Fig. 3** **a** Measurements of zeta potential for 0.5 wt%  $\text{Al}_2\text{O}_3$  nanofluids. **b** Measurements of zeta potential for 0.2 wt%  $\text{Al}_2\text{O}_3$  nanofluids. **c** Measurements of zeta potential for 0.1 wt%  $\text{Al}_2\text{O}_3$  nanofluids. **d** Measurements of zeta potential for 0.05 wt%  $\text{Al}_2\text{O}_3$  nanofluids. **e** Measurements of zeta potential for 0.02 wt%  $\text{Al}_2\text{O}_3$  nanofluids

<b>C</b>	<b>Mean (mV)</b>	<b>Area (%)</b>	<b>St Dev (mV)</b>
<b>Zeta Potential (mV): 44.9</b>	<b>Peak 1: 44.9</b>	100.0	5.01
<b>Zeta Deviation (mV): 5.01</b>	<b>Peak 2: 0.00</b>	0.0	0.00
<b>Conductivity (mS/cm): 0.0611</b>	<b>Peak 3: 0.00</b>	0.0	0.00
<b>Result quality : Good</b>			



<b>d</b>	<b>Mean (mV)</b>	<b>Area (%)</b>	<b>St Dev (mV)</b>
<b>Zeta Potential (mV): 43.6</b>	<b>Peak 1: 43.6</b>	100.0	4.32
<b>Zeta Deviation (mV): 4.32</b>	<b>Peak 2: 0.00</b>	0.0	0.00
<b>Conductivity (mS/cm): 0.0317</b>	<b>Peak 3: 0.00</b>	0.0	0.00
<b>Result quality : Good</b>			

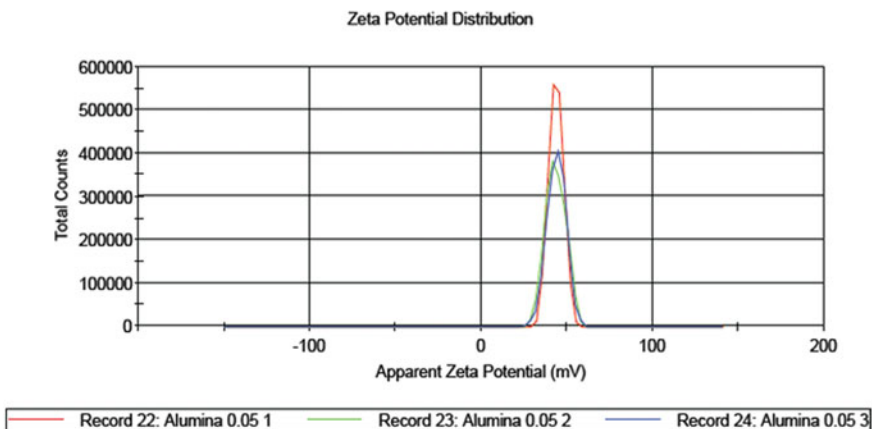


Fig. 3 (continued)

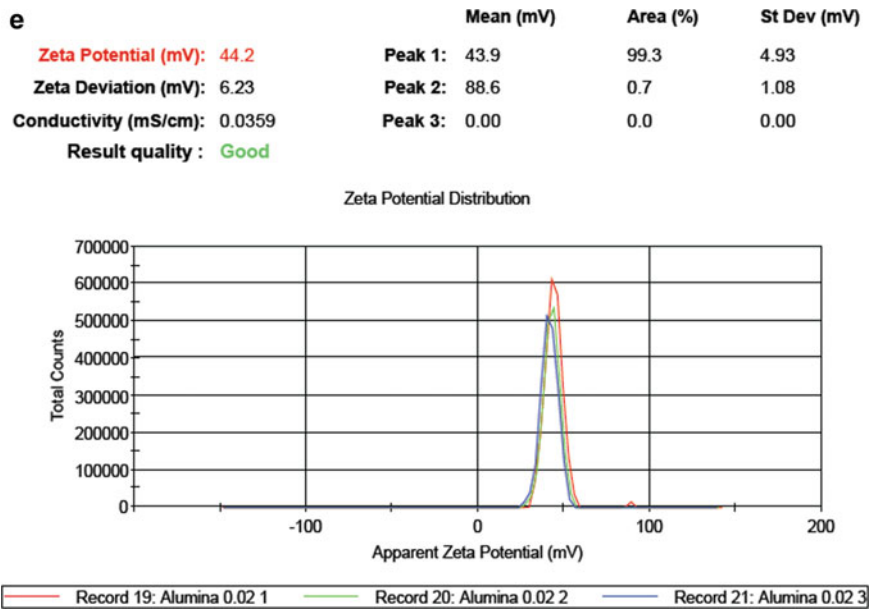


Fig. 3 (continued)

of nanoparticles in the solution. Figure 3a–e shows the zeta potential of different weight concentrations of nanofluids.

## 4 Conclusions

This study incorporates with the synthesis of  $\text{Al}_2\text{O}_3$ /water nanofluids at different weight concentrations. Different techniques were used for characterization of nanopowders and nanofluids. Experimental results state about high purity and good stability of synthesized nanofluids.

Noteworthy points are as follows:

- HRTEM images demonstrate the oval structure and nanometric range of  $\text{Al}_2\text{O}_3$  nanopowder.
- Highest absorbance in all the five nanofluid samples observed using 0.5 wt% concentration at wavelength 304 was 3.569. At the same wavelength, minimum value of 1.614 was achieved using nanofluids with 0.02 wt% concentration.
- While selecting the conditions for dispersion of particles, zeta potential is an important basis. 0.1 wt% nanofluids shows maximum zeta potential value of 44.9 ensuring best stability of nanofluids, whereas 0.5 wt% nanofluids shows minimum zeta potential value of 36.0 indicating towards less stability because of agglomeration of nanoparticles in the solution.

## References

1. Choi S, Eastman J (1995) Enhancing thermal conductivity of fluids with nanoparticles. In: International mechanical engineering congress and exposition, pp 12–17
2. Murshed SS, De Castro CN (2014) Nanofluids: synthesis, properties and applications. Nova Science Publishers, Inc., New York
3. Murshed SS, De Castro CN (2017) A critical review of traditional and emerging techniques and fluids for electronics cooling. *Renew Sustain Energy Rev* 78:821–833. <https://doi.org/10.1016/j.rser.2017.04.112>
4. Gupta M, Singh V, Kumar R, Said Z (2017) A review on thermophysical properties of nanofluids and heat transfer applications. *Renew Sustain Energy Rev* 74:638–670
5. Sezer N, Atieh MA, Koç M (2019) A comprehensive review on synthesis, stability, thermophysical properties, and characterization of nano fluids. *Powder Technol* 344:404–431. <https://doi.org/10.1016/j.powtec.2018.12.016>
6. Asadi A, Pourfattah F (2019) Heat transfer performance of two oil-based nanofluids containing ZnO and MgO nanoparticles; a comparative experimental investigation. *Powder Technol* 343:296–308. <https://doi.org/10.1016/j.powtec.2018.11.023>
7. Gupta M, Singh V, Kumar S, Dilbaghi N (2020) Experimental analysis of heat transfer behavior of silver, MWCNT and hybrid (silver + MWCNT) nanofluids in a laminar tubular flow. *J Therm Anal Calorim* 1–15
8. Gupta M, Singh V, Kumar S, Kumar S, Dilbaghi N, Said Z (2018) Up to date review on the synthesis and thermophysical properties of hybrid nanofluids. *J Cleaner Prod* 190:169–192
9. Asadi A, Asadi M, Siahmargoi M, Asadi T, Gholami Andarati M (2017) The effect of surfactant and sonication time on the stability and thermal conductivity of waterbased nanofluid containing Mg(OH)<sub>2</sub> nanoparticles: an experimental investigation. *Int J Heat Mass Transf* 108:191–198. <https://doi.org/10.1016/j.ijheatmasstransfer.2016.12.022>
10. Mehrali M, Sadeghinezhad E, Latibari ST, Kazi SN, Mehrali M, Zubir MNBM, Metselaar HSC (2014) Investigation of thermal conductivity and rheological properties of nanofluids containing graphene nanoplatelets. *Nanoscale Res Lett* 9:15. <https://doi.org/10.1186/1556-276X-9-15>

# Enhanced Electrocatalytic Activity of Poly (Trans-2,3-Dimethylacrylic Acid) Modified Electrode for Hydrazine Sensing



Rajasree G. Krishnan, Beena Saraswathyamma, S. Gopika, P. Vibhooshann, Anjitha Aravind, and M. G. Gopika

**Abstract** In this research work, authors have used poly (trans-2,3-dimethylacrylic acid) modified electrode as a novel electrocatalyst for the electrochemical sensing of environmental pollutant and group 2B carcinogen hydrazine. The modification was attained using potentiodynamic electropolymerization in phosphate buffer medium. Morphological analysis of the electropolymerized electrode was conducted using field-emission scanning electron microscope, and the catalytic effect was studied using cyclic voltammetry. A much lowered overpotential of +0.252 V versus Ag/AgCl (1 M KCl) was obtained for the electrochemical oxidation of hydrazine at the poly (trans-2,3-dimethylacrylic acid) film casted electrode. Differential pulse voltammetry was applied to measure the hydrazine concentrations varying from 20  $\mu\text{M}$  to 4 mM. Moreover, the sensor exhibited good selectivity, sensitivity, and repeatability. Practical usage of the sensor was tested in different kinds of water samples.

**Keywords** Hydrazine · Electrooxidation · Polymer

## 1 Introduction

Environmental pollution has now become a dominant concern across the world. Hydrazine ( $\text{N}_2\text{H}_4$ ) is known to be one of the chief environmental pollutants. But due to its widespread and multiple uses, it has become an indispensable part of chemical, pharmaceutical, and energy industry. Tons of hydrazine are expelled into air and aquatic bodies, and this in turn results in environmental hazards. Due to its highly volatile nature, it is being easily adsorbed through the skin and finds an easy way to enter into the body [1]. Prolonged exposure to hydrazine vapors in work places create impairment to the central nervous system, kidney, respiratory system, etc. [2]. Also it is recognized as a presumable carcinogenic chemical in

---

R. G. Krishnan · B. Saraswathyamma (✉) · S. Gopika · P. Vibhooshann · A. Aravind · M. G. Gopika

Department of Chemistry, Amrita Vishwa Vidyapeetham, Amritapuri, Kollam, India  
e-mail: [beenas@am.amrita.edu](mailto:beenas@am.amrita.edu)

human beings (group 2B) by International Agency for Research on Cancer (IARC) in 1999 [3]. Hydrazine is also found to exhibit hepatotoxic effects too [4]. Several methods like high performance liquid chromatography [5], spectrophotometry [6], and electrochemical methods [7] are reported for hydrazine determination. Being an easily oxidizable molecule and highly electroactive in nature, hydrazine can be determined using electrochemical techniques which retain high sensitivity, simple experimentation, cost-effective, fewer chemical utilization, etc., compared to other analyses' strategies [8, 9]. Electropolymerization is an established way of making selective and sensitive electrode modifiers with a highly tailorable thickness and morphology [10]. It produces homogenous, well adherent surface films in dimensions ranging from nano to micrometers [11]. Also thus formed films are highly stable in nature [12].

Herein, a facile and enhanced electrocatalytic ability of poly (trans-2,3-dimethylacrylic acid) modified pencil graphite electrode (poly DMAA/pencil graphite) for the effective quantification of hydrazine is presented. This is the first on the electropolymerization of trans-2,3-dimethylacrylic acid also known as tiglic acid in phosphate buffer medium to our knowledge best. Real sample analysis of the modified electrode was also verified in different water samples with externally added hydrazine.

## 2 Experimental

### 2.1 Chemicals

Hydrazine hydrate and potassium chloride (KCl) were obtained from Merck. Trans-2,3-dimethylacrylic acid was purchased from Sigma-Aldrich. Thin pencil was procured from a local shop. The brand of pencil is Cello. Analytical-grade reagents were used for the entire studies further purification. Room temperature was maintained for all the experiments.

### 2.2 Instrumentation

Electroanalysis using cyclic voltammetry (CV) and differential pulse voltammetry (DPV) were carried out with CHI 610E electrochemical workstation (CH Instruments, USA). Poly DMAA/pencil graphite was considered as the indicator electrode with platinum wire as auxiliary (counter) and silver/silver chloride [Ag/AgCl (1 M KCl)] as the reference electrode. The potentials mentioned in this report are in reference to Ag/AgCl (1 M KCl). Surface studies were carried out with field-emission scanning electron microscope FEI, NOVA NANOSEM 450.

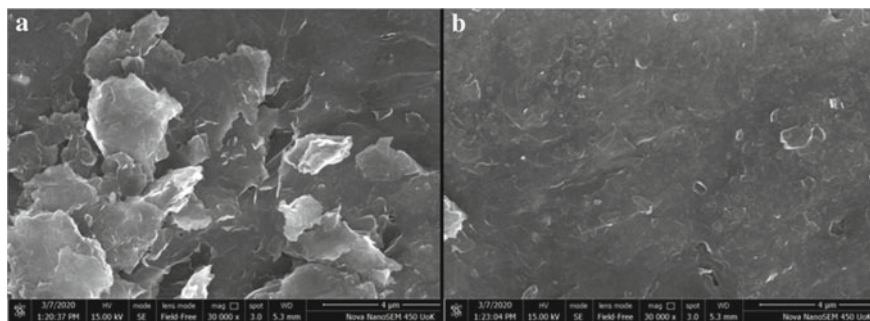


**Fig. 1** FE-SEM image of unmodified pencil graphite and poly DMAA/pencil graphite

### **2.3 Fabrication of Poly DMAA/Pencil Graphite**

The poly DMAA/pencil graphite was constructed using electropolymerization method. The film growth of trans-2,3-dimethylacrylic acid was achieved in 0.1 M phosphate buffer medium with pH 7. The potential sweeps were varied from  $-1$  to  $+1.5$  V at a scan rate of 100 mV/s. This potential-assisted polymerization of trans-2,3-dimethylacrylic acid in PB 7 medium is presenting for the first time to the best of our knowledge. The substrate to develop the polymer film was selected to be an easily available and low-cost pencil lead. Pencil lead was covered using Teflon tape with exposing 0.5 cm of its length to carry out the polymerization reaction.

## **3 Results**

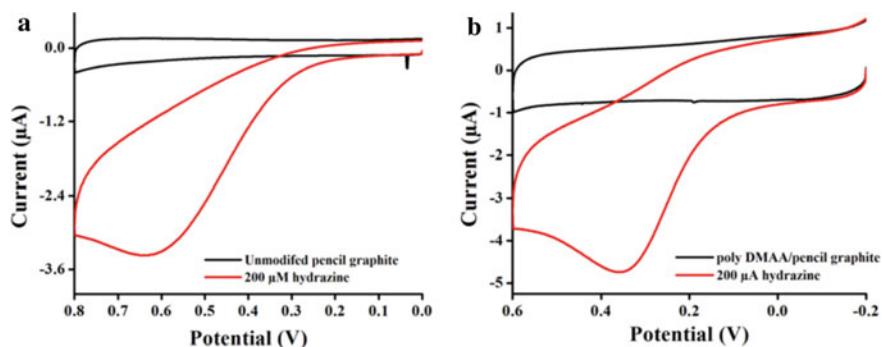
### **3.1 Surface Analysis of Bare and Polymer Coated Electrode**

Figure 1 represents the FE-SEM image of unmodified pencil graphite and poly DMAA/pencil graphite. Figure 1a shows the flakes morphologies of graphite, which is the chief constituent of the pencil material [13]. Also Fig. 1b proves that the flake like graphite structure is covered up by the polymer layer and hence can conclude that modification has been successfully incorporated onto the pencil material.

### **3.2 Electrochemical Behavior of Hydrazine at Poly DMAA Film**

Figure 2a, b shows the cyclic voltammogram obtained for the unmodified electrode and poly DMAA modified pencil graphite electrode with and without  $200 \mu\text{M}$





**Fig. 2** a CV of unmodified pencil graphite, b poly DMAA/pencil graphite with and without 200  $\mu\text{M}$  hydrazine in 0.1 M KCl

hydrazine in 0.1 M KCl solution, respectively. CV was carried out by sweeping the potentials from  $-0.2$  to  $0.8$  V by a scan rate of  $100$  mV/s. Upon anodic run, no characteristic peaks were noticed for the poly DMAA modified electrode at the potential window investigated. In the presence of  $200$   $\mu\text{M}$  hydrazine added into the KCl solution, a new faradic peak was observed at potential  $0.356$  and  $0.634$  V for poly DMAA/pencil graphite and unmodified pencil graphite, respectively. These oxidation peaks were not spotted to follow an electrochemical reduction process upon the reverse scan on both the modified and unmodified electrode surface.

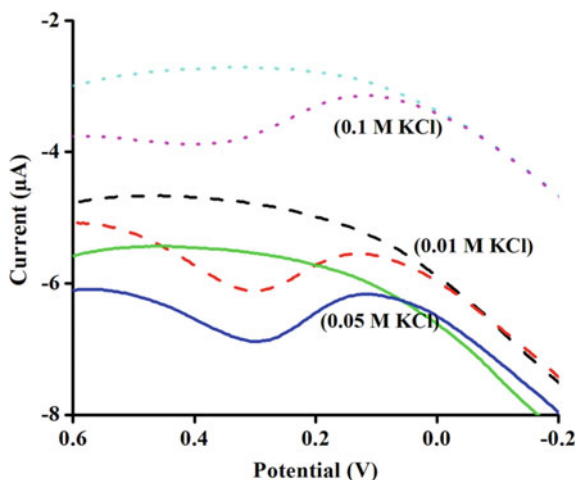
Even though there are peaks observed on both modified and unmodified electrodes, there exists a large potential difference of  $278$  mV for the electrooxidation of hydrazine at the two electrode surfaces. The overpotential was considerably reduced at the modified electrode surface showing its excellent electrocatalytic behavior toward the electrooxidation of the analyte.

### 3.3 Effect of Electrolyte

Effect of different electrolyte media was recorded and analyzed using DPV. The current response for  $200$   $\mu\text{M}$  hydrazine electrochemical oxidation at the poly DMAA/pencil graphite electrode in different electrolytes like  $0.1$  M phosphate buffer solution (PBS 7),  $0.1$  M NaOH,  $0.1$  M  $\text{H}_2\text{SO}_4$ ,  $0.1$  M  $\text{HClO}_4$  is given in Table 1. Results show that the maximum current response was obtained from  $0.1$  M KCl, and so it was specified as the medium of further studies.

**Table 1** Choice of electrolyte media

Electrolyte	Current ( $\mu\text{A}$ )		Potential (V)
<b>0.1 M KCl</b>	<b>1.387</b>		<b>0.295</b>
0.1 M PBS 7	0.845		0.317
0.1 M H <sub>2</sub> SO <sub>4</sub>		No peak	
0.1 M HClO <sub>4</sub>		No peak	
0.1 M NaOH		No peak	

**Fig. 3** DPV response of different supporting electrolyte concentration

### 3.4 Choice of Supporting Electrolyte Concentration

Finalizing KCl as the best electrolyte for hydrazine electrooxidation at poly DMAA/pencil graphite surface, the effect of various concentrations of KCl was examined. Results are shown in Fig. 3. Optimum response in respect of both peak current response and overpotential were noticed for 0.05 M KCl and hence chosen 0.05 M KCl as the optimum electrolyte concentration.

### 3.5 Influence of Polymerization Cycles

Further, the number of DMAA polymerization cycles was optimized using DPV. As the response current was higher for six cycles, it was chosen as the optimal polymerization cycle. Table 2 shows the data obtained by optimizing the polymerization cycles.

**Table 2** Influence of polymerization cycle

No. of scans	Current ( $\mu\text{A}$ )	Potential (V)
3	1.387	0.295
<b>6</b>	<b>1.53</b>	<b>0.248</b>
9	1.24	0.236

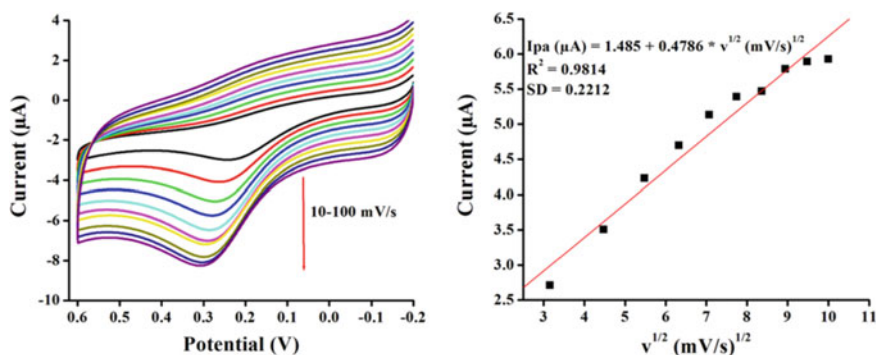


**Fig. 4** a CV of poly DMAA/pencil graphite in 0.05 M KCl containing 400  $\mu\text{M}$  hydrazine at varying scan rates from 10 to 100 mV/s, b linear plot between current versus square root of scan rate

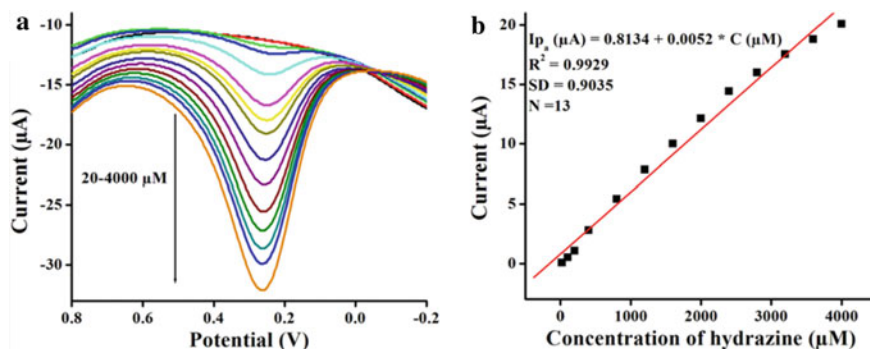
### 3.6 Variation of Scan Rate

Figure 4 A depicts the CV of poly DMAA in 0.05 M KCl containing 200  $\mu\text{M}$  hydrazine at scan rates varying from 10 to 100 mV/s. When the scan rates were varied from 10 to 100 mV/s, the peak current corresponding to the hydrazine electrochemical oxidation also got increased. A linear relation between the peak anodic current and square root of scan rate gives a linear fit narrating a diffusion-controlled process (Fig. 4 B). The corresponding linear equation is  $I_{pa} (\mu\text{A}) = 1.485 + 0.4786 * v^{1/2} (\text{mV/s})^{1/2}$  with  $R^2 = 0.9814$ .

### 3.7 DPV Response of Hydrazine at the Poly DMAA Film

Figure 5 A depicts the DPV response of poly DMAA/pencil graphite in 0.05 M KCl containing different concentrations of hydrazine from 20  $\mu\text{M}$  to 4 mM. New peak that formed at +0.252 V ascribed to hydrazine electrooxidation at the electropolymerized film was noted to be increasing as the quantity of hydrazine got increased. The possible mechanism of electrooxidation of hydrazine is [14–16]:





**Fig. 5** **a** DPV of poly DMAA/pencil graphite in 0.05 M KCl containing different concentrations of hydrazine in the range of 20  $\mu\text{M}$  to 4 mM, **b** calibration plot

Linear plot was generated with peak anodic current to the concentration of hydrazine, and a linear dynamic range was obtained from 20  $\mu\text{M}$  to 4 mM (Fig. 5 B). The equation describing linearity was obtained as  $I_{pa} (\mu\text{A}) = 0.8134 + 0.0052 * C (\mu\text{M})$  with regression coefficient  $R^2$  as 0.9929.

### 3.8 Effect of Interferants

To effectively utilize the developed sensor as a tool for hydrazine determination in water samples, it is necessary to ensure that it is free from interferences caused by other ions present in water bodies. For that, selectivity study was performed using DPV. The electrochemical response of hydrazine (100  $\mu\text{M}$ ) was drawn out along with 0.1 mM NaCl, 0.1 mM  $\text{Ca}^{2+}$ , 0.1 mM  $\text{SO}_4^{2-}$ , and 0.1 mM  $\text{NO}_2^-$ . DPV response for the effect of interferants is shown in Fig. 6. It was shown that only hydrazine exhibited faradic peaks, whereas other ions failed to exhibit faradic peaks. This proves that the fabricated sensor is applicable for hydrazine electroanalysis to use without any interference from commonly existing ions in water.

### 3.9 Practical Utility of the Sensor

Practical usage of the developed sensor was demonstrated in tap water and pond water samples. Standard addition method was employed by spiking hydrazine concentrations into the real sample matrix. DPV data was collected and is given in Table 3. Recovery percentages obtained were of acceptable range.

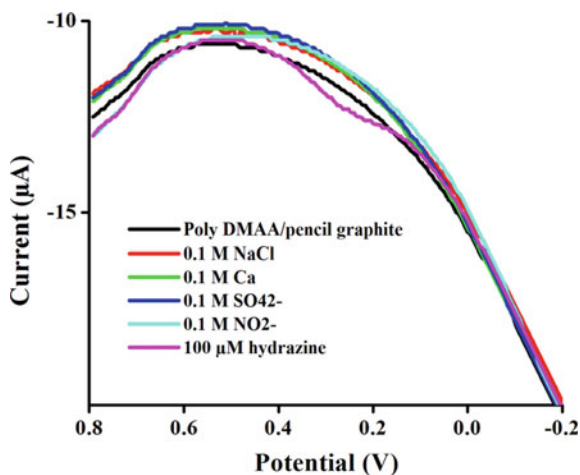


**Fig. 6** Selectivity study of the developed hydrazine sensor

**Table 3** Practical utility of the developed sensor toward the electrochemical sensing of hydrazine

Samples	Added ( $\mu\text{M}$ )	Found ( $\mu\text{M}$ )	Recovery (%)
Tap water	100	112.8	112.8
	200	214.5	107.25
Pond water	20	18.9	94.5
	400	418.26	104.56

### 3.10 Comparison Table

The as-fabricated sensor was compared with the recent literature reports of electrochemical hydrazine sensors. Our sensor was found to exhibit the highest linear range compared to other sensors. Also, the overpotential for hydrazine electrooxidation is the lowest for our sensor. This shows the excellent electrocatalytic ability of the poly DMAA modified pencil graphite electrode toward the electrooxidation of hydrazine. Table 4 shows the comparison data.

## 4 Conclusion

In short, the authors have employed a poly DMAA modified electrode for the electrochemical sensing of environmental pollutant and carcinogen hydrazine in KCl medium. The employed electrochemical polymerization using trans-2,3-dimethylacrylic acid was reported for the first time to the best of our knowledge.

**Table 4** Comparison of the as-fabricated hydrazine sensor with other electrochemical hydrazine sensors

S. No.	Electrode	Method	Medium	Potential (V)	Linear range ( $\mu\text{M}$ )	References
1	CSA-PTHA	Amperometry	PBS 7.4	0.5	10–90	[17]
2	PPy/CDs/PB/SAuNPE	Amperometry	KCl	0.3	0.5–80	[18]
3	AgNP@PANI-rGO/GCE	Amperometry	PB 8	0.51	0.4–2.2	[19]
4	ZnO NPs/PEDOT:PSS	Chronoamperometry	PBS 7.4	0.5	10–500	[20]
5	SPCE/p(TA)	CV	Tris buffer 8.5	0.3	0.1–100	[21]
<b>6</b>	<b>Poly DMAA/pencil graphite</b>	<b>DPV</b>	<b>KCl</b>	<b>0.25</b>	<b>20–4000</b>	<b>This work</b>

The developed electrode showed enhanced electrocatalytic ability toward the electrooxidation of hydrazine compared to bare pencil graphite. Also, it possesses higher anodic current response at the modified electrode surface. The voltammetric current response was increased linearly when the concentration of hydrazine was increased from 20  $\mu\text{M}$  to 4 mM with a regression coefficient 0.9929. The sensor is able to detect hydrazine in the presence of other interfering ions like  $\text{Ca}^{2+}$ ,  $\text{SO}_4^{2-}$ , etc. Practicality demonstration of the sensor was demonstrated in tap water and pond water sample matrix.

## References

1. Sudha V, Kumar SMS, Thangamuthu R (2020) NiCo<sub>2</sub>O<sub>4</sub> nanorod: synthesis and electrochemical sensing of carcinogenic hydrazine. *Inorg Chem Commun* 107927
2. Pei Y, Hu M, Xia Y, Huang W, Li Z, Chen S (2020) Electrochemical preparation of Pt nanoparticles modified nanoporous gold electrode with highly rough surface for efficient determination of hydrazine. *Sens Actuators B Chem* 304:127416
3. Lyon F (1994) IARC monographs on the evaluation of carcinogenic risks to humans. *Some Ind Chem* 60:389–433
4. Taei M, Salavati H, Banitaba SH, Shahidi L (2017) A novel hydrazine electrochemical sensor based on gold nanoparticles decorated redox-active 2-amino-4H-chromene-3-carbonitrile. *IEEE Sens J* 17:7325–7331
5. George GD, Stewart JT (1990) HPLC determination of trace hydrazine levels in phenelzine sulfate drug substance. *Anal Lett* 23:1417–1429
6. Kosyakov D, Amosov A, Ul'yanovskii N, Ladesov A, Khabarov YG, Shpigun O (2017) Spectrophotometric determination of hydrazine, methylhydrazine, and 1, 1-dimethylhydrazine with preliminary derivatization by 5-nitro-2-furaldehyde. *J Anal Chem* 72:171–177
7. Cao S, Zheng S, Pang H (2020) Ultrathin nanosheet-assembled accordion-like Ni-MOF for hydrazine hydrate amperometric sensing. *Microchim Acta* 187:1–9
8. Santhy A, Beena S, Namboothiri UK, Anupriya S, Sreeranjini C (2020) A pencil graphite electrode modified with poly nicotinamide as a framework for the electrochemical detection of

- propranolol hydrochloride. In: IOP conference series: materials science and engineering. IOP Publishing, p 012125
9. Krishnan RG, Greeshma D, Morris DS, Rameshan SS, Beena S (2019) Morphological studies of disposable graphite and its effective utilization for vitamin B12 analysis in pharmaceutical formulations. *Mater Today Proc* 18:3314–3320
  10. Krishnan RG, Rejithamol R, Saraswathyamma B (2020) Non-enzymatic electrochemical sensor for the simultaneous determination of adenosine, adenine and uric acid in whole blood and urine. *Microchem J* 104745
  11. Krishnan RG, Saraswathyamma B, Raj TA, Gopika M (2020) Poly (riboflavin) modified pencil graphite for the simultaneous electrochemical determination of serotonin and dopamine. In: AIP conference proceedings. AIP Publishing LLC, p 020007
  12. Golabi S, Zare H, Hamzehloo M (2001) Electrocatalytic oxidation of hydrazine at a pyrocatechol violet (PCV) chemically modified electrode. *Microchem J* 69:13–23
  13. Krishnan RG, Saraswathyamma B (2020) Disposable electrochemical sensor for coumarin induced milk toxicity in raw milk samples. *Measurement* 108709
  14. Habibi E (2019) Mesoporous Pd $\beta$ -SiCNW-nC based home made screen printed electrode for high sensitive detection of hydrazine. *Microchem J* 149:104004
  15. Tan C, Xu X, Wang F, Li Z, Liu J, Ji J (2013) Carbon black supported ultra-high loading silver nanoparticle catalyst for electro-oxidation and determination of hydrazine. *Science China Chem* 56:911–916
  16. Babu KJ, Zahoor A, Nahm KS, Aziz MA, Vengadesh P, Kumar GG (2016) Manganese dioxide–vulcan carbon@ silver nanocomposites for the application of highly sensitive and selective hydrazine sensors. *New J Chem* 40:7711–7720
  17. Vijeth H, Ashokkumar S, Yesappa L, Vandana M, Devendrappa H (2020) Camphor sulfonic acid surfactant assisted polythiophene nanocomposite for efficient electrochemical hydrazine sensor. *Mater Res Express* 6:125375
  18. Chen W, Wang H, Tang H, Yang C, Guan X, Li Y (2019) Amperometric sensing of hydrazine by using single gold nanopore electrodes filled with Prussian blue and coated with polypyrrole and carbon dots. *Microchim Acta* 186:350
  19. Kaladevi G, Wilson P, Pandian K (2020) Silver nanoparticle–decorated PANI/reduced graphene oxide for sensing of hydrazine in water and inhibition studies on microorganism, *Ionics* 1–11
  20. Beduk T, Bihar E, Surya SG, Castillo AN, Inal S, Salama KN (2020) A paper-based inkjet-printed PEDOT: PSS/ZnO sol-gel hydrazine sensor. *Sens Actuators B Chem* 306:127539
  21. Haque AMJ, Kumar S, Del Río JS, Cho YK (2020) Highly sensitive detection of hydrazine by a disposable, poly (tannic acid)-coated carbon electrode. *Biosens Bioelectron* 150:111927

# Effect of Temperature on the Sliding Wear Behavior of HVOF Sprayed Al<sub>2</sub>O<sub>3</sub> Composite Coating



Ankit Tyagi, S. M. Pandey, R. S. Walia, Qasim Murtaza, and Ajay Kumar

**Abstract** In present study, Al<sub>2</sub>O<sub>3</sub>-based composite coating has been deposited on mild steel substrate using HVOF thermal spray process in controlled process parameters. For analyzing the surface, FESEM of the developed coating was done. Its hardness, residual stresses, and tribological properties are studied at room temperature and at elevated temperature of 50, 100, and 150 °C. It is observed that with increased temperature its hardness, residual stresses, and tribological performance was enhanced, i.e., at 150 °C, wear and coefficient of friction decreased to a value of 120 μm and 0.35, whereas its hardness was 520 HV and residual stresses was -10 MPa, increased at evaluated temperature. This showed the temperature dependency of the coating, with increased temperature the coating showed better results.

**Keywords** Al<sub>2</sub>O<sub>3</sub> composite coating · FESEM · Hardness · Wear · COF

## 1 Introduction

In a world where metals and metal alloys are almost used everywhere, from the automotive industry, for military applications, to the aerospace industry, it is arduous to find a single material that is ideal for use in all conditions [1–4]. Wear has always

---

A. Tyagi (✉) · A. Kumar

Department of Mechanical Engineering, Faculty of Engineering & Technology, Shree Guru Gobind Singh Tricentenary University, Gurgaon, Haryana, India

S. M. Pandey

Department of Mechanical Engineering, NIT Patna, Patna, India

Q. Murtaza

Department of Mechanical Engineering, Delhi Technological University, New Delhi, Delhi 110042, India

R. S. Walia

Department of Production and Industrial Engineering, Punjab Engineering College, Chandigarh, India

© The Author(s), under exclusive license to Springer Nature Singapore Pte Ltd. 2021

23

C. Pandey et al. (eds.), *Advances in Materials and Mechanical Engineering*,

Lecture Notes in Mechanical Engineering,

[https://doi.org/10.1007/978-981-16-0673-1\\_3](https://doi.org/10.1007/978-981-16-0673-1_3)



been a major concern for design engineers. Wear is defined as “damage to a solid surface (generally involving progressive loss of material), caused by the relative motion between two substances.” Among the various components of an engine, the friction present at piston ring and cylinder liners accounts for 50% total loss [5] and also affects engine efficiency [6]. Nowadays, anti-wear coatings [7] have been used to reduced friction and wear for machine components. Reduction of COF helps in enlightening energy proficiency by decreasing depletion of energy due to frictional losses. Suitable range of materials and application of lubricants are some of the approaches of opposing losses due to friction. Surface alteration establishes new method, where a wear resistant layer on material is deposited to avoid losses due to friction [8]. As such, the tribological characteristics of materials with respect to hardness, resistance to erosion, and abrasion are considered for the selection for industrial applications, so that individual parts can have a longer life span [10]. However, the production of parts made entirely out of the materials with aforementioned properties is generally not always practical or economically feasible. This is where metal surface coatings come into play [11]. Surface metal coatings are an economical alternative to an entire solid body of metal of the coating material in cases where only surface interaction between two dissimilar materials is considered.

In the present study, development and characterization of  $\text{Al}_2\text{O}_3$ -based composite coating were studied. Aim of present work is to evaluate hardness, residual stress, COF, and wear of developed composite coating.

## 2 Experimental Procedure

The mild steel substrate of the size of  $50 \times 50 \times 5$  mm was ground using 100–2500 grit emery paper to get the smooth surface, and chemical composition of mild steel substrate is given in Table 1. After polishing, plates were grit blast at 0.6 MPa air pressure with  $\text{Al}_2\text{O}_3$ , to increase the adhesion strength. The high-quality  $\text{Al}_2\text{O}_3$ -based composite coating was developed using HVOF coating techniques. Initially, high velocity jet was used to sprayed  $\text{Al}_2\text{O}_3$ -based composite powder, in order to developed composite coating. The parameters of HVOF used to deposit the composite coating have been given in Table 2 while process parameters for experimentation have been shown in Table 3.

**Table 1** Chemical composition of mild steel substrate

Element	C	Mn	Si	S	P	Cr	Ni	Mo	Cu
% Composition	0.16	1.07	0.24	0.01	0.01	0.10	0.02	0.02	0.17

**Table 2** Parameters of HVOF used to deposit the composite coating

Sr. No.	Parameters used	Values
1	Deposition technique	HVOF process
2	Powder driving temperature (°C)	120
3	Hydrogen flow rate (mm <sup>3</sup> /min.)	13
4	Argon flow rate (mm <sup>3</sup> /min.)	112
5	Mixing powder time (min.)	90

**Table 3** Process parameters for experimentation of composite coating

Sr. No.	Process parameter	A <sub>1</sub>	A <sub>2</sub>	A <sub>3</sub>	A <sub>4</sub>
1	Load (N)	50	50	50	50
2	Sliding velocity (m/s)	1	1	1	1
3	Temperature (°C)	30	50	100	150

### 3 Results and Discussion

Figure 1a, b having magnification  $\times 2000$  and scale of 10 and 500  $\mu\text{m}$ , respectively, shows coating thickness while Fig. 1c having magnifications  $\times 4000$  and scale 1  $\mu\text{m}$  shows the surface characterization of  $\text{Al}_2\text{O}_3$ -based composite coating. It is quite clear from surface morphology that composite powder is properly mixed and formed a curved laminar structure. Carbide and oxides are formed might be during polishing process which finally may result in increasing the hardness value of the coating [9–11]. Figure 1d shows the EDS results of composite coating. SEM/EDS (Fig. 1d) for EDS) image over here to show the presence of oxygen which clearly depicts the formation of oxides in coating. Figure 1c of SEM images clearly shows that splash splat and melting bond droplet surface are illustrating that confirm homogeneous coating.

Figure 2 shows the experimental test result of residual stresses for  $\text{Al}_2\text{O}_3$ -based composite coating. The stresses values are  $-100$ ,  $-70$ ,  $-40$ , and  $-10$  MPa at 30, 50, 100, and 150 °C, respectively. The residual stress value is maximum at 30 °C ( $-100$  MPa), while minimum at 150 °C. While Fig. 3 shows the variation of hardness versus composite coating. The figure shows that the hardness is maximum at 150 °C, i.e., 520 HV and minimum at 30 °C, i.e., 350 HV. The increase in residual stresses may be occurred due to plastic deformation of coated sample under high temperature [9–11].

Figure 4 shows variation of COF while Fig. 5 shows the deviation of wear of  $\text{Al}_2\text{O}_3$  coating. The COF values are 0.7, 0.5, 0.45, and 0.35. The COF is maximum at 30 °C while minimum at 150 °C. The wear values are varied from 300 to 120  $\mu\text{m}$ . The wear is minimum at 150 °C while maximum at 30 °C. The increase in specific wear rate may be due to tribofilm formation on Mo blend composite coating [9–11].

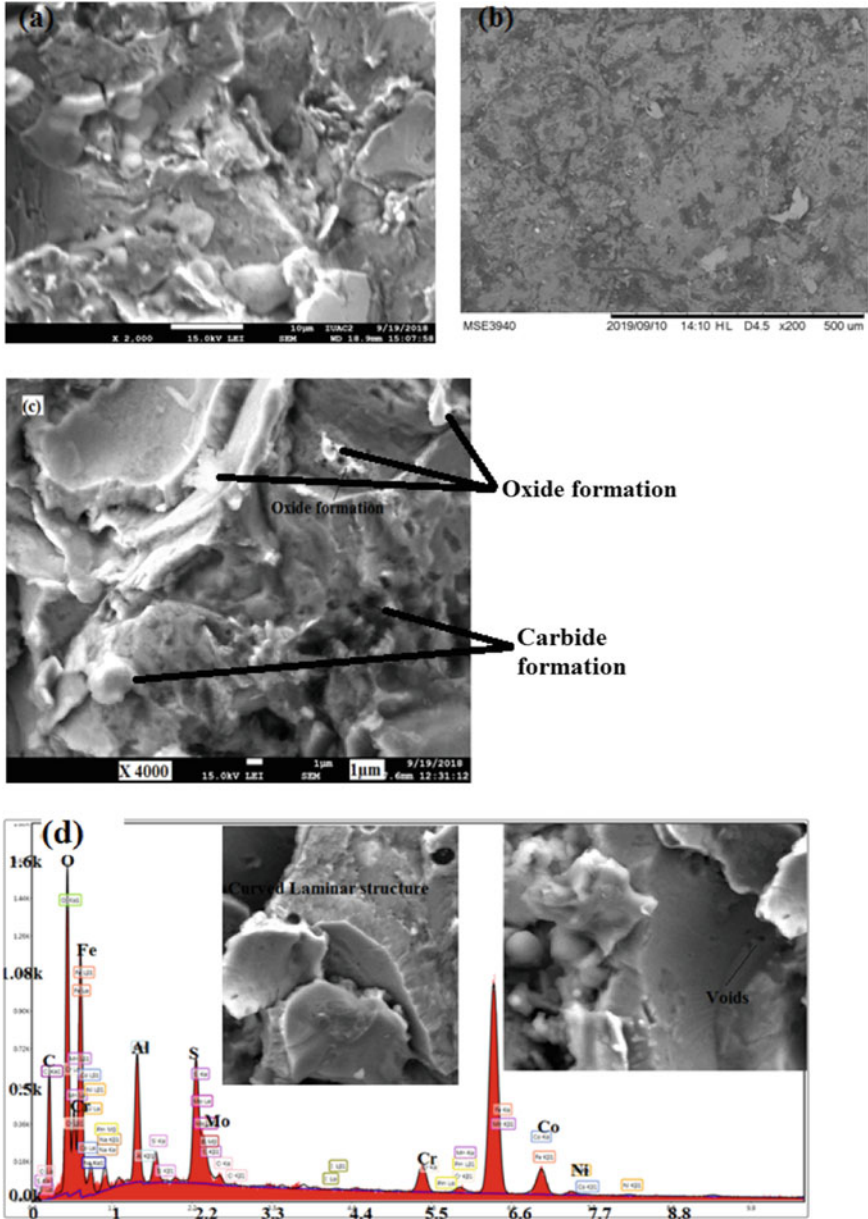


Fig. 1 a–c FESEM images, d EDS results of Al<sub>2</sub>O<sub>3</sub> composite coating

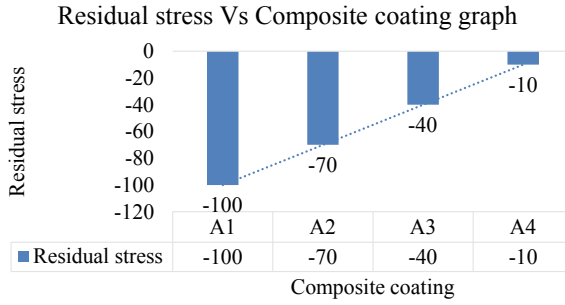


Fig. 2 Experimental results of residual stress versus Al<sub>2</sub>O<sub>3</sub> composite coating

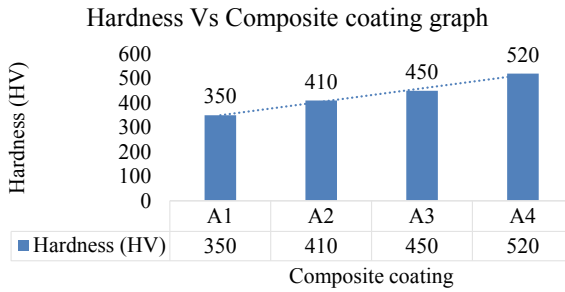


Fig. 3 Experimental results of hardness versus Al<sub>2</sub>O<sub>3</sub> composite coating

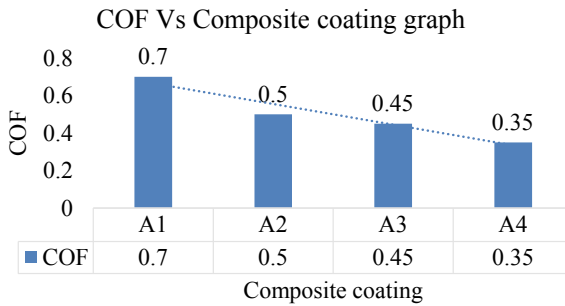
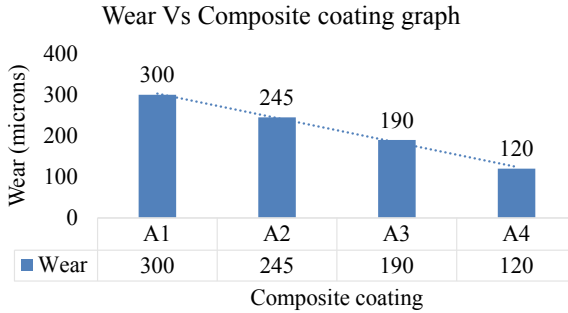


Fig. 4 Experimental results of COF versus Al<sub>2</sub>O<sub>3</sub> composite coating

### 4 Conclusions

The Al<sub>2</sub>O<sub>3</sub>-based composite coating was effectively developed with good surface morphology and enriched tribological properties using HVOF coating procedure for wear resistance applications. The hardness and residual stress values of composite coating are maximum at 150 °C. The experimental result of Al<sub>2</sub>O<sub>3</sub> coating shows



**Fig. 5** Experimental results of wear versus  $\text{Al}_2\text{O}_3$  composite coating

that as the temperature varies from  $30^\circ$  to  $150^\circ$ , COF decreases from 0.7 to 0.35, while wear was decreased from 300 to 120  $\mu\text{m}$ , respectively. The decrease in wear and decrease in COF may be due to the tribofilm formation on composite coating.

## References

1. Wang F, Zheng L, Li Q, Zhang F, Chen X, Zhang H (2018) Corrosion properties of carbon ions implanted chromium coating prepared on CSS-42L aerospace bearing steel. *Surf Coat Technol* 349:392–399
2. Tyagi A, Pandey S, Murtaza Q, Walia RS, Tyagi M (2019) Tribological behavior of carbon coating for piston ring applications using Taguchi approach. *Mater Today Proc*
3. Tyagi A, Pandey SM, Gupta K, Walia RS, Murtaza Q, Krishen K (2019) Tribological behavior of sustainable carbon based composite coating for wear resistance applications. *Mater Res Express* 6(12):125601
4. Tyagi A, Pandey SM, Walia RS, Murtaza Q (2019) Characterization and parametric optimization of tribological properties of Mo blend composite coating. *Mater Res Express* 6(8):086428
5. Shahmohamadi H, Mohammadpour M, Rahmani R, Rahnejat H, Garner CP, Howell-Smith S (2015) On the boundary conditions in multi-phase flow through the piston ring-cylinder liner conjunction. *Tribol Int* 90:164–174
6. Tung SC, Huang Y (2004) Modeling of abrasive wear in a piston ring and engine cylinder bore system. *Tribol Trans* 47:17–22
7. Bandyopadhyay PP, Siegmans S (2005) Friction and wear behavior of vacuum plasma-sprayed Ti e Zr e Ni quasicrystal coatings. *Surf Coat Technol* 197:1–9
8. Das S, Bandyopadhyay TK, Ghosh S, Chattopadhyay AB, Bandyopadhyay PP (2003) Processing and characterization of plasma-sprayed ceramic coatings on steel substrate: part I. On coating characteristics. *Metall Mater Trans A*, 34:1909–1918
9. Tyagi A, Murtaza Q, Walia RS, Pandey SM (2019) Characterization and parametric optimization of tribological properties of Mo blend composite coating. *Mater Res Express* (accepted, 2019)
10. Tyagi A, Walia RS, Murtaza Q (2019) Tribological behavior of temperature dependent environment friendly thermal CVD diamond coating. *Diam Relat Mater* 96:148–159
11. Tyagi A, Murtaza Q, Walia RS, Pandey SM, Tyagi P, Bajaj B (2019) A critical review of diamond like carbon coating for wear resistance applications. *Int J Refract Metal Hard Mater* 78:107–122

# Engine Friction Reduction Using Cu Nanofluid as Lubricant



Amar Kumar Jain , Manoj Kumar , and Gananath D. Thakre 

**Abstract** The experimental study on the use of Cu nanofluid as engine lubricant in reducing the friction between piston ring and liner contact has been undertaken. The Cu nanoparticles of CuS and CuO were synthesized and blended in commercial engine oil in varying concentrations for preparation of Cu nanofluid. The experiments were performed on reciprocating tribo-tester to simulate the piston ring and liner contact. The actual ring–liner specimens were used to perform the experiments. The contact was lubricated with commercial engine oil and blends of CuS and CuO in commercial engine oil. The contact friction was continuously recorded. Furthermore, the influence of nanoparticle concentration and applied load along with reciprocating frequency on the coefficient of friction was studied. It has been observed that the blending of Cu nanoparticles reduces engine friction. The optimum dose of the nanoparticles was observed to be 4% by weight. Of the two nanoparticles studied, the CuS nanoparticles resulted in significant reduction in coefficient of friction to the order of 33% as compared to the base lubricant. The findings of the study will be useful for lubricant chemists to develop new lubricants by blending the Cu nanoparticles.

**Keywords** Engine friction · Piston ring and liner · Cu nanoparticles · Reciprocating tribo-tester · Tribology

## 1 Introduction

The automotive sector is one of the major sectors around the globe that helps in transfer of persons and commodities. Hence, it can be considered that the automobiles drive the world economy. Considering the average number of automobiles

---

A. K. Jain · G. D. Thakre (✉)  
CSIR-Indian Institute of Petroleum, Dehradun 248005, India  
e-mail: [gdthakre@iip.res.in](mailto:gdthakre@iip.res.in)

M. Kumar  
DIT University, Dehradun 248009, India

© The Author(s), under exclusive license to Springer Nature Singapore Pte Ltd. 2021  
C. Pandey et al. (eds.), *Advances in Materials and Mechanical Engineering*,  
Lecture Notes in Mechanical Engineering,  
[https://doi.org/10.1007/978-981-16-0673-1\\_4](https://doi.org/10.1007/978-981-16-0673-1_4)

running on the roads, they are considered as one of the most energy-consuming commodity. Of the total energy generated by the combustion of fuel, a major chunk of it is lost in overcoming friction between various tribo-contacts of the automobile. The study undertaken by Holmberg et al. [1, 2] on the passenger cars, trucks and buses reveals that over 33% of energy generated by fuel combustion is consumed in overcoming friction in engine, gear box, tires, and brakes. Among these tribo-contacts, the engine has a lion's share of energy consumption and loss [3]. As the tribo-contacts are lubricated with either mineral or synthetic lubricating oils blended with high performance additives, they form thin films of sufficient thickness that tries to minimize the actual metal-to-metal contact thereby reducing the contact friction. The oils used for engine lubrication are characterized by physico-chemical characteristics on the basis of their chemistry and often the physico-chemical, rheological, and the tribo-performance of these lubricants can be correlated [4]. With the use and even high temperatures prevailing in the engines, degrade the performance of the lubricants, thereby increasing the contact friction [5]. In order to enhance the performance behavior of engine oils, they are often blended with additives such as ZDDP. The additives provide strong boundary films capable of protecting the surfaces from wear damage. However, with the presence of ZDDP, increased frictional losses are observed. These frictional losses are due to the friction encountered in the inter-layer shearing of the lubricating films. The higher values of pressure coefficient of boundary shear strength provide a suitable justification of higher contact friction [6]. Recently, use of nanoparticles as lubricant additives has gained significant interest. The nanoparticles due to their inherent physical characteristics impart desired performance characteristics to the lubricants [7]. The role of nanoparticles in reducing friction and wear has been reviewed by Sundeep et al. [8] and Shahnazar et al. [9]. The nanoparticles owing to their nano dimensions possess high surface energies and therefore are prone to agglomeration and settling down. The concentration of nanoparticles and their settling rate predicts the physico-chemical properties of the lubricants. Selvakumar and Wu [10] presented a theoretical model to predict the density of nanofluids. The developed model takes into account the aggregation of nanoparticles, interfacial layer formation, particle size distribution, etc.

The early use of nanoparticles as lubricant additives gained significant interest in heat transfer fluids, metal working fluids, and hydraulic fluids. Due to the promising values of thermal conductivities, the nanoparticles of  $\text{Al}_2\text{O}_3$ ,  $\text{CuO}$ ,  $\text{TiO}_2$  were extensively used in formulated oils and ethylene glycol [11]. The study revealed that the heat transfer capability increases with particle concentration. Wang and Xu [12] investigated the influence of  $\text{Al}_2\text{O}_3$  and  $\text{CuO}$  nanoparticles on the thermal conductivities of water and mineral base fluids. The study revealed higher thermal conductivity of nanoparticle-fluid mixture when compared with the base fluid. Because of their superior heat transfer capabilities, the nanoparticles are being used in metal working fluids [13]. The nanoparticles of PTFE, nanotori,  $\text{MoS}_2$ ,  $\text{WS}_2$ ,  $\text{g-C}_3\text{N}_4$ , etc., have been extensively studied by researchers in various mineral and synthetic base fluids [14–20]. The PTFE nanoparticles significantly enhanced the tribological characteristics of base fluids. Similarly, the nanotori nanoparticles enhanced the load carrying capacity by up to 950%. The  $\text{g-C}_3\text{N}_4$  nanoparticles reduced friction by nearly 32%

as compared to base fluid. Due to their improved tribological performance and heat transfer capabilities, use of nanoparticles was explored in engine applications. Ali and Xianjun [21] reviewed the recent developments in the use of nanoparticles in engine oils. The studies revealed that the particle shape and size influence the friction and wear behavior. The size of  $\text{Al}_2\text{O}_3$  nanoparticles in particular influences the wear of the coating applied on the internal surfaces of the engine [22]. However, most of the tribological studies pertaining to the use of nanoparticles in engine oils have been undertaken on pin on disk tribo-tester [23]. The pin-on-disk tribo-tester utilizes a rotary drive and hence is often incapable to simulate the reciprocating contact between the piston ring and liner. Recently, Rasheed et al. [24] investigated the tribological performance of graphene nanoflakes-blended engine oil in an actual engine. The study revealed that by mere blending of 0.01% graphene by weight in commercial engine oil reduces the friction coefficient by 21%. The use of graphene also decreases the ring wear over extended hour engine testing. The use of actual engines to test the efficacy of nanoparticles is a costly affair. Hence, Woydt and Kelling [25] developed a test procedure to investigate the tribological performance of lubricants outside the engines. The method uses actual piston ring segments and cylinder liner specimens. Similarly, Ali et al. [26] investigated the combined effect of  $\text{Al}_2\text{O}_3$  and  $\text{TiO}_2$  nanoparticles on the tribological performance in a reciprocating test rig and reported that 0.05 wt% each of  $\text{Al}_2\text{O}_3$  and  $\text{TiO}_2$  resulted in 40–51% reduction in contact friction.

Thus, literature survey undertaken reveals that use of various nanoparticles is being explored in the commercial engine oils. However, most of these studies are either being performed on a four-ball tribo-tester or pin-on-disk tribo-tester which is incompetent to simulate the actual piston ring–liner contact. Hence, the present communication is about the influence of CuS and CuO nanoparticles on the friction behavior of actual piston ring–liner contact in a reciprocating rig.

## 2 Materials and Methods

The CuS nanoparticles were synthesized by reacting copper acetate with  $\text{Na}_2\text{S}$  in equimolar ratios. The product thus obtained was isolated by centrifugation and dried in an oven. The dried CuS nanoparticles were then functionalized using oleic acid. Similarly, CuO nanoparticles were synthesized by reacting copper acetate with NaOH in equimolar ratios and functionalized using oleic acid. Prior to functionalization, the synthesized nanoparticles were examined using scanning electron microscope (SEM) to ascertain the shape and morphology of the particles. SEM micrographs revealed that the synthesized Cu nanoparticles are spherical in shape. The functionalized nanoparticles were then added to the base lubricant in varying doses. The lubricant blends were prepared by blending functionalized CuS and CuO nanoparticles in 0.1, 0.5, 1, 4, and 6% concentrations by weight. The base lubricant used for the blending purpose was a commercial fully formulated engine oil of SAE 5 W-40 grade. Table 1 shows the physico-chemical characteristics of the base lubricant.



**Table 1** Lubricant properties

Kinematic viscosity, cSt		Density @ 15 °C, kg/l	Pour point, °C	Flash point, °C
@40 °C	@100 °C			
74.4	13.1	0.840	-39	215

In order to obtain a homogeneous blend, the nanoparticles were stirred and sonicated using ultrasonic bath. The homogeneity of the blend was verified by using imaging and UV–Vis spectroscopy techniques. The blends were prepared for different concentrations of Cu nanoparticles and stored undisturbed in glass sample vials. The images of the undisturbed blends were captured on daily basis and settling/separation of nanoparticles were monitored. The images revealed clear lubricant solution with no visible settling/separation. This process was followed for a span of 30 days. A portion of prepared lubricant blends was inspected using UV–Vis technique. The UV light when passed through the sample is absorbed by the Cu nanoparticles. This absorbance causes a characteristic peak in the UV spectrum. The intensity of peak diminishes with decrease in concentration of the nanoparticles in the medium. In case the nanoparticles settle down or get separated, the intensity of peak will decrease with the extent of separation. In the present case, the prepared blends were tested over a span of 30 days, and almost negligible change in the intensity of peak was observed. This study proved that the developed blends were homogeneous.

The experiments to investigate the efficacy of the Cu nanoparticles in reducing the contact friction between ring–liner contact were performed on a tribo-test rig shown in Fig. 1. With the help of reciprocatory drive, the tribo-tester is able to simulate the

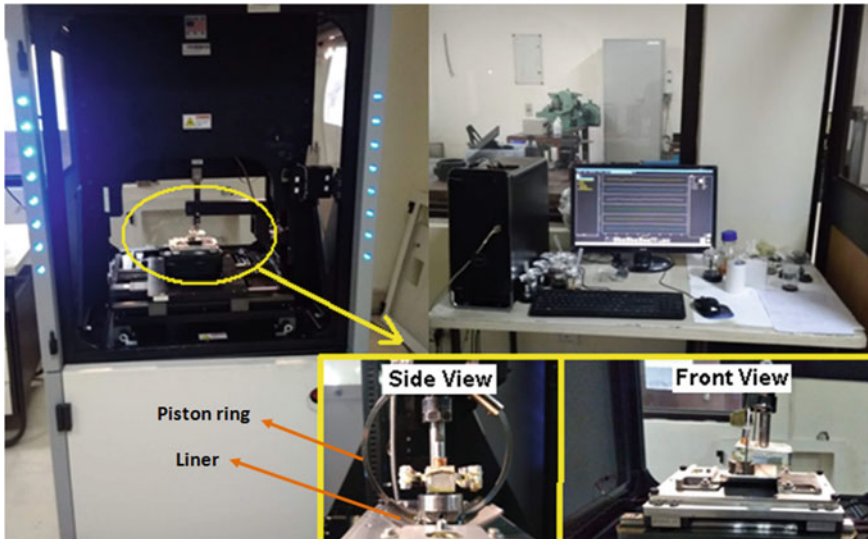


**Fig. 1** Experimental test setup

reciprocating motion between the piston ring and liner. The cut section of the liner was fixed on the stage that moved in a to-and-fro motion of desired stroke length and frequency. The ring was housed in a stationary fixture and loaded with the help of servo motor in the vertical direction. The liner was lubricated using base lubricant and the Cu nanoparticle-blended base lubricant. The experiments were performed over a range of operating conditions. The contact was loaded at 25, 50, and 100 N, while the reciprocating frequency was set to 1, 3, and 5 Hz. The experiments were performed at room temperature and the test duration of individual tests was maintained at 16 min. 40 s in line with the standard test method of ASTM G: 133. The contact friction in the form of coefficient of friction was continuously captured with the help of data acquisition system. The experiments were repeated to check the repeatability of the data. A fresh pair of ring, liner, and lubricant sample was used to perform each of the experiments.

### 3 Results and Discussion

The friction behavior of the base lubricant and nanoparticle-blended lubricant in the piston ring–liner contact is shown in Fig. 2. It is observed that the base lubricant has relatively higher friction as compared to that of the CuO- and CuS-blended lubricant. The base lubricant reported a kinetic friction of 0.1414 while the 1% CuO and 1% CuS blended in base lubricant reported a kinetic friction of 0.1339 and 0.1027, respectively. The percentage reduction in friction was 5.3 and 27.3% for the CuO- and CuS-blended lubricant. Thus, from the figure, it is revealed that blending of Cu nanoparticles helps in reducing the contact friction to a significant extent.

Figure 3 presents the influence of nanoparticle concentrations on the contact friction. It is observed that the contact friction decreased continuously with increase in nanoparticle concentration. The CuS nanoparticle-blended lubricant resulted in

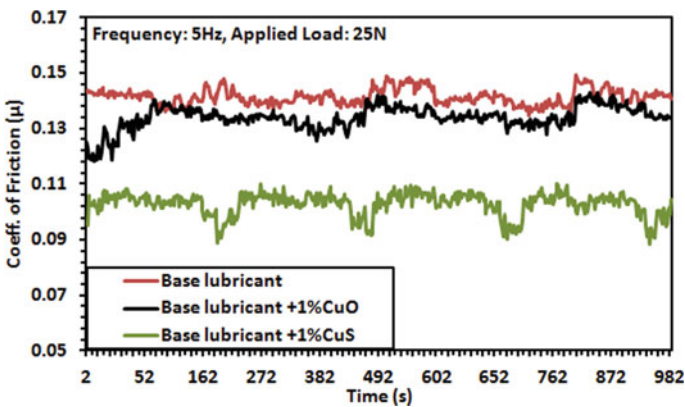
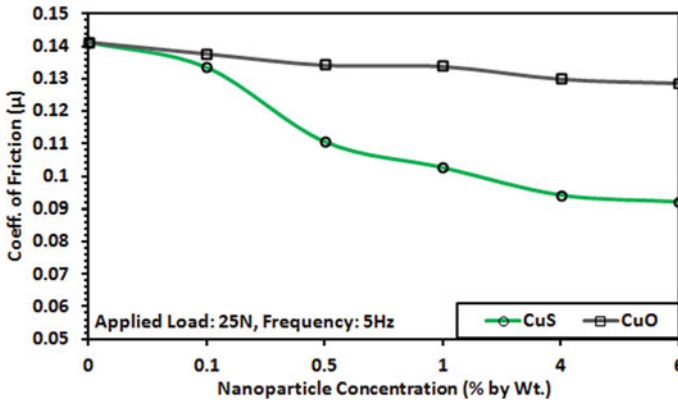


Fig. 2 Friction behavior of the lubricants



**Fig. 3** Effect of nanoparticle concentration on friction reduction

lower friction values as compared to the CuO nanoparticle-blended lubricant. The friction coefficient reduced from 0.1414 (base lubricant) to 0.0921 and 0.1287 in case of 6% (by wt.) CuS- and CuO-blended base lubricant. The percentage change in friction coefficient for 6% CuS and CuO is of the order of 34.87% and 8.98%, respectively.

The friction coefficient (kinetic) along with the percentage decrease in friction values with respect to base lubricant for different concentrations of the nanoparticles is given in Table 2. A steep decrease in friction till 4% concentration of nanoparticles has been observed. However, beyond 4%, the percentage decrease in friction is not that significant. The trend observed is same for both the CuS and CuO nanoparticle blends. Hence, it may be concluded that 4% by weight is the optimum concentration of nanoparticles for significant reduction in contact friction.

The influence of operating parameters viz. load and the reciprocating frequency on the friction within the contact lubricated with Cu nanofluids was investigated by varying the applied load and the reciprocating frequency. Figure 4 shows the coefficient of friction observed within the contact lubricated with CuS- and CuO-blended

**Table 2** Percentage decrease in friction

Lubricant sample	Coeff. of kinetic friction	% decrease in Friction	Lubricant sample	Coeff. of kinetic friction	% Decrease in friction
Base lubricant	0.1414	–	–	–	–
0.1% CuS	0.1336	5.5	0.1% CuO	0.1378	2.56
0.5% CuS	0.1107	21.71	0.5% CuO	0.1343	5.02
1% CuS	0.1027	27.37	1% CuO	0.1339	5.3
4% CuS	0.0942	33.38	4% CuO	0.1300	8.06
6% CuS	0.0921	34.87	6% CuO	0.1287	8.98

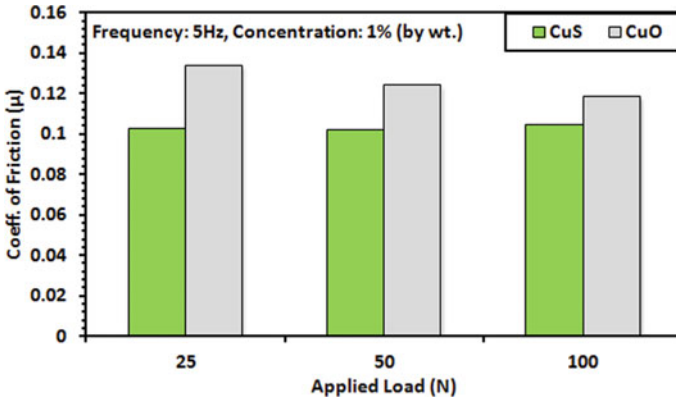


Fig. 4 Effect of load on the contact friction

lubricants for different loads. The coefficient of friction decreases with increase in load in case of CuO nanoparticle blends. The coefficient of friction observed at 25 N load is 0.1339 which reduces to 0.1185 at 100 N load. This accounts to 11.5% decrease in friction in case of CuO nanoparticle-blended lubricant. However, in case of CuS-blended lubricant, the friction coefficient observed is constant over the entire load range tested. The friction coefficient observed is 0.102. This may be due to the presence of sulfur in the CuS because of which enhanced lubricant film thickness and strong boundary film must have been formed. Due to this, no significant change in contact friction is observed in case of CuS with increase in load.

The effect of reciprocating frequency on the friction within the contact lubricated with CuS- and CuO-blended lubricants is shown in Fig. 5. It is observed that in case of CuS-blended lubricant, the contact friction remains almost constant at 0.101 irrespective of the reciprocating frequency. However, in the case of CuO-blended

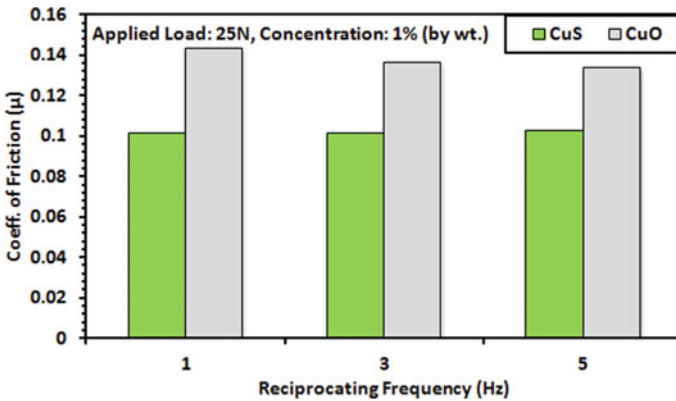


Fig. 5 Effect of reciprocating frequency on contact friction

lubricant, the coefficient of friction was 0.143 at 1 Hz and 0.134 at 5 Hz reciprocating frequency, respectively.

As the Cu nanoparticles are spherical in shape, they act as micro bearings in the contact vicinity because of which reduction in friction is observed. The blending of Cu nanoparticles in engine oils therefore helps in reducing the contact friction. Furthermore, due to the presence of S in CuS, improved tribological performance in terms of reduced friction is observed. The S molecules not only enhance the lubricity but also improve the strength of boundary film formed on the contacting surfaces.

## 4 Conclusions

An experimental study pertaining to the use of Cu nanoparticles in engine oils to reduce contact friction between the piston ring and liner was performed. The experiments were performed on a reciprocating rig utilizing actual piston ring and liner specimens. The Cu nanoparticles, namely CuS and CuO were synthesized and blended in commercial engine oils to prepare Cu nanofluid and the experiments performed. On the basis of the study undertaken following salient conclusions have been made:

- The friction coefficient within the contact reduces with the blending of Cu nanoparticles in the base lubricant.
- The friction coefficient decreases with increase in the concentration of the Cu nanoparticles.
- The optimum concentration of the Cu nanoparticles is 4% by weight that results into significant reduction in contact friction.
- At the optimum dose, the CuS nanoparticles result in 33% reduction, while CuO nanoparticles result in 8% reduction in the contact friction.
- With the use of CuO nanoparticles, the contact friction reduces with increase in load and reciprocating frequency. While the CuS nanoparticles report constant and lowest values of coefficient of friction irrespective of the applied load and reciprocating frequency.
- Of the two selected Cu nanoparticles, CuS nanoparticles result in significant reduction in the contact friction.

**Acknowledgements** The authors thank Director, CSIR-Indian Institute of Petroleum, Dehradun, India, for the financial support to carry out the experimental work and also to publish the findings.

## References

1. Holmberg, Kenneth, Peter Andersson, and Ali Erdemir.: Global energy consumption due to friction in passenger cars. *Tribology International*, 47, 221–234 (2012).
2. Holmberg K, Andersson P, Nylund N-O, Mäkelä K, Erdemir A (2014) Global energy consumption due to friction in trucks and buses. *Tribol Int* 78:94–114
3. Priest, M., and Christopher Mark Taylor: *Automobile engine tribology - approaching the surface*. *Wear* 241(2), 193–203 (2000).
4. Thapliyal, Prashant, and G. D. Thakre: Correlation study of physicochemical, rheological, and tribological parameters of engine oils. *Advances in Tribology* (2017).
5. Heredia-Cancino, J. A., Maziar Ramezani, and M. E. Álvarez-Ramos: Effect of degradation on tribological performance of engine lubricants at elevated temperatures. *Tribology International*, 124, 230–237 (2018).
6. Umer J, Morris N, Leighton M, Rahmani R, Balakrishnan S, Rahnejat H (2019) Nano and microscale contact characteristics of tribofilms derived from fully formulated engine oil. *Tribol Int* 131:620–630
7. Guo D, Xie G, Luo J (2013) Mechanical properties of nanoparticles: basics and applications. *J Phys D Appl Phys* 47(1):013001
8. Sundeep, D., S. Daniel Ephraim, and N. V. V. S. Satish: Use of nanotechnology in reduction of friction and wear. *IJIRAE* 1, 2349–2163 (2014).
9. Shahnazar S, Bagheri S, Hamid SBA (2016) Enhancing lubricant properties by nanoparticle additives. *Int J Hydrogen Energy* 41(4):3153–3170
10. Selvakumar R (2019) Deepak, and Jian Wu: A comprehensive model for effective density of nanofluids based on particle clustering and interfacial layer formation. *J Mol Liq* 292:111415
11. Jain, Ayush, Imbesat Hassan Rizvi, Subrata Kumar Ghosh, and P. S. Mukherjee: Analysis of nanofluids as a means of thermal conductivity enhancement in heavy machineries. *Industrial Lubrication and Tribology* (2014).
12. Wang X (1999) Xianfan Xu, and Stephen US Choi: Thermal conductivity of nanoparticle-fluid mixture. *J Thermophys Heat Transfer* 13(4):474–480
13. Singh RK (2017) Amit Rai Dixit, Amitava Mandal, and Anuj Kumar Sharma: Emerging application of nanoparticle-enriched cutting fluid in metal removal processes: a review. *J Braz Soc Mech Sci Eng* 39(11):4677–4717
14. Saini, Vinay, Jayashree Bijwe, Sarita Seth, and S. S. V. Ramakumar: Role of base oils in developing extreme pressure lubricants by exploring nano-PTFE particles. *Tribology International*, 143, 106071 (2020).
15. Sharma V, Timmons R, Erdemir A, Aswath PB (2017) Plasma-functionalized polytetrafluoroethylene nanoparticles for improved wear in lubricated contact. *ACS Appl Mater Interfaces* 9(30):25631–25641
16. Rico, E. Fernandez, I. Minondo, and D. Garcia Cuervo: The effectiveness of PTFE nanoparticle powder as an EP additive to mineral base oils. *Wear* 262, 1399–1406 (2007).
17. Peña-Parás L, Maldonado-Cortés D, Kharissova OV (2019) Karla Itzel Saldivar, Luisana Contreras, Patsy Arquieta, and Brenda Castaños: Novel carbon nanotori additives for lubricants with superior anti-wear and extreme pressure properties. *Tribol Int* 131:488–495
18. Saidi, M. Z., H. Akram, O. Achak, A. El Mouakibi, N. Canilho, C. Delgado-Sánchez, A. Celzard, V. Fierro, A. Pasc, and T. Chafik: Effect of morphology and hydrophobization of MoS<sub>2</sub> microparticles on the stability of poly- $\alpha$ -olefins lubricants. *Colloids and Surfaces A: Physicochemical and Engineering Aspects*, 572, 174–181 (2019)
19. An, Vladimir, Yuri Irtegov, and Charles De Izarra: Study of tribological properties of nanolamellar WS<sub>2</sub> and MoS<sub>2</sub> as additives to lubricants. *Journal of Nanomaterials*, (2014).
20. Kumar A, Thakre GD, Arya PK, Jain AK (2017) 2D Structured Nano-Sheets of Octadecylamine Grafted Graphitic-Carbon Nitride (g-C<sub>3</sub>N<sub>4</sub>) as Lubricant Additives. *Macromol Symp* 376(1):1700009

21. Ali, Mohamed Kamal Ahmed, and Hou Xianjun (2015) Improving the tribological behavior of internal combustion engines via the addition of nanoparticles to engine oils. *Nanotechnol Rev* 4(4):347–358
22. Singh, Shailesh Kumar, Somnath Chattopadhyaya, A. Pramanik, Sanjeev Kumar, and Navendu Gupta: Influence of Nano-particle on the Wear behaviour of Thin Film Coatings a Review. *International Journal of Applied Engineering Research*, 13(6), 4053–4058 (2018).
23. Mohan, Nishant, Mayank Sharma, Ramesh Singh, and Naveen Kumar: Tribological properties of automotive lubricant SAE 20W-40 containing nano-Al<sub>2</sub>O<sub>3</sub> particles. No. 2014-01-2781. SAE Technical Paper, (2014).
24. Rasheed AK, Khalid M, Javeed A, Rashmi W, Gupta TCSM, Chan A (2016) Heat transfer and tribological performance of graphene nanolubricant in an internal combustion engine. *Tribol Int* 103:504–515
25. Woydt, Mathias, and Norbert Kelling. Testing the tribological properties of lubricants and materials for the system “piston ring/cylinder liner” outside of engines. *Industrial Lubrication and Tribology* (2003).
26. Ali MK, Ahmed HX, Mai L, Bicheng C (2016) Richard Fiifi Turkson, and Cai Qingping: Reducing frictional power losses and improving the scuffing resistance in automotive engines using hybrid nanomaterials as nano-lubricant additives. *Wear* 364:270–281

# Review of Transformer Core and Winding Design with Material Used



Sumit Saroha, Vineet Shekher, Pankaj Kumar, and Suvir Kumar

**Abstract** Energy efficiency is the key issue in electricity supply network, so to assure higher efficiency there is requirement of higher energy-efficient devices from supply-to-consumer network end. On the basis of this fact, this is needed to go through the study of new technological advancement in the field of transformer design. Nowadays, in this field, number of research papers has been published in the design aspects with modern technologies. Therefore, this paper detailed a comparative analysis of core and winding design of transformer. The core has been analysed on the basis of material used, their annealing temperature with corresponding structure, core coating/making technique, magnetic or electric properties with loss of energy. Similarly, winding design is also analysed on the basis of material used, type of design (architecture/structure) with corresponding magnetic and electrical properties. Latest literature in the field of core and winding design has been reported. In addition to this, new technologies have been lime lighted in the field of transformer design.

**Keywords** Core · Magnetic material · Transformer · Winding

## 1 Introduction

The transformer is one of the most important components of the electricity supply network from generation to distribution part. The fault at any part will cause unreliable supply of electricity as a result of that power supply will be interrupted [1].

---

S. Saroha (✉)

Electrical Engineering, Guru Jambheshwar University of Science & Technology, Hisar, India

V. Shekher

Department of EEE, NIET, Greater Noida, India

P. Kumar

Department of IEWP, EWA, Manama, Bahrain

S. Kumar

Department of ECE, UCET, Vinoba Bhave University, Hazaribagh, India



Basically, transformer is a static induction principle-based electrical device which consists of single or two or more electrically or magnetically coupled windings. They have a variety of constructional features such as material used for winding, core, insulating mediums or agents with dielectric and thermal properties. Actually, energy conservation with its supply and efficiency is the very important task of power engineers, and in order to achieve this, highly efficient equipment must be required, from generation to distribution end of electric power supply network. In this, transformer will play a central role for maintaining the voltage balance among all distribution, transmission and generation of power systems [2].

From last 100 years, the electrical transformer has not faced any significant changes as per its function and operations. However, designers and manufacturers have reached in advance stage of design optimization with an aim to offer high efficiency with higher capacity and reliability of power supply with its continuous operation. The design aspects of transformer are quite complex job in which the designers have to ensure low manufacturing cost by keeping in mind all parameters with compatibility to meet out the desired specifications. Besides this, there is variation in the design aspects with their methodology as per the application of transformer such as sensor based, instrumental, distribution, power with corresponding operational frequency which may vary from 40 Hz to megahertz [3].

This paper detailed a comparative analysis of core and winding design of transformer. The core has been analysed on the basis of material used, their annealing temperature with corresponding structure, core coating/making technique, magnetic, or electric properties with loss of energy. Similarly, winding design is also analysed on the basis of material used, type of design (architecture/structure) with corresponding magnetic and electrical properties. In the next section, existing core and winding design are discussed. Section 3 highlights the different core material used, their annealing temperature with corresponding structure, core coating/making technique, magnetic or electric properties with losses; Sect. 4 presents key issues with findings of this review, and finally, review concludes in Sect. 5.

## 2 Existing Core and Winding Design

As per ANSI/IEEE [4], it is a static electrical device (machine) which consists of single or two or more than two (magnetically/electrically) coupled windings, in order to introduce mutual coupling between these electric circuits there may or may not be requirement of magnetic core. In electrical power systems, it is comprehensively used to transfer electrical power between circuits on the basis of electromagnetic induction at a constant frequency; generally, there is change of voltage and current values. It is one of the primary components for electrical supply networks for transmission and distribution electricity. Their constructional design mainly depends on the basis of application, rated power and level of voltage. During electrical energy conversion, the power loss accounts for a large percentage loss mainly heat dissipation at the time of transmission and distribution of electricity. This issue is not only felt by end

users in terms of efficiency at their power electronic components; but, also one of the major concern of high power applications in the power inverters generally utilized in solar power plant installations. There are two major loss involved in transformer no-load and load losses.

## 2.1 No-Load Loss

These losses are because of the core of transformer so they are also known for the core loss of transformer. The overall core or no-load components of power are broadly categories into three components, namely hystereses, eddy current and anomalous losses all are having different mechanisms. All these are highly dependent on the operating frequency of device as the frequency increase then the eddy current and anomalous losses will become more dominant (when  $f > 100$  kHz). Hysteresis losses are described by the type of magnetic material used for core. This is because of demagnetization and demagnetization of magnetic material. The loss occurs due to small circulating currents which actually oppose the main applied current (produce heating effect) in the core is called eddy current loss. Last component of loss in core is known as stray or anomalous loss, and they do not directly attribute to eddy current or hysteresis loss. The power loss in eddy current is defined by following Eq. (1):

$$P_e = K_e f^2 (B_{\max})^2 t^2 V \text{ W} \quad (1)$$

where  $B_{\max}$  maximum flux density in tesla ( $\text{Wb/m}^2$ ),  $t$  is thickness of laminations in metres,  $K_e$  is eddy current coefficient depends on type of core material,  $V$  is the volume of core material in  $\text{m}^3$ . The hysteresis loss can be defined as by Eq. (2):

$$P_h = K_h f (B_{\max})^{1.6} V \text{ W} \quad (2)$$

$K_h$  is hysteresis (Steinmetz) coefficient depends on range of flux density.

## 2.2 Load Loss

These losses are occurs only when load is applied to the transformer, i.e. because of load current. These are also known as winding or copper losses of transformer. These are derived from product of  $I^2 R$ ,  $I$  is the winding current and  $R$  is the winding resistance, both components of winging losses are the Joule losses and the stray losses. These losses are measured on the basis of measured DC resistance which is because of winding conductors used and current  $I$  measured at a given applied load [5–7].

### 3 Design Optimization

#### 3.1 Magnetic Core

It is the main component of transformer which is generally form by laminated stacks of grain-oriented or cold-rolled silicon steel. For the improvement of energy efficiency of magnetic core-based energy conversion devices, the soft magnetic material (SMM)-based core plays a key role. The magnetic properties of above-mentioned materials have material's intrinsic property which has been governed by magneto-crystalline anisotropy which is strongly correlated with hysteresis loss of core. Whereas, eddy current loss depends on extrinsic properties of materials, the magnitude of these losses decreases with decreasing thickness core material used. But the manufacturing cost of thinner core is higher as compared to thick. For low-frequency applications such as transformer used in power systems core with 200  $\mu\text{m}$  thickness is generally used; but, for high-frequency applications thickness of 50–100  $\mu\text{m}$  is widely used [8]. For amorphous and nanocrystalline, the thickness of single core lies between 20 and 30  $\mu\text{m}$  at a temperature of nearly 500 °C and 750 °C, respectively [9]. Core materials with on different parameters with coating and their magnetic properties are given in Table 1.

#### 3.2 Winding

Second most important component of transformer is its winding which carries the current. Over a century, the windings conductors of transformer are made of copper and aluminium. Lot of developments have been carried out in order to find new conductor materials with good conductivity to get better efficiency and mechanical performance. For the development of superconducting transformers, new research is in the recent trends for the development of high-temperature superconducting materials [1, 21]. The main objective is to design compact size (less core and winding material), highly efficient with higher overload capacity transformer. Over last two decades, due to unique excellent properties, the carbon nanotube (CNT) has also been studied and it is find that they are the true alternative of copper wire in transformer and other machines windings [22]. Reference [23] has designed a 630 kV high-temperature superconductor (HTS) winding base three-phase transformer which operates under liquid nitrogen with amorphous alloy core. The efficiency of transformer was upto 98.5%.

In electricity supply network, there is utilization of power, distribution and instrumental transformer. In power transformer with higher frequency (dual active bridge DC/DC converters & dual resonant DC/DC converters), one of the major concerns is the distribution of magnetic flux throughout the winding conductor. The diameter of winding conductor of power transformer is higher, and due to this, the skin effect will become dominant. Therefore, there is need to consider the physical structure of

**Table 1** Magnetic materials used for core with coating and their magnetic properties

Material	Structure with temp	Test size	Making/coating technique	Properties	Reference
Fe-Si-B-P-M	Amorphous (673 K) Nanocrystalline (813 K)	Thickness (20 μm) Width (0.8–1 mm)	Melt spinning technique	Amorphous, $M_s$ , $H_c$ (1.4 T, 4.4 A/m), Nanocrystalline $M_s$ , $H_c$ (1.4 T, 4.4 A/m)	[9]
Co-Fe-B-Si-Nb	Amorphous (500 °C)	Thickness (20 μm) Width (1 mm)	Melt spinning technique	Power Loss Decrease upto 75%, Power Loss (80 W/m <sup>3</sup> ) at 100 kHz	[10]
Fe-Si-B-Nb-Cu	Nanocrystalline (823 K)	Thickness (20 μm) Width (35 mm)		Magnetic Induction (0.52 T) Power Loss (36 W) at 30 kHz	[11]
Carbonyl iron coated with SiO <sub>2</sub> -Al <sub>2</sub> O <sub>3</sub>	Soft magnetic material (450 °C)		Hydrothermal Coating in N <sub>2</sub> atmosphere	Saturated Magnetic Flux Density (1.28 T), Resistivity (942 μΩm), Power Loss (106.9 W/kg) at 500 Hz	[12]
Fe based	Amorphous (500 °C)	Thickness (23 μm) Width (142 mm) Length (280 mm)		Saturated Magnetic Polarization (1.3 T) at 50 Hz Core Loss (0.22 W/kg) at 50 Hz	[13]
Fe-Si-B-C-Cr @SiO <sub>2</sub>	Phosphate Crystalline (550 °C)	Toroid Outer Dia (20.33 mm) Inner Dia. (12.7 mm) Height (5 mm)	Sol-gel method	Effective permeability (87.9–30) as frequency vary from (10 kHz–1 MHz)	[14]

(continued)

Table 1 (continued)

Material	Structure with temp	Test size	Making/coating technique	Properties	Reference
Carbonyl iron coated with phosphate & epoxy silicon	Soft magnetic material (500 °C)	Toroid Outer Dia (20 mm) Inner Dia (12 mm)	Phosphating & organic coating	Coating particle size decrease Complex Permeability increase from (18.2–27.8) at (5 Hz–1000 kHz)	[15]
Fe–Si–B–C–Cr @TiO <sub>2</sub>	Amorphous (480 °C)	Toroid Outer Dia. (20.33 mm) Inner Dia. (12.7 mm) Height (6 mm)	Ultrasonic treatment	Permeability (81.5) upto 10 MHz Core Loss (275 mW/cm <sup>3</sup> ) at 10 MHz	[16]
(Fe–Co)Si–B–P	Crystalline (923 K)	Thickness (30 μm) Width (2 mm)	Melt spinning technique	Coercivity (9.64–24.17 A/m) Saturation Magnetization (1.82 T)	[17]
Fe–Co–Ni–M–B	Amorphous (Curie Temp. 600 K)	Thickness (20–200 μm), Width (2–6 mm)	Melt spinning technique under Ar (Argon)	Coercive Field (6 A/m), Resistivity (180–230 × 10 <sup>-8</sup> μΩm) at (5 Hz–10 MHz), Magnetic Permeability (3 × 10 <sup>4</sup> ), Saturation Magnetization (1.2 T)	[18]
Fe–Si/ZrO <sub>2</sub> Nano Powder	Core shell structure sintering temp. (825 °C)	Ring Core Outer Dia (18 mm) Inner Dia.(12 mm) Thick (2.5 mm)	Spark Plasma Sintering	Coercivity (25.48 Oe), Resistivity. (688 μΩcm), Core Loss (147 W/kg), Max. Permeability (220), Saturation Magnetic Induction (1.2 T)	[19]
Co–Fe–Ni–Ti–B Powder	Amorphous (500 °C) Crystalline (800 °C)		Planetary Ball Mill under Ar	Coercivity (7.6 Oe), Saturation Magnetization (53.4 emu/g)	[20]

Saturation Magnetization ( $M_s$ ), Coercivity ( $H_c$ )

conductor also. Actually, skin effect is used to describe the distribution of current which is not uniform throughout the whole conductor and its associated resistance increases with increase in frequency of supply through the conductor. The reactance ( $X_L = 2\pi fL$ ) at the depth of conductor increase with increase in frequency ( $f$ ), due to the increase in reactance inside the conductor the distribution of current at surface of conductor will be more. Hence, current density at surface of conductor is more due to this entire conductor is not utilized properly. Now comes to magnetic flux part, the eddy current flows at inner depth of conductor which will oppose the effect of current or flux inside the conductor and the flux is always move towards air gap due to fringing effect; therefore, the flux linkage is outer surface of the conductor only. The skin effect has been compensated using multi-wire co-axial winding for testing a power transformer winding [24].

The foil winding can also be a good alternative to improve the thermal stability of high-frequency power transformer. In this, the cooling area of foil is large as a result of that it will allow higher current densities. But, the edges of foil are more due to this there is problem of skin, proximity, fringing and some other AC effects. Therefore, the presented research has presented different field shaping techniques which includes magnetic, non-magnetic, foil and winding techniques to reduce the above-mentioned effects [21]. The skin and proximity effect in high power medium-frequency transformers can also be compensated using Litz wire; but, the space occupied for the winding by Litz wire is more, i.e. require big size window and bobbin [25]. This large area window problem is minimized by foil winding. In order to compensate skin effect, the foil winding should be used at LV side as the flow of current is higher at that side. As the width of window and thickness of foil is limited (fixed), therefore, the overall winding thickness will be increased (number of winding layer is more); this will lead to proximity effect. Thus, for compensation the proximity effect, the LV winding (foil winding) layer needs to be wound in between HV windings [26].

A traction transformer of capacity 6.5 MVA has been designed using HTS conductor winding with an aim to achieve higher efficiency in with lighter in weight. For the winging four different single-phase winging units has been utilized in which Roebel cable of 5 mm wide is used for LV side winding and REBCO superconductor of 4 mm wire for HV side winding [27]. In 2016, Thummala et al. [28] have investigated the transformer winding self-capacitance, leakage inductance and AC resistance using analytical approach. The leakage inductance is the energy stored in the form of magnetic field in the winding, self-capacitance is the electric field energy stored which is considered as self-lumped element. The last one AC resistance is correlation with skin and proximity effect of transformer winding architecture (TWA). In this research, investigation of parameters has been carried out on four different schemes with seven TWA. Some of the important factors corresponding to transformer design are shown in Fig. 1.

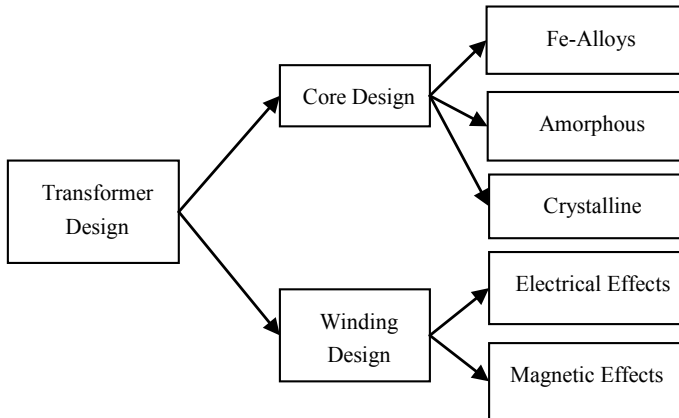


**Fig. 1** Important factors in transformer design

### 3.3 *Special Design*

While designing any of the devices, the saving of material is also very important subject of concern. Because it is highly correlated with cost of device designed. Reference [29] has proposed a 3-D wound core design, as per results 3-D design can also easily maintain the electromagnetic properties within permissible limits. The proposed model has been compared with three-phase three-column laminated core transformer, and there is saving of almost 27% of copper, 24% core material which makes the transformer cost almost 24% cheaper. In Ref. [30], Moghimi et.al designed a 3-D distribution network transformer and compared it with conventional transformer. For designing, silicon steel-based core with optimum transformer sizing theory is used and there is saving of 23.7% in overall cost of transformer design. On the other hand, Ref. [31] has designed a core on the basis of 3-D printing technology. By using 3-D printing, the thickness of coating material can be optimized easily as per requirement as a result of that transformer can be more responsive. In order to reduce the losses, Ref. [11] has designed a core sections with different materials as per the magnetic properties and load requirement and space between each section has been filled with Teflon and magnetic composite material made of Co–B–Nb–Si–Cu. Reference [32] has proposed a simulation algorithm for three-phase transformer with step lap wound joints.

## 4 Key Issues and Findings

This analysis of literature covers lot of research articles in the field of transformer design. But, in author's opinion the core design and winding design with their material and structure are very important topics of research. Therefore, both designs have

been taken into consideration for the analysis of review. It is observed that both the design (core and winding) concepts have their own characteristics and importance as per required specifications of device (core, shell, toroid, instrumental, 3-D, and auto-transformer). However, these are the following key issues and findings of this literature:

- Nanocrystalline and amorphous alloy-based cores have good electrical and magnetic properties with small no-load losses; but, their making process is not only time-consuming but also costly. Highly advanced machinery is required for making of such cores.
- The winding conductors with their structure/scheme and architecture must be designed by taking care of skin, proximity, fringing, line charging current, AC resistance and self-capacitance effects of winding.
- Thin core and winding conductor must be used to avoid different electrical and magnetic effects.
- It is found that there should be a good interlink between industry and academic to integrate the latest technology. Lot of research is going in the field of core and winding materials; but, it has not been implemented on ground level by industries.
- As per existing literature, it has also been observed that there is very limited use of adequate nano-technological concepts in the field of transformer design.

## 5 Conclusion

As the demand of electricity is growing at a very fast pace and energy-efficient devices can play a crucial role for conservation of energy. With an objective to analyse the energy efficiency of transformer with its design aspects, this paper provides an overview of latest literature concern to the transformer core and winding design with material used. For the proper analysis, latest research articles relevant to transformer core and winding designs have been also taken into consideration. For the comparative analysis, literature has been presented in tabular form with all necessary electrical and magnetic properties. By analysis, it has been observed that limited research work is in the field of winding design; whereas, core design with its structure and material used become a norm for most of the researchers. Currently, nanocrystalline structure of various alloys is being a latest topic of research in the field of core design because they show good magnetic and electrical properties among all structures of materials.



## References

1. Contreras JE, Rodriguez EA, Taha-Tijerina J (2016) Nanotechnology applications for electrical transformers—a review. *Electr Power Syst Res* 143:573–584
2. Feil DLP, Silva PR, Bernardon DP, Marchesan TB, Sperandio M, Medeiros LH (2017) Development of an efficient distribution transformer using amorphous core and vegetable insulating oil. *Electr Power Syst Res* 144:268–279
3. Amoiralis EI, Tsili MA, Kladas AG (2009) Transformer design and optimization: a literature survey. *IEEE Trans Power Delivery* 24(4):1999–2024
4. IEEE Standard Terminology for Power and Distribution Transformers. IEEE Std. C57.12.80 (2002)
5. Wood AJ, Wollenberg BF (2007) Power generation, operation and control, 2nd edn. Wiley, India
6. Elgard OI (1982) Electric energy system theory. TMH Edition
7. Sadat H (2002) Power system analysis. TMH Edition
8. Azuma D, Ito N, Ohta M (2020) Recent progress in Fe-based amorphous and nanocrystalline soft magnetic materials. *J Magn Magn Mater* (2020)
9. Zanaeva EN, Bazlov AI, Milkova DA, Churyumov AY, Inoue A, Tabachkova NY, Wang F, Kong FL, Zhu SL (2019) High-Frequency soft magnetic properties of Fe-Si-B-P-Mo-Cu amorphous and nanocrystalline alloys. *J Non-Cryst Solids* 526:119702
10. Baghbaderani HA, Masood A, Pavlovic Z, Alvarez KL, Mathuna CO, McCloskey P, Stamenov P (2020) On the mechanisms limiting power loss in amorphous CoFeB-based melt-spun ribbons. *J Magn Magn Mater* (2020)
11. Kolano-Buriana A, Kolano R, Zackiewicz P, Hreczka M, Kowalczyk M, Łukiewski M, Łukasiak P (2020) Investigation of the magnetic flux density dispersion  $B_d$  on the gaps of the FeSiBNbCu magnetically soft nanocrystalline block core. *J Magn Magn Mater* 500:166402
12. Suna K, Fenga S, Jianga Q, Lia X, Lia Y, Fana Y, Ana Y, Wang J (2020) Intergranular insulating reduced iron powder-carbonyl iron powder/SiO<sub>2</sub>-Al<sub>2</sub>O<sub>3</sub> soft magnetic composites with high saturation magnetic flux density and low core loss. *J Magn Magn Mater* 493:165705
13. Azuma D, Ito N, Ohta M (2019) Recent progress in Fe-based amorphous and nanocrystalline soft magnetic materials. *J Magn Magn Mater* (2019)
14. Zhou B, Dong Y, Chi Q, Zhang Y, Chang L, Gong M, Huang J, Pan Y, Wang X (2020) Fe-based amorphous soft magnetic composites with SiO<sub>2</sub> insulation coatings: a study on coatings thickness, microstructure and magnetic properties. *Ceram Int* (2020)
15. Chen D, Li K, Yu H, Zuo J, Chen X, Guo B, Han G, Liu Z (2019) Effects of secondary particle size distribution on the magnetic properties of carbonyl iron powder cores. *J Magn Magn Mater* (2019)
16. Zhou B, Chi Q, Dong Y, Liu L, Zhang Y, Chang L, Pan Y, He A, Li J, Wang X (2020) Effects of annealing on the magnetic properties of Fe-based amorphous powder cores with inorganic-organic hybrid insulating layer. *J Magn Magn Mater* 494:165827
17. Parra C, Perea D, Bolivar FJ (2019) Effect of cobalt addition on the microstructural evolution, thermal stability and magnetic properties of Fe-based amorphous alloys. *Vacuum* 169:108911
18. Chiriack H, Lupu N (2004) Design and preparation of new soft magnetic bulk amorphous alloys for applications. *Mater Sci Eng, A* 375–377:255–259
19. Geng K, Xie Y, Yan L, Yan B (2017) Fe-Si/ZrO<sub>2</sub> composites with core-shell structure and excellent magnetic properties prepared by mechanical milling and spark plasma sintering. *J Alloy Compd* 718:53–62
20. Avar B, Ozcan S (2015) Characterization and amorphous phase formation of mechanically alloyed Co<sub>60</sub>Fe<sub>5</sub>Ni<sub>5</sub>Ti<sub>25</sub>B<sub>5</sub> powders. *J Alloys Compd*
21. Kutkut NH (1997) Minimizing winding losses in foil windings using field shaping techniques. In: IEEE conference, pp 634–640
22. Pyrhönen J, Montonen J, Lindh P, Vauterin JJ, Otto M (2015) Replacing copper with new carbon nano-materials in electrical machine windings. *Int Rev Electr Eng* 10

23. Wang Y, Zhao X, Han J, Li H, Guan Y, Bao Q, Xiao L, Lin L, Xu X, Song N, Zhang F (2007) Development of a 630 kVA three-phase HTS transformer with amorphous alloy cores. *IEEE Trans Appl Supercond* 17(2):2051–2054
24. Rads MS, Novotny DW, Divan DM, Bacon RR, Gascoigne RW (1995) Multi-turn high frequency co-axial winding power transformers. *IEEE Trans Ind Appl* 31(1):112–118
25. Iyer K, Robbins W, Mohan N (2014) Design and comparison of high frequency transformers using foil and round windings. In: *Power electronics conference (IPEC)* (2014)
26. Iyer KV, Robbins WP, Mohan N (2014) Winding design of a high power medium frequency transformer. In: *IEEE international symposium on power electronics, electrical drives, automation and motion*, pp 665–669
27. Song W, Jiang Z, Staines M, Badcock RA, Wimbush SC, Fanga J, Zhang J (2020) Design of a single-phase 6.5 MVA/25 kV superconducting traction transformer for the Chinese Fuxing high-speed train. *Electr Power Energy Syst* 119:105956
28. Thummala P, Schneider H, Zhang Z, Andersen MAE (2016) Investigation of transformer winding architectures for high-voltage (2.5 kV) capacitor charging and discharging applications. *IEEE Trans Power Electron* 31(8):5786–5796
29. Guo X, Song D, Long L (2012) Study of material-saving effect of transformer with 3-D wound core. In: *International conference on electricity distribution*, pp 1–4
30. Moghimi MH, Moradnouri A, Vakilian M (2018) Feasibility of amorphous symmetric core transformer under distribution network planning. In: *IEEE electrical power distribution conference*, pp 57–62
31. Bollig LM, Hilpisch PJ, Mowry GS, Nelson-Cheeseman BB (2017) 3D printed magnetic polymer composite transformers. *J Magn Mater* 442:97–101
32. Mae A, Harada K, Ishihara Y, Todaka T (2002) A Study of characteristic analysis of the three-phase transformer with step-lap wound-core. *IEEE Trans Magn* 38(2):829–832

# Develop an Al-Alloy for High-Pressure–High-Temperature Applications by Enhancing Thermo-Mechanical Properties



J. Joy Mathavan, A. Kunaraj, and N. Sakthivelnathan

**Abstract** The aim of this research work is to develop an aluminium alloy which can be used in conditions like high temperature and high pressure. High pressure die castings, especially engine components of automobiles and heavy vehicles, are the important components which need to survive in such challenging working environment. Silicon, nickel and chromium found to be suitable filler materials to be used in high-pressure and high-temperature conditions based on the literature reviews. Based on the individual physical, chemical and thermo-mechanical properties of Si, Ni and Cr, these elements were selected as alloying elements and alloys Al–Si, Al–Si–Cr and Al–Si–Ni were prepared. The prepared samples were tested for various thermo-mechanical properties, and the results were analysed. Tensile strength values are obtained from hardness values based on Mayer’s hardness. Thermal conductivity values were obtained from electrical conductivity values based on Wiedemann–Franz law. Void content is calculated from practical and theoretical density values. At the end of the research, the new aluminium alloys proposed in this work found to be better replacements for aluminium metal which is currently in use for many high-pressure–high-temperature applications.

**Keywords** Thermo-mechanical property · Al-alloy · Engine components

## 1 Introduction

The automotive engines are to be operated in high temperature and under high pressure. Piston is the key component which has to undergo such challenging situation. Piston has to move back and forth rapidly; therefore, it must withstand high temperature, high pressure, and also, it should be wear resistant. For a long time, aluminium alloys are considered as the ideal material for piston. The high strength, good castability, wear resistance, low density and low thermal expansion make (Al–Si) alloys

---

J. J. Mathavan (✉) · A. Kunaraj · N. Sakthivelnathan  
Faculty of Technology, University of Jaffna, Jaffna, Sri Lanka

good for automobile industry [1]. But they still have disadvantages while considering their thermo-mechanical properties [2]. The focus of this paper is to find an aluminium alloy so as to reduce the drawbacks of piston alloy and to mitigate the issues in other related applications. It is sophisticate to identify an alloy (Al–Si, Al–Si–Cr and Al–Si–Ni) beyond technical and economic limitations to best suit the piston alloy by considering variation of thermal expansion and wear resistance.

## 2 Literature Review

M. Jinnah Sheik Mohamed mentioned in his paper that, the piston of internal combustion engines are alloys made up of aluminium–silicon cast alloys alloyed with chromium, nickel and magnesium. The reason is the ability of high wear resistance and low thermal expansion coefficient. Al–Si cast alloys are suitable for application less than 230 °C. Above this temperature, the microstructure strengthening mechanism of these alloys becomes unstable. Addition of nickel to Al–Si piston alloy will improve the high-temperature performance [1]. Cr increases strength at indoor and higher temperature [3].

Al–Ni–Si alloys are used for a wide range of engineering applications because of their high strength, good wear resistance, good castability, lightweight and low thermal expansion [4]. Aluminium alloys are generally used in the automobile industry particularly to reduce weight and thereby decrease fuel consumption and increase the efficiency [2]. Every 100 kg weight reduction in the weight of the vehicle can save around 0.5 l of petrol usage for 100 km drive [5–8]. Fuel economy can be significantly improved by reduction of weight in a vehicle [9, 10]. Onyebueke B Ifeanyi et al. further mentioned that, Al–Si alloy is the most cast friendly aluminium alloy. Addition of Co, Cr, Mn, Mo and Ni improves strength at high working temperature. Strength and fatigue resistance can be improved by adding copper without any harm to castability, but it will reduce corrosion resistance. Addition of magnesium increases the strength, especially after heat treatment, but it will affect ductility. Adding chromium to Al–Si alloy as a modifier at elevated temperatures suppresses the grain growth. It also decreases the vulnerability to stress corrosion cracking of the alloy. At elevated temperatures elements like Ni, Co, Cr and Mo with high melting points defend the decline in strength to some extent [2]. From these literature reviews, it can be observed that the strength is also playing an important role in the selection of piston alloy material. So it is appropriate to calculate the hardness and tensile values.

The reason behind the usage of Al–Si alloys as piston alloy over cast iron is its high thermal conductivity. The extraction of heat produced by combustion is more rapid in Al–Si alloys than cast iron. Low coefficient of friction and resistance to wear are the main features essential for engine block materials. Softening of hypoeutectic Al–Si piston alloys while operating in high temperature requires high-temperature strengthening of the Al–Si piston alloys. The thermal conductivity could be increased by liner-less Al–Si alloy cylinder blocks. The creep strength of the alloy improved

by the addition of nickel to the alloy; but, the effect of it is very small on the tensile strength at high temperature. The alloy containing nickel has fatigue strength almost 20% higher than that of the Al–Si–Mg alloy [11]. The ductility of the material can be increased significantly by adding nickel particles [12].

The AMAG Company in its report of 2012 mentioned that, the addition of alloying elements will reduce the thermal conductivity considerably. In Al–Si cast alloys, both electric conductivity and thermal conductivity decline very closely linearly with increasing nickel content. It is essential to understand the effects on thermal conductivity due to addition of nickel. For applications under high temperature, nickel is considered as a main alloying element with Al–Si cast alloys. Heat produced in compression cycle of a working engine needs to be removed as fast as possible to avoid hot spots and thermal stresses on the surface of the piston. Therefore, high thermal conductivity is also having a major impact on selection of the material for piston [13]. Aluminium has a conductivity-to-weight proportion twice that of copper and its strength-to-weight proportion is 30% more noteworthy than copper [14].

### 3 Methodology

The samples were prepared on burnout furnace. The aluminium rod is cut in to small pieces, and the surface is cleaned. Then it is introduced in a crucible made of silica and kept inside the burnout furnace. The time, maximum temperature and temperature increasing rate were set. Chromium, silicon and nickel were preheated and added according to the decided percentages to molten aluminium which is taken out of the furnace at 750 °C. Then the crucible containing this mixture was stirred well to emphasize the uniform mixture of all the components throughout the sample. Again it was kept inside the furnace for some time. Then the crucible was taken out of the furnace, stirred well and the slag formed on the surface of the molten mixture was removed. Then it was poured into the preheated split-type mould and allowed to cool for room temperature. Finally, the prepared samples were removed.

Impact of Ni and Fe in Al–Si alloys with Si content above 5% dramatically reduces corrosion resistance, fluidity and plasticity [3]. So in our studies, we did not add Ni or Cr above 5%. Different combinations of Al–Si, Al–Si–Cr and Al–Si–Ni matrix were prepared to analyse the change of various factors. The percentage addition of these elements is given in Table 1. Pure sample of aluminium also prepared.

#### 3.1 Vickers Hardness Test

The Vickers hardness testing method is based on visual dimension measuring system. The microhardness test is conducted according to ASTM E-384 procedure. The tests are conducted using an indenter, which may specify a range of light loads to make an indentation on the sample, and then it is measured, calculated and converted to a

**Table 1** Percentage addition of filler materials to base metal aluminium

Sample	Aluminium (%)	Silicon (%)	Chromium (%)	Nickel (%)
Al	100			
Al-2%Si	98	2		
Al-4%Si	96	4		
Al-2%Si2%Cr	96	2	2	
Al-2%Si4%Cr	94	2	4	
Al-2%Si1%Ni	97	2		1
Al-2%Si2%Ni	96	2		2
Al-2%Si3%Ni	95	2		3

hardness value. Since the indentation needs to be observed through microscope, the test samples must be highly polished. A square-based, pyramidal-shaped diamond inventor is used for testing the Vickers hardness. The range of loads can be from 10 gmf to 1 kgf. The hardness values obtained here are of the average of 10 readings. Tensile values are calculated using Eq. 1. This equation is used in several researches [15–17]. Tabor has developed an empirical correlation between hardness and tensile strength. This way of tensile and hardness testing methods is possible upon metals Al, Cu and steel, but not in Mg. The presence of profuse twinning at low stress levels can be the reason for not applying this equation in magnesium. Meyer, in 1908, propose this relationship  $H_m = 4w/\pi r^2$  (Meyer hardness has the dimensions of stress)  $H_m = 2.8 \sigma$  [17]. A cold-worked material's yield stress is given by  $\sigma_y = H/3$ . This formula is applicable for brass, steel in either hot-tempered or cold-rolled condition, and aluminium alloys in either aged or cold-rolled condition. Marcinkowski et al. found that for annealed Fe–Cr alloys, this expression appeared to be  $\sigma_y \approx H/5$  due to strain hardening. Speich and Warlimont showed that for Fe–Ni alloys and low carbon martensites,  $\sigma_y \approx H/4$  [15]. Here Hv represents Vickers's hardness and  $\sigma$  represents tensile strength. The specific reasons to use empirical equation to calculate the tensile values from hardness measurements are as follows. First, the preparation and testing of a hardness testing sample are less costly and need less experience and time when compared to the preparation and testing of tensile testing sample. Secondly, the tensile values could be obtained without destructing the sample, if the empirical equation is followed. This feature is smart from the production expense point of view.

$$Hv \approx 3\sigma \quad (1)$$

### 3.2 Density Calculation

The two major defects occurring in casting process which strongly weakens the fatigue strength is porosity and oxide enclosures [11]. Increase in porosity leads to poor tensile and fatigue strength. [18, 19]. The void content is under control in current research. It did not exceed more than 2%. Equation 2 is used to obtain the theoretical density of an alloy in terms of weight fraction.

$$\begin{aligned}\rho_{ms} &= 1/[(w_a/\rho_a) + (w_s/\rho_s) + (w_n/\rho_n)] \text{ or} \\ \rho_{ms} &= 1/[(w_a/\rho_a) + (w_s/\rho_s) + (w_c/\rho_c)]\end{aligned}\quad (2)$$

The weight fraction and density are represented by  $w$  and  $\rho$ , respectively. The suffix a, s, n, c and ms stand for aluminium, silicon, nickel, chromium and the mixture, respectively. Water immersion method is followed to calculate the actual density ( $\rho_{cm}$ ) of the specimen by experiment. Equation 3 is used to calculate the volume fraction of voids ( $V_v$ ) in the alloy. Here ct is theoretical density and cp is practical density

$$V_v = (\rho_{ct} - \rho_{cp})/\rho_{ct}\quad (3)$$

### 3.3 Thermal Conductivity

Parameters that improve thermo-mechanic fatigue (TMF) resistance are high thermal conductivity and low thermal expansion coefficient [20–22]. Thermo-mechanic fatigue resistance is improved by decreasing thermal expansion coefficient [11], and Ni decreases the coefficient of thermal expansion of Al alloys [3]. The thermal conductivity value of pure aluminium of the current experiment is very close to that of theoretical value.

The ratio between thermal conductivity  $K$  and electrical conductivity  $\sigma$  is proportional to the absolute temperature, at moderately low temperatures with a proportionality constant called “the Lorenz number”  $L = 2.45 \times 10^{-8} \text{ W } \Omega/\text{K}^2$ . This is known as Wiedemann–Franz law [23, 24]. In the current studies, the resistance is measured with a milli-ohm metre. It has precision of 0.01 milli-ohm. Subsequently, the value of resistivity and conductivity is determined by using appropriate Eqs. 4 and 5. Wiedemann–Franz law (Eq. 6) is used to find the thermal conductivity values from electrical conductivity values. In 1853, Gustav Wiedemann and Rudolph Franz reported that  $\kappa/\sigma$  has approximately the same value at the same temperature for different metals. Wiedemann–Franz law is named after this incident.

$$V = IR\quad (4)$$

**Table 2** Theoretical and practical density values

Sample	Theoretical density (g/cm <sup>3</sup> )	Practical density (g/cm <sup>3</sup> )	Void content
Al	2.7	2.66	1.481%
Al-2%Si	2.6917	2.65	1.549%
Al-4%Si	2.6828	2.62	2.34%
Al-2%Si2%Cr	2.725	2.662	2.311%
Al-2%Si4%Cr	2.76	2.71	1.811%
Al-2%Si1%Ni	2.71	2.682	1.033%
Al-2%Si2%Ni	2.729	2.717	0.439%
Al-2%Si3%Ni	2.7484	2.723	0.924%

$$R = \rho l/A \quad (5)$$

$$k/\sigma = LT \quad (6)$$

## 4 Results and Discussion

### 4.1 Density Values

Weight of the component should be considered while deciding material for piston alloy. It can be noticed from Table 2 that the density values of aluminium alloys are not varying significantly while comparing it with the density of aluminium sample. As mentioned earlier, the decrease in weight of the components is highly appreciated in the automobile industry. Nickel (density = 8.9 g/cm<sup>3</sup>), chromium (density = 7.15 g/cm<sup>3</sup>), and silicon (density = 2.33 g/cm<sup>3</sup>) are added as alloying elements, and the change in density is occurred. In current studies, the density of alloy samples did not show a wide variation. Rather, Al-2%Si, Al-2%Si2%Cr and Al-2%Si1%Ni show very close density values to that of aluminium. Since there is no significant increase in weight, the new proposed materials will neither lead to the increase in weight of parts nor to the decrease in performance of the vehicle.

### 4.2 Hardness and Tensile Values

Equation 1 is used to calculate the tensile values from hardness values. It can be noticed from the graph that, the tensile and hardness values are increasing with the



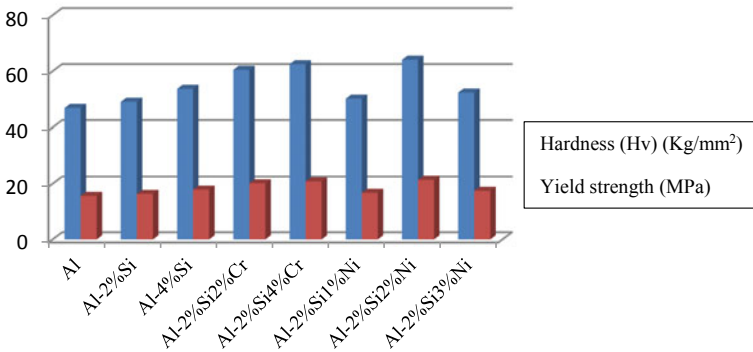


**Fig. 1** Hardness and tensile value comparison among the prepared samples

addition of Si and Cr. But with the addition of Ni, the hardness and tensile values started decreasing after 2% addition of Ni. It can be decided that 2% nickel addition would be the optimum value to obtain better results. All three alloying elements, namely chromium, nickel and silicon, are harder than aluminium which is the reason for the increase in hardness. These outcomes are shown in Fig. 1. Due to the better results obtained for hardness and tensile results of aluminium alloys than aluminium, the suggestion of new proposed alloys to automobile industry is meaningful.

### 4.3 Thermal Conductivity Values

The thermal conductivity value of aluminium obtained in current studies (238.19 W/mK) and the theoretical value (which is varying from 236 W/mK to 240 W/mK with temperature) are more or less similar in value. So it can be assumed that the errors in this practical are negligible. From Table 3, it is noticeable that

**Table 3** Electrical and thermal conductivity values

Sample	Electrical resistivity ( $\times 10^{-8} \Omega\text{m}$ )	Electrical conductivity ( $\times 10^7 \Omega^{-1} \text{m}^{-1}$ )	Thermal conductivity (W/mK)
Al	3.073	3.254	238.1928
Al-2%Si	3.763	2.657	194.4924
Al-4%Si	4.617	2.165	158.478
Al-2%Si2%Cr	3.57	2.801	205.0332
Al-2%Si4%Cr	3.922	2.549	186.5868
Al-2%Si1%Ni	3.202	3.123	228.6036
Al-2%Si2%Ni	3.451	2.897	212.0604
Al-2%Si3%Ni	3.599	2.778	203.3496

the addition of foreign material to aluminium slightly reduces the thermal conductivity. Except Al–4%Si, Al–2%Si4%Cr and Al–2%Si, the other compositions seem to have acceptable thermal conductivity. Si is a non-metal is the reason for the drastic reduction in thermal and electrical conductivity values of Al–4%Si and Al–2%Si.

## 5 Conclusion

Maximum hardness and tensile strength values are obtained for Al–2%Si4%Cr, Al–2%Si2%Ni and Al–2%Si4%Cr. These samples have far better results compared to other samples tested.

The density values of all the samples are almost equal to that of aluminium sample. Since the density values are not varying much, it can be stated that the weight will also be almost equal for all the samples. Due to this fact, the proposed material will not affect the weight of the vehicle; and thereby the performance of the vehicle will not be affected. Also, the void content of the sample is ranging only from 0.4 to 2.4%.

The thermal conductivity of Al–2%Si1%Ni and Al–2%Si2%Ni is slightly lower than that of aluminium sample. It is a slight drawback that these samples cannot conduct heat as fast as aluminium. But Al–2%Si1%Ni and Al–2%Si2%Ni will remove heat from engines in a slightly slower rate than aluminium. When considering other qualities, the slight reduction in thermal conductivity is acceptable.

When considering all the experiments, Al–2%Si2%Ni sample seems to be the better replacement for aluminium in high-pressure and high-temperature conditions, and it is followed by Al–2%Si2%Cr sample.

## References

1. Jinnah Sheik Mohamed M (2015) Influence of nickel addition and effect of heat treatment on aluminium-silicon piston alloys. *Int J Sci Res (IJSR)* 4(4):2319–7064
2. Onyebueke Ifeanyi B, Nwankwo Nkem E, Anene Amaechi F (2016) Effects of chromium and Molybdenum on the structure and mechanical properties of Al-Si alloys obtained by metal-mould casting. *J Sci Eng Res (JSERBR)* 3(3):383–389. ISSN: 2394-2630
3. Petrik J, Horvath M (2011) The iron correctors in Al-Si alloys. *Annals of faculty engineering Hunedoara. Int J Eng Tome IX (Year 2011). Fascicule 3.* ISSN 1584-2673
4. Böyü U (2012) Physical and mechanical properties of Al–Si–Ni eutectic alloy. *Met Mater Int* 18(6):933–938 (2012). <https://doi.org/10.1007/s12540-012-6004-5>
5. James M, Kihui JM, Rading GO, Kimotho JK (2011) Sustainable research and innovation conference proceedings, vol 3
6. Dawson S (2009) Compacted graphite iron—a material solution for modern diesel engine cylinder blocks and heads. *China Foundry* 6(3):241–246
7. Medraj M, Parvez A (2007) Analyze the importance of Magnesium-aluminium-strontium alloys for more fuel-efficient automobiles. *Automotive* 45:45–47
8. Allison JE, Cole GS (1993) Metal-matrix composites in the automotive industry: opportunities and challenges. *J Miner Met Mater Soc* 45:19–24

9. Kulekci MK (2008) Magnesium and its alloys applications in automotive industry. *Int J Adv Manuf Technol* 39:851–865
10. Eliezer D, Aghion E, Froes H (1998) Magnesium science, technology and applications. *Adv Perform Mater* 5:201–212
11. Javidani M, Larouche D (2014) Application of cast Al–Si alloys in internal combustion engine components. *Int Mater Rev* 59(3):132–158
12. Hashem El-Labban F, Abdelaziz M, Essam Mahmoud RI (2016) Preparation and characterization of squeeze cast Al–Si piston alloy reinforced by Ni and nano- $\text{Al}_2\text{O}_3$  particles. *J King Saud Univ Eng Sci* 28:230–239
13. Stadler F, Antrekowitsch H, Fragner W, Kaufmann H, Pinatel ER, Uggowitzer PJ (2013) The effect of main alloying elements on the physical properties of Al–Si foundry alloys. *Mater Sci Eng, A* 560:481–491. <https://doi.org/10.1016/j.msea.2012.09.093>
14. Logabharathi D, Rajaselvan S, Nitin S, Karthic Sankar S (2018) Analysis of transmission losses using grid system. *Int J Adv Res Eng Sci Technol* 5(4). e-ISSN: 2393-9877, p-ISSN: 2394-2444
15. Cahoon JR, Broughton WH, Kutzak AR (1971) The determination of yield strength from hardness measurements. *Metall Mater Trans B* 2:1979–1983. <https://doi.org/10.1007/BF02913433>
16. Zhang P, Li SX, Zhang ZF (2011) General relationship between strength and hardness. *Mater Sci Eng, A* 529:62–73
17. Lenhart RE (1995) The relationship of hardness measurements to the tensile and compression flow curves. WADC technical report 55–114. General Electric Research Laboratory, Wright Air Development Center
18. Aqida SN, Ghazali MI, Hashim J (2004) Effects of porosity on mechanical properties of metal matrix composite: an overview. *Jurnal Teknologi* 40(A):17–32
19. Mugica GW, Tovia DO, Cuyas JC, González AC (2004) Effect of porosity on the tensile properties of low ductility aluminum alloys. *Mater Res* 7(2)
20. Lee S-C, Weng L-C (1991) On thermal shock resistance of austenitic cast irons. *Metall Trans A* 22(8):1821–1831
21. Dieter GE (1986) *Mechanical metallurgy*, 3rd edn. McGraw-Hill, New York
22. Seruga D, Fatdiga M, Nagode M (2011) Creep damage calculation for thermo mechanical fatigue. *J Mech Eng* 57(5):371–378
23. Scott JF, Bohn HG, Schenk W (2000) Ionic Wiedemann-Franz law. *Appl Phys Lett* 77:2599. <https://doi.org/10.1063/1.1318939>
24. Christopher Seagle T, Cottrell E, Fei Y, Daniel Hummer R, Vitali Prakapenka B (2013) Electrical and thermal transport properties of iron and iron-silicon alloy at high pressure. *Geophys Res Lett* 40:5377–5381

# A Review on Mechanical Properties of Bamboo Fiber-Based Composites



Jagdeep Kumar, Shivaji Chaudhary, Vikas Goyat, and Amit Goyal

**Abstract** Composite materials can be tailored to provide application-based properties; therefore, they are suitable material for modern-age applications. Synthetic fiber-based composites are conventional composite materials and they possess excellent mechanical properties and applicability. Whereas synthetic fiber-based composites are not environment-friendly materials further, they are nonrenewable. Natural fiber-based composite materials can be a sustainable substitute for synthetic fiber-based composites as they are environment friendly, biodegradable, cost effective, low weight, good mechanical properties, and renewable. Bamboo fiber is one of the best natural fibers in terms of availability and mechanical properties. It is compatible with several matrix materials. This work presents a review on mechanical properties of bamboo fiber, bamboo fiber-based composites, and hybrid bamboo fiber-based composites.

**Keywords** Natural fiber · Bamboo fiber · Bamboo fiber-based composite · Mechanical properties

## 1 Introduction

Bamboo is a natural and traditional structural material, which is available around the Earth. Its fiber has unique antibacterial, UV protection, biodegradability, low cost, good thermal resistance, and superior mechanical properties among natural fibers [1, 2]. Bamboo fibers can be used as a reinforcement material for the matrix of rubber, plastics, and biopolymers. Nowadays, bamboo fiber is replacing the synthetic fibers to a significant extent in wide range of applications such as automobiles,

---

J. Kumar (✉)  
Sobhasaria Group of Institutions, Sikar, Rajasthan, India

S. Chaudhary  
Noida Institute of Engineering and Technology, Greater Noida, Uttar Pradesh, India

V. Goyat · A. Goyal  
SRM Institute of Science and Technology, Delhi NCR Campus, Ghaziabad, Uttar Pradesh, India

aerospace, railway coaches, building materials, ceiling, separation boards, furniture, packaging, consumer products, etc. [3]. Enhancement of bamboo fiber and its composite applications will surely increase the employment especially in the rural sector [4]. Researchers are working continuously to replace the harmful material with ecofriendly biodegradable materials and natural/bamboo fiber bio-composite is one of the significant outputs of their work [5]. The motivation of this study is to explore the scope, applications, and capabilities of natural bamboo fiber in comparison with conventional synthetic fibers. The recent improvements in mechanical properties of bamboo fiber composite is also discussed in this work.

## 2 Bamboo Fiber

Bamboo fibers are sustainable substitutes to synthetic fibers due to their low cost, easy availability, non-exhaustibility, environmental friendliness, good thermal resistance, and comparable mechanical properties [2]. Bamboo fiber constituents and their composition are depicted in Fig. 1. The major constituents of the bamboo fiber are cellulose, hemi-cellulose, and lignin. Due to high composition of cellulose, the bamboo fiber belongs to the family of cellulose fibers. The lignin is the unwanted constituent and need to be removed in order to produce the good fiber as well as composite. The Weibull statistics of tensile strength of bamboo fiber represents that the tensile strength of bamboo fiber depends on the gauge length of the fiber. The tensile strength decreases with an increase in the gauge length as the probability of a number of flaws increases with an increase in gauge length [6]. The transvers tensile strength of the bamboo fiber was noticed nearly 22 times less than the longitudinal strength [5]. It is observed from another Weibull analysis of mechanically extracted

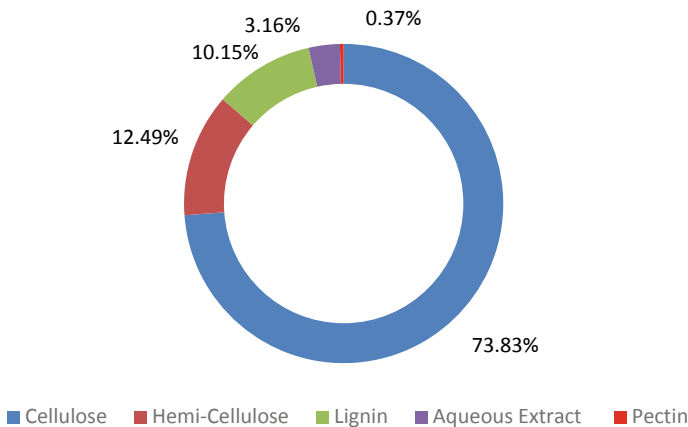


**Fig. 1** Bamboo fiber constituents and their composition [5]

(blasting extraction process) Moso bamboo fibers that the average mechanical properties also depend on the diameter of the fiber. Bamboo fiber with higher diameter shows the least tensile strength [7]. Trujillo et al. [8] presented a modified Weibull analysis for *Guadua Angustifolia* bamboo fibers extracted by the pure mechanical extraction process. The average tensile strength of bamboo fiber decreases with increase in the length of fiber as 943 MPa (1 mm) to 733 MPa (40 mm). Table 1 shows the tensile strength of different bamboo fibers.

**Table 1** Tensile strength of bamboo fiber

Gauge length (mm)	Fiber diameter (μm)	Bamboo type	Tensile strength (MPa)	Reference
1	132 ± 33	<i>Guadua angustifolia</i>	943 ± 94	[8]
2	137 ± 36	<i>Guadua angustifolia</i>	898 ± 124	[8]
5	90–250	<i>Guadua angustifolia</i>	833 ± 101	[2]
5	161 ± 27	<i>Guadua angustifolia</i>	833 ± 113	[8]
10	90–250	<i>Guadua angustifolia</i>	836 ± 119	[2]
10	156 ± 27	<i>Guadua angustifolia</i>	8221 ± 125	[8]
20	200 ± 15	–	555	[6]
20	196.6	Moso	568	[7]
20	317.3	Moso	553	[7]
20	398.4	Moso	523	[7]
20	508.8	Moso	491	[7]
20	584.3	Moso	483	[7]
20	164 ± 32	<i>Guadua angustifolia</i>	754 ± 72	[8]
30	200 ± 15	–	523	[6]
30	112 ± 8	<i>Guadua angustifolia</i>	733 ± 121	[8]
35	90–250	<i>Guadua angustifolia</i>	778 ± 122	[2]
40	90–250	<i>Guadua angustifolia</i>	772 ± 113	[2]
40	200 ± 15	–	492	[6]
40	156 ± 23	<i>Guadua angustifolia</i>	748 ± 115	[8]
50	200 ± 15	–	451	[6]
60	200 ± 15	–	442	[6]

### 3 Bamboo Fiber-Based Composites

The mechanical properties of bamboo fiber composites depend on different parameters such as fiber extraction method, fiber surface treatment, length of fiber, the orientation of fiber, volume fraction, aspect ratio, dispersion, matrix material, the chemistry between matrix, and fiber and fabrication method [4]. The orientation of fibers proportionally affect the mechanical properties of bamboo fiber composites. The longitudinal oriented fiber composite sample has comparably higher strength than an inclined fiber composite sample. Chattopadhyay et al. [9] investigated the applicability of Maleic anhydride-grafted polypropylene (MA-g-PP) as a compatibilizer for bamboo fiber-reinforced polypropylene composite. The 50% fiber and 5% MA-g-PP has been suggested for optimum mechanical and thermal properties. Afrin et al. [10] tested the degumming method so-called green method of bamboo fiber extraction and reported that bamboo fiber loses its antibacterial and UV protection properties during the degumming process. Osorio et al. [11] proposed a novel mechanical technique for extraction of long bamboo fiber. Obtained fibers have improved tensile strength (800 MPa) and Young's modulus (43 GPa). Aiping et al. [12] analyzed Young's modulus and the tensile strength of the natural bamboo fiber and its matrix using a hybrid approach. The Young's modulus and tensile strength have been observed as 30 GPa and 450 MPa for fiber whereas 120 MPa and 11 MPa for matrix. Copper sag and red mud can be used as a filler material for bamboo fiber epoxy composite to enhance the tensile strength whereas by doing so reduces the impact and flexural strength [13]. Addition of nanoclay (Cloisite) as a filler material in bamboo fiber epoxy composite ensures the significant improvements in tensile impact and flexural strength while it reduces the dielectric constant [14]. Bamboo fiber composites possess higher thermal insulation than ordinary glass fiber composites and the thermal conductivity increases with increase in fiber-orientation angle [15]. The alkali bamboo fiber extraction method is superior to steam explosion, and chemical extraction method in terms of the high tensile strength of fiber [16].

The cloisite nanoclay can be used as a filler material for bamboo fiber polylactic acid composite to enhance the compatibility between polylactic acid and bamboo fiber by increasing mechanical interlocking between them. This results in the improved mechanical properties and a significant decrease in dielectric constant [17]. Long *Guadua angustifolia* bamboo fibers can be extracted with a mechanical extraction process with tensile strength around 800 MPa. Long *G. angustifolia* bamboo fiber-reinforced polypropylene and maleic anhydride-grafted polypropylene thermoplastic composite consist longitudinal tensile strength of ~180 MPa and ~160 MPa, respectively. With epoxy resin, the Long *G. angustifolia* bamboo fibers produced tensile strength of ~222 MPa [2]. The starch-based biodegradable resin and stem explosion extracted long bamboo fiber composite exhibit a tensile strength of 270 MPa and flexural strength of 263 MPa that are comparable to glass fiber-reinforced composite [18]. The bamboo fiber mat and unsaturated polyester composite consist equivalent tensile strength with jute fiber mat and unsaturated polyester composite. Though kneaf fiber mat and unsaturated polyester composite

show higher tensile strength than bamboo- and jute fiber-based unsaturated polyester composite [19]. Polylactic acid is a biodegradable and environment-friendly polymer. Its compatibility with bamboo flour can be enhanced by grafting glycidyl methacrylate onto it. By adding glycidyl methacrylate-grafted polylactic acid in bamboo flour (15 %wt) and polylactic acid composite, the tensile and impact properties can be enhanced significantly [20]. The addition of long *Dendrocalmus giganteus* bamboo fibers in the polyester matrix will result in a considerable improvement in tensile strength. The interfacial shear stress has been found relatively low [21]. The mechanical properties such as tensile and flexural strength/modulus of high-density polyethylene can be improved by reinforcing 30% of bamboo pulp fiber as tensile strength 29 MPa, tensile modulus 1.4 GPa, flexural strength 45 MPa, and flexural modulus 2.15 GPa [22]. The composite of phenol-formaldehyde matrix and oriented bamboo (Maso) fiber mat produces tensile strength 248 MPa, compressive strength 173 MPa and shortbeam strength 19 MPa [23]. Leera and nordin [24] reported the effect of bamboo powder addition in the polyester matrix. The 25% bamboo powder composition ensures the maximum tensile and flexural strength whereas maximum impact strength can be achieved by adding 20% bamboo powder in the polyester matrix. Eberts et al. [25] fabricated single-ply plain-weaved and stockinette-weaved bamboo fiber composite with pinesap-based bio-resin using wet layup technique. The plain-weaved composite has a tensile strength of 19 MPa, while stockinette-weaved has a tensile strength of 14 MPa without pre-strain and 18 MPa with 100% pre-strain. The maximum tensile strength of bamboo fiber composites has been noticed one third to the glass fiber composite. Charpy toughness of giant *D. giganteus* bamboo fiber-reinforced epoxy composite increases with increase in reinforcement and it has a maximum value of 70 J/m with 30% bamboo fiber composition [26].

Latha et al. [27] evaluated the effect of stacking sequence on mechanical properties of bamboo/glass fiber mat-reinforced epoxy resin composite. Outer glass mat plies and inner bamboo mat plies show higher tensile modulus as well as tensile strength. All bamboo plies based epoxy composites have the maximum wear resistance. Abilash et al. [28] studied the delamination of bamboo fiber polyester composite and it is reported that the delamination can be minimum with 500 RPM, 18 mm/min feed and 4 mm tool diameter during the drilling process. Zuhudi et al. [29] explored the twill-woven bamboo fabric as reinforcement in a polypropylene matrix for automotive components. The introduction of the twill-woven bamboo fabric improved the impact, flexural, and tensile strength of polypropylene by 160%, 170% and 238%, respectively. Chopped *G. angustifolia* bamboo fibers reinforced potassium-based geopolymer provided flexural strength of 7.5 MPa in four-point flexural test [30]. Steam explosion processed and alkali-treated Moso bamboo fiber reinforced in biodegradable polylactic acid composite (cross-ply) shows a proportional increase tensile strength and Young's modulus with an increase in bamboo fiber compositions [31]. Sanchez et al. [32] successfully fabricated the agglomerated bamboo fiber composite with higuierilla resin made up from vegetable oil and Guadua bamboo fibers of 15 MPa compressive and 10 MPa tensile strength. Zhou et al. [33] investigated the effect of nanoparticles of Carbonized Ramosissima on the



mechanical properties of bamboo fiber-based epoxy composite. By adding the 0.5% nanoparticles, the tensile strength is increased by 18%.

## 4 Surface-Treated Bamboo Fiber-Based Composites

Concentrated NaOH treatment on bamboo fiber enhances the mechanical strength and Young's modulus but reduces the ductility. The NaOH-treated bamboo fiber and unsaturated polyester (Reservol P 9509) composite show higher interfacial shear strength compared to untreated bamboo fiber polyester composite [34]. Silane treatment on bamboo fiber epoxy composite is not suitable to enhance the mechanical strength of composite [35]. Alkali-treated bamboo fiber polylactide composite also shows significant improvement in mechanical and thermal properties. Further, the coupling agent silane (aminopropyl triethoxysilane) enhances the bonding strength between bamboo fiber and polylactide [36]. Kushwaha et al. [1] explored different chemical treatments for bamboo fiber to improve the mechanical (tensile strength, flexural strength, and impact strength) and water-resistant properties. They suggested permanganate treatment for bamboo epoxy composite and benzoyl chloride treatment for bamboo polyester composite. Alkali treatment of bamboo fibers ensures the high bonding strength between treated bamboo fiber and acrylonitrile-butadiene-styrene (ABS) matrix as it produces the rough surface of bamboo fibers. Impact strength and thermal stability of the composite have been improved by alkali treatment [37]. The surface treatment of bamboo fiber with alkali, silane, and combined alkali and silane shows combined alkali (5%) and silane (0.5%) surface treatment promise higher water resistance and mechanical properties in bamboo fiber vinyl ester resin composite [16]. The isocyanatoethyl methacrylate treatment on bamboo fiber considerably enhances the water resistance flexural strength and tensile strength in bamboo fiber composite with unsaturated polyester whereas it decreases the impact strength of composite [38]. Hot compressed water treatment on bamboo fibers enhances the mechanical properties [39]. The oxygen plasma treatment on bamboo fiber improved its crystallinity index and interfacial adhesion capabilities. The treated bamboo fiber-reinforced unsaturated polyester composite shows a significant value addition in tensile and fracture strength [40]. The elevation in the operating temperature from 40 to 80 °C enhances the tensile as well as flexural strength and a further increase in operating temperature will cause a significant decrement in all mechanical properties of alkali-treated bamboo fiber polyester composite. On the other hand, the increase in operating temperature diminishes the compressive strength and bending stiffness of composite [41].

Li et al. [42] explored the effect of surface treatment of bamboo fiber on mechanical properties of bamboo fiber-reinforced nanohydroxyapatite-poly(lactico-glycolic) composite. Alkali treatment on bamboo fiber surface enhanced the tensile strength of composite whereas silane treatment followed by alkali treatment improves the bending strength significantly. Azwa and Yousif [43] fabricated the untreated and NaOH treated randomly oriented bamboo fiber composite with a

polyester resin matrix to study the moisture and mechanical properties. The effect of moisture on thickness swelling has been observed same for treated–untreated bamboo fiber composite and it is comparably higher than pure polyester resin. The tensile strength of moisture degraded composites has been noticed poor than resin. The study of fracture mechanics of alkali-treated bamboo fiber-based epoxy composite reveals that debonding between fiber and matrix, fiber pulls out, and resin cracking are the causes of fracture. The higher value of fracture toughness has been noticed with 25 mm fiber length as 2.7 [44]. Dopamine treatment of bamboo fibers significantly enhanced the mechanical and interfacial properties of the bamboo-poly(lactic acid) composite. The 4% concentrated alkali treatment followed by dopamine treatment shows some improvements in mechanical properties of composite; however, further increase in concentration has a negative effect on tensile and flexural strength [45]. Nabinejad et al. [46] confirmed the advancement in tensile and flexural properties of NaOH-treated bamboo fiber-based unsaturated polyester composite prepared by vacuum assisted resin transfer molding technique. Alkali treatment on bamboo fiber surface enrich its adhesion and compatibility parameters in bamboo fiber-based poly(lactide acid) composite [47]. Liquid polypyrrole treatment on bamboo fiber slightly enhanced the tensile, flexural, and wear property of bamboo fiber polyamide composite [48]. Hybrid bamboo fiber-based composite in bamboo/glass fiber vinyl ester as well as unsaturated polyester hybrid composite, the bamboo fiber can replace 25% glass fiber without lowering down the tensile strength and other mechanical properties [49]. Replacing 30% glass fiber with bamboo fiber in a glass fiber polypropylene composite will result an enhancement of fire resistance without much compensating the impact strength [50].

Ramachandran et al. [51] have presented a comparative analysis of mechanical properties of bamboo fiber, bamboo–banana fiber, and bamboo–linen fiber-reinforced epoxy resin composites. Charpy test value of bamboo–banana fiber-based epoxy composite was found maximum as 5 J. Bamboo–linen fiber-based epoxy composite shows highest Rockwell hardness as 40 HRN. The hybrid composite of glass hollow micro-spheres and bamboo fiber with a matrix of maleic anhydride-grafted polypropylene and polypropylene as 1:9 showed the preferable mechanical properties [52]. A hybrid epoxy composite of flax and bamboo fiber shows high compatibility with resigning. However, the tensile strength of hybrid composite has been observed less than bamboo–epoxy composite and flexural strength has been noted lower than flax–epoxy composite [53]. Inserting carbon nanotubes in hybrid bamboo–epoxy composite results in a slight increase in tensile strength while flexural strength decreases by increasing nanotube volume fraction [54]. Haddou et al. [55] analyzed mechanical properties of bamboo fiber-reinforced polyamide 11 (a bio-based thermoplastic) composite, and they noticed that the Young's modulus is significantly increased to 11.9 GPa by adding the bamboo fibers. Huang and Young [56] investigated the untreated- and alkali-treated bamboo fiber epoxy composite. The density of the treated bamboo fiber was found increased as the alkali treatment remove the lignin and hemi-cellulose. Treated bamboo fiber composite has high strength in comparison with untreated bamboo fiber composite. Kumari et al. [57] fabricated Euphorbia coagulatum-treated polyester resin-based bamboo fiber composite.

The 40% fiber composition of pristine and 5% NaOH-treated bamboo fiber have optimal Young's modulus, flexural, and tensile strength. Chin et al. [58] investigated the alkali-treated *Gigantochloa scortechinii* bamboo fiber and their thermoset resin composites for microstructural, mechanical, and thermal properties. They noticed that the 10% NaOH treatment is best for bamboo fiber to remove unwanted constituents and offer high tensile strength, i.e., 319.52 MPa. The bamboo fiber-reinforced epoxy composite with 40% fiber concentration has the highest tensile strength of 119.39 MPa. Irawan et al. [59] fabricated the socket prosthesis with bamboo epoxy composite with 50% of bamboo fiber composition. The compressive strength was noticed significantly higher than the requirement of socket prosthesis. Zhang et al. [60] experimentally analyzed the failure of 6% NaOH-treated bamboo fiber reinforced poly-benzoxazine composite under impact loading. The bamboo fiber significantly added the impact strength to the poly-benzoxazine matrix. Table 2 shows the notable mechanical properties of different bamboo fiber composites.

## 5 Conclusion and Future Trends

In summary, bamboo fiber can replace the synthetic fibers in the future. To improve the mechanical properties as well as to make chemical-free bamboo fiber-based composites, following research interest needed to be explored.

- (a) The strength of bamboo fiber directly depends on the extraction method; thus, a sound environment-friendly extraction method may be developed to enhance the quality as well as mechanical properties of the fiber.
- (b) The first requirement to make a bamboo fiber-based green composite (Chemical free) is a biodegradable and renewable matrix material. Now, a few articles are available on such materials; therefore, biodegradable and renewable may be explored in pursuit of high mechanical strength and good compatibility with bamboo fiber.
- (c) To enhance the mechanical and surface properties of bamboo fiber, some non-ecofriendly chemical surface treatments have been noticed in this review. These chemical treatments may be replaced by other/ecofriendly surface treatment methods in the future.
- (d) A few articles have been found on additives and filler materials in bamboo fiber-based composites. This field may be explored to enhance the mechanical and water absorption properties.

**Table 2** Mechanical properties of bamboo fiber composites

Bamboo fiber type	Fiber weight %	Resin	Fiber treatment	Tensile strength (Mpa)	Young's Modulus (Gpa)	Flexural strength (Mpa)	Reference
Fiber	40	Epoxy	10 wt% NaoH	119.39		161.58	[58]
Fiber	40	Polyester	10 wt% NaoH	97.18		157.2	[58]
Fiber	40	Vinyl Ester	10 wt% NaoH	96.02		149.81	[58]
Fabric—10 layers		Epoxy (Carbonized ramosissima nanoparticles—0.5 wt%)		87.99			[33]
Fiber	40	Polyester		15.15	9.4	22.25	[57]
Fiber	40	Polyester	5 wt% NaoH	22.01	1.37	39.87	[57]
Fiber	40	Euphorbia coagulum treated polyester	5 wt% NaoH	24.41	2.03	43.22	[57]
Fiber	42	Epoxy		167.87	8.54		[56]
Fiber	42	Epoxy	NaoH—0.1 N	222.71	13.1		[56]
Fiber	60	Polyamide 11	3 wt% NaoH		11.9		[55]
Powder	10	Epoxy (MultiWalledCNT—0.5wt%)		79.763	1.866		[54]
Fiber	50	Poly lactide acid		10.7	7.45		[47]
Fiber	50	Poly lactide acid	4 wt% NaoH	16	5.86		[47]
Long fiber		Polyester	5 wt% NaoH	148.7		206	[46]
Fiber	40	Poly lactic acid		29.39	1.71	55.32	[45]
Fiber	40	Poly lactic acid	Dopamine hydrochloride 1 wt%	37.35	2.07	62.62	[45]

(continued)

**Table 2** (continued)

Bamboo fiber type	Fiber weight %	Resin	Fiber treatment	Tensile strength (Mpa)	Young's Modulus (Gpa)	Flexural strength (Mpa)	Reference
Fiber	40	Polylactic acid	Dopamine hydrochloride 1 wt% and 4 wt% NaOH	39.51	2.17	64.25	[45]

## References

1. Kushwaha PK, Kumar R (2011) Influence of chemical treatments on the mechanical and water absorption properties of bamboo fiber composites. *J Reinf Plast Compos* 30(1):73–85
2. Trujillo de los Rios EE, Osorio Serna LR, Van Vuure AW, Ivens J, Verpoest I (2013) Assessment of the properties of bamboo fibre and bamboo fibre composites. *Composites Week@ Leuven*, 1–9
3. Rohit K, Dixit S (2016) A review-future aspect of natural fibre-reinforced composite. *Polym Renewable Resour* 7(2):43–59
4. Liu D, Song J, Anderson DP, Chang PR, Hua Y (2012) Bamboo fiber and its reinforced composites: structure and properties. *Cellulose* 19(5):1449–1480
5. Khalil HA, Alwani MS, Islam MN, Suhaily SS, Dungani R, H'ng YM, Jawaid M (2015) The use of bamboo fibres as reinforcements in composites. In: *Biofiber reinforcements in composite materials*. Woodhead Publishing, pp 488–524
6. Shao J, Wang F, Li L, Zhang J (2013) Scaling analysis of the tensile strength of bamboo fibers using Weibull statistics. *Adv Mater Sci Eng*
7. Wang F, Shao J, Keer LM, Li L, Zhang J (2015) The effect of elementary fibre variability on bamboo fibre strength. *Mater Des* 75:136–142
8. Trujillo E, Moesen M, Osorio L, Van Vuure AW, Ivens J, Verpoest I (2014) Bamboo fibres for reinforcement in composite materials: strength Weibull analysis. *Compos A Appl Sci Manuf* 61:115–125
9. Chattopadhyay SK, Khandal RK, Uppaluri R, Ghoshal AK (2011) Bamboo fiber reinforced polypropylene composites and their mechanical, thermal, and morphological properties. *J Appl Polym Sci* 119(3):1619–1626
10. Afrin T, Tsuzuki T, Wang X (2010) Bamboo: a distinctive green fibre. In: *ICTA 2010: recent developments and challenges of textile and apparel industry: proceedings of the 1st international conference on textile and apparel*. Amin and Jahan Corporation, 14–19
11. Osorio L, Trujillo E, Van Vuure AW, Verpoest I (2011) Morphological aspects and mechanical properties of single bamboo fibers and flexural characterization of bamboo/epoxy composites. *J Reinf Plast Compos* 30(5):396–408
12. Zhou A, Huang D, Li H, Su Y (2012) Hybrid approach to determine the mechanical parameters of fibers and matrixes of bamboo. *Constr Build Mater* 35:191–196
13. Biswas S, Patnaik A, Kaundal R (2012) Effect of red mud and copper slag particles on physical and mechanical properties of bamboo-fiber-reinforced epoxy composites. *Adv Mech Eng* 4:1–6
14. Kumar V, Kumar R (2012) Dielectric and mechanical properties of alkali-and silane-treated bamboo-epoxy nanocomposites. *J Compos Mater* 46(24):3089–3101
15. Mounika M, Ramaniah K, Prasad AR, Rao KM, Reddy KHC (2012) Thermal conductivity characterization of bamboo fiber reinforced polyester composite. *J Mater Environ Sci* 3(6):1109–1116
16. Kim H, Okubo K, Fujii T, Takemura K (2013) Influence of fiber extraction and surface modification on mechanical properties of green composites with bamboo fiber. *J Adhes Sci Technol* 27(12):1348–1358
17. Kumar V, Sharma NK, Kumar R (2013) Dielectric, mechanical, and thermal properties of bamboo-polylactic acid bionanocomposites. *J Reinf Plast Compos* 32(1):42–51
18. Takagi H, Fujii T (2014) Mechanical characterization of bamboo fiber-reinforced green composites. In: *Key engineering materials*, vol 577. Trans Tech Publications Ltd., pp 81–84
19. Hojo T, Xu Z, Yang Y, Hamada H (2014) Tensile properties of bamboo, jute and kenaf mat-reinforced composite. *Energy Procedia* 56:72–79
20. Wang YN, Weng YX, Wang L (2014) Characterization of interfacial compatibility of polylactic acid and bamboo flour (PLA/BF) in biocomposites. *Polym Testing* 36:119–125
21. Neves Monteiro S, MuylaertMargem F, Barboza de Souza Martins L, LeiteLoiola R, Picanço Oliveira M (2014) Tensile strength of polyester matrix composites reinforced with giant bamboo (*Dendrocalmus giganteus*) fibers. In: *Materials science forum*

22. Ren W, Zhang D, Wang G, Cheng H (2014) Mechanical and thermal properties of bamboo pulp fiber reinforced polyethylene composites. *BioResources* 9(3):4117–4127
23. Yu Y, Huang X, Yu W (2014) A novel process to improve yield and mechanical performance of bamboo fiber reinforced composite via mechanical treatments. *Compos B Eng* 56:48–53
24. Noor Leha AR, Nordin NA (2014) Effect of filler compositions on the mechanical properties of bamboo filled polyester composite. In: *Advanced materials research*, vol 879. Trans Tech Publications Ltd., pp 90–95
25. Eberts W, Siniawski MT, Burdiak T, Polito N (2015) Mechanical characterization of bamboo and glass fiber biocomposite laminates. *J Renew Mater* 3(4):259–267
26. Glória GO, Margem FM, Ribeiro CGD, Moraes YMD, Cruz RBD, Silva FDA, Monteiro SN (2015) Charpy impact tests of epoxy composites reinforced with giant bamboo fibers. *Mater Res* 18:178–184
27. Latha PS, Rao MV, Kumar VK, Raghavendra G, Ojha S, Inala R (2016) Evaluation of mechanical and tribological properties of bamboo–glass hybrid fiber reinforced polymer composite. *J Ind Text* 46(1):3–18
28. Abilash N, Sivapragash M (2016) Optimizing the delamination failure in bamboo fiber reinforced polyester composite. *J King Saud Univ-Eng Sci* 28(1):92–102
29. Zuhudi NM, Jayaraman K, Lin RJT (2016) Mechanical, thermal and instrumented impact properties of bamboo fabric-reinforced polypropylene composites. *Polym Polym Compos* 24(9):755–766
30. Sankar K, Sá Ribeiro RA, Sá Ribeiro MG, Kriven WM (2017) Potassium-based geopolymer composites reinforced with chopped bamboo fibers. *J Am Ceram Soc* 100(1):49–55
31. Sukmawan R, Takagi H, Nakagaito AN (2016) Strength evaluation of cross-ply green composite laminates reinforced by bamboo fiber. *Compos B Eng* 84:9–16
32. Sánchez ML, Morales LY, Caicedo JD (2017) Physical and mechanical properties of agglomerated panels made from bamboo fiber and vegetable resin. *Constr Build Mater* 156:330–339
33. Zhou S, Li J, Kang S, Zhang D (2020) Effect of carbonized ramosissima nanoparticles on mechanical properties of bamboo fiber/epoxy composites. *J Nat Fibers*, 1–10
34. Wong KJ, Yousif BF, Low KO (2010) The effects of alkali treatment on the interfacial adhesion of bamboo fibres. *Proc Inst Mech Eng L: J Mater Des Appl* 224(3):139–148
35. Kushwaha PK, Kumar R (2010) Effect of silanes on mechanical properties of bamboo fiber-epoxy composites. *J Reinf Plast Compos* 29(5):718–724
36. Kang JT, Kim SH (2011) Improvement in the mechanical properties of polylactide and bamboo fiber biocomposites by fiber surface modification. *Macromol Res* 19(8):789–796
37. Ma L, He H, Jiang C, Zhou L, Luo Y, Jia D (2012) Effect of alkali treatment on structure and mechanical properties of acrylonitrile–butadiene–styrene/bamboo fiber composites. *J Macromol Sci B* 51(11):2232–2244
38. Liu W, Chen T, Wen X, Qiu R, Zhang X (2014) Enhanced mechanical properties and water resistance of bamboo fiber–unsaturated polyester composites coupled by isocyanatoethyl methacrylate. *Wood Sci Technol* 48(6):1241–1255
39. Chang F, Kwon JH, Kim NH, Endo T, Lee SH (2015) Effect of hot-compressed water treatment of bamboo fiber on the properties of polypropylene/bamboo fiber composite. *BioResources* 10(1):1366–1377
40. Liu W, Chen T, Xie T, Lai F, Qiu R (2015) Oxygen plasma treatment of bamboo fibers (BF) and its effects on the static and dynamic mechanical properties of BF-unsaturated polyester composites. *Holzforschung* 69(4):449–455
41. Manalo AC, Wani E, Zukarnain NA, Karunasena W, Lau KT (2015) Effects of alkali treatment and elevated temperature on the mechanical properties of bamboo fibre–polyester composites. *Compos B Eng* 80:73–83
42. Li Y, Jiang L, Xiong C, Peng W (2015) Effect of different surface treatment for bamboo fiber on the crystallization behavior and mechanical property of bamboo fiber/nanohydroxyapatite/poly (lactic-co-glycolic) composite. *Ind Eng Chem Res* 54(48):12017–12024

43. Azwa ZN, Yousif BF (2019) Physical and mechanical properties of bamboo fibre/polyester composites subjected to moisture and hygrothermal conditions. *Proc Inst Mech Eng L: J Mater Des Appl* 233(6):1065–1079
44. Khan Z, Yousif BF, Islam M (2017) Fracture behaviour of bamboo fiber reinforced epoxy composites. *Compos B Eng* 116:186–199
45. Lin J, Yang Z, Hu X, Hong G, Zhang S, Song W (2018) The effect of alkali treatment on properties of dopamine modification of bamboo fiber/poly(lactic acid) composites. *Polymers* 10(4):403
46. Nabinejad O, Debnath S, Beh JK, Mohammad YA (2018) Mechanical performance and moisture absorption of unidirectional bamboo fiber polyester composite. In: *Materials science forum*, vol 911. Trans Tech Publications Ltd., pp 88–94
47. Wang F, Zhou S, Yang M, Chen Z, Ran S (2018) Thermo-mechanical performance of polylactide composites reinforced with alkali-treated bamboo fibers. *Polymers* 10(4):401
48. Niu F, He R, Li J (2018) The influence of polypyrrole coatings on the mechanical and friction and wear properties of bamboo fiber filled PA6 composites. *Surf Interface Anal* 50(1):111–116
49. Mandal S, Alam S, Varma IK, Maiti SN (2010) Studies on bamboo/glass fiber reinforced USP and VE resin. *J Reinf Plast Compos* 29(1):43–51
50. Zuhudi NZM, Lin RJ, Jayaraman K (2016) Flammability, thermal and dynamic mechanical properties of bamboo–glass hybrid composites. *J Thermoplast Compos Mater* 29(9):1210–1228
51. Ramachandran M, Bansal S, Raichurkar P (2016) Experimental study of bamboo using banana and linen fibre reinforced polymeric composites. *Perspect Sci* 8:313–316
52. Kumar N, Mireja S, Khandelwal V, Arun B, Manik G (2017) Light-weight high-strength hollow glass microspheres and bamboo fiber based hybrid polypropylene composite: a strength analysis and morphological study. *Compos B Eng* 109:277–285
53. Sathish S, Kumaresan K, Prabhu L, Vigneshkumar N (2017) Experimental investigation on volume fraction of mechanical and physical properties of flax and bamboo fibers reinforced hybrid epoxy composites. *Polym Polym Compos* 25(3):229–236
54. Nor AFM, Sultan MTH, Jawaid M, Talib ARA, Azmi AMR, Harmaen AS, Asa'ari AZ (2018) The effects of multi-walled CNT in bamboo/glass fibre hybrid composites: tensile and flexural properties. *BioResources* 13(2):4404–4415
55. Haddou G, Dandurand J, Dantras E, Maiduc H, Thai H, Giang NV, Trung TH, Pontains P, Lacabanne C (2019) Mechanical properties of continuous bamboo fiber-reinforced biobased polyamide 11 composites. *J Appl Polym Sci* 136(23):47623
56. Huang JK, Young WB (2019) The mechanical, hygral, and interfacial strength of continuous bamboo fiber reinforced epoxy composites. *Compos B Eng* 166:272–283
57. Kumari S, Kumar R, Rai B, Kumar G (2019) Effect of fiber content on thermal and mechanical properties of euphorbia coagulum modified polyester and bamboo fiber composite. *Mater Res Express* 6(12):125341
58. Chin SC, Tee KF, Tong FS, Ong HR, Gimbin J (2020) Thermal and mechanical properties of bamboo fiber reinforced composites. *Mater Today Commun* 23:100876
59. Irawan AP, Sukania IW, Anggarina PT, Danendra AR, Baskara GD (2020) Socket prosthesis manufacturing process made from bamboo fiber composite materials. In: *IOP Conference Series: Materials Science and Engineering*, vol 852, no 1, p 012042
60. Zhang K, Sun Y, Wang F, Liang W, Wang Z (2020) Progressive failure and energy absorption of chopped bamboo fiber reinforced polybenzoxazine composite under impact loadings. *Polymers* 12(8):1809



# Review of the Approaches and Modeling Methodology for Lithium-Ion Battery Thermal Management Systems in Electric Vehicles



Indraneel Naik and Milankumar Nandgaonkar

**Abstract** The global level market penetration of electric vehicles (EVs) is rising every year. Faster adoption of electric vehicles has hindrances such as performance deficiencies, low range, and frequent need of charge. A common denominator of most of the roadblocks is the climatic sensitivity of the batteries leading to performance, life, and safety concerns. There lies a temperature range for the optimal performance, life and safety during the operation. Thus, maintaining the temperature in this range is the primary purpose of the battery thermal management system. There are mainly two categories in battery thermal management systems, namely active and passive systems. These systems manage the battery temperature in a vast range of climatic and usage conditions. They are continuously being researched and modified. Experimental techniques to determine the optimal performance of such systems are cost and time inefficient. Instead, modeling the battery along with the thermal management system provides a promising alternative. In recent years, hybrid systems are being proposed for effective thermal management.

**Keywords** Li-ion battery · Battery thermal management system · Electrochemical characteristics · Phase change materials · Heat pipe

## Abbreviations

$U$	Open-circuit voltage, V
$V$	Battery terminal voltage, V
$C$	Specific heat capacity, $\text{J kg}^{-1}\text{K}^{-1}$
$k$	Thermal conductivity, $\text{W m}^{-1}\text{K}^{-1}$
$I$	Current, A
$T$	Temperature, K or $^{\circ}\text{C}$
$\dot{q}_{\text{gen}}$	Rate of total heat generation, W

---

I. Naik (✉) · M. Nandgaonkar  
Department of Mechanical Engineering, College of Engineering Pune (COEP), Savitribai Phule  
Pune University, Pune, India

$\dot{q}_{\text{ohmic}}$	Rate of ohmic heat generation, W
$\dot{q}_{\text{entropic}}$	Rate of entropic heat generation, W
$\dot{q}_{\text{sink}}$	Rate of heat removal from battery, W
$h$	Convective heat transfer coefficient, $\text{W m}^{-2}\text{K}^{-1}$
$A$	Surface area of battery, $\text{m}^2$
$m$	Mass of battery, kg
DoD	Depth of discharge
$Q_T$	Theoretical battery capacity, Ah
$Y$	Conductance, $\Omega^{-1}$
$T_{\text{ref}}$	Reference temperature, K or C
Bi	Biot number
$t$	Time

### ***Subscripts***

bat	Battery
surr	Surrounding
ref	Reference
x	X-axis
y	Y-axis
z	Z-axis
PCM	Phase change material

## **1 Introduction**

The ‘Global EV outlook 2019’ report suggests that the year 2018 marks a milestone in the history of electric vehicles (EVs), since, for the first time, the worldwide stock of electric vehicles exceeded 5 million, representing a whopping 63% rise from the year before, number of charging points reaching close to 5.2 million, 44% more than previous year [1]. The recent advancements in electric vehicle technology have revolutionized the mobility concept all over the globe. The trend is likely to continue in forthcoming years despite the temporary slowdown of the auto-industry around the end of the year 2019. The whole dynamics are governed by a lot many factors such as technological advancements, fuel prices, sustainability objectives and government policies, to name a few. Especially in ambitiously developing countries, the mobility sector is expected to cater to the mobility requirements of billions of people, also meeting the ambitious ‘Go-Green’ goals set forth by the world toward a sustainable future. With ever-rising fuel prices and the alarming air pollution indices, the battery electric vehicles (BEVs), hybrid electric vehicles (HEVs), and plug-in hybrid electric vehicles (PHEVs) will be the future of the transportation sector. The prime features

of EVs, namely their high energy efficiency and low pollution rate, are responsible for their popularity.

There are still many roadblocks in a full-fledged implementation of EVs, battery replacement cost and battery life, availability of charging stations, charging time, and single-charge range, to name a few prominent ones. The high energy density (high capacity) and high charge–discharge rate (high performance), and more number of cycles (longer life) are the three most sought features of the batteries. Researchers are continuously striving to devise different battery chemistries to meet these requirements to make EVs compatible with conventional ICE vehicles.

Battery capacity and performance cannot be increased beyond a specific limit owing to the internal heat generation causing battery temperature to rise beyond allowable limits, which in turn poses a safety challenge in front of EVs. Maintaining the temperature of Li-ion battery (LIB) packs within safety limits is critical since a high temperature causes degradation of the electrodes. In contrast, extremely low temperature increases the internal resistance of the cells leading to a decrease in capacity and slower charge–discharge rates [2]. The cycle life of batteries is also adversely affected when operating at extreme-temperature conditions. Another factor that affects the life of a LIB is the cell temperature gradient. The cell-to-cell temperature gradient must be limited to maximize LIB life. The reduction in LIB cycle life, performance, and capacity ultimately affects the cost-to-customer, making EVs a less viable option for manufacturers and customers against conventional vehicles. Thus, researchers all over the world are concentrating their efforts to maintain the temperature of the batteries within limits to improve safety, life, and performance.

Battery thermal management systems (BTMSs) have a significant role in the overall implementation strategies of EVs. BTMS is expected to fulfill two primary requirements, to maintain the LIB temperature within limits of 15–35 °C [3] and to reduce the temperature gradient among the cells <5 °C [4]. Apart from these, there are several requirements for BTMS, mainly from vehicle manufacturers. It includes less dead weight and parasitic power consumption, compact and cost-effectiveness, secure packaging, and compatibility with the location in the vehicle, reliability, and easy accessibility for maintenance. BTMS has evolved from a simple natural convection system to as complicated as the hybrid ones that utilize the pros of two or more methods and try to eliminate the cons. Nevertheless, BTMS still fails in adverse usage or extreme climatic conditions and is hence continuously being researched upon and developed.

Researchers have been working in the area of battery thermal management for more than two decades. The systems are either active or passive in operation. There have been at least 4 groups of equally competent options for battery cooling, viz. air, liquid, and PCM and heat pipe, among few others. The selection criterion for the right BTMS approach is based on the overall feasibility, also considering the climatic variations and the usage conditions. It is not possible to experimentally test each BTMS option to find the best one that suits most of the requirements. Hence, modeling the cell and thermal management system becomes of utmost importance. To summarize, as said earlier, the temperature of the cell decides its performance,

life, and safety that, in turn, decide the acceptability of the EVs. The temperature of the cell depends on heat generation, thermo-physical properties, and heat removal.

Notable review papers in this area include Rao and Wang [5], who compared air-, liquid-, and PCM-based thermal management systems in BEV and HEVs. Another notable contribution is from Pan et al. [6], who reviewed different combinations of phase change materials (PCM) and detailed the ways of improving the thermal conductivity of PCMs. Wang et al. [7] reviewed different thermal characteristics of lithium-ion batteries and their importance in the design consideration of thermal management systems. In 2017, Liu et al. [8] analyzed recent advancements in thermal management systems based on solid–solid and solid–liquid phase change processes. Xia et al. [9] analyzed the problem of thermal management in cell level and module level perspectives separately. They dealt with the heat generation on the cell level and heat balance equation on the module level, where BTMS is implemented. In particular, air-based systems were compared to the liquid-based ones.

A review paper is required to take a holistic overview of battery thermal management systems from the below perspective.

- (a) System parameters involved in deciding the cell temperature (open-circuit potential, internal resistance, heat capacity)
- (b) System parameters that quantify the system performance (voltage, capacity) and the effect of (a) on (b)
- (c) Surrounding parameters involved in deciding the cell temperature (BTMS types)
- (d) Modeling methodology for the system (cell) and surroundings.

This paper is arranged as follows. Section 2 of this paper establishes in detail the need for thermal management of lithium-ion batteries, followed by a brief overview of a few of the fire incidents case studies. Section 3 introduces existing Li-ion cell chemistries and details the typical electrochemical and thermophysical parameters of Li-ion cells that characterize them. Section 4 briefs the battery and BTMS modeling philosophy followed by Sect. 5 that enlists research carried out in developing various battery thermal management systems. Lastly, a future direction to the ongoing research is proposed, which involves combining two or more BTMS options.

## 2 The Need for Thermal Management

BTMS has an impact on the performance, life, and safety of the EVs and hence is becoming an inseparable part of them. Generally, the acceptable operating range for LIB is  $-20$  to  $60$  °C, though the range for optimal performance and life is pretty narrow, about  $15$ – $35$  °C [10]. If the temperature is out of these bounds, it causes either the performance or life or the safety issues. Performance is measured in two aspects: power delivery and storage capacity. Most of the temperature effects on LIBs can be attributed to slowing down or speeding up chemical reactions. Other than that, the

ionic conductivity of the electrolyte and the electrodes also gets affected at adverse temperatures. The effect of temperature on these parameters can be split into 2 parts.

## 2.1 Effect of Low Temperature

There are various scenarios in which LIBs can be subjected to low temperatures. They include seasonal variation, high latitude countries, space missions, etc. There is much research on low-temperature performance degradation of LIBs. In 2001, Nagasubramanian [11] shown that the energy and power density a Panasonic 18,650 cylindrical cell dropped by over 95% when taken from 25 to  $-40$  °C. It will be seen in Sect. 3 how performance quantifying parameters like battery capacity and voltage get affected due to low temperature. The reasons for this were attributed to the loss in ionic conductivity due to increased viscosity of electrolyte, charge transfer resistance, slow diffusion of ions in the electrodes, and lithium plating. These all ultimately cause an increase in the internal resistance of the battery. Due to these effects, low temperature hampers the battery capacity far more than the high temperature, as shown in Fig. 1.

To avoid loss of ionic conductivity, various electrolyte additives like  $\text{LiPO}_2\text{F}_2$  were suggested [13] for NMC pouch cells. To counter other effects, the research is still ongoing. Nevertheless, managing the temperature by an external BTMS is still a cost-effective and promising option.

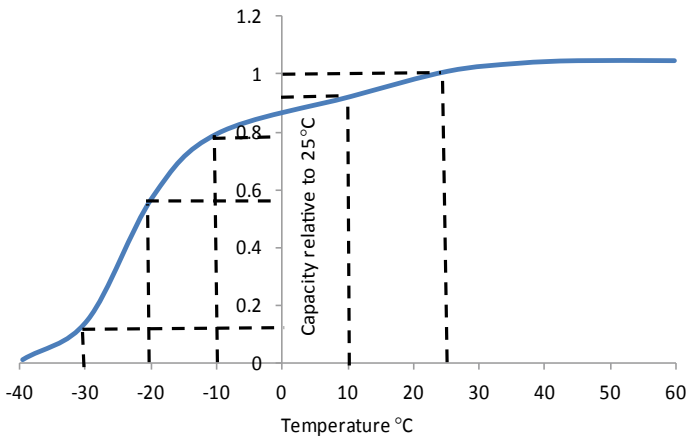


Fig. 1 Relative capacity retention at low temperatures [12]

## 2.2 Effect of High Temperature

High temperature is a more probable cause of performance and life sacrifice or, in cases, safety issues than low temperature. This is because there are several scenarios which can result in high temperature. High ambient temperatures are typical with low latitude countries, where most of the world's population is concentrated. High power applications demanding high discharge rates, and hence, high internal heat generations are another cause. Even in low ambient, high heat generation rates can supersede the heat rejection rates causing performance degradation due to high temperatures. Insufficient heat ventilation provided is another cause of high temperatures. The high-temperature effect is attributed to an increase in the charge transfer resistance at the interfaces and solid electrolyte interface (SEI) layer, increase in resistance of electrodes and electrolyte [14], inhomogeneous distribution or diffusion of lithium-ions, etc. [15]. As can be seen in the graph, at the  $n$ th cycle, the discharge capacity is less at a higher temperature.

High temperatures have an impact on the cycle and calendar life of LIBs as well, as shown in Fig. 2. The battery is considered unfit for EV applications after its capacity reaches below 80% of its nominal capacity. Cycle life is defined as the number of cycles a battery can perform before its capacity falls below 80% of the nominal capacity. This impacts the most onto the consumer's pocket and hence by and largely governs the EV acceptance.

Thermal aging is mostly because of the aging of electrodes or electrolytes. The electrode capacity irreversibly reduces due to the permanent intercalation of Li-ions into the cathode structure. The electrolyte also changes in chemical composition resulting in a life loss. Another result of high temperature is a significant roadblock

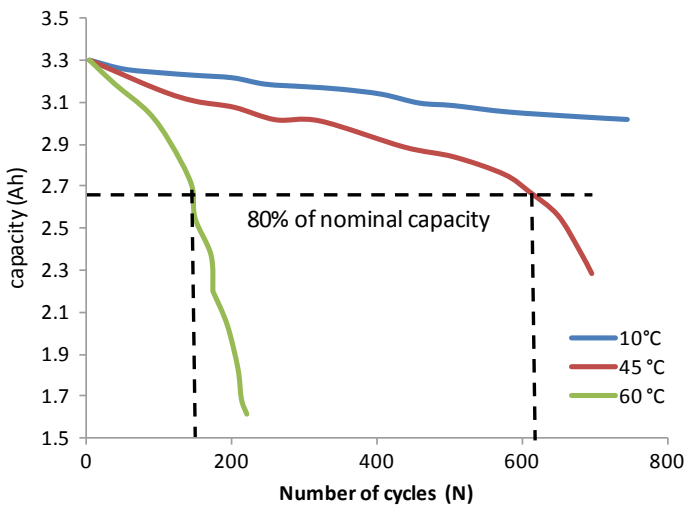


Fig. 2 Effect of high temperatures on cycle life [16]

in the overall implementation strategies of EVs. In case of faulty manufacturing or handling practices, high temperatures sites may witness thermal runaway, which finally can cause fire and explosion of the battery, posing a safety challenge. Although such mishaps are not very common, they are not something to get completely ignored. Table 1 briefs a few cases of fire hazards that, at times, made manufacturers call back all the vehicles sold.

The list is unending, and hence, an efficient BTMS is of utmost importance. The first step toward the design of an efficient BTMS is the understanding and modeling of cell behavior under versatile usage and climatic conditions. For this to happen, a study of electrochemical and thermophysical characteristics is essential in predicting the response of Li-ion cells to the electrical loads and climatic conditions. This will enable modeling the cell and the BTMS around it and designing an efficient BTMS accordingly.

### 3 Li-Ion Battery Characteristics

It is important to note that Li-ion cell is not a single chemistry, but the terminology covers a wide variety of chemistries. Li-ion cells have provided a promising option to electric vehicle technology due to their high power, high energy density, lightweight, low self-discharging behavior, and longer life cycle compared to their counterparts. Several Li-ion cell chemistries are being discovered to attain the goals of higher energy density and power density. Table 2 gives specifications of the typical chemistries that have been used with the electric vehicles for the last 3 decades. Although versatile in chemical composition, all types of cells possess a typical set of electrochemical and thermophysical characteristics that categorize them under the single umbrella of ‘lithium-ion cells.’ These characteristic parameters follow their unique patterns specific to cell chemistry and type, though the way these characteristics govern the overall cell performance is similar. The next section describes how these characteristic parameters respond to change in operating conditions such as discharge profile, temperature, and cycle age.

#### 3.1 *Electrochemical Characteristic Parameters*

Performance, life, and safety of the battery can be quantified in terms of electrochemical characteristics that include terminal voltage, open-circuit voltage (OCV), capacity, overpotential resistance, etc. The electrochemical parameters can again be split into two types. The first type is the governing parameters that include OCV, overpotential resistance, and entropic coefficient. As the name suggests, these parameters govern the overall electric and thermal behavior of the cell under operating conditions. The other category is performance parameters. This includes the voltage, capacity, and power, which quantify the performance. The operating conditions include the

**Table 1** List of BEV fire incidents [17, 18]

S. No.	Model	Battery specification	Range	Incident summary
1	Zotye M300 EV	LiFePO <sub>4</sub> , 35.2 kWh	160 km	China, in April 2011, Due to the leaking of battery cells, insulation was damaged between battery cells and containers. It led to short circuits, and the vehicle finally caught fire
2	Chevrolet Volt	16 kWh, Li-ion, hybrid	56 km electric only	June 2011, NHTSA subjected to side pole impact crash test followed by a post-impact rollover, caught fire three weeks later in the test center parking lot, burning nearby vehicles
3	Fisker Karma	20 kWh, Li-ion, hybrid	51 km electric only	2012, Texas and California, Fire at home, and in the parking lot. Fire because of the cooling fan. The battery was not identified as the cause
4	Mitsubishi iMIEV	16 kWh,	100 km	2013, Mizushima, Fire took place in the battery pack assembly plant itself during charging/discharging
5	Tesla Model S & X	60–85 kWh variants	350–500 km as per the variant	Multiple incidents during driving or charging 2013, Highway in Washington, Merida-Mexico, Murfreesboro-Tennessee, Irvine-California 2016, Norway, Biarritz-France, 2017, California 2018, Los Angeles 2019, Hong Kong, Belgium, Russia, England
6	Nissan Leaf	40 kWh	240 km	2015, Flower Mound, Texas
7	VW e-Golf	24.2 kWh	140 km	2017, Triangel, Germany
8	Porsche Panamera E-Hybrid	14.1 kWh, Li-ion, hybrid	50 km electric only	2018, fire during charging 2019, fire after an accident
9	Hyundai Kona Electric	64 kWh	400 km	Fire in household parking incidences 2019, Canada 2019, South Korea

(continued)



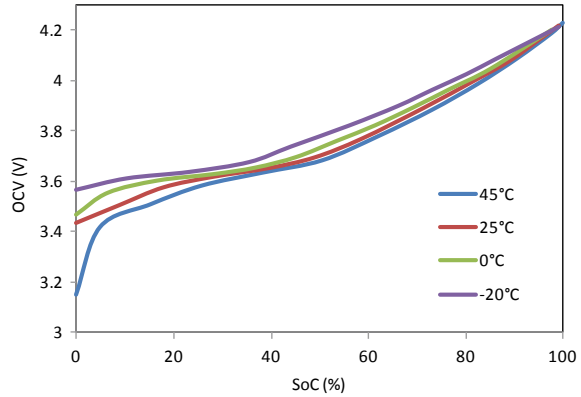
**Table 1** (continued)

S. No.	Model	Battery specification	Range	Incident summary
10	BMW i8 hybrid	7.1 kWh, hybrid	37 km electric only	2019, Netherlands, fire at the car dealership

**Table 2** Typical Lithium-ion chemistries used in electric vehicles

	Year introduced	Cathode (positive)	Anode (negative)	Nominal voltage (V)	Energy density (Wh kg <sup>-1</sup> )	Life-span (Cycles)	Runaway temp. (°C)
Lithium cobalt oxide (LCO)	1991	LiCoO <sub>2</sub>	Graphite	3.6	150–200	500–1000	150
Lithium iron phosphate (LFP)	1993	LiFePO <sub>4</sub>	Graphite	3.3	90–120	1000–2000	270
Lithium manganese oxide (LMO)	1996	LiMn <sub>2</sub> O <sub>4</sub>	Graphite	3.7	100–150	300–700	250
Lithium nickel cobalt aluminum oxide (NCA)	1999	LiNiCoAlO <sub>2</sub>	Graphite	3.6	200–260	500	150
Lithium nickel manganese cobalt oxide (NMC)	2008	LiNiMnCoO <sub>2</sub>	Graphite	3.7	150–220	1000–2000	210
Lithium titanate (LTO)	2008	LMO/NCA	Li <sub>4</sub> Ti <sub>5</sub> O <sub>12</sub>	2.4	70–80	3000–7000	–

**Fig. 3** OCV-SoC curves at various temperatures for NMC cell [21]



discharge profile and the ambient temperature decide the electrical and thermal state of the battery by defining the two parameters, namely state of charge (SoC) and battery temperature ( $T_{\text{batt}}$ ). A direct link of the performance, life, and safety can be established through SoC and  $T_{\text{batt}}$  with the operating conditions such as discharge profile and temperature.

*Open-circuit voltage (U):* Open-circuit voltage is the voltage across electrode terminals when there is no chemical reaction going on inside it to drive the current. Thus, it is the theoretical maximum terminal voltage across the cell when it is delivering no current. In other words, it is the theoretical voltage when two half cells are combined. During operation, when the cell delivers current, the voltage across it is less than the OCV. This is because the cell has its internal resistance that causes the potential to drop and hence results in loss of available energy. The open-circuit voltage is a function of the charge that is left on the cell-state of charge (SoC) and its temperature. It also is a function of the number of cycles performed by the cell [19, 20]. Battery terminal voltage and the rate of heat generation inside the cell depend on OCV, and hence its study carries importance in modeling the cell. Figure 3 shows the variation of OCV with respect to SoC, temperature. It is important to note that this curve is specific to the cell tested and every chemistry will have its typical curve that depicts the dependence of OCV on SoC and temperature. Especially, whether the increase or decrease in OCV with temperature depends on the next electrochemical characteristic parameter, the entropic coefficient, which indicates the sign of the change in  $U$  with respect to  $T$ .

*Entropic coefficient:* The entropic coefficient signifies the response of OCV toward the cell temperature. It is defined as the rate of change of OCV with respect to temperature,  $U/T$ . If the entropic coefficient is negative, it means the OCV decreases with the increase in temperature and vice versa. We have seen that the OCV is a function of SoC and temperature. It is observed that the OCV of a Li-ion cell follows approximately a linear trend with temperature when SoC is kept constant. Hence, its slope  $U/T$  will be a constant at a particular value of SoC. In other words, the entropic coefficient  $U/T$  is a function of SoC alone and hence is expressed as a polynomial

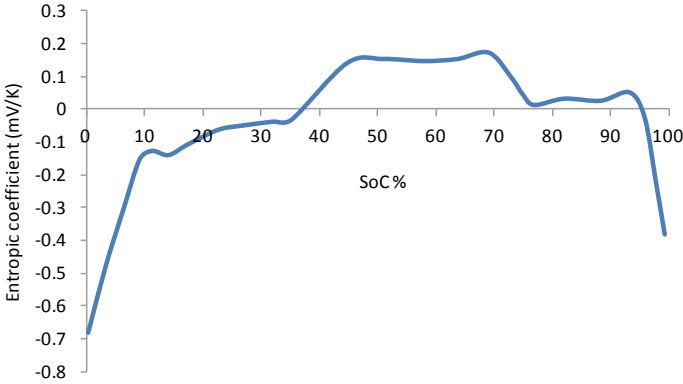


**Fig. 4** Entropic coefficient across all SoC levels for LFP cell [22]

in SoC. The significance of studying the entropic coefficient traces back to the rate of heat generation, which, as we will see in Sect. 4, is a combination of ohmic and entropic heat generations. The entropic heat generation is directly proportional to the entropic coefficient, and in fact, the sign of the entropic coefficient decides whether the entropic heat component will be liberated or absorbed. As we can see the typical nature of the curve in Fig. 4, the entropic coefficient is positive when the battery SoC is high, but shifts to negative values when the battery SoC is low. It is important to note that this curve is specific to the cell tested in the literature [22], and any other chemistry or other cells of the same chemistry need dedicated testing done to get their unique entropy coefficient profile.

*Battery terminal voltage (V), power delivery, and storage capacity:* Battery terminal voltage is the actual voltage that appears across the terminals of the cell when in operation. It is a function of DoD, temperature, and the current drawn from the cell. There is always an upper and lower cut-off on this voltage for the cell to function without compromising its life and safety of the operation. These cut-offs are different for different cells. Nevertheless, the family of lithium-ion cells generally follows typical curves for different charge–discharge rates.

Temperature also affects the terminal voltage as the temperature dictates the rates of chemical reactions and the properties of cell components. Figure 5 indicates the variation of terminal voltage with respect to the temperature and discharge current for an LFP cell [23]. The voltage decreases with decreasing temperature and increasing current. However, it can be evidently seen that the effect of current on the capacity is less dominant as compared to the temperature. Needless to say, that these curves are specific to the LFP cell tested and need to be established for different chemistries separately. The voltage curves get similarly affected while charging as well, as is came across in the literature [24].

The significance of studying battery terminal voltage is in deciding battery power delivery and storage capacity. Battery power delivery is defined as the product of terminal voltage and discharges current. It decides the torque and the speed of the

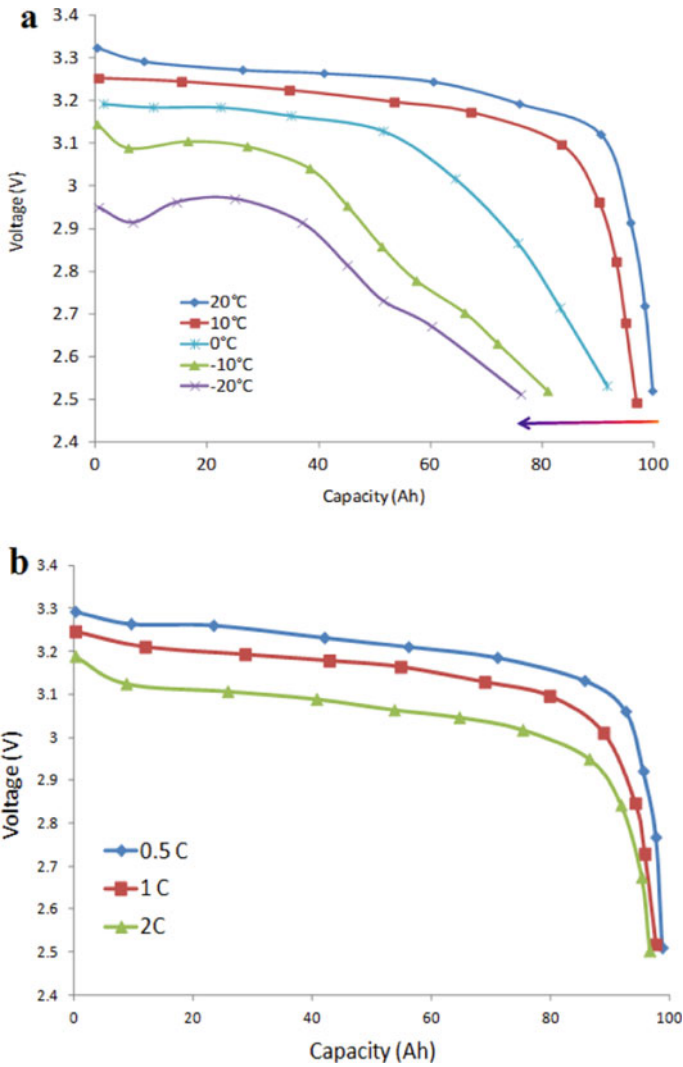


**Fig. 5** LFP battery voltage and capacity for varying **a** temperature, **b** discharge rate [23]

vehicle. Reduction in temperature reduces the power delivery. Hence at low climatic temperatures, higher charge–discharge rates are not possible. It is important to note here that the internal heat generation of the battery acts as a savior at low climatic temperatures. The overpotential resistance that is the next electrochemical parameter increases to such large values at low temperatures that the rate of heat generation is very high. This leads to self heating of the battery increasing its temperature and thereby reducing the resistance and increasing the available power and storage capacity. Storage capacity is defined as the total amount of charge the battery can

deliver (product of current and time of discharge) before its terminal voltage falls below the cut-off limit. Determination of the battery capacity holds its importance in the determination of time for which the battery will last at given discharge cycle and temperature; in essence, it tells us the range of an EV. It is also useful in the determination of the SoC of the battery. Reduction in temperature brings the terminal voltage close to the lower cut-off sooner, and hence, the storage capacity decreases at lower temperatures.

*Overpotential resistance (R):* When the current passes through the battery, there is a drop in the potential across its electrodes due to various effects, called the overpotential and the associated resistance is termed as overpotential resistance. It is given as  $R = (U - V)/I$ , where  $U$  is OCV,  $V$  is terminal voltage, and  $I$  is the current passing through the battery. It can also be defined as the slope of the voltage–current characteristics curve for a battery, as explained in the literature [25]. The V–I characteristics during discharge are linear and the slope, or in essence, the resistance changes as a function of SoC and temperature. Three effects sum up to this loss in the potential, namely activation overpotential, ohmic overpotential, and concentration overpotential. The first one deals with the energy required for the reaction to take place. Second is the resistance to the flow of electrons inside the electrolyte and across the interfaces. The third is generated due to spatial variations and is more prominent when the charge concentration on the electrodes is reduced. The reason for the existence of overpotential is the chemical reactions taking place inside the cell, and hence, temperature is another factor, apart from the SoC that affects it. Figure 6 represents a variation of overpotential resistance with respect to temperature and SoC and aging.

The inverse of this overpotential resistance is called conductance, denoted by  $Y$ . This parameter will be relevant in Sect. 4, where the modeling of the Li-ion cells is discussed.

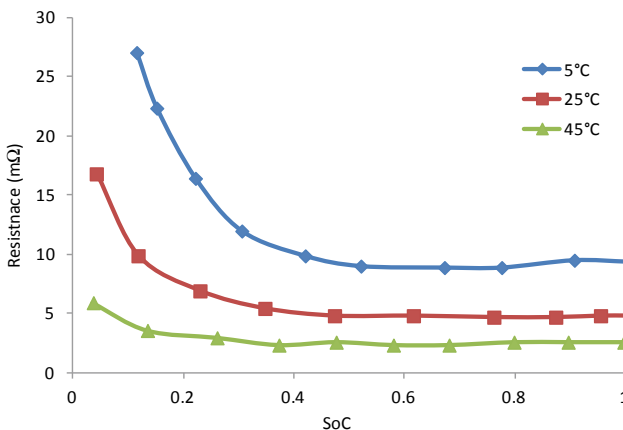


Fig. 6 Equivalent overpotential resistance of the LMO cell during the discharge [26]

### 3.2 Thermophysical Characteristic Parameters

Battery temperature dictates not just the safety and life of the battery, but also its performance. Temperature affects the OCV and overpotential resistance of the battery, which in turn controls the available terminal voltage and capacity of the cell. The rate of heat generation, if not entirely compensated by the battery heat sink, translates to the temperature of the cell depending on the thermophysical characteristics of the cell. Specific heat capacity is the most critical thermophysical characteristic parameter that decides the temperature of the cell.

*Specific heat capacity (C):* It is, in general, defined as the heat absorbed or released by a unit mass of material when it undergoes a unit temperature change, indicated in SI units as ( $\text{J kg}^{-1} \text{K}^{-1}$ ). The average specific heat capacity of a cell is a function of cell chemistry (NMC, LFP, LCO, and NCA), cell type (pouch, prismatic, cylindrical, etc.), and temperature. There are various methods of heat capacity determination, heat balance equation being at the heart of all. One approach is the method of calorimetry. There are different types of calorimeters, such as accelerating rate calorimeter, heat flow calorimeter, and differential scanning calorimeter [27, 28]. The second approach is to take a mass-weighted average of the specific heat capacity of each of the cell components such as cathode, anode, electrolyte, separator, container [29]. The third approach is by mixing method, where the Li-ion cell is brought in contact with another metal of known thermal capacity. From the final temperature, the heat capacity of the cell can be calculated [30]. The fourth method is the transient thermal resistance method, where the cell is preheated either using external means or by internal heat generation during discharging and then allowed to cool under natural convection. The rate of fall of temperature and natural heat transfer coefficient can give the specific heat capacity using Newton's law of cooling [31]. Evaluation of the heat capacity of the cell is essential since it decides the transient thermal response of the cell toward the heat generation and removal rates. The heat capacity of the Li-ion cell varies with respect to temperature and SoC, as indicated in Fig. 7.

*Thermal conductivity (k):* It is known that the thermal conductivity of electrode and electrolyte materials is so low (usually  $k \sim 1 \text{ W m}^{-1} \text{K}^{-1}$ ) [33] that they can be considered as insulating toward heat. The copper and aluminum foils that support the electrodes, on the other hand, are excellent conductors [34, 35]. The result of this is a very low thermal conductivity of the pouch and prismatic cells in thickness direction [34] and cylindrical cells in the radial direction [36]. Such low thermal conductivity causes a significant temperature gradient inside prismatic or cylindrical cell geometries since Biot number for them is usually  $>0.1$ ; unlike pouch cells, where small volume-to-area ratio reduces Biot number to  $<0.1$ . A significant temperature gradient is an indicator of temperature non-uniformity within the cell, making the core temperature higher than the surface [37]. Thus, thermal conductivity has a role to play in the performance, safety, and life of the battery. A typical method implemented in the determination of thermal conductivity of pouch/ prismatic cells is based on Fourier's law of heat conduction [32]. It involves sandwiching the cell between two metal plates, where one plate is given known heat flux. By measuring the temperature

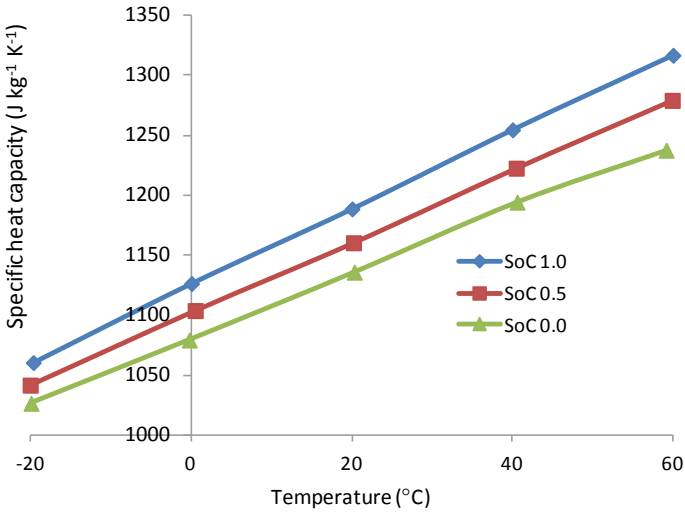


Fig. 7 Variation of specific heat capacity with temperature and SoC [32]

on either face of the cell, the thermal conductivity can be determined. The thermal conductivity of the Li-ion cell is as well a function of temperature and SoC, as indicated in Fig. 8.

High climatic temperatures, coupled with high discharge rates, can lead to high battery temperature and hence an effect on its performance and life. It is not always possible to carry out experimentation for the study of the impact of climate and usage conditions on cell performance, considering the time and the costs involved.

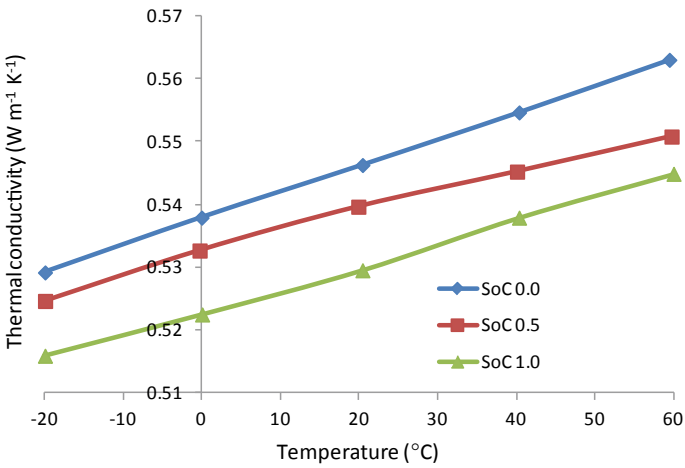


Fig. 8 Variation of thermal conductivity with temperature and SoC [32]



Modeling thus stands as the backbone of the modern BTMS design process. Modeling also helps in optimizing the system for performance and cost. An outstanding performing BTMS may not always be an economic one and vice versa. It is always a trade-off between performance and cost that makes modeling a crucial aspect of the whole BTMS design process.

## 4 Battery Modeling Approach: The Thermal Model

Newman, with other researchers, laid a foundation of battery modeling [38]. Since then, researchers all over the world have proposed various models to analyze the thermal behavior of a Li-ion cell under given climatic and usage conditions [39]. The modeling methodologies can be split into three categories, viz. mathematical models [38, 40, 41], physical models [42–44], and circuit models [45, 46]. Each category involves literature based on the prediction of electric, thermal, and aging aspects of the battery. These models can be one-, two-, or three-dimensional. The right model can be selected based on the nature of the physical problem, accuracy required, and computational power available.

The most popular modeling approach among all is the mathematical modeling due to its simplicity in implementation and low computational time. One of the first and still the most popular ‘thermal model’ was prescribed under this approach by Bernardi et al. [38]. The implementation of the thermal model can be split into two steps. The first step is the estimation of electrochemical parameters using experimental techniques. The second step is to evaluate the rate of heat generation and temperature using the thermal model. The former step gives parameters necessary for estimation of the rate of heat generation as a function of the battery discharge profile and temperature. Latter one gives the battery temperature as a function of the cell’s rate of heat generation, the rate of heat rejection to the surroundings, based on the geometrical parameters and thermophysical characteristics.

### 4.1 Estimation of electrochemical parameters

As said earlier, experimentation helps to establish functional relationships for the electrochemical parameters OCV ( $U$ ) and conductance ( $Y$ ).  $U$  and  $Y$  are both functions of the DoD and the temperature of the battery. They describe the battery chemistry, and hence, they are the link between the application environment and the battery behavior.

There are different polynomial function forms prescribed in the literature for expressing these parameters [19]. The most popular form is-

$$Y = \left[ \sum_{n=0}^5 b_n (\text{DoD}) a^n \right] e^{C_1 \left( \frac{1}{T_{\text{ref}}} - \frac{1}{T} \right)} \quad (1)$$

$$U = \left[ \sum_{n=0}^5 a_n (\text{DoD})^n \right] - C_2 (T - T_{\text{ref}}) \quad (2)$$

$a_n, b_n, C_1, C_2$  being the constants of the polynomial. The detailed process for the evaluation of these parameters and regression analysis for polynomial fitting can also be found in the literature [39, 47].

The DoD that appears in the above expressions depends on the usage discharge profile (I-t profile) and battery total deliverable capacity ( $Q_T$ ). It can be given as-

$$\text{DoD} = \frac{\int_0^t I dt}{Q_T} \quad (3)$$

$T_{\text{ref}}$  is taken as 298 K.  $T$ , the temperature of the battery, is not known in the beginning and is, in fact, an output of the thermal model. It is assumed as an initial guess for the evaluation of these parameters. They are then fed to the thermal model, which evaluates the temperature of the battery. This temperature is then given as feedback to the first step so that a revised estimate on the electrochemical parameters can be made.

## 4.2 Thermal Model

It gives the heat balance for the battery between the heat generation, rejection, and accumulation. The thermal model can either follow a differential equation approach where the cell's internal temperature gradients are taken into consideration [48], or a more commonly adopted approach of lumped model, where the entire cell is assumed at the same temperature. The lumped model can be used if  $\text{Bi} < 0.1$ , which is valid for thin pouch cells only. In either case, the thermal model uses the rate of heat generation based on the electrochemical parameters received from the previous step, and the rate of heat removal that is specific to the heat sink/BTMS. Based on the thermophysical properties of the battery, it can give the temperature of the battery at any time instant.

The heat generation rate in the battery is given as per the literature [38, 49–51].

$$q_{\text{gen}} = q_{\text{ohmic}} + q_{\text{entropic}} = I(U - V) - \frac{ITdU}{dT} \quad (4)$$

The voltage  $V$ , which is gauging parameter of the system performance, can be given as

$$V = U - \frac{I}{Y} \quad (5)$$

Hence, heat generation can be modified as,

$$\dot{q}_{\text{gen}} = \frac{I^2}{Y} - IT \frac{dU}{dT} \quad (6)$$

As can be seen in the above equation, the rate of heat generation has two components to it [52]. The first being ohmic generation, which is on account of the overpotential drop explained in the previous section. This is an irreversible component and is positive irrespective of whether the cell is charging or discharging. The second component, however, is a reversible component of heat generation, which means it can be positive or negative depending on whether the reaction is exothermic or endothermic. The entropy coefficient  $U/T$  discussed previously decides the nature of the reversible component of heat.

A lumped energy balance model for the battery then can be set as

$$mC \frac{dT}{dt} = \dot{q}_{\text{gen}} - \dot{q}_{\text{sink}} \quad (7)$$

In case, a three-dimensional differential heat conduction equation for pouch/prismatic cell can be set as,

$$\rho C \frac{T}{t} - \frac{\dot{q}_{\text{gen}}}{V} = k_x \frac{\partial^2 T}{x^2} + k_y \frac{\partial^2 T}{y^2} + k_z \frac{\partial^2 T}{z^2} \quad (8)$$

A similar equation for cylindrical cells can be set as

$$\rho C \frac{\partial T}{\partial t} - \frac{\dot{q}_{\text{gen}}}{V} = \frac{1}{r} \frac{\partial}{\partial r} \left( r \cdot k_r \frac{\partial T}{\partial r} \right) + \frac{1}{r^2} \frac{\partial}{\partial \theta} \left( k_{\theta} \frac{\partial T}{\partial \theta} \right) + \frac{\partial}{\partial z} \left( k_z \frac{\partial T}{\partial z} \right) \quad (9)$$

This model predicts the temperature and is then fed back to the previous step for the evaluation of electrochemical parameters for the next estimate of the rate of heat generation. The rate of heat generation by the battery and removal by the sink/BTMS in the above equation are both are functions of the battery temperature itself.

The rate of heat removal becomes a boundary condition for the heat balance equation considering the boundary between the battery as the system and BTMS as the surrounding. This boundary condition changes with a change in BTMS system design.

For example, if the battery is exposed to surroundings where natural convection is the only mode of heat rejection, we will have

$$\dot{q}_{\text{sink}} = hA(T_{\text{batt}} - T_{\text{surr}}) \quad (10)$$

If a passive BTMS that has PCM surrounding the cells is implemented, the boundary condition will be modified as, where  $x = t$  stands for the pouch/prismatic cell-PCM interface

$$\dot{q}_{\text{sink}} = -k_{\text{PCM}}A \left. \frac{dT}{dx} \right]_{x=t} \quad (11)$$

For cylindrical cell, the equation will be

$$\dot{q}_{\text{sink}} = -k_{\text{PCM}}A \left. \frac{dT}{dr} \right]_{r=R} \quad (12)$$

Hence, to set this boundary condition, the BTMS designer must have proper knowledge of the construction and properties of the BTMS. Different types of existing and under research BTMS will be discussed in the next section.

## 5 Battery Thermal Management Systems

BTMS has evolved from basic systems based on natural air convection to complicated systems such as PCM–liquid-based hybrid ones. As said earlier, there are two broad categories in which the BTMS can be split. They are active systems and passive systems. Active systems include forced air- and liquid-based cooling, which need external power to run. Though they can take higher loads, their operation adds to the cost/km of the EVs. Passive systems, on the other hand, are based on natural convection, phase change material (PCM), and heat pipe, which do not need external power. These systems cannot take higher loads since the rate of heat rejection ultimately depends on the natural convection heat transfer to the air. Both categories have their list of advantages and disadvantages which will be discussed at respective places. More recent research is on hybrid systems that combine the advantages of the two types and try to eliminate the cons. A comparative review among these systems is carried out at the end of this chapter considering the parameters such as heat removal rate, temperature uniformity, parasitic power consumption, compactness, range of climatic conditions, cost, and complexity.

### 5.1 Air Cooling

BTMS using air as a cooling medium came into existence as the pioneers in this field. There were two variants, viz. natural convection and forced convection-based systems, although forced convection is most widely used. The source of air also puts them into different categories as the systems using outside air, conditioned cabin air, and especially conditioned air. Air cooling has been the very first BTMS used for

the battery cooling application. This is primarily because of the easy availability and low complexity in its operation.

Natural convection is seldom used as a standalone system for battery thermal management due to the meager rate of heat transfer. It is found incapable of handling the heat generation rates that are encountered during higher discharge rates. Instead, natural convection is used in conjunction with other options. In the research involved with BTMS, natural convection is considered as a basis of comparison for gauging the effectiveness of a particular system. In 2002, forced BTMS was compared against the natural convection by Wu et al. [53]. The test set up consisted of a 12 Ah cylindrical, lithium-ion battery. They investigated the temperature distribution during discharging of the battery from 100% state of charge (SOC) till battery voltage falls to 2.8 V. They found that the temperature of the battery rises above the upper limit for a 0.5C discharge rate. Forced convection seems to lower the maximum temperature reached by about 15 °C, but the achieved temperature drop isn't found worth the parasitic power consumption and the non-uniformity generated.

Another innovative attempt was made by Mahamud and Park [54], where they proposed a forced air-based cooling system that reverses the direction of airflow in a fixed period. They found that with a 120 s reversal period, the temperature gradient reduced by 72%, and the maximum temperature came down by 1.5 °C compared with the unidirectional flow configuration.

Park [55], in the year 2013, worked on the air manifold shape design. He compared different manifold designs and found the one with a rectangular shape and tapered along the length that gives adequate heat and harmful gases removal. Fan et al. [56], in 2013, performed a 3D numerical analysis of a 15 Ah prismatic cell by changing the cell gap and the flow rate of air. It was observed that the decrease in either of these parameters causes the peak temperature of the cell to drop but with a simultaneous increase in temperature non-uniformity among the modules. Optimization of the numerical model is carried out, which yields 3 mm and 40.8 m<sup>3</sup>h<sup>-1</sup> as the optimized parameters.

The same year, Xun et al. [57] also came up with a similar conclusion when they numerically analyzed the effect of size and number of cooling channels on prismatic and cylindrical cell battery packs. They proposed two parameters to assess the cooling system performance, namely compactness of the battery stack, where smaller value means more compactness, and the energy efficiency that represents cooling performance compared to parasitic energy consumption. A smaller channel size is better for more energy density of the battery pack. But it increases the pumping power necessary, decreasing energy efficiency. So there is always a trade-off between energy efficiency and parasitic weight.

In 2014, Yu et al. [58] devised a system that has two inlet airports, one on each side of the battery. This facilitated the heat transfer to cells that were far off from one inlet, and they could directly receive the cold air from the second inlet. This helped in reducing the temperature gradient across the modules.

Xu and He [59] in 2015 analyzed the effect of changing the battery pack orientation from longitudinal to horizontal and adding a bottom duct of double I and double U type on maximum temperature rise and temperature gradient. Mohammadian and

Zhang [60] in the same year, numerically analyzed a thermal management system wherein a specially designed pin–fin was used to dissipate the heat from the 15 Ah prismatic cells. The system was considered for six different cases from no fin to as much as 40 pin fins of different length distributions between 1 and 36 mm. They found that these pin fins reduce the maximum temperature of the battery by 1.5% and temperature non-uniformity by about 13.7%.

There were subsequent attempts at the optimization of the airflow path, manifold design by several researchers, including Chen et al. [61] in the year 2017. Their numerical research included calculation of flow distribution using a flow resistance network model using the CFD tool. They suggested that the maximum temperature rise can be brought down by 41% by optimized flow distribution. In the same year, Xie et al. [62] worked on-air inlet and outlet angles and found that maximum temperature can be reduced by about 13% at angles of 2.5°. In the subsequent year, Hong et al. [63] added a secondary outlet vent in the duct and studied the effect of changing its size and shape. It was found that the temperature gradient was reduced by over 60%.

The use of air for battery cooling is the simplest and the cheapest approach. It is suitable for low power batteries. The other advantages of air-based cooling systems are low parasitic power consumption compared to liquid cooling, lightweight, easy maintenance, and no need for sealing as against liquid-based systems. These systems are also compatible with the location of the battery in the EVs since, in most of the cases, the battery is mounted at the base of the vehicle where the air is dragged over the base of the battery due to the motion of the vehicle. The forced air systems are still used in some of the EVs but are becoming less and less common owing to the high capacity and power batteries. These systems still prove to be useful when clubbed together with other passive systems.

By critical review of the literature, it is observed that with technological advancements, the batteries of higher energy density are being used in applications that demand higher discharge rates. The air cooling-based BTMS alone proves to be inefficient in such cases. This is evident because of the lower convective heat transfer coefficient of air, which in turn reduces the rate of heat withdrawn by an air-based BTMS. If an attempt is made to improve the heat transfer coefficient of air by increasing the Reynolds number, it will result in increased parasitic power demand by the BTMS. It also makes the air carrying ducts bulkier. Keeping sufficient space for the airflow between the cells results in lower volumetric energy capacity of the battery packs. Moreover, air cooling becomes ineffective at higher ambient temperatures.

## 5.2 *Forced Liquid Cooling*

This is another conventionally used BTMS. The coolants often used are water, oils, glycols, etc. The air cooling system discussed before is seen inadequate for high capacity, high power batteries due to low heat transfer coefficient and low specific heat capacity of air. There are two variants with forced liquid cooling systems. The first is where the battery directly comes in contact with the coolant, also called direct cooling.

The coolant, in this case, needs to be electrically insulating but thermally conducting. Obtaining such a combination has its own challenges and hence seldom used. The second variant is indirect cooling, where the coolant is pumped to the battery through a number of channels, which then absorbs heat from the battery. It is then sent to an external system, either an air-cooled heat exchanger or a dedicated chiller for re-circulation. The researches have focused mainly on three aspects regarding the force liquid cooling BTMS, namely geometry, number of channels, and the flow direction. In 2011, Jarret and Kim [64] studied BTMS with a cooling plate that had serpentine channels. They varied the width and the position of channels and studied the effect battery's maximum temperature and gradient, the pump pressure drop along the channel. They realized that wider channels give better performance in bringing down the maximum temperature, but less temperature gradient needs narrow channel tapering out toward the outlet. Thus, there was a trade-off, and all the three parameters could not simultaneously be optimized. In 2014, Jin et al. [65] worked on improving the decrease in convection performance along the length of the channel. They cut another mini-channel inclined with the original straight channels in the mini plate. They compared the two designs and found that the one with oblique channels gives better cooling performance even at low flow rates. Huo et al. [66] investigated the effect of changing the fluid mass flow rate, number of channels, and the direction of flow on the battery maximum temperature and gradient. They optimized these variables to attain maximum system performance. In 2015, Zhao et al. [67] investigate the effect of the mini-channel liquid cooling system on the 42,110 cylindrical  $\text{LiFePO}_4$  at 5C discharge. The number of mini-channels was varied from 2 to 16, and the mass flow rate was varied from  $5 \times 10^{-6} \text{ kg s}^{-1}$  to  $1 \times 10^{-3} \text{ kg s}^{-1}$ . The results were optimized for peak temperature, temperature gradient, and the cost of the system, and an optimum number of channels was prescribed as 8 with an overall mass flow rate of  $1 \times 10^{-4} \text{ kg s}^{-1}$ . In the year 2016, Lan et al. [68] numerically investigated the performance of microchannel-based BTMS with the battery for varying discharge rates, flow rates, number of mini-channels, flow direction through mini-channel. The flow rate of 0.8 LPM was found optimum for discharge rates up to 2C. The performance was assessed for optimum pumping power and cooling efficiency.

Nieto et al. [69] devised a BTMS for a battery developed for a traction application directed to the railway industry. Prismatic cells of NMC chemistry with 40 Ah nominal current and 3.7 V each were used. Two models were generated, optimized, and the results of numerical simulation, viz. coolant flow rate and inlet temperature were validated with the experimental setup. Qian et al. [70] analyzed the thermal performance of the mini-channel cooling system numerically. When the number of channels was varied from 2 to 7 with a width from 3 to 6 mm with a constant discharge rate of 5C and a mass flow rate of  $1 \text{ g s}^{-1}$ , 5 channels were found to be optimum with 6 mm channel width to reduce the pressure drop. Panchal et al. [71] investigated prismatic 20Ah  $\text{LiFePO}_4$  battery at discharge rates upto 4C in various climatic conditions from 5 to 35 °C. The highest rate of heat generation was observed at 4C discharge and 5 °C temperature, the lowest being at 1C and 35 °C. Rao et al. [72] attached an aluminum block with the battery and circulated cooling fluid through it. They found

that the maximum cooling effect is observed by increasing the length of the block and fluid velocity. Malik et al. [73] analyzed the battery pack with a cooling plate on either side of individual cells and by changing the fluid temperature for different discharge rates and drive cycles. They concluded that the liquid temperature of 30 °C was sufficient to maintain the battery within the safe temperature range.

These systems are more efficient in terms of heat removal as compared to air cooling systems. This is because of the high heat transfer coefficient and specific heat capacity of liquids compared to air. Thus such systems are often seen in EVs or series HEVs wherein higher heat generation rates are observed [74]. The cooling rates observed by these systems are found satisfactory for reducing the peak temperatures. The temperature gradient among the cells is reduced when compared to air cooling but still remains a challenge.

It is observed that these systems consume more power and are more complicated, mainly because of the insulation required over the cells from direct contact with the liquid. The weight of these systems is more compared to the air-based systems due to bulky components. The inherent limitation of the forced convection mechanisms of having a temperature gradient along the cooling path lies in this method. Special attention is needed for the optimization of the cooling path, considering the cooling performance and the pressure drops.

### ***5.3 Phase Change Materials***

This method works on the latent heat absorption principal. The phase change material absorbs heat generated by the battery and thus starts melting at its melting point. The heat released is thus absorbed as latent heat, and hence, the temperature cannot rise unless the entire PCM melts. The PCM rejects this heat to the surrounding through natural convection, in which case it needs to be operated intermittently [75]. It can reject the heat to another secondary cooling system, in which case it increases parasitic power consumption. Selecting the right quantity of PCM is also a crucial decision considering the improvement in performance against the added weight and cost. PCM should not react with the battery material, should be non-toxic, and have high latent heat. Paraffin is the most favored substance that satisfies these requirements but comes with an inherent disadvantage of low thermal conductivity. Hence, most of the research work in recent years concentrates on increasing the thermal conductivity of PCM.

In 2000, Al-Hallaj and Selman [76] introduced a method to integrate PCMs with the existing battery thermal management system. The results were obtained from a numerical solution with 100 Ah battery, discharge varying up to 1C. They showed that PCM not only lowers the temperature but also assist in uniform temperature distribution. In 2004, Khateeb et al. [77] introduced a PCM couple BTMS for an 11 Ah electric scooter battery. The battery was tested for discharge rate up to 2.4C, with ambient temperature from 0 to 40 °C, 3 different configurations, and 2 different PCMs with melting temperatures 12 and 42 °C. The numerical solutions were validated



by the experiments. The results proved that the third configuration PCM with metal foam matrix and aluminum fins provided repetitive satisfactory results for continuous three charge–discharge cycles. In 2005, once again, Al-Hallaj et al. [78] investigated the performance of a passive BTMS using PCM coupled with a graphite matrix. The ambient was controlled from 30 to 45 °C with cylindrical cells consisting of a battery pack. The performance was tested for currents varying from 4.8 to 10 A, and a significant improvement in BTMS performance was observed. In 2008, Kizilel et al. [79] compared air-based active BTMS with PCM-based passive system and concluded that the PCM performs better, especially when the battery is subjected to abusive conditions. They performed numerical simulations where PCM was embedded with the graphite matrix and surrounded the cylindrical cells. The ambient temperature was kept 40 °C, and the battery was discharged at 6.67C.

In 2014, Javani et al. [80] numerically analyzed a PCM-based BTMS, where they varied the thickness of the PCM layer over the cell. They found that increasing the PCM thickness helped in reducing the peak temperature and optimized the design to meet the cost, weight, and performance goals. The same year they worked on a hybrid system that combined PCM with cooling plates on either side of the cells. The cooling plates consisted of aluminum microchannels with ethylene glycol as a coolant. The BTMS was tested upto the 5C discharge rate.

In the subsequent year, Ling et al. [51] worked on a BTMS that consisted of paraffin PCM with expanded graphite surrounding the cells. The expanded graphite increases the thermal conductivity of the PCM. By changing the concentration of EG in paraffin, they could get PCM with different melting points, conductivities, and latent heats. Heaters were used to simulate the batteries experimentally. Using a numerical solution, they found that the optimum paraffin concentration was 75% with 890 kg m<sup>-3</sup> density and 44 °C temperature. Wu et al. [81] proposed a pyrolytic graphite sheet for increasing the effective thermal conductivity of the PCM. They could achieve better cooling performance and thermal uniformity as compared to the only PCM case. Zhao et al. [82] used PCM with a heat pipe as a medium to conduct away the heat from PCM. They investigate the effect of changing the velocity of air at the condenser section of the heat pipe. They could achieve <50 °C battery temperature with this hybrid system. Hemery et al. [83] developed a PCM–liquid hybrid system where cooling plates were attached above and below the PCM. The liquid temperature was maintained at 22 °C. They could achieve 2C discharge rates by keeping battery temperature within safe limits. Rao et al. [84] and Wu et al. [85] added copper foam to the PCM to improve its heat transfer efficiency. They, later in 2018, studied the effect of changing the thickness of the PCM and convective heat transfer coefficient to optimize the performance considering the cost of the system [86]. Table 3 gives the effect on the thermal properties of PCM due addition of expanded graphite, which is the most preferred method in the literature, apart from adding copper mesh or providing metal fins.

The PCMs prove to an efficient technique in BTMS applications due to their high latent heats. Moreover, since the heat absorption takes place passively, the auxiliary power requirement is low. They are easy to handle when they are in a solid state. In general, the PCMs having their melting point from 35 to 45 °C are found most

**Table 3** Some typically used organic PCMs with modifications for battery thermal management

Compound	Latent heat (kJ kg <sup>-1</sup> )	Thermal conductivity (W m <sup>-1</sup> K <sup>-1</sup> )	Phase change temperature (°C)	Specific heat (kJ kg <sup>-1</sup> .K <sup>-1</sup> )	Density (kg m <sup>-3</sup> )	Reference
Paraffin Expanded Graphite (EG) composite (85% paraffin)	103.2	6.2	36	2.9	700	[51]
Paraffin EG composite (75% paraffin)	87.9	10.1	44	2.5	796	[51]
Paraffin EG composite (75% paraffin)	87.9	10.8	44	2.5	890	[51]
Paraffin EG composite(75%paraffin)	87.9	11.2	44	2.5	1040	[51]
Paraffin EG composite(85%paraffin)	119.5	5.3	52	2.9	700	[51]
PCM composite (6% expanded graphite)	258.5	1.23	41–44	1.926	–	[87]
PCM composite (9% expanded graphite)	250.3	3.15	41–44	1.889	–	[87]
PCM composite (12% expanded graphite)	242	5.74	41–44	1.852	–	[87]
PCM composite (20% expanded graphite)	220	10.6	41–44	1.754	–	[87]
PCM composite (30% expanded graphite)	192.5	13.85	41–44	1.631	–	[87]
RT44–HC composite	181	7.85	42	2.5	714	[51]
PCM/graphite composite	123	16.6	42–45	1.98	789	[79]
Paraffin EG composite (85% paraffin)	98.6	6.8	44	2.9	700	[51]

effective for the purpose. Cost-wise these systems are found to be advantageous. They are reliable as long as the discharge rates and ambient temperatures are low, or they are supported by active systems. Paraffin-based PCMs are found compatible with the Li-ion cells, and hence, there is no risk of damage due to leakage like that in the liquid cooling. One major drawback of the PCMs is the lower thermal conductivity. PCM composites with EG or incorporation of a metallic foam/matrix are some of the methods to increase the effective thermal conductivity of PCMs. The heat thus being conducted out from the PCMs is to be released to the surroundings so that a regeneration of the melted PCM occurs. An air or liquid-based active cooling system serves the purpose of auxiliary cooling. Another disadvantage of PCMs is its dead weight that, in turn, reduces the specific energy of the battery pack. So, in finding the right quantity of PCM, it is always a trade-off between the cost of the reduced specific energy and that of the improved performance and life.

## 5.4 Heat Pipe

Heat pipes are known to have versatile applications in the cooling domain. They perform based on the successive evaporation–condensation mechanism between heat source and sink. The rate of transfer of heat from the evaporator end to the condenser end is governed by gravity, buoyancy, and capillary effect.

Wu et al. [53] suggested the use of a heat pipe with metallic fins for cooling lithium-ion battery. The surface temperature of the battery was achieved as 32 °C. But a uniform cooling was not achieved at the center of the battery. Burban et al. [88] cooled electronics in hybrid EVs using a pulsating heat pipe. The effect of change in the working fluid, inclination, airspeed, etc., was tested on the steady-state and transient performance of the heat pipe. Tran et al. [89] studied the performance of a flat heat pipe under natural and forced convection for various positions. They found that the heat pipes are superior to natural and forced convection by about 30% and 20%, respectively. They found that natural convection in the condenser section was not sufficient to maintain battery temperature within limits. Heat pipe with liquid cooling at the condenser end was studied by Rao et al. [90]. The water bath was maintained at 25 °C, and the heat pipe was inserted between the cells of commercial prismatic LiFePO<sub>4</sub> batteries. Ye et al. [91] numerically studied copper heat sink and fin-based heat pipes for faster heat removal rates. The results of numerical simulation established that fins enhanced the heat transfer at the cell level. Liu et al. [92] used ultra-thin micro-heat pipe and compared natural convection and forced convection at the condenser end. They found that forced convection is the only effective method to control the battery temperature. Wang et al. [93] studied the performance of modified L-shaped heat pipes where the condenser end of the heat pipe was immersed in liquid below the battery, and the evaporator end was attached to the aluminum plate and inserted between the cells. Zhao et al. [94] established that a combination of air cooling and wet cooling at the condenser end of the heat pipe is the best strategy to cool the battery pack.

Heat pipe has the main advantage that it is a passive cooling strategy, consuming no parasitic power and hence does not affect the energy efficiency of the battery pack much [95]. The deadweight is very less, and the systems are not complex. Apart from this, they are found very efficient conductors of heat, unlike the previously discussed passive technology, the PCMs, which have very low thermal conductivity. The sheer size, flexibility in geometry, long lifetime with almost no maintenance of heat pipes makes them a competing alternative in BTMS technology.

Heat pipe strategy has, like the other passive systems, a limitation on account of ambient temperature. They are ineffective in higher temperature zones. Moreover, the rate of heat removal from the condenser end is governed by the convection rate to surrounding air. If this does not match the rate of generation of heat, it may give rise to certain other complications such as drying out of the heat pipe. In high load cases, a liquid cooling system might be used at the condenser end, with an additional cost burden. A small contact area in the evaporator section is another disadvantage of heat pipes. The feasibility of heat pipe as a cooling strategy in Li-ion batteries considering the material weight, compatibility, the effect of varying thermal loads, vibrations, etc., still needs an examination.

## 5.5 *Other Methods*

There are other methods either in the concept stage or in the development stage for achieving the task of battery thermal management. Hydrogel-based system is one such option that is under study. The system is compact, easy to manufacture, and cheap [96]. Another option, though not very popular due to its low efficiency, is thermoelectric cooling [97]. Another intuitive technology is refrigerant-based cooling. Incorporating either the battery in the cabin air-conditioning loop or to have a separate refrigerant loop are the two possible approaches [98]. But this technology involves more complexity and hence not being widely used. An innovative technology is proposed based on the boiling phenomenon of propane or ammonia in the liquid phase [99]. The battery is submerged partially in these coolants. The pressure over the coolant can be varied to change their boiling point as desired. There are many hybrid technologies, even as discussed before, such as the ones that use heat pipes [82] or liquid cooling [83] or metal fins [100] with PCM. Heat pipe with liquid cooling at the condenser end [90] is another example of such hybrid BTMS. The logic behind designing hybrid systems is to couple a passive, and an active system together so that the hybrid BTMS can utilize the high heat transfer rate of active systems and low power consumption of passive systems.

Thus, it can be seen that passive systems are better compared to the active systems when considered from an auxiliary power consumption point of view, whereas active systems prove to be effective for high discharge rate applications. The advantages and disadvantages of each type of system discussed strengthen this argument. At the same time, it is very important to note that only passive systems cannot suffice the purpose for the sole reason that they reject the heat to surrounding via natural

convection, making it a slow heat rejection process. For this reason, when there is a higher heat generation rate involved, as in most cases nowadays, due to higher battery capacity and power requirements and higher climatic temperatures, a passive system must be assisted by an active system making it a hybrid BTMS. With ongoing research in this field, more and more options are opening up in both passive and active approaches. The feasibility of a combination should only be judged based on all the above-discussed decision variables.

## 6 Discussion

EV manufacturers promise an average of 500 cycles of battery life with 80% DoD, which the battery researchers are trying to extend over 2000 cycles. This cycle life, however, is observed to depend on many variables; the most critical among all is the battery temperature. The operating temperature range of Li-ion batteries considering the versatility of climates in different applications over different geographical locations and seasonal variations is wide. Li-ion cells are found to have optimum performance and life in a relatively narrow range from 15 to 35 °C. The performance, life, and safety may get severely compromised if the temperature of the battery crosses these bounds, costing money to the user and life in worst cases. To control the temperature within bounds is possible with a thermal management system, but is a task that costs money, both in installation and operation of BTMS. To design and develop an efficient and cost-effective BTMS is thus a challenge that is faced by the industry. Such an efficient and effective design demands the knowledge of

- (a) Application requirements (I-t profile, SoC)
- (b) Surrounding characteristics ( $Q_{\text{sink}}$ )
- (c) Impact of above on the system's (battery) characteristics ( $U, Y, C, k = f(\text{SoC}, T)$ )
- (d) Dependence of heat source on the above parameters ( $Q_{\text{source}} = f(I, U, Y, T)$ )
- (e) Impact of system and surroundings parameters on system temperature profile ( $T = f(Q_{\text{source}}, Q_{\text{sink}}, C, k)$ )
- (f) Impact of application, system, and surrounding on the system performance parameters ( $V = f(U, I, Y)$ ).

It was established that a study of Li-ion cell's characteristics and their dependency is of utmost necessity to gauge the response of the battery to varying application requirements and surrounding conditions. It was also discussed how modeling is the feasible option compared to experimentation for this task. The paper then discussed modeling fundamentals and established a relationship of the application requirements, surrounding conditions, and system characteristics with the system performance. With application requirements and the corresponding system (battery) already fixed, the only thing that remains in control is the surrounding conditions of the battery. Developing a BTMS around the battery can modify the surroundings of the battery so that its performance gets optimized. The point that is to be remembered

while designing BTMS is that the cost of improvement in performance should supersede the cost of operation of BTMS. The paper then reviews the literature on different BTMS alternatives, their advantages and disadvantages. They can be broadly classified into two types, passive and active. Passive systems include the use of PCM and heat pipes. Researchers have tried modifying the thermal properties of PCMs to optimize their performance. Heat pipes have been studied with different working fluids, wick structures, orientations, and shapes. Passive systems, though energy economical, are less efficient. Active systems include forced air or forced liquid cooling. Researchers have established that the flow path design plays a vital role in the efficient and effective implementation of active systems. These are found to be more efficient in bringing down the temperature compared to passive ones but come at a higher operating cost. The paper lists requirements from a good BTMS at the end and compares various alternatives for BTMS. A comparative analysis between these alternatives suggests that PCM and heat pipe are equally competent options in the passive category. The right choice is to be made based on a list of requirements specific to the application. In the active category, liquid cooling undoubtedly wins over air cooling due to the superior thermal properties of liquids over the air. Liquid cooling, though, should be carefully designed for preventing any leakages into the battery.

As said earlier, an efficient system might not be cost-effective, and vice versa, and hence, a single BTMS option is not sufficient for modern batteries. Optimization of a BTMS should be done considering the performance and cost aspects. A combination of passive and active systems is thus advised, termed as hybrid BTMS. Many such hybrid BTMS are being continuously researched upon. Such hybrid BTMS should be so designed that they make use of the pros of both passive and active systems and eliminate the cons. Finally, it is noteworthy that due to reducing the costs of the batteries, the adoption of EVs is happening at an increasing pace. An efficient and cost-effective BTMS will thus be a significant factor deciding the future of EVs.

**Funding** This work was supported by the All India Council for Technical Education (AICTE), India. [Grant number:8–23/RIFD/RPS-NDF/Policy-1/2018–19].

**Conflicts of Interest/Competing Interests** The authors declare that they have no known competing financial interests or personal relationships that could have appeared to influence the work reported in this paper.

## References

1. (2019) Global EV Outlook-2019, Scaling up the transition to electric mobility, IEA Technology report—May 2019
2. Buchmann I (2012) Basic to advanced battery information from battery university. <https://batteryuniversity.com/>

3. Pesaran AA, Santhanagopalan S, Kim GH (2013) Addressing the impact of temperature extremes on large format Li-Ion batteries for vehicle applications. In: 30th international battery seminar
4. Pesaran AA (2002) Battery thermal models for hybrid vehicle simulations. *J Power Sources*
5. Rao Z, Wang S (2011) A review of power battery thermal energy management. *Renew Sustain Energy Rev*
6. Pan D, Xu S, Lin C, Chang G (2016) Thermal management of power batteries for electric vehicles using phase change materials: a review. In: SAE Technical Papers. SAE International
7. Wang Q, Jiang B, Li B, Yan Y (2016) A critical review of thermal management models and solutions of lithium-ion batteries for the development of pure electric vehicles. *Renew Sustain Energy Rev* 64:106–128. <https://doi.org/10.1016/J.RSER.2016.05.033>
8. Liu H, Wei Z, He W, Zhao J (2017) Thermal issues about Li-ion batteries and recent progress in battery thermal management systems: a review. Elsevier
9. Xia G, Cao L, Bi G (2017) A review on battery thermal management in electric vehicle application. *J Power Sources* 367:90–105
10. Ismailov K, Adair D, Massalin Y, Bakenov Z (2017) On using splitter plates and flow guide-vanes for battery module cooling. *Heat Mass Transf Und Stoffuebertragung*. <https://doi.org/10.1007/s00231-016-1794-5>
11. Nagasubramanian G (2001) Electrical characteristics of 18650 Li-ion cells at low temperatures. *J Appl Electrochem* 31:99–104. <https://doi.org/10.1023/A:1004113825283>
12. Chang C (2019) Factors affecting capacity design of lithium-ion stationary batteries. *Batteries* 5:58. <https://doi.org/10.3390/batteries5030058>
13. Yang B, Zhang H, Yu L et al (2016) Lithium difluorophosphate as an additive to improve the low temperature performance of LiNi<sub>0.5</sub>Co<sub>0.2</sub>Mn<sub>0.3</sub>O<sub>2</sub>/graphite cells. *Electrochim Acta* 221:107–114. <https://doi.org/10.1016/j.electacta.2016.10.037>
14. Leng F, Tan CM, Pecht M (2015) Effect of temperature on the aging rate of Li-ion battery operating above room temperature. *Sci Rep* 5. <https://doi.org/10.1038/srep12967>
15. Nyman A, Zavalis TG, Elger R et al (2010) Analysis of the polarization in a Li-ion battery cell by numerical simulations. *J Electrochem Soc* 157:A1236. <https://doi.org/10.1149/1.3486161>
16. Diao W, Saxena S, Han B, Pecht M (2019) Algorithm to determine the knee point on capacity fade curves of lithium-ion cells. *Energies* 12. <https://doi.org/10.3390/en12152910>
17. List of production battery electric vehicles (table). [https://en.wikipedia.org/wiki/List\\_of\\_production\\_battery\\_electric\\_vehicles\\_\(table\)](https://en.wikipedia.org/wiki/List_of_production_battery_electric_vehicles_(table))
18. Electric vehicle fire incidents. [https://en.wikipedia.org/wiki/Plug-in\\_electric\\_vehicle\\_fire\\_incidents](https://en.wikipedia.org/wiki/Plug-in_electric_vehicle_fire_incidents)
19. Yu QQ, Xiong R, Wang LY, Lin C (2018) A comparative study on open circuit voltage models for lithium-ion batteries. *Chinese J Mech Eng (English Ed)* 31. <https://doi.org/10.1186/s10033-018-0268-8>
20. Skoog S (2017) Electro-thermal modeling of high-performance lithium-ion energy storage systems including reversible entropy heat. In: 2017 IEEE applied power electronics conference and exposition (APEC). IEEE, pp 2369–2373
21. Zhang R, Xia B, Li B et al (2018) A study on the open circuit voltage and state of charge characterization of high capacity lithium-ion battery under different temperature. *Energies*. <https://doi.org/10.3390/en11092408>
22. Bazinski SJ, Wang X (2014) The influence of cell temperature on the entropic coefficient of a Lithium iron phosphate (LFP) pouch cell. *J Electrochem Soc* 161:A168–A175. <https://doi.org/10.1149/2.082401jes>
23. Feng F, Lu R, Zhu C (2014) A combined state of charge estimation method for lithium-ion batteries used in a wide ambient temperature range. *Energies* 7:3004–3032. <https://doi.org/10.3390/en7053004>
24. Mastali M, Foreman E, Modjtahedi A et al (2018) Electrochemical-thermal modeling and experimental validation of commercial graphite/LiFePO<sub>4</sub> pouch lithium-ion batteries. *Int J Therm Sci* 129:218–230. <https://doi.org/10.1016/j.ijthermalsci.2018.03.004>

25. Abdul-Quadir Y, Laurila T, Karppinen J et al (2014) Heat generation in high power prismatic Li-ion battery cell with LiMnNiCoO<sub>2</sub> cathode material. *Int J Energy Res* 38:1424–1437. <https://doi.org/10.1002/er.3156>
26. Liu G, Ouyang M, Lu L et al (2014) Analysis of the heat generation of lithium-ion battery during charging and discharging considering different influencing factors. *J Therm Anal Calorim* 116:1001–1010. <https://doi.org/10.1007/s10973-013-3599-9>
27. Vertiz G, Oyarbide M, Macicior H et al (2014) Thermal characterization of large size lithium-ion pouch cell based on 1d electro-thermal model. *J Power Sources*. <https://doi.org/10.1016/j.jpowsour.2014.08.092>
28. Tang Y, Li T, Cheng X (2019) Review of specific heat capacity determination of lithium-ion battery. In: *Energy Procedia*. Elsevier, pp 4967–4973
29. Lin C, Xu S, Li Z et al (2015) Thermal analysis of large-capacity LiFePO<sub>4</sub> power batteries for electric vehicles. *J Power Sources* 294:633–642. <https://doi.org/10.1016/j.jpowsour.2015.06.129>
30. Yu G, Zhang X, Wang C et al (2013) Experimental study on specific heat capacity of lithium thionyl chloride batteries by a precise measurement method. *J Electrochem Soc*. <https://doi.org/10.1149/2.148306jes>
31. Ruan H, Jiang J, Ju Q et al (2017) A reduced wide-temperature-range electro-thermal model and thermal parameters determination for lithium-ion batteries. In: *Energy procedia*
32. Sheng L, Su L, Zhang H (2019) Experimental determination on thermal parameters of prismatic lithium ion battery cells. *Int J Heat Mass Transf* 139:231–239. <https://doi.org/10.1016/j.ijheatmasstransfer.2019.04.143>
33. An Z, Jia L, Wei L et al (2018) Investigation on lithium-ion battery electrochemical and thermal characteristic based on electrochemical-thermal coupled model. *Appl Therm Eng* 137:792–807. <https://doi.org/10.1016/j.applthermaleng.2018.04.014>
34. Tourani A, White P, Ivey P (2014) A multi scale multi-dimensional thermo electrochemical modelling of high capacity lithium-ion cells. *J Power Sources* 255:360–367. <https://doi.org/10.1016/j.jpowsour.2014.01.030>
35. Li J, Cheng Y, Jia M et al (2014) An electrochemical-thermal model based on dynamic responses for lithium iron phosphate battery. *J Power Sources*. <https://doi.org/10.1016/j.jpowsour.2014.01.007>
36. Drake SJ, Wetz DA, Ostanek JK et al (2014) Measurement of anisotropic thermophysical properties of cylindrical Li-ion cells. *J Power Sources* 252:298–304. <https://doi.org/10.1016/j.jpowsour.2013.11.107>
37. Wu X, Lv S, Chen J (2017) Determination of the optimum heat transfer coefficient and temperature rise analysis for a lithium-ion battery under the conditions of Harbin city bus driving cycles. *Energies* 10
38. Bernardi D, Pawlikowski E, Newman J (1985) A general energy balance for battery systems. *J Electrochem Soc* 132:5–12
39. Shabani B, Biju M (2015) Theoretical modelling methods for thermal management of batteries. *Energies* 8:10153–10177
40. Ng KS, Moo CS, Chen YP, Hsieh YC (2009) Enhanced coulomb counting method for estimating state-of-charge and state-of-health of lithium-ion batteries. *Appl Energy*. <https://doi.org/10.1016/j.apenergy.2008.11.021>
41. Barcellona S, Brenna M, Foiadelli F et al (2015) Analysis of ageing effect on Li-polymer batteries. *Sci World J*. <https://doi.org/10.1155/2015/979321>
42. Cai L, White RE (2009) Reduction of model order based on proper orthogonal decomposition for lithium-ion battery simulations. *J Electrochem Soc*. <https://doi.org/10.1149/1.3049347>
43. Kim US, Yi J, Shin CB et al (2011) Modelling the thermal behaviour of a lithium-ion battery during charge. *J Power Sources*. <https://doi.org/10.1016/j.jpowsour.2011.01.103>
44. Li J, Lai Q, Wang L et al (2016) A method for SOC estimation based on simplified mechanistic model for LiFePO<sub>4</sub> battery. *Energy*. <https://doi.org/10.1016/j.energy.2016.08.080>
45. Hu Y, Yurkovich S, Guezennec Y, Yurkovich BJ (2009) A technique for dynamic battery model identification in automotive applications using linear parameter varying structures. *Control Eng Pract*. <https://doi.org/10.1016/j.conengprac.2009.05.002>



46. Forgez C, Vinh Do D, Friedrich G et al (2010) Thermal modeling of a cylindrical  $\text{LiFePO}_4$ /graphite lithium-ion battery. *J Power Sources*. <https://doi.org/10.1016/j.jpowsour.2009.10.105>
47. Liu Y, Liao YG, Lai M-C (2019) Transient temperature distributions on lithium-ion polymer SLI battery. *Vehicles*. <https://doi.org/10.3390/vehicles1010008>
48. Peng P, Sun Y, Jiang F (2014) Thermal analyses of  $\text{LiCoO}_2$  lithium-ion battery during oven tests. *Heat Mass Transf Und Stoffuebertragung*. <https://doi.org/10.1007/s00231-014-1353-x>
49. Javani N, Dincer I, Naterer GF, Rohrauer GL (2014) Modeling of passive thermal management for electric vehicle battery packs with PCM between cells. *Appl Therm Eng* 73:307–316. <https://doi.org/10.1016/j.applthermaleng.2014.07.037>
50. Lazrak A, Fourmigué JF, Robin JF (2018) An innovative practical battery thermal management system based on phase change materials: numerical and experimental investigations. *Appl Therm Eng* 128:20–32. <https://doi.org/10.1016/j.applthermaleng.2017.08.172>
51. Ling Z, Wang F, Fang X et al (2015) A hybrid thermal management system for lithium ion batteries combining phase change materials with forced-air cooling. *Appl Energy* 148:403–409. <https://doi.org/10.1016/j.apenergy.2015.03.080>
52. Yunyun Z, Guoqing Z, Weixiong W, Weixiong L (2014) Heat dissipation structure research for rectangle  $\text{LiFePO}_4$  power battery. *Heat Mass Transf Und Stoffuebertragung*. <https://doi.org/10.1007/s00231-013-1284-y>
53. Wu MS, Liu KH, Wang YY, Wan CC (2002) Heat dissipation design for lithium-ion batteries. *J Power Sources* 109:160–166. [https://doi.org/10.1016/S0378-7753\(02\)00048-4](https://doi.org/10.1016/S0378-7753(02)00048-4)
54. Mahamud R, Park C (2011) Reciprocating air flow for Li-ion battery thermal management to improve temperature uniformity. *J Power Sources*. <https://doi.org/10.1016/j.jpowsour.2011.02.076>
55. Park H (2013) A design of air flow configuration for cooling lithium ion battery in hybrid electric vehicles. *J Power Sources*. <https://doi.org/10.1016/j.jpowsour.2013.03.102>
56. Fan L, Khodadadi JM, Pesarana AA (2013) A parametric study on thermal management of an air-cooled lithium-ion battery module for plug-in hybrid electric vehicles. *J Power Sources*. <https://doi.org/10.1016/j.jpowsour.2013.03.050>
57. Xun J, Liu R, Jiao K (2013) Numerical and analytical modeling of lithium ion battery thermal behaviors with different cooling designs. *J Power Sources*. <https://doi.org/10.1016/j.jpowsour.2013.01.095>
58. Yu K, Yang X, Cheng Y, Li C (2014) Thermal analysis and two-directional air flow thermal management for lithium-ion battery pack. *J Power Sources*. <https://doi.org/10.1016/j.jpowsour.2014.07.086>
59. Xu XM, He R (2013) Research on the heat dissipation performance of battery pack based on forced air cooling. *J Power Sources*. <https://doi.org/10.1016/j.jpowsour.2013.03.004>
60. Mohammadian SK, Zhang Y (2015) Thermal management optimization of an air-cooled Li-ion battery module using pin-fin heat sinks for hybrid electric vehicles. *J Power Sources*. <https://doi.org/10.1016/j.jpowsour.2014.09.110>
61. Chen K, Song M, Wei W, Wang S (2018) Structure optimization of parallel air-cooled battery thermal management system with U-type flow for cooling efficiency improvement. *Energy* 145:603–613. <https://doi.org/10.1016/j.energy.2017.12.110>
62. Xie J, Ge Z, Zang M, Wang S (2017) Structural optimization of lithium-ion battery pack with forced air cooling system. *Appl Therm Eng*. <https://doi.org/10.1016/j.applthermaleng.2017.07.143>
63. Hong S, Zhang X, Chen K, Wang S (2018) Design of flow configuration for parallel air-cooled battery thermal management system with secondary vent. *Int J Heat Mass Transf*. <https://doi.org/10.1016/j.ijheatmasstransfer.2017.09.092>
64. Jarrett A, Kim IY (2011) Design optimization of electric vehicle battery cooling plates for thermal performance. *J Power Sources*. <https://doi.org/10.1016/j.jpowsour.2011.06.090>
65. Jin LW, Lee PS, Kong XX et al (2014) Ultra-thin minichannel LCP for EV battery thermal management. *Appl Energy* 113:1786–1794. <https://doi.org/10.1016/j.apenergy.2013.07.013>

66. Huo Y, Rao Z, Liu X, Zhao J (2015) Investigation of power battery thermal management by using mini-channel cold plate. *Energy Convers Manag.* <https://doi.org/10.1016/j.enconman.2014.10.015>
67. Zhao J, Rao Z, Li Y (2015) Thermal performance of mini-channel liquid cooled cylinder based battery thermal management for cylindrical lithium-ion power battery. *Energy Convers Manag.* <https://doi.org/10.1016/j.enconman.2015.06.056>
68. Lan C, Xu J, Qiao Y, Ma Y (2016) Thermal management for high power lithium-ion battery by minichannel aluminum tubes. *Appl Therm Eng.* <https://doi.org/10.1016/j.applthermaleng.2016.02.070>
69. Nieto N, Díaz L, Gastelurrutia J et al (2014) Novel thermal management system design methodology for power lithium-ion battery. *J Power Sources.* <https://doi.org/10.1016/j.jpowsour.2014.07.169>
70. Qian Z, Li Y, Rao Z (2016) Thermal performance of lithium-ion battery thermal management system by using mini-channel cooling. *Energy Convers Manag.* <https://doi.org/10.1016/j.enconman.2016.08.063>
71. Panchal S, Dincer I, Agelin-Chaab M et al (2016) Experimental and theoretical investigations of heat generation rates for a water cooled LiFePO<sub>4</sub> battery. *Int J Heat Mass Transf* 101:1093–1102. <https://doi.org/10.1016/j.ijheatmasstransfer.2016.05.126>
72. Rao Z, Qian Z, Kuang Y, Li Y (2017) Thermal performance of liquid cooling based thermal management system for cylindrical lithium-ion battery module with variable contact surface. *Appl Therm Eng.* <https://doi.org/10.1016/j.applthermaleng.2017.06.059>
73. Malik M, Dincer I, Rosen MA et al (2018) Thermal and electrical performance evaluations of series connected Li-ion batteries in a pack with liquid cooling. *Appl Therm Eng.* <https://doi.org/10.1016/j.applthermaleng.2017.10.029>
74. Panchal S, Dincer I, Agelin-Chaab M et al (2017) Experimental investigation and simulation of temperature distributions in a 16Ah-LiMnNiCoO<sub>2</sub> battery during rapid discharge rates. *Heat Mass Transf Und Stoffuebertragung.* <https://doi.org/10.1007/s00231-016-1870-x>
75. Ramandi MY, Dincer I, Naterer GF (2011) Heat transfer and thermal management of electric vehicle batteries with phase change materials. *Heat Mass Transf Und Stoffuebertragung.* <https://doi.org/10.1007/s00231-011-0766-z>
76. Al HS, Selman JR (2000) A novel thermal management system for electric vehicle batteries using phase-change material. *J Electrochem Soc.* <https://doi.org/10.1149/1.1393888>
77. Khateeb SA, Farid MM, Selman JR, Al-Hallaj S (2004) Design and simulation of a lithium-ion battery with a phase change material thermal management system for an electric scooter. *J Power Sources* 128:292–307. <https://doi.org/10.1016/j.jpowsour.2003.09.070>
78. Al-Hallaj S, Kizilel R, Lateef A et al (2005) Passive thermal management using phase change material (PCM) for EV and HEV Li-ion batteries. In: 2005 IEEE vehicle power and propulsion conference, VPPC
79. Kizilel R, Sabbah R, Selman JR, Al-Hallaj S (2009) An alternative cooling system to enhance the safety of Li-ion battery packs. *J Power Sources.* <https://doi.org/10.1016/j.jpowsour.2009.06.074>
80. Javani N, Dincer I, Naterer GF, Yilbas BS (2014) Heat transfer and thermal management with PCMs in a Li-ion battery cell for electric vehicles. *Int J Heat Mass Transf.* <https://doi.org/10.1016/j.ijheatmasstransfer.2013.12.076>
81. Wu W, Wu W, Wang S (2017) Thermal optimization of composite PCM based large-format lithium-ion battery modules under extreme operating conditions. *Energy Convers Manag* 153:22–33. <https://doi.org/10.1016/j.enconman.2017.09.068>
82. Zhao J, Lv P, Rao Z (2017) Experimental study on the thermal management performance of phase change material coupled with heat pipe for cylindrical power battery pack. *Exp Therm Fluid Sci.* <https://doi.org/10.1016/j.expthermflusci.2016.11.017>
83. Hémerly CV, Pra F, Robin JF, Marty P (2014) Experimental performances of a battery thermal management system using a phase change material. *J Power Sources.* <https://doi.org/10.1016/j.jpowsour.2014.07.147>

84. Rao Z, Huo Y, Liu X, Zhang G (2015) Experimental investigation of battery thermal management system for electric vehicle based on paraffin/copper foam. *J Energy Inst* 88:241–246. <https://doi.org/10.1016/j.joei.2014.09.006>
85. Wu W, Yang X, Zhang G et al (2016) An experimental study of thermal management system using copper mesh-enhanced composite phase change materials for power battery pack. *Energy*. <https://doi.org/10.1016/j.energy.2016.07.119>
86. Wu W, Wu W, Wang S (2018) Thermal management optimization of a prismatic battery with shape-stabilized phase change material. *Int J Heat Mass Transf* 121:967–977. <https://doi.org/10.1016/j.ijheatmasstransfer.2018.01.062>
87. Jiang G, Huang J, Fu Y et al (2016) Thermal optimization of composite phase change material/expanded graphite for Li-ion battery thermal management. *Appl Therm Eng* 108:1119–1125. <https://doi.org/10.1016/j.applthermaleng.2016.07.197>
88. Burban G, Ayel V, Alexandre A et al (2013) Experimental investigation of a pulsating heat pipe for hybrid vehicle applications. In: *Applied thermal engineering*, pp 94–103
89. Tran TH, Harmand S, Desmet B, Filangi S (2014) Experimental investigation on the feasibility of heat pipe cooling for HEV/EV lithium-ion battery. *Appl Therm Eng* 63:551–558. <https://doi.org/10.1016/j.applthermaleng.2013.11.048>
90. Rao Z, Wang S, Wu M et al (2013) Experimental investigation on thermal management of electric vehicle battery with heat pipe. *Energy Convers Manag*. <https://doi.org/10.1016/j.energconman.2012.08.014>
91. Ye Y, Saw LH, Shi Y, Tay AAO (2015) Numerical analyses on optimizing a heat pipe thermal management system for lithium-ion batteries during fast charging. *Appl Therm Eng*. <https://doi.org/10.1016/j.applthermaleng.2015.04.066>
92. Liu F, Lan F, Chen J (2016) Dynamic thermal characteristics of heat pipe via segmented thermal resistance model for electric vehicle battery cooling. *J Power Sources*. <https://doi.org/10.1016/j.jpowsour.2016.04.108>
93. Wang Q, Jiang B, Xue QF et al (2014) Experimental investigation on EV battery cooling and heating by heat pipes. *Appl Therm Eng*. <https://doi.org/10.1016/j.applthermaleng.2014.09.083>
94. Zhao R, Gu J, Liu J (2015) An experimental study of heat pipe thermal management system with wet cooling method for lithium ion batteries. *J Power Sources*. <https://doi.org/10.1016/j.jpowsour.2014.10.007>
95. Rao Z, Wang Q, Zhao J, Huang C (2017) Experimental investigation on the thermal performance of a closed oscillating heat pipe in thermal management. *Heat Mass Transf Und Stoffuebertragung*. <https://doi.org/10.1007/s00231-017-2049-9>
96. Zhao R, Zhang S, Gu J et al (2014) An experimental study of lithium ion battery thermal management using flexible hydrogel films. *J Power Sources*. <https://doi.org/10.1016/j.jpowsour.2013.12.138>
97. Liu Y, Yang S, Guo B, Deng C (2014) Numerical analysis and design of thermal management system for lithium ion battery pack using thermoelectric coolers. *Adv Mech Eng*. <https://doi.org/10.1155/2014/852712>
98. Scrosati B, Garche J, Tillmetz W (2015) *Advances in battery technologies for electric vehicles*
99. Al-Zareer M, Dincer M, Rosen MA (2017) Electrochemical modeling and performance evaluation of a new ammonia-based battery thermal management system for electric and hybrid electric vehicles. *Electrochim Acta*. <https://doi.org/10.1016/j.electacta.2017.06.162>
100. Lv Y, Yang X, Li X et al (2016) Experimental study on a novel battery thermal management technology based on low density polyethylene-enhanced composite phase change materials coupled with low fins. *Appl Energy* 178:376–382. <https://doi.org/10.1016/j.apenergy.2016.06.058>

# **Future Trends in Mechanical Engineering**

# Failure Criteria for Composite Blades with Wavy Edge in Aerospace Applications



Prakash Jadhav

**Abstract** In many structural applications, either a notch or a hole is used for some specific design intent. The notch could be contained within the plane of structure, or it could be partially located along the edge of the structure. Although theoretical formulae are available for computing the stress variation along the section passing through a simple hole or a notch, for complicated structure or loading conditions, it becomes difficult to evaluate the stress variation. One such example of complicated structure is proposed wavy trailing edge on the composite fan blade where waviness on the edge of blade could be in-plane as well as out of plane. It is important that for evaluation of stress variation in these type of structures, a methodology (i.e., failure criteria based on notch or hole strength) should be developed which will help in predicting the mechanical behavior/failure load of new designs of these structures. Based on preliminary coupon bending tests (coupons with and without wavy trailing edge) and FEA analysis of the coupon models, the characteristic distance from the edge is evaluated and later used to predict the failure for new wavy trailing edge designs for composite fan blade.

**Keywords** Wavy trailing edge · Failure criteria · Notch sensitivity

## 1 Introduction

There are many attempts to make composite blades perform better in the aircraft engine. As part of the efforts, there were many attempts by the author to implement design changes in the composite fan blade to increase its efficiency and reduce the weight [1–5]. Recently, there are some papers published which talks about the ways to reduce the stress concentration near rectangular, circular, and other shaped holes, using functionally graded material layers near the regions of interest [6–8]. They use the finite element modeling to demonstrate the effect of use of functionally graded material. Taheri-Behrooz computes characteristic distance as a failure criterion for

---

P. Jadhav (✉)

Department of Mechanical Engineering, SRM University, AP, Andhra Pradesh, India  
e-mail: [prakash.j@srmmap.edu.in](mailto:prakash.j@srmmap.edu.in)

© The Author(s), under exclusive license to Springer Nature Singapore Pte Ltd. 2021  
C. Pandey et al. (eds.), *Advances in Materials and Mechanical Engineering*,  
Lecture Notes in Mechanical Engineering,  
[https://doi.org/10.1007/978-981-16-0673-1\\_9](https://doi.org/10.1007/978-981-16-0673-1_9)

113

a woven composite plate with a hole using numerical and experimental investigation and progressive failure [9]. They used the characteristic distance to predict the strength of notched composite under tensile loading. Characteristic length-based failure criterion has also been proposed by Chen.P, who used 0 degree plies failure and tried to predict the tensile and compressive strength of notched (with a circular hole) fiber reinforced composite laminates [10]. Srivastava [11] again has investigated notched strength prediction of laminated composites under tensile loading using point stress criterion, characteristic length, and numerical calculations for a plate with a hole. He proves the dependence of characteristic length on the hole size and width of the plate. Zhang [12] demonstrates the use of numerical progressive damage method to obtain characteristic lengths in order to predict failure of multi-bolt joints. Small computation is enough, and time-consuming expensive tests are avoided. He [13] also demonstrates the characteristic length method using testing of composite plates with circular holes and semicircular notches under tensile and compressive loading. Designing the edge of composite fan blade as wavy edge is also part of the effort to increase the aeroefficiency which was demonstrated by some researchers in their publications and patents [14, 15]. The problem under consideration here prediction of strength of wavy edge for composite blade is unique, and no published work is available on this so far.

## 2 Methodology

Many wavy edge designs needed to be evaluated for mechanical stress concentration happening at the notch-like shapes due to waviness; and for that purpose, this research work was proposed. Here, with the help of preliminary tests of composite coupons with a couple of wavy edge designs incorporated inside them and also the FEA analysis of the same coupon models, a method is devised, which can be used to predict the mechanical behavior (stress concentration) of new wavy edge designs without even testing them. For this study, three types of carbon composite coupon FEA models were built, baseline flat, case 3 with in-plane waviness with bigger wave size and case 19 with in-plane waviness with smaller wave size. As seen in Fig. 1,

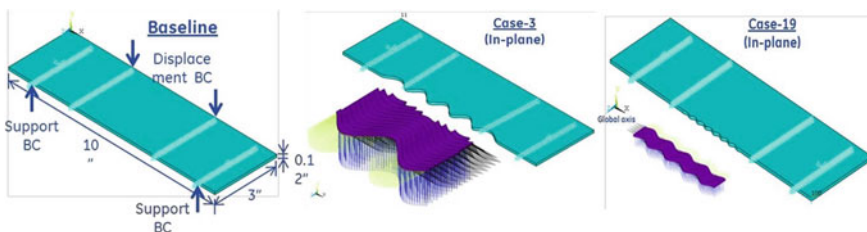


**Fig. 1** Baseline, case 3 and case 19 type of coupon models



**Fig. 2** Case 3 and case 19 type coupons under 4-point bend configuration

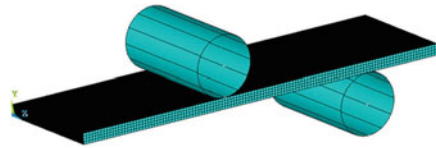
coupon models were built with symmetric and balanced quasi-isotropic layup of IM7-8551 plies and based on this design, carbon composite coupons were manufactured using hand layup and autoclave curing. The wavy shapes were designed in CAD, and then using water jet cutting, the shapes were carved out on coupons. Coupons were then tested under four-point bend boundary condition as shown in Fig. 2. As can be seen, sculpted or wavy trailing edge was incorporated on one edge of the coupons. This introduction of wavy features is supposed to create stress concentration on the edge and supposedly lead to early coupon failure compared to the flat baseline coupons. These 300 mm long coupons were tested in loading span of 100 mm and support span of 200 mm configuration. A point stress criteria is used as given in the theory for a transversely loaded hole in a plate. If the stress distribution is seen along the cut section which is passing through the hole, 3 times higher stress level is observed as per theory at the hole edge point compared to the far field stress.

Figure 3 shows the experimental failure strains and failure load results obtained for baseline, case 3 and case 19 specimens at the locations shown in the figure. Strain gage locations 1, 2, and 3 are on compression side while at location 2, there is also a strain gage on tension side. In this study, the strains will be monitored at a certain characteristic distance “a” from the scallop valley. Tensile and compressive

Sample	Max Strain (far field Tension)	Max Strain (far field compression)	Max load N	Scallop strain compression			Scallop strain tension
				1	2	3	2
Average of baseline specimens	12971	16000	3650				
Average of STE Specimens	11825	14934	3700	13529	12236	12493	15318
FEA-STE	11700	11700	3850	12900			

**Fig. 3** Strain and load results for specimen

Trial	Compressive modulus GPa	Tensile modulus GPa
1	63	98
2	77	105
3	84	91
4	84	112
5	105	119



**Fig. 4** Baseline model for analysis and different moduli trials

side material moduli were tweaked in FEA to get the best possible representation of load–displacement behavior. Using this modified moduli, baseline, case 3 and case 19 composite coupon models analysis were run in FEA and characteristic distance “a” was found for which case 3 and case 19 failure strain level is equal to the baseline failure strain. Based on the characteristic distance obtained from this FEA study, failure load in new designs of wavy edge coupons STE 15 and 17 can be predicted. This predicted load can be validated with the experimental failure load, and thus, characteristic distance “a” can be proposed for particular new wavy edge design. These case numbers 3, 19, 15, 17 are just the randomly selected design numbers of the wavy features from the available 30 designs.

For all the finite element analysis runs, Ansys structural analysis software was used with user-defined parametric codes as inputs. These codes allow the variation in any geometrical parameters quickly and see the effect of it on the results.

For all the FEA runs, material properties of IM7-8551 carbon-epoxy fiber-reinforced laminated composite available from literature are used. Due to space limitations, the material properties input is not listed here. These are basically linear static runs, and strain levels are monitored at the locations of interest at different load levels (which is achieved through the displacement loading). Figure 4 shows the baseline coupon symmetric model with rollers to include sliding contact effects. For this model, top half thickness coupon model and bottom half thickness coupon model are assigned combination of different modulus values as shown in the accompanied table. From the load–displacement plots obtained using this nonlinear geometry static analysis with roller contacts, and it can be seen that the trial 4 modulus combination model generates much closer results to the experimental one. Hence, this modulus combination is used for the further analysis.

### 3 Results and Discussions

Figure 5 shows the longitudinal strain variation obtained over the distance from the edge (baseline flat edge specimen) or scallop valley (wavy edge specimen) along the width of specimens by running the FEA models for baseline, case 3 and case



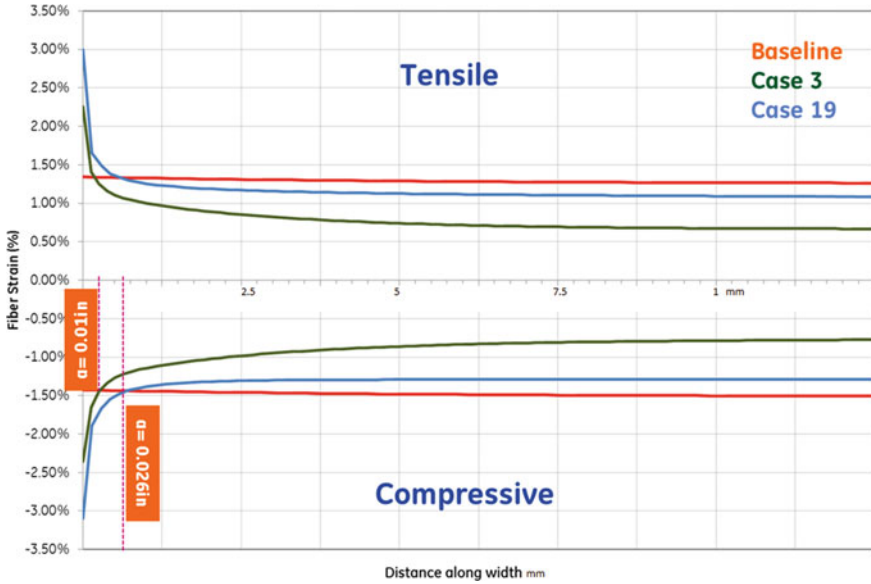


Fig. 5 Strain over distance from the edge

19 models. Experimental failure load obtained using earlier experimental trials was used in FEA to determine the failure strain variation along the width cross section. For case 3 specimen, 1300 N failure load was used while for case 19 specimen 3700 N failure load was used. If the compressive side is considered for computing characteristic distance “a,” as can be seen for case 3, “a” distance is 0.25 mm and for case 19 the “a” distance is 0.65 mm. Therefore, the average “a” distance is 0.45 mm.

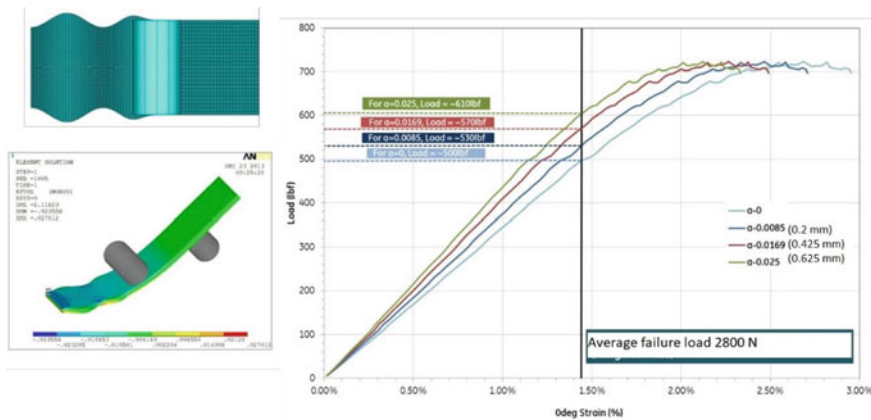


Fig. 6 STE 15 failure load prediction

Now as shown in Fig. 6, the new design STE 15 coupon model can be used to predict the experimental failure load. The load at which strain at characteristic distance “a” is equal to baseline flat edge compressive failure strain is computed for different characteristic distances of 0, 0.212, 0.42, and 0.625 mm. The average failure load obtained for experiments is around 2800 N. While  $a = 0.425$  mm predicts the most accurate load or strength of 2850 N. Figure 7 shows similar failure load prediction for new STE 17 coupon designs. The distance “a” of 0.215 mm and 0.425 mm predicts the accurate failure load of 3100 N which is closer to the experimental failure load of 3150 N.

Figure 8 shows failure load predictions compared with experimental one for tensile and compressive side. These failure load predictions clearly show the correctness of prediction capability of this methodology. The slight difference in characteristic distance “a” as listed in Fig. 9 is due to the difference in mesh density and scallop geometry. So it can be said that characteristic distance of 0.4325 mm can be used for all the cases successfully for predicting the failure load. In this way, Fig. 10 shows that the same characteristic distance can be used to predict the failure load for any

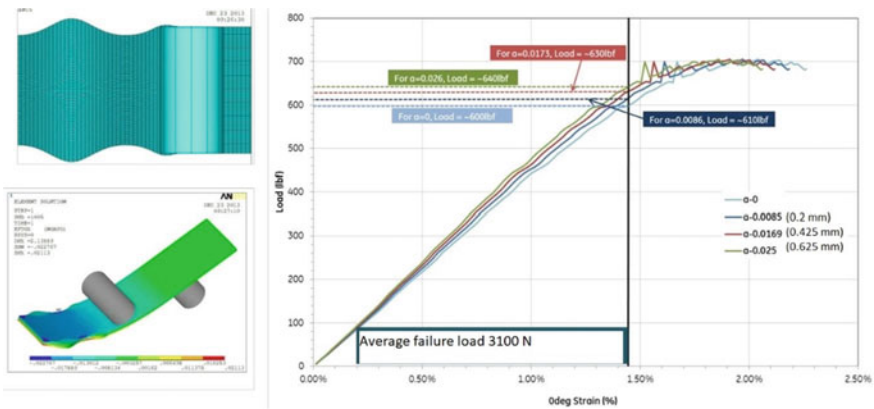


Fig. 7 STE 17 failure load prediction

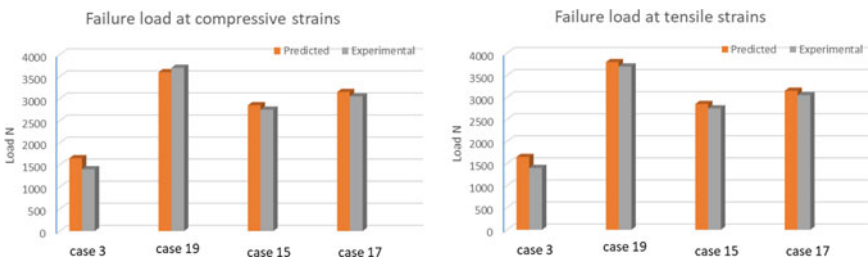
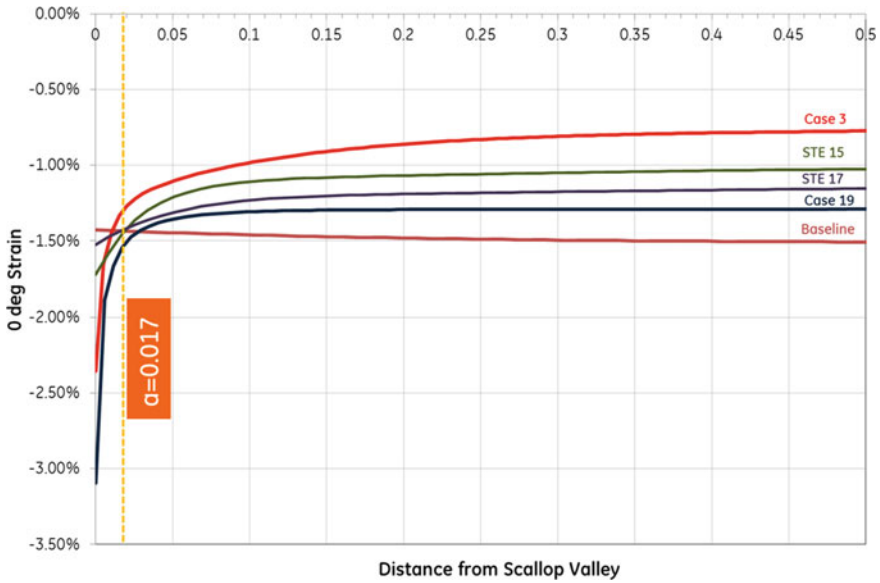


Fig. 8 Experimental and predicted failure loads

**Fig. 9** Characteristic distance “a” for all cases

Case	distance a mm
Case 3	0.5
Case 19	0.4325
STE 15	0.425
STE 17	0.4325



**Fig. 10** Characteristic distance 0.04325 mm (0.017 in.) for all cases (compressive)

new design case just by analyzing the model in finite element analysis, and there is no need to make the new design specimens and test them experimentally.

The significance of this result is huge for the blade designers. As the composite blade is very costly to actually make and test for every small change in the design, the coupon method is devised here. Representative coupons were designed using FEA and then manufactured using similar layup and material that of blade and tested under representative boundary condition; and based on their behavior, we can come to some conclusions that how the blade may behave under certain design conditions. So this method can help reduce substantial efforts/cost of making and testing the actual size blades. The design methodology devised here can help evaluate any sculpted edge design which can increase the aeroefficiency of the blade.

## 4 Conclusions

New prediction method is devised here which can predict the mechanical stress concentration behavior of any new wavy edge/sculpted design of composite blade, using the test database of few preliminary coupons tests with and without wavy features inside them and the FEA analysis of similar coupon models. The characteristic distance “a” which is the parameter of monitoring the stress concentration is used here to compare different wavy edge designs. Three coupon configurations baseline, case 3, and case 19 were used to compute the characteristic distance “a,” and then this distance a was used to predict the failure loads for the coupons of case 15 and case 17. It can be concluded here that a characteristic distance “a” from the edge can be computed/obtained using some preliminary experimental test data for wavy edge and baseline flat edge specimens along with FEA analysis of similar coupons and can be successfully used to predict the failure load for any new such designs with notched/wavy edges. This can really help reduce the efforts of modifying the blade designs, by eliminating most of the blade making and testing cost/efforts.

## References

1. Kray JN et al (2019) Composite compressor blade and method of assembling, US Patent 10247014 B2
2. Spoonire RA (2016) Hybrid turbine blade including multiple insert sections, US Patent 9309772B2
3. Shim D-J (2013) Fan blade, US Patent 2013/0287588A1
4. Jadhav P (2020) Effect of ply drop on aerospace composite structures. *Key Eng Mater* 847:46–51
5. Prakash Jadhav, Innovative designs of embedded foam inserts in aerospace composite structures, *Materials Today Proceedings*, volume 21, part 2, pages 1164–1168 (2020)
6. Goyat V, Verma S, Garg RK (2018) Reduction in stress concentration around a pair of circular holes with functionally graded material layer. *Acta Mech* 229:1045–1060. <https://doi.org/10.1007/s00707-017-1974-5>
7. Goyat V, Verma S, Garg RK (2017) Reduction of stress concentration for a rounded rectangular hole by using a functionally graded material layer. *Acta Mech* 228:3695–3707. <https://doi.org/10.1007/s00707-017-1907-3>
8. Goyat, V., Verma, S., and Garg, R.K. ‘Stress Concentration Reduction Using Different Functionally Graded Materials Layer Around the Hole in an Infinite Panel’. 1 Jan. 2019: 31–45.
9. F.Taheri Behrooz and H. Bakhshan, Characteristic length determination of notched woven composites, *Advanced composite material*, vol 27–1, pp 67–83 (2018)
10. Puhuri chen, Zhen shen, Jun yang wang, Prediction of strength of notch fiber dominated composite laminate, *Composite science and technology*, vol 61, pp 1311–1321 (2001)
11. Srivastava VK (2002) Notched strength prediction of laminated composite under tensile loading. *Material Science and Engineering* a 328:302–309
12. Zhang J, Liu F, Zhao L, Chen Y, Fei B (2014) A progressive damage analysis based characteristic length method for multi bolt composite joint. *Compos Struct* 108:915–923

13. Zhang J, Liu F, Zhao L, Shan M (2015) Investigation on characteristic length testing methods for failure prediction of composite multi bolt joints. *Reinforced Plastic and Composites* 34(8):636–648
14. Nicholas Joseph Kray et al, US Patent 9121294B2 (Sept 1, 2015)
15. John Sullivan, et al, US Patent 8573541B2 (Nov 5, 2013)

# Stress and Deformation Analysis of Hip Joint for Design of Hip Prosthesis



Amiya Kumar Dash, K. Sai Vishwak, and Vaibhav Pahuja

**Abstract** Biomechanics is a study of the musculoskeletal system and the resulting forces acting on them. Hip joint plays a vital role in the musculoskeletal system, which is why there is a need to analyze it more critically. However, with today's knowledge of the mechanism of the hip, the study and analysis of stress distribution over the joint are limited. Recreating the environment according to daily activities is very important in the experimental analysis of the joint. This approach is difficult to conduct without and changes to the physiological environment. Numerical methods like finite element methods are used to analyze these systems without any damage or invasive processes. This paper has adopted a novel approach to analyze hip joint using 3D volumetric model generation techniques and finite element method. The hip joint is segmented from the computed tomography (CT) scans of a patient, and the bone model is developed with thresholding and volume generation algorithms. The joint along with the complete hip anatomy has been meshed with octahedral elements. A static load has been considered to apply at the hip joint, and the effect of the load is computed and analyzed. The analyzed data will help for effective design of hip prosthesis and an appropriate selection of material.

**Keywords** Hip · Stress · Deflection · Prosthesis · Design

## 1 Introduction

Biomechanics is a study on the motion of various body segments under the application of forces. Study of various forces acting on different parts of the body helps surgeons to keep the right amount of forces during operations, exact position for fixation, etc., and for doctors, it will be helpful to give exact medication for the patient. To study and analyze these forces and the impacts of them on the bones, it is very difficult to conduct experiments each time and perform an analytical study. To eliminate these restrictions, finite element analysis was introduced into the study of biomechanics.

---

A. K. Dash (✉) · K. Sai Vishwak · V. Pahuja  
BML Munjal University, Gurgaon, Haryana, India  
e-mail: [amiya.dash@bmu.edu.in](mailto:amiya.dash@bmu.edu.in)

© The Author(s), under exclusive license to Springer Nature Singapore Pte Ltd. 2021  
C. Pandey et al. (eds.), *Advances in Materials and Mechanical Engineering*,  
Lecture Notes in Mechanical Engineering,  
[https://doi.org/10.1007/978-981-16-0673-1\\_10](https://doi.org/10.1007/978-981-16-0673-1_10)

123

Finite element method (FEM) is a numerical method which is used to solve physical models that are represented in partial differential equations. Finite element methods can be used to solve many engineering and scientific problems. It has much more scope than the analytical approach because it can solve problems that cannot be solved analytically. Main applications of finite element method are to find the stresses that are produced in a body when subjected to various types of loads. Finite element method, when applied to a real-life problem, requires a large amount of computation and calculations. The method is now applied to a wide range of problems such as heat flow, fluid flow, electrostatics, vibrations, and many more. Scope of using various types of materials is also a very powerful feature of finite element analysis. Raja et al. [1] have used the concept of reverse engineering and analyzed human hip femur joint which was made by polycaprolactone material. After examining in ANSYS software, it was obtained that the maximum pressure to be given for the artificial femur to fail is 0.5 MPa. The calcium hydroxyapatite is used on many artificial hips that enhance the attachment of implement on living bone. Trask et al. [2] have determined whether the current criteria for microfracture are correct for chondral lesions in the hips. It was observed that the patients with high cartilage defects have high chances for total hip arthroplasty. Patients who underwent microfracture surgery had grade-IV changes to either femoral head or acetabulum. The current method should be divided through sex, age, size, and shape of the chondral defect. Henak et al. [3] used finite element method to evaluate the chondrolabral contact mechanics and congruency in dysplastic hips and normal hips. The labrum supported more load in dysplastic hips as compared to normal hips. He evaluated that the contact area on superior labrum was more in dysplastic than the normal hips. Spikes of contact stresses were found larger in normal than dysplastic hips. Labrum experienced 2.8–4.0 times the load of a normal hip when there is a dysplastic hip. There is no significant difference between the congruency of normal hip and dysplastic hip. Hua et al. [4] have investigated edge loading and effects caused by it on the contact mechanics of a modular metal-on-polyethylene total hip replacement. The maximum Von-Mises stress was obtained when 2000  $\mu\text{m}$  of micro-separation was much higher than that of stresses due to acetabulum inclination angle. Piao et al. [5] after implementing the total hip joint simulation in vitro compared the stress shielding effect of implantable anatomical and traditional prosthesis. Lee et al. [6] has reconstructed labrum using iliotibial band autografts and semitendinosus improved the biomechanical properties by increasing contact areas and decreasing contact pressure. There is no significant change in the contact area of the joint than the native intact state. Robert et al. [7] has presented the results of the initial study on the structural analysis of the hip joint, by considering changes that occur in mechanical properties of articular cartilage of the joint. Articular cartilage of the joint main function is for smooth movement of the joint, and it absorbs shocks. The capability of absorbing shocks decreases with the increase in age and degeneration of cartilage. Henak et al. [8] developed and validated a series of finite element models which are specimen specific, so that the characterization of the local response of human hip cartilage in compression can be done. Moreover, the assessment of the effects of material nonlinearity, inhomogeneity, and material coefficients on finite element analysis predictions of cartilage contact stress and contact area. Hanz et al. [9] has

estimated the hip-joint center using Harrington Equation and Geometric sphere fit. Moreover, identification of most accurate functional and predictive methods along with adequate range of motion was done. Elkins et al. [10] investigated the effects femoral head size that will influence the stability in THA for several dislocation prone motion and the mechanics of the wear at the trunnion surface by relating the wear potential, the head size and also, they investigated cup orientation, type of hip motion, and impaction load. Greater the cup orientation angle, greater was the contact stress and contact pressure, causing instability. Wear was noticed at the trunnion due to slipping and the horizontal cup orientation and edge loading resulted in maximum contact stress. Christen et al. [11] developed a reverse approach for the deriving of joint loads from bone microstructures which were acquired from micro-tomography. Peak forces in human being were concentrated at a single point, i.e., femoral head, whereas in case of a dog, peak force start from head, and then, it distributes accordingly to full area. The force intensity of normal human is twice as that of osteoporotic because of the lag in bone density. Askari et al. [12] analyzed the effect of friction-induced vibration and contact mechanism due to the maximum contact pressure and moment of artificial hip joints. Friction influenced hip implant moment, and it influences the system dynamic response because of negative gradient of friction coefficient. Moreover, the temperature of the articular cartilage, i.e., film, influenced the value of friction coefficient between the femoral head and acetabulum.

The main purpose of this paper is to study the stress distribution on the hip joint under different loading conditions and compare the results for the study of stress distribution and displacement. In this research, MIMICS was used for three-dimensional reconstruction of the hip joint and ANSYS R18.1 for finite element analysis. The results obtained will help the engineers for effective design of hip prosthesis and appropriate material selection. The research done in this paper will also help experts from various fields like osteologists, archeologists, pathologist, etc.

## 2 Methodology

### 2.1 Forces Acting on the Hip Joint

The three major ligaments in the hip joint are iliofemoral ligament, ischiofemoral ligament, and pubofemoral ligament. These ligaments are the ones which attach the hip joint and the femur. These play an important role in the movement of the leg. Any damage to the pubofemoral ligament results in excess abduction, and extension causes muscle strains. The femur bone is one of the strongest bones in the human body. Actions like walking, jumping, etc., result in application of forces on femur which in turn act on the hip joint. So, it is very important to understand the forces and the effects of these forces acting on the hip joint. Joint reaction forces in hip joint can be calculated with Eq. 1.



$$\text{Joint Force Reaction} = \text{Body Weight} + \text{Abductor Force} \quad (1)$$

The main elements in determining the joint force reaction are bodyweight, bodyweight momentum arm, abductor force, and abductor force arm.

The resultant force is more in dislocated hip than in normal hip. These forces are used to determine the behavior of hip with other constraints.

## 2.2 Segmentation of the Hip Joint

Segmentation process plays an important role in 3D reconstruction of the bone structures from computed tomography (CT) scans. In this study, MIMICS was used to perform segmentation of the required region by applying global thresholding technique with appropriate Hounsfield unit (HU) values. These HU values are carefully selected, so that there is not much loss in the structure. Selecting only the required region in all the three views for every frame makes this process cumbersome and difficult. Any small details missed during this process can affect the final finite element analysis results. Figure 1 shows the segmentation in coronal, transverse, and sagittal views and a 3D reconstructed surface model of the segmentation.

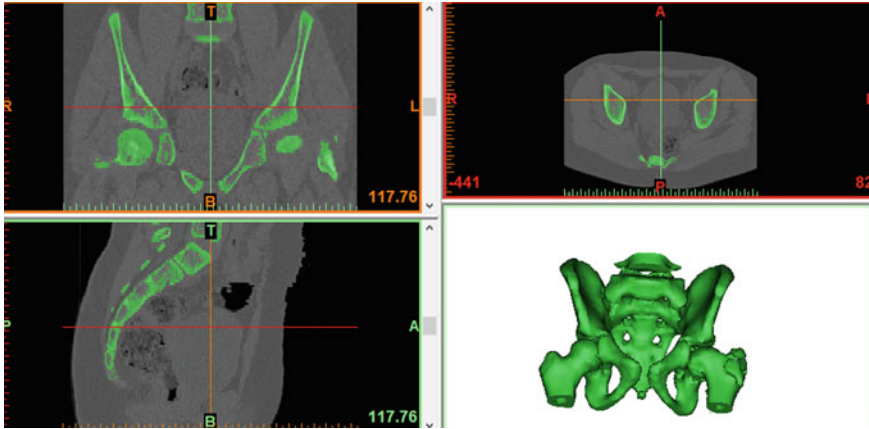


**Fig. 1** Segmented regions in coronal, transverse, and sagittal views along with 3D reconstructed surface model

**Table 1** Mechanical properties of the model

Parameter	Value
Density (Kg/m <sup>3</sup> )	1980
Young's modulus (MPa)	2413
Poisson's ratio	0.33

### 2.3 Generation of Volumetric Model and Material Assignment

The resultant surface model generated from the segmented regions now needs to be converted into a volumetric model for meshing and finite element simulation. The surface model generated is in STL format, and in-built MIMICS 3-MATIC software can be used to create a volumetric model with meshing. Open-source software's like GMSH can also be used to achieve similar results. But MIMICS has better functionality while performing meshing and model refinements. Usually, the segmented process will not be very accurate. So, the model is to be refined and removed from all minute damages.

Meshing is performed in MIMICS 3-MATIC software with an average element size of 1 mm. Mesh refinements were performed of the model to remove the segmentation errors and make the model more appropriate for the finite element analysis. Material properties assigned to the model are considered to be isotropic in nature and constant density throughout the model. In this research, the material properties are considered as isotropic in nature rather than anisotropic because the interest is in analyzing local phenomena, and this assumption can be made to reduce the complexity of the model and reduce the computational time required to perform the simulation. Table 1 shows the material properties of the model.

### 2.4 Finite Element Method

Finite element model for a simple rod in one-dimension can be expressed with Eq. 2.

$$dp/dx + f = 0 \tag{2}$$

$$P = EA \times \left( \frac{du}{dx} \right) \tag{3}$$

where  $u$  is the displacement in the rod element,  $P$  is the stress,  $E$  is Young's modulus, and  $A$  is the area of cross section. In finite element method,  $u$  is a continuous variable which is an approximate for the nodal values  $u_1$  and  $u_2$  with respect to shape functions.

$$U = u_1 N_1 + u_2 N_2 \tag{4}$$

$$U = [N_1 \ N_2]\{u_1; u_2\} = [N]\{u\} \quad (5)$$

In Eq. 4,  $N_1$  and  $N_2$  are the shape functions, and in here, only a single element is considered; hence, only two nodes exist.

$$\int_0^L \begin{Bmatrix} N_1 \\ N_2 \end{Bmatrix} EA \frac{d^2}{dx^2} [N_1 \ N_2] dx \begin{Bmatrix} u_1 \\ u_2 \end{Bmatrix} + \int_0^L \begin{Bmatrix} N_1 \\ N_2 \end{Bmatrix} F dx = \begin{Bmatrix} 0 \\ 0 \end{Bmatrix} \quad (6)$$

The main purpose in solving these equations is to reduce the residual to zero. If the residual becomes zero, then the solution is said to be analytical which is the optimal solution that can be achieved.

Many methods are available to achieve this, but the Galerkin method became famous in finite element world where the residual is multiplied to each shape function and integration over the entire element and equating it to zero. In practice, the entire element is discretized into a number of elements and solve Eq. 6 for each element and calculate the displacements at each node. Once all the equations for the elements are formulized, a global matrix is formed which is in the form

$$[k] \times [u] = [f] \quad (7)$$

where  $k$  is the global stiffness matrix. Finally, with stress–strain relation, the stress at each node can be calculated, and it can be interpolated on the entire element. Boundary conditions are applied to these equations to solve the required physical model. This ideology can be used to solve many engineering problems which are difficult to calculate with analytical methods and models with complex geometries.

In this research, the 3D reconstructed volume model generated in MIMICS software is imported into ANSYS R18.1 and connected to a static structural analysis module. The boundary conditions are considered as the force acting from femur trochanter with the iliac fossa as the support. 42.47 N force was applied with  $10^\circ$  angle with respect to the global Z-axis. The current boundary condition simulates sitting position with lumbar inclined at  $10^\circ$ . Figure 2 shows the boundary conditions that were applied to the model.

### 3 Results and Discussion

In this simulation, Von-Mises stresses and displacement were calibrated over the entire model. The simulation was carried out using an Intel(R) Core (TM) i3-6100 T CPU @ 3.20 GHz processor with 12 GB ram. This section depicts the discussion of the results obtained from the analyses at the end.

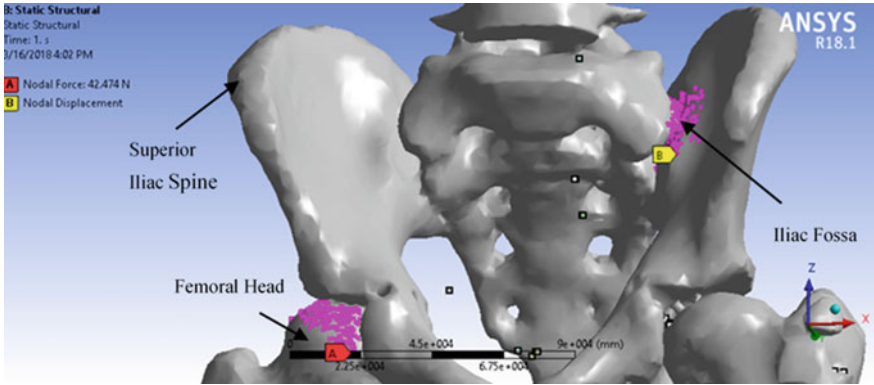


Fig. 2 Application of boundary conditions

### 3.1 Deformation

A uniform load of 42.47 N acting at an angle of 10° from femur trochanter with iliac fossa as support resulted with maximum deformation of 0.35 μm at the acetabular rim and minimum deformation of 0.0397 μm at iliac fossa. Figure 3 shows the deformation contour of the simulation.

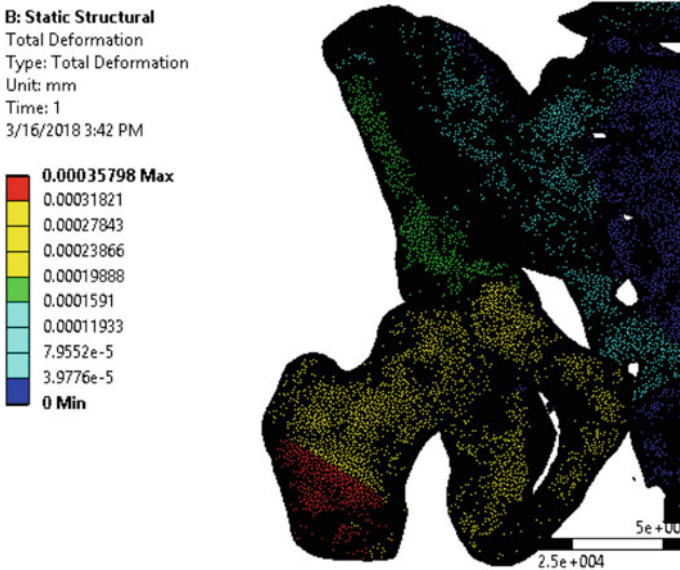
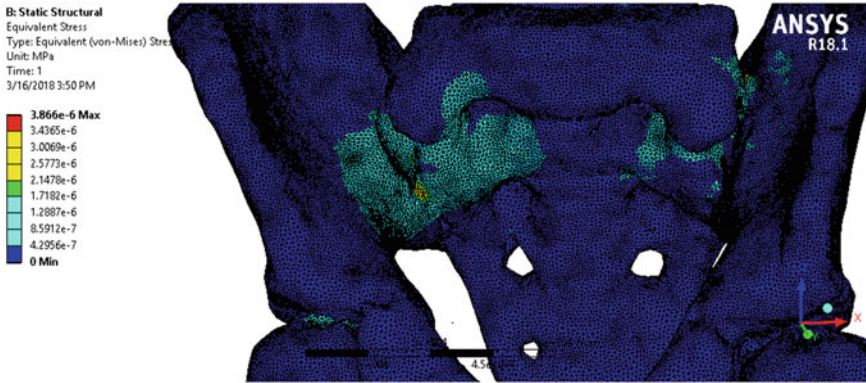


Fig. 3 Deformation contour of femur and hip joint



**Fig. 4** Von-Mises stress contours of femur and hip joint

### 3.2 Von-Mises Stress

A uniform load of 42.47 N acting at an angle of  $10^\circ$  from femur trochanter with iliac fossa as support resulted with maximum Von-Mises stress of  $3.8 \times 10^{-6}$  MPa at the iliac fossa and minimum Von-Mises stress of  $4.29 \times 10^{-7}$  MPa at acetabular rim. Figure 4 shows the Von-Mises contour of the simulation.

The results obtained from the analysis indicate that during standing position load passes through the femur head and subsequently passes through the trochanter of the femur. The load results in stress and deformation at the pelvis area which is primarily used as a major load-bearing part of the body. Detailed analysis of the results indicates that the critical area is the posterior superior iliac spine, as this part is subjected to a maximum stress of magnitude  $3.8 \times 10^{-6}$  MPa. Hence, the joint of the spine with pelvis should be strengthened to avoid uneasiness of patient with any kind of deformity in the pelvis including the femur joint.

## 4 Conclusion

The computational approach used for this study showed the stress and deformation associated with the human pelvis while standing. The analysis reflected that the ischial tuberosity (IT) is subjected to the maximum deformation while standing position came out to be  $+0.00035798$  mm. This value being extremely small signifies that a grown human pelvis is most stable when a person is in standing position.

Von-Mises stress analysis showed the maximum stress concentrated over the posterior superior iliac spine. The maximum stress value came out to be  $3.8 \times 10^{-6}$  MPa. This result can help the orthopedic surgeon to advice the patient, the inclination at which the stress associated with standing would be minimum.

This paper investigated the stress and displacement experienced by hip joint during standing of a male subject of 34 age. The computational procedure was employed to evaluate the stress and deformation during loading conditions. The results obtained from the current analysis will help for effective design of hip prosthesis and suitable material selection.

## References

1. Raja SKR, Mageshwaran G (2015) Analysis of hip femur joint for material polycaprolactone 8:488–494
2. Trask DJ, Keene JS (2016) Analysis of the current indications for microfracture of chondral lesions in the hip joint. *Am J Sports Med* 44(12):3070–3076. <https://doi.org/10.1177/0363546516655141>
3. Henak CR, Abraham CL, Anderson AE, Maas SA, Ellis BJ, Peters CL, Weiss JA (2014) Patient-specific analysis of cartilage and labrum mechanics in human hips with acetabular dysplasia. *Osteoarthritis Cartilage* 22(2):210–217. <https://doi.org/10.1016/j.joca.2013.11.003>
4. Hua X, Li J, Wang L, Jin Z, Wilcox R, Fisher J (2014) Contact mechanics of modular metal-on-polyethylene total hip replacement under adverse edge loading conditions. *J Biomech* 47(13):3303–3309. <https://doi.org/10.1016/j.jbiomech.2014.08.015>
5. Piao C, Wu D, Luo M, Ma H (2014) Stress shielding effects of two prosthetic groups after total hip joint simulation replacement. *J Orthop Surg Res* 9:71. <https://doi.org/10.1186/s13018-014-0071-x>
6. Lee S, Wuerz TH, Shewman E, McCormick FM, Salata MJ, Philippon MJ, Nho SJ (2015) Labral reconstruction with iliotalibial band autografts and semitendinosus allorrafts improves hip joint contact area and contact pressure: an in vitro analysis. *Am J Sports Med* 43(1):98–104. <https://doi.org/10.1177/0363546514553089>
7. Karpiński R, Jaworski Ł, Zubrzycki J (2016) Structural analysis of articular cartilage of the hip joint using finite element method. *Adv Sci Technol Res J* 10:240–246. <https://doi.org/10.12913/22998624/64064>
8. Henak CR, Kapron AL, Anderson AE, Ellis BJ, Maas SA, Weiss JA (2014) Specimen-specific predictions of contact stress under physiological loading in the human hip: validation and sensitivity studies. *Biomech Model Mechanobiol* 13(2):387–400. <https://doi.org/10.1007/s10237-013-0504-1>
9. Kainz H, Carty CP, Modenese L, Boyd RN, Lloyd DG (2015) Estimation of the hip joint centre in human motion analysis: a systematic review. *Clin Biomech (Bristol, Avon)* 30(4):319–329. <https://doi.org/10.1016/j.clinbiomech.2015.02.005>
10. Elkins JM, Callaghan JJ, Brown TD (2014) Stability and trunnion wear potential in large-diameter metal-on-metal total hips: a finite element analysis. *Clin Orthop Relat Res* 472(2):529–542. <https://doi.org/10.1007/s11999-013-3244-8>
11. Christen P, Ito K, Galis F, van Rietbergen B (2015) Determination of hip-joint loading patterns of living and extinct mammals using an inverse Wolff's law approach. *Biomech Model Mechanobiol* 14(2):427–432. <https://doi.org/10.1007/s10237-014-0602-8>
12. Askari E, Flores P, Dabirrahmani D, Appleyard R (2014) Study of the friction-induced vibration and contact mechanics of artificial hip joints. *Tribol Int* 70:1–10. <https://doi.org/10.1016/j.triboint.2013.09.006>

# Stress and Displacement Propagation Analysis of Lumbar L4 Vertebrae for Prosthesis Design



Amiya Dash and Vaibhav Pahuja

**Abstract** Spine plays an important role to facilitate mobility in humans. It has four distinct parts such as cervical, thoracic, lumbar and coccyx which have respective role to play. The lumbar part of the spine is responsible to bear the torso load. This part of the spine is subjected to maximum load. In the present paper, lumbar vertebrae number 4 has been considered for stress analysis and displacement analysis. The stress distribution profile indicates the maximum and minimum stressed part for a given amount of load. The modelling of the L4 vertebrae has been done with Blender, and analysis has been done using Abaqus. The output of this has helped us that the lumbar vertebrae is subjected to dynamic load not only during walking or running but also during standing, sitting and bending. From the results, we have identified that annulus of L4 vertebrae is subjected to maximum stress and anterior annulus is subjected to maximum displacement during normal standing position of a human. The research outcome will help in effective design of spine prosthesis.

**Keywords** Lumbar · Stress · Deflection · Prosthesis · Design

## 1 Introduction

The spine is a combination of 33 individual bones stacked on top of each other. These 33 bones run along the back of an individual helping a person to perform day-to-day normal activities such as sitting, standing, bending and running along with providing a rigid support to the back. A healthy spine constitutes various organs such as ligaments, tendons and soft nerves. The spinal vertebrae are divided into five regions, cervical, thoracic, lumbar, sacrum and coccyx. The vertebrae in each region have unique features that help them perform their main functions [1].

The weight of head is supported by the cervical spine divided into seven cervical vertebrae numbered C1–C7. There are 12 thoracic vertebrae numbered T1–T12. The range of motion in the thoracic spine is limited. The sacrum plays a crucial role in

---

A. Dash (✉) · V. Pahuja  
BML Munjal University, Gurgaon, Haryana, India  
e-mail: [amiya.dash@bmu.edu.in](mailto:amiya.dash@bmu.edu.in)

© The Author(s), under exclusive license to Springer Nature Singapore Pte Ltd. 2021  
C. Pandey et al. (eds.), *Advances in Materials and Mechanical Engineering*,  
Lecture Notes in Mechanical Engineering,  
[https://doi.org/10.1007/978-981-16-0673-1\\_11](https://doi.org/10.1007/978-981-16-0673-1_11)

133

connecting the spine to the hip bones (iliac). There is a total of five sacrum vertebrae stacked and fused together. The four connected bones of the coccyx or tailbone provide attachment for ligaments and muscles of the pelvic floor. The present paper is addressed to carry out the stress and deformation analysis of L4 for taking clinical decision by the practitioner. In this regard, researchers have carried out various researches to help provide an insight over the analysis of various regions of spine. Researchers have made some contributions in this domain, and few of them are discussed here.

Zysset et al. [2] have developed new official positions that can be used clinically for the quantitative computed tomography which is based on finite element analysis of hip and spine. Wang et al. [3] has developed modified finite element models which can be used to simulate degenerative lumbar scoliosis which is based on the normal lumbar spine model, and they investigated the facet joint force of the degenerative lumbar scoliosis. The result obtained was such that if the Cobb angle was less than  $20^\circ$ , then the impact of stresses was more on the convex side; but if the Cobb angle was more than  $20^\circ$ , then the stresses were much concentrated on the concave side. Wang et al. [4] has tested the in vivo loads in the lumbar L3–4 disc during a weight-lifting extension. The anterior shear displacement was found to be largest at the flexion positions among the three subjects. Maximum compression of L3–4 occurred at upright position as compared to flexion position. Compression was higher during upright position, and shear was higher during flexion position. Villa et al. [5] has done the finite element analysis of the lumbar fixation rod when it is subjected to ASTM and ISO standards. When FE simulations and experiments were compared, it was observed that they had a good agreement between results and thus confirming the suitability of the finite element analysis. Sterba et al. [6] has studied the biomechanical analysis of spino-pelvic postural configurations in spondylosis when subjected to various sport-related dynamic loading conditions. Three cases with spondylosis were built and were tested with 16 types of dynamic loading. It was observed that combined flexion and axial rotation with compression tend to generate the highest stress conditions related to risks of spondylosis. Song et al. [7] have studied the three-dimensional finite element model of the lower cervical spine, and they further compared the stress distribution of the four lateral mass screw fixation (LSF) techniques, following laminectomy which is basically to explore the risks after fixation. The lateral mass screw fixation techniques of Magerl and Roy-Camille are safer methods that can be used for stabilising the lower cervical spine. Therefore, these methods potentially possess a lower risk of failure after fixation. Ali et al. [8] investigated the biomechanical response of the trunk musculoskeletal system when it is subjected to sudden forward load, taking into account the pre-perturbation conditions and post-loading magnitudes. They used finite element analysis for determining the spinal forces and central nervous response for 12 healthy pieces, pre and post-perturbation periods. Pre-loading the trunk significantly increased the pre-perturbation back muscle forces. Mustafy et al. [9] compared the spinal load sharing under pure compression and sagittal extension when subjected to two different impact rates using a biofidelic FE model of the ligamentous cervical functional spinal unit C2–C3. The experiments resulted in dependency of resistance of spinal component



to impact load on loading rate and direction. The stresses increased for the loads applied and were concentrated in intervertebral disc. Mc Grill et al. [10] analysed the muscle activity and spine loading in pushing exercises. Stable labile exercises were used for examining. It was seen that there was much more torso muscle activity when instable labile exercises were done as compared to stable labile exercises. There was no significant impact on spine compression due to exercise. Ganbat et al. [11] investigated whether mechanical loading results in the substantial formation of heterotopic ossification. It was seen that for the compressive force, most of the HO formation occurred on the vertebra end plates uncovered by the implant foot plate. For the shear force, the HO was dominantly seen in the anterior of upper and lower vertebrae. The strain energy showed a reduction after the formation of HO. Fabio et al. [12] investigated the degenerative changes of the intervertebral disc after ageing and also their impact on spinal flexibility. Due to lack of water, it was observed that the lower back started to pain due to changes in the flexibility of disc. Marcel et al. [13] compared and critically reviewed different literature paper to estimate the loads on human lumbar spine. They compared various postures, i.e., sitting, standing, or lying as well as the dynamic activities in order to come to the conclusion. They observed that pressure increases significantly from standing to forward bending. Arun et al. [14] modelled the lumbar vertebrae L2–L4 for the analysis of stress concentration and displacement of an osteoporotic patient compared to that of a normal one. The results showed a significance increase in both the stress and displacement of the osteoporotic patient. Alexander et al. [15] studied the effect on the lumbar L3–4 due the size variation in the interarticular regions. The results showed an increase in 35–40% of stress after the half reduction of interarticular thickness. Koichi et al. [16] developed a nonlinear three-dimensional pediatric lumbar spine finite element model to identify the reasons for the apophyseal bony ring fracture occurring mechanically. The results showed that higher compression stresses over long time in the flexion may be the reason for the apophyseal ring fracture.

Previous literature review indicate that research has been carried out to evaluate the stress and strain of different parts of spine for different position of patient. However, little work can be seen particularly on load and stress analysis of lumbar vertebra L4, which is subjected to major load during standing and sitting and bending position. Therefore, this paper helps in giving a clear insight on the stress distribution in the lumbar L4 for common bodily postures such as bending and standing.

## 2 Methodology

This section depicts the modelling and analysis method used for examining of lumbar L4 vertebrae.

Finite element analysis. The finite element analysis (FEA) is the simulation of some random physical phenomenon utilizing the numerical system called finite element method (FEM). Typical problem areas of interest include the traditional fields

of structural analysis, heat transfer, fluid flow, mass transport and electromagnetic potential.

General equation for a FEM:

$$S_{ij} = \sum C_{ij} * N_{ij} \quad (1)$$

where  $S_{ij}$  is the equation of discretised element,  $C_{ij}$  is the nodal values, and  $N_{ij}$  is the shape function or blending function.

Lumbar spine (L4) was modelled using Blender from the MRI data. Discretisation (volume meshing) of geometry was done in Blender, and the model was assigned material properties in congruent to a bone. Model was taken to ANSYS 18.2 and discretized, afterwards the boundary conditions are applied for further analysis. Load was simulated, and the results obtained were analysed in Abaqus. Furthermore, a flex sensor was used to compare the results obtained from simulation to those in actual scenario. The results obtained from computation were as such: The stress developed is in the annulus  $-752.9$  Pa. The displacement in the cortical rim is  $1.072 \times 10^{-2}$  mm. Therefore, the stress developed is not large for the actual loading conditions, and the displacement is negligible and does not cause any pain for the obtained computational result. The second case is the bent condition, flex sensor was used for its analysis, and the results were plotted.

## 2.1 Computational Analysis

MRI data of a person's lumbar vertebrae was taken and was converted into a 3D model as shown in Fig. 1 using Blender.

ANSYS was used for the discretisation of geometry because it provides an advantage on triangular mesh formation (shown in Fig. 2) on complex surfaces over other software. The number of nodes and number of elements (linear tetrahedral elements of type C3D4) generated are 20,297 and 101,418, respectively.

Lumbar L4 vertebrae were assigned bone material properties as shown in Fig. 3, and Abaqus was used for stress and displacement analysis because the propagation obtained in Abaqus is more refined and accurate than other software.

Fixed support (Fig. 4) was given on the bottom of lumbar L4 vertebrae to simulate the exact conditions experienced by the L4 while standing.

Load was applied as shown in Fig. 5 on the body of cortical rim for the exact simulation while standing.

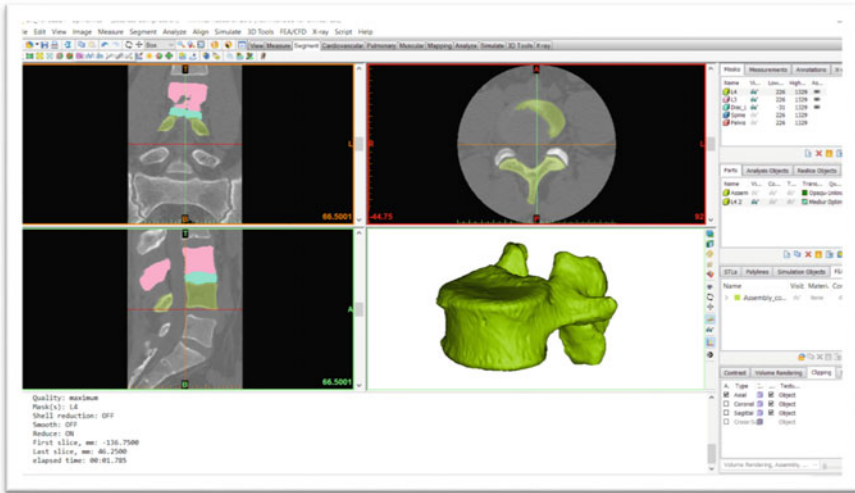


Fig. 1 Lumbar L4 vertebrae modelling in blender

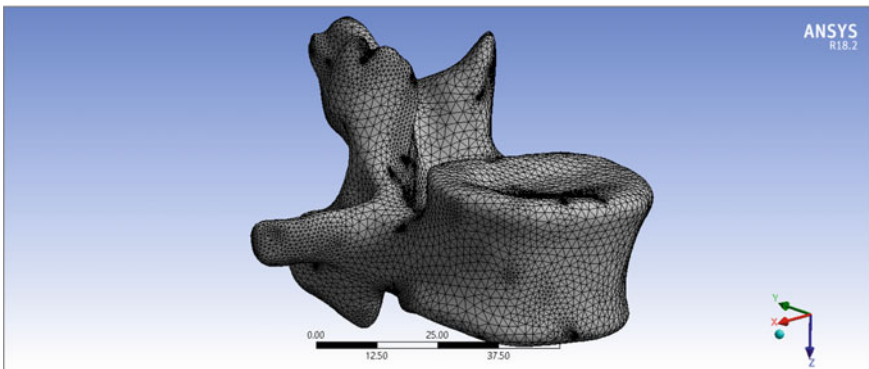


Fig. 2 Meshing of lumbar L4 vertebrae model

## 2.2 Flex Sensor Analysis

Flex sensor was placed on a person’s back, and he was allowed to stand for a specific amount of time. The reading on the deflection with respect to time was plotted (Figs. 6 and 7).

Flex sensor was placed on a person’s back, and he was allowed to bend. The graph for deflection w.r.t. time was plotted.

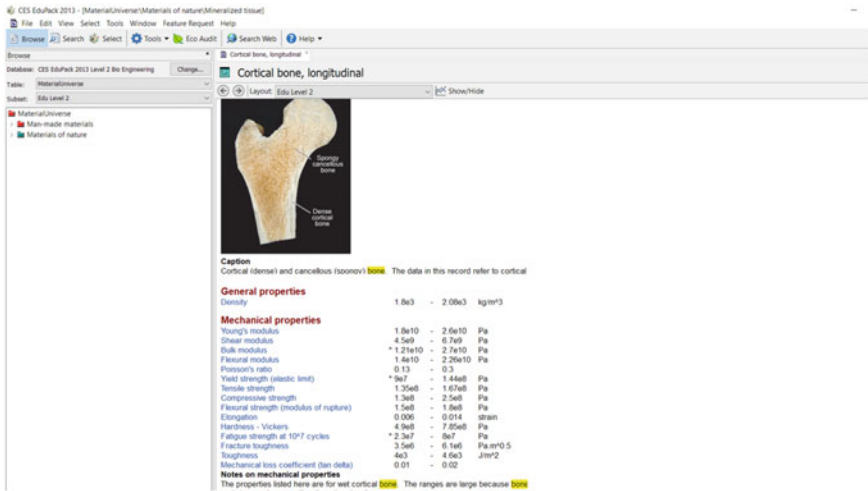


Fig. 3 Bone material assignment

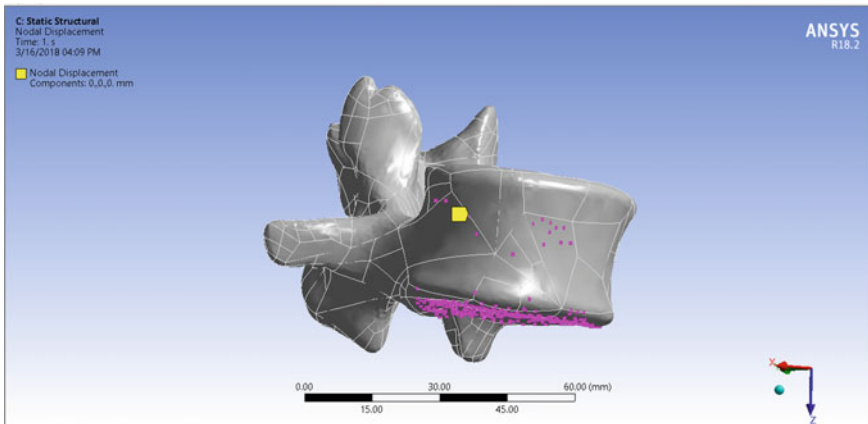


Fig. 4 Applying boundary condition: support

### 3 Results

#### 3.1 Computational Analysis

##### Von-Misses Stress

From Fig. 8, it can be seen that the stress is concentrated on annulus of lumbar L4 vertebrae, and it is the point experiencing the maximum stress (+4.500e+02) while standing.

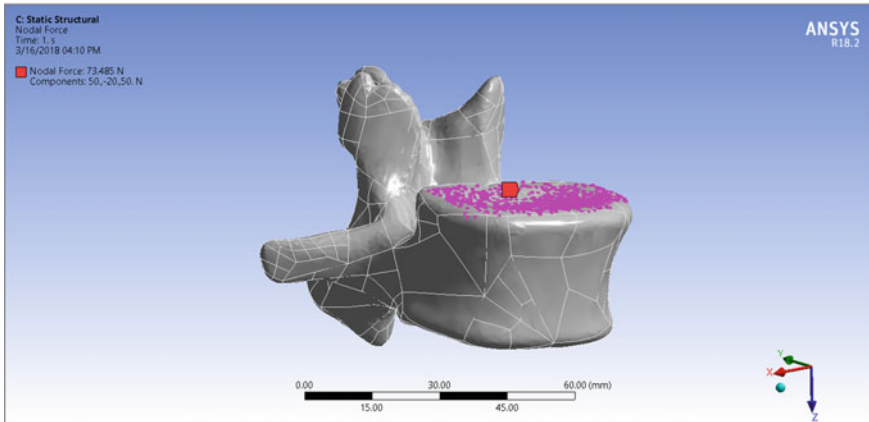


**Fig. 5** Applying boundary condition: load

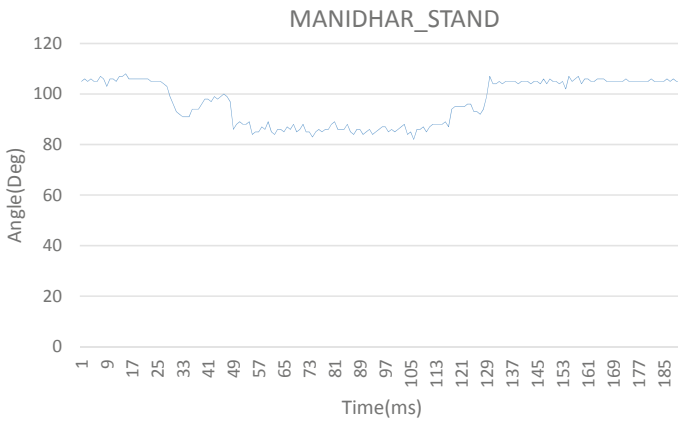


**Fig. 6** Angle/time plot for lumbar L4 vertebrae while standing

**Displacement**

Figure 9 illustrates that the maximum amount of displacement ( $+1.072e-05$ ) was found on the cortical rim of lumbar L4 vertebrae.

**3.2 Flex Sensor Analysis**

The results obtained from flex sensor showed that the lumbar L4 vertebrae experiences dynamic loads even when a person is standing in an upright position. This dynamic load leads to the change in the stress concentration point on the lumbar L4

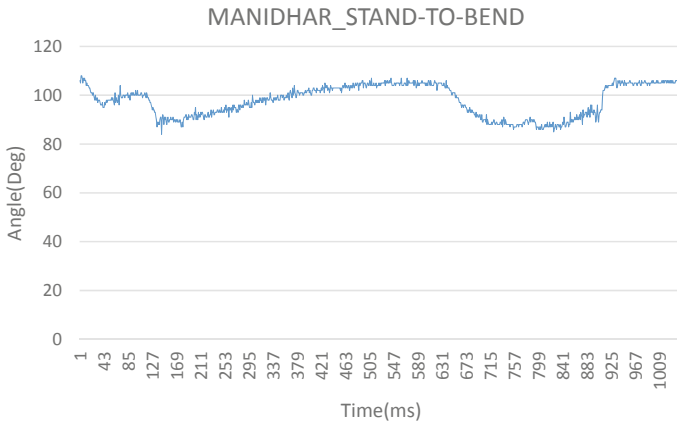


Fig. 7 Angle/time plot for lumbar L4 vertebrae while bending

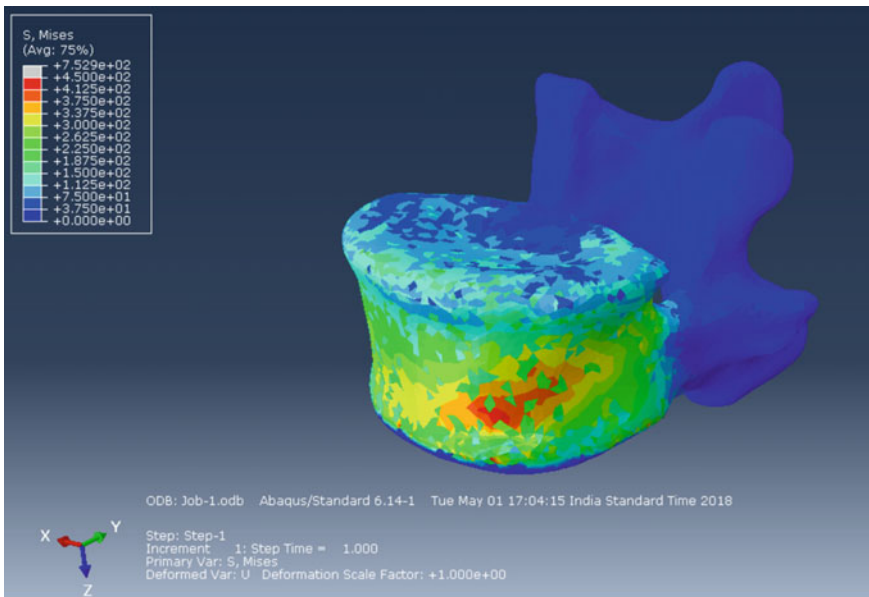
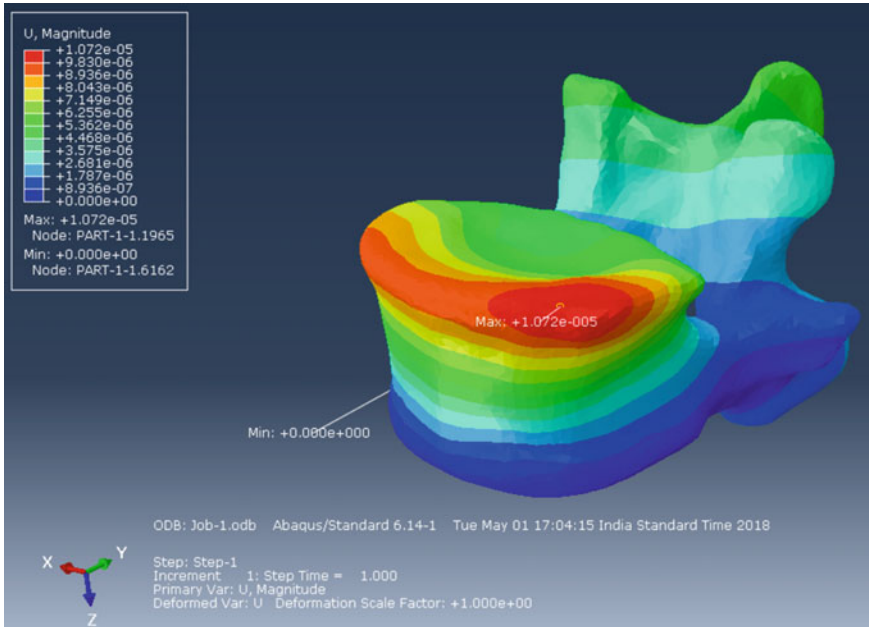


Fig. 8 Stress analysis profile obtained in Abaqus

vertebrae (as shown in Fig. 6) that is why, the computational analysis showed the stress concentrated over a region rather than a point. The same is the case with the displacement profile.

The change in dynamic load while bending is more than the change obtained in the upright position as shown in Fig. 7, which can help the doctors inform the patients



**Fig. 9** Displacement profile obtained in Abaqus

in the absolutely precise manner as to what should be the angle at which the pain associated with bending and standing would be minimum.

## 4 Conclusion

This paper aims to evaluate the stress and displacement experienced by lumbar L4 vertebrae during standing and bending. Both the computational and experimental procedures were employed to evaluate the stress during these loading conditions. The conclusions drawn from the analyses are depicted below.

1. Computational approach showed that the cortical rim in the anterior position of a lumbar bone experiences the maximum amount of displacement and the annulus of lumbar bone experiences the maximum amount of stress.
2. Results obtained using the flex sensor were found to be similar to that of computational approach.
3. Results obtained from flex sensor showed that the lumbar L4 vertebrae experiences dynamic load even while standing and bending.
4. This research can be further extended by putting load on various inclinations angles to lumbar L4 vertebrae, so that it can help an orthopedic surgeon to

decide and suggest the patient; the most optimum angle at which the stress and displacement associated to the lumbar L4 vertebrae would be minimum.

5. The results obtained from the current analysis will help for effective design of spine prosthesis.

## References



1. <https://mayfieldclinic.com/pe-anat spine.htm>. Developed by Mayfield Clinic, Cincinnati, Ohio
2. Zysset P, Qin L, Lang T, Khosla S, Leslie WD, Shepherd JA, Schousboe JT, Engelke K (2015) ISCD position development conference on clinical use of quantitative computed tomography-based finite element analysis of the hip and spine in the management of osteoporosis in adults, vol 18(3), pp 359–392. The International Society for Clinical Densitometry
3. Wang L, Zhang B, Chen S, Lu X, Li Z-Y, Guo Q (2016) A validated finite element analysis of facet joint stress in degenerative lumbar scoliosis. *World Neurosurg* 95:126–133
4. Wang S, Park WM, Kim YH, Cha T, Wood K, Li G (2014) In vivo loads in the Lumbar L3–4 disc during a weight lifting extension. *Clin Biomech* 29(2):155–160
5. Villa T, La Barbera L, Galbusera F (2014) Comparative analysis of international standards for the fatigue testing of posterior spinal fixation systems. *Spine J* 14:695–704 (2014)
6. Sterba M, Arnoux P-J, Labelle H, Warner WC, Aubin C-E (2018) Biomechanical analysis of spino-pelvic postural configurations in spondylolysis subjected to various sport-related dynamic loading conditions. *Eur Spine J* 27(8):2044–2052
7. Song M, Zhang Z, Lu M, Zong J, Dong C, Ma K, Wang S (2014) Four lateral mass screw fixation techniques in lower cervical spine following laminectomy: a finite element analysis study of stress distribution. *BioMed Eng Online* 13:115
8. Shahvarpour A, Shirazi-Adl A, Lariviere C, Bazrgari B (2015) Trunk active response and spinal forces in sudden forward loading-analysis of the role of perturbation load and pre-perturbation conditions by a kinematics-driven model. *J Biomech* 48:44–52
9. Mustafy T, El-Rich M, Mesfar W, Moglo K (2014) Investigation of impact loading rate effects on the ligamentous cervical spinal load-partitioning using finite element model of functional spinal unit C2–C3. *J Biomech* 47:28912903
10. McGill SM, Cannon J, Anderson JT (2014) Analysis of pushing exercise: muscle activity and spine load while contrasting techniques on stable surfaces with a labile suspension strap training system. *J Strength Conditioning Res* 28(2):105–116
11. Ganbat D, Kim YH, Kim K, Jin YJ, Park WM (2015) Effect of mechanical loading on heterotopic ossification in cervical total disc replacement: a three dimensional finite element analysis. *Biomech Model Mechanobiol* 15(5):1191–9
12. Galbusera F, van Rijsbergen M, Ito K, Huyghe JM, Brayda-Bruno M, Wilke H-J (2014) Ageing and degenerative changes of the intervertebral disc and their impact on spinal flexibility. *Eur Spine J* (23)324–332
13. Dreischarf M, Shirazi-Adl A, Arjmand N, Rohlmann A, Schmidt H (2015) Estimation of loads on human lumbar spine: a review of in-vivo and computational model studies. *J Biomech* 49(6):833–845
14. Arun Prasath S., Dhasan R, Vijayaragavan E (2016) A study of biomechanical behaviour of lumbar vertebra L2–L4 region for osteoporosis condition in endplates. *Indian J Sci Technol* 9(34)
15. Ivanov AA, Faizan A, Ebraheim NA, Yeasting R, Goel VK (2007) The effect of removing the lateral part of the pars interarticularis on stress distribution at the neural arch in lumbar foraminal micro-decompression at L3–L4 and L4–L5: anatomic and finite element investigations. *Spine* 32:2462–2466



16. Sairyo K, Goel VK, Masuda A, Vishnubhotla S, Faizan A, Biyani A, Ebraheim N, Yonekura D, Murakami R-I, Terai T (2006) Three-dimensional finite element analysis of the pediatric lumbar spine part I: pathomechanism of apophyseal bony ring fracture. *Eur Spine J* 15:923–929

# Design Optimization of Torque Link of an Aircraft Landing Gear Assembly



Srishti Singh , Rishabh Chaudhary , Vaibhav Kumar Pathak ,  
and Vipul Saxena 

**Abstract** In the landing gear assembly of an aircraft, the torque links connect the two telescoping cylinders and prevent the relative rotation of the piston to maintain the wheel alignment during taxiing on ground. However, it contributes to the dead weight during flight of the aircraft. Thus, reducing the weight of the torque link will turn down the overall weight of the aircraft. This can improve fuel economy which in turn will benefit the aviation industry remarkably. Topology optimization is a method of simultaneously optimizing the topology and orientation of the boundaries to obtain most efficient design. Topology optimization of torque link is carried out with objective function to minimize the compliance. The torque link is designed in CREO3.0, and optimization is executed in ANSYS 19.2. The weight of torque link is reduced from 6.28 to 5.61 kg, resulting in optimize percent of 12.09. This will result in efficient design with reduced mass, fulfilling all the functional requirements.

**Keywords** Landing gear · Pseudo-density · SIMP technique · Torque link · Topology optimization

## 1 Introduction

In aviation industry, every gram count and thus reduction in weight is fundamental. Fuel efficiency and weight goes hand in hand. Every decrease in weight significantly reduces operating cost of airlines and also lowers the emission of carbon dioxide [1]. Topology optimization is an approach of design that allows best material distribution in given space [2]. Topology optimization helps in minimizing or maximizing the objective function for the given constraints [3].

According to objective and response constraint, the optimization of a continuum structure is categorized as shape, size, and topology optimization [4]. In shape optimization, the structure is optimized to change its geometry while the topology is retained within the structure [5]. The size optimization is used to derive the optimum

---

S. Singh · R. Chaudhary (✉) · V. K. Pathak · V. Saxena  
Department of Mechanical Engineering, JSSATE, Noida 201301, India

model parameters, for instance thickness of the given geometry. In some cases, the structure's topology is unknown and thus topology optimization is used to find the ideal topology for the given shape [6].

The in-built topology optimization module in finite element tool ANSYS 2019 interpret and performs the analysis with a couple of available option, namely optimal approach and sequential approach. In ANSYS, topology optimization maximizes the stiffness or minimizes the compliance, while reducing the volume for the set limits or range. Every problem of topology optimization in ANSYS is converted into shape optimization with a new configuration, and optimization parameter is the material distribution. The objective is achieved by reducing strain energy of the structure while meeting the given constraints.

The torque links connect the telescoping cylinders in the landing gear assembly. The piston is free to rotate inside the upper strut. To constraint the motion of wheel in straight path, the torque links prevent relative rotation between the piston and the strut while taxiing on the ground [7, 8]. Hence, a moment acts on the torque link. Torque links also allow controlled steering when connected to the actuator.

Jing-Kui et al. [9] used solid isotropic material with penalization (SIMP) interpolation method of shape optimization module in ANSYS Workbench with a goal to minimize the flexibility of the structure and volume constraint of 20% and achieve a weight reduction of 16.7% for the torque arm. Wong et al. [10] used multiple multi-body dynamics topology optimization iterations within the design space for Sukhoi Superjet slave links of main landing gear and obtained two revised design. For the first revised design, he achieved an overall 67% weight reduction but no cost saving due to complexities in the design, and for the second design, he achieved 36% weight reduction with approximately 60% cost saving.

In this paper, lower torque link of an American-based single turboprop utility aircraft is modeled in CREO3.0 and optimized using topology optimization module of ANSYS 2019 to minimize weight of the torque arm without altering its functional requirements in the assembly.

## 2 Static Structural Analysis for Preprocessing of Optimization

Most of the studies suggest landing gear as a nonlinear multi-degree of freedom mechanical system [11]. The foremost requirement of topology optimization is a pre-stressed structure. In other words, it requires some initial values of stress and strain to find out the optimum solution for the given problem. For given purpose, the analysis is split in two steps: The first step will have pre-stress effect to account for initial strain and stress. In this analysis, a lower torque link with 424.47 mm length and 44 and 36 mm bore, at lower and upper end, respectively, is designed in CREO3.0 as shown in Fig. 1 and the geometry is imported into ANSYS in IGES format.

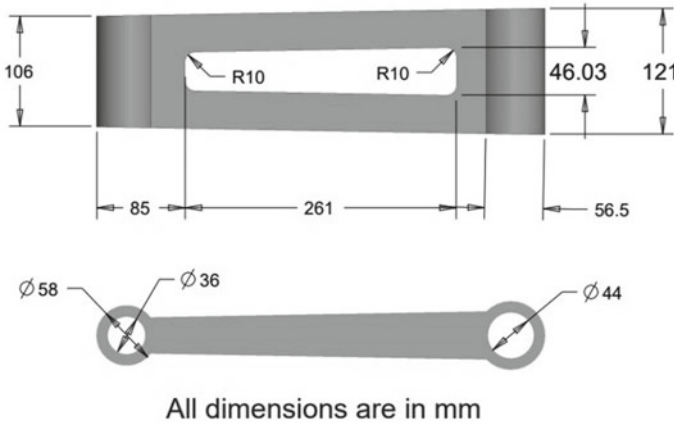


**Fig. 1** Detailed drawing of torque link

A patch conforming mesh with tetrahedral elements and inflated boundary is used to discretize the torque link as shown in Fig. 2. As the aspect ratio of tetrahedral mesh element is near to unity, the tetrahedral mesh is selected to ensure the accuracy of results. A total of 26,753 nodes and 11,363 elements are generated on the basis of convergence analysis as shown in Fig. 3.

A fixed support is provided at one end of the link while another end is connected to the piston which is loaded with a moment of  $7 \times 10^6$  N mm in the counterclockwise direction about the z-axis [9] as shown in Fig. 4.

Titanium alloys and composites are employed for manufacturing of aircraft components because these are exceptional alternatives to steel and aluminum alloys [12]. In this analysis, the material assigned to the torque link is TIMETAL 834, properties are given in Table 1, which is a near-alpha titanium alloy.

Figures 5 and 6 illustrate the deformation and maximum equivalent stress for the pre-stressed torque link in the static structural module.

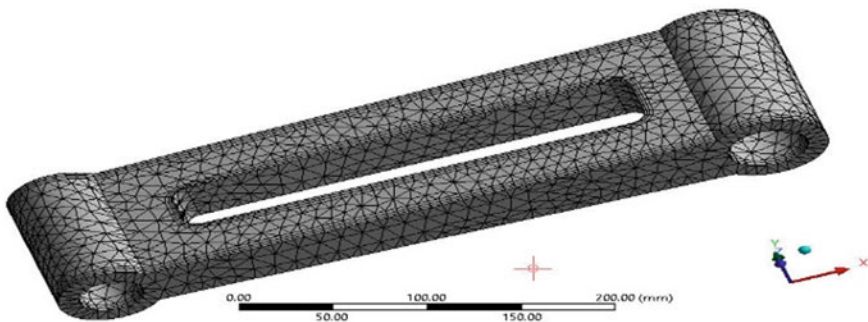


**Fig. 2** Discretized torque link

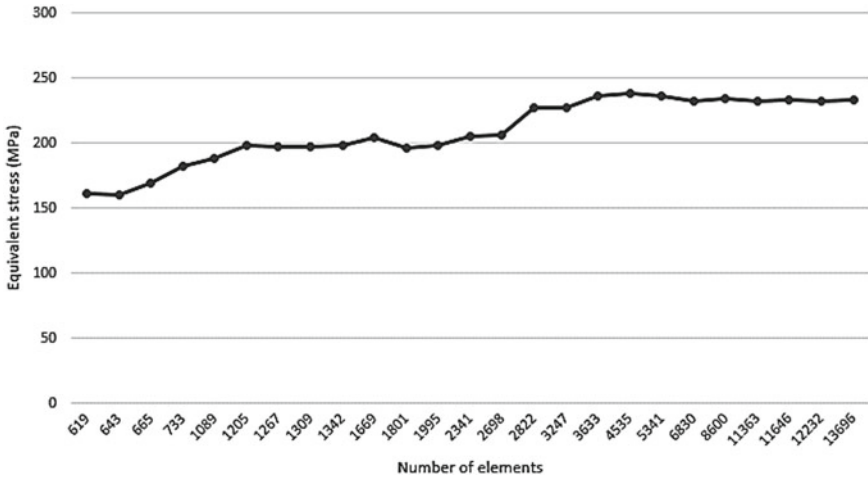


Fig. 3 Convergence plot

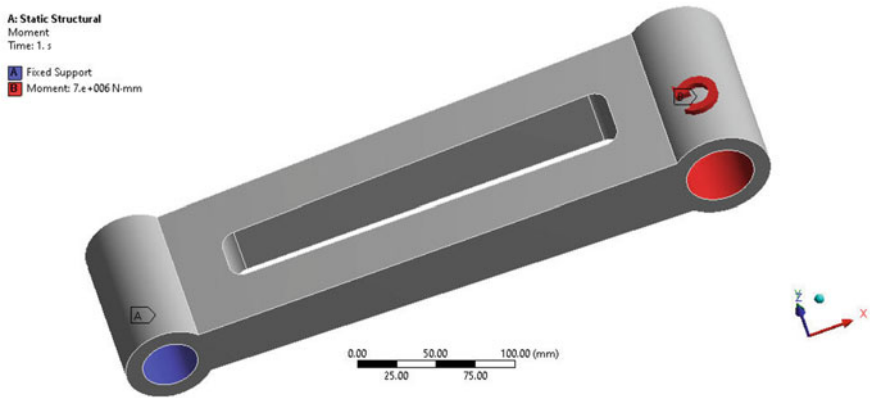


Fig. 4 Fixed support and moment applied on torque link

Table 1 Properties of TIMETAL 834 [13]

Material	Density (g cm <sup>-3</sup> )	Young's modulus (GPa)	Poisson's ratio	Tensile yield strength (MPa)	Tensile ultimate strength (MPa)
TIMETAL 834	4.55	120	0.32	930	1050

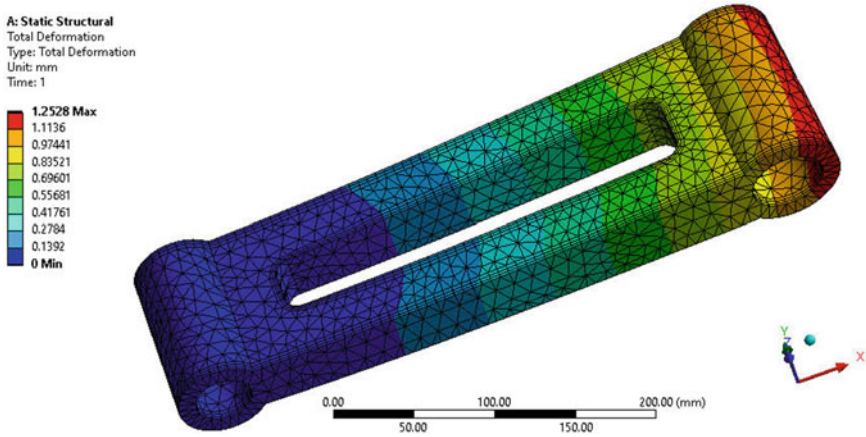


Fig. 5 Total deformation before optimization

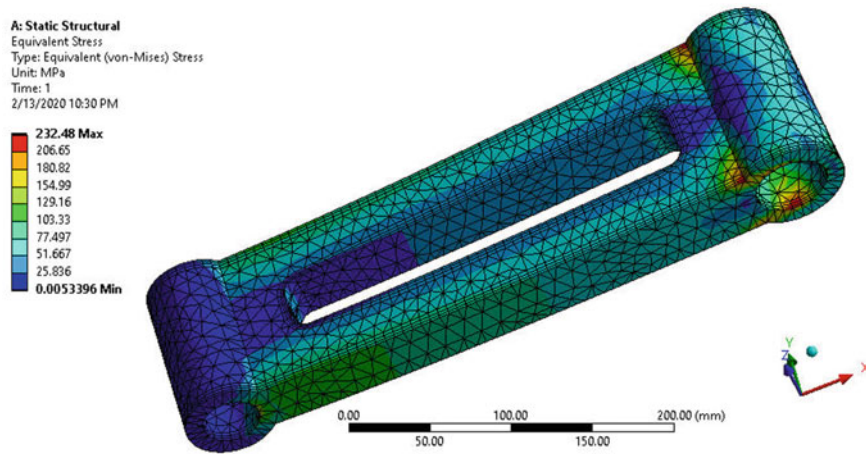


Fig. 6 Equivalent stress before optimization

### 3 Methodology

The model of torque link is created in CREO3.0, and then torque link is imported into ANSYS. The static structural analysis is performed after the assignment of material. Then the pre-stressed structure is optimized under topology optimization module in ANSYS, where the response constraint is volume. Then the geometry is optimized and validated.

The topology optimization works on the principle of SIMP technique in which the design variable ( $\eta$ ) assigns pseudo-density to every finite element ( $\eta_a$ ) in the structure [14]. The magnitude of pseudo-density lies between 0 and 1 [15]. If  $\eta$  is

almost equal to zero, then a zero magnitude of density is assigned to that element while it is assigned as one if the  $\eta$  is almost equal to one. This pseudo-density alters the elasticity tensor and hence the stress vector which is governed by Eq. (1).

$$[\sigma_a] = [E_a][\epsilon_a] \quad (1)$$

where  $\sigma_a$  is the stress vector,  $E_a$  is the elastic tensor, and  $\epsilon_a$  is the strain tensor.

For minimizing the compliance, take an example, the volume has to be constrained and hence the strain energy has to be reduced for the given boundary conditions and loads. For this case, the governing equation is

$$C = \min F(\eta_a) \quad (2)$$

where  $C$  is the compliance,  $\eta_{la}$  is the pseudo-density for the element  $a$  and  $0 \leq \eta_{la} \leq 1$ .

## 4 Result of Topology Optimization

The optimization region is defined as the surface of the link excluding the cylindrical surface at both ends as it will change the bore, which holds the pin, of the torque link. The objective is to minimize the compliance in the static structural environment of ANSYS. Geometric density is the design variable in optimization process. The response constraint is set to retain 81% of total volume after multiple iterations until the solution is converged. The optimal structure is obtained finally in 13 iterations, and the final iteration has processing time of 1 min and 41 s.

The approach to optimize torque link is to maximize the stiffness of structure and minimize the volume while fulfilling its functional requirements. The number of elements over which stress is distributed and has reduced after optimization because the material is stipulated on the basis of pseudo-density value assigned by decision variable ( $\eta$ ). The results are given in Table 2. The results for optimized geometry, as shown in Figs. 7 and 8, illustrate that the increase in stress, deformation, and other important performance parameters are not exceeding the permissible stress limit for the torque link, and thus, satisfactorily meets the need. The weight of link after optimization reduced from 6.38 to 5.61 kg, thus obtaining the optimize percent

**Table 2** Results of topology optimization

Parameter	Before optimization	After optimization
Total deformation (mm)	1.25	1.26
Maximum equivalent stress (MPa)	232.48	234.79
Weight (kg)	6.38	5.61
Optimize percent	12.09	

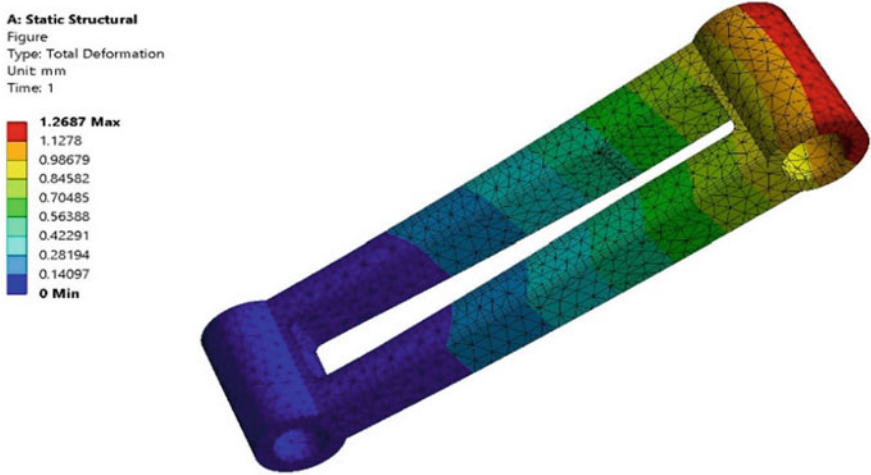


Fig. 7 Maximum total deformation after optimization

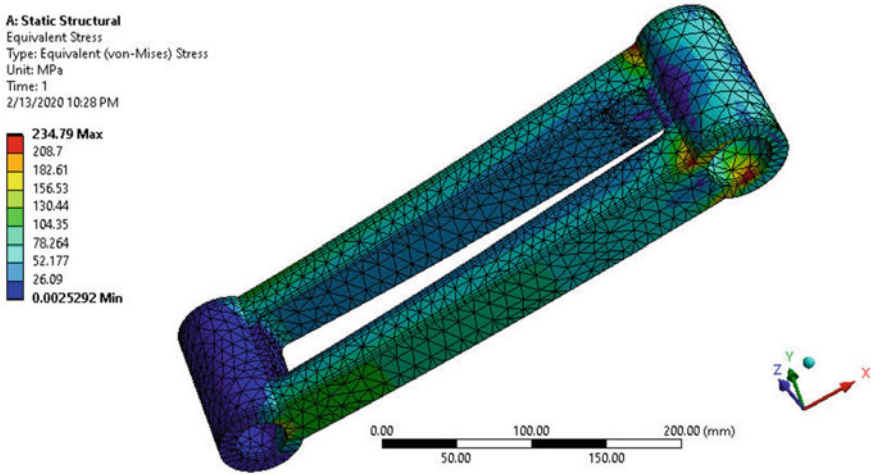


Fig. 8 Maximum equivalent stress after optimization

of 12.09. The maximum total deformation after optimization is 1.26 mm, and the maximum equivalent stress is 234.79 MPa.



## 5 Conclusion

In this paper, ANSYS platform, that is finite element tool, is used to carry out the numerical processing for the optimization of continuum structure of torque link using the SIMP technique in topology optimization module.

Some of the concluding remarks are given below:

1. The topology optimization module is selected to optimize the torque link in order to ensure the proper functioning of the model in landing gear assembly.
2. The objective to minimize the compliance is achieved by arresting the percent of volume reduction.
3. With the application of optimized geometry in landing gear assembly, an overall weight reduction of 12.09% is achieved.
4. The methodology used in this research paper for topology optimization can be used to optimize other components of aircraft. This approach can be used in various applications which include the optimization of automobile transmission housing, turbine disk.

## References

1. Grote M, Williams I, Preston J (2014) Direct carbon dioxide emissions from civil aircraft. *Atmos Environ* 95:214–224
2. Saleem W, Yuqing F, Yunqiao W (2008) Application of topology optimization and manufacturing simulations—a new trend in design of aircraft components. In: *Proceedings of the international multi conference of engineers and computer scientists*, vol 2
3. Zhu JH, Zhang WH, Xia L (2016) Topology optimization in aircraft and aerospace structures design. *Arch Comput Methods Eng* 23(4):595–622
4. Deaton JD, Grandhi RV (2014) A survey of structural and multidisciplinary continuum topology optimization: post 2000. *Struct Multi Optim* 49(1):1–38
5. Chen J, Shapiro V, Suresh K, Tsukanov I (2007) Shape optimization with topological changes and parametric control. *Int J Numer Methods Eng* 71(3):313–346
6. Luo Z, Wang MY, Wang S, Wei P (2008) A level set-based parameterization method for structural shape and topology optimization. *Int J Numer Methods Eng* 76(1):1–26
7. Gowda AC, Basha N (2014) Linear static and fatigue analysis of nose landing gear for trainer aircraft. *Measurement* 2:5
8. Freitas M, Infante V, Baptista R (2019) Failure analysis of the nose landing gear axle of an aircraft. *Eng Fail Anal* 101:113–120
9. Jing-Kui LI, Fei-Fei DUAN, Rui-Guan LIN (2017) Topology optimization to torque arm in landing gear system based on ANSYS workbench. *DEStech Trans Eng Technol Res (icmeca)* 46–50
10. Wong J, Ryan L, Kim IY (2018) Design optimization of aircraft landing gear assembly under dynamic loading. *Struct Multi Optim* 57(3):1357–1375
11. Somieski G (1997) Shimmy analysis of a simple aircraft nose landing gear model using different mathematical methods. *Aerosp Sci Technol* 1(8):545–555
12. Thuis HGSJ (1999) Development of a composite torque link for helicopter landing gear applications. National Aerospace Laboratory NLR
13. Matweb <http://www.matweb.com/>. Accessed 14 Feb 2020

14. Zuo W, Saitou K (2017) Multi-material topology optimization using ordered SIMP interpolation. *Struct Multi Optim* 55(2):477–491
15. Vatanabe SL, Lippi TN, de Lima CR, Paulino GH, Silva EC (2016) Topology optimization with manufacturing constraints: a unified projection-based approach. *Adv Eng Softw* 100:97–112

# System Modeling, Simulation, and Analysis of Electrohydrostatic Actuator for Armoured Recovery Vehicles



Manish Kumar and Shweta Singh

**Abstract** The electrohydrostatic actuator (EHA) is an emerging technology which is being used extensively and effectively in the field of aviation to control the aircraft which otherwise was the difficult task. It is a modular and compact design obtained by combining various cutting edge technologies. This technology has replaced the bulky and leak prone centralized hydraulic system with a compact and modular design. Fixed pump variable motor simulation (FPVM) model is developed to analyze the digital prototype of physical model to predict its performance in real world by using the software tool advanced modeling environment for performing simulations of engineering systems (AMESim). The performance of the simulation model is tested with and without load. The open- and the closed-loop system analysis are carried out. The thermal analysis is also done using proportional integral derivative (PID) controller.

**Keywords** EHA · AMESim · PID · FPVM

## 1 Introduction

Electrohydrostatic actuator (EHA) system is a multi-disciplinary integrated modular design comprising of electrical, hydraulic, mechanical, and control subsystems [1]. It is also known as power-by-wire technology [2]. The need of PBW actuation system for the next-generation all-electric armoured fighting vehicle concept has been well-envisaged for the future [3]. EHA has mainly three possible configuration based on pump and motor arrangement which are fixed pump and variable motor (FPVM), variable pump and variable motor (VPVM), and variable pump and fixed motor (VPFM) depending on requirements these are used for various applications [4]. The main component of EHA is Brushless Direct Current (BLDC) Motor, control

---

M. Kumar (✉)  
Jawaharlal Nehru University, New Delhi, India

S. Singh  
J.K. Institute, University of Allahabad, Allahabad, Uttar Pradesh, India

element, Actuator and PID Controller, pump [5, 6]. Due to its compact size and very high reliability, this system is predominantly used in flight control applications [3]. It has replaced the bulky defect-prone centralized hydraulic system from the Modern days Aircraft [7]. In spite of its utilization in aviation, the full potential of the EHA are still unexplored [2]. It can be used in Military Applications for the replacement of centralized hydraulic system in Armoured recovery Vehicles which is completely dependent on hydraulic system for its operations. The future of armored fighting vehicle will be more agile lightweight multi-terrain and multirole [8].

The work presented in this paper in the form of analyzing the dynamic behaviour of EHA in no-load and loaded conditions and also its behaviour in open-loop and closed-loop systems to understand the suitability of EHA in military grade equipments and function as standalone system. Further, the novel work carried out by analysing the thermal behaviour of EHA and the effect of rise in temperature on the working fluid inside the EHA [9]. Since the military grade equipments are subjected to various terrains with huge variation in temperature, these equipment needs to be rugged. To carry out the above analysis, the system model was developed on AMESim software which deals with the development of mathematical description of a system to predict its dynamic behavior. The description includes the first-order or higher-order equations based on the required accuracy level of the model. As we tend to improve the accuracy level of the model, the complexity and the total consumed power of the model proportionately increase for simulation. There is always a tradeoff between model accuracy and model complexity [10]. Hence, a simple model with required level of accuracy is considered to predict the system dynamic behaviour [11]. In addition, system model provides a platform to vary different parameters and study how each parameters affect the performance of system. Simulation provides an easy and cost-effective method to understand the dynamic system behavior. The system model developed has represented the actual dynamics. It also has all system information, which plays a major role in affecting the system dynamics.

Section 1 explains about the literature survey and working principle of EHA. Section 2 of this paper provides an insight on configuration considered in present research work. The system modeling of EHA using collaborative approach and AMESim tool is explained in Sect. 3. Section 4 illustrates the simulation results recorded through AMESim-based bond graph-based analysis [12]. Section 5 explains about the analysis of open-loop and closed-loop systems using PID controller and also draws the comparison between both. Section 6 explains the thermal analysis which is carried out by raising the temperature of the hydraulic fluid from room temperature to 80 °C followed by conclusion.

## 2 System Configuration

In the present study, fixed displacement and variable motor (FPVM) configuration is considered because of its simple structure and relatively higher efficiency [13]. EHA with symmetric cylinder is considered because of its wide applicability in the field of aviation and its applications in the industries. In addition, EHA brings the energy efficiency, modularity, and localization of present actuating system; this configuration has one fix displacement pump and variable displacement motor [14].

### 2.1 System Description

The schematic of EHA configuration considered in the present work is shown in Fig. 1. It is the combination of electrical, hydraulic, mechanical, and controller domains. Electrical domain consists of brushless direct current (BLDC) servomotor [15], displacement sensor, and speed sensor. Hydraulic domain consists of fixed displacement bidirectional pump (FDBP), non-return valves (NRV) [1], pressure relief valves (PRV), single-rod double acting symmetric cylinder and reservoir. The control domain consists of PID controller and its algorithm and data acquisition system. The PID controller is given with a position set point, and it acquires displacement sensor signal as a feedback. Controller gives motor speed signal as controller output [16]. BLDC servomotor drives the bidirectional pump based on controller output [14]. The pump has suction and delivery lines connected to the double

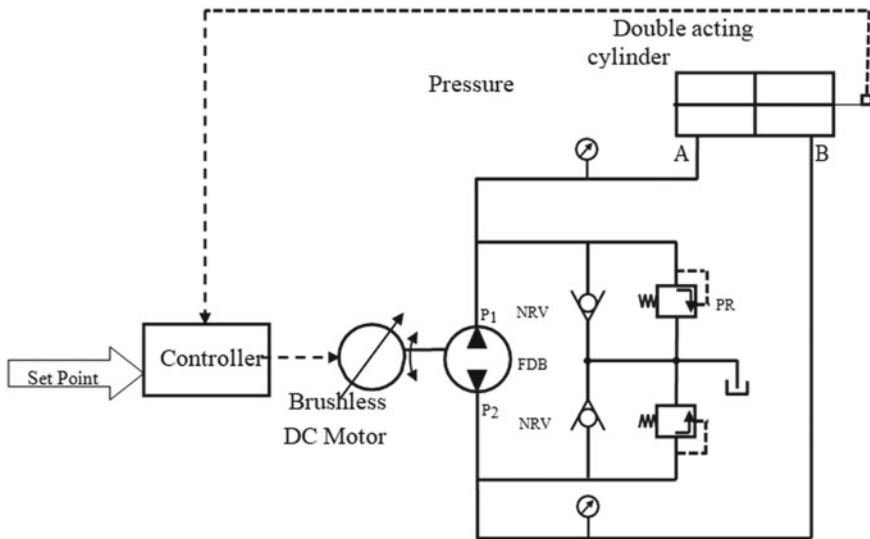


Fig. 1 Schematic of FPVM electrohydraulic actuator (EHA) system

acting symmetric cylinder. Non-return valve (NRV) is used to allow the flow to suction side and restrict the flow in discharge side of pump depending on the direction of rotation of pump, pressure relief valve (PRV) is used to limit the maximum pressure at inlet and outlet lines of cylinder. The tank serves as a reservoir for oil. The circuit forms the closed-loop position control of symmetric cylinder using fixed displacement pump and variable speed motor [17].

## 2.2 Working Principle

A position set point is given to the controller. The controller gives output signal based on difference between the desired displacement (set point) and measured displacement (position feedback) [3]. The controller output is a speed signal to the BLDC servomotor. The servomotor drives the fixed displacement bidirectional pump. The variable speed of the pump provides different flow rates to cylinder in forward motion of piston,  $P1$  is the delivery side, and  $P2$  is the suction side of pump. The pump sucks oil from the tank through NRV 2 to suction side ( $P2$ ) of the pump. The pump rotates and delivers the oil to port A of the cylinder (piston side). In case of return motion of cylinder, the motor rotates in the opposite direction based on the controller output signal. The  $P1$  becomes suction side, and  $P2$  becomes delivery side of the pump. The pump sucks oil from the tank through NRV 1 and delivers to port B of cylinder and piston moves in return direction. If pressure exceeds the safe limit, then the oil goes to tank through PRV 2. In the subsequent motion of cylinder, the oil is sucked from the piston side of cylinder instead of tank [18]. If oil is required in addition, then only oil is sucked from the reservoir. In the present work, experimental investigations have been carried out on both symmetric and asymmetric actuators, and it is important to note that the asymmetric cylinder has volume difference in the forward and return direction. Hence, the amount of oil required for forward and return stroke is different for the same amount of pump flow. The oil is re-circulated from cylinder to pump [19]. The oil from the tank is sucked only due to flow difference or due to the loss of oil by leakage. The controlling of asymmetric cylinder becomes more challenging when compared to symmetric cylinder due to the different flow in forward and return direction.

## 3 System Model

System model has been developed by using the library of AMESim software. The system model replicates the physical model in the digital form. This model has been developed to carry out various analysis [13]. The system contains all necessary information to give out the dynamic behavior of system. It plays an important role in analyzing system parameters, and it also helps in evaluating the controller performance for the future application in various different types of equipments.

### 3.1 AMESim System Modeling and Simulation

Advanced modeling environment for creating the simulations of any type of dynamic engineering systems (AMESim) software is based on bond graph modeling concept [20]. In the current world of smart, automated and electrified products it is clear that the development and performance validation of such products is increasingly more complex. AMESim is an integrated, scalable, mechatronic system simulation platform [4]. The software has various inbuilt modeling literary such as electrical, hydraulic, mechanical, pneumatic, control, thermal, vehicle dynamics, and so on. It provides the platform to analyze, simulate, and study various parameters. It includes optimization, energy management, activity analysis, sensitivity analysis, frequency, and time domain analysis. It also provides interface with other software's like MATLAB, LabVIEW, and Modelica [10]. A collaborative simulation provides effective way for analysis of multi-disciplinary system. Hence, collaborative simulation is carried out using AMESim and LabVIEW software. The electrical, hydraulic, and mechanical subsystem is modeled in AMESim. The controller subsystem is developed in LabVIEW and interfaced with AMESim software. The advantage of modeling control part in LabVIEW is that the same control module can be used for both simulation and experimental studies. EHA system modeled using AMESim tool is shown in Fig. 2. The AMESim system model has one to one relation with the system configuration shown in Fig. 2. The model has subsystems such as brushless DC servomotor, pump, valve manifold and reservoir, actuation system, and controller subsystems. Motor subsystem has BLDC motor attached with the inertial element [21]. The inertia element signifies combined inertia of motor-pump and mechanical coupling. Valve manifold has necessary NRV and PRV to ensure proper working of the circuit and keeps pressure levels within the safe limit. The controller subsystem has interface block which interfaces AMESim with LabVIEW software. The piston

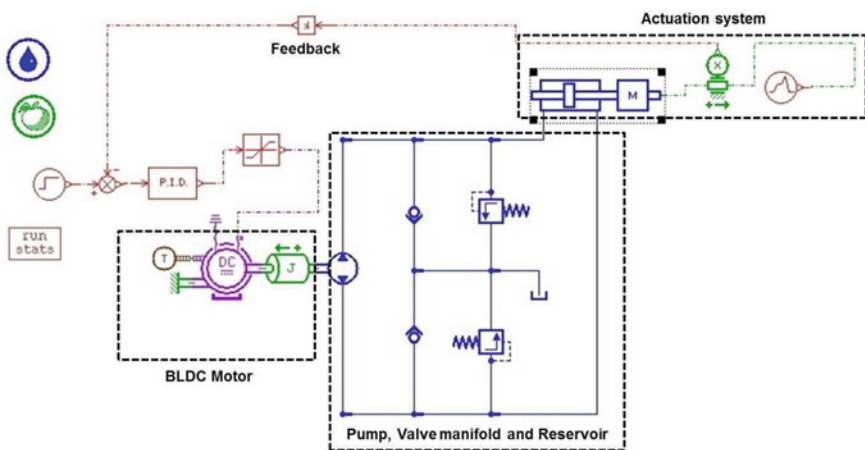


Fig. 2 AMESim model of electrohydraulic actuator (EHA)

displacement is given as a feedback to the controller, and its output is given to the motor [22].

The absolute viscosity, density, and bulk modulus of hydraulic oil incorporated into hydraulic fluid properties module in AMESim model [11]. System simulation has been carried out to study the closed-loop behavior of the system.

Table 1 shows the parameters of EHA system considered for simulation. The simulation is carried out using Livermore Solver for Ordinary Differential Equations (LSODA) available in LMS AMESim tool (AMESim, 2014).

**Table 1** Input parameters to AMESim model

	Components	Parameters	Value
1.	Brushless DC servomotor	Armature resistance	0.8 $\Omega$
		Armature inductance	$1.3 \times 10^{-3}$ H
		Speed constant	0.11 Vs/rad
		Torque constant	0.11 Nm/A
		Motor inertia	$3 \times 10^{-5}$ kg m <sup>2</sup>
		Viscous friction in motor	$2.54 \times 10^{-3}$ Nm/rpm
2.	Bidirectional pump	Pump displacement	1.48 cc/rev
		Volumetric efficiency	0.93
		Mechanical efficiency	0.87
3.	Symmetric cylinder	Piston diameter	29.88 mm
		Rod diameter	20.38 mm
		Stroke length	50 mm
		Coulomb friction	0.981 N
		Static friction	14.7 N
		Viscous friction	0.01 NS/m
4.	Valves	PRV cracking pressure	10 bar
		NRV cracking pressure	0.3 bar
5.	Reservoir	Tank pressure	1 bar
6.	Oil properties	Density	857 kg/m <sup>3</sup>
		Bulk modulus	$1 \times 10^6$ N/m <sup>2</sup>
		Absolute viscosity	28 cP
7.	Gain parameters	Proportional gain	8400
		Integral time	0
		Derivative time	0.002



## 4 Simulation Result

This section shows the results obtained by subjecting the developed model to different environments. The dynamic behavior of the model was first analyzed without load condition or in no-load condition. Subsequently, the same model was subjected to load condition by attaching 1 kg of load and the behavior of the model was observed. To further ascertain the nature of the model, it was tested in open-loop and closed-loop environment and the behavior of the model observed and documented.

### 4.1 Symmetric Actuator Without Load

Graph shown in Fig. 3 is the displacement of the symmetric actuator for the full stroke when the inputs are as per Table 1. For the above simulation result, a PID controller is used. The major factors that contribute to the actuator response are the bulk modulus, Coulomb, and static friction. As we understand from the result graph using PID controller that actuator will take 1.64 s of time 0 move 50 mm length.

Figure 4 shows the actuator velocity profile over a stroke length of 50 mm, as we see the actuator takes 1.64 s to complete the stroke. The velocity of the actuator reaches a maximum value of 0.10 m/s at the start and the velocity tends to slow as the actuator travels through the stroke and eventually dies down to zero at the end of the stroke.

The actuator acceleration profile is shown in Fig. 5. It is seen that there is an initial spike in the acceleration, and thereafter, the acceleration of the actuator reduces instantly to zero. It is the momentum generated after the initial spike in acceleration that powers the actuator to complete the stroke.

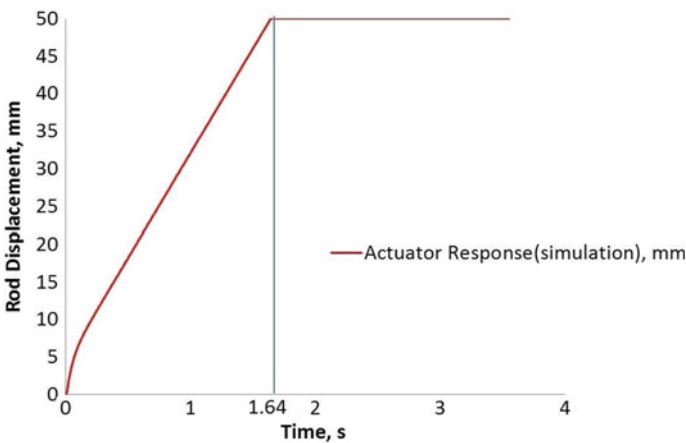


Fig. 3 Actuator displacement with PD controller

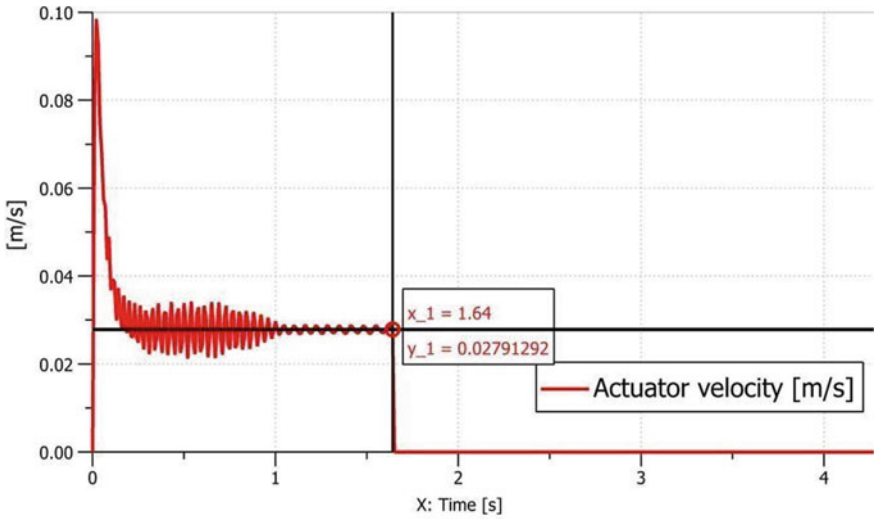


Fig. 4 Actuator velocity profile

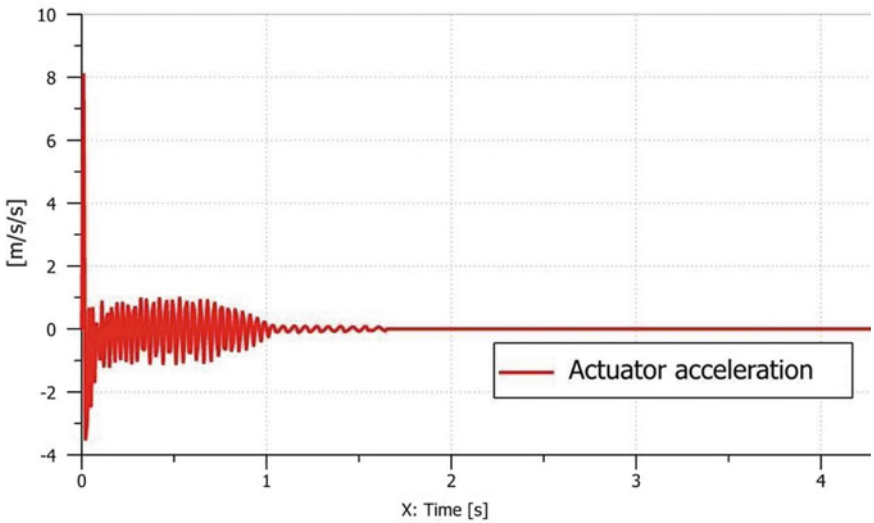


Fig. 5 Actuator acceleration profile

### 4.2 Symmetric Actuator with 1 kg Load

The simulation study has been carried out by subjecting the symmetric actuator to a load of 1 kg. Figure 6 shows the response of the symmetric actuator when subjected to 1 kg load. It is seen that at no-load condition, the symmetric actuator takes 1.64 s

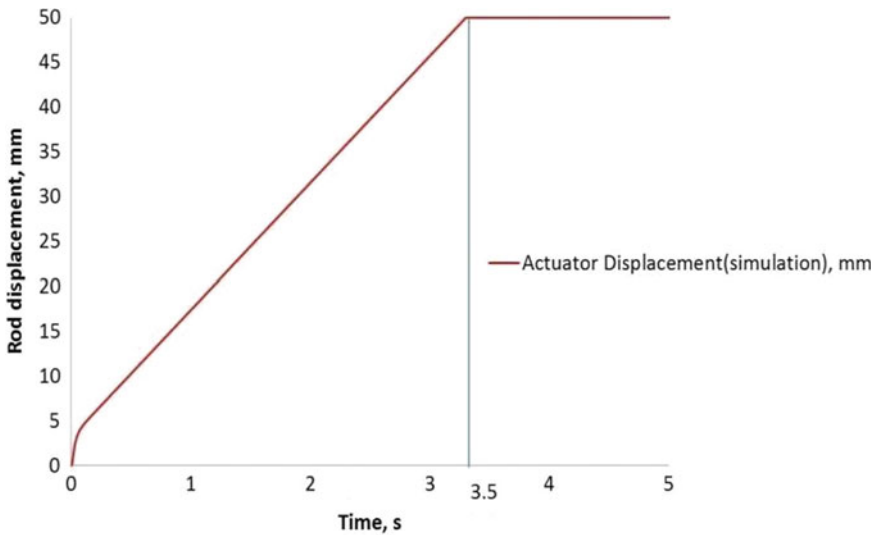


Fig. 6 Actuator response with 1 kg load with PID controller

to complete the full stroke; however, at 1 kg load the actuator records a time of 3.5 s to complete the same stroke length. With the same parameters and PID controller as it was in no loaded condition.

### 5 Analysis of Actuators Behavior in Open- and Closed-Loop Conditions

The analysis of various parameters such as actuator displacement, actuator velocity, and flow rate is carried out on simulated model for the open-loop system and closed-loop system based on PID controller. PID controller works on the instantaneous error  $e(t)$  between measured value  $y(t)$  and desired value  $r(t)$ . The instantaneous error is given by

$$e(t) = r(t) - y(t) \tag{1}$$

The PID controllers calculate the controller output  $u(t)$  as

$$u(t) = K_p \left[ e(t) + \frac{1}{T_i} \int e(t)dt + T_d \frac{de(t)}{dt} \right] \tag{2}$$

where  $K_p$  is the controller gain,  $T_i$  is the integral time also called as reset time, and  $T_d$  is the derivative time also called as rate limit. The proportional part of controller gives output proportional to error value. The integral part of controller gives output

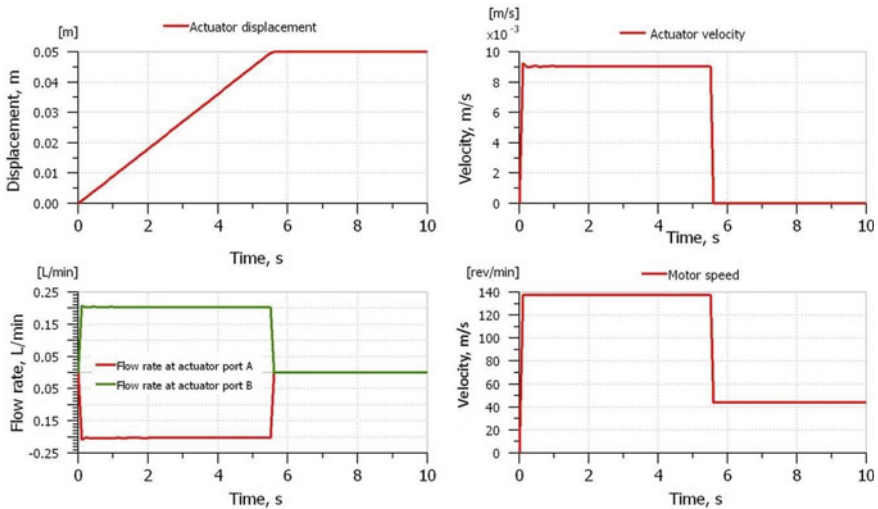


**Fig. 7** Open-loop actuator response for PID controller

by integrating error over the time [16]. The derivative part of controller gives output based on the rate of error, and the results are presented in the graphical form.

### 5.1 Open-Loop Actuator Response PID Controller

Open-loop and closed-loop analyses have been carried out on the symmetric actuator. The main purpose of this simulation exercise is to record the actuator response to the two different environments. In the open-loop system, there is no displacement feedback to the controller; however, in closed loop a potentiometer/LVDT is placed which provides instant displacement feedback to the controller with the help of which motor speed and direction is controlled [23].

Graphs in Fig. 7 represent the actuator response, velocity, and the flow rate through ports A and B, respectively. The symmetric actuator takes 5.7 s to complete a full stroke of 50 mm in case of open loop system with the PID controller [21]. With the parameters given in Table 1 the motor speed is also shown in Fig. 7.

### 5.2 Closed-Loop Actuator Response PID Controller

Closed-loop symmetric actuator response is illustrated in Fig. 8. The advantage of closed-loop analysis over open loop is that it provides instant positional feedback to the controller, thereby improving the response time of the actuator. It is seen that the

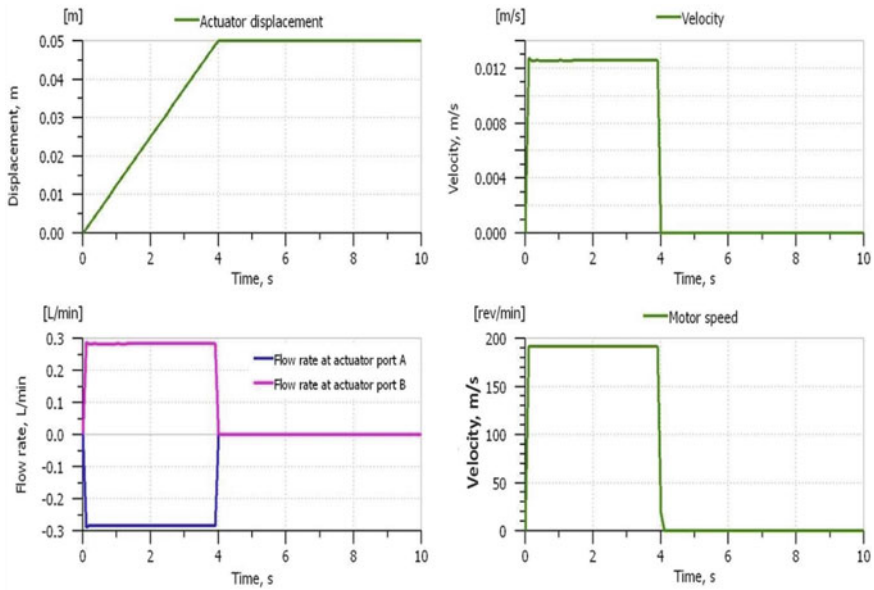


**Fig. 8** Closed-loop actuator response for PID controller

actuator takes 4 s to complete the full stroke of 50 mm when compared to 5.7 s in open-loop analysis using PID controller.

### 5.3 Comparison of Open-Loop and Closed-Loop PID Controlled Actuator

The graph obtained from open-loop actuator is superimposed on closed-loop actuator graph to draw comparison between the two in the same frame as shown in Fig. 9. It is clearly evident from the graphs the response of closed loop is much better than open loop in terms of displacement velocity, fluid flow rate, and velocity.

## 6 Thermal Analysis

The symmetric actuator is most responsive to the PID controller; hence, it has been used for this experiment. The hydraulic oil is heated gradually, the temperature of the oil in the tank rises [9]. At specified temperatures, the setup is run and the actuator response is recorded. The experiment has been carried out with temperatures ranging from room temperature to 80 °C. The response of the EHA system with the symmetric actuator is recorded with varying oil temperatures as shown in Fig. 10. It is noted

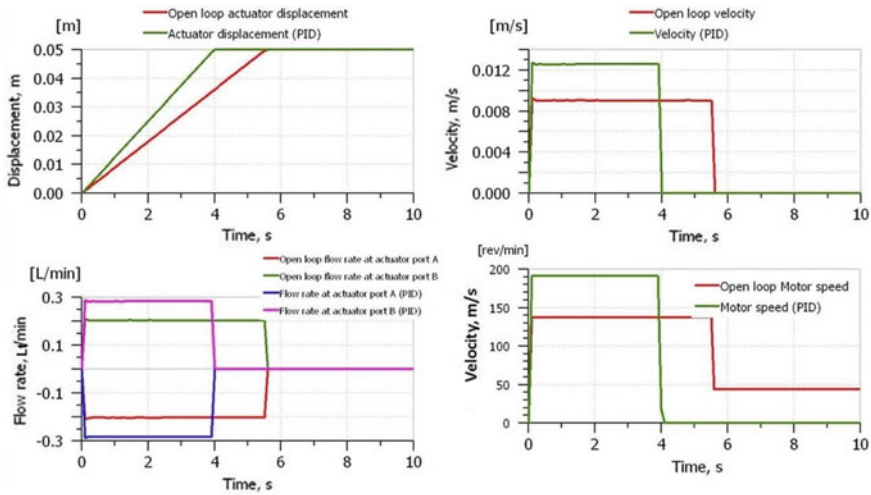


Fig. 9 Comparison of open-loop and closed-loop actuators

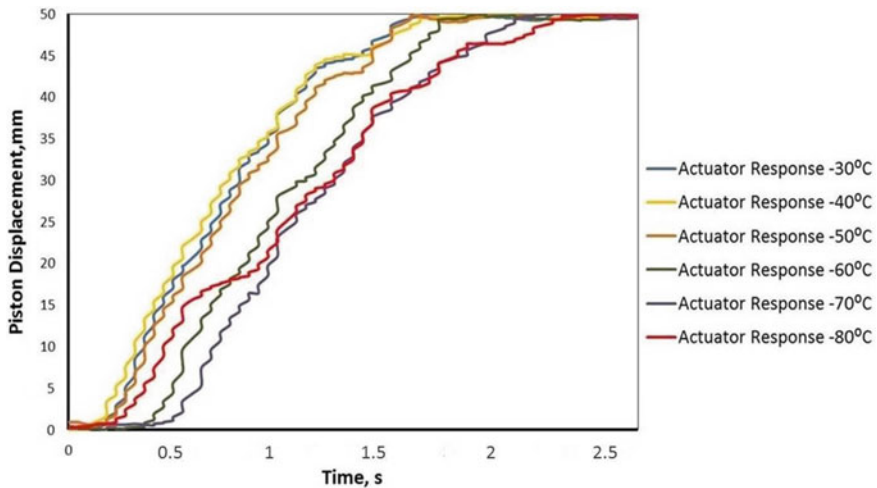


Fig. 10 Thermal analysis graphs at various temperature

that as the temperature of the oil increases the response of the actuator gets sluggish. With the increase in temperature, the viscosity of the hydraulic oil tends to reduce this change in viscosity effect the chemical composition and behavior of the hydraulic fluid, resulting in inadequate energy transfer from the hydraulic oil to the actuator when pressurized. This change negatively impacts the performance of the EHA and subsequently results in the increase in raise time.

**Table 2** Values of rise and settling times at different temperature

Temperature (°C)	Rise time (s)	Settling time (s)
30	1.6	1.6
40	1.7	1.7
50	2	2
60	2.3	2.3
70	2.4	2.4
80	2.5	2.5

At 30 °C, the raise time of the symmetric actuator is 1.6 s; however, as the temperature is increased to 80 °C the raise time is recorded at 2.5 hydraulic fluid. And the property of hydraulic fluid varies on variation of temperature. The EHA analyzed in the paper with the aim of using it as a standalone system to operate Armoured Recovery vehicle. As elucidated in Table 2, the study of thermal analysis is imperative in EHA as the system operates in isolation at high-temperature environment also.

## 7 Conclusion

EHA system is an emerging domain which is drawing attention of lot many researchers these days due to its inherent merits and widescale application as a standalone system in heavy equipments. Due to its integrated self-operated modular design, this can also be used in Armoured vehicular technology. It has several advantages over the conventional hydraulic system. The present study involves the development of the digital simulation model of electrohydrostatic actuator with symmetrical cylinder. The system model is developed on AMESim software. AMESim tool interfaced with LabVIEW to obtain the result. The behavior of the system model is checked for various dynamic factors. Load conditions, open-loop, closed-loop, and thermal analysis aspects are covered in this paper. While load conditions, open-loop and closed-loop analyses are available in the literature; however, we have extended the existing concept by finding its dynamic and thermal behaviors for different temperature conditions. The dynamic and thermal analyses of EHA has its vital significance for establishing its suitability for various applications which forms the main focus of this paper. While analyzing no-load and loaded conditions, it is understood from the result that the response time of the actuator without load is almost half vis-a-vis loaded condition. Simulation of open-loop and closed-loop analyses has also been carried out to record the actuator response for the two different environments, and it is clear from. After comparison, it is found that PID controller gives the better result than any other controller while using with EHA. Due to the position feedback, the closed-loop system is much accurate and quick as compared to open-loop system. The thermal analysis yields important relations between the studied parameters like with increase in temperature the viscosity of the oil increases and the response of

the actuators slow down. Based on the various analysis carried out in this paper, it is concluded that due to many advantages EHA could be used in the Armoured Recovery Vehicle as a standalone system. In future work, the experiment needs to be carried out physically on experimental setup to compare the results and carry out sensitivity analysis.

## References

1. Alle N, Hiremath SS, Makaram S, Subramaniam K, Talukdar A (2016) Review on electro hydrostatic actuator for flight control. *Int J Fluid Power* 2332–2343
2. Alden R (1991) Power-by-wire flight control systems. In: *Proceedings of the IEEE conference on national aerospace and electronics NAECON*, vol 2, pp 535–539
3. Botten SL, Whitley CR (2000) Flight control actuation technology for next-generation all electric aircraft. *Technol Rev J Millennium Issue* 23(6):55–68
4. Rongjie K, Zongxia J, Shaoping W, Lisha C (2009) Design and simulation of electro-hydrostatic actuator with a built-in power regulator. *Chin J Aeronaut* 700–706
5. Park B, Kim TS, Ryu J-S, Hyun DS (2006) Fault tolerant strategies for BLDC motor drives under switch faults. In: *Proceedings of the conference on industry applications*
6. Wheeler PW (2004) An electrohydrostatic aircraft actuator using a matrix converter permanent magnet motor drive. In: *Second IEE international conference on power electronics, machines and drives*. <https://doi.org/10.1049/cp:20040332>. <https://www.sci-hub.se/10.1049/cp:20040332>
7. Huang X, Gerada C, Goodman A, Bradley K, Zhang H, Fang Y (2011) A brushless DC motor design for an aircraft electro-hydraulic actuation system. In: *Proceedings of IEEE international conference on electric machines & drives*, pp 223–232
8. Boglietti A, Cavagnino A, Tenconi A, Vaschetto S (2009) The safety critical electric machines and drives in more electric aircraft: a survey. In: *Proceeding of the IECON*, pp. 2587–2594
9. Kong X, Wang F, Xing J (2011) Temperature rise calculation of high-speed PM machine based on thermal-circuit method and 3D fluid field method. In: *Proceedings of international conference on electrical machines and systems*, 20–23 Aug 2011
10. Bellad K (2014) Modeling, simulation and experimental investigations on electro-hydraulic actuator system—asymmetric cylinder. Thesis (Master), Indian Institute of Technology Madras
11. Ramakrishnan R, Hiremath SS, Singaperumal M (2014) Design strategy for improving the energy efficiency in series hydraulic/electric synergy system. *Energy* 162–169
12. Langlois O, Roboam X, Mare JC, Piquet H, Gandanegara G (2004) Bond graph modelling of an electro-hydrostatic actuator for aeronautic applications. France
13. Rongjie K, Zongxia J, Shaoping W, Lisha C (2010) Design and simulation of electro-hydrostatic actuator with a built-in power regulator. *Chin J Aeronaut* 22(6):700–706
14. Ivantysyn J, Ivantysynova M (2003) *Hydrostatic pumps and motors: principles, design, performance, modelling, analysis, control and testing*. Tech Books International, New Delhi
15. Matsuse K, Saito S, Tadakuma S (2013) History of motor drive technologies in Japan. *IEEE Ind Appl Mag* 19(6):10–17
16. Chinniah Y, Burton R, Habibi S (2006) Failure monitoring in a high-performance hydrostatic actuation system using the extended Kalman filter. *Mechatronics*
17. Navatha A, Bellad K, Hiremath SS, Karunanidhi S (2016) Dynamic analysis of electro hydrostatic actuator system. *Procedia Technol* 25:1289–12296. <https://doi.org/10.1016/j.protcy.2016.08.223>
18. Fu Y, Zhang W (2010) The deadband analysis of the electro-hydraulic actuator of the motor-pump coordinated control. In: *IEEE international conference on mechatronics and automation*, pp 37–39



19. Zattoni E (2005) Detection of incipient failures using an  $h_2$ -norm criterion: application to electric point machines. IFAC Proc Volumes 36–39
20. Bellad K, Hiremath SS, Singaperumal M, Karunanidhi S (2014) Optimization of PID parameters in electro hydraulic actuator system using genetic algorithm. Appl Mech Mater 535–539
21. Muenchhof M, Beck M, Isermann R (2009) Fault tolerant actuators and drives—structures, fault detection principles and applications. Ann Rev Control 33(2):136–148
22. Khan H, Abou SC, Sepehri N (2005) Nonlinear observer-based fault detection technique for electro hydraulic servo-positioning systems. Mechatronics
23. Hu X, Mao Z, Jiao Z, Wu S, Yu X, Li F (2014) Analysis of the characteristics by modeling and simulation of actuator in flight control system. In: Proceedings of conference on IEEE Chinese guidance, navigation and control. IEEE

# An Improved Hydro-mechanical Braking System to Maintain a Constant Pedal Feel During Deceleration of Electric Vehicle



Sutapa Mondal and Arup Kumar Nandi

**Abstract** In the present paper, an improvement of conventional hydro-mechanical braking system is presented which increases the regenerative performance of parallel regenerative braking used in electric vehicles. Realizing that brake pedal feel of driver during deceleration is important for the safety, an appropriate brake pedal feel measurement is proposed here. Moreover, it was noticed that perception of brake pedal feel varies with the driver's attitude. The improved hydro-mechanical braking system maintains a constant desired brake pedal feel throughout the braking process.

**Keywords** Electric vehicle · Hydro-mechanical · Parallel regenerative braking system · Pedal feel · Energy

## 1 Introduction

Regenerative braking (RB) is a unique approach applied to electric vehicles (EV) for energy conversion from mechanical braking (kinetic) energy to electrical energy. Electric energy generated through RB is used to charge the battery. Thus, besides protection of environmental pollution (by reducing the heat dissipation in frictional braking), RB minimizes the (fuel) energy consumption.

In most of the braking situations, the regenerative torque delivered by a generator is limited to cope up the required braking torque. Thus, a combination of (friction) brake and regenerative brake is used. The way of dividing the required braking torque among the regenerative and mechanical braking systems in order to recuperate the vehicle kinetic energy (KE) as much as possible without losing the required braking performance is the most challenging, and it motivates the designer for developing

---

S. Mondal

Academy of Scientific and Innovative Research (AcSIR), Ghaziabad, Uttar Pradesh, India

Birla Institute of Technology, Mesra, Off-campus, Deoghar, India

A. K. Nandi (✉)

CSIR-Central Mechanical Engineering Research Institute, Durgapur, West Bengal, India

e-mail: [nandi@cmeri.res.in](mailto:nandi@cmeri.res.in)

© The Author(s), under exclusive license to Springer Nature Singapore Pte Ltd. 2021

171

C. Pandey et al. (eds.), *Advances in Materials and Mechanical Engineering*,

Lecture Notes in Mechanical Engineering,

[https://doi.org/10.1007/978-981-16-0673-1\\_14](https://doi.org/10.1007/978-981-16-0673-1_14)

different braking strategies which are fall under the two categories: serial regenerative braking (SRB) and parallel regenerative braking (PRB). Switching of mechanical brake and regenerative brake is an important factor, and several studies were carried out on this issue [1–3]. The braking force distributions of regenerative braking and friction braking in SRB and PRB systems are presented in [4], and it is obvious to appear that SRB recovers more KE than PRB.

Unlike to SRB, in PRB, regenerative brake works parallel with friction brake, where total brake force reaches the same deceleration as in conventional mechanical braking system. In addition to energy recovery, safe braking is also important which is affected by the brake pedal feel (BPF) to the driver. During the entire braking period, it is required to be maintained a constant BPF.

BPF is the feedback force experienced by the driver from the brake pedal during braking [5], and it is normally measured in terms of deceleration per unit pedal force [6]. Since there is no such mechanical connection of brake pedal with regenerative braking force, conventional BPF as experienced in mechanical braking system is not realized during regenerative braking [5]. In order to improve the pedal feel in regenerative braking, various concepts were proposed such as utilizing predetermined force-displacement relationship for the brake pedal [7], decoupling mechanical connection among the brake pedal and braking system [8], adopting brake pedal simulator [9, 10], etc. In [11], a cooperative control of regenerative braking and friction braking was proposed in order to improve the conventional parallel braking system where the similar driver's feel as realized in only friction brake system in terms of brake force ( $F_b$ ) versus pedal displacement was tried to maintain.

But in reality, required brake force for a certain deceleration varies with vehicle speed (lower the vehicle speed ( $v$ ) higher the braking force) which creates an ambiguity to driver's feeling. It is explained as follows. The deceleration,  $d$  due to the applied brake force is calculated as

$$d = \frac{F_b + mg f_r + \frac{1}{2} \rho_a C_d A_f v^2}{m} \quad (1)$$

For a given vehicle, air density and rolling friction coefficient,  $d$  varies with  $F_b$  and  $v$ . Now if  $F_b$  is fixed for a certain pedal displacement,  $d$  is varying with  $v$ . So, for the same pedal displacement, different deceleration rates are achieved for different  $v$ , resulting varying brake pedal feel. But, driver's brake pedal feel is required to be same during the entire period of braking as well as in any driving situation. Moreover, brake pedal feel should be robust so that it is insensitive to the drift and variation of system characteristics [12]. How the driver's pedal feel changes with the variation of pedal force with respect to pedal displacement due to brake pad stiffness, temperature and brake pad wear was demonstrated in [13]. Thus, instead of brake force with respect to pedal displacement, driver's feel can be appropriately defined by the deceleration rate per unit pedal displacement [14, 15].

Present work proposes a parallel RBS which comprises a hydro-mechanical braking and a regenerative braking. The regenerative braking is being performed by the electric motor which acts as a generator during deceleration. An improvement

is made in the hydro-mechanical braking system by incorporating a linear actuation. Such improvement not only increases the energy regeneration as observed in SRB but also maintains a driver's desired BPF throughout the deceleration period. In the following, how a constant BPF can be maintained during deceleration using the proposed improved hydro-mechanical braking system is explained, and it is the primary motivation of the present research.

## 2 Proposed PRB System

### 2.1 Improvement of Hydro-mechanical System

The proposed improvement (as presented in Fig. 1) requires a very little modification of the conventional hydro-mechanical braking system. The primary components used in a conventional mechanically controlled hydraulic brake system are as follows. Brake pedal lever rotates around a fixed pivot point during braking, and after releasing, it restores to its initial position with the help of a spring. An input pushrod which is attached to the brake pedal lever pushes the booster input rod once a force is applied on the brake pedal through pedal displacement. The normal position of booster input rod is maintained using a spring that is positioned around it. Figure 1a demonstrates the normal position (no-braking condition) of the system where the input pushrod and booster input rod are close in contact at a position (p1). During braking, as the force applied to brake pedal, the input pushrod pushes the booster input rod (from p1 to p2 as shown in Fig. 1b). The brake booster increases the pedal force which is used to actuate the master cylinder during braking.

In the proposed braking system, a reversing linear solenoid is positioned inside the input pushrod, and it is connected to the friction brake controller. Two magnetic coils are attached in the electromagnet that acts as a reversing linear solenoid. The armature stroke motion from one end position to the other or vice versa is achieved by means of electromagnetic force. The desired operating direction and stroke movement are obtained through excitation of the respective solenoid coil with an appropriate current through friction brake controller.

A sensor (transducer) is connected with the booster input rod to measure its displacement that is fed to the friction brake controller. Other components as used in conventional braking system are same in the proposed system. Figure 1b demonstrates the initial braking situation. During braking, as the vehicle speed reduces, the required braking torque increases and it is mitigated by the reversing linear solenoid through its desired forward stroke (towards brake booster) resulting further pressing of booster input rod. In such situation, the effective force on the hydraulic cylinder increases without any additional pedal displacement. Such situation is demonstrated in Fig. 1c. On the other hand, when the mechanical brake torque produced corresponding to the given pedal displacement is found to be more, it is diminished through the solenoid's reverse stroke. As a result, a constant deceleration is sustained during

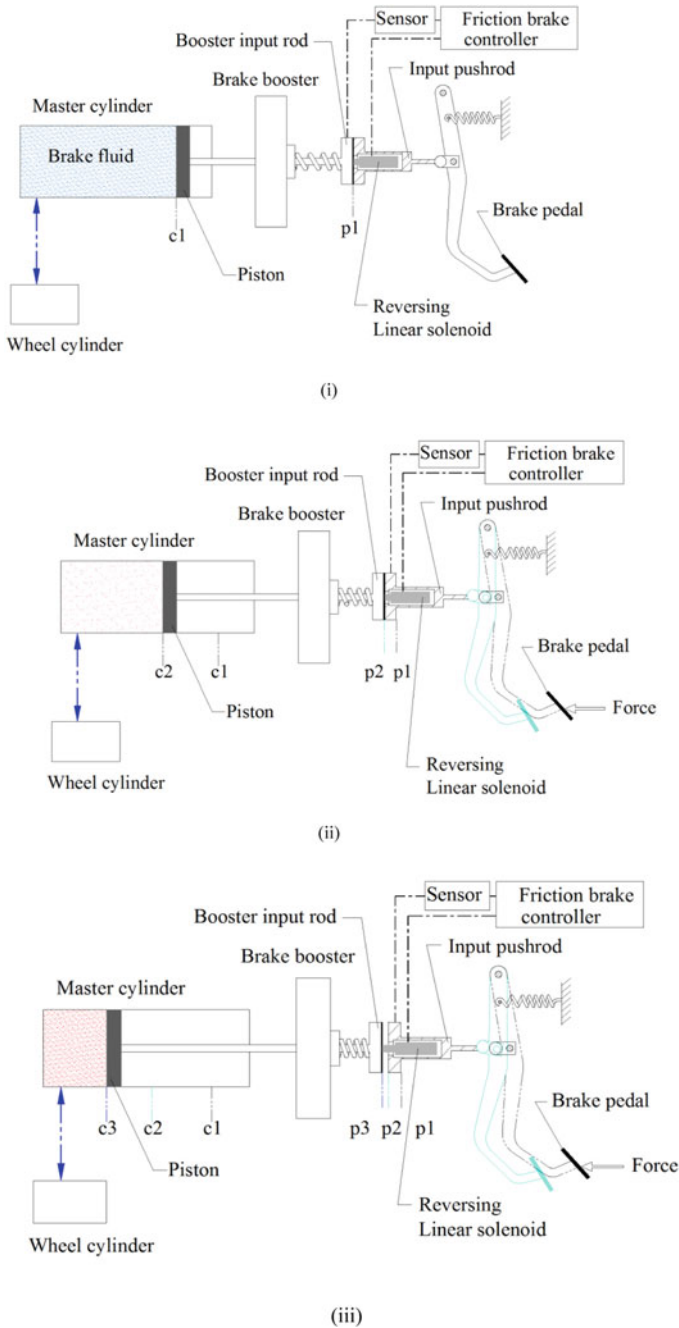


**Fig. 1** Hydro-mechanical braking system layout towards maintaining a constant desired pedal feel with proposed PRB operation strategy for different situations. **a** No-braking. **b** Initial braking. **c** Speed changing

the entire braking period for a fixed pedal displacement, thereby maintaining a desired pedal feel of the driver.

There exists a certain relation of the amount of pedal force required to make a desired pedal displacement, and it depends on the spring and other mechanical components of the system.

### 2.2 Control System Design for the Improved Parallel Regenerative Braking

The control system designed for the proposed improved parallel regenerative braking system is presented in Fig. 2.

The control system comprises of two PI controllers: regenerative brake controller and friction brake controller which are connected to brake control logic. Regenerative brake controller is used to control the motor speed and charges the battery. The regenerative torque ( $\tau_{regen}$ ) generated by the motor along with the friction brake torque ( $\tau_{friction}$ ) is used to decelerate the EV speed. During braking, the motor works like a generator and converts the KE into electricity that is used to charge the battery. Reference deceleration ( $d_{ref}$ ), deceleration error, speed error ( $e$ ), EV actual deceleration ( $d_{actual}$ ), vehicle and route/environmental parameters and motor speed ( $\omega$ ) are the inputs to brake control logic. According to the driver's brake pedal feel characteristics, brake control logic divides the total required brake torque,  $\tau_{Total\_br}$  for a given pedal displacement.  $\alpha_1$  fraction of  $\tau_{Total\_br}$  is the input of regenerative brake controller, and  $\alpha_2$  fraction of  $\tau_{Total\_br}$  is fed to friction brake controller, where  $\alpha_1 + \alpha_2 = 1$ .

The maximum values of  $\alpha_1 \tau_{Total\_br}$  are the maximum torque capacity of generator at  $\omega$ . Friction brake controller decides the required booster input rod displacement to

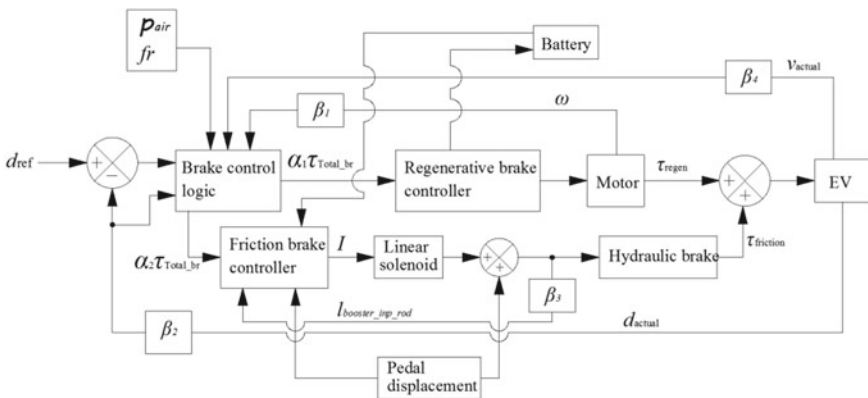


Fig. 2 Schematic diagram of control system design

generate  $\alpha_2 \tau_{Total\_br}$  through friction brake. There exists a certain relationship (linear in most of the cases) of the booster input rod displacement with the pedal displacement.

If pedal displacement is not sufficient or excessive according to the brake control logic, friction brake controller supplies a current,  $I$  to actuate the linear solenoid either forward or reverse direction, respectively.  $\beta_3$  fraction of actual booster input rod displacement ( $l_{booster\_inp\_rod}$ ) is fed back to the friction brake controller in opposite phase to stabilize the system. According to Fig. 1c,  $l_{booster\_inp\_rod}$  equals to  $p3-p2$ .

### 2.3 Operational Procedure of the Proposed System Corresponding to a Desired Brake Pedal Feel

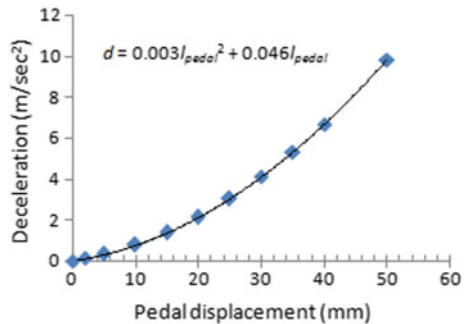
The operational strategy of the proposed PRB system is as follows.

- Step 1:  $d$  is decided corresponding to the pedal displacement,  $l_{pedal}$  from the desired BPF characteristics model. A typical driver brake pedal feel characteristics (for a maximum value of  $l_{pedal} = 50$  mm and  $d_{max} = 1$  g) is presented in Fig. 3 [6].
- Step 2: Calculation of total braking force,  $F_{Total\_br}$ , and corresponding total braking torque,  $\tau_{Total\_br}$  required to obtain  $d$ .  
 $F_{Total\_br} = \text{vehicle mass} * d$ , and  $\tau_{Total\_br} = F_{Total\_br} * \text{tyre radius}$
- Step 3: Determination of maximum regenerative braking torque,  $\tau_{Max\_regen}$  delivered by the motor/generator based on the current motor speed,  $\omega$ . The frictional braking torque,  $\tau_{Friction\_br}$  produced by the hydraulic brake due to the  $l_{pedal}$  is as follows:

$$\tau_{Friction\_br} = 2r\mu \frac{A_w}{A_m} (fR_p + F_b) \tag{2}$$

where  $f$  is the force applied due to the booster input rod movement (for instance from p1 to p2 in Fig. 1b) corresponding to  $l_{pedal}$ .  $R_p$  and  $F_b$  are the pedal lever ratio and booster assist force, respectively.  $A_m$ ,  $A_w$ ,  $\mu$  and  $r$  are

**Fig. 3** A typical brake pedal feel characteristics



the master cylinder piston area, caliper piston area, coefficient of friction of the lining and effective radius of the caliper, respectively.

- Step 4: Now if  $\tau_{\text{Total\_br}} \leq \tau_{\text{Max\_regen}}$ , only RB is applied. In this situation,  $\tau_{\text{Friction\_br}}$  is to be kept zero, and it is possible by solenoid's reverse stroke to make  $f = 0$ . Otherwise, calculate the additional frictional braking torque,  $\tau_{\text{Friction\_br}}$  required to meet the  $\tau_{\text{Total\_br}}$  and the corresponding  $f$ .
- Step 5: Determination of current to be passed through solenoid to obtain the desired  $f$

### 3 Discussion

The energy regeneration capacity of the present PRB system with the improved hydro-mechanical braking is expected to be similar to a SRB system. With the proposed design of regenerative braking system presented in Fig. 1, a fixed desired brake pedal feel is achieved at every time throughout the entire braking period. The other advantage of the proposed braking system is that any kind of brake pedal feel characteristic can be achieved as explained in Sect. 2.3.

Authors are presently working to model the above-presented parallel regenerative braking system for simulation study. Through simulation study, the design parameters of the proposed regenerative braking system will be optimized. A prototype of the system will also be fabricated based on the optimum design parameters and tested for evaluation of its effectiveness towards implementation in electric vehicle.

### 4 Conclusions

An improvement in the design of a conventional hydro-mechanical braking system is presented here. The system architecture and working principle of the proposed PRB system based on the improved hydro-mechanical braking are described. The proposed PRB is found to be simple in nature and easy to implement in small EVs. A more realistic brake pedal feel measurement in terms of deceleration rate vs pedal distance is proposed here. The regeneration capability of the proposed system is expected to be similar to a serial regenerative braking system. In addition, the proposed braking system can provide a constant brake pedal feel to the driver throughout the entire braking process, and it is essential for safety reason.



## References

1. Paterson J, Ramsay M (1993) Electric vehicle braking by fuzzy logic control. In: ORTECH international 2395, Ontario, L5K 1B3, Canada
2. Bai ZF, Li SX, Cao BG (2005)  $H_\alpha$  control applied to electric torque control for regenerative braking of an electric vehicle. *J Appl Sci* 5(6):1103–1107
3. Fenzhu J, Lijum L (2011) Study of braking stability of electro-mechanical hybrid braking system in electric vehicles based on ECE regulation. In: 2011 international conference on computer distributed control and intelligent environmental monitoring, Changsha, China
4. Varocky BJ (2011) Benchmarking of regenerative braking for a fully electric car. TNO Automotive, Helmond & Technische Universiteit Eindhoven (TU/e). Report No. D&C 2011.002
5. Caliskan U, Apaydin A, Otaran A, Patoglu V (2018) A series elastic brake pedal to preserve conventional pedal feel under regenerative braking. In: 2018 IEEE/RSJ international conference on intelligent robots and systems (IROS), Madrid, Spain
6. Mortimer RG, Segel L, Dugoff H (1978) Brake force requirement study: driver-vehicle braking performance as a function of brake system design variables. Highway Safety Research Institute, University of Michigan. Report No. UM-HSRI-78-53
7. Zehnder JW, Kanetkar SS, Osterday CA (1999) Variable rate pedal feel emulator designs for a brake-by-wire system. Delphi Automotive Systems Chassis Systems. Technical Report 1999-01-0481 (1999)
8. Yu L, Liu X, Xie Z, Yi Chen Y (2016) Review of brake by wire system used in modern passenger. In: ASME international design engineering technical conference and computers and information in engineering conference, paper no: DETC2016-59279, V003T01A020
9. Flad M, Rothfuss S, Diehm G, Hohmann S (2014) Active brake pedal feedback simulator based on electric drive. *SAE Int J Passeng Cars* 189–200
10. Abey Siriwardhana WSP, Abeykoon AHS (2014) Simulation of brake by wire system with dynamic force control. In: 7th IEEE international conference on information and automation for sustainability, Srilanka
11. Kumar CSN, Subramanian SC (2016) Cooperative control of regenerative braking and friction braking for a hybrid electric vehicle. *Proc ImechE Part D: J Automobile Eng* 230(1):103–116
12. Sellgren U, Söderberg A (2019) Robust brake feel design. In: NAFEMS world congress 2009, Crete, Greece
13. Breuer B, Bill K (2008) Brake technology handbook. SAE International, Warrendale, PA, USA
14. Park S (2005) Effect of brake pedal impedance on braking performance in EH-BBW System. *Int J Autom Technol* 6(4):391–402
15. Johnston M, Leonard E, Monserre P, Riefe M (2005) Vehicle brake performance assessment using subsystem testing and modeling. SAE 2005-01-0791. SAE International, Warrendale

# Design of Sandwich Panel Using Taguchi Analysis



Prashank Sharma, Chandan Singh Mehra, Utkarsh Jha, Sachin, and Anil Kumar

**Abstract** The aim of the present paper is to optimize the dimensions of honeycomb sandwich structure through simulating three-point bending test. The sandwich structure consists of epoxy carbon woven prepreg face sheets separated by a Kevlar honeycomb core. Based on the analysis, panel structure parameters considered are honeycomb core cell size, core height, face sheet thickness and panel size. L9 orthogonal array is generated using Taguchi design of experiments considering three levels of each parameter. The models generated in Taguchi design are numerically analysed by finite element analysis for ultimate force and equivalent stiffness. Taguchi analysis is carried out to find the optimum design levels of parameter. The levels obtained were further verified by grey relation analysis.

**Keywords** Taguchi analysis · Grey relation analysis · Three-point bending test

## 1 Introduction

Composite materials are the combination of two or more materials bonded to each other and this bonding utilizes the properties of each material in order to form an improved structure. The honeycomb sandwich panel consists of a honeycomb core sandwiched between two face sheets of same or different materials. Generally, the core is of low density so that sandwich panel has less weight and high section modulus. The face sheets carry the bending load and core carries the shear load. This unique combination of materials provides high-specific strength along with high specific stiffness, and the whole assembly becomes lighter than their counterparts. Therefore, these structures have got wide applications in the automotive industry, commercial aerospace industry because of high fuel efficiency in transportation vehicles due to reduction in weight. Sandwich panel is also used in satellites, marine structures, defence, locomotives, bridge decks and supercars. With the use of Kevlar which is the strongest textile fibre available today, these structures become

---

P. Sharma (✉) · C. S. Mehra · U. Jha · Sachin · A. Kumar  
Department of Mechanical and Automation Engineering, G. B. Pant Government Engineering College, Okhla Phase III, New Delhi, India

© The Author(s), under exclusive license to Springer Nature Singapore Pte Ltd. 2021  
C. Pandey et al. (eds.), *Advances in Materials and Mechanical Engineering*,  
Lecture Notes in Mechanical Engineering,  
[https://doi.org/10.1007/978-981-16-0673-1\\_15](https://doi.org/10.1007/978-981-16-0673-1_15)

179

more advantageous. Kevlar is a Para-Aramid fibre synthesized from p-phenylene diamine and terephthaloyl chloride. The three-point bending flexural test is used to calculate bending stiffness, shear stiffness, deflection, facing stress, core stress and the flexural stress–strain response of the material. Grey relation analysis (GRA) is one of the most widely used models for optimization of multi-objective functions. And Taguchi design of experiments is also very popular that reduces the analysing time and also the resources required are less. Kaushik and Singhal (2018) observed that the Taguchi approach is one of the most helpful tools for single objective optimization [1]. Taguchi analysis is used to find optimum values of various levels. The primary goal of this method is to keep the variance in the output very low, even in the presence of noise inputs.

Simonidis Vartholomaïos et al. [2] performed the finite element analysis on sandwich beams with homogeneous or FGM faces under three-point bending. Five different models were numerically analysed to study the influence of FGMs faces. The faces and the core material were considered as isotropic. It was concluded that the presence of the homogeneous faces decreases the stresses and the maximum deflection of the core of the sandwich beams. Cracks were initiated at the introduction of the load from the supports.

J. Suresh Kumar et al. [3] presented an experimental study of aluminum honeycomb core sandwich structure under low velocity impact test. Taguchi orthogonal array was constructed to design the experiments. Three input parameters which were cell wall thickness, core thickness, cell size were considered to minimize density, maximize energy absorption and peak force. Grey relation analysis along with ANOVA was performed to find the most influencing parameter. It was observed that cell thickness along with cell height was the most influencing structural parameters, and the core height was the least influencing one.

Rupani et al. [4] presented the aspects of design, modelling and manufacturing of honeycomb sandwich structures. Core gives compressive strength while face sheets give shear strength. Modelling and numerical analyses of the sandwich panel with actual cell geometry require high computational resources and time. Hence, core of sandwich is generally modelled as solid equivalent plate. The elastic properties of the equivalent core can be found analytically, experimentally, or numerically.

Altan Kayran et al. [5] presented the assessment of effective elastic properties of honeycomb cores by finite element analysis of sandwich panels. Several equivalent core models were prepared by replacing the actual honeycomb hexagonal geometry with a solid bulk. The elastic constants of different equivalent core models were found using combination of continuum models of honeycomb core. To find the best equivalent model, a comparison was made between the reaction forces generated when displacement is applied on the equivalent model and its reference model. The reference model is made with actual honeycomb geometry. The model with the least percentage difference in the reaction forces is the best performing model. It was concluded that the equivalent core model which uses Masters and Evans model to find the in-plane elastic constants and Grediac model to find out-of-plane elastic constants gives the best result.

Thomas et al. [6] observed that most of the properties of composite depend on the different geometrical parameters like core cell size and core cell walls thickness.

## 2 Methodology

The various steps in the design of the sandwich panel having the Kevlar honeycomb core and Epoxy carbon woven (230 GPa) prepreg face sheet can be represented as Fig. 1.

In the first step, design parameters which are face sheet thickness, honeycomb cell size, honeycomb core height, panel size are identified. In this work, three levels

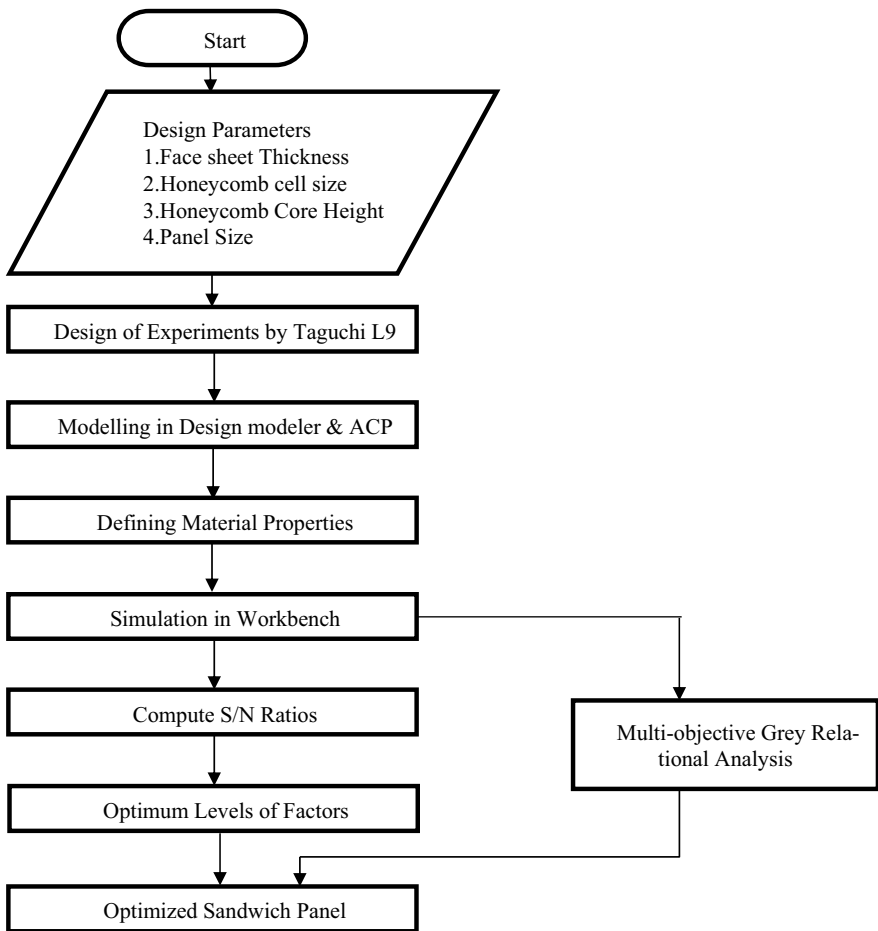


Fig. 1 Methodology flowchart

of each parameter are considered. Minitab 18 is used for design of experiments by Taguchi L9 orthogonal arrays. The homogenized cores of the generated 9 configurations are modelled in design modeller while face sheets are modelled in Ansys composites Prep-Post (ACP). Three-point bending test simulation is performed in workbench according to the ASTM C393 standards. Then analysis of the computed output is done by the Taguchi method to find out the best configuration. The results of Taguchi analysis are verified by GRA.

### 3 Material Properties

The mechanical properties of the Kevlar honeycomb are obtained from the Plascore which is a leading manufacturer of the Para-Aramid. To model the honeycomb core as homogenized orthotropic material, nine constants are needed to be determined in order to construct the stiffness matrix. These nine engineering constants are  $E_1^* E_2^*, E_3^*, \nu_{12}^*, \nu_{23}^*, \nu_{13}^*, G_{12}^* E_{13}^*, E_{23}^*$ . Here  $E^*, G^*, \nu^*$  represents Young's modulus, shear modulus and Poisson's ratio of honeycomb core, respectively.  $\rho^*, \rho_s$  are the density of honeycomb and honeycomb material, respectively.

The suffixes of the constants represent the axis system that is given in Fig. 2 and are followed throughout this work. These engineering constants are found using formulae developed by Gibson and Ashby [7] for honeycomb with double thickness vertical walls (Figs. 2 and 3).

$$\frac{\rho^*}{\rho_s} = \left(\frac{t}{l}\right) \frac{(1 + h/l)}{\left(\frac{h}{l} + \sin \theta\right) \cos \theta} \tag{1}$$

$$\frac{E_1^*}{E_s} = \left(\frac{t}{l}\right)^3 \frac{\cos \theta}{\left(\frac{h}{l} + \sin \theta\right) (\sin \theta)^2} \tag{2}$$

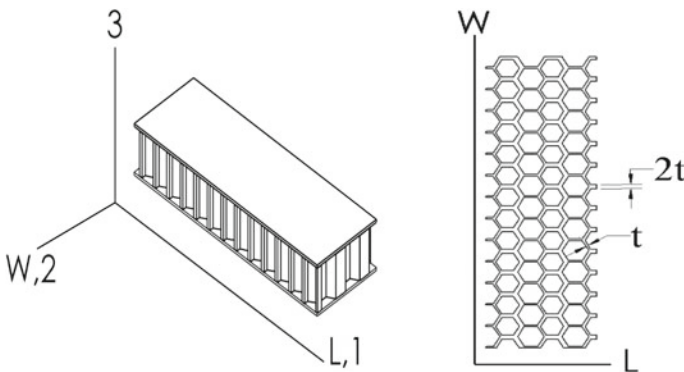
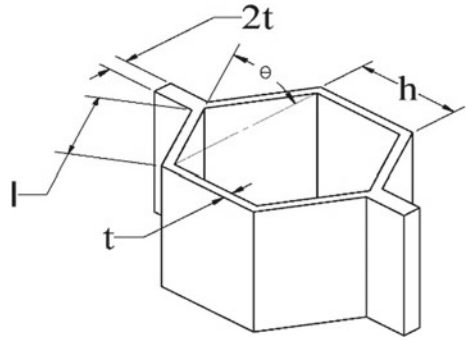


Fig. 2 Honeycomb axis system

**Fig. 3** Honeycomb cell with double thickness wall



$$\frac{E_2^*}{E_s} = \left(\frac{t}{l}\right)^3 \frac{\left(\frac{h}{l} + \sin \theta\right)}{(\cos \theta)^3} \tag{3}$$

$$\nu_{12}^* = \frac{(\cos \theta)^2}{\left(\frac{h}{l} + \sin \theta\right) \sin \theta} \tag{4}$$

$$\nu_{21}^* = \frac{\left(\frac{h}{l} + \sin \theta\right) \sin \theta}{(\cos \theta)^2} \tag{5}$$

$$\frac{G_{12}^*}{E_s} = \left(\frac{t}{l}\right)^3 \frac{\left(\frac{h}{l} + \sin \theta\right)}{\left(\frac{h}{l}\right)^2 \cos \theta (1 + 16h/l)} \tag{6}$$

$$\frac{E_3^*}{E_s} = \left(\frac{t}{l}\right) \frac{(1 + h/l)}{\left(\frac{h}{l} + \sin \theta\right) \cos \theta} \tag{7}$$

$$\nu_{13}^* = \nu_{23}^* \approx 0 \tag{8}$$

$$G_{23}^* \cong G_{23 \text{ lower}}^* \left(\frac{0.787}{h/l}\right) (G_{23 \text{ upper}}^* - G_{23 \text{ lower}}^*) \tag{9}$$

$$\left(\frac{t}{l}\right) \left(\frac{\left(\frac{h}{l} + \sin \theta\right)}{\left(\frac{h}{l} + 1\right) \cos \theta}\right) \leq \frac{G_{23}^*}{G_s} \leq \left(\frac{t}{l}\right) \left(\frac{\left(\frac{h}{l} + (\sin \theta)^2\right)}{\left(\frac{h}{l} + \sin \theta\right) \cos \theta}\right) \tag{10}$$

$$\frac{G_{13}^*}{G_s} = \left(\frac{t}{l}\right) \frac{\cos \theta}{\left(\frac{h}{l} + \sin \theta\right)} \tag{11}$$

The material properties of the face sheet are available in Ansys library by default.

## 4 Finite Element Analysis

Solid 186 & Shell 181 elements were used to mesh the homogenized core and face sheet of the sandwich panel, respectively. To make the sandwich panel act as an integrated unit, the contact between the core and face sheets is considered as bonded. Bonded contact is assigned such that face sheet has ‘contact body’ and core has ‘target body’ setting. Default ‘program controlled’ was used to set up the formulation of contact, and hence, it considers the FEA approach as penalty method. Flat support and flat loading bar each of width 25 mm are used in the analysis. A load is applied until the failure of the panel according to the standards. The shear strength of the Kevlar core in ‘L’ direction is less than both the bending strength of face sheet and the bond strength between the core and face sheet. Hence, the sandwich panel is considered to fail when the shear stress in the Kevlar core equals to the shear strength of the core. This load is called the ultimate load. The computed results of nine configurations are Table 1.

**Table 1** FEA results

Configuration number	Face Sheet thickness (mm)	Honeycomb core cell size (mm)	Honeycomb core height (mm)	Panel size B × L (mm × mm)	Ultimate load (N)	Deflection (mm)	Equivalent stiffness (N/mm)
1.	0.4	3.2	8	40 × 150	1078	2.823	381.86
2.	0.4	4	10	45 × 150	1325	2.459	538.84
3.	0.4	4.8	12.7	50 × 150	2050	2.72	753.68
4.	0.6	3.2	10	50 × 150	1705	2.294	743.24
5.	0.6	4	12.7	40 × 150	1504.5	2.045	735.70
6.	0.6	4.8	8	45 × 150	1225.3	2.623	467.14
7.	0.8	3.2	12.7	45 × 150	1949.5	2.016	967.01
8.	0.8	4	8	50 × 150	1254	1.989	630.47
9.	0.8	4.8	10	40 × 150	1374	2.298	597.91

### 5 Analytical Method

The results obtained through FEA are verified using analytical methods (Fig. 4).

$P$  is the load applied. Shear stress in the core is determined by

$$\tau = \frac{P}{(d + c)b} \tag{12}$$

Bending stiffness in the case of same facings

$$D = \frac{E(d^2 - c^2)}{12} \tag{13}$$

Panel shear rigidity  $U$  can be determined as

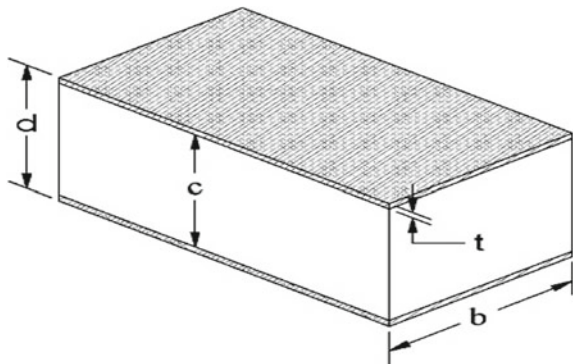
$$U = \frac{G(d + c)^2b}{4c} \tag{14}$$

Sandwich panel deflection

$$\Delta = \frac{PL^3}{48D} + \frac{PL}{4U} \tag{15}$$

The analytical calculations were performed for each configuration. A maximum of 2 and 15% difference is observed between the calculated and simulated values for shear stress in the core and deflection of panel, respectively.

Fig. 4 Sandwich panel





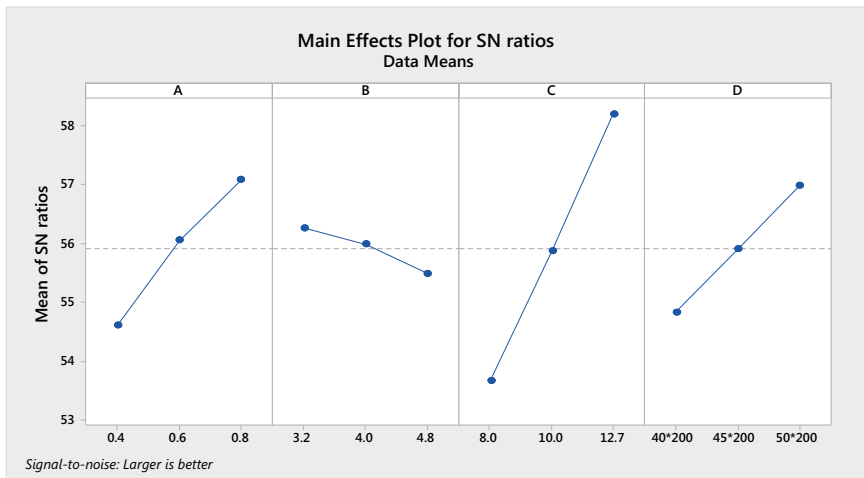


**Fig. 5** Main effects for  $S/N$  ratios for equivalent stiffness. **a** Face sheet thickness. **b** Honeycomb cell size. **c** Honeycomb core height. **d** Panel size ( $B \times L$ )

## 6 Taguchi Analysis for Optimum Parameters

The Taguchi analysis is carried out on the computed output to identify the most influencing parameter. There are three available categories of quality characteristics which are smaller the better, nominal the better and higher the better. Since higher ultimate force and equivalent stiffness (force required to produce unit displacement) are desirable, higher the better is selected for analysis. The first two runs are performed on the ultimate force and equivalent stiffness alone, and then the third run is performed by considering both the characteristics simultaneously. Response table of  $S/N$  represents the influence of various factors on output. Lower the rank in the table higher the effect of that particular parameter on the output. Irrespective of the quality characteristics used the parameter setting having the highest  $S/N$  ratio yield optimum quality with minimum variance (Figs. 5, 6 and 7; Tables 2, 3 and 4).

From the above  $S/N$  plots, it is observed that for maximum ultimate force and equivalent stiffness the optimum parameter levels are same, i.e. face sheet thickness 0.8 mm, honeycomb cell size 3.2 mm, honeycomb core height 12.7 mm and panel size ( $B \times L$ )  $50 \times 200$  mm.

## 7 GRA

As designing the optimum sandwich panel is a multi-objective problem, the levels obtained from Taguchi analysis are verified by GRA. Equal weightage is given to

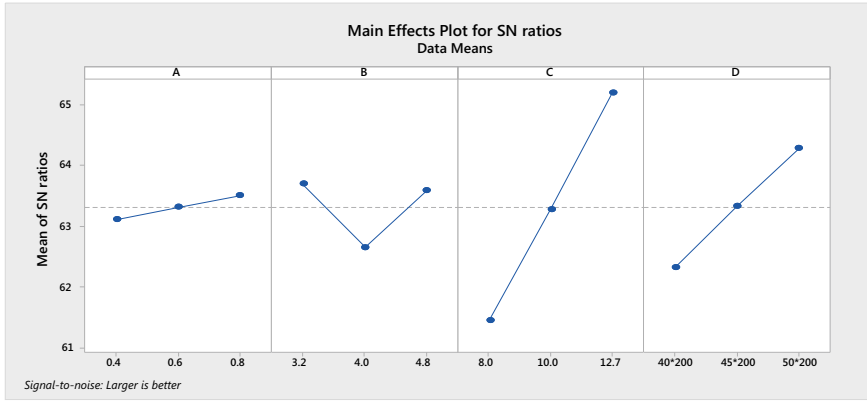


Fig. 6 Main effects for S-N ratios for ultimate force

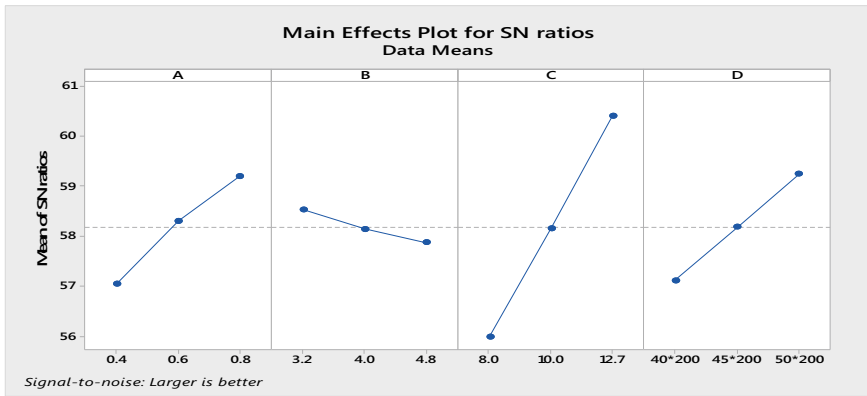


Fig. 7 Main effects for S-N ratios for equivalent stiffness and ultimate force

Table 2 Response table for signal-to-noise ratios (larger is better) for equivalent stiffness

Level	Face sheet thickness (mm) (A)	Honeycomb core cell size (mm) (B)	Honeycomb core height (mm) (C)	Panel size (B × L) (mm × mm) (D)
1.	54.60	56.26	53.67	54.83
2.	56.05	55.99	55.86	55.91
3.	57.08	55.49	58.20	56.99
Delta	2.47	0.77	4.52	2.15
Rank	2	4	1	3

**Table 3** Response table for signal-to-noise ratios (larger is better) for ultimate force

Level	Face sheet thickness (mm) (A)	Honeycomb core cell size (mm) (B)	Honeycomb core height (mm) (C)	Panel size (B × L) (mm × mm) (D)
1	63.11	63.70	61.46	62.32
2	63.32	62.65	63.28	63.34
3	63.51	63.59	65.19	64.28
Delta	0.40	1.04	3.73	1.96
Rank	4	3	1	2

**Table 4** Response table for signal-to-noise ratios (larger is better) for ultimate force and equivalent stiffness

Level	Face sheet thickness (mm) (A)	Honeycomb core cell size (mm) (B)	Honeycomb core height (mm) (C)	Panel size (B × L) (mm × mm) (D)
1	57.04	58.53	55.99	57.11
2	58.30	58.14	58.15	58.18
3	59.19	57.87	60.39	59.24
Delta	2.16	0.66	4.40	2.12
Rank	2	4	1	3

every parameter. The grey relation coefficients and grades for each configuration in L9 orthogonal array is listed in the Table 5.

The average grey relation grade for each factor level is calculated and listed in Table 6. The level associated with the highest value of the average grey relational grade for each column is the optimum level of that factor.

Hence, face sheet thickness at level 3, HC cell size at level 1, HC height at level 3 and panel size at level 3 are the conditions for the optimal design parameter

**Table 5** Grey relational coefficients and grey relational grades

Configuration number	Grey relational coefficient		Grey relational grade
	Equivalent stiffness	Ultimate force	
1.	0.333333333	0.333333333	0.333333333
2.	0.405934138	0.401321222	0.40362768
3.	0.57832004	1	0.78916002
4.	0.566626965	0.584837545	0.575732255
5.	0.558471802	0.471158507	0.514815155
6.	0.369205434	0.370794232	0.369999833
7.	1	0.828644501	0.914322251
8.	0.465058058	0.379095164	0.422076611
9.	0.442173272	0.418244406	0.430208839

**Table 6** Average grey relational grade for factors and levels of the experiment

Level	Face sheet thickness	HC cell size	HC core height	Panel size
1.	0.5087070	0.607795946	0.375136592	0.426119109
2.	0.4868490	0.446839815	0.469856258	0.398568041
3.	0.5888692	0.529789564	0.739432475	0.759738175

combination of sandwich panel. The results obtained in GRA are matching with Taguchi analysis.

### 8 FEA of Optimum Model

The optimum input parameter level setting obtained from the Taguchi and GRA is not in the L9. So the sandwich panel is modelled with optimum dimensions. The meshing of the panel and the bonding of homogenized core with face sheets is done as described in Sect. 5. The bottom face of the lower face sheet is split into 3 faces with length 25, 150, 25 mm, respectively. To simulate the effect of the flat support, the displacement and rotation of the outer faces on the bottom face of the lower face sheet are restricted in horizontal and vertical direction. A three-point bending load is applied until the failure of the panel. The computed results are as follows (Figs. 8 and 9).

Ultimate load and equivalent stiffness of the optimum model are 2,159 N and 1,074.13 N/mm, respectively.

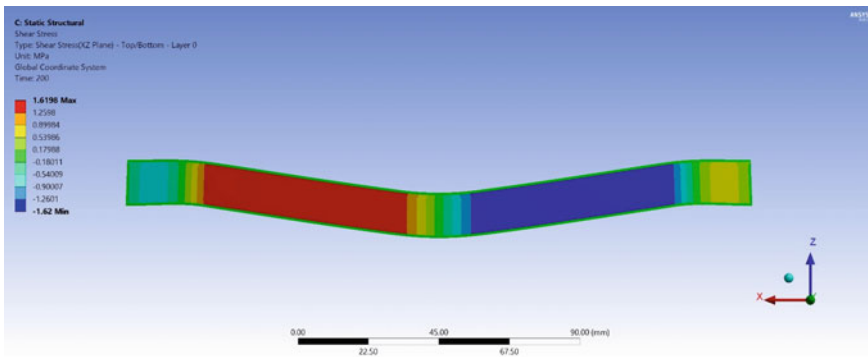


**Fig. 8** Shear stress at failure

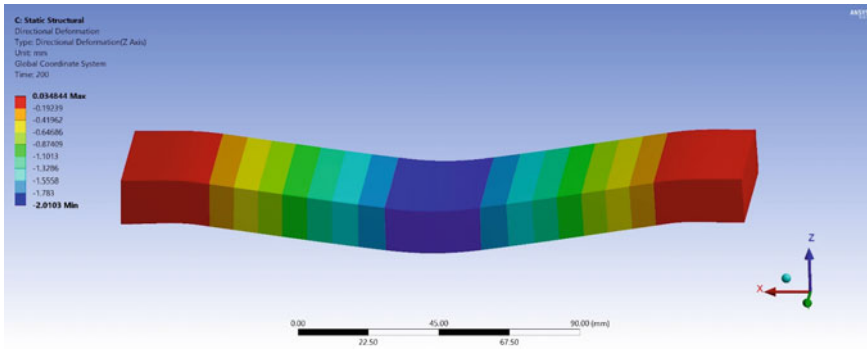


**Fig. 9** Deflection of panel at failure

## 9 Conclusion

This study aims to design the sandwich panel having Kevlar honeycomb core and epoxy carbon woven (230 GPa) prepreg face sheet by dimensional optimization using the performance measures of the three-point bending test. Taguchi analysis was performed to find out the optimum level of each factor and its influence on the ultimate force and equivalent stiffness. The results of Taguchi analysis were further verified by GRA. It is observed that the effects of various input factor on equivalent stiffness of panel according to their rank are core height, face sheet thickness, panel size and honeycomb cell size. Similarly, for ultimate force the effects of various input factor according to their rank are core height, panel size, honeycomb cell size and face sheet thickness. The optimum level of each factor in this study is honeycomb core cell size 3.2 mm, core height 12.7 mm, face sheet thickness 0.8 mm and panel size ( $B \times L$ )  $50 \times 200$  mm, respectively.

## References

1. Kaushik N, Singhal S (2018) Optimization of wear properties in aluminum metal matrix composites using hybrid taguchi-GRA-PCA. *Int J Performability Eng* 14(5):857–870. <https://doi.org/10.23940/ijpe.18.05.p4.857870>
2. Vartholomaios S, Theotokoglou E (2015) Numerical study of fractured sandwich beams with homogenous or FGM faces under three-point bending. *Int J Struct Integrity* 6:142–156. <https://doi.org/10.1108/ijsi-05-2014-0022>
3. Kumar JS, Kalaichelvan K (2017) Taguchi-grey multi-response optimization on structural parameters of honeycomb core sandwich structure for low velocity impact test. *Silicon* 10:879–889. <https://doi.org/10.1007/s12633-016-9544-3>
4. Rupani S, Jani S, Acharya G (2017) Design, modelling and manufacturing aspects of honeycomb sandwich structures: a review. *Int J Sci Eng Dev Res* 2:526–532
5. Aydinçak İ, Kayran A (2009) An approach for the evaluation of effective elastic properties of honeycomb cores by finite element analysis of sandwich panels. *J Sandwich Struct Mater* 11:385–408. <https://doi.org/10.1177/1099636209102891>

6. Thomas T, Tiwari G (2019) Crushing behavior of honeycomb structure: a review. *Int J Crashworthiness* 24:555–579. <https://doi.org/10.1080/13588265.2018.1480471>
7. Gibson LJ, Ashby MF (2001) *Cellular solids: structure and properties*. Cambridge University Press, Cambridge

# A Review on Solar Desalination Still Designs



Rajat G. Kawalkar, Samish M. Fale, and Satish P. Lokhande

**Abstract** The modern state-of-the-art techniques involved in the human community is continuously been challenged for energy and fresh drinking water needs. To an extent, efforts made by researchers have tried to address the urgency of the orthodox methods involving solar still technology. However, many of the limitations involved in different types of solar stills include lean of glass, area of absorbing plate, and volume of water. The major implication of maintaining the required water volume in the conventional method is rectified to some extent in inclined stills. Hence, many of the recent developments in still design inculcate the knowledge in the application of wicks and steps in the container to maintain the desired efficiency. For water desalination techniques involving the above-mentioned technology, the influential promise of trusting with the renewable sources of energy like solar, wind, geothermal, hydraulic, biomass is discussed in detail. In this review, Present research is a try to present the current state and feasibility of applications of various still designs to desalinate the water from salts to convert into freshwater in order to enhance the productive capacity of suggested methodologies.

**Keywords** Desalination · Solar still design · Inclined solar still · Basin and wick solar still · Active and passive stills

## 1 Introduction

The water crisis in modern times appears to call out for catastrophic situations all over the world. As per estimates declared by UNO, approximately 2 billion people are estimated to suffer from water scarcity by 2025 [1]. Hence, to get this situation

---

R. G. Kawalkar (✉)  
Technocool HVAC Engineers, Nagpur, India

S. M. Fale  
Department of Mechanical Engineering, NIT Polytechnic, Nagpur, India

S. P. Lokhande  
Department of Mechanical Engineering, Priyadarshini College of Engineering, Nagpur, India

under control, researchers are coming up with improvements in existing desalination technology to enhance the productivity of fresh drinking water despite limitations such as relatively low operating efficiency of this mechanized process. However, with the ever depleting resources and consequently raising population demands have shouldered the need of desalination on an ever-increasing demand. With the major advancements happening in Middle East (with Saudi Arabia being the largest user of this technology for the treatment of seawater) and the USA, parts of Asian Pacific countries such as India, China, and Japan along with global powers like Germany and UK have been heavily involved in the development of this technology [2]. However, the treated water when discharged has a surreal impact on the aquamarines.

Desalination, as interpreted, is a continuous process in which salts are eradicated from saline water, which later can be used for different purposes. The prominent methods to achieve this are characterized mainly into two categories: membrane and thermal. With nearly 3/5th of entire world desalinated water is being treated on the application of solar desalination, present work looks upon the further insights of this ever-developing process. Few of the prominent recent developments having a vital importance in contributing to this work are as listed below:

- (1) Yousef [3] conducted the experimental study on single slant solar still. The experimentation was performed in the Egypt. For doing experimentation, five different conditions are undertaken and comparison was done between them. The various conditions are (a) condition only traditional still was used, (b) condition was traditional still with phase change material, (c) condition are traditional solar still with phase change material and pin finned, (d) condition are solar still with steel wool fiber and phase change material is used, and the last condition is (e) solar still with steel wool fiber only. After experimentation, it is found that when phase change material with the pinned surface has used the output of freshwater were increased by 17% and 7% more as compared to traditional and still with phase change material, respectively. When steel wool with phase change material has used the output of freshwater during sun time was increased by 14%, and during off shine, there was a drop of 80% as compared to still with phase change material.
- (2) Al-harahsheh [4] performed the investigation study on solar still with external heat exchanger and phase change material. In this experimentation, the distillation of water is done by two methods: first by directly absorbing heat from solar rays and second by supplying hot water from the heat exchanger. From experimentation, they found that the 10 ml/s supply of cooled water is optimal. As the level of water increases, the productivity of still decreases. The 4.3 lit/m<sup>2</sup> per day output is obtained from this still from which was 40% were obtained after evening. From the financial analysis, it was exposed that this system was more useful in rural areas (Fig. 1).
- (3) Sahota [5] studied the consequences of nanofluids on the double slope solar still. In this experimentation, the three different nanoparticles are used such as aluminum oxide, tin oxide, and copper oxide. The 0.25% concentration of nanoparticles is used for experimentation. After experimentation, it is found



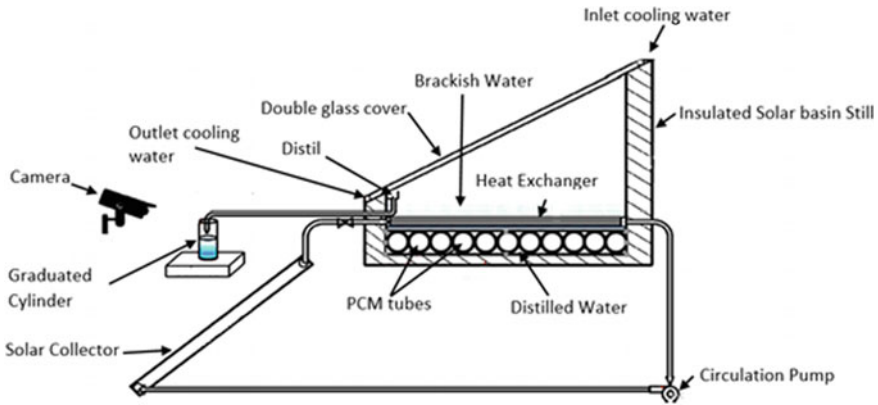


Fig. 1 A systematic representation of exploratory arrangement [4]

that when aluminum oxide nanoparticles are used 50.34% efficiency was found, similarly when tin oxide was used as nanoparticles 46.10% efficiency were found and lastly, for copper oxide 43.81% efficiency was found as compared to traditional solar still. The yield was calculated for a different condition in March for the projected design.

## 2 Renewable Energy Desalination

With the need to increase the productivity of the plants, involved in this process and the implementation of fossil fuels-driven mechanized processes, the implications observed in carbon content in the atmosphere led to the abolishment of the technology and application of renewable sources as fuel for the plants. This practice is widely used in the majority of the gulf countries. The varied sources are as discussed below:

- (a) Solar: The heat generated from the sun’s radiation is used in wide applications across the plants.
- (b) Wind: With the help of windmill plants, electricity being generated from mechanical generators.
- (c) Hydroelectric: Energy generated by a huge volume of water flow majorly observed in dams.
- (d) Biomass: Energy obtained from burning/degrading waste such as woods and cow dung cakes.
- (e) Geothermal: Energy utilized beneath the earth’s crust in the form of particulate/liquid form for electricity generation.

With the help of different technologies, the scientific community has tried to explore the majority of sources available for disposal. However, it is the solar desalination technology that is widely preferred over others due to the abundance of energy and fewer finances being involved in the installation of mechanics.

### 3 Solar Desalination

The solar desalination technique is broadly classified in the management of solar energy. Hence, it is widely dissolved into two main categories:

- (a) Direct: The absorption process and desalination take place in the same apparatus.
- (b) Indirect: Both absorption of solar energy and desalination are done through different processes and systems (Fig. 2).

The conventional methodology involving basin solar still is the most used method for ages and is hassle-free for aspects related to convenience and maintenance. The basin which is covered up with a see-through cover and contains saline water which is unveiled in the presence of solar radiation is usually black stained to facilitate maximum radiation [7]. Once water changes its state of form (due to evaporation), it is made to condense once its particulates comes in interaction with the upper surface. Finally, the residual water is thereafter circulated to different facilities through proper mediums. However, major limitations involved in this simplified apparatus are its

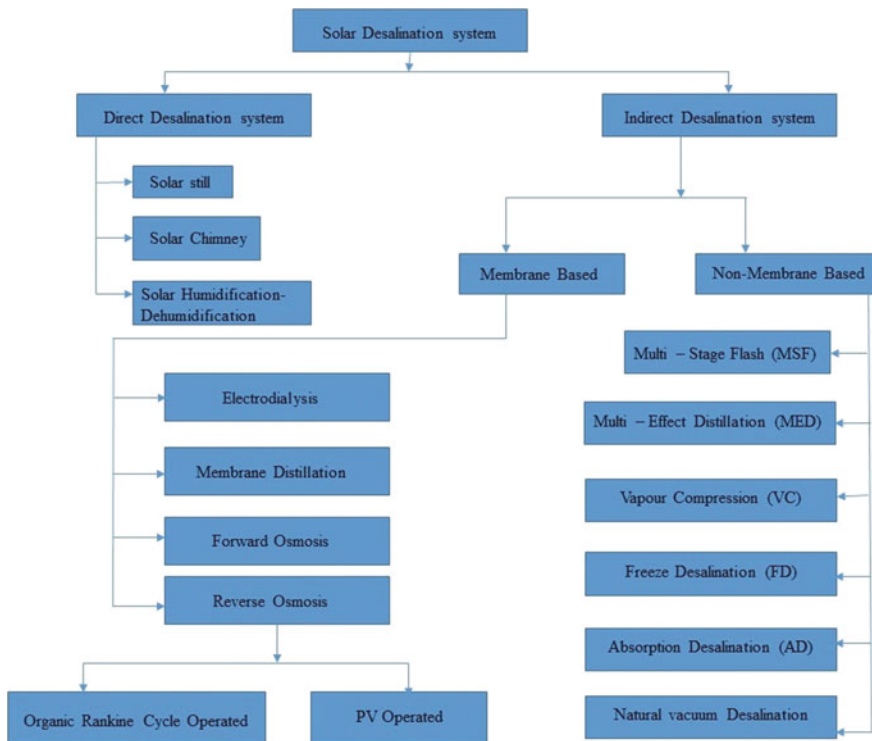


Fig. 2 Stratification of different solar desalination technologies [6]

significant low efficiency due to liberated latent heat of condensation and the slow rise in water’s evaporation temperature [8].

### 4 General Classification of Solar Still Designs

The designs of solar stills are segregated into two major categories: active and passive stills, altogether depending upon the process involved in heat source used for evaporation of saline water. Usually, solar heaters, photovoltaic thermal hybrid solar collectors, and concentrators are used for this purpose. However, these stills are further categorized into single and multi-effect based on number of glazing layers over the surface of the water.

#### Single effect passive solar stills

They are the most conventional stills used ever. They are easily constructible while having only a glazed layer over the surface of the water. Despite all, the major limitation is the loss of thermal energy in the form of latent heat of condensation from the application of glazing. Hence, this limitation can be worked upon significantly for achieving substantial efficiency. Various still designs are analyzed and worked upon by researchers which can be brought into implementations for incorporating the desired efficiency of the still (Fig. 3).

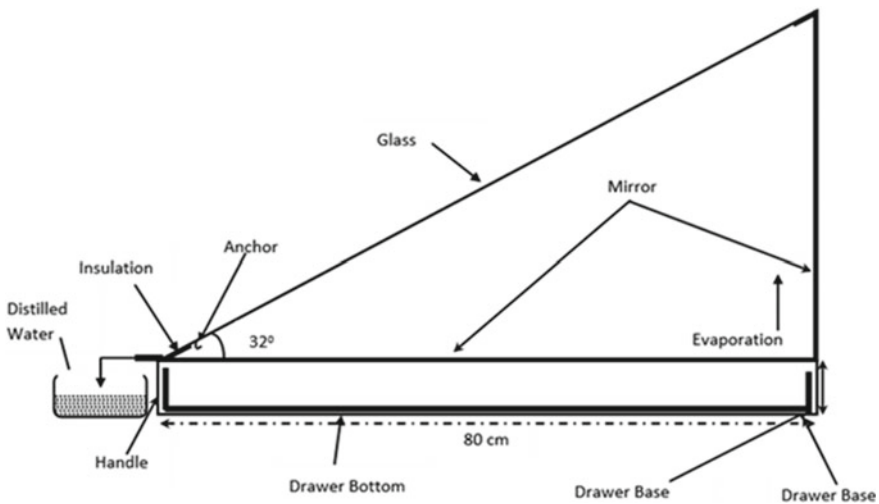


Fig. 3 Diagram Illustrating a single effect passive solar still [9]

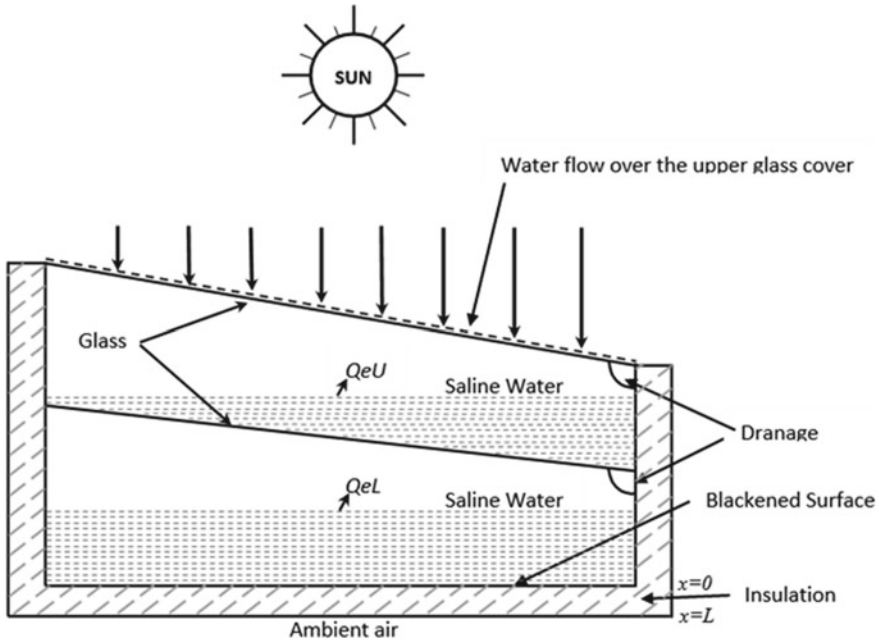


Fig. 4 Diagram Illustrating multi-effect passive solar still [10]

### Multi-effect passive solar stills

These stills are developed with the intent of employing and using max. dissipated heat. This type of still designs incorporates more than a single layer of glazing sheet, hence utilizing the latent heat of condensation for increasing the productivity of the still. Since it is more efficient than the single still due to its utilization of the abundant thermal energy compared to single still. Therefore, various still designs are analyzed and worked upon by researchers which can be brought into implementations for incorporating the desired efficiency of the still (Fig. 4).

### Single effect active solar stills

Since the evaporation temperature of the water can only be increased by the direct contact of sun's radiation in the case of passive stills, this is somewhat rectified by the modern design of active stills. As illustrated in case of single effect passive solar still (with a single glazed layer), there is a supply of thermal energy from an additional exterior source to raise the evaporation temperature of the water which effectively results in faster heat transfer rate (causing a surge in evaporation rate) and invariably increases the efficiency of active still (Fig. 5).

### Multi-effect active solar stills

This is the most productive and efficient among all the discussed stills. They preferably consist of layers of many glazed covers. Similar to single slit active solar still,

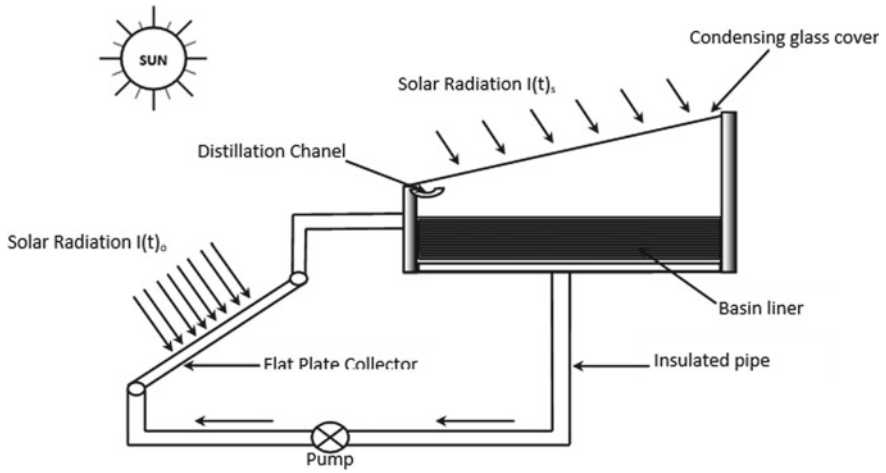


Fig. 5 Diagram Illustrating a single effect active solar still [11]

a supplementary thermal energy source is supplied to the rearmost basin since it receives the least solar thermal energy than other higher placed basins due to the abated transitivity by the presence of additional basins (Fig. 6).

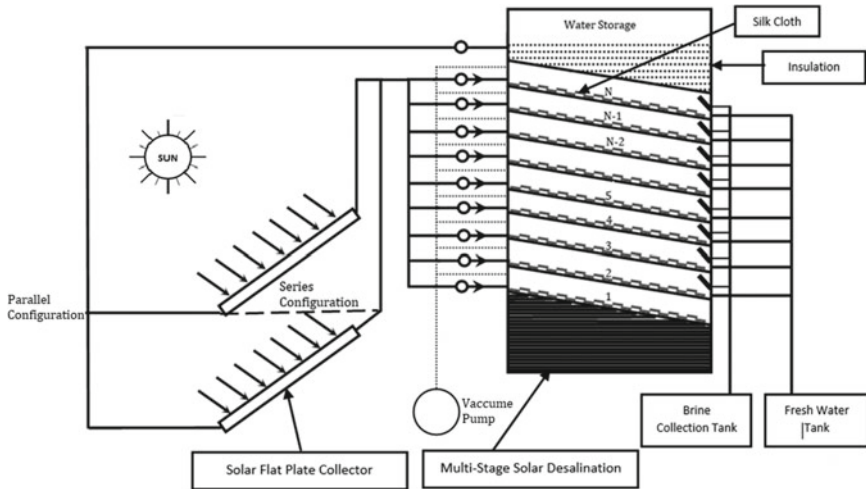


Fig. 6 Diagram illustrating multi-effect active solar still [12]

## 5 Inclined Solar Stills

See Fig. 7.

As the terminology suggests, the still is tilted at an angle from the horizontal in this type of design. The formulation for this type of design is derived from the consideration that the evaporation rate is directly proportional to the quantitative flow of water quantity on the absorber plate which invariably results in the added volume of distilled water. Hence, the efficiency of the still also increases with solar radiation hitting a larger area due to the position of the still. The major advantage in this over other orthodox stills is the volume content which is significantly less as compared to other stills which facilitate the thermal energy to heat up the contained water at a faster rate [13]. Over the years, the basic theoretical facts developed by extensive research prove that (a) The solar radiation angle when aligned with basin increases efficiency, (b) low water streamline on cover increases more productivity of distillate, and (c) basic combinations of different still designs can be more effective [14]. The basic types of inclined solar stills are as discussed below.

### Wick-Type Solar Still

With the implementations of wick material, the contact time between the water molecules increases on the absorber plate which helps the streamline flow to heat up rapidly which results in a faster evaporation rate. However, the edge in this still is the application of brine to glib the brine to avoid dark spots. Moreover, parameters such as conductance, absorption, and capillarity define the efficacy of wick. Materials used as wick are inclusive of either commercial crops, stones, etc. and are validated to be the most suitable. This is generally aligned to horizontal (Fig. 8).

### Basin-Type Solar Still

In this type of design, water containing salts are feed to the basin from the tank. The solar radiation causing refraction activity on the glass due to the basin containing

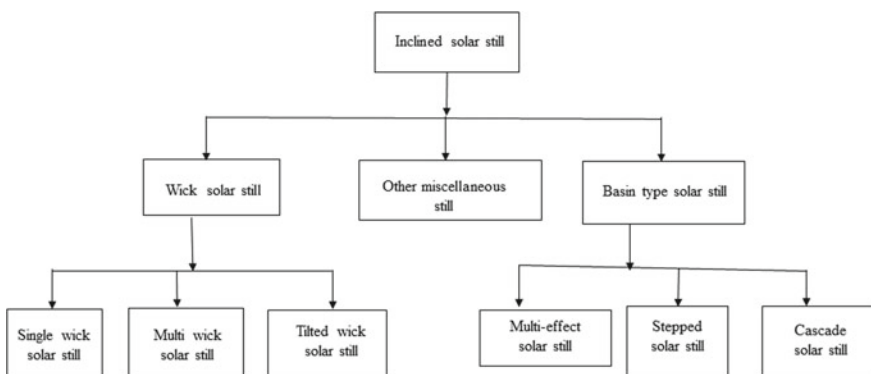
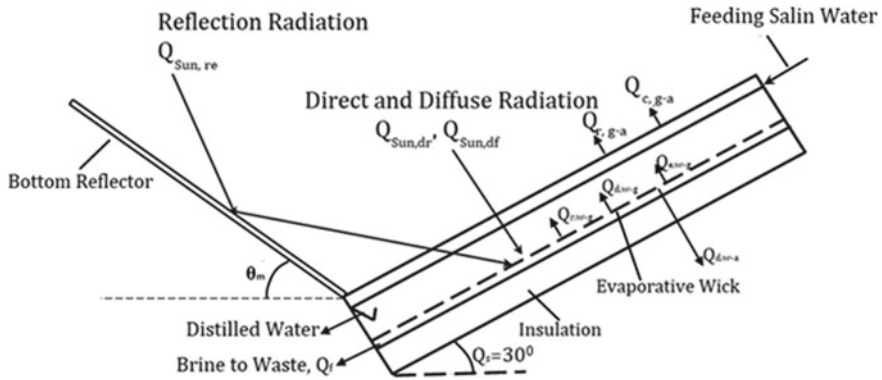


Fig. 7 Different types of inclined solar stills [7]



**Fig. 8** A representation of Inclined wick-type solar still with reflectors placed at top and bottom [15]

water makes a sequential process of evaporation and condensation occurring simultaneously which invariably causes to heat the water. Factors such as the volume of water contained, basin alignment, geographical, and climatically conditions influence the efficiency of this type of still (Fig. 9).

**Other Designs**

This includes developing designs such as solar still with a reciprocating spraying system, solar still with continuous water flow, weir-type inclined solar still, hybrid solar still, plastic solar water purifier, solar still with the sun tracking system, and inverted trickle solar still.

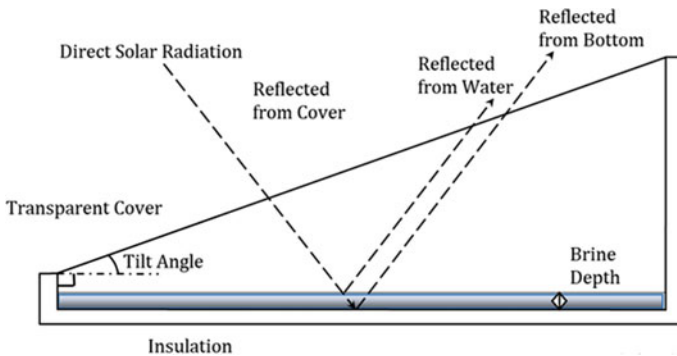


**Fig. 9** An Illustrative diagram for basin type solar still [16]

## 6 Scope of Improvement

From many years now, the work on different solar still has been done but still there is huge scope to increase the efficiency of solar still. Due to simple construction and working, single slope solar still is most popular among different other types of solar stills. To increase the efficiency of still, many researchers have developed different types of solar still. Due to various parameters, solar still design up till now is not suitable for long time. During examination, it is found that the few region of work are not yet discovered due to complication in experimentation. A feasible design can be made which comprises of development of a hybrid system by combining the solar water heater system with the basin-type solar still. The solar water tube is placed inside the basin. The saline water is made to flow inside the tubes, and further, the tube is surrounded by saline water. The tube acts like an absorber which absorbs the solar radiation from the sun and heats the saline water after some time. As the temperature of water increases, it starts to evaporate and as the vapour is collected on the top glass cover of basin post-condensation, the water is collected separately and can be used for drinking purpose. Furthermore, an arrangement to provide the reflector to incident all the solar rays on the tubes which will be reflecting from the glass surface can also be made. During experimentation, the angle of the tube can be changed as well as reflectors to give us optimized results as to what inclination of tubes and reflector should be maintained to generate maximum output from the setup. Mathematical modelling for the above experimental work suit can also be validated through CFD technology.

## 7 Conclusion

In this paper, discussion regarding different facets related to inclined solar still designs is made. With this, substantial accomplishments are made regarding new findings and developments, efficient designs, and further scope for improvements taking into consideration the various limitations. The major findings are as listed below:

- (a) After analyzing various designs, step solar still with condenser and reflector is the most efficient.
- (b) Wick-basin passive solar still is as well a convenient method to use with yields proportional to nearly 4/5th.
- (c) Pre-heating of water containing salts gives up excellent results that enhance its condensing and evaporating capabilities.
- (d) A low streamline flow of water is preferred over higher quantity produces better condensation on the application of glass cover.
- (e) Re-usage of different forms of energy can also prove to worth but the initial cost for installing this equipment with processes is significantly high.
- (f) With the help of wick material, and with a suitable volume of water in still, there are higher chances of achieving desired productivity.



- (g) Other upcoming designs with hybrid systems application produce better desalination with improved efficiency.

Although, inclined solar still is one of the best designs among the majority of desalination systems. However, important additions such as solar projection, design, finances involved, water flow, evaporation rate, the volume of the basin, flexible alignment, etc., make them one of the trusted technologies to efficiently perform desalination.

## References

1. U. WATER (2019) The United Nations World Water Development Report
2. Water supply and sanitation in Saudi Arabia—Wikipedia. Available: [https://en.wikipedia.org/wiki/Water\\_supply\\_and\\_sanitation\\_in\\_Saudi\\_Arabia#Desalination](https://en.wikipedia.org/wiki/Water_supply_and_sanitation_in_Saudi_Arabia#Desalination). Accessed 15-Feb-2020
3. Yousef MS, Hassan H (2019) An experimental work on the performance of single slope solar still incorporated with latent heat storage system in hot climate conditions. *J Clean Prod* 209:1396–1410
4. Al-harahsheh M, Abu-Arabi M, Mousa H, Alzghoul Z (2018) Solar desalination using solar still enhanced by external solar collector and PCM. *Appl Therm Eng* 128:1030–1040
5. Sahota L, Tiwari GN (2016) Effect of Al<sub>2</sub>O<sub>3</sub> nanoparticles on the performance of passive double slope solar still. *Sol Energy* 130:260–272
6. Sharon H, Reddy KS (2015) A review of solar energy driven desalination technologies. *Renew Sustain Energy Rev* 41:1080–1118
7. Kaviti AK, Yadav A, Shukla A (2016) Inclined solar still designs: a review. *Renew Sustain Energy Rev* 54:429–451
8. He T, Yan L (2009) Application of alternative energy integration technology in seawater desalination. *Desalination* 249:104–108
9. Durkaieswaran P, Murugavel KK (2015) Various special designs of single basin passive solar still—a review. *Renew Sustain Energy Rev* 49:1048–1060
10. Fath HES (2010) Multi-effect solar stills. *renewable energy system and desalination*, 3
11. Sampathkumar K, Arjunan TV, Pitchandi P, Senthilkumar P (2010) Active solar distillation—a detailed review. *Renew Sustain Energy Rev* 14:1503–1526
12. Reddy KS, Kumar KR, O'Donovan TS, Mallick TK (2012) Performance analysis of an evacuated multi-stage solar water desalination system. *Desalination* 288:80–92
13. Manokar AM, Murugavel KK, Esakkimuthu G (2014) Different parameters affecting the rate of evaporation and condensation on passive solar still—a review. *Renew Sustain Energy Rev* 38:309–322
14. Murugavel KK, Anburaj P, Samuel Hanson R, Elango T (2013) Progresses in inclined type solar stills. *Renew Sustain Energy Rev* 20:364–377
15. Manikandan V, Shanmugasundaram K, Shanmugan S, Janarthanan B, Chandrasekaran J (2013) Wick type solar stills: a review. *Renew Sustain Energy Rev* 20:322–335
16. Khalifa AJN, Hamood AM (2009) Performance correlations for basin type solar stills. *Desalination* 249:24–28

# Design and Fabrication Errors of Foil Bearings: A Review



Vishal Mourya and Skylab P. Bhore

**Abstract** Aerodynamic gas foil bearing (GFB) is a self-acting hydrodynamic bearing that used ambient air as a working fluid to carry small turbomachinery with medium load capacity. The compliant structure of foil bearings provides more reliability to a high-speed rotating system. The thin flexible structure of top foil and bump foil assists the foil bearings to accommodate shaft misalignment with better stiffness characteristics. Due to frictional interactions, the GFBs also provide coulomb damping with nonlinear behavior. As a consequence, the complexity of GFBs is increased. With compliant structure, the foil bearings offer many advantages such as the capability to operate at high speed with elevated temperature, longer service life (due to air lubricant), and less operating cost. But there are some limitations of GFBs, i.e., high friction loss at low speed. Due to small and complex structure, the manufacturing process of FBs is large and slightly challenging. As a consequence, many undesirable manufacturing errors are developed in FBs design such as foil thickness error, bump pitch error, and bump height error. This paper reviews the present research related to manufacturing techniques which are used for developing the compliant corrugate shape of foil bearings. These manufacturing techniques are blanking–punching, metal cutting, etc. To overcome these manufacturing errors and make the fabrication process of the FBs with more accurate, heat treatment and quenching process are also used. Currently, the advanced manufacturing technique such as rapid prototyping is used to avoid any error and developing accurate foil bearings.

**Keywords** Gas foil bearings · Manufacturing errors · Geometrical parameters

---

V. Mourya (✉) · S. P. Bhore

Rotor Dynamic and Vibration Diagnostic Lab, Mechanical Engineering Department, Motilal Nehru National Institute of Technology, Allahabad, Uttar Pradesh, India

# 1 Introduction

For the past two decades, the applications of gas foil bearings (GFBs) are increased with superior advantages such as high-speed stability. Since the 1960s, these GFBs starts implementing in many high-speed rotating machineries such as turbo blower, turbocharger [1]. The reasons for the increased requirement of GFBs are that it provides more reliability under the high-speed condition with a large temperature range capability. In addition, there are some additional advantages of GFBs such as no degradation of lubricant properties under extreme conditions and less friction loss (due to the presence of air lubricant) [2].

Due to thin and flexible structure, the foil bearings are capable to accommodate shaft misalignment under high-speed conditions [3]. This experiment results demonstrate that foil bearings have more capability to tolerate high level of misalignment than other bearings (Table 1).

Reference [4] This is due to the formation of wedge profile between the rotor surface and top foil surface. Therefore, the foil bearing is also known as self-acting bearings. With air lubricant as a working fluid, the contamination problem of lubricant in foil bearings is inattentive. However, there is high friction loss at starting or stopping condition due to less viscous characteristics of air lubricant. Whereas, the issues of load capacity and friction coefficient in miniature (mesoscale) air journal bearing can be addressed by adopting surface texture [25]. Specifically, employing square-shaped textures in the convergent zone of the bearing gives improved load capacity and friction coefficient [26].

## 1.1 Background and History of Foil Bearings

Since the origin of gas foil bearings (GFBs) technology, many research papers on GFBs had been published with various objectives such as improve load capacity and rotordynamic characteristics. With progressive development in the structural configuration of foil bearing, the bump-type gas foil bearing is classified into three distinct generations such as generations I, II, and III. In the generation I bump-type GFBs, the top foil and bump foil is uniform in the axial and radial direction, (see Fig. 1). Whereas the generation II or generation III have cut bump strip in axial and circumferential direction, respectively. However, the performance of small high-speed rotating machinery majorly depends upon the structural parameters of foil bearings [27].

Walowit et al. [28] modeled the single bump by considering it as a spring. In this study, the friction at the interface between the top and bump foil and between two consecutive bumps is negligible. Heshmat et al. [5] introduced the friction in the single bump model and evaluated its performance characteristics with variation in friction coefficient. Heshmat [6] performed testing on two configurations of foil bearings with different objectives such as higher load capacity and better whirl

**Table 1** Comprehensive summary of literatures

Focus area	Work	Major findings
Experiment analysis [1]	Investigation of foil bearings design and coatings at high temperature	With foil bearings, the maximum possible weight reductions is upto 30% and cost reduction upto 20% may be possible by eliminating the bearing lubrication system
Misalignment in gas foils journal bearings [3]	Experimentally investigated the misalignment by laser alignment system	Gas foil bearings force coefficient is affected by misalignment
Structural damping of foils journal bearings [4]	Influence of amplitude on dynamic characteristics of FBs	The direct stiffness and damping decrease with increasing dynamic amplitude. This investigation shows bearing stiffness and damping increased with bearing number
Theoretical analysis [5]	The analysis of two different configuration of foil bearings: one is single pad and other is multi-pad	Multi-pad foil bearings decrease the load-carrying capacity. With increase in compliance, the torque and the load capacity of foil bearings is also decreased
Experiment analysis [6]	Design two different types of foil bearing for different purposes: stability and load capacity	The single pad bearing achieved maximum steady state load. Whereas the three-pad bearing shows better whirl stability
Load capacity estimation of foil air journal bearings [7]	A simple thumb rule to estimate the load capacity of foil bearings	The rule of thumb (ROT) concept establishes a standard for estimating the load capacity of foil journal bearings

(continued)

Table 1 (continued)

Focus area	Work	Major findings
Fabrication and experiment analysis of foil bearings [8]	The development of discrete and continuous bump foil bearings involves determination of bump geometry for the desired load capacity	Continuous bump foil bearings have edge over the discrete bump foil bearings in low load and high-speed applications
Theoretical analysis of bump foils geometry [9]	The theoretical model of corrugated bump considers the friction between the bump foil, top foil and bearing sleeve	An increase in friction b/w top and bump foil improve the coulomb damping and stiffness. The loading condition also influences the stiffness of foil bearings
Stiffness and damping coefficients of gas foil bearings [10]	Perturbation method is used to obtain the dynamic coefficients	The stiffness and damping coefficients are reduced by the elastic foundation. The results were computed using the finite difference method
Dynamic analysis [11]	The equivalent viscous damping of the Coulomb friction caused by the foil relative motion is included in the structural calculation	The existence of the foil membrane stiffness affects the bearing dynamic coefficients
Dynamic analysis [12]	Dynamic load versus foil bearing structural deflection measurements for increasing shaft temperatures, from ambient to 188 °C	As the amplitude of dynamic load increased, the FB stiffness increased by 57%. The frequency of dynamic load improves the FB dynamic stiffness. But FB stiffness reduced with increase in shaft temperature from 22 °C -188 °C
Thermo-hydrodynamic analysis of bump-type gas foil bearings: [13]	Thermal analysis of FBs by considering heat transport in the gas film region	The gas film temperature is increase significantly with increased in static load and rotor speed
Dynamic analysis of air foil bearings [14]	Investigates the two different types of foil bearings: one is single continuous top foil circular cylindrical bearings and other is non-circular	Preloaded three-pad bearings have significantly reduced load capacity compared to circular bearings due to a small pad arc length of only 120 deg
Structural parameters of the multi leaf gas foil journal bearing [15]	Evaluate the load-carrying capacity of multi-leaf foil bearing under various geometric parameters	At optimum values of the geometric parameters, the load capacity of multi-leaf foil bearing is improved significantly

(continued)

Table 1 (continued)

Focus area	Work	Major findings
Adaptive and nonlinear structure [16]	Represent the self-adaptability and nonlinear behavior of foil bearings by numerical and experimental study	The stiffness of foil bearings is increased with increase in pressure load. The vibration level is low at high rotor speed
Structural modifications by using metal shims [17]	Numerical simulation is performed to calculate the stiffness and damping by adding metal shims in the first generation FBs	The shims decreased the eccentricity and minimum film thickness in GFBs and increased the FBs stiffness significantly. The load-carrying capacity of foil bearings is also increased
The effect of Coulomb friction on the static performance of foil journal bearings [18]	Evaluate the influence of friction on the foil bearing performance	The multiple equilibrium position in FBs is observed for one load due to hysteresis effect. The influence of friction on the minimum film thickness is negligible
Manufacturing of compliant foil bearings [19]	DOE technique used to quantify the different manufacturing parameters and define optimizes manufacturing process	The FEA suggests that the stress within the foil is sensitive to the shape of the die. By changing die, the mean stress is reduced by 17.4% and springback error by 69%
Manufacturing error [20]	Three realistic manufacturing error bump height. Bump length and radius of bump are analyzed	Manufacturing error in bump height affect the bump stiffness. i.e., 4% of bump height induce 40% reduction in stiffness
Stiffness and damping Coefficient [21]	Establish a new Rule of Thumb (ROT) for estimate the stiffness and damping coefficients of FBs	The preloaded foil bearing increased the stiffness and damping coefficients
Design, manufacturing, and modeling [22]	This paper introduces a novel design of FBs by using lithography manufacturing processes	The fabricated foil bearings shows minimal effect of damping on the onset synchronous vibration
Bump height manufacturing errors [23]	Synchronous amplitude of rotor are investigated by consider bump height manufacturing error	Manufacturing error decreases the damping of bump foil bearings
Manufacturing errors [24]	Numerical simulation performed to evaluate the static and dynamic response of foil bearings with bump height manufacturing error and without error	The effects of manufacturing error are evaluated in terms of orbit and stability

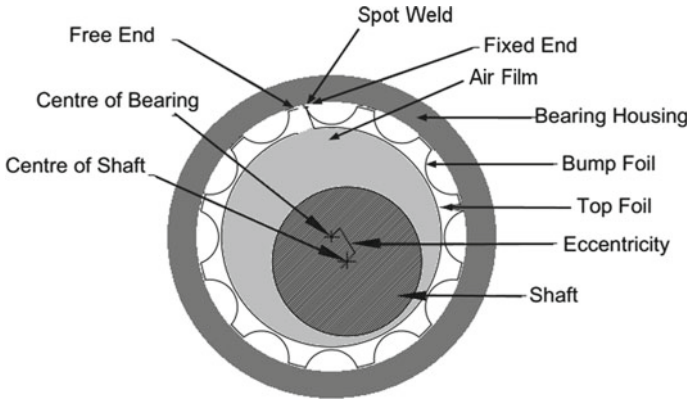


**Fig. 1** Schematic view of generation I bump-type foil bearings

stability. In this study, the results demonstrate that three-pad bearings provide more whirl stability at high rotor speed. Whereas, the single pad bearings show better load capacity under similar condition. To measure the load capacity of foil bearings without any experiment, Dellacorte [7] introduced empirical formula for estimating the load capacity of foil bearings. In this literature, author relates the load capacity of foil bearings with its geometrical parameters and is given as Eq. (1).

$$W = D(L \times d)(d \times Nrpm) \tag{1}$$

where

- $W$  = Maximum load-carrying capacity of bearing
- $D$  = load-carrying capacity coefficient ( $N/(mm^3 \times Nrpm)$ )
- $L$  = Bearing length in axial direction (mm)
- $d$  = Bearing diameter (mm)
- $N$  = rotor speed in thousand rpm.

Whereas some author developed different foil bearings for the desired speed and load capacity [8]. In this study, the author analyzed two different foil bearings, named discrete and continuous bump foil bearings. The analysis results demonstrate that possibility of axial dislocation in discrete bump is more under high-speed condition. But the continuous bumps are linked with each other and no dislocation occurs in continuous bump foil bearings. In addition, the minimum speed required to lift off the rotor in continuous FBs is smaller than discrete FBs.

Ku and Heshmat [9] proposed a theoretical model to investigate the effect of friction between the top foil and bump foil and bump foil and bearing housing. This study also considered the interactions between the bumps. These investigation results show the increase in friction improves the stiffness and damping of foil bearings. It is also observed that bump stiffness near to welded end is more than the free end. Peng and Carpino [10] calculated the dynamic coefficients of foil bearings by using

the perturbation method. Further, Peng and Carpino [11] evaluated the rotordynamic coefficients by finite element method. This study evaluates the influence of various geometric parameters such as bearing number, bearing compliance, and bending on stiffness and damping coefficients of foil bearings. Ku and Heshmat [29] extend their previous work and theoretically investigate the viscous damping of bump strip. The author predicted the stiffness and damping characteristics of FBs by using a periodic perturbation method. In addition, the dynamic stiffness and damping of foil bearing are majorly depending upon the frequency and amplitude of perturbation. In the second part [30], the parametric study was done to investigate the effect of amplitude and frequency of perturbation with accuracy. The results demonstrate that the direct stiffness and damping coefficient decreased with an increase in the amplitude of perturbation. From the analysis, it was observed that stiffness was not much affected at small friction value. But the stiffness value increased abruptly with increased friction value. Whereas the damping of foil bearing increased up to the certain value of with friction (0.4) and after that value, the damping starts to decrease slightly.

Heshmat [31] conducted tested on various types of advanced coatings with an objective to develop foil bearings that will operate at high temperature. Thereafter, the author evaluated tribological characteristics of several coatings such as Korolon 700, 800, and 1350. This investigation demonstrates that hard chrome coatings were found unsuitable for high-temperature applications, whereas the Korolon and PS304 coatings show good result under high temperature (upto 800 °C). Fanning [32] evaluated the impact of PS304 and Korolon 1350A coatings on thrust bearings performance at 540 °C and 3.44 kPa at startup/shutdown condition. In addition, when these two coating (PS304 on and K1350A) were coupled, then the hydrodynamic performance improved significantly. Whereas, Zywicka [33] performed an experimental analysis of foil bearings with sliding coatings (hard chrome coating on journal and polymer coating on top foil) made up of synthetic materials. This test used to evaluate the tribological characteristics of foil bearings under different operating conditions. The rotation speed 12,500–10,000 and 9000 rpm, the increased in temperature was found to be 1 °C and the maximum temperature (32 °C) was found at 5000 rpm. Kim [12] performed experimental to evaluate the dynamic coefficients variation with increase in shaft temperature. This analysis results shows that FBs structural stiffness and damping coefficients decreased significantly with increase in shaft temperature. San Andres [13] performed thermal analysis of FBs by considering external cooling medium inside the shaft. This analysis also considered the change in material properties due to temperature.

Kim [14] performed parametric study for two different types of foil bearings: (a) circular bearing with single top foil, (b) non-circular(preloaded). This analysis results demonstrate that preloaded bearing had low load capacity in comparison with normal FBs. In addition, the bearings rotordynamic characteristics are also influenced by the bearing shape. In other words, the load capacity and rotordynamic characteristics of FBs depend upon the overall bearing shape. Li [15] introduced theoretical model to evaluate the impact of structural parameters on load capacity of multi-leaf gas foil bearings [MLFB]. The variable parameters in this study are foil overlapping



ratio, radial clearance, and foil thickness. Kim and Andres [34] introduced the three metal shims with lobe-like structure in foil bearings to improve the load-carrying capacity and whirl stability of GFB. These results show that the shimmed GFBs developed extra load to generate more hydrodynamic pressure. With shimmed, the rotor critical speed was increased due to enhanced in direct stiffness. In comparison with simple GFBs, the shimmed GFB demonstrates larger stiffness and damping coefficient at smaller eccentricity and journal attitude angle. Hoffmann [35] modified the generation I bump-type foil bearings by inserting three metal shims in between the sleeve and bump foil. In this study, the variable parameters such as static preload, dynamic amplitude, and excitation frequency are considered. With these results, the author analyzed the effect of shim on the dynamic characteristics (stiffness and damping) of foil bearings. Liebich [17] performed numerical simulation to evaluate the impact of shim on radial clearance in GFB-rotor system. This analysis results demonstrate that shim increase the stiffness of foil bearings.

Sim et al. [36] performed an experiment to investigate the impact of preload and radial clearance on the rotordynamic characteristics of lobed gas foil bearings. In this study, five different GFBs (three circular GFB with radial clearance 50, 100, and 150  $\mu\text{m}$  and two-lobed GFB with preload 100 and 150  $\mu\text{m}$ ) were experimentally analyzed. This experiment results show that system natural frequency increased due to mechanical preload which improved the rotordynamic performance of oil-free TC. Sim et al. [37] evaluated the influence of preload on the performance of three-pad foil journal bearing under static and dynamic conditions. However, it is observed that stiffer foil is implemented in foil journal bearing to avoid sagging problem. In addition, bump foil can also be used into multi-stage to achieve large load-carrying capacity of foil bearings. In addition, foil bearings show self-adaptability feature at high-speed condition [16]. From the results, it is observed that the dynamic and thermal properties of GFBs change simultaneously with their working environment.

Feng et al. [38] performed experimental analysis of novel hybrid bump-metal mesh foil bearings (HB-MFBs) to evaluate its static and dynamic characteristics. These results demonstrate that the HB-MFBs show brilliant damping characteristics because the number of micro-slips occurs inside the mesh blocks. In contrast, the HB-MFBs show twice advantages, namely as better precision control by BFBs and larger damping characteristics by MMBs. With continue to previous work, Feng et al. [39] proposed another model of hybrid bump-metal mesh foil bearing (HB-MFBs) by inserting metal mesh block inside the bump foil structure. In this study, the spring model is used for calculating the stiffness and damping coefficients of metal mesh. These theoretical results show that structural stiffness of HB-MFBs for 40% mesh density is larger than mesh density 25%.

Feng and Kaneko [40] developed the theoretical model to examine the dynamic analysis of bump foil bearings in terms of instability and unbalance response. These simulations were performed by considering it as link-spring model. The results demonstrated that load capacity increased with increase in bump number or length ratio. The load capacity was also enhanced with foil thickness and Young's modulus. It is important to note that the bump height never influence the load capacity of bump-type foil bearings.

Zhang et al. [41] developed the 3D model of GFBs and performed numerical analysis through fully coupled fluid–structure interaction (FSI). In each FSI iteration, the fluid model solves Navier–Stokes equation and transfers the developed pressure on the top foil surface in structural model. These results show that load-carrying capacity is increased with increasing in eccentricity ratio. Aksay and Coskun [42] performed the fully coupled 3D analysis of foil journal bearings through FSI. Its result demonstrates that load-carrying capacity is increased with increase in rotor speed. Whereas the altitude angle decreased gradually with rotor speed which depict that film thickness moves toward to load axis.

Salehi [43] design foil bearing for performing experiment to investigate the dynamic characteristics of bump foil bearing. In this analysis, the two methods were adopted for calculating damping values which are energy method and single degree of freedom method. The result demonstrate that the damping values increased with increased in friction coefficient upto certain value (threshold limit), and after that values, the damping starts to decrease with increase in friction value, whereas the damping values decreased with increased in frequency. In addition, the variation in stiffness with frequency is not much significant. Lez et al. [44] developed the finite element structural model for analyze the static and dynamic characteristics of bump-type foil bearings. The static results demonstrate that structural stiffness is decreased from weld end to free end. It is also important to note that dynamic stiffness and equivalent viscous damping decreased with increased in amplitude of dynamic pressure, whereas the dynamic stiffness increased with increased in friction coefficient.

Hou et al. [45] proposed numerical study of double-layer protuberant foil bearing to calculate its static and dynamic characteristics. In this study, the contacts between different layers have been considered to evaluate the deflection of each foil. These results depicts that load capacity of this bearings is increased with increased with bearing number and eccentricity ratio.

Han et al. [46] proposed numerical and experimental analyses to investigate the effect of stiffness and excitation force on harmonic response in air cycle machines (ACM). By modal and resonance analysis, the author observed two different whirling: cylindrical whirling and conical whirling critical speed which shows the dynamic behavior of foil bearings. From the graph, it depicts that vertical bearing stiffness is more than the horizontal stiffness. Whereas the critical speed in horizontal direction is less than the vertical direction.

Lee et al. [18] developed the structural model of foil bearing to investigate the hysteretic effect on its static performance. In this study, the FEM model of foil bearings developed and then algorithm used to provide the frictional contact and its direction at the mating surfaces. The average pressure acting on the top foil is 0.2 MPa. The analysis results demonstrate that friction force influence the dynamic characteristics of foil bearings significantly. Due to friction, the various static equilibrium positions were obtained for on static load.

## 2 Manufacturing of Foil Bearings and Its Errors

In bump-type foil bearings, the various geometrical parameters such as bump height, bump width, foil thickness, bump length and bump pitch etc. These parameters are mutually dependent. It is also observed that any small change in one design parameter can influence the overall performance of foil bearings. Therefore, it is necessary to manufacture the foil bearings with accuracy. Shalash [19] evaluate the manufacturing process and set the optimum manufacturing process by design of experiment (DOE) techniques. This study predicts the process variables which induced springback error. Fatu [20] performed numerical analysis to evaluate the influence of various manufacturing error on stiffness and damping characteristics of foil bearings.

The static and dynamic characteristics of foil bearings (load capacity, stiffness and damping) can be influenced by a small variation in the shape of foil structure [21]. Kulkarni [47] investigate the influence of geometric error on stiffness characteristics of foil bearings. This paper introduced a mathematical relation between geometrical parameters with stiffness characteristics are as follows:

$$\text{Stiffness (K)} = \frac{\text{Load}}{\text{Deflectin}} = \frac{6G}{r^3} \quad (2)$$

where  $G$  is flexural stiffness per unit width of the foil strip

$$G = \frac{Et^3}{12(1 - \nu^2)} \quad (3)$$

where

$t$  = bump foil thickness (mm)

$r$  = bump foil radius (mm)

$E$  = Young's Modulus (N/mm<sup>2</sup>)

$\nu$  = Poisson ratio.

Xu [48] also investigate the impact of geometrical parameters on the rotordynamic characteristics of bump foil bearings. In this study, the author derived an empirical formula for calculating the deformation in a bump. The empirical formula which relates the geometrical parameters with the deflection of an individual bump is as follows:

$$D_b = -\frac{3(1 - \cos \theta)}{EIt^3} \times \left( l^2 \theta + r^2 \frac{\theta}{2} + 2lr \cos \theta - \frac{r^2}{4} \sin 2\theta - 2lr \right) + \frac{3Fr^2}{2EIt^3} (4l \sin \theta - 4l \cos \theta - 4r \cos \theta + 4r \cos^2 \theta + 2r \cos 2\theta - r) \quad (4)$$

where

- $D_b$  = Bump deflection ( $\mu\text{m}$ )
- $F$  = Vertical load on the bump (N)
- $2l$  = Bump length (mm)
- $r$  = Bump radius (mm)
- $\theta$  = Bump angle ( $^\circ$ )
- $E$  = Young's Modulus ( $\text{N}/\text{mm}^2$ )
- $L$  = Bearing length (mm).

From these equations, it was observed that small variation in any geometrical parameter can influence the deflection and stiffness of foil bearings. Therefore, it is necessary to make a proper sequence of the manufacturing processes for developing each part of foil bearings and then assembly of these parts with bearing housing with spot welding. As a consequence, the possibility of any error during manufacturing steps will be reduced. The fabrication steps of FBs can (see in Fig. 2).

Kim [22] introduced a novel design of bump foil bearings by fabricating it with lithography manufacturing techniques. This literature describes new manufacturing tools with various advantages, i.e., the high precision in design and easy assembly. But the compliant structure of foil strip makes that the manufacturing process is slightly difficult. Therefore, the possibility of manufacturing error in design of foil bearings is increased. However, the manufacturing errors in the design of foil bearings,

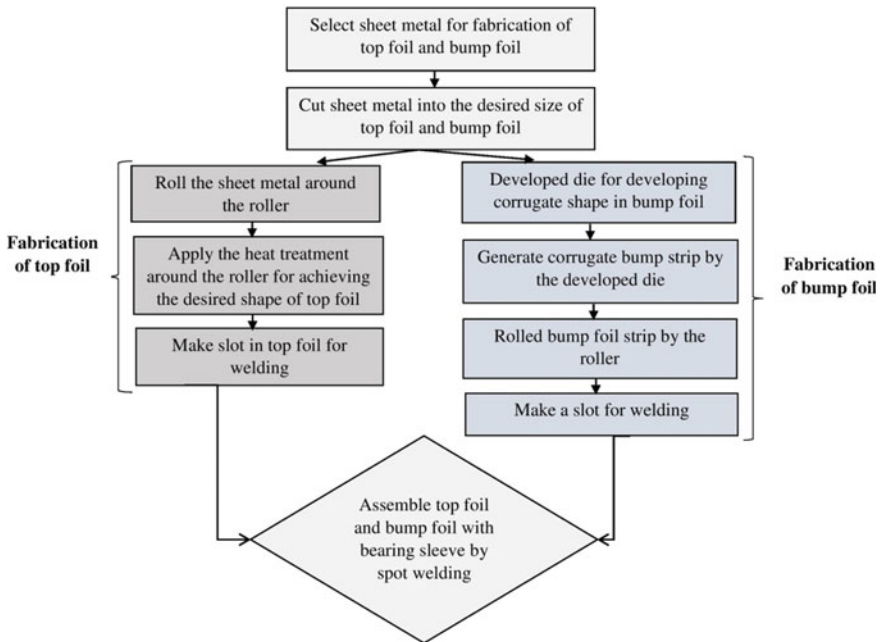


Fig. 2 Flowchart of design, fabrication, and manufacturing of foil bearings

namely foil thickness, pitch, and bump height, influences the overall performance of turbomachinery (Fig. 3).

### **2.1 Foil Thickness Error**

The foil thickness error influences the static and dynamic characteristics of foil bearings (Fig. 3a). The major causes of foil thickness error are non-uniform pressure or using inappropriate die shape during forming process. To reduce this error, the pressure is applied uniformly during forming process. The advanced manufacturing tools such as laser cut or lithography techniques can be used for developing accurate die shape.

### **2.2 Bump Pitch Error**

The bump pitch is another important parameter in design of foil bearings (Fig. 3b). The main causes of this error are inaccurate die (used for developing corrugate shape of foil) or may be due to springback effect. To diminish this error, heat treatment and quenching process can be used during the forming process. Another method to reduce this error by putting some extra load during forming so that final shape of foil is nearest to desired size.

### **2.3 Bump Height Error**

The error in bump height influences the performance of foil bearing [23], as shown in Fig. 3(c). This error may be due to non-uniform pressure or non-uniform foil thickness. To avoid or diminish this error, the hydraulic press can also be used for uniform deformation.

The manufacturing processes such as machining, rolling, bending, forming, and welding are used for developing compliant structure of FBs. But these manufacturing processes have various limitations which can result into manufacturing error in foil bearings. The major reasons of these manufacturing errors are traditional manufacturing techniques, inaccurate die shape or inappropriate pressure during forming process.

Fatu and Arghir [24] performed numerical analysis to estimate the stiffness of foil bearings. This study considered three distinguish manufacturing errors in foil bearings model such as bump height, radius of bump foil, and bump length. From the analysis, the author observed that radius of bump foil never affects the structural stiffness of foil bearings significantly, whereas the bump height influences the structural stiffness (i.e., 20  $\mu\text{m}$  error in bump height leads to 40% decreased in structural

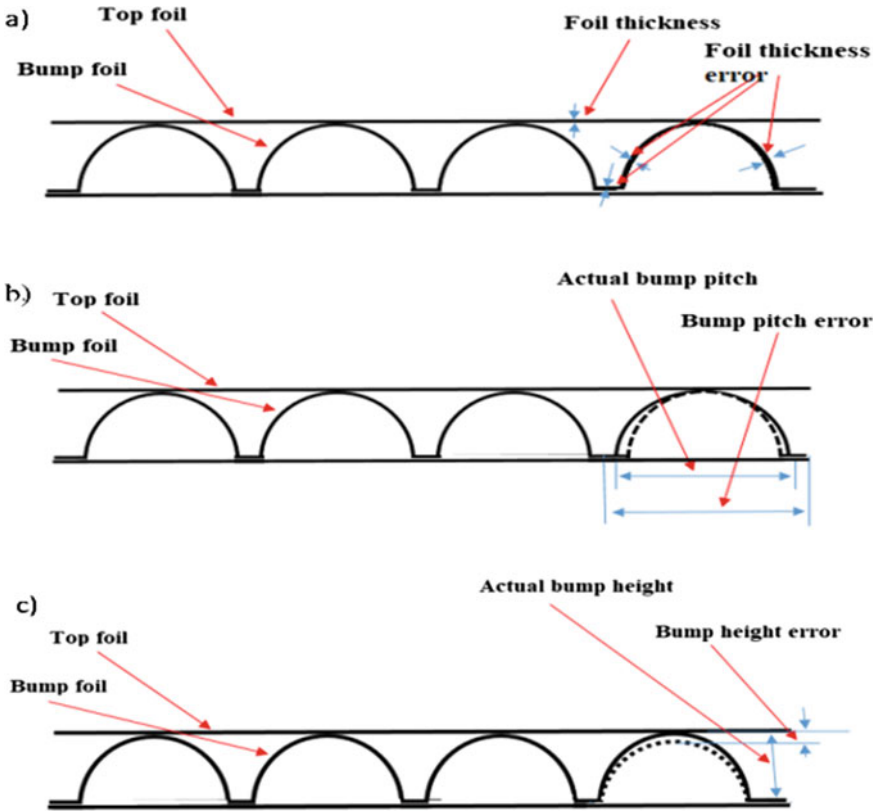


**Fig. 3** Various manufacturing errors in FBs: **a** Foil thickness error, **b** bump pitch error, **c** bump height error

stiffness). However, it is also observed that the bump length error never influences the structural stiffness significantly.

### 3 Concluding Remarks

This paper represents the comprehensive overview of bump foil bearings and describes the various fabrication errors, i.e., foil thickness error, bump pitch error, and bump height error in the design of foil bearings. There are many research papers related to structural configuration, and rotordynamic characteristics of foil bearings have been published. From the literature survey, it was observed that there is less number of research paper related to its fabrication and manufacturing of foil bearings. As a consequence, there is some deficiency in accuracy of manufacturing process of foil bearings. In foil bearings technology, small variation in geometrical parameters

of foil strip can influence the stiffness and load-carrying capacity of foil bearings. Thus, it is necessary to develop foil bearings with more accuracy. In other words, the major focus of this review paper is to describe the relation between the geometrical parameters with the stiffness characteristics of foil bearings. This paper also introduced a design and fabrication process by reducing the manufacturing errors in foil strip. Thus, we have concluded some key points which are: (a) Any fabrication error in foil strip can influence the overall performance of foil bearings. (b) The most influencing parameter in design of foil bearings are foil thickness, bump height, and bump radius. (c) Rapid prototyping techniques can be used for developing foil bearings with accuracy.

**Acknowledgements** The authors acknowledge the Office Coordinator, Computational Research Lab, Mechanical Engineering Department, Motilal Nehru National Institute of Technology Allahabad, Prayagraj (India), for providing the system in Computational Lab. Authors also thanks to staff of Rotor Dynamics Laboratory, Mechanical Engineering Department, MNNIT Allahabad, for their constant support.

## References

1. Heshmat H (2005) Demonstration of a turbojet engine using an air foil bearing. In: Turbo expo: power for land, sea, and air, 46997:919–926. <https://doi.org/10.1115/GT2005-68404>
2. Agrawal GL (1997) Foil air/gas bearing technology—an overview. In: ASME 1997 international gas turbine and aeroengine congress and exhibition. American Society of Mechanical Engineers Digital Collection. <https://doi.org/10.1115/97-GT-347>
3. Howard (2009) Misalignment in gas foil journal bearings: an experimental study. *J Eng Gas Turbines Power* 131(2). <https://doi.org/10.1115/1.2966392>
4. Heshmat H (1994) Structural damping of self-acting compliant foil journal bearings. *ASME J Tribol* 116:76–82. <https://doi.org/10.1115/1.2927050>
5. Heshmat H (1983) Analysis of gas-lubricated foil journal bearings. *J Lubr Technol* 105:647–655. <https://doi.org/10.1115/1.3254697>
6. Heshmat H (1982) Development of foil journal bearings for high load capacity and high speed whirl stability. *ASME J Lubr Technol* 104:149–156. <https://doi.org/10.1115/1.3253173>
7. DellaCorte C (2000) Load capacity estimation of foil air journal bearings for oil-free turbomachinery applications. *Tribol Trans* 43(4):795–801. <https://doi.org/10.1115/1.3253173>
8. Kulkarni S (2013) Development of foil bearings for small rotors. In *Gas Turbine India Conference*, vol 35161, p V001T05A010. American Society of Mechanical Engineers. <https://doi.org/10.1115/GTINDIA2013-3644>
9. Ku C-PR: Compliant foil bearing structural stiffness analysis part I: theoretical model-including strip and variable bump foil geometry. *ASME J Tribol* 114(2):394–400 (1992). <https://doi.org/10.1115/1.2920898>
10. Peng J-P (1993) Calculation of stiffness and damping coefficients for elastically supported gas foil bearings. *ASME Trans J Tribol* 115:20–27. <https://doi.org/10.1115/1.2920982>
11. Peng J-P (1997) Finite element approach to the prediction of foil bearing rotor dynamic coefficients. *ASME J Tribol* 119:85–90. <https://doi.org/10.1115/1.2832484>
12. Kim TH (2008) Characterization of foil bearing structure for increasing shaft temperatures: part ii—dynamic force performance. In: turbo expo: power for land, sea, and air, vol 43116, pp 689–695. <https://doi.org/10.1115/GT2008-50570>

13. San Andrés (2010) Thermohydrodynamic analysis of bump type gas foil bearings: a model anchored to test data. *J Eng Gas Turbines Power* 132(4). <https://doi.org/10.1115/1.3159386>
14. Kim D (2007) Parametric studies on static and dynamic performance of air foil bearings with different top foil geometries and bump stiffness distributions. *ASME J Tribol* 129:354–364. <https://doi.org/10.1115/1.2540065>
15. Li C (2019) Effects of structural parameters on the load carrying capacity of the multi-leaf gas foil journal bearing based on contact mechanics. *Tribol Int* 131:318–331. <https://doi.org/10.1016/j.triboint.2018.09.003>
16. Żywica G (2019) Investigation of gas foil bearings with an adaptive and non-linear structure. *Acta mechanica et automatica* 13(1):5–10. <https://doi.org/10.2478/ama-2019-0001>
17. Liebich RHTPR (2015) A numerical performance analysis of a gas foil bearing including structural modifications by applying metal shims. In: 11th international conference on vibrations in rotating machines, Magdeburg, Deutschland, 23–25.
18. Lee DH (2010) The effect of Coulomb friction on the static performance of foil journal bearings. *Tribol Int* 43(5–6):1065–1072. <https://doi.org/10.1016/j.triboint.2009.12.048>
19. Shalash K (2017) On the manufacturing of compliant foil bearings. *J Manuf Process* 25:357–368. <https://doi.org/10.1016/j.jmapro.2016.12.021>
20. Fatu A (2018) Numerical analysis of the impact of manufacturing errors on the structural stiffness of foil bearings. *J Eng Gas Turbines Power* 140(4). <https://doi.org/10.1115/1.4038042>
21. DellaCorte C (2011) Stiffness and damping coefficient estimation of compliant surface gas bearings for oil-free turbomachinery. *Tribol Trans* 54(4):674–684. <https://doi.org/10.1080/10402004.2011.589966>
22. Kim D, Creary A, Chang SS, Kim JH (2009) Mesoscale foil gas bearings for palm-sized turbomachinery: design, manufacturing, and modeling. *J Eng Gas Turbines Power* 131(4). <https://doi.org/10.1115/1.3077643>
23. Benchekroun O, Arghir M, Impact of bump height manufacturing errors on the unbalance response of a 4dof rigid rotor.
24. Fatu A, Arghir M (2018) Influence of manufacturing errors on the unbalance response of aerodynamic foil bearings. In: International conference on rotor dynamics. Springer, Cham, pp 281–291. [https://doi.org/10.1007/978-3-319-99262-4\\_20](https://doi.org/10.1007/978-3-319-99262-4_20)
25. Hingawe ND (2019) Tribological performance of a surface textured meso scale air bearing. *Ind Lubr Tribol*. <https://doi.org/10.1108/ILT-04-2019-0146>
26. Hingawe N (2019) Effect of partial texture on the hydrodynamic performance of meso scale air bearings for mesoscale turbo-machines. In: Gas Turbine India Conference, vol 83532, p V002T11A004. American Society of Mechanical Engineers. <https://doi.org/10.1115/GTINDI A2019-2517>
27. Xu F (2019) Effect of bump structural friction on the performance of bump foil bearing and rotor dynamic behavior: Experimental study. *Proc Inst Mech Eng, Part J: J Eng Tribol* 233(5):702–711. <https://doi.org/10.1177/1350650118794536>
28. Walowit J (1975) Modern development of lubrication mechanics. Applied Science Publishers, Ltd., London. <https://doi.org/10.1115/1.3453088>
29. Ku C (1994) Structural stiffness and coulomb damping in compliant foil journal bearings: theoretical considerations. *Tribol Trans* 37(3):525–533. <https://doi.org/10.1080/10402009408983325>
30. Ku CPR (1994) Structural stiffness and coulomb damping in compliant foil journal bearings: parametric studies. *Tribol Trans* 37(3):455–462. <https://doi.org/10.1080/10402009408983317>
31. Heshmat H (2005) Low-friction wear-resistant coatings for high-temperature foil bearings. *Tribol Int* 38(11–12):1059–1075. <https://doi.org/10.1016/j.triboint.2005.07.036>
32. Fanning CE (2008) High-temperature evaluation of solid lubricant coatings in a foil thrust bearing. *Wear* 265(7–8):1076–1086. <https://doi.org/10.1016/j.wear.2008.02.009>
33. Żywica G (2016) Experimental studies on foil bearing with a sliding coating made of synthetic material. *J Tribol* 138(1). <https://doi.org/10.1115/1.4031396>
34. Kim TH (2009) Effects of a mechanical preload on the dynamic force response of gas foil bearings: measurements and model predictions. *Tribol Trans* 52(4):569–580. <https://doi.org/10.1080/10402000902825721>



35. Hoffmann R (2017) Experimental and numerical analysis of the dynamic behaviour of a foil bearing structure affected by metal shims. *Tribol Int* 115:378–388. <https://doi.org/10.1016/j.triboint.2017.04.040>
36. Sim K (2012) Thermohydrodynamic analysis of bump-type gas foil bearings using bump thermal contact and inlet flow mixing models. *Tribol Int* 48:137–148. <https://doi.org/10.1016/j.triboint.2011.11.017>
37. Sim K (2013) Effects of mechanical preload and bearing clearance on rotordynamic performance of lobed gas foil bearings for oil-free turbochargers. *Tribol Trans* 56(2):224–235. <https://doi.org/10.1080/10402004.2012.737502>
38. Feng K (2016) Analysis of novel hybrid bump-metal mesh foil bearings. *Tribol Int* 103:529–539. <https://doi.org/10.1016/j.triboint.2016.08.008>
39. Feng K (2016) Experimental evaluation of the structure characterization of a novel hybrid bump-metal mesh foils bearing. *J Tribol* 138(2). <https://doi.org/10.1115/1.4031496>
40. Feng K (2010) Parametric studies on static performance and nonlinear instability of bump-type foil bearings. *J Syst Des Dyn* 4(6):871–883. <https://doi.org/10.1299/jsdd.4.871>
41. Zhang W (2017) A fully coupled fluid–structure interaction model for foil gas bearings. *J Eng Gas Turbines Power* 139(2). <https://doi.org/10.1115/1.4034343>
42. Aksoy S (2011) A Fully Coupled 3D finite element analysis for a bump-type compliant foil bearing. In: ASME/STLE 2011 international joint tribology conference, pp 131–134. <https://doi.org/10.1115/IJTC2011-61066>
43. Salehi M (2007) Advancements in the structural stiffness and damping of a large compliant foil journal bearing: an experimental study. *J Eng Gas Turbines Power* 129(1):154. <https://doi.org/10.1115/1.2360598>
44. Le Lez, S (2007) A new bump-type foil bearing structure analytical model, vol 5: Turbo Expo. <https://doi.org/10.1115/GT2007-27078>
45. Hou Y (2015) The numerical study of static and dynamic characteristics of multi-layer protuberant foil bearing. *J Adv Mech Des, Syst, Manuf* 9(5). <https://doi.org/10.1299/jamdsm.2015jamdsm0058>
46. Han D (2018) Dynamic characteristics of air cycle machine rotor system. *Shock Vib* 1–16. <https://doi.org/10.1155/2018/1257274>
47. Kulkarni S (2020) Influence of geometric parameters on the bump foil bearing performance. *Proc Inst Mech Eng, Part J: J Eng Tribol* 234(7):1017–1026. <https://doi.org/10.1177/1350650119887043>
48. Xu H (2020) The influences of bump foil structure parameters on the static and dynamic characteristics of bump-type gas foil bearings. *Proc Inst Mech Eng, Part J: J Eng Tribol* 1350650120912609. <https://doi.org/10.1177/1350650120912609>

# Computational Investigation on Dynamics of Drop Formation: Effect of Viscosity



Pardeep Bishnoi, Mukesh Kumar Sahu, and M. K. Sinha

**Abstract** This paper deals with the effect of Newtonian fluid's viscosity variation on the drop formation through the computational domain. The simulation is performed on a two-dimensional domain and the "volume of fluid" method is used to investigate the impact of dispersed phase fluid's viscosity on the dynamics of the droplet that expels from a vertical capillary tube. The computational results are validated with the experimental results. Below  $\mu/\mu_w \sim 100$ , the simulation reveals the linear variation in the dimensionless thread length  $L_i/R$ . Above this ratio, an exponential increase in the dimensionless thread length is observed. The dimensionless thread length depends strongly on the fluid's viscosity. Meanwhile, viscosity tends to damp the undulations developed by the breakup of the initial droplet.

**Keywords** Volume of fluid · Computational simulation · Liquid thread · Newtonian fluid

## 1 Introduction

The phenomenon of drop formation is widely used in scientific events even it is also used in daily life processes. It is a tough task to predict the size of the droplet or the dynamics of the drop formation. Because of the industrial application of the drop formation in spray painting, chemical processing, ink-jet printing, and silicon chip technology, the research works in this area gained the momentum. The term drop formation is firstly mentioned by the Mariotte [1] in his book on the motion of

---

P. Bishnoi (✉)

Department of Mechanical Engineering, Chandigarh Engineering College, Mohali, Punjab, India  
e-mail: [pardeep.4318@cgc.edu.in](mailto:pardeep.4318@cgc.edu.in)

M. K. Sahu

Department of Mechanical Engineering, Cambridge Institute of Technology, Ranchi, Jharkhand, India

P. Bishnoi · M. K. Sahu · M. K. Sinha

Department of Mechanical Engineering, National Institute of Technology, Jamshedpur, Jharkhand, India

fluids. In an accidental incident, it was noticed that the water flowing from a hole in the bottom of the container turned into water droplets. He assumed that gravity, or other external forces, is responsible for this drop formation process but in the nineteenth century, Rayleigh [2] derived the analytical solution of the droplet generation caused by jet instabilities. Later, several researchers began the analytical study on the droplet generation. These studies are based on the simplification of Navier–Stokes equation, such as axisymmetric, stable flow with free surface to describe the separation of droplets. However, the general analytical description of droplet generation is limited by the complexity of basic differential equations such as Navier–Stokes equations. Shi et al. [3] investigated the experiments and computational simulation to understand the shape of the liquid. It reveals the effect of discrete liquid's viscosity on liquid thread length and suggests that the main thread made from the concentrated solution of glycerin may produce micro-threads or even a series of necks. Eggers [4] reviewed the various theoretical development and experimental work in the drop dynamics process. Renardy et al. [5] numerically revealed the influence of inertia on the rupture of a droplet using the continuous surface force algorithm along with the volume of fluid (VOF), where the droplet exhibits a self-similar damped oscillation similar to the one-dimensional mass spring system. Later Renardy and Renardy [6] developed a new algorithm, i.e., PROST: parabolic reconstruction of surface tension, which can accurately represent the body force developed due to surface tension which effectively eliminate stray currents. Suryo et al. [7] studied the nonlinear droplet deformation and rupture of the composite jet through time analysis. The result suggests that the development of compound drops is ideally possible at low Reynolds number.

Ong et al. [8] performed a computational simulation on the drop formation from a 3D nozzle device. Distilled water and silicon are considered as the primary fluid for the simulation. With increasing the flow rate of the silicon oil, the velocity profile, as well as the size of the droplets, gets affected. Also, the size of the droplet becomes smaller and smaller with respect to the rise in the flow rate. Dravid et al. [9] studied the evolution of shear-thinning liquids jet on an experimentally verified computational model. For the Reynolds number = 5, it was observed that increase in the shear-thinning initially increases the size of the satellite droplet but latter it decreases. Gupta et al. [10] studied the effect of geometry on the drop generation with the help of the lattice Boltzmann method. For different capillary number, the dimensional effect of the geometry on the mechanism of the drop formation is investigated. As the (a) width of the hole and (b) the distance from the entrance increase, the droplet size can be seen to increase. Bishnoi and Sinha [11] explored the influence of design parameters on the pattern of the drop formation. Through simulation, it was investigated that increasing the contact angle, reduced the drop's breakup time along with increasing the breakup velocity and thread length of the drop. Moreover, the increased hydrophobicity leads to distortion of the droplet shape, which is not suitable for spraying or ink-jet printing. Later Bishnoi et al. [12] revealed the instability of the droplet under different transition regimes and also examined the vorticity variation on the drop generation.

In this manuscript, the impact of viscosity is investigated on the dynamics of drop formation with the help of computational fluid dynamics.

## 2 Physical Description of the Computational Domain

Figure 1 shows the physical schematic diagram of the capillary modeled in ANSYS design modeler software. The domain consists of two areas (chambers), i.e., discrete phase fluid and the continuous phase fluid. In this work, air is used as the continuous phase fluid and glycerin is used as the discrete phase liquid. For the study of dynamics of drop development, glycerin is used as the discrete phase liquid and air as the continuous liquid. Table 1 shows the description of the geometric model which is represented in Fig. 1. The computational results [13] obtained through the domain model are already validated with the available literature [14].

The inner surface of the capillary tube is neutrally wettable, while the surface around the capillary nozzle is not wettable. Our base fluid comprises of varying compositions of glycerin which acts as a Newtonian fluid and is incompressible as

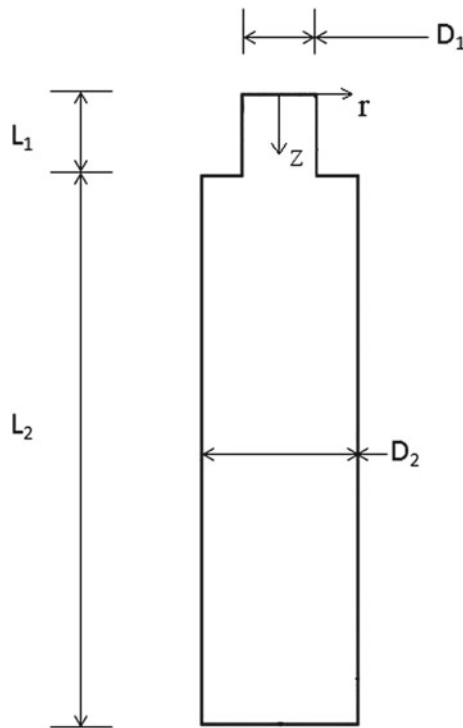


Fig. 1 Schematic of computational domain model

**Table 1** Description of schematic computational domain

Notation	Description	Measurement (m)
$D_1$	Diameter of glycerin-85% chamber	0.0032
$D_2$	Diameter of air chamber	0.0100
$L_1$	Length of glycerin-85% chamber	0.0020
$L_2$	Length of air chamber	0.0170

**Table 2** Physical properties of glycerin [14]

Liquid	Density ( $\times 10^3$ kg/m <sup>3</sup> )	Viscosity ( $\times 10^{-3}$ Ns/m <sup>2</sup> )	Surface tension ( $\times 10^{-3}$ N/m)
85% Glycerin	1.223	112.9	66.0
70% Glycerin	1.182	22.9	68.5
50% Glycerin	1.272	6.1	70.0
20% Glycerin	1.048	1.8	72.4

shown in Table 2. The VOF model in Fluent version 15.0 is used to analyze the development of droplets from the capillary to the surrounding air. At the start of the analysis, the capillary tube is filled with glycerin, while the rest of the domain is filled with air. The fluids at this moment are both assumed to be at rest. As ejection is initiated, the velocity of glycerin at inlet boundary increases from 0 to 1 ml/min with a fully developed profile. This simulation includes the effects of gravity in the  $z$ -direction. Due to the axial symmetry of the problem, two-dimensional geometric model is used.

### 3 Governing Equations

The mathematical model involves mainly vector-shaped mass–momentum conservation equations related to assumptions and boundary conditions. In order to study the free surface flow in the capillary, the Navier–Stokes equation and the mass conservation equation are used together to adjust the volume fraction of the glycerol phase in the domain. Navier–Stokes equation is composed of continuity equation and momentum equation and is used to express the physics involved in fluid flow. The dynamics of droplet formation depends on many factors, such as the flow rate of the inlet liquid, the viscosity of the liquid phase ( $\mu$ ), the density ( $\rho$ ) of the two phases, i.e., discrete and continuous phases, the surface tension between the glycerol and air ( $\sigma$ ), and the diameter of the capillary nozzle ( $D_1$ ). For the computational work, certain assumptions are made which includes the wall of the capillary tube is smooth and the flow as laminar.

### 4 Boundary Conditions

The boundary conditions for the simulation problem are shown pictorially in Fig. 2. The inlet of the domain is considered as velocity inlet. The domain has axisymmetric axis along with free slip condition hooked near the walls of the computational domain. The outlet of the computational domain is open to the atmospheric pressure outlet.

The flow is assumed to be fully developed at capillary tube’s exit with a velocity profile,

$$v_z = \frac{2Q}{\pi R^2} \left\{ 1 - \left( \frac{r}{R} \right)^2 \right\}, \quad 0 \leq r \leq R, \tag{1}$$

where  $r$  is the radial coordinate of drop phase and  $v_z$  is the flow velocity in the  $z$ -direction or axial component of the velocity within the contact circle formed by the pinning of liquid to the edge of the capillary tube exit. On putting  $r = 0$  in Eq. 1, flow velocity becomes,  $U = \frac{2Q}{\pi R^2}$ , which is the maximum flow velocity at the center of the flow.

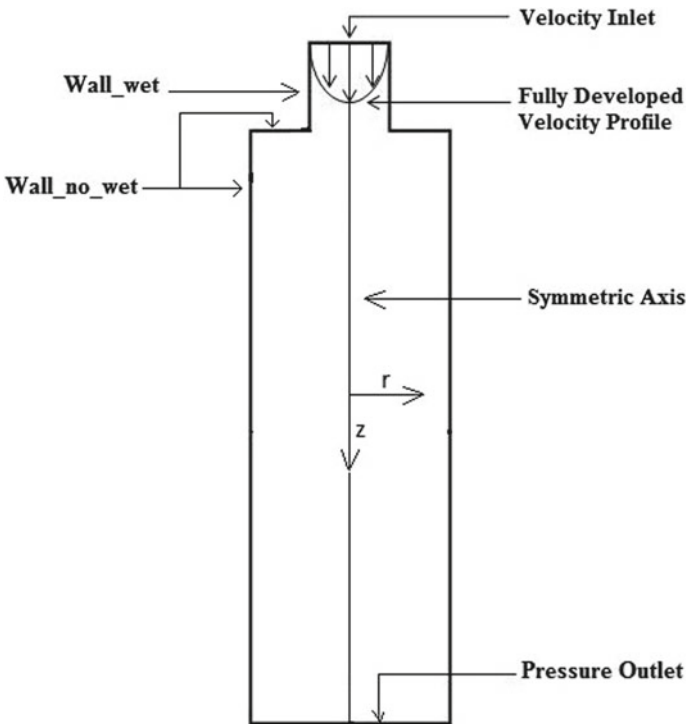
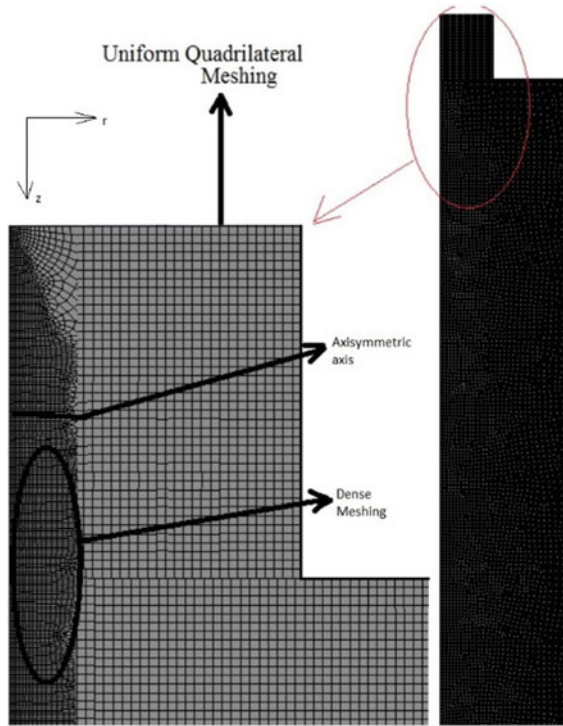


Fig. 2 Boundary conditions



**Fig. 3** Meshing of the computational domain

## 5 Grid Generation

The cell arrangement of the computational domain is shown in Fig. 3. It can be marked that the cells are fine near the axisymmetric axis as compared to the other region in the capillary tube. The development and detachment process of the droplet are executed near the axisymmetric axis of the tube so smaller cells are placed near the axisymmetric axis. 35,000 grid cells are considered for the simulation. As the computational model is axisymmetric, therefore meshing is performed on the half model. Figure 4 shows the grid sensitivity test of the domain. The grid sensitivity test is used to determine the correctness of the calculation results under different grid conditions.

## 6 Numerical Solution Procedure

The finite volume method is used to integrate 2D equations of mass and momentum over a control volume and the subsequent equations are discretized over control

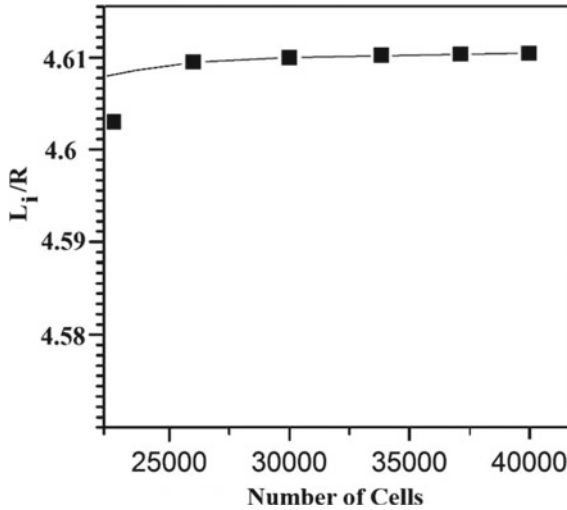


Fig. 4 Grid sensitivity test

volume. The resultant equations, imposed by the above boundary conditions, are solved in an iterative manner using the multigrid solver of Fluent 15.0. Pressure-Implicit with Splitting of Operators (PISO) algorithm is recommended for transient flow conditions. The SIMPLE and SIMPLEC algorithms have a common limitation that they do not satisfy the momentum balance with new velocities and corresponding fluxes after the pressure-correction equation is solved. Consequently, all the calculations have to be solved again until balance is achieved.

## 7 Results and Discussion

### Comparison of Drop detachment thread length: Computational versus Experimental Result

The comparison of the computed results data point with the experimental results is plotted in Fig. 5. According to the plot, the variation in the results lies within the error range of  $\pm 5\%$ . The above comparison shows that the computational techniques can be used to study the drop formation process. Pardeep et al. [13] illustrate the comparison of the detachment profiles of the droplet for the experimental and calculation methods in different time series.



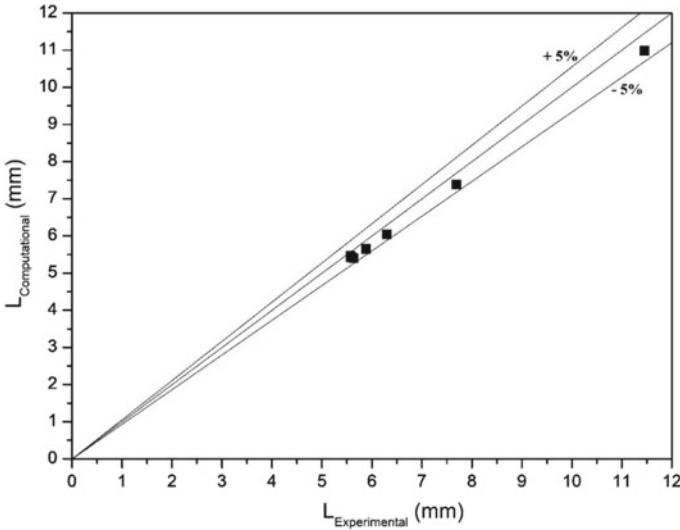


Fig. 5 Comparison of computed results with the experimental results

### 7.1 Effect of Viscosity on the Drop Generation

After comparison of the thread length between the computational domain and the experimental, the investigation prompted to study the viscosity impact on the droplet features with the computational results. The viscosity of the discrete phase fluid is an important parameter to control the fluctuation of the separated droplet interface. It can smooth the separation contour of the droplet at each stage before breaking.

Before going to the parametric study, all must know about the dynamics of the drop formation. In the evolution process of the drop formation, gravity tends to pull the drop downwards and elongating it axially as the inertial force pushes it away from the nozzle. For a while, the inertial force, surface tension, and gravitational force are in equilibrium and the drop continues to grow while still attached to the tube. When the volume of the drop reaches a certain value, equilibrium cannot be maintained, and the gravitational and inertial forces take over, creating a downward acceleration. The bottom part of the fluid starts moving down. Since it has a higher weight, so the pressure on the middle section increases. The diameter of the middle region gets thinner as the velocity increases.

The liquid continues to flow from the capillary tube; however, once necking is initiated, the fluid does not come into the thin ligament because the detachment of the drop occurs shortly after the necking has started. The time for break up is very short and is in order of milliseconds as per the present study. Once the necking happens, three distinctive liquid parts can be noticed, with the first one being the portion of mass still attached to the nozzle, the second being a fluid ligament and the last one, a nearly formed drop. The newly formed drop is called the primary drop and has a

flat surface at the place where it used to be attached to the neck (at 98 ms in Fig. 6). The drop has a flattened side because after the breakup, the inertial force is dominant and the velocity pushes down on the top part. A moment later, because of surface

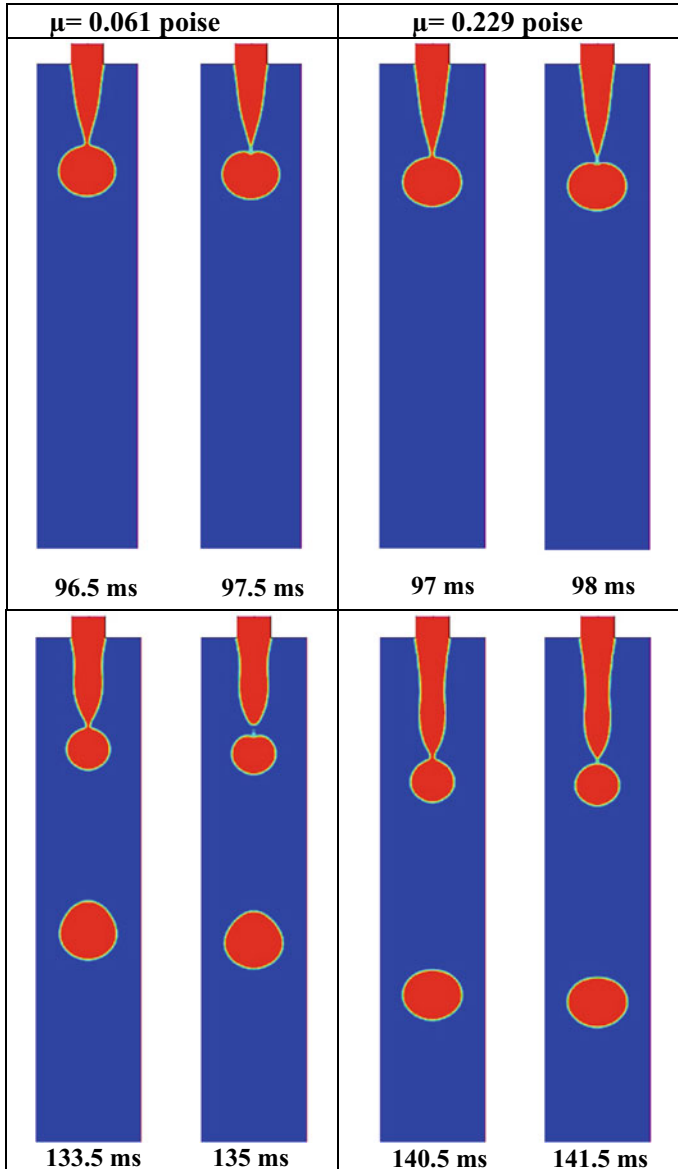


**Fig. 6** Images of the drop detachment for the systems with different viscosity of the disperse phase through a capillary tube of diameter 3.2 mm the velocity of the disperse phase is  $v_z = 0.15$  m/s

tension force the tip of the ligament becomes rounded and moves up. The reduction in thread length at 133.5–135 ms is shown in Fig. 6. All these variations are because of the development of recoil forces in the ligament.

As the viscosity increases, the drops formed attain more volume and take longer time to detach. The formation of a drop is affected by the detachment of the previous drop. In fact, after the pinch-off from a drop, there is a creation of ripples that affects the mechanism subsequent drop formation. The greater the effect of the ripples, the lesser time it will take for the following drop generation. The viscosity tends to damp the action of the ripples. As the viscosity increases, the time of formation of the secondary drops comes closer to that of the primary drop.

Figure 6 shows the detachment process of the droplet from a capillary tube for two different viscosities, i.e., for 0.061 poise and 0.229 poise. It is clearly seen in the above figure that at each time step, the thread length of 0.229 poise liquid is more than that of 0.061 poise liquid. There is a consistent flow in the nozzle, which pushes the liquid ligament downwards. Due to this reason, the thread length of the successive drop is more than that of previous ones.

On comparing the drop dynamic system with the spring balance system, the viscosity of the liquid used in the drop process plays a similar character as the damping force plays in the spring balance system. With an increment in the viscosity of the liquid, the oscillations occurring during the formation of the drop get eliminated and the break-off period of the process also increases. The limit of glycerin composition varies from 0 to 100%. Thread length increases exponentially with the increase in the percentage content of the glycerin. The percentage content of the glycerin's dependence on the thread length follows an exponential curve as represented by our Eq. (2). The fitted curve is shown in Fig. 7. The coefficient of determination for the

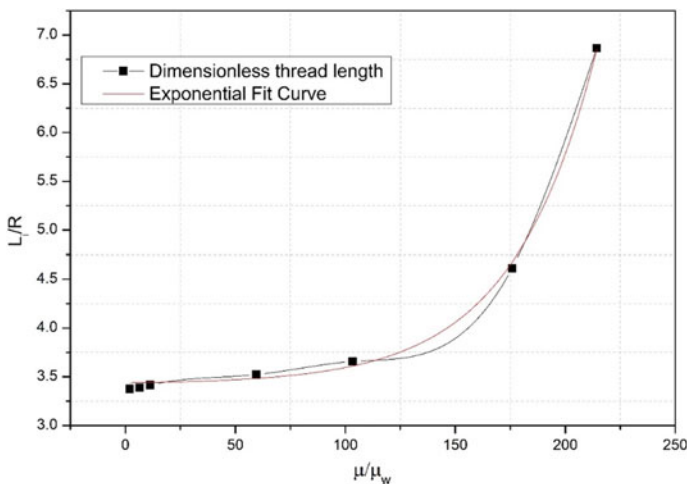


**Fig. 7** Curve fitting plot for dimensionless thread length versus dimensionless viscosity of the liquid phase

fitted curve is 0.99984, which represent the best fit for the regression curve for the given data. Relation shown in Eq. (2), exists only on the initial boundary conditions of the system, i.e., for  $Q = 1.0$  ml/min, and the values of viscosity ratios at different glycerin compositions used in the computational analysis that is shown in Fig. 7.

$$\frac{L_i}{R} = 3.42 + 0.12 \exp\left(0.26 \times \frac{\mu}{\mu_w}\right), \quad (2)$$

where

$L_i/R$  = Dimensionless Thread Length (mm) and  $\mu/\mu_w$  = Dimensionless Viscosity ratio of the liquid (poise).

## 8 Conclusions

Simulation is performed on the axisymmetric two-dimensional domain which comprises the Navier–Stokes equation linked with the volume of fluid model to determine the effect of viscosity on the behavior of the drop’s geometric profile in a glycerin fluid. ANSYS Fluent 15.0 has been used which hooked with the Geo-Reconstruct interface scheme and PISO algorithm. The time evolution of glycerin liquid that is ejected from a vertical capillary tube having different viscosity values was investigated. The validated computational model is used for further simulation. The numerical simulation has many advantages since it permits us to observe in detail the mechanism of drop formation in different conditions. In order to observe the effect of fluid property, certain parameters like the diameter of the capillary tube, flow rate are assumed as constant. Viscosity plays a damper role for the pendant fluid ligament. For the value of viscosity ratio from 0 to 150, the dimensionless thread length varies linearly with a very less slope. But at the higher concentration of glycerin or at high viscosity ratio, a significant increase in drop’s dimensionless thread length is being observed. The thread extends over a distance exceeding 2–3 times the capillary tube radius  $R$ , resulting in a significant increase in drop thread length. An increase in the viscosity also increases the chance of satellite drop formation.

## References

1. Mariotte E (1686) Treats water movement of other fluids. E. Michallet, Paris
2. Rayleigh L (1878) On the instability of jets. Proc Lond Math Soc 10(4):4–13
3. Shi XD, Brenner MP, Nagel SR (1994) A cascade of structure in a drop falling from a faucet. Science 265(5169):219–222
4. Eggers J (1997) Nonlinear dynamics and breakup of free-surface flows. Rev Mod Phys 69(3):865
5. Renardy YY, Cristini V (2001) Effect of inertia on drop breakup under shear. Phys Fluids 13(7)

6. Renardy Y, Renardy M (2002) Prost—a parabolic reconstruction of surface tension for the volume-of-fluid method. *J Comput Phys* 183:400–421
7. Suryo R, Doshi P, Basaran OA (2006) Nonlinear dynamics and breakup of compound jets. *Phys Fluids* 18:082107(1–31)
8. Ong WL, Hua J, Zhang B, Teo TY, Zhuo J, Nguyen NT, Ranganathan N, Yobas L (2007) Experimental and computational analysis of droplet formation in a high-performance flow-focusing geometry. *Sens Actuators, A* 138(1):203–212
9. Dravid V, Loke PB, Corvalan CM, Sojka PE (2008) Drop formation in Non-Newtonian jets at low Reynolds numbers. *J Fluids Eng* 130:081504(1–8)
10. Gupta A, Matharoo HS, Makkar D, Kumar R (2014) Droplet formation via squeezing mechanism in a microfluidic flow-focusing device. *Comput Fluids* 100:218–226
11. Bishnoi P, Sinha MK (2018) Influence of the wettability nature of the nozzle wall on the dynamics of drop formation. *Int J Heat Technol* 36(3):1005–1009. <https://doi.org/10.18280/ijht.360329>
12. Bishnoi P, Jeeva Chithambaram S, Singh A, Kumar P, Khatkar SK, Sinha MK (2020) Investigation of drop's instability under different transition stages on axisymmetric flow model. *Comput Fluids* 104673
13. Pardeep SM, Sinha MK (2018) Numerical simulation of dynamics of the drop formation at a vertical capillary tube. In: Singh MK et al (eds) *Applications of fluid dynamics*, LNME. Springer, Singapore, pp 371–381. [https://doi.org/10.1007/978-981-10-5329-0\\_27](https://doi.org/10.1007/978-981-10-5329-0_27)
14. Wilkes ED, Phillips SD, Basaran OA (1999) Computational and experimental analysis of dynamics of drop formation. *Phys Fluids* 11(12):3577–3598

# Viscous Oscillatory Exponentially Stratified Flow Through Parallel Plates



L. Prasanna Venkatesh

**Abstract** The research work in this article proposes a mathematical model and its results to the flow which is oscillatory and vertically exponential density stratified viscous fluid induced by constant suction through one side of the channel. The region of the flow is assumed to be rectangular formed by two parallel plates of which the right-hand side plate is porous and the fluid is taken out through this plate inducing the flow with constant velocity. The mathematical system explaining the above problem is solved using variable separable similarity solution and was interpreted through graphs for various parameters involved in the system. The stratification is considered to be exponentially distributed in the vertical direction, and the results reveal that the flow in the vertical direction is mainly affected by the stratification parameter, and significant comparisons are established with the case of linearly distributed density stratification. Further for second-degree approximation, the exponential stratification reduces to the results of linear stratification results, which are already available in the literature.

**Keywords** Density stratification · Oscillatory flow · Exponential stratification · Similarity transformation · Boussinesq approximation

## 1 Introduction

Fluid flows that take into account of density variations are categorized as density stratified flows. The stratification needs to be addressed mainly in two different situations, firstly when the fluid is in an undisturbed state and secondly when the fluid gets disturbed by some external forces. When at the disturbed state, the stratification depends almost on all parameters, while in the undisturbed state, it is dependent on only gravitational and vertical parameters. The density in an unperturbed state has predominantly two characterizations which are the exponential and linear distribution of height. The literature study reveals that the exponential distribution of density in

---

L. P. Venkatesh (✉)

Department of Mathematics, Sathyabama Institute of Science and Technology, Chennai, India  
e-mail: [prasannavenkatesh.maths@sathyabama.ac.in](mailto:prasannavenkatesh.maths@sathyabama.ac.in)

© The Author(s), under exclusive license to Springer Nature Singapore Pte Ltd. 2021  
C. Pandey et al. (eds.), *Advances in Materials and Mechanical Engineering*,  
Lecture Notes in Mechanical Engineering,  
[https://doi.org/10.1007/978-981-16-0673-1\\_19](https://doi.org/10.1007/978-981-16-0673-1_19)

233

the vertical direction is a natural phenomenon, whereas the linear distribution is its approximation, taking the first two terms of expansion in exponential form. However, the higher-order terms that occur in the exponential case are very small and hence are very little significant when it comes to the effects of it on various parameters. Hence, in the current discussion, we compare the exponential stratification effects with that of the linear distribution of density in the direction of gravity.

Khandelwal and Jain [1] discussed in detail about “flow of unsteady and MHD heterogeneous fluid through pervious medium over a plate which is moving in slip flow condition” by presenting a perturbation solution for various characteristics associated with the flow. The problem considers the plate velocity being time-dependent varying exponentially with respect to time and the suction velocity applied perpendicular to the plate. Attia [2] studied the influences of inclusion and removal of fluid on the unsteady flow (amid two permeable parallel plates) with varying characteristics through a channel which is rectangularly shaped by assuming the thermal conductivity and viscous effects to be dependent on temperature. The effects of heat transfer and magnetohydrodynamics on dusty viscoelastic stratified fluid flowing through an angled surface in permeable space under varying viscosity were experimented by Chakraborty [3] by discussing the variations in particle and liquid speeds and temperature with corresponding changes in stratification factor. By assuming the functional expression for pressure in terms of the two-dimensional variables  $x$ ,  $y$ , and unknown function of  $t$ , the exact solution was presented. “Transfer of heat on dusty and MHD flow of non-Newtonian heterogeneous fluid with variable viscosity in porous medium” was presented by Prakash [4] by considering both vertical and horizontal velocity expressions as an expression of  $y$ ,  $t$  and by depicting the variable separable substitution for deriving a class of exact solution to fluid velocity.

While considering fluids with moderate Reynolds number and channel with length significantly larger than breath, the flow equations simplify to narrow channel flows. Such simplification in momentum equations is known as lubrication approximation which was originated basically from lubrication industry. Such flows also draw interest from various other similar industries that are similar and supportive to the lubrication field. Panton [5] discussed the concept of lubrication approximation problem which we refer to as narrow channel problems for plane Poiseuille flow by assuming the time independency for the flow. Krechetnikov [6] elaborated on the various uses and purposes of applications of narrow channel simplification to coating flows in multi-direction with clear and wet boundaries by establishing weak ellipticity different from the usually accepted parabolic structures allowing lubrication analysis capturing topologies of the flow in and around points of stagnation. He further extended it for bearing problems and expressed the exact solution for velocity functions by considering pressure dominated fluid flow. It is Reynolds [7] from whom the theory and applications of the lubrication concept in industries evolved through Beauchamp tower’s experiments.

Krishna and Sharma [8] solved the problem on “the motion of an axisymmetric body in a rotating stratified fluid confined between two parallel planes” by considering the direction of planes to be vertical of the perpendicular axis of circulations. Naidu [9] explained the detailed solution to “stratified viscous flow between two oscillating

cylinders” by formulating density stratification as exponentially distributed with governing equations of motion of fluid in the polar form. Prasanna Venkatesh [10] analyzed the “magnetohydrodynamics oscillating viscous flow in a very thin channel induced by removal or inclusion of fluid through the pervious plate” by considering the electrically conducting fluid in both axial and transverse direction and its effects on channels which are very thin in nature. Prasanna Venkatesh [11] presented the effect of “stratification in rectangular channel problem” with the assumption that the density when there is no disturbance in the fluid as a function of depth only and also the flow being time-dependent. When the channel of the flow becomes narrower when compared to its length, the influences due to the inertial terms are very small and hence can be neglected based on the type of flow considered. Considering this aspect, Prasanna Venkatesh and Prabha [12] studied the “effect of narrow channel approximation on viscous oscillatory density stratified fluid flow through rectangular channels” by comparing the cases of flow without applying the lubrication approximation with that when it is applied. Shah et al. [13] discussed on “combined effect of magnetic and electric field on micropolar nanofluid between two parallel plates in the rotating system.” Bonzanini et al. [14] analyzed “velocity profiles description and shape factors included in a hyperbolic, one-dimensional, transient two-fluid model for stratified and slug flow simulations in pipes” by computing velocity profiles in stratified conditions. Waqas [15] presented a “mathematical and computational framework for heat transfer analysis of ferromagnetic non-Newtonian liquid subjected to heterogeneous and homogeneous reactions.”

The most common stratification characteristic in literature available is linear distribution in an unperturbed state which is an approximation to naturally existing exponential stratification. In some of the research works where exponential stratification considered was suitably substituted in order to get negotiated during the process of evaluation of the solution. Hence, in our present discussion, we consider the flow of exponential density stratified flow of viscous oscillatory fully developed flow between parallel plates generalizing linearly distributed density stratified fluid flow for the same case.

## 2 Mathematical Model and Solution to the Problem

The region of the flow is between two plates where the left side plate is fixed to be exactly on  $y$ -axis and the right-side plate is assumed to be adjacent to it which is separated by a distance ‘ $h$ ’. The plate on the right side is porous, and the other is non-porous. The fluid is removed or included with a periodic constant suction or injection velocity through the pervious plate. As the fluid flow considered is fully developed, the initial velocity of the fluid is assumed to be constant. The fluid is considered to be density stratified in such a way that in an unperturbed state, it is considered to be exponentially distributed as a function of  $y$ . In disturbed condition, density distribution is a function of all parameters pertaining to space and time. The representation of the flow in terms of mathematical equations is presented here.



$$\frac{\partial u}{\partial x} + \frac{\partial v}{\partial y} = 0 \tag{1}$$

$$\rho \frac{\partial u}{\partial t} = -\frac{\partial p}{\partial x} + \mu \left( \frac{\partial^2 u}{\partial x^2} + \frac{\partial^2 u}{\partial y^2} \right) \tag{2}$$

$$\rho \frac{\partial v}{\partial t} = -\frac{\partial p}{\partial y} + \mu \left( \frac{\partial^2 v}{\partial x^2} + \frac{\partial^2 v}{\partial y^2} \right) - \sigma_e B_0^2 v - \rho g \tag{3}$$

$$\rho = \rho_0(y) + \rho'(x, y, t) \tag{4}$$

$$\rho_0(y) = \rho'_0 e^{-\beta y} \tag{5}$$

$$\frac{\partial \rho}{\partial t} = \rho'_0 \beta e^{-\beta y} v \tag{6}$$

The following explains the notations used in the above system of equations. (i)  $\mu$ —coefficient of viscosity, (ii)  $\rho$ —density of the fluid, (iii)  $\sigma$ —electrical conductivity, (iv)  $B_0$ —electromagnetic induction, (v)  $\mu_e$ —magnetic permeability, (vi)  $\rho'_0$ —constant density, (vii)  $\rho'(y, t)$ —perturbation density, (viii)  $\beta$ —stratification parameter, (ix)  $N$ —Brunt–Vaisala frequency  $N. N^2 = \beta g$ , (xi)  $g$ —gravity, (xii)  $v_0$ —initial average velocity,  $u_0 = v_0 h_0 / L$ . Using mathematical simplification process on (2), (3), and (6), we get

$$\begin{aligned} \rho'_0 \frac{\partial^2}{\partial t^2} \left( \frac{\partial u}{\partial y} - \frac{\partial v}{\partial x} \right) &= \mu \frac{\partial}{\partial t} \nabla^2 \left( \frac{\partial u}{\partial y} - \frac{\partial v}{\partial x} \right) \\ &+ \rho'_0 N^2 e^{-\beta y} \frac{\partial v}{\partial x} \end{aligned} \tag{7}$$

The time component in both velocity and pressure function are chosen based of the fluid oscillation in the following manner

$$\begin{aligned} u(x, y, t) &= u(x, y) e^{i\omega t}, \quad v(x, y, t) = V(x, y) e^{i\omega t}, \\ \text{and } p(x, y, t) &= p(x, y) e^{i\omega t} \\ -\rho'_0 \omega^2 \left( \frac{\partial u}{\partial y} - \frac{\partial v}{\partial x} \right) &= \mu i \omega \nabla^2 \left( \frac{\partial u}{\partial y} - \frac{\partial v}{\partial x} \right) \\ + \rho'_0 N^2 e^{-\beta y} \frac{\partial v}{\partial x} & \end{aligned} \tag{8}$$

We define stream function  $\psi$  such that

$$u = \frac{\partial \psi}{\partial y}, \quad v = -\frac{\partial \psi}{\partial x} \tag{9}$$

$$\left( \nabla^2 - \frac{i\rho'_0\omega}{\mu} \right) \nabla^2 \psi - \frac{\rho'_0 N^2}{\mu i \omega} e^{-\beta y} \frac{\partial^2 \psi}{\partial x^2} = 0 \tag{10}$$

where

$$\nabla^2 = \frac{\partial^2}{\partial x^2} + \frac{\partial^2}{\partial y^2} \quad \text{and} \quad \psi(x, y, t) = \psi(x, y) e^{i\omega t}$$

The values of velocity on the boundary are assumed to be

$$u = 0 \text{ at } x = 0, \quad u = u_1 \text{ at } x = h$$

$$v = 0 \text{ at } x = 0, \quad v = 0 \text{ at } x = h$$

$$\Psi = \left( u_0 - \frac{v_1 y}{h} \right) f(\eta) \tag{11}$$

where  $\eta = \frac{x}{h}$  and  $u_0$  is the average entrance velocity. Equation (10) becomes

$$\left( D^4 - \frac{1}{\mu} \left( \rho'_0 - \frac{i\rho'_0 N^2}{\omega} e^{-\beta y_0} \right) D^2 \right) f(\eta) = 0 \tag{12}$$

where

$$D^2 = \frac{d^2}{d\eta^2}, \quad \alpha^2 = \frac{1}{\mu} \left( \rho'_0 - \frac{i\rho'_0 N^2 e^{-\beta y_0}}{\omega} \right)$$

$$\Rightarrow \alpha = \sqrt{\frac{1}{\mu} \left( \rho'_0 - \frac{i\rho'_0 N^2 e^{-\beta y_0}}{\omega} \right)}$$

In Eq. (12) by considering particular values for  $y_0$ , the above equation reduces to a linear differential equation with constant complex coefficient. Here  $\alpha^2$  is a complex number; hence, there is only one possibility. Two of the roots are distinct and complex, and the other two are zero (i.e.,  $m^2(m + \alpha)(m - \alpha) = 0$ ).

$$f(\eta) = c_1 + c_2\eta + c_3e^{\alpha\eta} + c_4e^{-\alpha\eta} \tag{13}$$

The transformed velocity values at the boundary in terms of  $f(\eta)$  are

$$\left. \begin{aligned} f(0) &= 0 \\ f(1) &= -1 \\ f'(0) &= 0 \\ f'(1) &= 0 \end{aligned} \right\} \tag{14}$$

The equations using (14) to determine the arbitrary constants in  $f(\eta)$  are

$$c_1 + c_3 + c_4 = 0 \tag{15}$$

$$c_1 + c_2 + c_3e^\alpha + c_4e^{-\alpha} = -1 \tag{16}$$

$$c_2 + \alpha c_3 - \alpha c_4 = 0 \tag{17}$$

$$c_2 + \alpha c_3e^\alpha - \alpha c_4e^{-\alpha} = 0 \tag{18}$$

In expression for  $\psi$  and (9) after substituting the constants, the velocity components are

$$u(x, y) = -u_1 \left( \frac{e^\alpha - 1 - \alpha(1 + e^\alpha)X + e^{\frac{\alpha x}{h}} - e^\alpha e^{-\frac{\alpha x}{h}}}{(\alpha + 2) + (\alpha - 2)e^\alpha} \right) \tag{19}$$

$$v(x, y) = -(v_0 - u_1 y) \left( \frac{-\alpha(1 + e^\alpha) + \alpha e^{\frac{\alpha x}{h}} + \alpha e^\alpha e^{-\frac{\alpha x}{h}}}{(\alpha + 2) + (\alpha - 2)e^\alpha} \right) \tag{20}$$

### 3 Results and Discussion

The pictorial presentations on the effects of stratification number ( $N$ ) and constant density ( $\rho_0$ ) on velocity both in transverse and axial directions are represented for the possible estimations of special variables  $x$  and  $y$  being assumed to lie within the range 0–1 while that of each of the other parameters are varied. There are significant

effects of Brunt Vaisala frequency  $N$  on transverse velocity in many regions of the flow region at specific lengths.

Figure 1 explains how transverse velocity profile changes for different values of  $x = 0$  to 10 and  $y = 0$  to 10, while values of  $\rho = 1$ ,  $\mu = 0.894 \times 10^{-3} \text{ kg m}^{-1} \text{ s}^{-1}$ ,  $\omega t = 0$ ,  $u_0 = 10$ ,  $h = 10$ ,  $N = 0.5 \times 10^{-4} \text{ s}^{-1}$ , and  $v_1 = 2$ , by allowing the time parameter  $\omega t$  to vary from 0 to  $\pi$  with values of  $x$  substituted from 0 to 1. Figures 2 and 3 are plotted for transverse velocity profiles for  $y = 10$  and  $y = 1$ , respectively. It

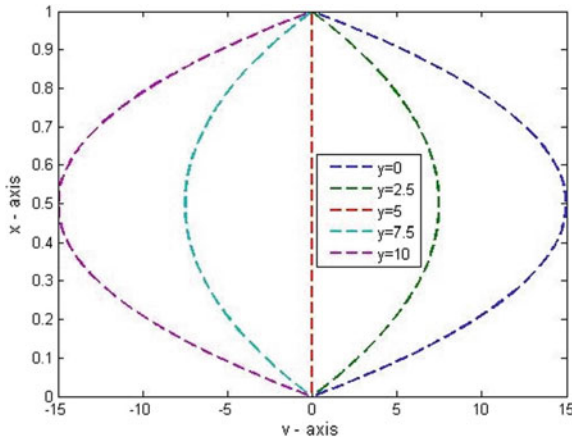


Fig. 1 Velocity in transverse direction for varying heights  $y = 0$  to 10

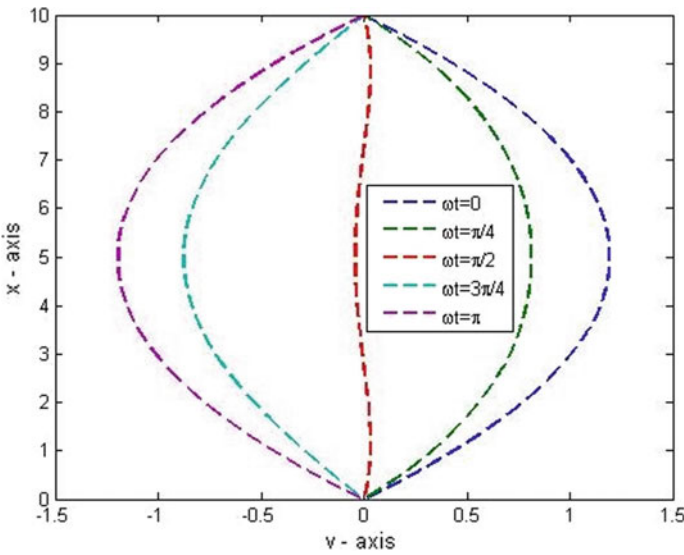
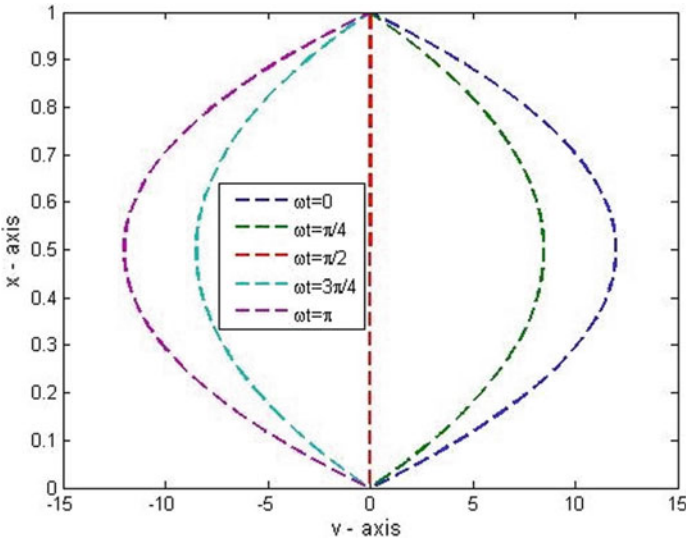


Fig. 2 Velocity in transverse direction for varying time at  $y = 10$



**Fig. 3** Velocity in transverse direction for varying time at  $y = 1$

is noted from Figs. 2 and 3 that whenever the values of time parameter increased, the value of transverse velocity decreases and hence can be concluded that transverse velocity varies inversely with time.

When distance between plates is substituted as 25 and value of  $y = 1$ , then transverse velocity can be projected in the form of Fig. 4.

The graphical interpretations of velocity profiles are in confirmation with their parabolic nature. It can also be easily concluded that the symmetricity of the velocity in transverse direction is disturbed as the breadth of the channel tends to increase.

In Fig. 5, black colored velocity profiles are drawn for  $y = 1$ , red colored are drawn for  $y = 2$ , and blue colored are for  $y = 3$ , respectively. It can be observed from these figures that transverse velocity varies directly as average entrance velocity  $u_0$ .

Figure 6 shows the influences in the vertical velocity for various values of stratification variable from soft water to hard water ( $N = 0.000012$  to  $0.000020$ ). Only on the centre part of the channel, the resulting influences of stratification are observed. As the water becomes harder, its flow on the center part of the channel is restricted and reversed. By varying time parameter  $\omega t$ , axial velocity profiles were presented for the values  $\omega t = 0$  to  $\pi$  by Fig. 7.

Figure 8 explains how the effects of stratification influence the axial velocity profiles near non-porous plate ( $x = 0$  to  $1$ ) for different values of  $N$ . Also, it is observed from Fig. 8 that hard water tends to move faster in axial direction while having opposite nature in transverse direction. It can be noted from the above graphs for axial velocity profiles that it varies inversely with respect to stratification and time. These properties are very similar to that of flows with linearly density stratification under the similar boundary condition.

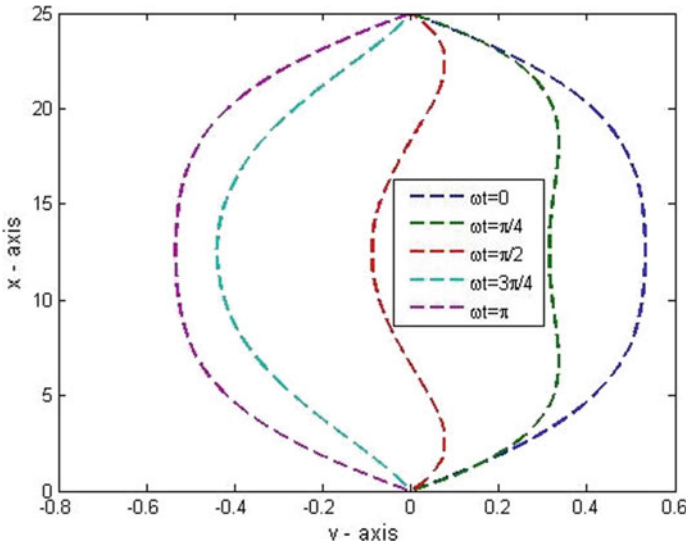


Fig. 4 Velocity in transverse direction for different  $\omega t$  values and  $h = 25$

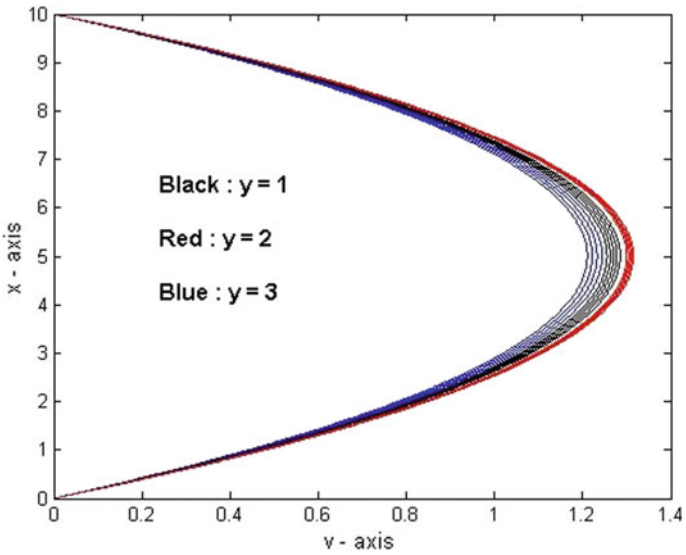


Fig. 5 Velocity in transverse direction for varying  $\nu_1$  values from 2 to 4

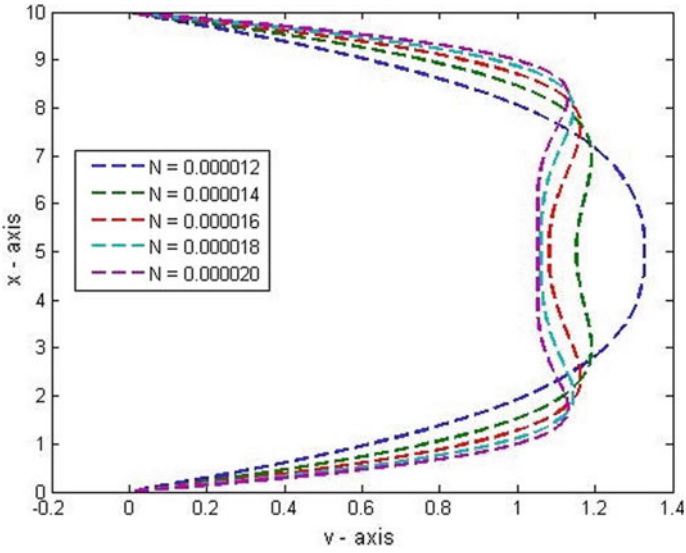


Fig. 6 Velocity in transverse direction for varying stratification parameter values

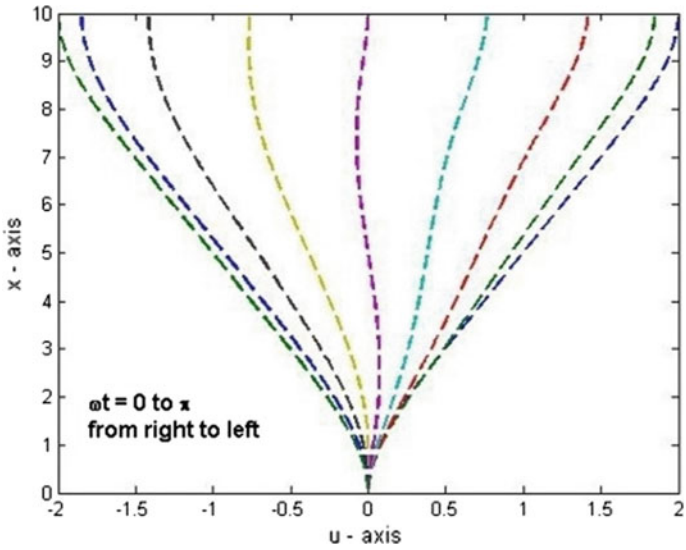


Fig. 7 Velocity in axial direction for varying time

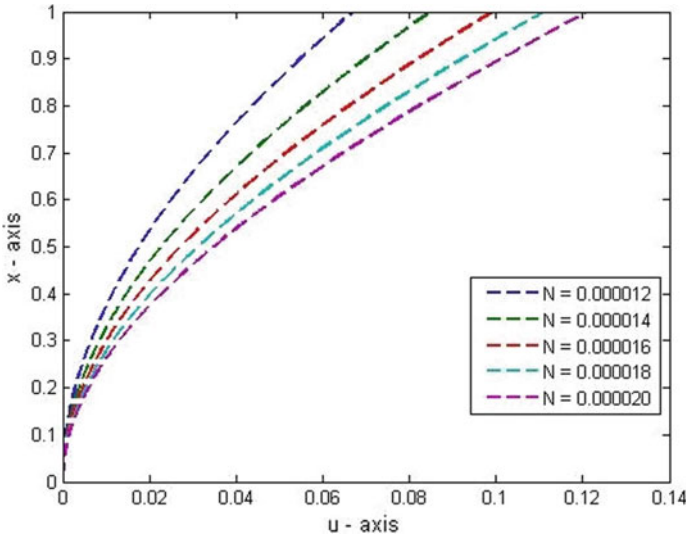


Fig. 8 Velocity in axial direction for varying  $N$  values

## 4 Conclusions

The effects of exponential stratification in vertical rectangular channel problem having a pervious wall are analyzed in this paper. Similarity transformation is applied to reduce the system of partial differential equation, and the solutions are obtained using suitable boundary conditions. The outcome is compared with that of linearly distributed density stratification problems. The following observations are obtained as a result of the analysis. Higher values of  $N$  make the flow to be slower around the center of the channel, whereas it allows the flow to be increasingly nonlinear in transverse direction nearer to the boundary. On the other hand, for axial velocity, it increases with increase in  $N$  values. Transverse velocity varies inversely with time, suction velocity, and stratification. Hence, stratification obstructs the movement of fluid in upright path. Axial velocity profiles vary inversely with time, whereas it has opposite effects nearer to non-porous and porous plates.

## References

1. Khandelwal AK, Jain NC (2005) Unsteady MHD flow of stratified fluid through porous medium over a moving plate in slip flow regime. *Indian J Theoret Phys* 53(1):25–35
2. Attia HA (2005) The effect of suction and injection on the unsteady flow between two parallel plates with variable properties. *Tamkang J Sci Eng* 8(1):17–22
3. Chakraborty S (2001) MHD flow and heat transfer of a dusty viscoelastic stratified fluid down an inclined channel in porous medium under variable viscosity. *Theoret Appl Mech* 26:1–14



4. Prakash O, Kumar D, Dwivedi YK (2012) Heat transfer in MHD flow of dusty viscoelastic (Walters' liquid model-B) stratified fluid in porous medium under variable viscosity. *Pramna* 79(6):1457–1470
5. Panton RL (2013) *Incompressible flow*. Wiley
6. Krechetnikov R (2010) On application of lubrication approximation to non-unidirectional coat flows with clean and surfactant interfaces. *Phys Fluids* 22:1–10
7. Reynolds O (1886) On the theory of lubrication and its application to Mr. Beauchamp tower's experiments, including an experimental determination of the viscosity of olive oil. *Philos Trans R Soc London* 177:157–234
8. Krishna DV, Sarma LV (1969) Motion of an axisymmetric body in a rotating stratified fluid confined between two parallel planes. *J Fluid Mech* 38(4):833–842
9. Naidu KB (1974) Stratified viscous flow between two oscillating cylinders. *Indian J Pure Appl Math Indian Natl Sci Acad* 5(12):1127–1136
10. Prasanna Venkatesh L (2018) Magneto hydrodynamics viscous oscillatory flow in a narrow channel due to suction or injection through the porous wall. *J Adv Res Dyn Control Syst* 3(3):1354–1361
11. Prasanna Venkatesh L (2018) Effects of stratification in rectangular channel problems. *Int J Pure Appl Math* 119(15):1211–1219
12. Prasanna Venkatesh L, Prabha BS (2017) Effects of narrow channel approximation on viscous oscillatory density stratified fluid flow through rectangular channels. In: *International conference on innovations in information, embedded and communication systems (ICIIECS) proceedings*. IEEE, New York, 2018, ©2017, India, pp 1–5
13. Shah Z, Islam S, Gul T, Bonyah E, Khan MA (2018) The electrical MHD and hall current impact on micropolar nanofluid flow between rotating parallel plates. *Results Phys* 9:1201–1214
14. Bonzanini A, Picchi D, Ferrari M, Poesio P (2019) Velocity profiles description and shape factors inclusion in a hyperbolic, one-dimensional, transient two-fluid model for stratified and slug flow simulations in pipes. *Petroleum* 5(2):191–198
15. Waqas M (2020) A mathematical and computational framework for heat transfer analysis of ferromagnetic non-Newtonian liquid subjected to heterogeneous and homogeneous reactions. *J Magn Magn Mater* 493:165646

# A Review of Various Kinds of Cascade Refrigeration Cycle and Application of Ejector Mechanism



Sachin Kumar and Virender Chahal

**Abstract** Various kinds of refrigeration cycles and the effect of various design parameters are reviewed in this paper. A simple vapor compression absorption cycle provides cooling at low temperature up to  $-50\text{ }^{\circ}\text{C}$  but cannot produce cooling and heating effect simultaneously, whereas this limitation overcome by cascading two vapor compression cycle to produce both cooling and heating effect simultaneously by taking  $\text{CO}_2$  as a refrigerant in the high-temperature side and other refrigerants in the low-temperature side which provides a larger cooling range as compared to the conventional cycle. An EES computer program was built to investigate the properties of some blends such as R744/125, R744/41, and R744/32, and the effect of subcooling, superheating, and approach temperature was calculated. The effect of some design parameters, such as evaporator temperature and isentropic efficiency of the compressor, is analyzed, and results show that the COP of the cycle increases with an increase in evaporative temperature but decreases with increasing condenser temperature. The isentropic efficiency of the compressor has little effect on system performances. A transcritical cycle can give heating effect above the critical temperature which makes the cycle more efficient as compared to the subcritical cycle. Furthermore, cycle performances of both subcritical and transcritical cycles can improve by using a two-phase ejector as a replacement of the throttle valve. The effect of various design parameters of the ejector to increase system performance is also discussed moreover for large-scale industrial applications of ejector-enhanced refrigeration cycle.

**Keywords** Subcritical cycle · Transcritical cycle · Design parameters · Two-phase ejector mechanism · Carbon dioxide

---

S. Kumar (✉)

Department of Mechanical Engineering, Jagan Nath University, Bahadurgarh, Jhajjar, Haryana, India

V. Chahal

Department of Mechanical Engineering, Chandigarh Group of Colleges, Ladran, Punjab, India

© The Author(s), under exclusive license to Springer Nature Singapore Pte Ltd. 2021

245

C. Pandey et al. (eds.), *Advances in Materials and Mechanical Engineering*,

Lecture Notes in Mechanical Engineering,

[https://doi.org/10.1007/978-981-16-0673-1\\_20](https://doi.org/10.1007/978-981-16-0673-1_20)

## Nomenclature

AT	Approach temperature
COP	Coefficient of performance
DT	Heat exchanger temperature difference
$\varepsilon$	Heat exchanger effectiveness
$h$	Enthalpy
HT cycle	Higher temperature cycle
IT	Intermediate temperature
LT Cycle	Lower temperature
$m_L, m_H$	Mass transfer in low and high-temperature cycles respectively (kg)
$\eta_c$	Isentropic efficiency of compressor
OT	Overlap temperature
$Q_H$	Heat transfer in higher temperature cycle (kJ)
$Q_L$	Heat transfer in lower temperature cycle (kJ)
$T_C$	Condenser Temperature
$T_E$	Evaporative temperature
$T_H$	Temperature of heat sink fluid
$T_L$	Temperature of heat source fluid
$W_T$	Total work done by the compressor

## 1 Introduction

The process of producing cold by extracting heat from a body is known as refrigeration. The refrigeration process is widely used in industries for freezing applications such as cold storage, food preservations, air conditioning, and many more. Its vast scope in daily life has encouraged many researchers to do research in this field. The refrigeration effect can be produced naturally and artificially. In 1756, William Cullen, developed the first artificial refrigeration method at the University of Glasgow, Scotland, using diethyl ether as a refrigerant to absorb heat from surrounding air after passing through a pump which creates a vacuum. But, unfortunately, the system had no practical application at that time even though it can produce a small amount of ice. In 1758, Benjamin Franklin and John Hadley conduct an experiment with a bulb of mercury thermometer, for the rapid cooling of an object by evaporation. The temperature of any object can drive down by evaporation of highly volatile liquids such as ether and alcohol.

Producing refrigeration effect by using chemical solutions or volatile liquids like ethyl ether was compensated by the invention of simple vapor compression cycles, which, firstly, is designed by Oliver Evans in 1805 and built by Jacob Perkins in 1834, but could not succeed commercially, but the model was furthered converted in working prototype by John Hague. The first patent on the practical application of the vapor compression refrigeration system was filed in 1856 by James Harrison,

which is composed of refrigerants like ether, alcohol, or ammonia. This system reduced the requirement of vacuum on the low-pressure side due to the lower boiling point of ammonia, i.e.,  $-33.3\text{ }^{\circ}\text{C}$ , which in turn made ammonia as a widely used refrigerant in refrigeration plants at that decade. In a simple vapor compression refrigeration cycle, refrigerant first passes through a compressor where the refrigerant gets compressed and then allows cooling in the condenser. The refrigerant then after passing through the condenser now expands in the throttle valve and then finally reaches the evaporator. The refrigerating effect is produced in the evaporator where the refrigerant absorbs heat from the cooling space to maintain the cooling space temperature at the desired level. This whole process contributes to an ideal vapor compression system, but whereas, a practical vapor compression cycle consists of irreversibility due to internal friction in components and also non-ideal gas behavior of the refrigerant in a cyclic process. The vapor compression refrigeration cycle has its applications in domestic as well as commercial refrigeration plants such as in air conditioning and food storage.

A simple vapor compression cycle consists of a mechanical device like a compressor that causes the irreversibility of the system due to its internal friction and also noisy in operation which are the main disadvantages of this cycle. Consumption of high electricity for driving the compressor of the cycle is also a drawback of the vapor compression refrigeration system which increases the running cost of the system. Further, the compressor of the cycle runs at very high speed which causes vibration and noise, and also the maintenance cost of the cycle is also high. All these limitations are covered up by the use of the vapor absorption refrigeration system. The first gas absorption refrigeration system was invented by a French scientist Ferdinand Carré in 1859 using aqua ammonia solution (gaseous ammonia dissolved in water) by replacing the compressor with an absorber in which gaseous ammonia was absorbed by water for making aqua ammonia solution. This solution further passed through the condenser after pumped by the pump at high pressure, and the refrigerating effect is produced in the evaporator same like in case of vapor compression system but with an advantage that the refrigerant can pump in the absorption system more efficiently as compared to being compressed in the compressor as in case of the vapor compression cycle. The further advantage of the vapor absorption cycle is that, in the absorption cycle, the refrigerant is pumped at a higher pressure, so less evaporative pressure is required as compared to a simple vapor compression cycle. In 1925, Carl Munters and Baltzer Von Plantan built the first domestic absorption refrigeration system using ammonia as refrigerant and water as an absorber. As absorber refrigeration system require an external heating system to operate rather than electric power, this disadvantage of the system limited its use to commercial purpose only which make vapor compression system more suitable for domestic purpose. Another reason to use the vapor compression cycle in domestic refrigeration is its high COP as compared to the absorption refrigeration cycle. To extend volumetric potency and refrigerant results and to cut back power consumption, the time-period vapor compression cycle with intercooling is usually used [1].

The limitations of a single-stage refrigeration system such as lower temperature range and also availability of lower evaporator pressure were overcome by cascade the refrigeration system by cascading two different or two same types of refrigeration systems using different refrigerants in each cycle. R12 and R13 refrigerants were of most interest in research in the past. However, these refrigerants contained chlorine that causes ozone gas depleting. Therefore, eco-friendly refrigerant area unit is most appropriate for industrial applications connected to food preservation, such as in supermarkets, cold storages, and blast cooling, wherever refrigeration temperature down to  $-80\text{ }^{\circ}\text{C}$  is needed [2]. Hydrocarbons as refrigerants cause environmental hazards and also reduce the energy consumption and offer good drop-in replacements for the existing halogenated refrigerants [3].

With relation to world environmental protection, the employment of natural refrigerants in the cascade refrigeration system helps to satisfy the obligations of environmental treaties [4]. A single-compressor-driven auto-cascade system uses zeotropic mixtures as refrigerants where evaporator condenser attained a cascade between low and high boiling point components to pertain refrigeration effect at lower evaporator temperature as compared to a single refrigerant system. Refrigeration capacity and system performance of an auto-cascade refrigeration system decreases in course of increased condenser temperature and mass fraction of R744, whereas compressor power increases at the same [5]. COP of the auto-cascade cycle can be increased by charging concentration about 30% (weight) with stable system conditions. Suction and discharge pressure of the auto-cascade system decrease with a decrease in cooling water outlet temperature which leads to less power consumption by the compressor [6]. Implementing the ejector mechanism in the auto-cascade system reduces the pressure ratio of the compressor, and thus, COP of cycle increases at low refrigerating temperature [7]. Jianlin et. al. [8] proposed an internal auto-cascade refrigeration cycle (IARC) operating with the zeotropic mixture of R290/R600 composed of a cascade heat exchanger associated with a phase separator to enhance the overall system performance. The refrigeration system producing a refrigerating effect at lower evaporative temperature is in increasing demand nowadays especially for rapid freezing, storage of medical materials, etc. Somewhere refrigerating effect at low temperature, say  $-20\text{ }^{\circ}\text{C}$ , is needed which cannot be achieved by using a single-stage refrigeration process such as vapor-compression or absorption system alone. For example, an  $\text{H}_2\text{O}/\text{LiBr}$  absorption system can produce a refrigerating effect at temperature up to  $0\text{ }^{\circ}\text{C}$  only limiting its use for subfreezing refrigeration, whereas the  $\text{NH}_3/\text{H}_2\text{O}$  absorption refrigeration system can produce refrigerating effect at evaporation temperatures up to  $-20\text{ }^{\circ}\text{C}$ . In 2005, vapor absorption cascade system was analyzed keeping the R744-717 vapor compression refrigeration system at low-temperature side to achieve a refrigerating effect at low temperatures and the absorption cascade system ( $\text{NH}_3/\text{H}_2\text{O}$ ) at the high-temperature stage. The intermediate temperature has a direct effect on system performance and higher COP can be achieved by varying intermediate temperature. The evaporation temperature affected optimal intermediate temperature in a more significant way by using  $\text{NH}_3$  as a refrigerant in the compression system rather than  $\text{CO}_2$  [9]. A compression absorption system assisted with geothermal energy can improve cycle efficiency by 37–54% in

comparison with conventional cycle under the same operating conditions which can be an alternative to electrical consumption as well as to reduce greenhouse emission [10].

Garimella et al. [11] proposed a waste-heat-driven compression absorption system for naval ship applications that uses the waste heat of onboard gas turbine to drive the absorption cycle. By the use of waste heat as free energy for the absorption system, overall performance of the absorption cascade system was high as compared to conventional cycles with reducing electrical consumption by 31%. Use of LiBr-H<sub>2</sub>O as a refrigerant in the cascade system increases system performance up to 33% higher than the conventional cycles using NH<sub>3</sub> refrigerant in the absorption section of the cascade system by reducing thermal energy consumption up to 35% [12]. When a simple vapor compression cycle is coupled with the absorption cycle, space requirement increases but electrical consumption and running cost decrease simultaneously due to the use of waste heat of vapor compression cycle available at a much low cost almost free compared to the running cost of a single-stage system [13, 14]. System performances and rational efficiency were maximized by optimal cascade condenser temperature, whereas the irreversibility rate of the cycle was minimized. The overall system performance of the compression absorption cascade system is affected by cascade condensing temperature. Lower the condensing temperature, higher the system performances, as well as, cost of the system, which is not so economical. Nonlinear programming (NLP) tool was used by Jain et al. [15] to optimize system performances which reduce the annual cost by 12% following the reduction in investment cost up to 22.4%.

A heat-driven compression absorption system consisting of three subsystems, viz., ammonia–water mixture power generation subsystem, ammonia–water absorption system, and a CO<sub>2</sub> compression refrigeration system, can produce a cooling effect to a temperature as low as  $-60\text{ }^{\circ}\text{C}$  without any additional electricity unit [16].

The vapor compression absorption cascade refrigeration cycle cannot provide heat and cold effect simultaneously, which can be achieved by cascade two vapor compression cycles with CO<sub>2</sub> as a refrigerant in the high-temperature cycle to provide heating effect and another refrigerant like NH<sub>3</sub>, propane, propylene, etc., in the low-temperature cycle to produce the cold effect. Further, these cascade cycles cannot provide heating effect above the temperature of  $31.06\text{ }^{\circ}\text{C}$  which was overcome by using transcritical and supercritical refrigeration cycles. The effect of various design parameters such as evaporator temperature, condenser temperature, and isentropic efficiency on system performance, i.e., COP of the cycles, is discussed in the next sections of the present paper.

## 2 Subcritical Cascade Refrigeration Cycles

### 2.1 Subcritical Cycles for Cooling Only

Jain and Bansal [1] reviewed two circuit cascade refrigeration systems using R-22, R-32, R-717, R290, and R-1270 as high-temperature fluids and R-744, HFC-23, R-508B, etc., as lower temperature fluids resulting in maximum COP with R-717. Much research has been done on the cascade refrigeration system to improve the efficiency of the cycle. In 2006, Lee [4] provides an equation for optimal condensing temperature at which maximum COP can be attained. A study by Dopazo et al [17] revealed that the COP of the system diminished by 45% with an increase in condenser temperature for R744/R717 cascade refrigeration system.

Nicola et al. [18] have given a comparative analysis on the performance of a cascade refrigeration cycle operated with blends of carbon oxide (R744) and HFCs (R23, R32, R41, and R125) because the low-temperature operating fluid and R717 because the warmth operating fluid. In the present paper, a simulation program was built in EES for analyzing COP of subcritical cycle using different refrigerants and was compared with results of Nicola study which results in 5% higher COP as comparable to the former (Fig. 1, 2).

In 2011, an experimental study on R744/717 cascade refrigeration system for the freezing process was performed by Dopazo et al. [19]. Evaporator temperature ranged from  $-40$  to  $-50$  °C. COP was increased by 6.5% at an evaporator temperature of  $-50$  °C. But with the implementation of economizer, 19% increment in COP was measured, whereas an experimental study performed by Huagen et al. [20] shows the adverse effect of cascade heat exchanger temperature difference as the cooling capacity of the system decreases with an increase in cascade heat exchanger temperature difference and thus COP also.

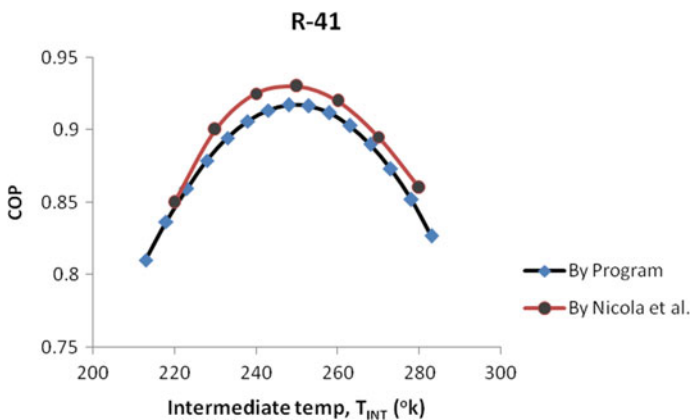


**Fig. 1** Variation of COP with intermediate temperature for R-41

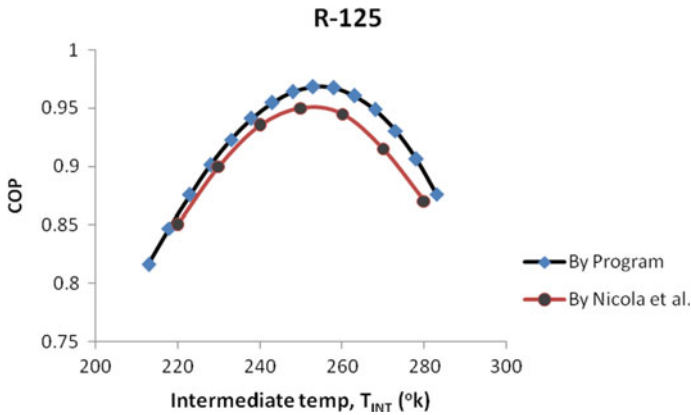


Fig. 2 Variation of COP with intermediate temperature for R-125

The cost of the system can be reduced by optimizing the various design parameters of the system like heat exchangers, etc. Exergy analysis of CO<sub>2</sub>-NH<sub>3</sub> cascade refrigeration system done by Behbahaninia et al. [21] revealed the decrease in the total annual cost of the cycle by 9.34% as compared to already existed subcritical cycles and find the optimal values of various decision variables such as condenser temperature equal to 56.27 °C and evaporator temperature value which was found equal to -50 °C. A linear regression analysis developed by Getu and Bansal [22] defines the optimum thermodynamic parameters, and it was found that an increase in subcooling increases system performances and mass flow ratio, whereas the effect of superheating is reversed as that of subcooling. The first experimental study on the use of R290 as a secondary refrigerant in the cascade system was done by Zhang et al. [23] and found that R744/ R290 blends have more refrigeration capacity than R13 as well as COP with zero ODP and smaller GWP. Properties of some refrigerants used for cooling purpose in the subcritical cycle are given in Table 1.

A two-stage subcritical cascade system consists of two vapor compression cycles cascade to each other as shown in Fig. 3 and works with two completely different refrigerants one in lower temperature circuit and other in the high-temperature circuit. In the low-temperature cycle, a primary refrigerant with a lower boiling

Table 1 Thermo-physical properties of refrigerants

Properties	R12	R22	R23	R41	R135
Environmental classification	<i>CFC</i>	<i>HCFC</i>	HFC	HFC	<i>HFC</i>
Chemical formula	<i>CCl2F2</i>	<i>CHClF2</i>	CHF3	CH3F	<i>C2H2F4</i>
Molecular Weight (Kg/Kmol)	120.9	86.5	70	34	102
Boiling point (°C)	-29.8	-40.7	-82.1	-78.2	-26.3
Critical temperature (°C)	111.97	96.2	25.92	44.13	101.06
Critical pressure (bar)	41.36	49.36	48.36	58.97	40.59



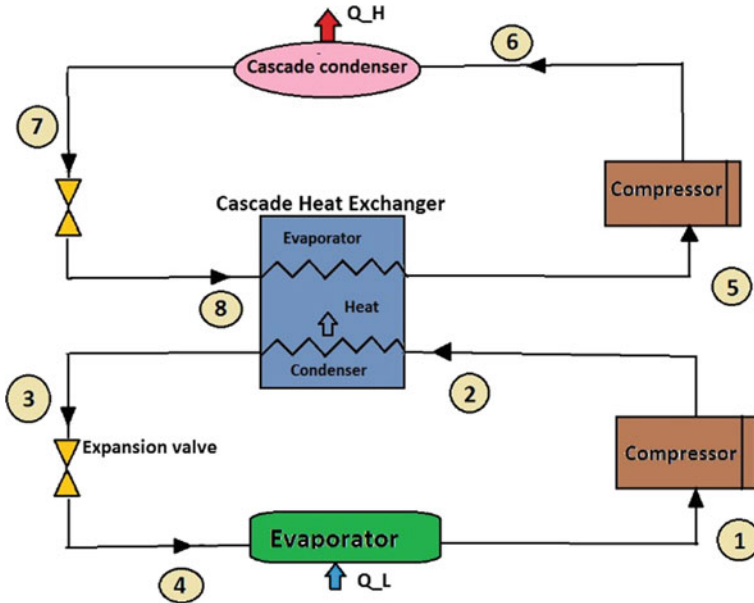


**Fig. 3** Systematic cascade refrigeration cycle with an evaporator, condenser, and cascade condenser

point produces a refrigerating effect in the evaporator of the lower circuit and then allows to compress in the compressor and passed to the cascade condenser where it releases heat to the secondary refrigerant flowing in the high-temperature cycle. Rejected heat of primary refrigerant in the cascade heat exchanger is absorbed by the evaporator of the high-temperature circuit containing secondary refrigerant which then condensed in the condenser of the high-temperature circuit after passed through the compressor of the high-temperature cycle. The evaporator of the low-temperature circuit produces the desired refrigerating effect. Cascade heat exchanger temperature difference is an important factor for designing the cascade system as it directly affects the system performances. The effect of subcooling and superheating and approach temperature was studied, and system performance increases with intermediate temperature which reaches up to optimum temperature and after that the effect reversed (Fig. 4).

Furthermore, the mass flow rate increases around 3% by superheating and subcooling because the load on the cascade condenser increases due to the combined effect of an increase in compressor work and refrigerating effect. Increasing the mole fraction of carbon dioxide mass flow rate decreases for R-125 and R-23 and increases for R-41 and R-32. But as condenser temperature increases, the mass flow rate in the high-temperature circuit increased, and also the same results were countered when the cycle was implanted with a liquid vapor heat exchanger in the low-temperature cycle (Fig. 5).

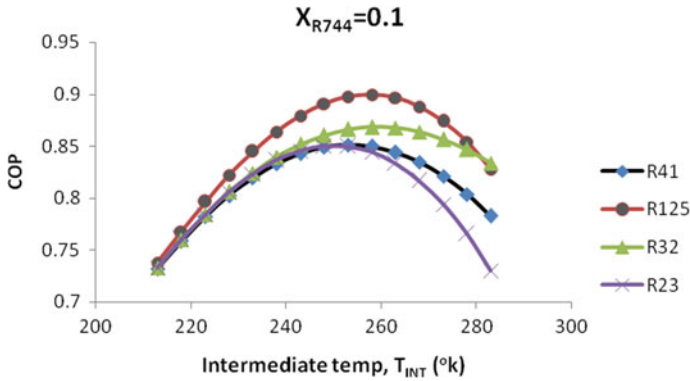


Fig. 4 Comparison of COPs for different refrigerating fluids with approach 5 °C

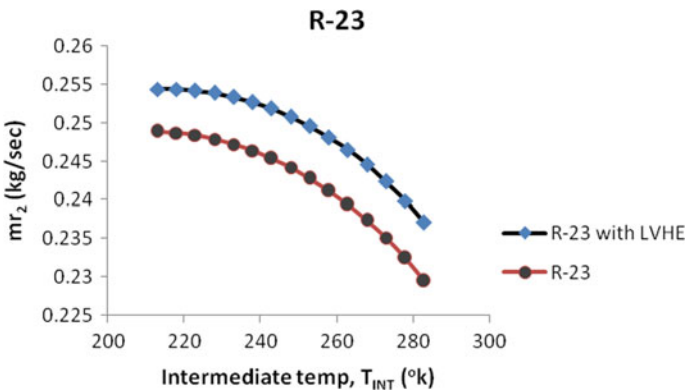


Fig. 5 Effect of liquid vapor heat exchanger on mass flow rate

## 2.2 Subcritical Cycles Used for Cooling and Heating Purpose Simultaneously.

Using R-744 as high-temperature fluid and other refrigerants such as R-290 and R-1270 in lower temperature cycle makes a cascade cycle to operate as Refrigerator and heat pump simultaneously. The main advantage of using refrigerants other than R744 in the LT circuit is to provide a larger cooling effect as R744 can cool the system up to  $-56\text{ }^\circ\text{C}$ , whereas other refrigerants give larger temperature lift say about  $-60$  to  $-70\text{ }^\circ\text{C}$  and more. In 1985, Gupta [24] had done numerical optimization of a cascade refrigeration system using R12 and R13 as a working fluid for providing cold and heat effects. This research put the basics of implementing a double vapor compression cascade cycle as a refrigerator and heat pump. Overall system performance was recorded as 7.4 with temperature limits of  $-30$  to  $10\text{ }^\circ\text{C}$  for low- and high-temperature circuits and 2.5 for  $-70\text{ }^\circ\text{C}$  to  $60\text{ }^\circ\text{C}$  temperature limits. Murthy [25] experimented on

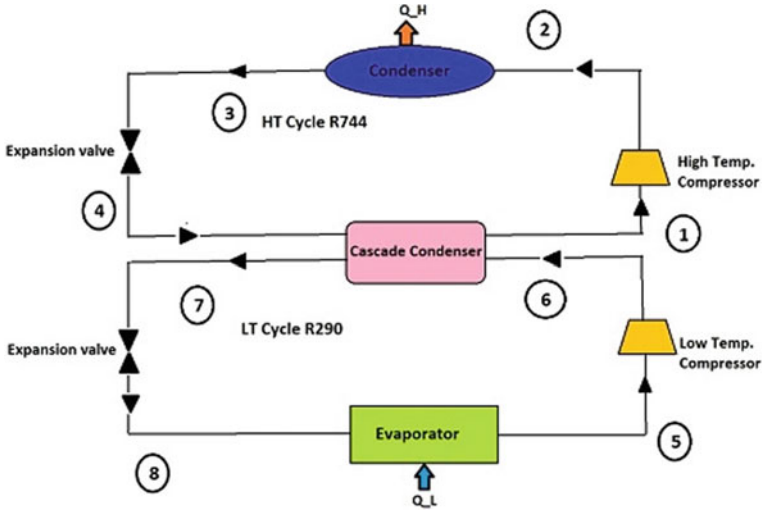


Fig. 6 Cascade refrigeration cycle for heating and cooling purpose

the R11-R12 cascade system used for cogeneration of cold and heat and 65 to 95 °C condensing temperature of R11 refrigerant which could be achieved by varying the evaporative temperature of R12 from -20 to + 8 °C with the achievement of system performance in the range of 1.2–1.7.

Figure 6 represents the cascade system using R744 as a refrigerant in the high-temperature circuit and R290 as a refrigerant in the low-temperature circuit. Heat ( $Q_H$ ) released from the HT cycle is used to produce a heating effect and in LT circuit Propane absorbs heat ( $Q_L$ ) in the LT evaporator to give refrigerating effect to outside space. For simplification of the analysis, heat transfer in the condenser of the HT cycle, the evaporator of the LT cycle, and cascade heat exchanger are considered as isobaric. The isentropic efficiency of the cycle is taken as 0.78 for simplification.

The cooling and heating output from the system is given by,

$$Q_L = m_L(h_5 - h_8) \quad \text{and} \quad Q_H = m_H(h_2 - h_3) \tag{1}$$

Total work input to the compressors (LT stage and HT stage) is expressed as,

$$W_T = m_L(h_6 - h_5) + m_H(h_2 - h_1) \tag{2}$$

Hence, the system COP (combined heating and cooling) can be written as,

$$COP_{sys} = (Q_H + Q_L)/W_T \tag{3}$$

In the present study, an EES program was built to calculate the effect of various design parameters such as evaporator temperature, isentropic efficiency of the

compressor, and outlet temperature of the condenser of higher temperature cycle keeping the intermediate temperature constant. On basis of the results obtained by simulation of the mathematical model in EES software, it was found that the COP of the system increases with an increase in evaporator temperature as increasing evaporator temperature reduced the compressor work in LT circuit (Fig. 7), but the effect of gas cooler exit temperature is adverse on system performance. As gas condenser temperature increases, the work requirement of the compressor of the HT cycle increases due to an increase of pressure ratio and thus system performance decreases (Fig. 8), whereas isentropic efficiency has little effect on system performances (Fig. 9).

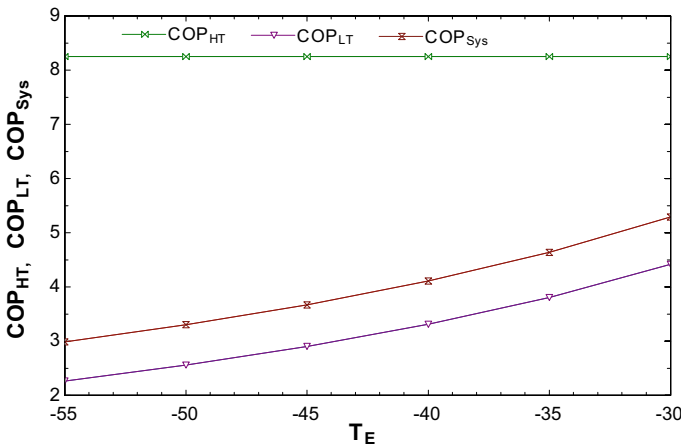


Fig. 7 Effect of evaporator temperature on COP of the system

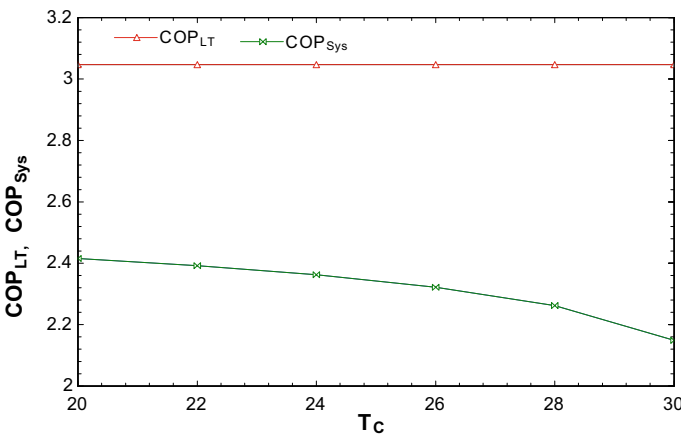


Fig. 8 Effect of condenser temperature on COP of the system

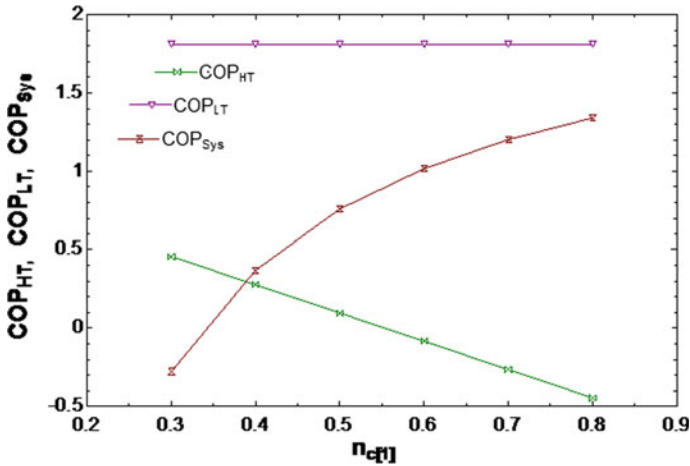


Fig. 9 Variation of COP with compressor isentropic efficiency

### 3 Transcritical CO<sub>2</sub> Cycle Used for Cooling and Heating Purpose

A transcritical CO<sub>2</sub> cycle is a modified form of simple vapor compression refrigeration cycle with the implementation of an internal heat exchanger. The waste of condenser outlet is used for heating the fluid, whereas the refrigerating effect is produced in the evaporator (Fig. 10). Sarkar et al. [26] optimized a transcritical CO<sub>2</sub> cycle and found that the system performance is less affected by internal heat exchanger effectiveness, whereas the effect of the gas cooler exit temperature and evaporator temperature effect on COP of the system are more predominant. Groll et al. [27] uses the ejector mechanism as a replacement of evaporator and improves

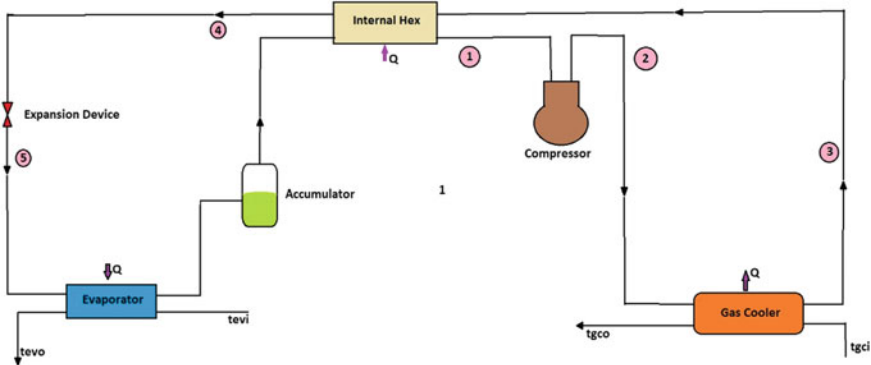


Fig. 10 Transcritical CO<sub>2</sub> cycle for cold and heat

the system performances by 16% to that of the basic transcritical system. Again in 2011, Yari [28] analyzed two new CO<sub>2</sub> cascade cycles, one as ejector-enhanced transcritical CO<sub>2</sub> cycle and the other as a subcritical cycle. COP of the transcritical cycle with the ejector mechanism was increased up to 10.8–17.2% and while COP of the supercritical CO<sub>2</sub> cycle was increased up to 31% as compared to the basic transcritical cycle. A basic transcritical cycle used for cooling and heating purpose has high throttling losses which can be reduced by using an expander. In the present study, effects of evaporator temperature, internal heat exchanger effectiveness, and gas cooler exit temperature were considered. The heat rejected in the gas cooler can be given as  $Q_H = m_r (h_2 - h_3)$ , and heat absorbed by the system in the evaporator can be calculated as  $Q_L = m_r (h_6 - h_5)$ . Compressor work is given as  $W_C = m_r (h_2 - h_1)$ , and cooling and heating performance of the system were calculated as  $COP_{HT} = Q_H/W_C$ ,  $COP_{LT} = Q_L/W_C$  and whole system performance was calculated as  $COP_{sys} = (Q_H + Q_L)/W_C$ .

Figure 11 shows the variation of various COPs with evaporator temperature. It was seen that evaporator temperature has positively affected the system performances with less work load requirement for compressor. Cooling the CO<sub>2</sub> fluid at gas cooler exit with the implementation of an auxiliary cycle (an assisted vapor compression cycle) results in increased COP of the transcritical CO<sub>2</sub> cycle [29].

Many researchers have shown interest in finding advantages of using a transcritical CO<sub>2</sub> based cascade refrigeration system as a refrigerator and heat pump. In 2005, Bhattacharya et al. [30] performed a thermodynamic analysis of R744/R290 transcritical cycle used for cooling and heating purpose showing results that this cycle provides a larger cooling range as compared to a subcritical R744/717 cascade system. The main factor is using the CO<sub>2</sub> transcritical cycle to give heating range up to 120 °C, and the cooling range of propane was estimated as -40 °C which is

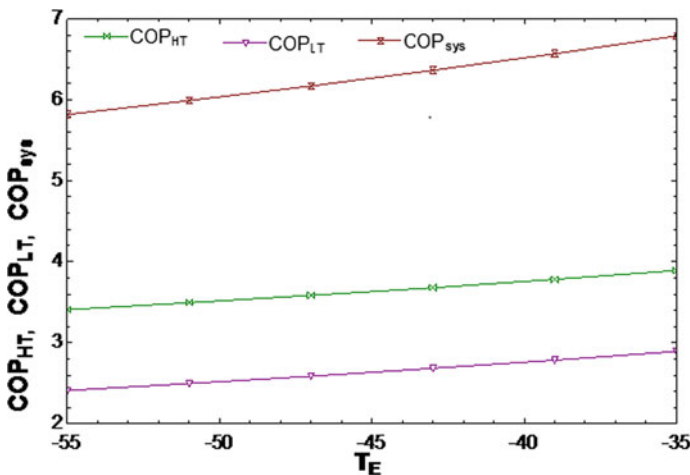


Fig. 11 Variation of COP with evaporative temperature of transcritical CO<sub>2</sub> cycle

**Table 2** Properties of refrigerants [32, 33]

Properties	R290	R1270	R170	R744	R744A
Environmental classification	<i>HC</i>	<i>HO</i>	HC	–	<i>HFC</i>
Molecular Weight (kg/Kmol)	44	42	30	44	97.6
Boiling point (°C)	–42.1	–47.7	–88.8	–88.47	–46.2
Critical temperature (°C)	96.8	94.4	32.2	36.37	72
Critical pressure (bar)	42.56	46	48.9	36.37	72
O.D.P	0	0	0	0.017	0
Ashare standard safety rating	A3	A3	A3	A1	A1

much higher than the subcritical cycle discussed before. A new refrigerant  $N_2O$  was supposed by Sarkar et al. [31] studying the COP as a function of approach temperature (AT), intermediate temperature (IT), and overlap temperature (OT). Optimized intermediate temperature varies with gas cooler and low-temperature cycle evaporator temperature for attaining maximum COP of the system keeping the condensing temperature of nitrous oxide same in the cascade heat exchanger. Alok et al. [32, 33] use propylene as a secondary fluid in a lower temperature cycle for  $CO_2$  based transcritical cycle and compares the COPs of various existing cycles with results of achieving the highest COP among all cycles proposed before (Table 2).

In 2007, Exergy analysis of the transcritical  $CO_2/C_3H_8$  cascade refrigeration system was performed by Bhattacharya et al. [34]. The temperature of heat sink  $T_H$  was optimized, and the study revealed that with increasing  $T_H$  system performances also increases. Cascade heat exchanger temperature difference does not affect the COP of high-temperature cycle, whereas the COP of lower temperature cycle and that of the whole system reduces with an increase in the cascade heat exchanger temperature. The overall COP of transcritical  $CO_2$  based two-stage cascade refrigeration system is more than that of the subcritical cycle which in turn could be a topic of interest for future researches for implementation in supermarket refrigeration systems.

Exergetic efficiency and component irreversibility analysis for a transcritical  $CO_2$  cycle performed by Bhattacharya et al. [35] revealed that the internal heat exchanger has little effect on the system irreversibility, whereas maximum COP of the system was achieved at values 1.8 and 1.9 countered for internal heat exchanger area ratio. Furthermore, the system component's irreversibility can also be decreased to a significant amount by implementing a “thermo-electric sub-cooler” and thus, in results, increasing the system COP as well, about 16% higher than the conventional cycle [36]. However, exergy destruction for compressor, gas cooler, and expansion valve is counted, so significantly that some serious efforts should be made for designing these components to improve cycle efficiency. System irreversibility can be reduced by increasing the rate of heat transfer in the gas cooler between the refrigerant and water flow [37].

### 4 Application of Ejector Mechanism in Cascade Cycles

The use of ejector in cascade refrigeration cycles, as a replacement of the throttle valve (Fig. 12), is to recover the expansion work wasted in the throttling process. Two-phase ejector modification is more emphasized due to its low cost and simple structure. Also, the ejector has no moving parts, so its running cost is low. Implementing an ejector as an expansion device in replacement of the throttle valve in a simple vapor compression cycle raises the suction pressure higher than that in evaporator results in reducing compressor work and thus improves the system performance. The first ejector-enhanced vapor compression cycle was proposed by Kornhauser [38] using R12 as working fluid by the implementation of a two-phase ejector mechanism, and a liquid–vapor separator results in improving system performance by 21% over the standard cycle under the same operating conditions. Types of the working fluid used in the cycle also affect the system performances, strongly, in an ejector-enhanced cycle as R134a as working fluid gives more COP as compared to R404a, R407, and R410 [39]. Further, a two-phase ejector mechanism has more COP, about 3.9–7.6%, as compared to a single-phase ejector system with R134a as a refrigerant [40].

Second law analysis of subcritical ejector-enhanced cycle was performed by Yari [41] using R134a as a refrigerant and found that total energy destruction of simple vapor compression cycle was found 24% higher as compared to ejector-enhanced cycle, whereas by using ejector mechanism, COP of the system was increased about 16% as compared to simple subcritical cycle. In second law analysis, isentropic efficiency of the motive nozzle, suction nozzle, and diffuser is of most interest as they affect the system performance directly [42]. As the throat diameter of the primary nozzle increases, both cooling capacity and system performances improve due to an increase in circulation ratio. Besides all these, the compressor pressure ratio was affected negligibly by changing throat diameter [43].

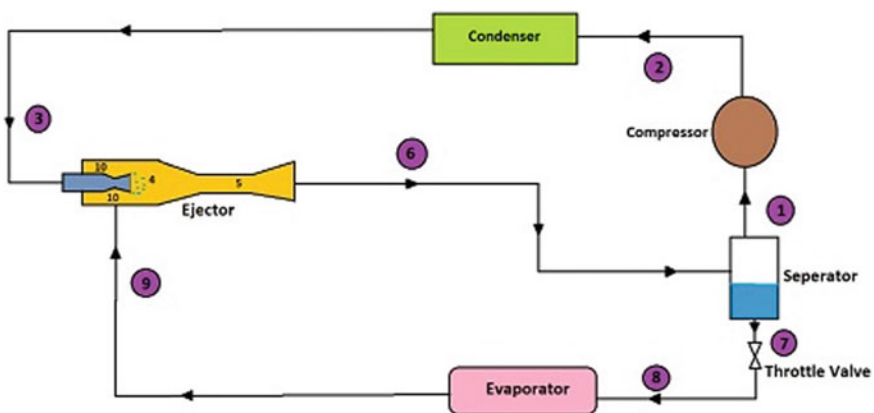
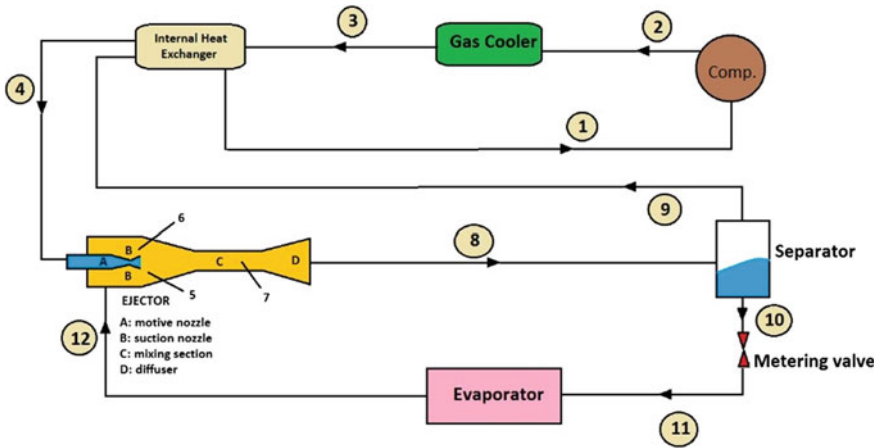


Fig. 12 Ejector-enhanced subcritical cycle





**Fig. 13** Ejector-enhanced transcritical CO<sub>2</sub> cycle

Motive nozzle efficiency can increase by providing a larger length of the diverging section of the nozzle as it provides a longer time period to achieve equilibrium, and thus, COP of the system increases [44]. The outlet diameter of the motive nozzle has a negligible effect on system performances [45]. The area ratio of the mixing section to motive nozzle also affects the system performances as COP of the cycle increases until the area ratio reaches to a peak point and then decreases with an increase in area ratio which means that if ejector operates beyond the optimal values causes waste of energy results in an increase in compressor work and decrease in COP of the system.

The small expansion ratio of the transcritical CO<sub>2</sub> cycle as compared to the conventional cycle makes ease of implementation of the ejector mechanism. Figure 13 shows an ejector-enhanced transcritical CO<sub>2</sub> cycle that comprises of a suction line internal heat exchanger for superheating (9–1) the gas before it gets compressed in the compressor. This heat exchanger also performs the subcooling (3–4) of gas after gas cooler. In an ejector-enhanced cycle, there is a reduction in mass flashed into vapor due to lower throttling pressure difference, making easier evaporator tube arrangement in the ejector expansion cycle [46]. The energy losses in the throttling process are lower in ejector-enhanced transcritical cycle as compared to the conventional cycle. Studies also revealed that there is negligible change in energy losses of evaporator, whereas energy losses due to compression and condenser are reduced quite significantly [46]. The balance between pressure lift and ejector entrainment ratio can be controlled by installing the metering valve below the liquid–vapor separator [47]. The ejector entrainment ratio gets directly affected by evaporator temperature, whereas gas cooler exit temperature harms the ejector entrainment ratio. The use of an internal heat exchanger in the ejector-enhanced transcritical CO<sub>2</sub> cycle reduces the optimal pressure of the high-temperature side that why lower improvement in COP of the cycle achieved as compared to the conventional cycle. The effect of the

mixing area is not so significant in the transcritical cycle as that of the subcritical cycle.

Entrainment ratio gets affected by mixing length (Point 'C' in Fig. 14) as higher-pressure recovery is achieved with larger mixing length, as well as, entrainment ratio, system performance also increased with larger mixing length. Mixing length has also some adverse effects on the COP of the cycle. There will be a minor change in pressure recovery if a much larger mixing length is taken which also causes a reduction in entrainment ratio. For the maximum mass flow rate in the suction nozzle, the COP of the cycle reaches its maximum value [48]. There was 10% COP difference which was achieved by using a larger mixing length as compared to the smaller one [49]. An experimental study on the effect of the internal heat exchanger on system performances for ejector-enhanced transcritical CO<sub>2</sub> cycle performed by Marasigan et al. [50] discovered that internal heat exchanger length has a significant effect on system performance. A 60 cm internal heat exchanger can provide a larger COP about 27% higher than that of the conventional cycle. Implementation of double ejectors in a two-stage transcritical CO<sub>2</sub> cycle, arranged in high and low-pressure stage, reduces the throttling loss with recovering more available expansion work in turns providing more volumetric heating capacity as well as higher COP as compared to the conventional cycle [51]. Jianlin et al. [52] performed an advanced exergy analysis of ejector-enhanced transcritical CO<sub>2</sub> cycle by splitting exergy destruction into endogenous/exogenous and unavoidable/avoidable parts showing that the compressor has the highest rate of exogenous exergy destruction which is significantly affected by discharge pressure. Hongxia Zhao et al. [53] improved the system performances of the conventional booster R744 two-temperature supermarket refrigeration cycle by adding an ejector to the cycle. Adding an ejector to the cycle reduces the compressor work by 10% as compared to the conventional cycle which in turn increases the COP by 11%.

An experimental study was performed [54] on a prototype of an ultra-low temperature upright freezer equipped with a modified cascade refrigeration system by implementing an ejector in the first stage. The experiment conducted at 25 °C ambient temperature results in lower energy consumption of the system, approx 4.77% lower, as compared to the baseline freezer. Yan et al. [55] performed an experimental study of ejector-enhanced auto-cascade refrigeration cycle taking R134a/R23 as refrigerants and compare the results with the conventional cycle. The experimental results show 9.6% and 25.1% improvement in COP and energy efficiency, respectively, of the ejector-expanded cycle as compare to the conventional cycle. The system performances were affected by the mass fraction ratio of R23, and the maximum system exergy efficiency was obtained at an optimal mass fraction ratio of 0.30. An ejector-enhanced power cycle combined with the ejector-enhanced refrigeration cycle to make a combined power, and refrigeration cycle was studied by Shafii et al. [56] to improve the thermal and exergy efficiency up to 10.226% and 9.551%, respectively. The cooling capacity increases with an increase in inlet turbine pressure which results in decreasing the exergy efficiency keeping energy efficiency constant, whereas increasing evaporator temperature results in a rise of cooling capacity with constant power output. Nebot-Andrés et al. [57] performed an experimental study of a

transcritical CO<sub>2</sub> refrigeration plant with integrated mechanical subcooling to determine the optimal working conditions. The optimal COP values were determined by varying evaporator temperatures at different ambient temperatures, and results show that optimum COP values vary from 1.40 to 2.48 with gas cooler inlet temperature ranges from  $-1.3$  to  $10$  °C. Furthermore, the optimum pressure varies linearly with the gas cooler outlet temperature, without getting affected by the evaporation temperature.

## 5 Conclusion

Various kinds of cascade refrigeration systems used for cooling only and for both cooling and heating purposes simultaneously have been reviewed, and their performance characteristics were analyzed in this paper. The effect of various operating parameters such as evaporator temperature, isentropic compressor efficiency, and intermediate temperature on the system performance of subcritical and transcritical cycles was studied in this paper. Vapor absorption cascade cycle can provide only cooling effect, whereas subcritical cascade cycle consists of two vapor compression cycle can be used for providing simultaneously cooling and heating effect. In the earliest research in the field of the cascade refrigeration system to provide cooling and heating effect simultaneously, the first refrigerant used was CO<sub>2</sub> but was replaced by synthetic refrigerants in the 1930s. Because of its safe, economic, and environmentally sustainable characteristics have focused the interest of the researchers to use CO<sub>2</sub> as a working fluid again especially in transcritical cycles. The main limitation of CO<sub>2</sub> as a refrigerant in the cascade cycle is its low critical point which was recovered by using it as a refrigerant in the transcritical cycle as unlike of subcritical cycle, the transcritical cycle provides the heating effect through the condenser of the high-temperature side at a temperature above the critical point. COP of the transcritical cycle is affected by various design parameters such as internal heat exchanger effectiveness, evaporator exit temperature, condenser outlet temperature, and isentropic efficiency of the compressor. For a two-stage CO<sub>2</sub> based cascade transcritical cycle system, the COP of the system increases with an increase in evaporator exit temperature and decreases with an increase in condenser outlet temperature, whereas internal heat exchanger effectiveness has a negligible effect on system performances.

Further COP of each cycle viz., subcritical and transcritical cycles, can improve by replacing throttle valve by ejector as an expansion device. COP of the ejector-enhanced cycle depends on various design parameters such as the size of the motive nozzle, length of the mixing area, size of the suction nozzle, and diffuser. The experimental studies of ejector-enhanced cycles show that changing the nozzle's throat area and optimal value of gas cooler temperature can be achieved which enhances the COP of the cycle. The maximum COP of the cycle as well as the ejector can achieve through adjusting the design parameters to an optimal value such as the length of the mixing section can increase system performances but after increasing the length beyond optimal value can reduce the COP of the cycle.

## References

1. Bansal PK, Jain S (2007) Cascade systems: past, present, and future. *ASHRAE Trans* 113(1):245–252
2. Sharma V, Fricke B, Bansal P (2014) Comparative analysis of various CO<sub>2</sub> configurations in supermarket refrigeration systems. *Int J Refrig* 46(2), 86–99 (2014).
3. Harby K (2017) Hydrocarbons and their mixtures as alternatives to environmental unfriendly halogenated refrigerants: an updated overview. *Renew Sustain Energy* 73:1247–1264
4. Lee T-S, Liu C-H, Chen T-W (2006) Thermodynamic analysis of optimal condensing temperature of cascade-condenser in CO<sub>2</sub>/NH<sub>3</sub> cascade refrigeration systems. *Int J Refrig* 29(7):1100–1108
5. Kim MS, Kim SG (2002) Experiment and simulation on the performance of an auto-cascade refrigeration system using carbon dioxide as a refrigerant. *Int J Refrig* 25(8):1093–1101
6. Du K, Zhang S, Xu W, Niu X (2009) A study on the cycle characteristics of an auto-cascade refrigeration system. *Exp Thermal Fluid Sci* 33(2):240–245
7. Yu J, Zhao H, Li Y (2008) Application of an ejector in auto-cascade refrigeration cycle for the performance improvement. *Int J Refrig* 31(2):279–286
8. Yan G, Hu H, Yu J (2014) Performance evaluation on an internal auto-cascade refrigeration cycle with mixture refrigerant R290/R600a. *Appl Thermal Eng* 75:994–1000
9. Fernandez-Seara J, Sieres J, Vazquez M (2005) Compression–absorption cascade refrigeration system. *Appl Thermal Eng* 26:502–512
10. Kairouani L, Nehdi E (2006) Cooling performance and energy saving of a compression–absorption refrigeration system assisted by geothermal energy. *Appl Therm Eng* 26(2):228–294
11. Garimella S, Brown AM, Nagavarapu AK (2011) Waste heat driven absorption vapor-compression cascade refrigeration system for megawatt scale, high-flux, low temperature cooling. *Int J Refrig* 234(8):776–1785
12. Cimsit C, Tekin Ozturk I (2012) Analysis of compression-absorption cascade refrigeration cycles. *Appl Thermal Eng* 40:311–317
13. Jain V, Kachhwaha SS, Sachdeva G (2013) Thermodynamic performance analysis of a vapor compression–absorption cascaded refrigeration system. *Energy Convers Manage* 75:685–700
14. Jain V, Sachdeva G, Kachhwaha SS (2014) Thermodynamic modeling and parametric study of a low temperature vapour compression-absorption system based on modified Gouy-Stodola equation. *Energy* 79(1):407–418
15. Jain V, Sachdeva G, Kachhwaha SS (2015) NLP model based thermo-economic optimization of vapor compression–absorption cascaded refrigeration system. *Energy Convers Manage* 93:49–62
16. Chen Y, Han W, Jin H (2017) Proposal and analysis of a novel heat-driven absorption–compression refrigeration system at low temperatures. *Appl Energy* 185:2106–2116
17. Alberto Dopazo J, Fernández-Seara J, Sieres J, Ufía FJ (2009) Theoretical analysis of a CO<sub>2</sub>-NH<sub>3</sub> cascade refrigeration system for cooling applications at low-temperatures. *Appl Therm Eng* 29(8–9):1577–1583
18. Nicola GD, Giuliani G, Polonara F, Stryjek R (2005) Blends of carbon dioxide and HFCs as working fluids for the low-temperature circuit in cascade refrigerating systems. *Int J Refrig* 28(2):130–140 (2005)
19. Alberto Dopazo J, Fernandez-Seara J (2011) Experimental evaluation of a cascade refrigeration system prototype with CO<sub>2</sub> and NH<sub>3</sub> for freezing process applications. *Int J Refrig* 34(1):257–267
20. Bingming W, Huagen W, Jianfeng L, Ziwen X (2009) Experimental investigation on the performance of NH<sub>3</sub>/CO<sub>2</sub> cascade refrigeration system with twin-screw compressor. *Int J Refrig* 32(6):1358–1365
21. Rezayan O, Behbahaninia A (2011) Thermo-economic optimization and exergy analysis of CO<sub>2</sub>/NH<sub>3</sub> cascade refrigeration systems. *Energy* 36(2):888–895

22. Getu HM, Bansal PK (2008) Thermodynamic analysis of an R744–R1717 cascade refrigeration system. *Int J Refrig* 31(1):45–54
23. Niu B, Zhang Y (2007): Experimental study of the refrigeration cycle performance for the R744/R290 mixtures. *Int J Refrig* 30(1):37–42
24. Gupta VK (1985) Numerical optimization of multi-stage cascaded refrigeration-heat pump system. *Heat Recov Syst* 5(4):305–319
25. Murthi SS, Krishna Murthi MV (1985) Experiments on a cascaded R11-R12 vapour compression system for cogeneration of heat and cold. *Heat Recov Syst* 5(6):519–526
26. Sarkar J, Bhattacharyya S, Ram Gopal M (2004) Optimization of a transcritical CO<sub>2</sub> heat pump cycle for simultaneous cooling and heating applications. *Int J Refrig* 27(8):830–838
27. Li D, Groll EA (2005) Transcritical CO<sub>2</sub> refrigeration cycle with ejector-expansion device. *Int J Refrig* 38(8):766–773
28. Yari M, Mahmoudi SMS (2011) Thermodynamic analysis and optimization of novel ejector-expansion TRCC (transcritical CO<sub>2</sub>) cascade refrigeration cycles (Novel transcritical CO<sub>2</sub> cycle). *Energy* 36(12):6839–6850
29. Dai B, Lui S, Sun Z, Ma Y (2017) Thermodynamic performance analysis of CO<sub>2</sub> transcritical refrigeration cycle assisted with mechanical subcooling. *Energy Procedia* 105:2033–2038
30. Bhattacharyya S, Mukhopadhyay S, Kumar A, Khurana RK, Sarkar J (2005) Optimization of a CO<sub>2</sub>–C<sub>3</sub>H<sub>8</sub> cascade system for refrigeration and heating. *Int J Refrig* 28(7):1284–92
31. Bhattacharyya S, Garaia A, Sarkar J (2009) Thermodynamic analysis and optimization of a novel N<sub>2</sub>O–CO<sub>2</sub> cascade system for refrigeration and heating. *Int J Refrig* 32(7):1077–1084
32. Dubey AM, Kumar S, Agrawal GD (2014) Thermodynamic analysis of a Transcritical CO<sub>2</sub>/propylene (R744–R1270) cascade system for cooling and heating applications. *Energy Convers Manage* 86:774–783
33. Dubey AM, Kumar S, Agrawal GD (2015) Numerical optimization of a transcritical CO<sub>2</sub>/propylene cascaded refrigeration-heat pump system with economizer in HT cycle. *Ind Acad Sci* 40:437–454
34. Bhattacharyya S, Bose S, Sarkar J (2007) Exergy maximization of cascade refrigeration cycles and its numerical verification for a transcritical CO<sub>2</sub>-C<sub>3</sub>H<sub>8</sub> system. *Int J Refrig* 30(4):624–632
35. Sarkar J, Bhattacharyya S, Ram Gopal M (2005) Transcritical CO<sub>2</sub> heat pump systems: exergy analysis including, heat transfer and fluid flow effects. *Energy Conversion Manage* 46:2053–2067
36. Sarkar J (2018) Performance optimization of transcritical CO<sub>2</sub> refrigeration cycle with thermoelectric subcooler. *Int J Energy Res* 37:121–128
37. Ozgur AE, Bayrakci HC (2008) Second law analysis of two-stage compression transcritical CO<sub>2</sub> heat pump cycle. *Int J Energy Res* 32:1202–1209
38. Kornhauser AA (1990) Use of an ejector as a refrigerant expander. Proceedings of USNC/IIR-Purdue refrigeration conference. USA
39. Takeuchi H, Kume Y, Oshitani H, Ogata G (2002) Ejector cycle system. U.S. Patent 6, 438, 993 B-2
40. Harrell GS, Kornhauser AA (1995) Performance tests of a two-phase ejector. In: Proceedings of 30th inter society energy conversion engineering conference. Orlando, FL
41. Yari M (2008) Exergetic analysis of the vapor compression refrigeration cycle using ejector as an expander. *Int J Exergy* 5:326–340
42. Ersoy HK, Bilir N (2010) The influence of ejector component efficiencies on performance of ejector expander refrigeration cycle and exergy analysis. *Int J Exergy* 7:425–438
43. Chaiwongsa P, Wongwises S (2007) Effect of throat diameters of the ejector on the performance of the refrigeration cycle using a two-phase ejector as an expansion device. *Int J Refrig* 30:601–608
44. Nakagawa M, Takeuchi H (1998) Performance of two-phase ejector in refrigeration cycle. In: Proceedings of third international conference on multi-phase flow, Lyon, France
45. Chaiwongsa P, Wongwises S (2008) Experimental study on R-134a refrigeration system using a two-phase ejector as an expansion device. *Appl Therm Eng* 28:467–477

46. Deng J, Jiang P, Lu T, Lu W (2007) Particular characteristics of transcritical CO<sub>2</sub> refrigeration cycle with an ejector. *Appl Therm Eng* 27:381–388
47. Hrnjak ES (2007) Experimental investigation of transcritical CO<sub>2</sub> ejector system performance. In: 22nd IIR international congress of refrigeration, Beijing
48. Lee JS, Kim MS, Kim MS (2011) Experimental study on the improvement of CO<sub>2</sub> air conditioning system performance using an ejector. *Int J Refrig* 34:1614–1625
49. Nakagawa M, Marasigan AR, Matsukawa T (2010) Experimental analysis of two-phase ejector system with varying mixing cross-sectional area using natural refrigerant CO<sub>2</sub>. *Int J Air-Cond Refrig* 18:297–307
50. Nakagawa M, Marasigan AR, Matsukawa T (2014) Experimental analysis on the effect of internal heat exchanger in transcritical CO<sub>2</sub> refrigeration cycle with two-phase ejector. *Int J Refrig* 34:1577–1586
51. Xing M, Yu J, Liu X (2014) Thermodynamic analysis on a two-stage transcritical CO<sub>2</sub> heat pump cycle with double ejectors. *Energy Convers Manage* 88:677–683
52. Bai T, Yu J, Yan G (2016) Advanced exergy analyses of an ejector expansion transcritical CO<sub>2</sub> refrigeration system. *Energy Conversion Manage* 126:850–861
53. Huang Z, Zhao H, Yu Z, Han J (2018) Simulation and optimization of a R744 two-temperature supermarket refrigeration system with an ejector. *Int J Refrig* 90:73–82
54. Li Y, Yu J, Qin H, Sheng Z, Wang Q (2018) An experimental investigation on a modified cascade refrigeration system with an ejector. *Int J Refrig* 96:63–69 (2018)
55. Bai T, Yan G, Yu J (2019) Experimental investigation of an ejector-enhanced auto-cascade refrigeration system. *Appl Therm Eng* 129:792–801
56. Behnama P, Faegh M, Shafii MB (2019) Thermodynamic analysis of a novel combined power and refrigeration cycle comprising of EKalina and ejector refrigeration cycles. *Int J Refrig* 104:291–301
57. Nebot-Andres L, Catalan-Gil J, Sanchez D, Calleja-Anta D, Cabello R, Llopis R (2020) Experimental determination of the optimum working conditions of a transcritical CO<sub>2</sub> refrigeration plant with integrated mechanical subcooling. *Int J Refrig* 113:266–275

# Microstructure and Mechanical Properties of Rapid Solidified Hypereutectic AlSi<sub>24</sub>Cu<sub>3.8</sub>Mg<sub>0.8</sub> Alloys by UV-Assisted Stir–Squeeze Casting Method Under T-6 Condition



M. Peeru Naik and K. T. Balaram Padal

**Abstract** Hypereutectic aluminum–silicon composites are the prominent alloys in most automotive and manufacturing sectors due to their superior tribological and mechanical properties. However, the characteristics of the alloy much rely upon the production technique they involve. In this manner, many fabrication commerce aims attention at new production techniques to manufacture the right efficient materials. In this study, the alloys (AlSi<sub>24</sub>) were prepared by UV-assisted stir (UVS) casting and UV-assisted stir–squeeze (UVSS) casting processes under the T-6 condition. UVSS as a manufacturing method improves the hardness, tensile, and microstructural characteristics significantly by 20–50%. However, the best hardness (161.5) was obtained with AlSi<sub>24</sub>Cu<sub>3.8</sub>Mg<sub>0.8</sub> with UV-assisted stir–squeeze under T-6 condition. The enhancement in metallurgical and mechanical characteristics was primarily imputed to the dispersion and size of Si-particles due to the production process. Hardness and tensile characteristics are obtained with Tensometer and Brinell hardness tester. Additionally, EDS, metallurgical microscope, and SEM are used for microstructure observation.

**Keywords** Stir–squeeze · AlSi alloys · Hardness · Tensometer

## 1 Introduction

Aluminum alloys acquire considerable researchers' attention due to their great strength, reduced weight, ductility, and excellent tribological properties. The aluminum alloys with silicon particles have outstanding advantages, such as strength, hardness, and excellent wear rate [1, 2]. However, hypereutectic aluminum–silicon composites produced great automotive significance from the latest manufacturing methods due to their excellent wear and physical properties [3]. Even though adding of Si particles in molten metal possesses some difficulties like poor dispersion and size due to increased surface area [4], the poor dispersion and size problems are

---

M. P. Naik (✉) · K. T. B. Padal  
Andhra University, Visakhapatnam, Andhra Pradesh 530003, India

ousted by choosing the latest production processes [5]. Yuan et al. conducted experiments on AlSi composite and revealed that the microstructure and hardness of the alloy are substantially enhanced by UV-assisted producing course [6]. Sahu et al., in their examination, clarified that the metal matrix characteristics and added nanoparticles rely upon the stirring criterion of the manicuring techniques [7]. The investigations of Hekmat et al. [8] detailed that the composite microstructure is better for an excess cooling differentiated to the reduced cooling rate. Additionally, Ramesha et al. [9] played out a progression of investigations by changing ZrSiO<sub>4</sub> particle weight percentages and presumed that the stir casting course significantly improved mechanical properties. So, the manufacturing of hypereutectic AlSi composite with the mechanical stir process route improves the mechanical and microstructures characteristics [10–12].

Further, many researchers continued their experiments by adding ultrasonic vibration to the mechanical stir casting technique. Poovazhagan et al. [13] described their experimental results that the tribo-mechanical characteristics of Al composite are broadly enhanced by UV-treated manufacturing course [14]. Numerous scholars explained that the squeeze casting process enhances the AlSi composite characteristics distinguished from the usual methods such as sand and stir casting [15–18]. Yuan-Ji Shi et al. described by their experiments that squeeze cast AlSi composite improves mechanical and microstructure characteristics significantly [15, 16]. However, the study carried on by treating the mold with UV with a squeeze casting method. Wei Dai et al., by their experiments, described that the grain diameter was shortened with the raised load, and notable developments in the physical characteristics were observed with the excess temperature [17].

Moreover, Chattopadhyay et al. described that the even distribution and less porosity and uniform size of silicon carbide are achieved by the stir–squeeze casting method [19, 20]. Besides, Tirth et al. [21] reported that the increased load and heat treatment enhance the mechanical properties significantly. So it is apparent that the rapid solidified hypereutectic AlSi composites produced by the stir–squeeze casting method with T-6 have superior physical and wear characteristics distinguished to the usual manufacturing processes [22–31].

By the above references, it is apparent that no one investigated the effect of UV-assisted stir–squeeze process on tensile and hardness characteristics of AlSi<sub>24</sub>Cu<sub>3.8</sub>Mg<sub>1</sub> alloys. Accordingly, the current study explores the effect of UV-assisted stir–squeeze casting with the T-6 condition process on mechanical and microstructural characteristics of rapid solidified AlSi alloys.

## 2 Materials and Methods

The manufacturing of AlSi<sub>24</sub>Cu<sub>3.8</sub>Mg<sub>0.8</sub> composite (Table 1) is carried out by (Fig. 1) UV-assisted stir–squeeze casting (UVSS) process; however, in starting part, the composite is produced by using UVS coming after it was carried on by squeeze casting method.



**Table 1** AlSi composite chemical composition

Alloy	Production process	Chemical composition (wt%)			
		Si	Cu	Mg	Al
AlSi24	UVS and UVSS	24	3.8–4	0.8–1	Balance

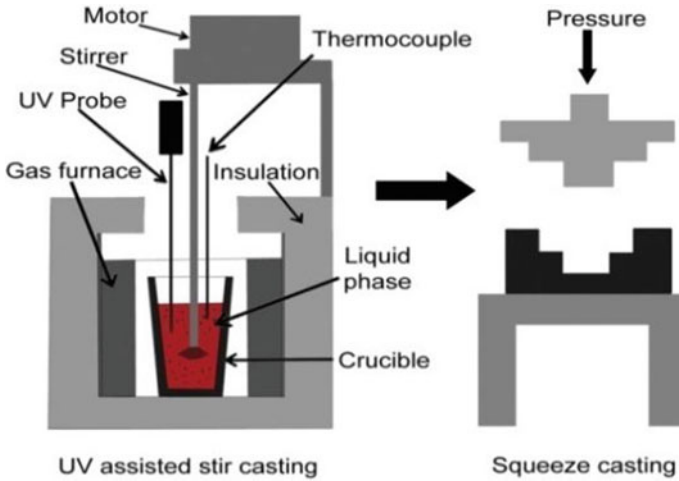


**Fig. 1** Ultrasonic vibration-assisted stir–squeeze casting

The method starts with liquefying the Al and Cu plates in a crucible. When the composite was melted (1200 °C), it was again cooled to 750 °C for stirring. Preheated Si and Mg powders were added into the mechanically stirred composite by keeping up the 300 rpm for 15 min. The composite was heated again (1200 °C) and grasped for 20 min. Next, the liquid composite was dealing with ultrasonic vibration about 5min for the distribution of Si powder. After UV-assisted stir casting process completed, the melted composite was discharged into a 200 °C heated die, and then squeeze casting activity was accomplished. Here, the composite was pressed at 150MPa and obtained a rapidly solidified AlSi composite billets. Further, the prepared AlSi24 composite is sustained through the hardening process under the T-6 process. The T-6 process includes heating the prepared billets at 450 °C for by 4 hours of soaking time; later the billets placed in water (not more than 50 °C) for rapid quenching and finally undergone through an artificial-aging process where the billets again heated at 165 °C and held for 4 hours and then cooled at room temperature.

The AlSi composites billets are sliced into 10 mm thick plates to investigate the microstructural and physical characteristics. However, the specimens are polished with SiC papers (900 grit size) coming after, applied 1 μm diamond paste for the final finishing of the AlSi composites. Specimens were cleaned with benzene to remove any scrap that may have been left during machining and polishing. EDS, SEM, and microstructural analysis are performed on the plates to reveal the composition and



**Fig. 2** Hardness test specimens

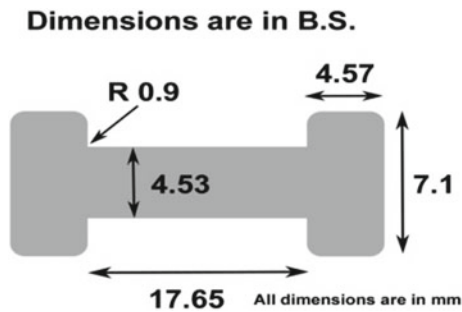


**Fig. 3** Tensile test specimen

microstructures of AlSi composite. The physical properties of the AlSi composites are investigated using Brinell (load=250 kgf, ball diameter = 5 mm) (Fig. 2) and Tensometer (20 N) (Fig. 3) analysis techniques.

### 3 Results and Discussion

#### 3.1 Microstructural Observations

Figures 4 and 5 represent metallurgical images of UVS and UVSS-T6 cast AlSi composite. However, image (Fig. 4) shows that the alloy prepared with UVS include uneven polygon forms and irregular dispersion of Si grains. Additionally, there is a significant enhancement seen in the distribution of Si grains and microstructure by UVSS-T6 fabrication process (Fig. 5). Compositional analysis (EDS) is (Table 2) evident that uneven polygonal elements shown in Fig. 6 are similar elements Si, Al, Mg, and Cu, as shown in Table 2. Images (Figs. 7 and 8) show the SEM micrographs of AlSi24 composites. From Fig. 7, it is evident that the UVSS-T6 process gives even

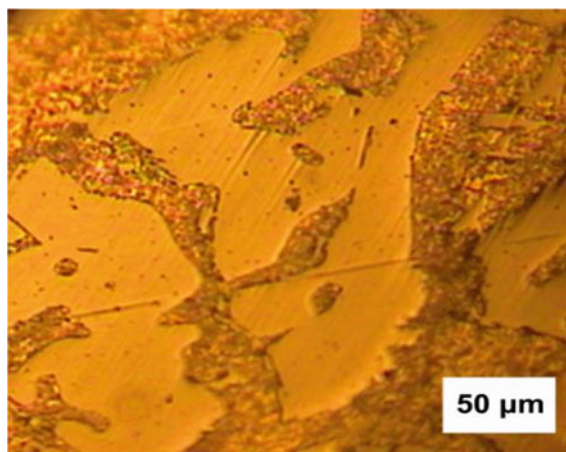


**Fig. 4** Microstructure of UVS-casted AlSi24 alloy

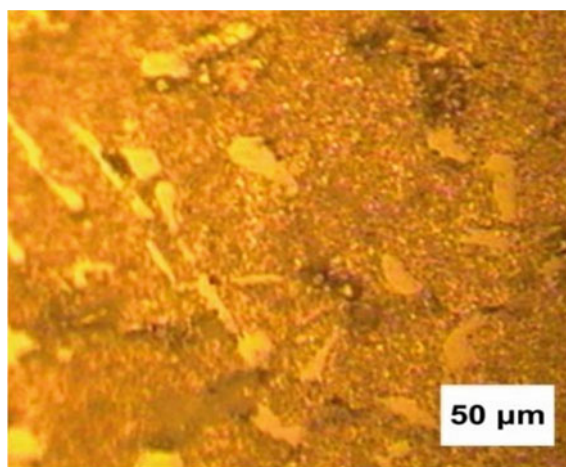


**Fig. 5** Microstructure of UVSS-T6-casted AlSi24 alloy

**Table 2** AlSi composite EDS analysis

S. No.	Composite	Elements (wt%)					
		Si	Cu	O	Mg	C	Al
1	AlSi24	21.47	3.57	0.89	0.51	5.86	67.7

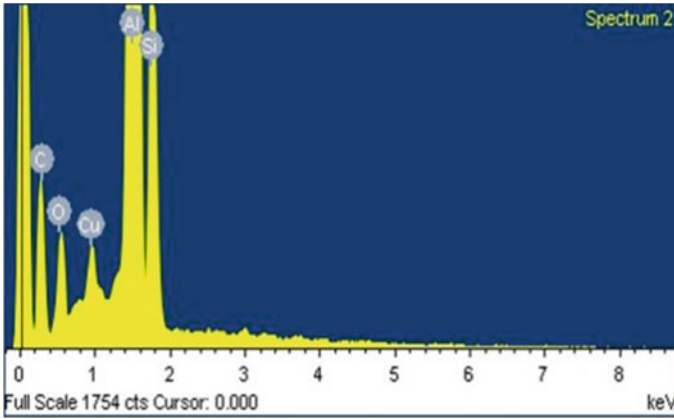


Fig. 6 EDS analysis of AlSi24 alloy

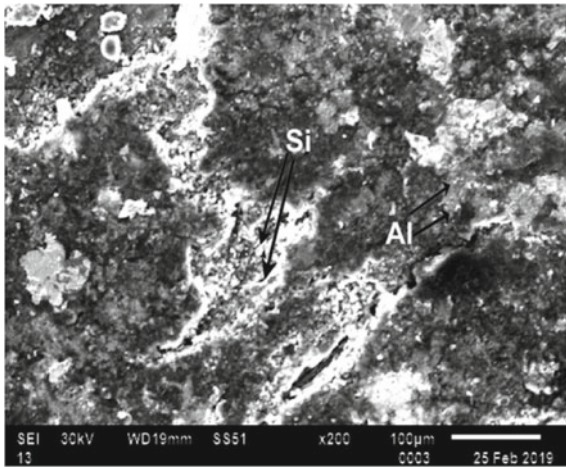


Fig. 7 SEM microstructure of UVS-casted AlSi24 alloy

size and uniform distribution of Si grains in the composite compared to the UVS-casted composites (Fig. 8). From the micrographs, it is evident that the UVSS-T6 casting method improves the grain size, low porosity, and grain distribution.



**Fig. 8** SEM microstructure of UVSS-T6-casted AlSi24 alloy

## 3.2 Mechanical Characterization

### 3.2.1 Hardness

The hardness results of the UVSS-T6 cast composites are enhanced and distinguished to the UVS cast composites due to the even size and dispersion of Si grains. Additionally, the UVSS-T6 method contributes a significant improvement in the hardening of AlSi24 composites. The study values of Fig. 9 show that the hardness of the AlSi24 composite is improved for UVSS-T6 manufactured samples.

### 3.2.2 Tensile Strength

The UTS, YS, and elongation results (ASTM E8/E8M) of AlSi24 composite at ambient air are added in Figs. 10 and 11. Images represent that the UVSS-T6 technique leads to superior strengthening effects for AlSi24 composite. Simultaneously, AlSi24 composite with UVSS-T6 attained high tensile values compared to UVS composites due to the existence of wholly distributed Si granules in the composite. However, the YS and UTS of composite AlSi24(UVSS-T6) are observed as 369 MPa and 387 MPa respectively, which are enhanced by 50% and 28% independently, if compared with the AlSi24(UVS) composite. Likewise, UVSS-T6 cast composites elongation percentage is enhanced by 20% in comparison with UVS composite.

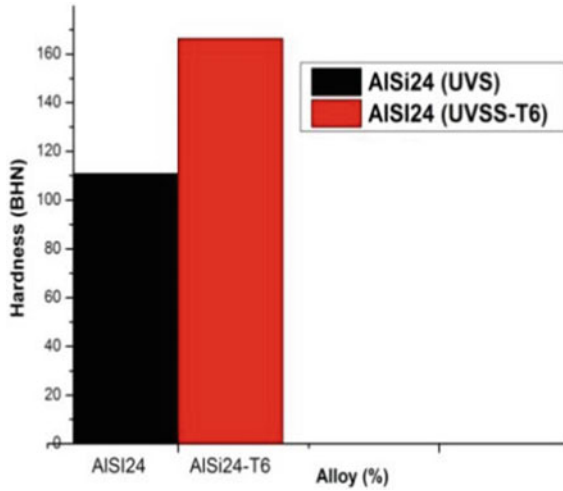


Fig. 9 Hardness values of AISi24 alloy

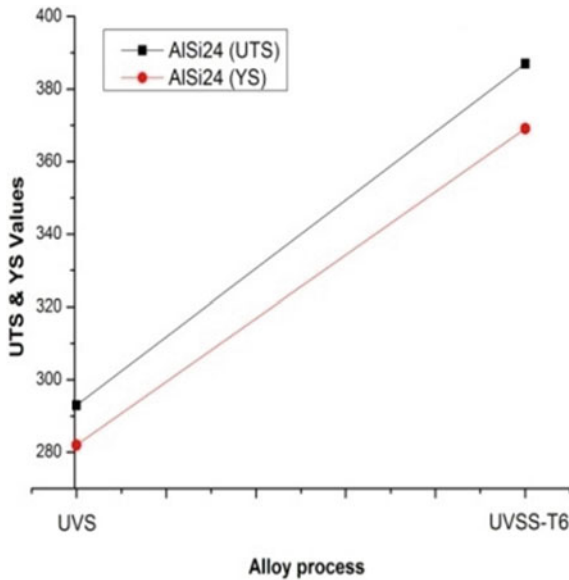
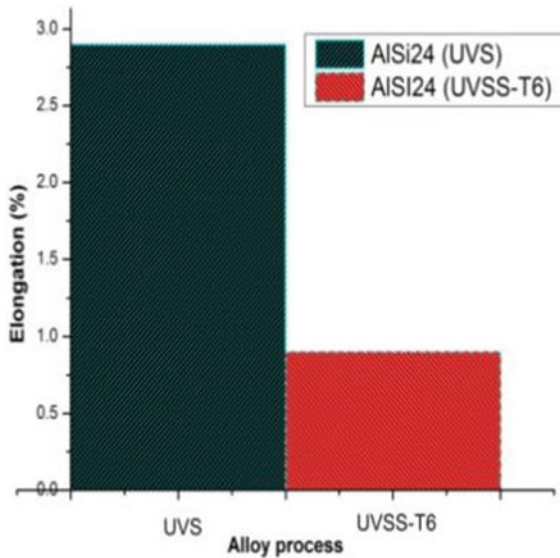


Fig. 10 UTS and YS values of AISi24 alloy

### 4 Conclusion

In this study, we investigated the hardness and tensile characteristics of the hypereutectic rapid solidified AISi24Cu3.8Mg0.8 composite under the T-6 condition, where



**Fig. 11** Elongation percentages of AISi24 alloy

UV-assisted stir-squeeze method is utilized for the production of AlSi composites. The values reveal that UVSS-T6 casting had a critical impact on microstructure enhancement. However, SEM, metallurgical microscope, and EDS analysis of composite reveal that the microstructure and Si dispersion enhanced significantly. Moreover, Tensometer and Brinell's hardness tester values explain that the mechanical characteristics of AlSi24Cu3.8Mg1 composites enhanced greatly by about 20–50%. This is evident that the UVSS process with T6 condition aided not only in the improvement of microstructure but also in tensile and hardness characteristics development.

## References

1. Chen G, Wan J, He N, Zhang H, Han F, Zhang Y (2018) Strengthening mechanisms based on reinforcement distribution uniformity for particle reinforced aluminum matrix composites. *Trans Nonferrous Met Soc China* 28(12):2395–2400. [https://doi.org/10.1016/S1003-6326\(18\)64885-X](https://doi.org/10.1016/S1003-6326(18)64885-X)
2. Al-Aqeeli N, Abdullahi K, Hakeem AS, Suryanarayana C, Laoui T, Nouari S (2013) Synthesis, characterisation and mechanical properties of SiC reinforced Al based nanocomposites processed by MA and SPS. *Powder Metall* 56(2):149–157. <https://doi.org/10.1179/1743290112Y.0000000029>
3. Ye H (2003) An overview of the development of Al-Si-alloy based material for engine applications. *J Mater Eng Perform* 12:288–297. <https://doi.org/10.1361/105994903770343132>
4. Canakci A, Varol T, Erdemir F (2016) The effect of flake powder metallurgy on the microstructure and densification behavior of B<sub>4</sub>C nanoparticle-reinforced Al–Cu–Mg alloy matrix

- nanocomposites. Arab J Sci Eng 41:1781–1796. <https://doi.org/10.1007/s13369-015-1969-2>
5. Kosnikov GA, Figovsky OL, Eldarkhanov AS (2014) Liquid phase production technologies of metal matrix composites (review). Int Lett Chem Phys Astron 6:69–77
  6. Hu Z., Wu G, Xu J, Mo W, Li Y, Liu W, Zhang L, Ding W, Quan J, Chang Y-W (2016) Dry wear behavior of rheo-casting Al–16Si–4Cu–0.5Mg alloy. Trans Nonferrous Met Soc China 26:2818–2829
  7. Sahu MK, Sahu RK (2018) Fabrication of aluminum matrix composites by stir process parameters. Adv Casting Technol. <https://doi.org/10.5772/intechopen.73485>
  8. Alireza Hekmat A, Frank A (2010) Effect of conventional and rheocasting processes on microstructural characteristics of hypereutectic Al–Si–Cu–Mg alloy with variable Mg content. J Mater Process Technol 210:767–775
  9. Ramesha V, Prasad TB, Nayak V, Neelakantha VL (2018) A study on mechanical properties of Al-17Si metal matrix composites. Mater Sci Eng 376:012100. <https://doi.org/10.1088/1757-899X/376/1/012100>
  10. Lloyd DJ (1989) The solidification microstructures of particulate reinforced aluminium/SiC composites. Compos Sci Technol 35:159–179
  11. Kolsgaard A, Brusethaug S (1993) Settling of SiC particles in an AlSi7Mg melt. Mater Sci Eng A 173:213–219
  12. Iseki T, Kameda T, Maruyama T (1984) Interfacial reactions between SiC and aluminium during joining. J Mater Sci 19:1692–1698
  13. Poovazhagan L, Kalaichelvan K, Sornakumar T (2015) Processing and performance characteristics of aluminum-nano boron carbide metal matrix nanocomposites. Mater Manuf Process 31(10):1275–1285. <https://doi.org/10.1080/10426914.2015.1026354>
  14. Wu S, Du Y, Lü S, Hu K, An P (2018) Nano-SiCP particles distribution and mechanical properties of Al-matrix composites prepared by stir casting and ultrasonic treatment. Res Dev China Foundry 15:203–209
  15. Shi YJ et al (2017) Effect of squeeze casting process on microstructures and flow stress behavior of Al-17.5Si-4Cu-0.5 Mg alloy. J Iron Steel Res Int 24:957–965
  16. Mao W, Zheng Q, Zhu D (2010) Rheo-squeeze casting of semi-solid A356 aluminum alloy slurry. Trans Nonferrous Met Soc China 20:1769–1773
  17. Dai W, Wu S, Lü S, Lin C (2012) Effects of rheo-squeeze casting parameters on microstructure and mechanical properties of AlCuMnTi alloy. Mater Sci Eng A 538:320–326. <https://doi.org/10.1016/j.msea.2012.01.051>
  18. Lin C et al (2018) Effects of high pressure rheo-squeeze casting on Fe-containing intermetallic compounds and mechanical properties of Al-17Si-2Fe-(0, 0.8) V alloys. Mater Sci Eng A 713:105–111. <https://doi.org/10.1016/j.msea.2017.12.050>
  19. Chattopadhyay J, Singh R, Prakash O (eds) (2017) Innovation in materials science and engineering, vol 2. [https://doi.org/10.1007/978-981-13-2944-9\\_7](https://doi.org/10.1007/978-981-13-2944-9_7)
  20. Sarfraz MH, Jahanzaib M, Ahmed W et al (2019) Multi-response parametric optimization of squeeze casting process for fabricating Al 6061-SiC composite. Int J Adv Manuf Technol 102:759–773. <https://doi.org/10.1007/s00170-018-03278-6>
  21. Tirth V, Ray S, Kapoor ML (2009) Effect of squeeze pressure on aging and mechanical properties of AA2218-5 Wt Pct Al<sub>2</sub>O<sub>3</sub> (TiO<sub>2</sub>) composites. Metall Mater Trans A 40:1246–1254. <https://doi.org/10.1007/s11661-009-9815-3>
  22. Malleswararao NDK, Niranjan Kumar IN (2019) Investigation of tribological behaviour of DLC coating on hypereutectic Al-Si alloys, a review. Mater Today: Proc 18(7):2581–2589. <https://doi.org/10.1016/j.matpr.2019.07.116>
  23. Prasad BK, Venkateswarlu K, Modi OP et al (1998) Sliding wear behavior of some Al-Si alloys: role of shape and size of Si particles and test conditions. Metall Mat Trans A 29:2747–2752. <https://doi.org/10.1007/s11661-998-0315-7>
  24. Prasad SV, Rohatgi PK (1987) Tribological properties of Al alloy particle composites. JOM 39:22–26. <https://doi.org/10.1007/BF03257531>
  25. Malleswararao NDK, Niranjan Kumar IN (2019) Mechanical characterization of rapid solidified alsicumg alloys by new CRSS casting method under T6 condition. Int J Innov Technol Explor Eng (IJITEE) 8(12):2897–2902. <https://doi.org/10.35940/ijitee.K1577.1081219>



26. Shanmugasundaram P, Subramanian R (2013) Wear behaviour of eutectic Al-Si alloy-graphite composites fabricated by combined modified two-stage stir casting and squeeze casting methods. *Adv Mater Sci Eng* 2013:1–8. <https://doi.org/10.1155/2013/216536>
27. Cantor B (1986) Fundamentals of rapid solidification. In: Sahn PR, Jones H, Adam CM (eds) *Science and technology of the undercooled melt*. Nato Asi Series (E: Applied Sciences), vol 114. Springer, Dordrecht. [https://doi.org/10.1007/978-94-009-4456-5\\_1](https://doi.org/10.1007/978-94-009-4456-5_1)
28. Malleswararao NDK, Niranjana Kumar IN (2020) Investigation of wear behavior of rapid solidified Al–Si alloys. In: Yang LJ, Haq A, Nagarajan L (eds) *Proceedings of ICDMC 2019*. Lecture Notes in Mechanical Engineering. Springer, Singapore. [https://doi.org/10.1007/978-981-15-3631-1\\_29](https://doi.org/10.1007/978-981-15-3631-1_29)
29. Kumar P, Wani MF (2017) Friction and wear characterization of hypereutectic Al-Si alloy/steel tribopair under dry and lubricated conditions. *J Tribol* 15:21–49
30. Gruzleski JE, Closset BM (1990) *The treatment of liquid aluminum-silicon alloys*. AFS, Illinois
31. Hatch JE (1984) *Aluminum: properties and physical metallurgy*. ASM, Ohio

# A Complete Study on Various Area Filling Strategies Used in Weld Deposition-Based Additive Manufacturing



Kishore Kumar Panchagnula  and Jayaprakash Sharma Panchagnula 

**Abstract** Achieving the optimal toolpath as well as obtaining the desired physical and geometrical properties for bulk metallic parts through weld deposition-based additive manufacturing (AM) is a challenging task. The current work aims in identifying the suitable toolpath for bulk weld deposition-based AM applications by comparing the various toolpath (eleven types) techniques. These toolpaths were evaluated based on the final layer thickness attained after face milling (skinning) operation, minimum amount material machined during the face milling, average hardness achieved, length of the heat-affected zone (HAZ) and the microstructural behaviour. Amongst the various toolpath patterns considered, hybrid toolpath (Single Contour Out with Hilbert In) is ideal for bulk deposition-based AM owing to its maximum final layer thickness and the minimum amount of material removed in skinning operation. On the other hand, it has been observed that Spiral Out to In toolpath pattern is inferior for bulk deposition-based AM. Additionally, the average grain size is presented for some of the toolpath patterns in the current article.

**Keywords** Additive manufacturing · Toolpath generation · Weld deposition-based AM · Mechanical and microstructural properties

## 1 Introduction

Nowadays, aerospace, automobile and biomedical industries are aiming at the functional components rather than prototyping. With the dedicated research in the fields of metallic additive manufacturing (AM), the same can be achieved in a shorter lead time. Several researchers tried to combine the traditional machining process with the weld deposition technique to enhance the surface quality of the arc-based AM

---

K. K. Panchagnula

Department of Mechanical Engineering, Vignana Bharathi Institute of Technology, Aushapur, Hyderabad, Telangana, India

J. S. Panchagnula (✉)

Department of Mechanical Engineering, SRM University-AP, Amaravati, India  
e-mail: [jayaprakash.p@srmmap.edu.in](mailto:jayaprakash.p@srmmap.edu.in)

components [1–4]. Karunakarn et al. proposed a technique named as hybrid layer manufacturing (HLM) to manufacture complex metallic components through arc-based AM with an industrially acceptable surface finish. The same is adopted in the current research in which a GMAW-based welding machine is retrofitted with a computer numerically controlled (CNC) milling centre to build complex metallic objects arc-based metallic AM. Manufacturing of thin-walled structures (component is comprised with a single weld-bead and multilayer) using arc-based weld deposition was extensively studied by few researchers [5]. Nevertheless, for dense components (component is comprised with multiple weld-beads with optimal stopover values and multilayer) manufactured using weld deposition-based metallic AM, in spite of intense research done, there is a technical gap when it comes to identifying an optimized area filling technique.

In multibead deposition process, identification of optimal step-over value between the successive weld-bead plays an important role which decides the dimensional accuracy and quality of the deposition. Several mathematical models have been proposed by the researchers to find the same for optimizing material utilization during the deposition process. By assuming the cross section of the deposited weld-bead as a circular arc, Aiyiti et al. proposed an overlapping model of two adjacently deposited weld-beads [6]. Similarly, Donghong et al. proposed an overlapping model named tangent overlapping model (TOM) to optimize the step-over value between the consecutive weld-beads by considering the cross section of the deposited bead as various trigonometric functions and parabola to provide stable overlap [7]. By approximating the cross section of the weld-bead geometry as a symmetric parabola, Suryakumar et al. had arrived at the optimal step-over value to be two-third (66% overlap) of the single weld-bead width [8]. The same is adopted throughout this work.

Ideally, for bulk metallic deposition, identifying the optimal toolpath is crucial and an ideal toolpath for the same should possess the following properties:

- Continuous without self-intersections,
- Minimum number of starts and stops,
- Easy to implement and minimum convoluted patterns.

Nevertheless, the toolpath techniques available for AM in the literature are unable to achieve the above-listed requirements. In addition to that, there is no one to one comparisons of these toolpath in detail in the literature. The present work aims in comparing various toolpath (including special toolpaths such as Hilbert and hybrid) techniques based on final layer thickness, minimum material removed during face milling (in other words amount of material removed in face milling operation) and the average hardness achieved. The author assumes that the final layer thickness is the deposited layer thickness after face milling operation and the same considered in the entire article. The various area filling techniques used in the current research, its merits and limitations, details of the experimental set-up, the experimental procedure followed and detailed microstructures for some toolpath patterns are explained in the subsequent sections. At last significant conclusions based on the experimentation and suitable toolpath strategy for various applications and situations are also presented.

## 2 Various Area Filling Techniques Used in AM

The various regularly used area filling patterns with its merits and limitations for AM are tabulated in Table 1. The preferred toolpath characteristics for the defect-free and uniform material deposition in weld-based AM are the minimum numbers of starts and stops, avoiding self-intersection, sharp turns and easy to implement. There has been numerous researches done to attain at a toolpath with above-mentioned features. Nevertheless, the toolpath techniques available for AM in the literature are unable to achieve the above-listed requirements. In addition to that, there is no one to one comparisons of these toolpath in detail in the literature. Hence, a comparison on various toolpath techniques based on minimum material removed during face milling, final layer thickness and average hardness achieved for each toolpath pattern is presented in the current article. These toolpaths are developed by an in-house developed MATLAB code, which converts the coordinates of the geometry into CNC G-code. In other words, the toolpath for a single layer consists of two or more path patterns with an appropriate connection. The same G-code is executed in the CNC controller for the weld deposition. In addition to that the average length of the heat-affected zone (HAZ) and average grain size for the significant toolpath are a part of this work.

## 3 Experimental Set-Up and Procedure

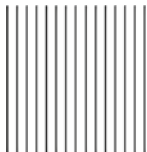
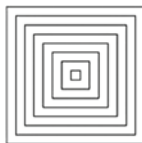

The weld deposition (GMAW weld deposition)-based AM experimental set-up is illustrated in Fig. 1. The experimental set-up is comprising of two major units; weld deposition (additive) unit and computer numerically controlled (subtractive) milling unit.

For performing the weld deposition, a mild steel (MS) plate is used as a substrate. In the current study, ER70S-6 is used as deposition material. During this processes, the electrode (filler wire) is surrounded by a gas mixture. The gas mixture ratios are 82% argon and 18% carbon dioxide. The weld deposition torch is attached close to CNC milling cutter for positioning the torch with the desired speed and feed for performing the continuous and smooth welding. These two units are working on a single station synchronously without disturbing its actual purpose.

Based on preliminary experiments, it is found that the optimal process parameters for uniform and continuous weld-bead are as follows:

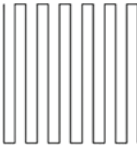
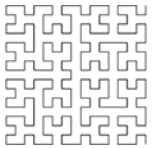
- Voltage ( $V$ ) = 19 V,
- Current ( $I$ ) = 135 Amps,
- Torch speed ( $T_s$ ) = 0.36 m/min,
- Wire feed ( $W_f$ ) = 4.5 m/min, and
- Contact tip to workpiece distance (CTWD) = 10 mm.

**Table 1** Description, merits and limitations of frequently used toolpaths for weld-based AM

Type of toolpath	Description	Merits	Limitations
 <p>Raster/Line</p>	<p>The toolpath is combinations of straight lines. In the beginning, tool moves horizontally left-to-right at a constant torch speed. At the end of each line, the welding torch returns to the left side and begin depositing the next scan line with suitable step-over value</p>	<p>(1) Simple to implement and suitable for any arbitrary geometry</p>	<p>(1) Too many weld stops and starts, which results in non-uniform weld-bead height and layer thickness                      (2) Since the toolpath is one-directional, the deposited part may have anisotropy in its mechanical and physical properties                      (3) Does not capture the slice outer boundary exactly, especially for those, geometries neither perpendicular nor parallel to the deposition direction. This is due to the discretization errors at the edges</p>
 <p>Contour</p>	<p>The path is produced by offsetting the boundary of the geometry towards Out to In or In to Out with suitable step-over value. Another name for this toolpath is contour parallel toolpath and as there is no straight forward formula for generating the same, mostly it was dealt with in the literature for machining applications [9]</p>	<p>(1) Suitable for any arbitrary geometry with pockets                      (2) Captures outer boundary of the slice accurately and as the toolpath is in several directions, there is minimum material and physical anisotropy in the object</p>	<p>(1) At the beginning and end, the path has too many discontinuities. This results in too many starts and stop                      (2) Achieving a uniform layer thickness is difficult</p>
 <p>Spiral</p>	<p>The spiral toolpath is generated by suitably connecting the offset contours. This toolpath starts from a point and proceeds either In to Out or Out to In in a continual spiral to trace the complete area. This type of curve is more suitable for some special geometrical models for faster toolpath generation [10]</p>	<p>(1) The path is continuous such that leading to the minimum number of starts and stops                      (2) Similar to the contour path captures the outer boundary of the slice accurately and as the path is continuous, material and physical anisotropy of the part is minimum</p>	<p>(1) Toolpath generation for arbitrary shapes and special cases like the geometries with islands or pockets is difficult</p>

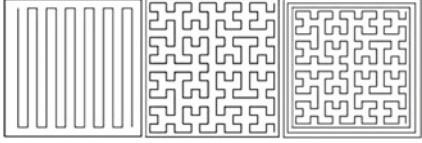
(continued)

**Table 1** (continued)

Type of toolpath	Description	Merits	Limitations
 <p>Zigzag</p>	<p>The path captures the entire area in an alternate fashion. This toolpath changes its direction abruptly left-to-right and/or right-to-left with a suitable step-over increment. This toolpath was a well-studied strategy for machining operations and the alternative name for this is directional parallel toolpath [11]</p>	<p>(1) Suitable for somewhat complex geometries and simple to implement                  (2) As the deposition happens alternative opposite directions, material and physical anisotropy of the part can be reduced                  (3) Since the toolpath is continuous, significant reduction in the number of stops and starts</p>	<p>(1) Similar to the raster toolpath, it does not capture the slice outer boundary exactly, especially for those, geometries neither perpendicular nor parallel to the deposition direction. This is due to the discretization errors at the edges</p>
 <p>Fractal curves (Hilbert)</p>	<p>In case of Hilbert curve (space filling curve), portion of the curve is repeated at various locations to area fill the entire region. Though the curve has many intricacies, the length of the curve is almost the same as zigzag and other conventional paths. So the same has been used cover a complete region in the current research</p>	<p>(1) Similar to contour and spiral toolpath pattern, the path is continuous, which results in material and physical anisotropy of the part is minimum</p>	<p>(1) The path is highly complex                  (2) Arriving at an optimal order of curve and generation of toolpath for complex contours is difficult</p>

(continued)

**Table 1** (continued)

Type of toolpath	Description	Merits	Limitations
 <p data-bbox="652 1495 676 1571">Hybrid</p>	<p data-bbox="217 326 382 573">These paths are generated by combining or in combination with more than one existing patterns to achieve a continuous and void-free toolpath. These toolpaths are much popular to leverage the advantages of various toolpath generations, minimize the errors and to enhance the geometrical accuracy</p>	<p data-bbox="217 590 652 979">(1) Ability to explore all the benefits of independent toolpaths and minimizing their drawbacks to capture all the geometric details accurately (2) Suitable for any complex geometry and the toolpath expanded in mostly all the directions, physical and material properties of the part tends to isotropic</p>	<p data-bbox="217 996 382 1571">(1) While shifting the toolpath pattern from one to another, especially in combination with Hilbert, identification of the curve order and the optimal step-over value, toolpath is difficult</p>

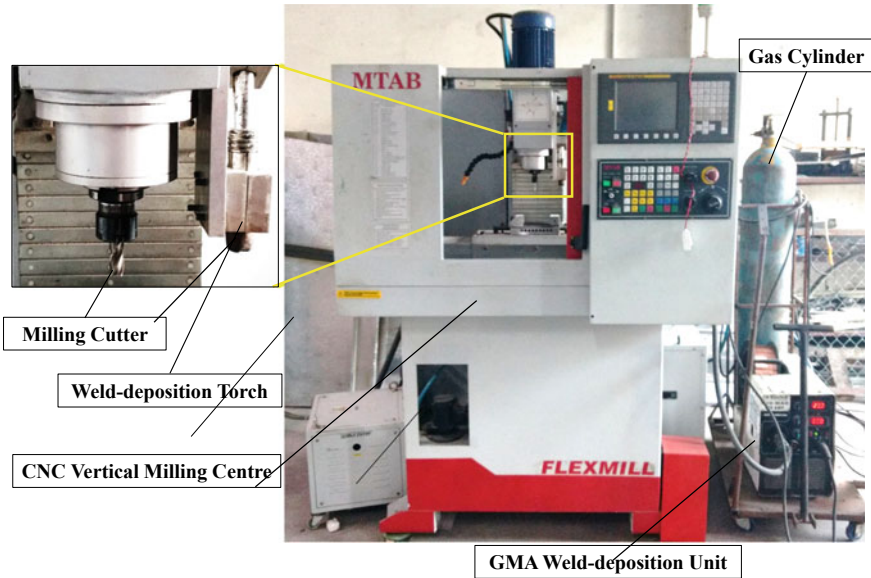


**Fig. 1** Experimental set-up for weld deposition

The weld-bead height ( $h$ ) and width ( $w$ ) obtained with the above-stated optimal process parameters are 3.80 mm and are 5.01 mm, respectively. The step-over (road width) value is considered as 3.30 mm ( $2/3$ rd of the single weld-bead width). A square geometry of 45 mm side is chosen for weld deposition to compare the various toolpath patterns which are listed in Table 1. After a layer is deposited with the given toolpath pattern, face mill skinning operation is performed to measure the final layer thickness and min. material removed during face milling. This face mill skinning operation helps in achieving the Z-accuracy for the next layer deposition. After face milling operation, the height of the layer (in other words layer thickness) is measured using a digital Vernier calliper. Instead of considering a single reading, three readings were taken at three different locations of the top flat surface and the average of those readings is considered as final layer thickness. To avoid the uncertainties in the readings, a similar procedure has been followed for all kinds of measurements in the entire research. The final layer thickness obtained for various toolpaths is mentioned in Table 2. After the layer thickness is measured, the samples are cut using wire electric discharge machine (EDM) and then mechanical polishing operation is performed. At final, polishing paste having an avg. grain diameter of diamond powders of the orders one to two microns is used. For the microstructural analysis, the polished samples are etched in Nital (5% nitric acid with 95% ethanol) solution. Microstructures of the deposited specimens are observed at various locations of the samples under the optical microscope (magnification ranges from 50 to 1000 $\times$ ). The hardness measurement is carried out using Rockwell hardness tester. To ensure the hardness distribution across the machined surface, the hardness has been measured



**Table 2** One-to-one comparison of several toolpaths used in weld deposition-based AM

S. No.	Type of toolpath	Substrate weight (g)	Substrate + weld deposition weight (g)	Weight of the substrate + deposition after face milling (g)	Weight of the material skinned (g)	Layer height after face milling (mm)	Average hardness (HRB)	Outer boundary captured (yes/no)
1	Raster/line unidirectional	668	734	724	10	2.90	85.0	No
2	Raster/line bidirectional	662	730	716	14	2.88	85.4	No
3	Contour Out to In	660	726	716	10	2.71	86.0	Yes
4	Contour In to Out	664	734	722	12	2.68	84.3	Yes
5	Spiral Out to In	664	730	714	16	2.64	81.3	Yes
6	Spiral In to Out	666	732	720	12	2.83	83.3	Yes
7	Zigzag	652	718	708	10	2.91	85.6	No
8	Hilbert	664	730	716	14	2.84	87.0	No
<i>Hybrid toolpaths</i>								
9	Contour Out + Zigzag In	670	736	722	14	3.00	85.0	Yes
10	Single Contour Out + Hilbert In	666	740	731	9	3.04	88.6	Yes
11	Three Contours Out + Hilbert In	660	740	725	15	3.02	88.0	Yes

**Table 3** Average length of HAZ and average grain size for some toolpath patterns

S. No.	Type of toolpath	Average HAZ length ( $\mu\text{m}$ )	Average grain size ( $\mu\text{m}$ )
1	Spiral Out to In	1372	9.28
2	Single Contour Out + Hilbert In	904	8.13
3	Contour In to Out	644	8.02
4	Contour Out to In	1589	8.21

at various locations of the specimen (at least 9 locations for each sample). In other words, hardness measurement at a single point is less significant. The average hardness values for the various toolpath patterns are also listed in Table 2. In addition to the above, the average length of the HAZ and the average grain size is also measured for some toolpath patterns and listed in Table 3.

## 4 Results and Discussion

As mentioned previously, for the comparison of several toolpaths patterns listed in Table 1, a square (45 mm side) geometry is considered for arc-based weld deposition. Figure 2 depicts the weld deposition (single layer) of listed toolpath patterns with the given area filling, and Fig. 3 illustrates the machined surface to achieve the plain smooth upper surface for the measurement of final layer thickness. Table 2 represents the comparison of several toolpaths used for weld deposition-based AM based on the amount of material deposited in grams, the weight of the material is removed (skinning) during the face milling operation and the final layer thickness.

Figure 4 illustrates the final layer thickness achieved for the various toolpath patterns. Similarly, Figs. 5 and 6 depict the amount of material removed in face milling (skinning) operation and measured average hardness values for the various toolpath patterns, respectively. Based on the final layer thickness achieved and the amount of material removed in the face milling operation, the significant samples are identified and the same is considered for the microstructural study.

It has been observed from the experimentation that, the lowest final layer thickness (2.64 mm) and the maximum amount of material skinned (16 g) are from Spiral Out to In pattern. On the other hand, the highest final layer thickness (3.04 mm) and the minimum amount of material skinned (9 g) are from Single Contour Out with Hilbert In pattern and both are considered for the microstructural study. In addition to the above-mentioned toolpath patterns, Contour Out to In and Contour In to Out are also considered for the microstructural study. As described previously, after the layer thickness is measured, the sample size on 10 mm in length at the centre of the deposited layer was considered in microstructural studies and the same was cut using wire EDM along the deposition direction and then polished using polishing paste. Figure 7 shows the cut hot mounted specimen with the region of interest for

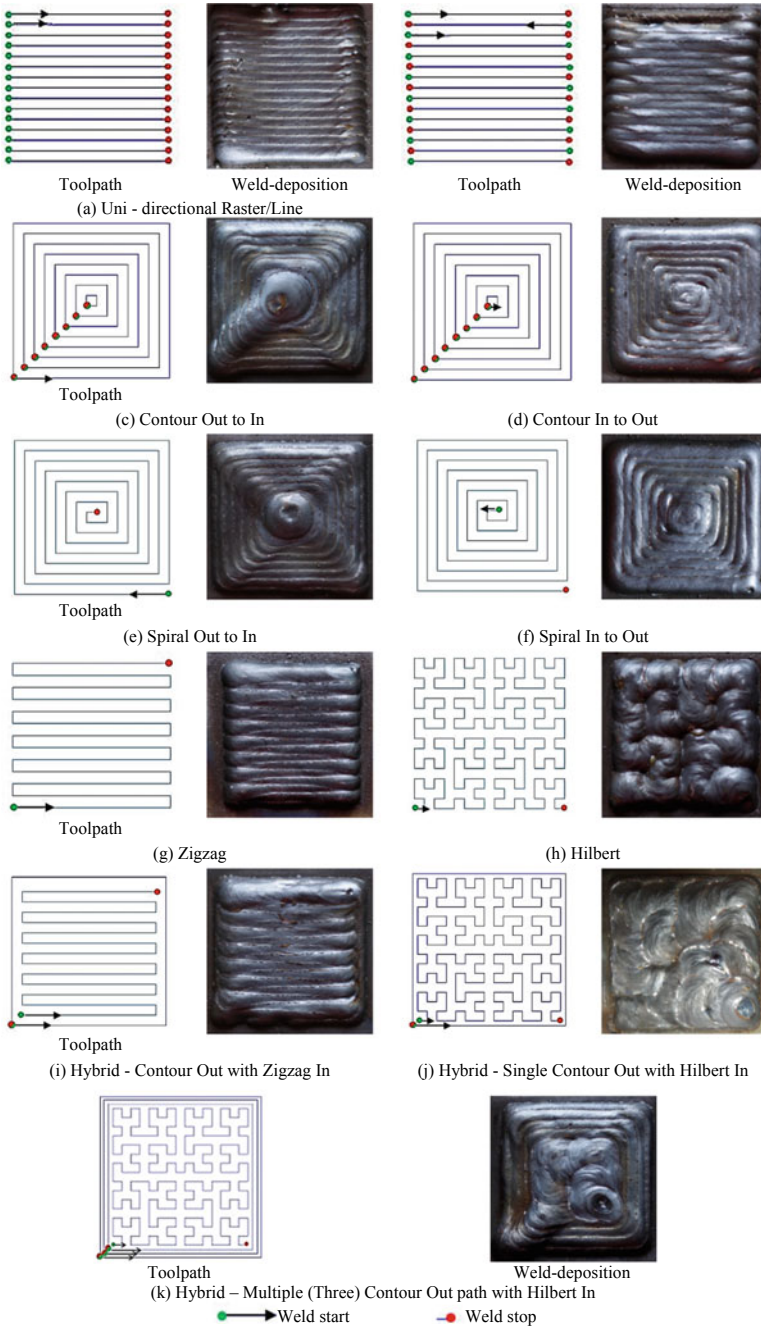
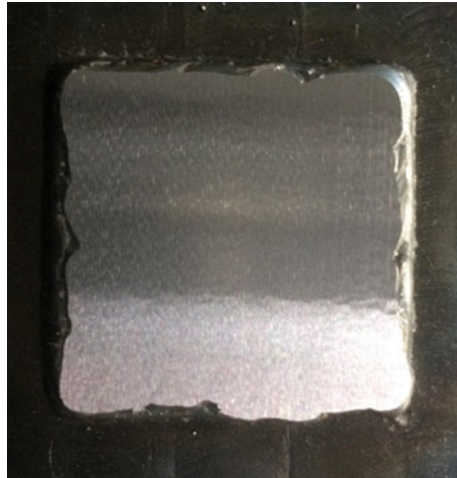
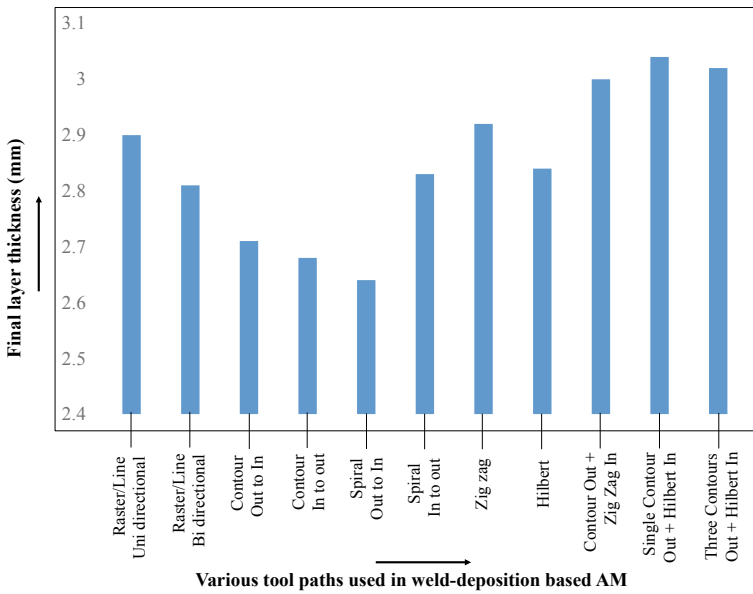


Fig. 2 Various toolpaths used in weld deposition-based AM



**Fig. 3** Face milled surface for final layer thickness measurement



**Fig. 4** Final layer thickness (mm) achieved for the various toolpath patterns used in weld deposition-based AM

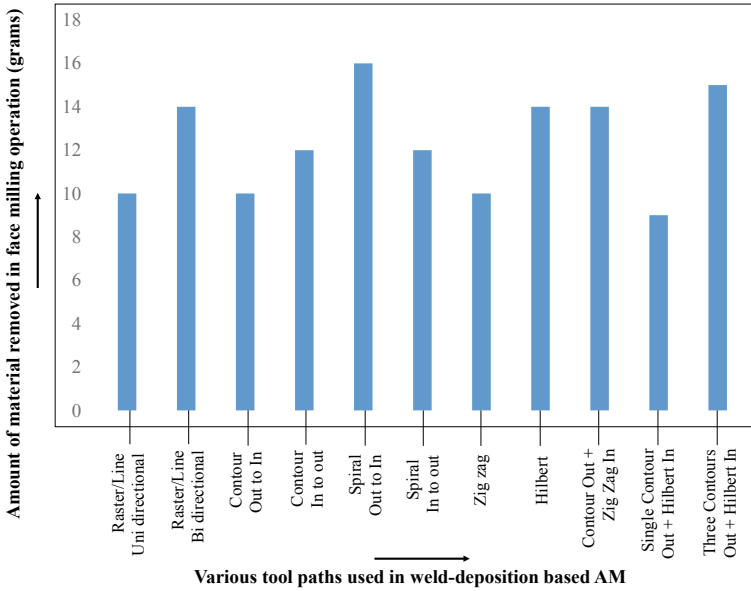


**Fig. 5** Amount of material removed (in grams) in face milling operation for the various toolpath patterns used in weld deposition-based AM

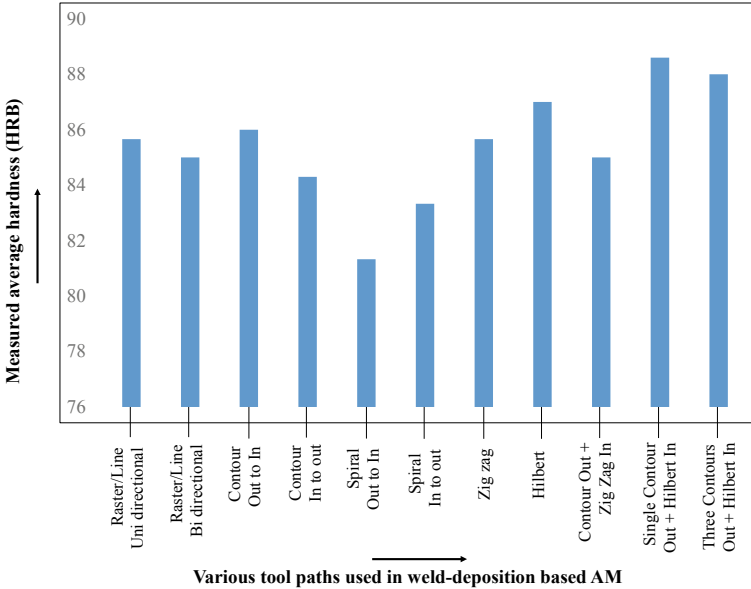


**Fig. 6** Measured hardness (HRB) values for the various toolpath patterns used in weld deposition-based AM

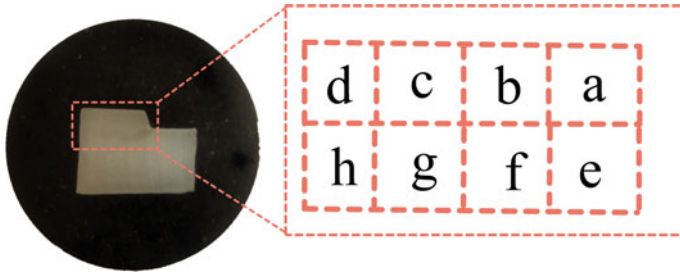


**Fig. 7** Region of interest for microstructural observation in a sample

microstructural observation. Although Fig. 7 depicts the region of interest for Spiral Out to In pattern for remaining toolpath patterns, the same procedure is followed. From Fig. 7 it is clear that the region 'a' to region 'd' is weld deposition portion and region 'e' to region 'h' is HAZ. For observing the microstructures of the samples, Nital is used as an etchant. From the microstructures, it is observed that the entire sample is the mixture of ferrite and pearlite phases with diverse grain sizes.

Ferrite appears grey colour, pearlite appears dark (Black colour). From the available literature, it was found that, for low carbon steels, phase transition takes place from austenite to ferrite subjected to the gradual cooling to atmospheric temperature [12–15]. The same has been observed in the current research. However, the phase change may also be affected by the cooling rate. It is also observed from the microstructures that the samples approximate composition (in percentage) 75% of ferrite and 25% of pearlite. The percentage of ferrite and pearlite has been identified using IMAGEJ software, and Fig. 8 depicts the solid solution of ferrite and pearlite for low carbon steel.

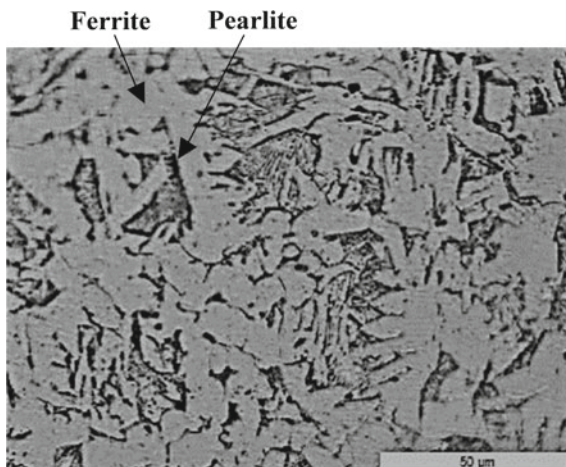


**Fig. 8** Microstructure of low carbon steel with ferrite and pearlite

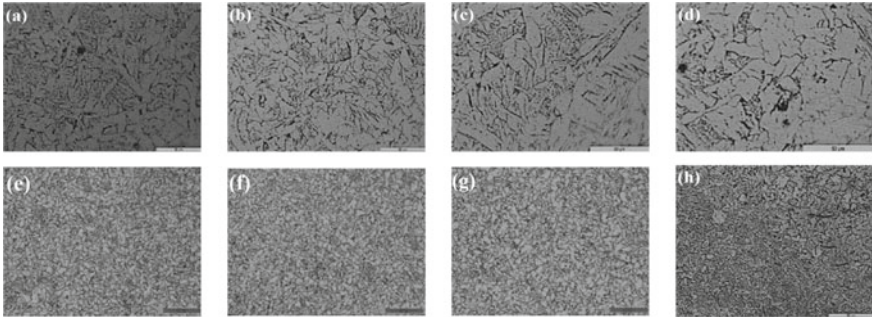


**Fig. 9** Microstructure of Spiral Out to In pattern at several locations of region of interest (RoI)

Through visual inspection, the ferrite phase has sharp and irregular shaped boundaries. The grey colour ferrite grains indicate that more amount of ferrite is present, which generally records less hardness value than pearlite. It has been observed from the microstructures that the percentage of ferrite and pearlite differ severely from 75–25% to 50–50% in the HAZ portion which results in an increase in the hardness in HAZ; except in hybrid (Single Contour Out with Hilbert In) toolpath pattern. The reason for the same is slow cooling after the weld deposition because of the virtue of the toolpath. It has been observed from the microstructures that, Contour In to Out possess high amount of pearlite owing to its fast cooling rate. From the above discussion, it was found that the average hardness of the deposited parts is varying with the toolpath pattern. From the microscopic analysis, ferrite–pearlite structure is identified in the deposited specimens and the hardness of the specimen is indirectly proportional to the percentage of ferrite in ferrite–pearlite composition. This reinforces the hypothesis that the properties of the weld-deposited parts can be controlled in a localized manner by changing the toolpath pattern or area filling technique. The length of the HAZ and the grain size is measured using an optical microscope at various locations of the specimen. The average value of the length of the HAZ and the average grain size values are listed in Table 3. Figure 9 illustrates the microstructure of Spiral Out to In pattern along the deposition direction at various locations of the sample including HAZ. Likewise, Figs. 10, 11 and 12 depict the microstructures of (at the region of interest) for Single Contour Out with Hilbert In, Contour Out to In and Contour In to Out, respectively.

According to Hall–Petch relation, the highest strength (theoretical strength) can be achieved by reducing grain size. In other words, hardness of the given material is inversely proportional to its grain size of the same. In agreement with the above statement, Spiral Out to In toolpath pattern may possess with lowest yield strength in comparable with the other toolpath patterns.

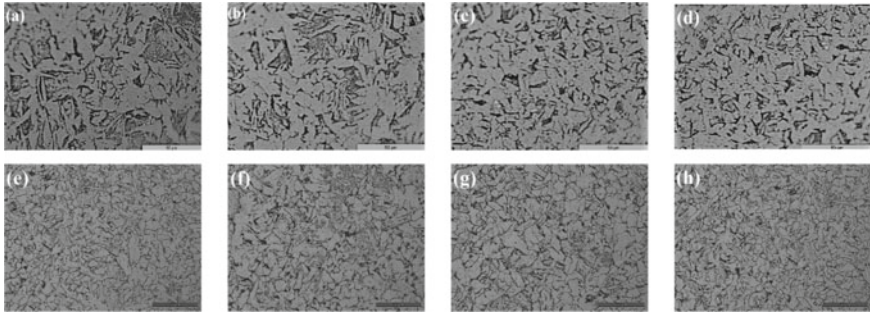


**Fig. 10** Microstructure of Single Contour Out with Hilbert In pattern at several locations of region of interest (RoI)

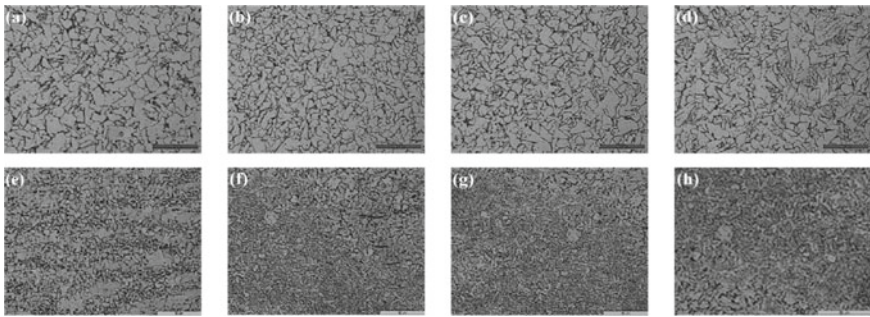


**Fig. 11** Microstructure of Contour Out to In pattern at several locations of RoI (Region of Interest)

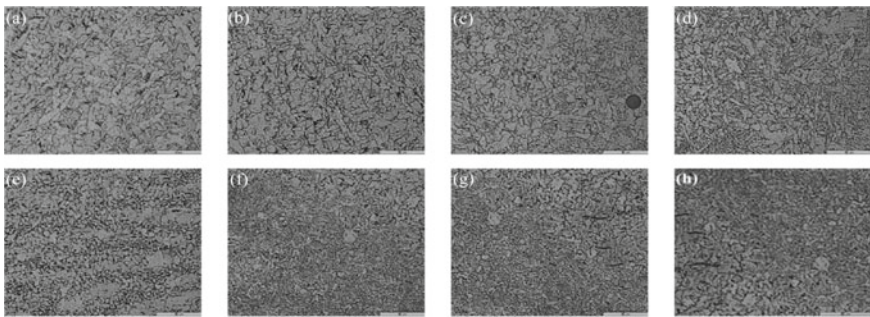


**Fig. 12** Microstructure of Contour In to Out pattern at several locations of RoI (Region of Interest)



## 5 Conclusions

The deposition path strategy selection has significant importance in arc (weld deposition)-based AM. The several toolpath patterns available for weld deposition-based AM, its advantages and limitations are explained in details in the current article. A square (45 mm side) geometry is chosen for realization of weld deposition to compare the several toolpath patterns. A weld deposition-based metallic additive manufacturing workstation (welding torch is retrofitted with a CNC milling centre) is used for realizing the same. Further, one-to-one comparison of these toolpath patterns in various aspects is also presented in detail. The results presented in the current article provide the necessary information for the selection of toolpath for bulk weld deposition-based AM. Based on the experimental results and the observations, the following conclusions are drawn:

- The hybrid toolpaths such as Contour Out with Zigzag In, Single Contour Out with Hilbert In and three Contours Out with Hilbert In capture the outer boundary accurately and also provides maximum final layer thickness. The values of the same are as follows:
  - (a) 3.00 mm for Contour Out with Zigzag In,
  - (b) 3.04 mm and 3.02 for Single Contour Out with Hilbert In and
  - (c) Three Contours Out with Hilbert In, respectively.
- Hilbert curves In and Contours Out registers the highest hardness values (HRB 87.0 for Hilbert, HRB 88.6 for Single Contour Out with Hilbert In and HRB 88.0 is for three Contours Out with Hilbert In).
- The layer thickness after face milling operation and the average hardness values of raster unidirectional, raster bidirectional and zigzag are almost identical. At the same time, the outer boundary of the geometry is not completely captured in all three toolpath patterns.
- Single Contour Out with Hilbert In requires the lowest material to be skinned (9 g) and on the other hand Spiral Out to In records highest amount of material to be skinned (16 g) during the face milling operation.
- The final layer thickness of Contour toolpaths and Spiral path patterns is comparable and also captures the outer profile precisely.
- Spiral In to Out records moderate final layer thickness after skinning operation, and the average hardness value than Spiral Out to In toolpath pattern. Also, Spiral In to Out records less material to be skinned than Spiral Out to In pattern.
- From the microscopic analysis, ferrite–pearlite structure is identified in the deposited specimens and the hardness of the specimen is indirectly proportional to the percentage of ferrite in ferrite–pearlite composition.
- The ferrite–pearlite composition for hybrid toolpath (Single Contour Out with Hilbert In) in HAZ does not alter significantly. This is due to the slow cooling after the weld deposition because of the virtue of the toolpath.
- It has been observed from the microstructures that, Contour In to Out possess a high amount of pearlite owing to its fast cooling rate and also reports both

lowest average HAZ value (644 microns) and the average grain size values (8.02 microns). The reason for the same is the uniform heat dissipation and cooling rate comparing with the other toolpath patterns.

- The properties of the weld-deposited parts can be controlled in a localized manner by changing the toolpath pattern or area filling technique.

The above-mentioned conclusions provide the basic information about the several toolpath patterns used for weld deposition-based additive manufacturing. The author proposes that the hybrid toolpath (Single Contour Out with Hilbert In) is ideal for bulk deposition-based AM. This fulfils most of the requirements for AM such as easy to implement, highest layer thickness, the minimum amount of material to be skinned after deposition, captures outer boundary accurately, avoids self-intersections, the minimum number of starts and stops and highest hardness comparing with the other toolpath patterns for bulk deposition-based AM. Nevertheless, its average length of HAZ and average grain size values are slightly higher than the Contour In to Out toolpath pattern.

## References

1. Song Y-A, Park S (2006) Experimental investigations into rapid prototyping of composites by novel hybrid deposition process. *J Mater Process Technol* 171(1):35–40
2. Simhambhatla S, Karunakaran KP (2015) Build strategies for rapid manufacturing of components of varying complexity. *Rapid Prototyp J* 21(3):340–350
3. Karunakaran KP, Suryakumar S, Pushpa V, Akula S (2010) Low cost integration of additive and subtractive processes for hybrid layered manufacturing. *Robot Comput-Integr Manuf* 26(5):490–499
4. Panchagnula JS, Simhambhatla S (2016) Inclined slicing and weld-deposition for additive manufacturing of metallic objects with large overhangs using higher order kinematics. *Virtual Phys Prototyp* 11(2):99–108
5. Kazanas P, Deherkar P, Almeida P, Lockett H, Williams S (2012) Fabrication of geometrical features using wire and arc additive manufacture. *Proc Inst Mech Eng Part B J Eng Manuf* 0954405412437126
6. Aiyiti W, Zhao W, Bingheng Lu, Tang Y (2006) Investigation of the overlapping parameters of MPAW-based rapid prototyping. *Rapid Prototyp J* 12(3):165–172
7. Ding D, Pan Z, Cuiuri D, Li H (2015) A multi-bead overlapping model for robotic wire and arc additive manufacturing (WAAM). *Robot Comput-Integr Manuf* 31:101–110
8. Suryakumar S, Karunakaran KP, Bernard A, Chandrasekhar U, Raghavender N, Sharma D (2011) Weld bead modeling and process optimization in hybrid layered manufacturing. *Comput-Aided Des* 43(4):331–344
9. Persson H (1978) NC machining of arbitrarily shaped pockets. *Comput-Aided Des* 10(3):169–174
10. Romero-Carrillo P, Torres-Jimenez E, Dorado R, Díaz-Garrido F (2015) Analytic construction and analysis of spiral pocketing via linear morphing. *Comput-Aided Des* 69:1–10
11. Park SC, Choi BK (2000) Tool-path planning for direction-parallel area milling. *Comput-Aided Des* 32(1):17–25
12. Thijs L, Verhaeghe F, Craeghs T, Kruth JP (2010) A study of the microstructural evolution during selective laser melting of Ti–6Al–4V. *Acta Mater* 58(9):3303–3312
13. Hejrípour F, Binesh F, Hebel M, Aidun DK (2019) Thermal modeling and characterization of wire arc additive manufactured duplex stainless steel. *J Mater Process Technol* 272:58–71

14. Stützer J, Totzauer T, Wittig B, Zinke M, Jüttner S (2019) GMAW cold wire technology for adjusting the ferrite–austenite ratio of wire and arc additive manufactured duplex stainless steel components. *Metals* 9
15. Zhang XY, Wang KH, Zhou Q, Ding JL, Ganguly S, Marzio G, Yang DQ, Xu XF, Dirisu P, Williams SW (2019) Microstructure and mechanical properties of TOPTIG-wire and arc additive manufactured super duplex stainless steel (ER2594). *Mater Sci Eng A* 762

# Characterization and Optimization of Machining Parameters for High-Strength Steel



Gagandeep Garg, Bhaskar Thakur, and Satish Kumar Sharma 

**Abstract** During machining of die steels, better surface quality of machined surface and larger amount of material removal are the main concerns of the machinist. In present study, three important cutting parameters (depth of cut, feed rate and cutting speed) are varied as process parameters during turning of EN 24 steel with objectives to get minimum surface roughness (SR) and maximum material removal rate (MRR). Experiments are planned as per Taguchi's L9 orthogonal array with three parameters where each parameter is varied at three levels. Using analysis of variance (ANOVA), effect of the cutting parameters on the process responses is deduced and quantified. To validate the outcome of signal-to-noise ratio approach, confirmatory experiments were conducted at optimized levels of parameters and results for surface smoothness and material removal rate had improved by 41.88% and 51.14% as compared to initial settings of cutting parameters.

**Keywords** Machining · Surface roughness · High-strength steel · Material removal rate · Taguchi

## 1 Introduction

Owing to its high strength, EN24 steel is widely used for making dies in manufacturing industries [1]. Desired shape of die is given using both traditional [2–5] as well as non-traditional machining operations [6–8]. In small-scale industries or the applications where little bit compromise with precision is acceptable, conventional machining is given preference over non-conventional machining. Moreover, conventional machining is comparatively more economical for less complex jobs. Initial set-up cost is also lesser in case of conventional machining. In any machining

---

G. Garg · S. K. Sharma (✉)

Department of Mechanical Engineering, Thapar Institute of Engineering & Technology, Patiala, Punjab, India

B. Thakur

International Association of Engineers, Hong Kong, China

operation, selection and control of its cutting parameters is very important to obtain the desired results. In machining processes, better surface finish on workpiece is required for desired shape and its accurate dimensions. Moreover, larger MRR is also desired for economic machining. In machining of high-strength steel like EN24, it is a challenge for machinist to find out the optimized levels of machining parameters which gives better surface finish along with higher MRR. It is worth to mention here that the machinist have to do a trade-off between two for setting the optimized process parameters. This is because the set value of parameters for higher MRR will lead to poor surface finish and vice versa [2].

For few advanced and non-conventional processes, optimization of process parameters is proposed and reported in literature by many researchers such as fused deposition modelling-assisted investment casting [9], fused deposition modelling [10], electric discharge machining [11], travelling wire electrochemical spark machining [12], submerged arc welding [13, 14] and friction stir welding [15]. However, studies concerning optimization of conventional machining process parameters, specifically for die steels, are reported very scantily in literature or have different objectives such as optimization with two levels of process parameters [16], considered different process outcomes [17, 18].

Therefore, objective of present experimental investigation is to fulfil the demand of modern industry to machine the high-strength steel like EN24 at low cost and with high quality.

To provide a sustainable solution for the problem, scientific approach is a necessity as it ensures a wide acceptance to the results of the investigation. Therefore, in this study, Taguchi method is used in its totality including its orthogonal array approach for experimentation and ANOVA test to quantify the contribution of process parameter on process output measures [6]. Quality approach of Taguchi in terms of signal-to-noise (S/N) ratio is also applied to find out the optimal level of process parameters for desired outcome of machining operation [7].

From the literature, most effective and influencing process parameters of machining known as cutting parameters (depth of cut, feed rate and cutting speed) are selected and varied at three levels. In the present investigation, experiments are conducted on EN 24 steel which is a high-strength grade of die steel category. As process outcome, SR and MRR are measured and calculated, respectively. To ensure the dimensional accuracy by limiting the human intervention, CNC turning machine is used. Other process parameters such as coolant condition and tool geometry which can also disturb the surface quality and MRR are kept at optimized conditions as per the experience of machinist and are kept constant for all experiments.



**Fig. 1** CNC lathe machine used in study

**Table 1** Chemical composition of EN 24 steel

Element	Ni	Cr	Mn	Mo	Ti	Bi	Fe
Percentage of element	1.28	1.09	0.52	0.21	0.21	0.03	96.65

## 2 Materials and Methods

### 2.1 Material and Machine Selection

For present study, EN24, a special grade of hard steel is selected as it have high hardness and wear resistance, therefore, more suitable for die making. EN 24 steel rod of 25 mm diameter and 70 mm length was turned over a length of 50 mm on CNC lathe (EMCO PC TURN 345 II), (refer Fig. 1) having maximum speed 5000 RPM and 6.7 kW power with FANUC control. CNC machine is selected for accurate machining by eliminating any operator specific deviation. As in CNC machining, quality of machined surface and production rate are not dependent on the skill of the operator. Moreover, for better output and smooth process, carbide inserts were used for machining of EN24 steel. Chemical composition of EN24 steel used as work material is given in Table 1.

### 2.2 Selection of Process Parameter

In present investigation, three cutting parameters, depth of cut, feed rate and cutting speed are selected as process input variables. Selection of these parameters is done

**Table 2** Cutting parameters and their levels

Factors	Parameters	Unit	Level 3	Level 2	Level 1
C	Depth of cut	mm	0.75	0.50	0.25
B	Feed	mm/rev	0.16	0.12	0.08
A	Cutting speed	m/min	140	120	100

as per their importance and significant role during mechanism of machining operation as reported in literature and given theories of machining. In addition to that, for calculation of MRR, all these parameters in quantities are the requirement of the study. Level and their values are selected on the basis of the results of trial experiments. For experimentation purpose, the process parameters and their values at three levels are given in Table 2.

### 2.3 Measurement and Calculation of Machining Output

For any machining process, the quality of machined surface and production rate is two main concerns. As quality of machined surface is evaluated in terms of its finish and production rate is expressed in terms of MRR, therefore, SR and MRR are selected as output measures of machining process. The measurement of SR was performed by a ‘Talysurf’ surface roughness tester (refer Fig. 2) with a 2.5 mm sampling length and transverse speed of 0.3 mm/s. The measurement was repeated three times at different locations and average value (Ra in microns) is reported in

**Fig. 2** Set-up for ‘Talysurf’ roughness tester

the results, whereas MRR is calculated by the multiplication of cutting parameters (depth of cut, feed rate and cutting speed) and expressed in cm<sup>3</sup>/min.

### 2.4 Selection of DOE Approach

As Taguchi’s approach for design of experiments is very robust, systematic and economic as compared to other, therefore, Taguchi’s standard orthogonal array L9 design is used for designing of the experiments. Combination of levels of considered input parameters for each experiment is listed in Table 3 for each experiment. For optimization of process parameters, S/N ratio for SR and MRR is calculated as per the ‘smaller-the-better’ and ‘larger-the-better’ concept of quality characteristics as expressed in Eqs. 1 and 2.

The larger-the-better

$$S/N = -10\log_{10}\left(\frac{1}{n} \sum \frac{1}{y_i^2}\right) \tag{1}$$

The smaller-the-better

$$S/N = -10\log_{10}\left(\frac{1}{n} \sum y_i^2\right) \tag{2}$$

where  $Y_i$  is the output for the  $i$ th test in the trial,  $n$  = number of measurement in trial.

**Table 3** L9 orthogonal array for design of experiments with results for SR and MRR

Run no	Depth of cut (mm)	Feed rate (mm/rev)	Cutting speed (m/min)	Surface roughness (μm)	S/N ratio for SR	Material removal rate (cm <sup>3</sup> /min)	S/N ratio for MRR
1	0.25	0.08	100	1.953	-5.812	2.0	6.021
2	0.50	0.12	100	0.623	4.117	6.0	15.563
3	0.75	0.16	100	3.936	-11.900	12.0	21.584
4	0.50	0.08	120	0.280	11.057	4.8	13.625
5	0.75	0.12	120	0.472	6.530	10.8	20.669
6	0.25	0.16	120	1.482	-3.414	4.8	13.625
7	0.75	0.08	140	0.370	8.648	8.4	18.486
8	0.25	0.12	140	4.779	-13.546	4.2	12.465
9	0.50	0.16	140	5.143	-14.224	11.2	20.984



### 3 Results and Discussion

Experimental result for SR, MRR and their corresponding  $S/N$  ratio for each experiment is listed in Table 3. Moreover, ANOVA test was performed to see the significance of effect of each factor on individual response. Mean value of  $S/N$  ratio was calculated for each level of individual process parameter and used to predict the optimal combination of process parameter for both responses.

#### 3.1 ANOVA Results for SR and MRR

Results of ANOVA for SR and MRR are shown in Tables 4 and 5, respectively. From Table 4, it can be observed that order of process parameters for percentage contribution in ascending order in deciding the SR of the machined surface is C (depth of cut), B (feed rate) and A (cutting speed). Effect of cutting speed and feed rate variation on SR comes out to be almost equal.

However, results of ANOVA test showed that depth of cut has least role in controlling the SR. From ANOVA test results for MRR listed in Table 5, it is clear that depth of cut has dominating role in deciding the MRR during machining operation and it comes out to be 66.59% followed by feed rate (26.75%) and depth of cut (2.84%). Moreover, from the ANOVA results for both SR and MRR, another significant outcome is that role of external or noise factors in terms of error is more in case of SR as 25.07% as compared to 3.83% only in case of MRR. It can be understood from the mechanics of machining operation where many factors such as tool chatter,

**Table 4** ANOVA table for SR

Source	DF	Adj SS	Adj MS	F-value	P-value	Percentage contribution
Cutting speed	2	10.836	5.418	1.38	0.420	34.69
Feed rate	2	10.667	5.333	1.36	0.423	34.14
Depth of cut	2	2.012	1.006	0.26	0.796	6.44
Error	2	7.833	3.916			25.07
Total	8	31.241				

**Table 5** ANOVA table for MRR

Source	DF	Adj SS	Adj MS	F-value	P-value	Percentage contribution
Cutting speed	2	2.907	1.453	0.74	0.574	2.84
Feed rate	2	27.387	13.693	6.99	0.125	26.75
Depth of cut	2	68.187	34.093	17.39	0.054	66.59
Error	2	3.920	1.960			3.83
Total	8	102.40				

tool wear, machine structure and its rigidity, types of chips play very important role in controlling the surface finish of machined component.

### 3.2 Parametric Optimization for Surface Roughness

According to ‘signal-to-noise ratio’ approach, the term ‘signal’ represents desired outcome while ‘noise’ being undesirable. The outcome having highest *S/N* ratio is always desired. For SR, mean value of *S/N* ratio at all three levels of each process parameters is calculated and tabulated in Table 6.

The plot for mean *S/N* ratios for SR corresponding to each level of all three parameters is shown in Fig. 3. It is clearly evident from the graph that major effect on SR is primarily due to feed and cutting speed. Moreover, based on the results of mean *S/N* ratio at each level, the optimal level of process variables is determined for

**Table 6** Table of mean *S/N* ratios for SR

Level	Depth of cut (mm)	Feed rate (mm/rev)	Cutting speed (m/min)
1	-7.5918	4.6309	-4.5315
2	0.3166	-0.9673	4.7244
3	1.0927	-9.8461	-6.3753
Delta	8.6844	14.4770	11.0997
Rank	3	1	2

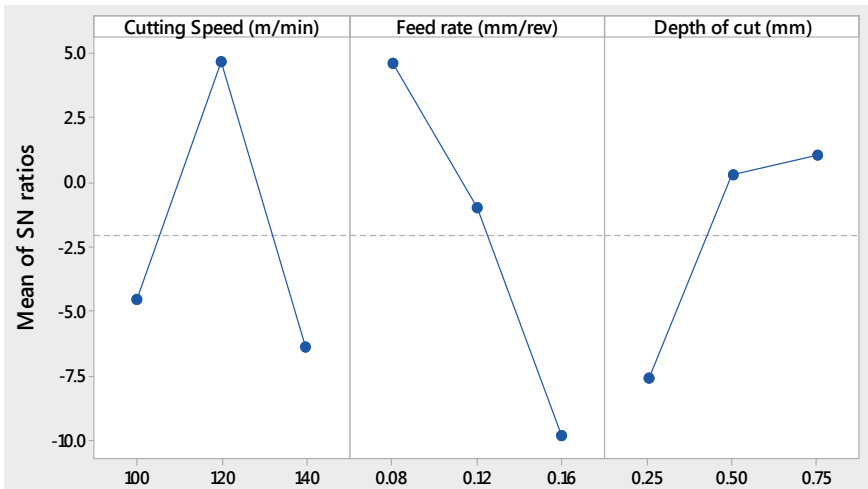


**Fig. 3** Plots of mean *S/N* ratios for SR

SR as follows: 0.75 mm (level 3) of depth of cut, 0.08 mm/rev (level 1) of feed rate and 120 m/min (level 2) of cutting speed.

### 3.3 Parametric Optimization for Material Removal Rate

Similarly, for MRR the mean value of *S/N* ratio at each level of every process parameter is listed in Table 7. According to Table 7, first rank is given to depth of cut. Feed rate and cutting speed have second and third rank, respectively. These results support the findings of ANOVA test.

The plot for mean *S/N* ratios for MRR corresponding to each level of all three parameters is shown in Fig. 4. The optimal level of each process parameter for larger MRR is as follows: 140 m/min (level 3) of cutting speed, 0.16 mm/rev (level 3) of feed rate and 0.75 mm (level 3) of depth of cut.

**Table 7** Table of mean *S/N* ratios MRR

Level	Depth of cut (mm)	Feed rate (mm/rev)	Cutting speed (m/min)
1	10.70	12.71	14.39
2	16.72	16.23	15.97
3	20.25	18.73	17.31
Delta	9.54	6.02	2.92
Rank	1	2	3

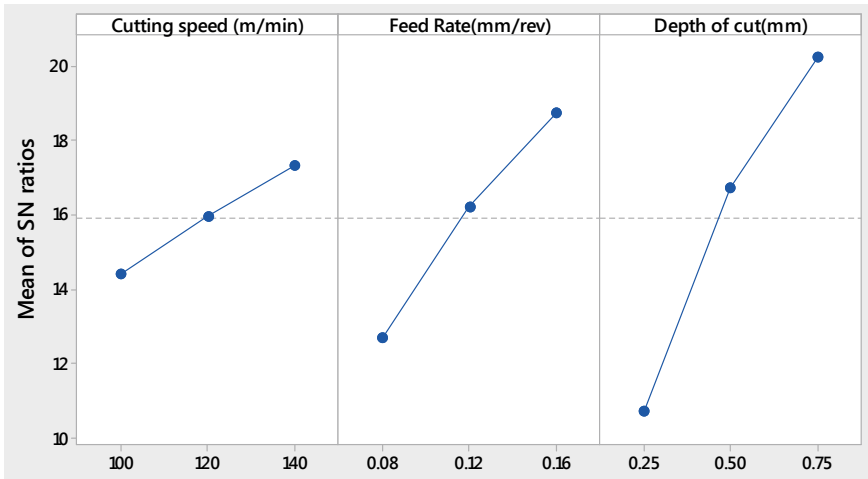


**Fig. 4** Plots of mean *S/N* ratios for MRR

**Table 8** Results of confirmatory experiments

Condition	Cutting speed (m/min)	Feed rate (mm/rev)	Depth of cut (mm)	SR (micron)	MRR (cm <sup>3</sup> /min)
Initial level	120	0.12	0.50	0.468	8.80
Optimal level for SR	120	0.08	0.75	0.272	–
Optimal level for MRR	140	0.16	0.75		13.30
Improvement in percentage				41.88	51.14

### 3.4 Confirmatory Experimentation

To verify the results of *S/N* ratio approach which was applied to predict the optimal level of each process parameter for smaller SR as well as larger MRR, confirmatory experiments were performed. Results of SR and MRR observed in confirmatory experiments are tabulated in Table 8 which are found much better than the results in experiments carried out at initial level of process parameters. Middle level value of each process parameter is taken as its initial level value. Initial level values of process parameters are those values which a machinist generally selects for machining of hard materials.

## 4 Conclusion

In present investigation, parametric characterization of machining operation on EN24 steel for SR and MRR is carried out. On the basis of the study findings, following conclusions were drawn from this study:

1. Taguchi approach comes out to be an appropriate statistical technique to understand the relationship between input and output parameters of machining operation. In this study, SR and MRR, both are found to be strongly influenced by cutting parameters.
2. From the percentage contribution, it is evident that cutting speed and feed rate are the most influencing process parameters for SR while feed rate and depth of cut are found to be the most deciding parameters for MRR.
3. Based on the signal-to-noise ratio analysis, the optimum process parameters for SR are as follows: 0.75 mm (level 3) of depth of cut, 0.08 mm/rev (level 1) of feed rate and 120 m/min (level 2) of cutting speed. Similarly, for MRR, optimal level is level 3 of each process parameter as 140 m/min (level 3) of cutting speed, 0.16 mm/rev (level 3) of feed rate and 0.75 mm (level 3) of depth of cut.

4. Results of confirmatory experiments for SR and MRR at suggested optimal levels of process parameters are found much better than the results in experiments carried out at initial level of process parameters. Improvement of 41.88% and 51.14% is observed in SR and MRR, respectively.
5. Findings of present study can be a guide work for machinist for machining the high-strength materials like EN24 for obtaining better surface finish and larger material removal.

## References

1. Das A, Patel SK, Hotta TK, Biswal BB (2019) Statistical analysis of different machining characteristics of EN-24 alloy steel during dry hard turning with multilayer coated cermet inserts. *Measurement* 134:123–141
2. Thakur A, Manna A, Samir S (2019) Performance evaluation of different environmental conditions on output characteristics during turning of EN-24 steel. *Int J Precis Eng Manuf* 20:1839–1849
3. Rizvi SA, Ali W (2017) Determination the effect of machining parameter on roughing operation of DIN 17210 steel using Taguchi Technique. *J Prod Eng* 20:7–12
4. Das A et al (2019) A comparison of machinability in hard turning of EN-24 alloy steel under mist cooled and dry cutting environments with a coated cermet tool. *Fail Anal Prev* 19:115–130. <https://doi.org/10.1007/s11668-018-0574-6>
5. Tyagi G, Bhaskar J, Singhal SK, Bartarya G (2019) Experimental study on machining of EN24 using minimum quantity lubrication. In: Shunmugam M, Kanthababu M (eds) *Advances in forming, machining and automation. Lecture Notes on Multidisciplinary industrial engineering*. Springer, Berlin. [https://doi.org/10.1007/978-981-32-9417-2\\_44](https://doi.org/10.1007/978-981-32-9417-2_44)
6. Payal H, Maheshwari S, Bharti PS, Sharma SK (2019) Multi-objective optimisation of electrical discharge machining for Inconel 825 using Taguchi-fuzzy approach. *Int J Inf Technol*. <https://doi.org/10.1007/s41870-018-0102-7>
7. Payal H, Sharma SK, Aakash, Kumar A, Kumar A, Himanshu (2019) Study of MRR and TWR in electric discharge machining of AISI D2 tool steel. In: Shanker K et al (eds) *Advances in industrial and production engineering, Lecture Notes in Mechanical Engineering*. [https://doi.org/10.1007/978-981-13-6412-9\\_8](https://doi.org/10.1007/978-981-13-6412-9_8)
8. Kumar A, Maheshwari S, Sharma C, Beri N (2010) A study of multi-objective parametric optimization of silicon abrasive mixed electrical discharge machining of tool steel. *Mater Manuf Process* 25:1024–6914
9. Singh S, Prakash C, Antil P, Singh R, Królczyk G, Pruncu CI (2019) Dimensionless analysis for investigating the quality characteristics of aluminium matrix composites prepared through fused deposition modelling assisted investment casting. *Materials (Basel)* 12(12):1907. <https://doi.org/10.3390/ma12121907>
10. Srivastava M, Maheshwari S, Kundra TK, Rathee S, Yashaswi R, Sharma SK (2016) Virtual design, modelling and analysis of functionally graded materials by fused deposition modeling. *Mater Today: Proc* 3(10):3660–3665
11. Prakash C, Singh S, Singh M, Antil P, Aliyu AAA, Abdul-Rani AM, Sidhu SS (2018) Multi-objective optimization of MWCNT mixed electric discharge machining of Al–30SiCp MMC using particle swarm optimization. In: Sidhu S, Bains P, Zitoune R, Yazdani M (eds) *Futuristic composites. Materials Horizons: From Nature to Nanomaterials*. [https://doi.org/10.1007/978-981-13-2417-8\\_7](https://doi.org/10.1007/978-981-13-2417-8_7)
12. Rattan N, Mulik RS (2017) Experimental investigations and multi-response optimization of silicon dioxide (Quartz) machining in magnetic field assisted TW-ECSM process. *SILICON* 9:663–673. <https://doi.org/10.1007/s12633-016-9521-x>

13. Sharma SK, Maheshwari S (2016) Multi-objective optimization of HAZ characteristics for submerged arc welding of micro-alloyed high strength pipeline steel using GRA-PCA approach. *J Manuf Sci Prod* 16(4):263–271. <https://doi.org/10.1515/jmsp-2016-0027>
14. Kumar A, Maheshwari S, Sharma SK (2015) Fuzzy logic optimization of weld properties for SAW using silica based agglomerated flux. *Procedia Comput Sci* 57:1140–1148. <https://doi.org/10.1016/j.procs.2015.07.403>
15. Ghangas G, Singhal S (2018) Modelling and optimization of process parameters for friction stir welding of armor alloy using RSM and GRA-PCA approach. *Mater Res Express* 6:026553. <https://doi.org/10.1088/2053-1591/aaed9b>
16. Motorcu AR (2010) The optimization of machining parameters using the Taguchi method for surface roughness of AISI 8660 hardened alloy steel. *Strojniški Vestnik—J Mech Eng* 56(6):391–401
17. Tzeng CJ, Lin YH, Yang YK, Jeng MC (2009) Optimization of turning operations with multiple performance characteristics using the Taguchi method and Grey relational analysis. *J Mater Process Technol* 209(6):2753–2759
18. Aslan E, Camuşcu N, Birgören B (2007) Design optimization of cutting parameters when turning hardened AISI 4140 steel (63 HRC) with Al<sub>2</sub>O<sub>3</sub> + TiCN mixed ceramic tool. *Mater Des* 28(5):1618–1622

# An Alternative Approach for Turning of Inconel 825: Feasibility Analysis of Process Parameters



Neel Sanghvi, Dhairya Vora, Jash Patel, and K. N. Vijayakumar

**Abstract** This paper is an attempt to design and configure a mathematical system to optimize a subtractive manufacturing process by considering the feasibility of the considered values of the inputs. A turning experiment consisting of 18 trials conducted with Inconel 825 is taken as a reference. The initial phase of the process consists of normalization of the input data so that a numerical analysis can be done. Linguistic input data is processed using a fuzzy logic system by considering three factors related to the type of tool used: tool cost, flank wear and the roughness of the machined surface. A normalization scheme based on feasibility is developed to process the numerical input data. Three multiple attribute decision-making methods (MADM methods): simple additive weighting, weighted product and technique for order preference by similarity to ideal solution (TOPSIS) are used to optimize the process. The results are tabulated and the first ranked experiment with the highest feasibility score, given by the three methods is the first alternative among the chosen combinations. It is very well observed that the optimization results obtained by the three methods are coherent.

**Keywords** Inconel · Turning · Machining · Optimization · Comparison · Feasibility · Manufacturing · TOPSIS · MADM · Super-alloy · Fuzzy · GRA

## 1 Introduction

Turning can be defined as a subtractive manufacturing process which is generally used for producing convex cylindrical surfaces. Similar to all machining processes, turning has a perpetual disadvantage that a large amount of energy is spent in removing the unneeded material. Many innovations have been developed to optimize the turning process by influencing the force interactions in the specific cutting zone. But various mathematical techniques like fuzzy logic, grey relational analysis and others attempt to optimize the turning process by considering the significance of the outputs. Thus,

---

N. Sanghvi (✉) · D. Vora · J. Patel · K. N. Vijayakumar  
Dwarkanadas J. Sanghvi College of Engineering, Vile Parle, Mumbai, India

the mathematical techniques optimize the machining process at the macrolevel and can contribute to efficient process planning. Therefore, it can be very well concluded that it is in the best interest of the manufacturing industry that new mathematical methods be developed to optimize machining process from the cost, energy and material perspectives. In this paper, the authors attempt the development of a mathematical method based on the significance of the values of the process parameters.

Studies conducted for optimization of machining processes generally have been focused on the performance characteristics like material removal rate, tool wear, surface roughness and others [1–4]. But it is important to understand that the cost of resources used to manufacture the product with the optimized performance characteristics is also important. In this paper, the authors have tried to develop an optimization scheme with respect to the input parameters (process parameters). A system to normalize the inputs is developed, when the inputs are in numerical form. When the inputs are in linguistic form, a fuzzy system is used to obtain the corresponding numerical normalized form. Data of an experiment of turning of Inconel 825 is taken as an example and the proposed concepts are explained. Vasudevan et al. [5] have performed an optimization of turning of Inconel 825 with PVD- and CVD-coated carbide tools for optimum material removal rate and surface roughness. It is important to understand at this point of time that this problem is a multiple attribute decision-making (MADM) problem where decision-making (selecting the inputs) is done with consideration of multiple attributes (Ra and MRR have been taken here). Rao [6, 7] has commented that MADM problems are normally discrete with a predetermined number of alternatives. It must be noted here that the MADM methods, namely SAW, WP and TOPSIS that have been used up to this point of time, have been generally used to optimize machining processes by considering the outputs of the process. But this paper serves to optimize a machining process by considering the feasibility of the various values of the inputs that are considered. The above-mentioned MADM methods are applied to the inputs, not to the outputs as is conventionally done.

### ***1.1 Simple Additive Weighting (SAW) Method***

This MADM method is one of the simplest and the input data used is in the normalized form to take care of the differences between the larger-the-better and smaller-the-better nature of the inputs. This method was given by Fishburn [8]. The normalized value of the inputs for each alternative is added to obtain an additive feasibility index (AFI) which will be a larger-the-better type of index to rank the overall feasibility of the alternatives



### 1.2 Weighted product (WP) method

This MADM method is simple to implement and the input data used is in the normalized form to take care of the differences between the larger-the-better and smaller-the-better nature of the inputs. This method was given by Miller and Starr [9]. The normalized value of the inputs for each alternative is multiplied, as opposed to added in SAW method, to obtain an multiplicative feasibility index (MFI) which will be a larger-the-better type of index to rank the overall feasibility of the alternatives.

### 1.3 TOPSIS Method

The technique for order preference by similarity to ideal solution (TOPSIS) was invented by Yoon and Hwang [10] based on the logic that the preferred choice must be the most distant from the negative ideal solution and at the shortest distance from the ideal solution. Umamaheswarrao et al. [11] have applied TOPSIS method to optimize inputs for turning of AISI 52100 steel. Sharma et al. [12] have implemented TOPSIS to identify and arrange in appropriate order the critical success factors for implementation of TQM in Indian Manufacturing Industry. Ahmed et al. [13] have implemented TOPSIS method for optimization of cryogenic drilling of the Ti-6Al-4V alloy.

## 2 Materials and Methods

The combinations of the values of inputs that are chosen for this experiment are based on the work done by Vasudevan et al. [5] Inconel 825 is taken as a workpiece material for the study presented as a metal of high industrial importance, with a wide range of applications in the chemical, nuclear and marine industries. Table 1 shows the details of the process parameters. The details of factors and inputs are shown in Table 2.

**Table 1** Details of process parameters [5]

Process parameters	Levels		
	One	Two	Three
Cutting tool insert	PVD	CVD	–
Cutting speed ( $N$ ) (m/min)	100	120	140
Feed rate ( $f$ ) (mm/rev)	0.075	0.15	0.225
Depth of cut (mm)	0.3	0.6	0.9

**Table 2** L18 array used for design of experiment

Expt.	Coded input				Absolute input			
	Type	Speed	Feed	RDOC	Type	Speed	Feed	RDOC
1	1	1	1	1	PVD	100	0.075	0.3
2	1	1	2	2	PVD	100	0.15	0.6
3	1	1	3	3	PVD	100	0.225	0.9
4	1	2	1	1	PVD	120	0.075	0.3
5	1	2	2	2	PVD	120	0.15	0.6
6	1	2	3	3	PVD	120	0.225	0.9
7	1	3	1	2	PVD	140	0.075	0.6
8	1	3	2	3	PVD	140	0.15	0.9
9	1	3	3	1	PVD	140	0.225	0.3
10	2	1	1	3	CVD	100	0.075	0.9
11	2	1	2	1	CVD	100	0.15	0.3
12	2	1	3	2	CVD	100	0.225	0.6
13	2	2	1	2	CVD	120	0.075	0.6
14	2	2	2	3	CVD	120	0.15	0.9
15	2	2	3	1	CVD	120	0.225	0.3
16	2	3	1	3	CVD	140	0.075	0.9
17	2	3	2	1	CVD	140	0.15	0.3
18	2	3	3	2	CVD	140	0.225	0.6

### 2.1 Consolidation of Input Data

Use of fuzzy logic to convert linguistic input into numerical input:

In a machining experiment which may be aimed at optimizing the inputs by checking the feasibility, some inputs may comprise of linguistic terms like tool type, coolant type and so on. For mathematical analysis, a numerical equivalent of the linguistic term is needed. Such conversion from linguistic to numerical feature if done arbitrarily will not be mathematically consistent. Hence, a fuzzy system must be used.

Two types are tools are considered, PVD coated and CVD coated [5]. It can be easily understood that the decision whether a particular type of tool is good or not depends on the magnitude of its properties, like wear and cost and roughness of machined surface. In this case, these three factors are considered, but for an in-depth analysis more properties can be considered. Thakur et al. [4] have concluded after a series of experiments that PVD-coated tools give lower surface roughness and lower flank wear compared to CVD-coated tools. Aliofkhazraei et al. [14] have concluded that PVD process is costlier compared to the CVD process. Hence, we assign numerical values (0.5 or 1) to the low or high value of each property depending on whether it was a higher-the-better or lower-the-better type. For example, surface

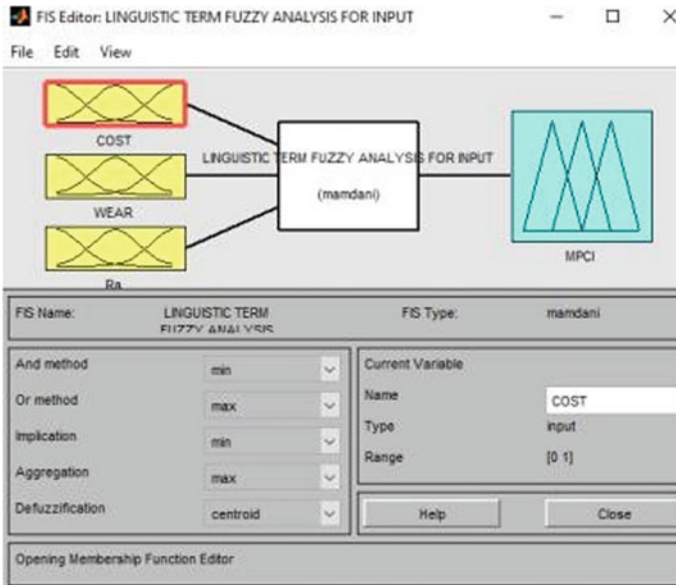


Fig. 1 Fuzzy inference system built on MATLAB

roughness (Ra) is a lower-the-better type of property and low Ra was assigned a value of 1 and high Ra was assigned a value of 0.5 (Figs. 1 and 2; Table 3).

A three input one output fuzzy inference system was built on MATLAB. Two membership functions were used for each input and output. Thus, a number of rules required for this system are equal to  $2^3 = 8$  (number of membership functions  $\wedge$  number of inputs). The mathematical formulation of the rules is a very important role in the optimization process for the three scenarios. The GRC input after the fuzzification will be related to one of the membership functions, 1 or 2. The category of the MPCI is equal to the weighted mean of the categories of the inputs, which had been approximated to the nearest integer. This process is elaborated with help of suitable example; the formulation of the second rule.

Weights given to Ra, wear, cost:

Weighted mean of the membership functions =  $(1/3) * 1 + (1/3) * 1 + (1/3) * 2 = 1.333$ .

This value has to be rounded to the nearest integer = 1.

Thus, if the cost is '1', the wear is '1' and the Ra is '2', the MPCI will be '1'. An MPCI of 0.727 is obtained for PVD and 0.5 for CVD-coated tools is obtained as the output. Thus, in this manner, a fuzzy system has been effectively used for converting the linguistic input ('PVD' or 'CVD') into a numerical input (0.727 or 0.5). It is worth mentioning here that Rao [15] has compiled a copious amount of previous research regarding fuzzy MADM problems.

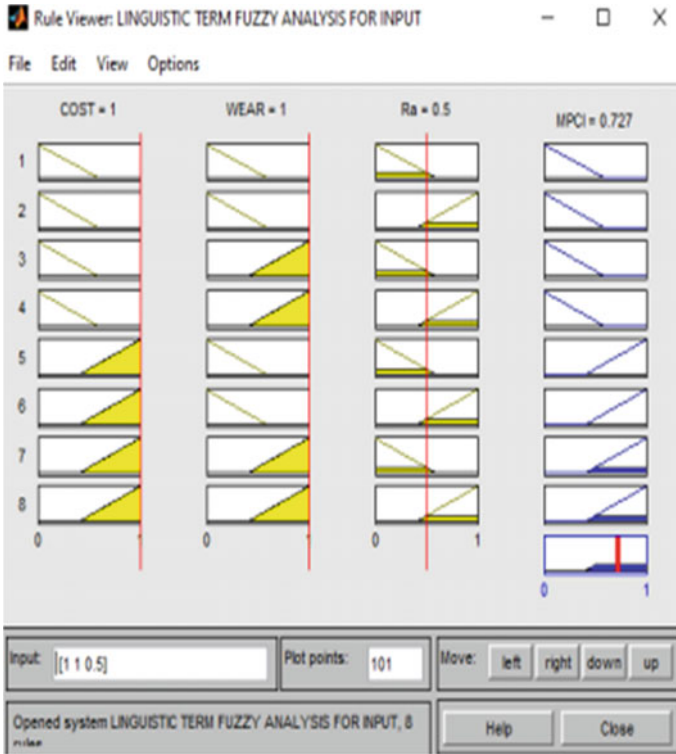


Fig. 2 Obtaining MPCl using rule viewing window

### 2.2 Assignment of Feasibility Levels to Numerical Inputs:

There are three numerical inputs that are chosen in this experiment, speed, feed and radial depth of cut with three values for each input. An attempt has been made to numerically express the comparative feasibility of each value of a given input. For this feasibility index to be consistent with MPCl obtained for the tool type, limits for zero and full feasibility are decided as 0 and 1. We then express the feasibility index of the lowest feasible and highest feasible values as 0.1 and 0.9. Expressing these as 0 and 1 will be incorrect as a values for that input may exist which are lower and higher than lowest and highest values given in Table 4 and the feasibility index for the middle value of the input is expressed as the average of the other two, which is 0.5 (Table 5).

For the speed values, the lowest speed is given highest feasibility, because the lowest speed will consume the least power. For feed, the highest feed is given lowest feasibility, as increasing feed rate increases flank wear [16]. For radial depth of cut, the highest value is given lowest feasibility, as the surface roughness increases with the depth of cut.

**Table 3** Values of recorded output

Expt.	MRR (cm <sup>3</sup> /min)	Ra (μm)
1	1.027	0.2222
2	1.3	1.1667
3	2.105	1.6
4	0.402	0.3333
5	1.037	1.2
6	2.52	1.6
7	0.364	0.4167
8	1.002	1.2
9	2.446	1.6
10	1.905	0.2353
11	0.969	1.1667
12	1.78	1.4
13	0.515	0.2667
14	0.869	1
15	1.264	1.6
16	0.556	0.2222
17	0.6	1
18	0.843	2

**Table 4** Values assigned for various cases

	Ra		Wear		Cost		MPCI
PVD	Low	1	Low	1	High	0.5	0.727
CVD	High	0.5	High	0.5	Low	1	0.5

**Table 5** Assignment of feasibility levels to numerical inputs

	Levels		
	1	2	3
Speed	100	120	140
Index	0.9	0.5	0.1
DOC	0.3	0.6	0.9
Index	0.9	0.5	0.1
Feed	0.075	0.15	0.225
Index	0.9	0.5	0.1

### 2.3 SAW and WP Methods Application

The SAW and WP methods are applied to the normalized input data, in order to obtain the additive feasibility index and the multiplicative feasibility index, respectively. Results have been tabulated in Table 7.

### 2.4 TOPSIS Method Application

According to the TOPSIS process, which has been explained by Rao [7], the decision table D, which lists all the  $j$  relevant attributes for all the  $i$  alternatives, is composed of the feasibility levels mentioned in Table 6. Each element in D is represented as a  $mij$ . A uniform decision matrix denoted as  $R$  will be obtained, the elements of which are denoted as  $Rij$ . Equation 1 shall be used for normalizing Table D of decisions as follows:

The elements of the weighted normalized matrixes are calculated from the following relation: With this, the negative (worst) and positive (best) solutions are obtained

**Table 6** Inputs with their corresponding feasibility indexes

Absolute inputs				Feasibility levels			
Type	Speed	Feed	RDOC	Type	Speed	Feed	RDOC
PVD	100	0.075	0.3	0.727	0.9	0.9	0.9
PVD	100	0.15	0.6	0.727	0.9	0.5	0.5
PVD	100	0.225	0.9	0.727	0.9	0.1	0.1
PVD	120	0.075	0.3	0.727	0.5	0.9	0.9
PVD	120	0.15	0.6	0.727	0.5	0.5	0.5
PVD	120	0.225	0.9	0.727	0.5	0.1	0.1
PVD	140	0.075	0.6	0.727	0.1	0.9	0.5
PVD	140	0.15	0.9	0.727	0.1	0.5	0.1
PVD	140	0.225	0.3	0.727	0.1	0.1	0.9
CVD	100	0.075	0.9	0.5	0.9	0.9	0.1
CVD	100	0.15	0.3	0.5	0.9	0.5	0.9
CVD	100	0.225	0.6	0.5	0.9	0.1	0.5
CVD	120	0.075	0.6	0.5	0.5	0.9	0.5
CVD	120	0.15	0.9	0.5	0.5	0.5	0.1
CVD	120	0.225	0.3	0.5	0.5	0.1	0.9
CVD	140	0.075	0.9	0.5	0.1	0.9	0.1
CVD	140	0.15	0.3	0.5	0.1	0.5	0.9
CVD	140	0.225	0.6	0.5	0.1	0.1	0.5

**Table 7** Summary of optimization results for SAW, WP and TOPSIS methods

Rank	SAW method		WP method		TOPSIS	
	Expt.	AFI	Expt.	MFI	Expt.	$P_i$
1	1	3.427	1	0.529983	1	0.553028
2	4	3.027	4	0.294435	13	0.534492
3	11	2.8	11	0.2025	4	0.534247
4	2	2.627	2	0.163575	11	0.527118
5	10	2.4	13	0.1125	5	0.510209
6	13	2.4	5	0.090875	2	0.509147
7	5	2.227	10	0.0405	10	0.483982
8	7	2.227	7	0.032715	14	0.478478
9	12	2	12	0.0225	17	0.472059
10	15	2	15	0.0225	7	0.465376
11	17	2	17	0.0225	15	0.463774
12	3	1.827	14	0.0125	12	0.462038
13	9	1.827	3	0.006543	16	0.43676
14	14	1.6	9	0.006543	18	0.419421
15	16	1.6	16	0.0045	9	0.413985
16	6	1.427	6	0.003635	3	0.410559
17	8	1.427	8	0.003635	8	0.395384
18	18	1.2	18	0.0025	6	0.387807

$$V^+ = \left[ \text{Max} \left( \frac{v_{ij}}{j} \varepsilon J \right) \text{Min} \left( \frac{v_{ij}}{j} \varepsilon J' \right) / i \quad i = 1, 2, \dots, N \right] \tag{1}$$

$$V^- = \left[ \text{Min} \left( \frac{v_{ij}}{j} \varepsilon J \right) \text{Max} \left( \frac{v_{ij}}{j} \varepsilon J' \right) / i \quad i = 1, 2, \dots, N \right] \tag{2}$$

where  $J = [(j = 1, 2, \dots, M)]/j$  is associated with the beneficial attributes. Where  $J' = [(j = 1, 2, \dots, M)]/j$  is associated with the non-beneficial attributes.

$V_j^+$  is essentially the optimal meaning of the variable. For a non-beneficial attribute like Ra,  $V_j^+$  is equal to the smallest value of the attribute, while for a beneficial attribute like MRR;  $V_j^+$  is equal to the largest value of the attribute. After that, the separation measures will be taken. The separation measures ( $S_i^-$  and  $S_i^+$ ) indicate distance between the solution and the negative ideal and the positive ideal solutions.

$$S_i^+ = \left\{ \sum_{j=1}^M (V_{ij} - V_j^+)^2 \right\}^{0.5} \quad i = 1, 2, \dots, N \tag{3}$$

$$S_i^- = \left\{ \sum_{j=1}^M (V_{ij} - V_j^-)^2 \right\}^{0.5} \quad i = 1, 2, \dots, N \tag{4}$$

For the final step, the relative proximity of a particular alternative to the ideal solution, we can express the value of  $P_i$  as follows:

$$P_i = \frac{S_i^-}{S_i^- + S_i^+} \quad (5)$$

The quantity of  $P_i$  can be referred to as the composite score of that particular alternative. Alternatives shall be ordered in the descending order of their composite score. Results have been tabulated in Table 7.

### 3 Results and Discussions

The optimization scheme obtained by these methods, SAW, WP and TOPSIS have been tabulated in Table 7. The optimal combination of input parameters as given by all three methods is the values of the inputs in the first experiment. The first alternative is concluded to represent the most optimum (feasible) combination of input parameters. The terms AFI, MFI and Pi can be labelled as feasibility scores for further comparative analysis.

### 4 Conclusion

In this paper, an optimization scheme for the turning of Inconel 825 based on the input parameters has been developed. The foundational idea for this scheme is that various values of the same input will have different values of feasibility. A unique system has been proposed to quantify the feasibility in case of numerical inputs. A fuzzy-based system is used to quantify the feasibility in case of linguistic inputs. In the optimization results, the first ranked experiment with the highest feasibility score, given by the three methods, is the first alternative among the chosen combinations. This paper serves as an effective starting point to perform input based optimization of machining process. An extension of this study may be focused on combined input–output-based optimization methods.

### References

1. Deshpande Y, Andhare A, Sahu N (2017) Estimation of surface roughness using cutting parameters, force, sound, and vibration in turning of Inconel 718. *J Braz Soc Mech Sci Eng* 39:5087–5089. <https://doi.org/10.1007/s40430-017-0819-4>
2. Gandhi A, Abhishek K, Kumari S (2019) Effect of speed on various machinability criteria in dry turning of nickel–iron–chromium-based superalloy. In: Deb D, Balas V, Dey R (eds) *Innovations in infrastructure: advances in Intelligent systems and computing*. Springer, Singapore, p 757



3. Tamang SK, Chandrasekaran M (2016) Integrated optimization methodology for intelligent machining of Inconel 825 and its shop-floor application. *J Braz Soc Mech Sci Eng* 39:865–877. <https://doi.org/10.1007/s40430-016-0570-22>
4. Thakur A, Gangopadhyay S (2018) Evaluation of micro-features of chips of Inconel 825 during dry turning with uncoated and chemical vapour deposition multilayer coated tools. *Proc Inst Mech Eng Part B: J Eng Manuf* 232(6):979–994. <https://doi.org/10.1177/0954405416661584>
5. Vasudevan H, Rajguru R, Jain S, Kaklotar M, Desai J, Mathur S (2019) Optimization of machining parameters in the turning operation of Inconel 825 using grey relation analysis. In: Vasudevan H, Kottur V, Raina A (eds) *Proceedings of international conference on intelligent manufacturing and automation. Lecture Notes in Mechanical Engineering*. Springer, Singapore, pp 413–424
6. Rao RV (2007) Introduction to decision making in the manufacturing environment. In: *Decision making in the manufacturing environment*. Springer Series in Advanced Manufacturing. Springer, London, pp 8–12
7. Rao RV (2007) Introduction to multiple attribute decision-making (MADM) methods. In: *Decision making in the manufacturing environment*. Springer Series in Advanced Manufacturing. Springer, London, pp 27–41
8. Fishburn PC (1967) Methods of estimating additive utilities. *Manage Sci* 13(7):435–453. <https://EconPapers.repec.org/RePEc:inm:ormnsc:v:13:y:1967:i:7:p:435-453>
9. Miller DW, Starr MK (1969) *Executive decisions and operations research*. Prentice-Hall. <https://books.google.co.in/books?id=XypVAAAAMAAJ>
10. Yoon K, Hwang LI (1981) *Multiple attribute decision making*. Springer, Berlin
11. Umamaheswarrao P, Raju DR, Suman KNS, Sankar BR (2019) Topsis based optimization of process parameters while hard turning of AISI 52100 Steel. *Acta Mechanica Malaysia (AMM)* 2(2):28–31
12. Khanna H, Sharma D, Laroia S (2011) Identifying and ranking critical success factors for implementation of total quality management in the Indian manufacturing industry using TOPSIS. *Asian J Qual* 12(1):124–138
13. Shakeel Ahmed L, Pradeep Kumar MJ (2016) Multiresponse optimization of cryogenic drilling on Ti-6Al-4V alloy using TOPSIS method. *J Mech Sci Technol* 30:1835–1841. <https://doi.org/10.1007/s12206-016-0340-1>
14. Aliofkhaezai M, Ali N (2014) Fabrication of micro/nanostructured coatings by CVD techniques. In: Hashmi S, Batalha GF, Van Tyne CJ, Yilbas B (eds) *Comprehensive materials processing*. Elsevier, pp 85–117. <https://doi.org/10.1016/B978-0-08-096532-1.00706-8>
15. Rao RV (2007) A logical approach to fuzzy MADM problems. In: *Decision making in the manufacturing environment*. Springer Series in Advanced Manufacturing. Springer, London, pp 39–43
16. Anil KC, Vikas MG, Teja BS, Rao KYS (2017) *IOP Conf Ser: Mater Sci Eng* 191:12–25

# Analysis of PMEDM Parameters for the Machining of Inconel-800 Material Using Taguchi Methodology



Satish Kumar, Sanjeev Kumar, Rajdeep Singh, Pardeep Bishnoi, and Virender Chahal

**Abstract** In the present scenario, copper tools and Inconel-based materials became popular due to their unique properties and are widely used for manufacturing various materials, airplane parts, furnace parts, etc. That is why, copper as a tool and nickel-based superalloy as a material, we have chosen for further experimentation. In order to study behavior of Inconel material, the content material removal rate (MRR) has been selected as a response parameter. After reviewing the literature, the process parameters, i.e. current, pulse on time ( $T_{on}$ ), pulse off time ( $T_{off}$ ), and electrical discharge machining (EDM) have been chosen for the experiment. After analysis, results indicated that, the peak current more effect the MRR as compared with the other two process parameters, i.e.  $T_{on}$  and  $T_{off}$ .

**Keywords** Inconel-800 · Material removal rate · Design of experiment · Signal-to-noise ratio

## 1 Introduction

Inconel material, i.e., nickel-based super alloy is more popular because of their good mechanical properties such as relatively high abrasion resistance and toughness at high hardness. These materials are widely used to manufacture various materials, parts of airplanes, parts of furnaces, etc. However, some features such as high temp and work hardening make it difficult to machine the alloy with conventional techniques, as higher temperatures are produced that shorten the life of the cutting tool. One of the most suitable manufacturing and non-contact material removal processes is EDM. The layer formed on the machined surface has microscopic cracks that slow down the wear and corrosion resistance of the EDM surface [1]. Series of craters are formed on machined surface when worked with turned off the pulse [2]. Powder particles were mixed with dielectric fluid to improve MRR and TWR [3–5]. PMEDM has one of the impressive methods of augmenting the capabilities of EDM. In this

---

S. Kumar (✉) · S. Kumar · R. Singh · P. Bishnoi · V. Chahal  
Department of Mechanical Engineering, Chandigarh Engineering College, Landran, Punjab, India  
e-mail: [satish.4310@cgc.edu.in](mailto:satish.4310@cgc.edu.in)

© The Author(s), under exclusive license to Springer Nature Singapore Pte Ltd. 2021  
C. Pandey et al. (eds.), *Advances in Materials and Mechanical Engineering*,  
Lecture Notes in Mechanical Engineering,  
[https://doi.org/10.1007/978-981-16-0673-1\\_25](https://doi.org/10.1007/978-981-16-0673-1_25)

321

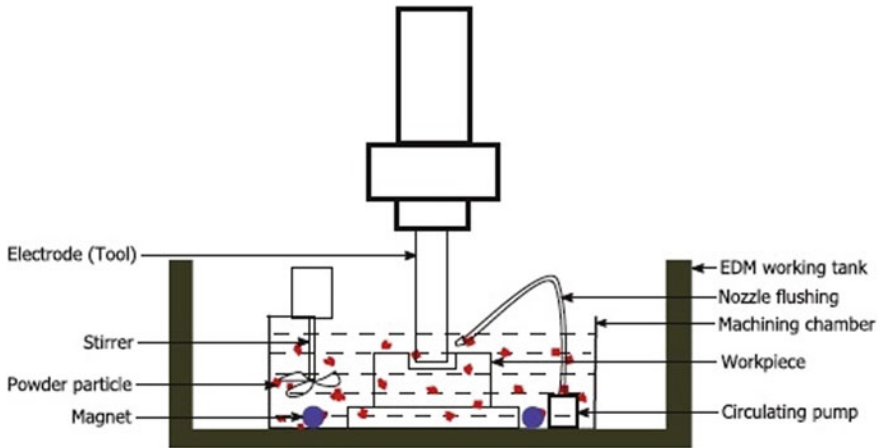


**Fig. 1** Schematic diagram of PMEDM experimental setup

process, a fine powder of conductive material is added to the EDM oil to fill the spark gap. The PMEDM process was invented in the late 1970s and the first publication was in 1980 [6]. In PMEDM, a fine powder of suitable material is mixed in EDM oil which leads to better surface finish and machining rate than conventional EDM. Additive conductive particles dissociate the insulating properties of the dielectric fluid so that it becomes more stable and thus improves machining rate and surface refinement [7, 8]. The two-tank system for EDM was first developed by Mitsubishi [9]. Larger tanks contain standard EDM oils while smaller tanks have EDM oil with powder. After the initial operation, the tool head moved to the smaller tank to perform machining operations. For the circulation of powder material in small tanks, a stirring mechanism is used. Figure 1 shows the modified circulation system for continuous reuse of powder.

At the first discharge, the fine powder particles become active and accelerated by the electric field so that on moving with ions further, these particles strike with another molecules and generate more ions. Thus, there will be more electric charges in PMEDM compared to traditional EDM [10]. After that, particles form the chain like structures between both the electrodes and interlocking take place between the particles. Chain formation helps to reduce the discharge gap between the two electrodes [11].

From the literature, it has been found that, almost work has been reported on the machining of die steel, titanium, composite matrix elements, etc., but no work has been reported on the Inconel-800. The purpose of this study is to investigate the effect of powder particles, i.e., tungsten carbide on Inconel-800 material along with Cu–Cr as a tool material.

**Table 1** Level values of input process parameters

S. No.	Symbols	Factors	Levels		
			1	2	3
1	A	$T_{on}$	60	90	120
2	B	$T_{off}$	30	45	60
3	C	Current	4	8	12

**Table 2** L9 design matrix

Exp. No.	$T_{on}$ ( $\mu$ s)	$T_{off}$ ( $\mu$ s)	Current (amp)
E1	60	30	4
E2	60	45	8
E3	60	60	12
E4	90	30	8
E5	90	45	12
E6	90	60	4
E7	120	30	12
E8	120	45	4
E9	120	60	8

## 2 Methodology and Experimental Setup

### 2.1 Methodology

To select the factors and their levels, one factor at a time approach is used. Parameters such as peak current,  $T_{on}$ , and  $T_{off}$  were varied to examine their effect on MRR. Powder concentration 9 g/L was kept constant during the experimentation. Degrees of freedom for the three factors were calculated to be 8.

Thus, Taguchi  $L_9$  matrix was a suitable design for the present study. In  $L_9$  ( $3^3$ ) array, three columns in nine rows represent nine experiments to be conducted with three levels of the same factor. Table 1 shows the level values of input process parameters while Table 2 shows the design matrix for the machining of Inconel-800 material.

### 2.2 Experimental Setup

For the experimentation, a die sinking EDM machine is used. The pictorial view of EDM machine is as shown in Fig. 2. A separate tank having dimension (250 × 100 × 100) mm was installed on the machine for mixing powder with the dielectric

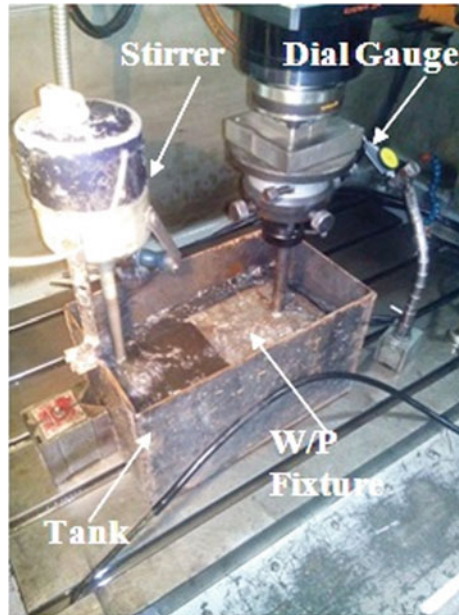


**Fig. 2** Experimental set up

along with a stirrer mechanism to avoid settling of powder particles. Based on literature survey and pilot experiment, powder concentration, i.e., 11 g/L has been taken for achievement of MRR. Figure 2 shows a photograph of the experimental set up while Fig. 3 shows the pictorial view of EDM machine. Table 3 shows the chemical composition of the work specimen. The specimen has been taken in the form of rectangular plate having dimensions 150 mm × 15 mm × 6 mm. The inhomogeneous composition of the Inconel-800 was made from the Ashapura Metal Alloy Testing Service.

### 3 Results and Discussions

#### 3.1 Material Removal Rate

Table 4 illustrates the experimental results of MRR and its consequent signal-to-noise ratio (S/N), while Table 5 shows the analysis of variance (ANOVA) results. The ANOVA results and  $F$ -test values, it has been clear that the most significant factor is current with contribution of (63.99%) compared to other factors, i.e.,  $T_{on}$  (20.76%) and  $T_{off}$  (14.47%).



**Fig. 3** Pictorial view of EDM machine

**Table 3** Chemical composition of Inconel-800

Element	Ni	Fe	Cr	C	Mn	S	Si	Cu
%	Base material	7.78	14.56	<0.15	<1.0	0.015	0.5	0.5

**Table 4** Average results of MRR and S/N ratio

Exp. No.	MRR (mm <sup>3</sup> /min)			Mean value	S/N ratio
	R-1	R-2	R-3		
E1	3.514	3.514	3.522	3.516	10.92
E2	9.755	9.755	9.755	9.755	19.784
E3	13.554	13.526	13.526	13.535	22.629
E4	13.831	13.831	13.831	13.831	22.817
E5	22.661	22.661	22.661	22.661	27.105
E6	2.998	3.004	3.004	3.002	9.548
E7	28.478	28.478	28.478	28.478	29.09
E8	3.619	33.619	3.619	13.619	22.682
E9	10.651	10.651	10.627	10.643	20.541

$R^2 = 99.2\%$   $R^2$  (adj.) = 97.0%

From Fig. 4, it is clear that the MRR hikes with the current. With the increased current, discharge energy is also increased resulting in higher temperature which

**Table 5** ANOVA analysis for MRR

Control factors	DOF	Seq. SS	Adj. SS	Adj. MS	F-value	P-value	% Contribution
<i>ANOVA for MRR</i>							
$T_{on}$	2	112.113	112.113	56.056	27.34	0.035	20.76
$T_{off}$	2	78.132	78.132	39.066	19.06	0.05	14.47
Current	2	345.447	345.447	172.724	84.25	0.012	63.99
Residual error	2	4.1	4.1	2.05			0.759
Total	8	539.793					100

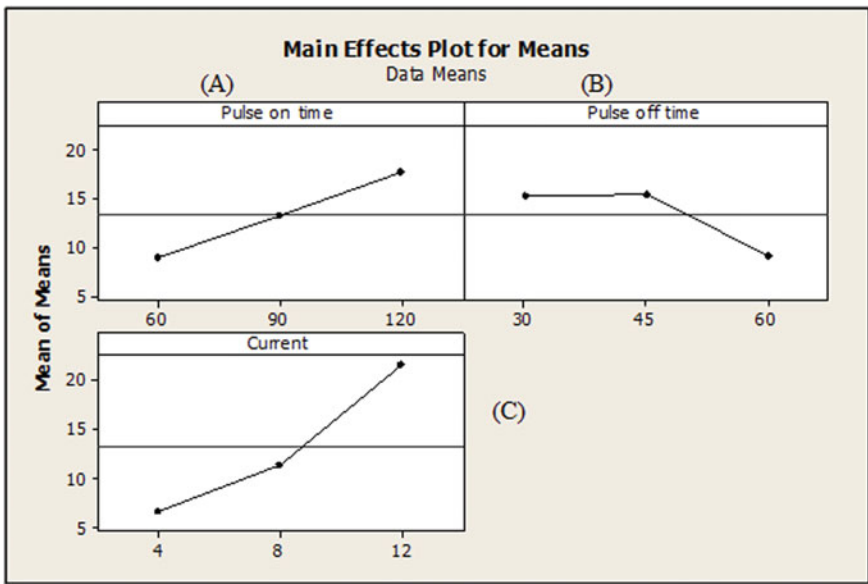


**Fig. 4** Main effects plot for means of means for MRR

causes evaporation and better impulsive forces acting on machine area resulting higher MRR [11]. It indicates that current is the key factor for higher MRR.

Figure 4 (A) shows the effect of  $T_{on}$  on the MRR. With the minimum value of  $T_{on}$ , i.e., factor (A) MRR is also the minimum value. As value of A increased, MRR is also increased, this is because when  $T_{on}$  hike, sparking frequency of the tool is also hike and more erosion takes place at the surface of the specimen. Figure 4 (B) shows the influence of  $T_{off}$  on the MRR and from the figure, it is clear that with the hike value of  $T_{off}$  (C) MRR decreased gradually. This is because when pulse off time increases, time taken by the tool increases that increase the tool life but decrease the MRR. Figure 4 shows the  $A_3B_3C_1$  parameters, i.e., current of 12 A,  $T_{on}$  of 120  $\mu$ s and  $T_{off}$  of 30  $\mu$ s, respectively, are the optimal conditions for better MRR.

**Table 6** Factor level values of each factor and their ranking

Level	$T_{on}$	$T_{off}$	Ip
1	17.78	20.94	14.38
2	19.82	23.19	21.05
3	24.1	17.57	26.27
Delta	6.33	5.62	11.89
Rank	2	3	1

ANOVA for  $S/N$  ratio is summarized in Table 5 and it is observed that current is the most prominent factor which effects the MRR maximum with percent contribution of 63.99% followed by  $T_{on}$  with percent contribution 20.76% then  $T_{off}$  with percent contribution 14.47%. Table 6 shows the factor level values of each factor and their ranking.

## 4 Conclusions

In the present study, Inconel-800 a super alloy was machined with the help of copper–chromium as a tool material. From the result of ANOVA, current (C) has the highest effect on material removal rate of workpiece material. MRR at optimum condition, i.e.,  $A_3B_3C_1$  is hike along with the current and  $T_{on}$ . From the result, delta value obtained for the current is 11.89 followed by pulse on time and pulse off time, i.e., 6.33 and 5.62. High delta value among the factors means high significant factor. On the bases of delta value, current has first rank, pulse on time has second rank, and pulse off time has third rank. Third rank means that pulse off time has least effect on the material as compared to other factors.

## References

1. Ekmekci B, Erdenl A (2004) Remarks on surface integrity of electric discharge machined surfaces: a state of art review. Paper presented at 11th international conference on machine design and production, Antalya, Turkey, pp 411–428
2. Foteyey NK (1997) Electro-physical machining surface quality after electric discharge machining. Russ Eng Res 17:73–79
3. Klocke F, Lung D, Antonoglou TG (2004) The effects of powder suspended dielectrics on the thermal influenced zone by electro-discharge machining with small discharge energies. J Mater Process Technol 149:191–197
4. Abbas NM, Solomon DG, Bahari MF (2007) A review on current research trends in electrical discharge machining (EDM). Int J Mach Tools Manuf 47(7–8):1214–1228
5. Kumar A, Maheshwari S, Sharma C, Beri N (2009) Performance evaluation of silicon additive in electrical discharge machining of EN 24 steel based on Taguchi method. J Mech Eng 60(5–6):298–304



6. Erden A, Bilgin S (1980) Role of impurities in electric discharge machining. In: Proceedings of the 21st machine tool design and research conference, Swansea, Macmillan, London, pp 345–350
7. Gudur S, Potdar VV, Gudur S (2014) A review on effect of aluminum & silicon powder mixed EDM on response variables of various materials. *Int J Innov Res Sci Eng Technol* 12:17937–17945
8. Talla G, Gangopadhyay S, Biswas CK (2016) State of the art in powder-mixed electric discharge machining: a review. *J Eng Manuf* 1–16
9. Silicon powder additives proven safe and effective in EDM. *Modern Machine Shop*, Apr 2000, <https://www.mmsonline.com/articles/silicon-powder-additivesproven-safe-and-effective-in-edm>
10. Zhao WS, Meng QG, Wang ZL (2002) The application of research on powder mixed EDM in rough machining. *J Mater Process Technol* 129(1–3):30–33
11. Kansal HK, Singh S, Kumar S (2005) Parametric optimization of powder mixed electrical discharge machining by response surface methodology. *J Mater Process Technol* 169(3):427–436

# Influence of Wall Angle, Feed Rate, and Sheet Thickness on Forming Force in SPIF



Ajay Kumar , Parveen Kumar, and Hari Singh

**Abstract** Single point incremental forming (SPIF) technique is a choice of green manufacturing that can produce complicated shapes from sheet materials with reduced power and energy using simple tools. This technique further exempts use of expensive forming dies and punches due which makes it cost effective for rapid prototyping and batch-type manufacturing. The prediction and measurement of forming forces during SPIF process determine the size of forming machinery and additional hardware along with preventing the failures of facilities. In this work, maximal axial forming forces have been investigated under the effects of interactions of significant input variables like sheet thickness, wall angle, and feed rate. The minimal axial peak force (836 N) required to produce conical frustums was observed during trial 1 when a wall angle of 60 was employed with minimum sheet thickness (0.8 mm, in this case). On the other hand, the maximal axial peak force (1577 N) required to produce conical frustums was observed during trial 12 when a wall angle of 72 was employed with greater sheet thickness (1.6 mm, in this case) which can be the limiting factor of forming tool and machinery and that should obviously be avoided.

**Keywords** Incremental sheet forming · Single point incremental forming · Forming force · AA-2024 · Input parameters

## 1 Introduction

The conventional sheet forming techniques require customized and specific tooling to meet the requirements of particular shape and sizes of components to be formed. This leads to hike in cost of initial setup and time required to produce the user ready components [1, 2]. Enough time is consumed in designing and fabricating the

---

A. Kumar (✉)

Department of Mechanical Engineering, Faculty of Engineering and Technology, Shree Guru Gobind Singh Tricentenary University, Gurugram, Haryana, India

P. Kumar · H. Singh

Department of Mechanical Engineering, National Institute of Technology, Kurukshetra, Haryana, India

© The Author(s), under exclusive license to Springer Nature Singapore Pte Ltd. 2021

329

C. Pandey et al. (eds.), *Advances in Materials and Mechanical Engineering*,

Lecture Notes in Mechanical Engineering,

[https://doi.org/10.1007/978-981-16-0673-1\\_26](https://doi.org/10.1007/978-981-16-0673-1_26)

punches and dies involved in conventional forming processes [3]. In addition, large amount of forces is required to shape the sheet material into required shape and size due to the nature of these forming processes. Furthermore, batch-type production and rapid prototyping are not economical using these techniques. The level and ability of frontier sectors, like aerospace, can be enhanced by manufacturing complicated thin-walled sheet material components with greater performance using certain flexible forming techniques to fulfill the need of rapid prototyping and batch-type production in short delivery time [4]. Incremental sheet forming (ISF) technique has been proved as a viable and flexible method that has full potential to solve the above issues and to produce complicated shapes without using dedicated punches and dies. ISF involves moving a simple stylus, generally hemispherical-ended, over the surface of blank deforming the material layer by layer by following predetermined trajectory defined by CAM software [5–7]. The numerical instructions are usually generated from CAD file of the desired shape. This concept of forming the sheet material was envisaged by two patents [8, 9], both issued in 1967. By backtracking the publications on ISF, Mason's [10] work can be considered as the origin of the true ISF process. The applications of ISF include, but not limited to, automobile components, aerofoil and fuselage parts, ankle and knee implants, cranial plate, customized channels, etc.

Single point incremental forming (SPIF) is a subclass of ISF process which is also known as “negative incremental forming” or “die-less forming”. SPIF technique eliminates the use of any kind of dies for producing components of sheet material. Lesser lead time and lower tooling cost allow the SPIF technique to become suitable for producing the components in batches economically and efficiently [11–13]. Moreover, the absence of specific dies and punches, which otherwise are essential in traditional forming technique, increases the versatility and flexibility of SPIF technique. Figure 1 shows the schematic of SPIF technique.

Furthermore, forming forces required to produce deformation are comparatively small enough during ISF technique due to the fact that the deformation is purely local which allows utilization of smaller forming machinery and hence, saving the energy and cost of hardware [14]. Hence, energy can be saved up to large context by using negative incremental forming. In addition, determination of maximum forming forces required for producing components from specific material under specific set of parameters delineates the capability of forming machinery that should be employed for this process. Therefore, assured utilization of forming setup can be promised by investigating and determining maximum forming force [15].

In SPIF, forming force can be measured by load cells or force dynamometers using various methods. Most of the researchers [14–23] have employed table-type dynamometer fixing it between machine table and sheet clamping device or fixture as shown in Fig. 2. Kumar et al. [14] also studied impact of various process variables on axial forming forces on AA2024 sheets using forming tool of hemispherical shape. Conical frustums of various wall angles ( $52^\circ$ ,  $56^\circ$ ,  $60^\circ$ ,  $64^\circ$ ) were formed using helical tool path. Forming forces raised by 20.03% tool radius were raised from 3.76 to 7.83 mm for a wall angle of  $64^\circ$ . Kumar et al. [15] focused on the influence of interactions of tool radius—tool shape and wall angle—tool shape on forming forces on AA2024 sheets. It was observed that forces were increased by 17.46% when tool

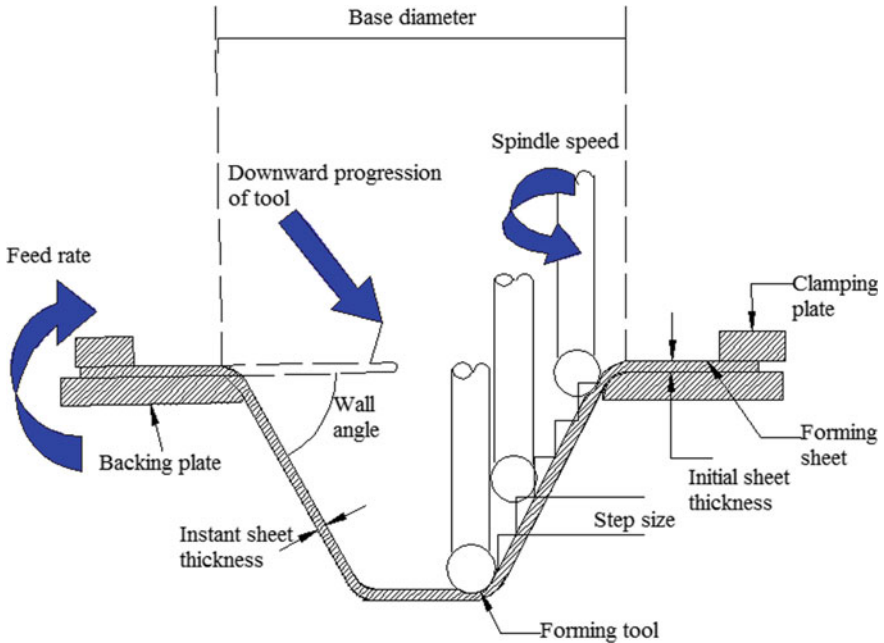


Fig. 1 Single point incremental forming [1]

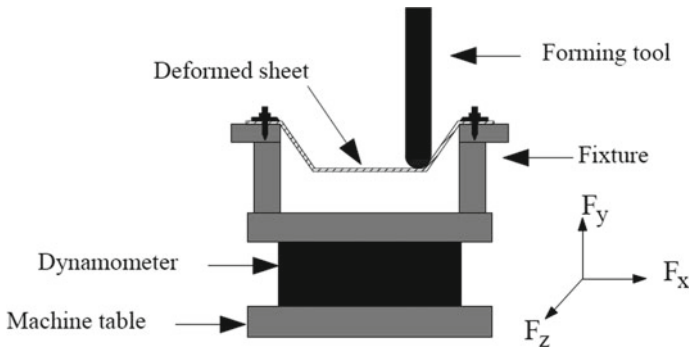


Fig. 2 Schematic of measurement of forming force during SPIF

radius of 5.80 mm of flat end was employed as compared to hemispherical shape. The increase in tool radius (from 3.76 to 7.83 mm) resulted in the decrement of forces by 35.49%. Uheida et al. [16] studied the impact of feed rate and spindle speed on vertical forming forces on titanium grade 2 sheets of 0.8 mm thickness using hemispherical-end forming tool of 10 mm to produce varying wall angle conical frustum (VWACF). Results showed that, although, forming force decreased with the increase in spindle speed but sheet fracture was noticed after spindle speed of

4000 rpm. Ali et al. [17] optimized the SPIF process for forming forces taking step size, feed rate, sheet thickness and tool radius into account on AA1050-H14 sheets. Furthermore, a model was established to estimate the forces by artificial intelligence techniques. Sakhtemanian et al. [18] developed a theoretical model for predicting the energy that can be transferred to heat from the ultrasonic vibrations used in the study. In addition, the temperature attained by forming tool was also analyzed.

Lon et al. [19] studied the influence of feed rate, material of sheet (AA1050-H14, AA5052-H34), vibration amplitude (0, 6, 9, 12, 15, 18  $\mu\text{m}$ ), ultrasonic power and tool radius on forming force and temperature induced during ultrasonic-assisted SPIF process. The reduction in forming forces was lower when higher feed rate was used. Honarpisheh et al. [20] investigated the forming force, thickness distribution, and geometrical accuracy of bimetal sheets of AA1050 and copper (C-10100). The results showed that the axial forming forces increased from 1464 and 1357 N to 1636 and 1730 N for numerical and experimental tests, respectively, when tool diameter was raised from 10 to 16 mm. Zhai et al. [21] investigated the effects of spindle speed, sheet thickness, and step size on forming forces during ultrasonic-assisted ISF (U-ISF) and ISF on AA1050-O sheets to produce pyramidal frustums. Forming forces were found to reduce up to 40% when ultrasonic amplitude was increased from 0 to 10  $\mu\text{m}$ . Moreover, the forming forces increased gradually in the initial stages because of work hardening effects and then became stable due to equilibrium between work hardening and sheet thinning, and, this is in accordance of [22]. Kumar and Gulati [22] studied impact of various process variables for axial forming forces and optimized the SPIF process using Taguchi method for AA6063 and AA2024 sheets. A statistical model was also developed for estimating the axial forming forces which was validated with further experimentation work. Authors also explored the gradient of force curve that could be employed as a spy variable for safe implementation of SPIF operation. Kumar and Gulati [23] studied impact of various process variables for axial forming forces and thickness reduction, and optimized the SPIF process using Taguchi method on AA2014 sheets. Conical frustums were formed using two different tool path approaches, viz. profile and helical and these are well described by [1, 13, 22]. Lubricants were found to affect forces negligibly as compared to the impact of other factors taken into account. A statistical model was proposed for predicting the forming which was further validated experimentally. Chang et al. [24] developed an analytical model for predicting forming forces in single pass SPIF, multipass SPIF, and incremental hole flanging processes and validated the same with experimental results by varying impact factors for AA5052 and AA3003 alloys sheets.

It has also been observed in literature [13, 25, 26] that the axial forming forces ( $F_z$ ) are much greater than other two components of forming forces (i.e.,  $F_x$  and  $F_y$ ). Therefore, secure implementation of forming machinery and forming tools can be ensured by determining the maximum axial forces required to execute the SPIF process. The knowledge about the effects of input factors on forming forces would lead to efficient prediction of failures of components as well as machinery used for executing the process. Furthermore, the prediction of forming forces helps

**Table 1** Chemical compositions of AA2024 sheet

Element	Al	Cr	Cu	Fe	Mg	Mn	Si	Ti	Zn
Weight %	91.50	0.10	4.60	0.30	1.70	0.80	0.50	0.10	0.20

**Table 2** Levels of input variables under investigation

Variable	Level 1	Level 2	Level 3	Level 4
Sheet thickness (mm)	0.8	1.2	1.6	–
Wall angle (°)	60	64	68	72
Feed rate (mm/min)	1000	1500	2000	2500

in controlling the process online and estimating the power needed by forming machinery.

This paper aims at filling this gap by investigating impact of wall angle, feed rate, and interactions of these with the sheet thickness. To the best of authors' knowledge, the interactions of these parameters have not been studied on AA2024 sheets during SPIF process so far. AA2024 is a popular aluminum alloy which is known for its favorable characteristics in sheet metal applications like lightweight, high strength, corrosion resistance, etc. Table 1 represents the chemical compositions of AA2024 sheets extracted by using an optical emission spectrometer (Foundry Master, Oxford Instruments, Uedem, Germany). Table 2 represents the levels of impact factors investigated in the current work. While varying the set of input factors, other parameters were kept constant according to previous work [15].

## 2 Experimental Setup

The experimental setup of this work (Fig. 3) includes forming tool of hemispherical end, a hollow fixture to clamp the blank firmly, a load-cell to measure forming forces, a data logger system to record the measured forces, and a CNC milling machine to execute this die-less process. To produce conical frustums of 120 mm major diameter and 70 mm height, CAD model was designed in Solidworks® software and the same was imported to Delcam™ software for generating numerical instructions for CNC milling machine taking helical tool path into consideration. Castrol Alpha SP 320 oil has been used as lubricant during forming operation.

## 3 Results and Discussion

The recorded values of the maximal vertical downward forces ( $F_{z_{max}}$ ) are depicted in Table 3. The influence of interaction of sheet thickness and wall angle is depicted

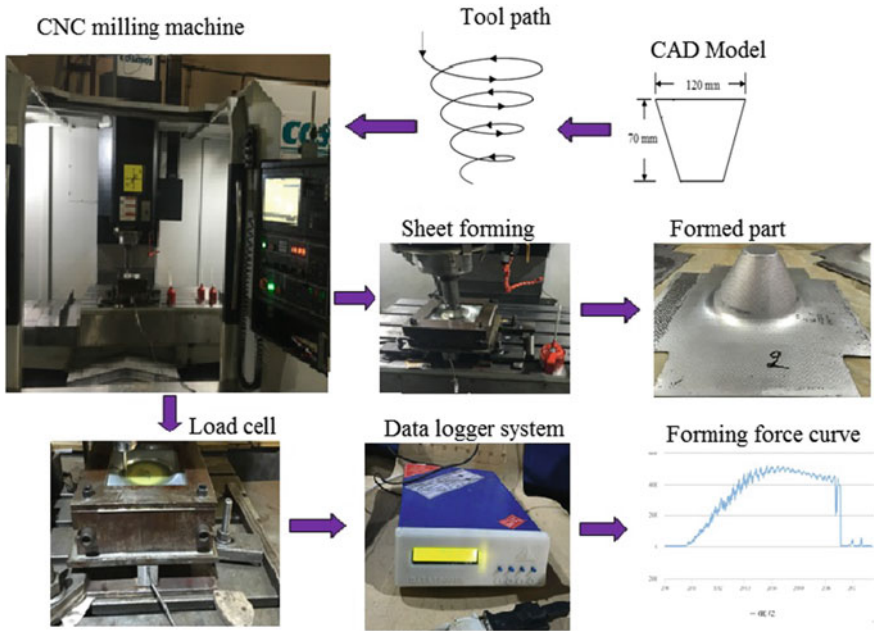


**Fig. 3** Experimental setup and measurement of forming force

**Table 3** Experimental results for the designed conditions on maximal axial forces

Effects of wall angle and sheet thickness				Effects of feed rate and sheet thickness			
Run	Wall angle (°)	Sheet thickness	$F_{z,max.}$ (N)	Run	Feed rate	Sheet thickness	$F_{z,max.}$ (N)
1	60	0.8	836	13	1000	0.8	903
2	60	1.2	907	14	1000	1.2	972
3	60	1.6	998	15	1000	1.6	1084
4	64	0.8	931	16	1500	0.8	933
5	64	1.2	1007	17	1500	1.2	1009
6	64	1.6	1122	18	1500	1.6	1121
7	68	0.8	1068	19	2000	0.8	950
8	68	1.2	1183	20	2000	1.2	1033
9	68	1.6	1338	21	2000	1.6	1156
10	72	0.8	1247	22	2500	0.8	968
11	72	1.2	1403	23	2500	1.2	1055
12	72	1.6	1577	24	2500	1.6	1178

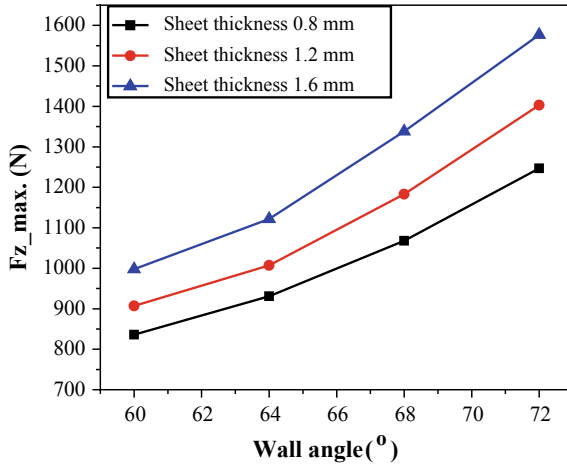


**Fig. 4** Influence of sheet thickness and wall angle on maximal axial forces

by Fig. 4. The maximal axial force was increased dramatically when the amount of sheet thickness and wall angle was raised because the larger wall angle results in deforming the material in large amount at an instant.

For higher sheet thickness, large amount of material is deformed which requires much forming load to produce local deformation. When combination of higher levels of these two factors is employed, the forming force increases very rapidly and hence, become the limiting factor of forming tool and machinery that should obviously be avoided. On the other hand, employment of higher wall angle resulted in the fracture of sheet material well before achieving the designed height of conical frustums. Sheet material was fractured at a height of 58 mm when combination of higher sheet thickness (1.6 mm, in this case) and wall angle (72°, in this case) was employed. When same wall angle (72°) was employed with lower level of sheet thickness (0.8 mm, in this case), sheet fractured at a relatively lower height (43.5 mm). This is due to the fact that excessive thinning of sheet is occurred when wall angle increases (according to sine law [27]) and hence, less material is available to delay the fracture for thinner sheets. The combination of lower sheet thickness and higher wall angle can deform material by lower forming forces at the expense of formability.

The influence of interaction of sheet thickness and feed rate is depicted by Fig. 5. The maximal axial force was found to rise dramatically when the feed rate and sheet thickness were raised because forming tool has to deform the material rapidly for a higher rate. The rate of increasing forming force was found to reduce for higher levels of feed rate due to the fact that the greater feed rate results in increasing coefficient of friction at forming zone which lead to increase in forming temperature. When combination of higher levels of these two factors is employed, the forming force increases very rapidly and hence, become the limiting factor of forming tool and machinery that should obviously be avoided.



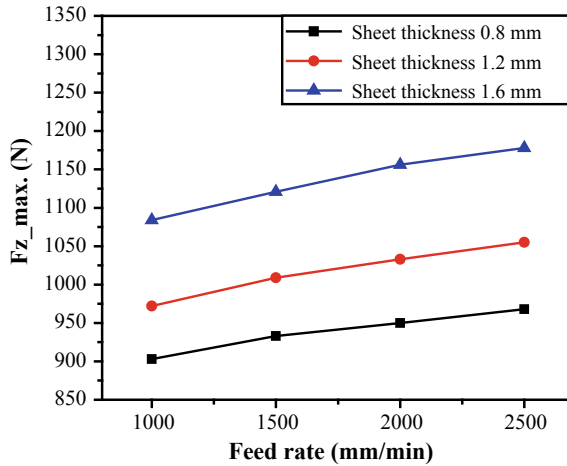


Fig. 5 Influence of sheet thickness and feed rate on maximal axial forces

## 4 Conclusion

The objective of this study is to investigate the maximal axial forming forces required to produce conical frustums during SPIF technique by using helical tool path. The input variables like sheet thickness, feed rate, and wall angle have been investigated to check their effects on maximal axial forces. The effects of interactions of these factors have also been discussed. It was observed that the investigated factors were of great significance that can affect and control the process. When combination of higher levels of sheet thickness, wall angle, and feed rate is employed, the forming force increases very rapidly and hence, become the limiting factor of forming tool and machinery that should obviously be avoided. The combination of lower sheet thickness and higher wall angle can deform material by lower forming forces at the expense of formability. Future work would target the investigation of effects of interactions of input variables on formability and surface roughness of formed components.

## References

1. Kumar A, Mittal RK (2020) Incremental sheet forming technologies: principles, merits, limitations, and applications, 1st edn. CRC Press, Taylor and Francis. ISBN: 978-0-367-27674-4
2. Kumar A, Gulati V (2019) Experimental investigation and optimization of surface roughness in negative incremental forming. *Meas J Int Meas Confederation* 131:419–430
3. Kumar A, Gulati V, Kumar P (2018) Investigation of surface roughness in incremental sheet forming. *Procedia Comput Sci* 133:1014–1020. In: International conference on robotics and smart manufacturing. Elsevier, Amsterdam

4. Kumar A, Gulati V, Kumar P (2018) Effects of process parameters on surface roughness in incremental sheet forming. *Mater Today Proc* 5(14):28026–28032. In: International conference on composite materials, manufacturing, experimental techniques, modeling and simulation. Elsevier, Amsterdam
5. Bagudanch I, Centeno G, Vallellano C, Garcia-Romeu ML (2013) Forming force in single point incremental forming under different bending conditions. *Procedia Eng* 63:354–360
6. Gulati V, Kumar A (2018) Investigation of some process parameters on forming force in single point incremental forming. *Int Res J Eng Technol* 4(4):784–791
7. Gulati V, Aryal A, Katyal P, Goswami A (2020) Process parameters and thickness reduction in single point incremental forming. *Int Res J Eng Technol* 7(1):473–476
8. Leszak E, Ave H (1967) Apparatus and process for incremental dieless forming. United States Patent, United States
9. Berghahn WG, Murray GF (1967) Method of dieless forming surfaces of revolution. United States Patent, New York
10. Mason B (1978) Sheet metal forming for small batches. PhD thesis, University of Nottingham
11. Kumar A, Gulati V, Kumar P, Singh V, Kumar B, Singh H (2019) Parametric effects on formability of AA2024-O aluminum alloy sheets in single point incremental forming. *J Market Res* 8(1):1461–1469
12. Kumar A, Gulati V, Kumar P, Singh H, Singh V, Kumar S, Haleem A (2018) Parametric investigation of forming forces in single point incremental forming. In: International conference on “advances in materials and manufacturing applications (IConAMMA 2018)” Amrita Vishwa Vidyapeetham, Bengaluru Campus, Karnataka, India, 16th–18th Aug 2018
13. Kumar A, Gulati V (2019) Forming force in incremental sheet forming: a comparative analysis of the state of the art. *J Braz Soc Mech Sci Eng* 41
14. Kumar A, Gulati V, Kumar P (2018) Investigation of process variables on forming forces in incremental sheet forming. *Int J Eng Technol* 10(3):680–684
15. Kumar A, Gulati V, Kumar P (2019) Experimental investigation of forming forces in single point incremental forming. In: Shankar K, Shankar R, Sindhwani R (eds) International conference on future learning aspects of mechanical engineering, LNME. Springer, Berlin, pp 423–430
16. Uheida EH, Oosthuizen GA, Dimitrov D (2017) Investigating the impact of tool velocity on the process conditions in incremental forming of titanium sheets. *Procedia Manuf* 7:345–350
17. Ali A, Ragab AE, Dabwan A, Mustafa M, Hidri L (2019) Prediction of formation force during single-point incremental sheet metal forming using artificial intelligence techniques. *PLoS One* 14(8)
18. Sakhtemanian MR, Honarpisheh M, Amini S (2019) A novel material modeling technique in the single-point incremental forming assisted by the ultrasonic vibration of low carbon steel/commercially pure titanium bimetal sheet. *Int J Adv Manuf Technol* 102:473–486
19. Lon Y, Li Y, Sun J, Ille I, Li J, Twiefel J (2018) Effects of process parameters on force reduction and temperature variation during ultrasonic assisted incremental sheet forming process. *Int J Adv Manuf Technol* 97:13–24
20. Honarpisheh M, Keimasi M, Alinaghian I (2018) Numerical and experimental study on incremental forming process of Al/Cu bimetals: influence of process parameters on the forming force, dimensional accuracy and thickness. *J Mech Mater Struct* 13(1):35–51
21. Zhai W, Li Y, Cheng Z, Sun L, Li F, Li J (2020) Investigation on the forming force and surface quality during ultrasonic-assisted incremental sheet forming process. *Int J Adv Manuf Technol* 106:2703–2719
22. Kumar A, Gulati V (2018) Experimental investigations and optimization of forming force in incremental sheet forming. *Sādhanā* 43:159
23. Kumar A, Gulati V (2020) Optimization and investigation of process parameters in single point incremental forming. *Indian J Eng Mater Sci*. ISSN: 0975-1017 (Online); 0971-4588 (Print), accepted
24. Chang Z, Li M, Chen J (2019) Analytical modeling and experimental validation of the forming force in several typical incremental sheet forming processes. *Int J Mach Tools Manuf* 140:62–76

25. Oleksik V, Pascu A, Gavrus A, Oleksik M (2010) Experimental studies regarding the single point incremental forming process. *Acad J Manuf Eng* 8:51–56
26. Fiorentino A, Ceretti E, Attanasio A, Mazzoni L, Giardini C (2009) Analysis of forces, accuracy and formability in positive die sheet incremental forming. *IntJ Mater Form* 2:805–808
27. Jeswiet J, Micari F, Hirt G, Bramley A, Duflou J, Allwood J (2005) Asymmetric single point incremental forming of sheet metal. *CIRP Ann Manuf Technol* 54:88–114

# Laser Polishing of Laser Additive Manufactured Hastelloy-X: Parametric Dependence and Process Optimization



Poonam Deshmukh, Ambar Choubey, A. N. Jinoop, C. P. Paul, S. S. Mohite, and K. S. Bindra

**Abstract** The components built using laser additive manufacturing (LAM) suffer from various issues, like—stair-stepping effect, balling effect and presence of partially melted powders, which results in higher surface roughness. Thus, the surface finish of LAM built components is not suitable for various engineering applications in the as-built condition. Therefore, post-processing is necessary to improve the aesthetics and surface quality of LAM built components. Laser polishing is one of the advanced post-processing techniques that can be used for improving the surface quality of LAM built components. Laser polishing can be used to improve the surface quality of various engineering components for aerospace, automobile, biomedical, construction, cryogenics and nuclear industries due to its inherent advantages, like—smaller processing time, ability to access intricate shapes and smaller areas, etc. Hastelloy-X is the one of the nickel superalloys processed by LAM for building complex shaped components for nuclear and aerospace sector. As LAM is used for building components with complex geometry, it is difficult to deploy conventional polishing techniques for polishing of LAM built components. Thus, laser polishing can be considered as an ideal choice for improving the surface finish of such components. In the present work, an experimental investigation is carried out to optimize the process parameters during continuous wave fibre laser-based laser polishing of LAM built Hastelloy-X surface. The parametric dependence is investigated through design of experiments as per Taguchi L9 array with laser power, process speed, percentage of laser line overlapping and stand-off distance. Analysis of variance (ANOVA) is performed to identify significant laser parameters and it is observed that the laser power and line overlapping are the most significant factors. An improvement in average surface finish by ~30% (from a value of  $R_a = 8.46 \mu\text{m}$  to  $5.7 \mu\text{m}$ ) is achieved at the optimum process parameters. The study open avenues

---

P. Deshmukh · S. S. Mohite  
Government College of Engineering, Aurangabad, Maharashtra, India

A. Choubey · A. N. Jinoop · C. P. Paul (✉) · K. S. Bindra  
Laser Technology Division, Raja Ramanna Centre for Advanced Technology, Indore, India

A. N. Jinoop · C. P. Paul · K. S. Bindra  
Homi Bhabha National Institute, Anushaktinagar, Mumbai, India

for the potential deployment of laser polishing for post-processing of LAM built components.

**Keywords** Laser additive manufacturing · Laser polishing · Process optimization · Hastelloy-X

## 1 Introduction

Hastelloy-X (Hast-X) is a nickel–chromium–iron–molybdenum alloy with high oxidation resistance, good ductility, excellent forming, resistant to stress-corrosion cracking and high-temperature strength [1–3]. It is commonly used for the furnace, petrochemical, automobile, aircraft, space applications, thermal power plants and high-temperature nuclear reactors. In order to fabricate complex shaped engineering components using Hast-X, researchers are investigating on the process development to build defect-free Hast-X using laser additive manufacturing (LAM). LAM is an advanced manufacturing process with capability of fabricating the complex shaped components directly from solid models with shorter lead time. LAM is best suited for the fabrication of mass-customized components and lightweight engineering components [4, 5]. LAM processes can be primarily classified into laser powder bed fusion (LPBF) and laser directed energy deposition (LDED) based on the material feeding mechanism. The surface finish of LDED built samples is not suitable for various engineering applications in as-built condition and requires post-processing to achieve the surface finish requirements of engineering applications. Conventionally many methods are deployed to improve the surface finish of LAM components, like—milling, mechanical polishing, chemical polishing, electrochemical polishing, buffing, etc. [6, 7]. Laser-based post-processing is one of the advanced post-processing techniques that can be used to improve the surface properties of LAM parts. Among them, laser polishing is a technique, which can improve the surface finish of LAM built parts. In laser polishing process, the laser spot irradiates the sample surface with laser beam at a certain range of laser power density that causes a surface melting, yielding improvement in surface finish. Laser polishing method is superior to conventional techniques due to its inherent advantages. Being a non-contact, highly flexible and automated process, it can be used to polish complex metallic components. In addition, it is also possible to polish the components, three dimensionally of the order of average surface roughness up to submicron and nanometer levels, within geometrical tolerances [8, 9]. Willenborg [10], Perry et al. [11] and Wang et al. [12] deployed laser polishing of LPBF samples and developed methods to achieve highly smoothed surfaces. To the best of authors' knowledge, there are no published reports in public domain on laser polishing of LDED built samples. Thus, in the present work, an attempt is made to understand the effect of process parameters during laser polishing of LDED built Hast-X through a systematic investigation.

## 2 Experimental Plan

An indigenously developed 2 kW continuous wave fibre laser-based laser directed energy deposition (LDED) system at Raja Ramanna Centre for Advanced Technology (RRCAT), Indore, India, is used to build Hast-X samples. The gas atomized Hast-X powder employed for LDED process is supplied by Sandvik Osprey Ltd., UK with a chemical composition in weight percentage (wt%) of Ni balance: Cr 21.70%, Fe 18.60%, Mo 9.20%, Co 1.82%, Si 0.36%, W 0.90%, O 0.017% and C 0.056%. The samples are built using optimized parameters of laser power 1600 W, scan speed 0.5 m/min, powder feed rate 8 g/min and laser spot diameter 2.5 mm [1]. Laser polishing is performed on an experimental setup developed at RRCAT as shown in Fig. 1, having a 500 W continuous wave (CW) Yb: Fibre laser. CW laser is preferred over pulsed laser in the present work, as it can produce continuous melt pool yielding superior surface finish due to advantages of fluid properties. The laser beam is delivered to the sample surface using a galvano-scanner that directs the laser beam in the *xy* plane. Further, the beam passes through a F-theta lens having a focal length of 500 mm. On the sample surface, a focused beam spot diameter of about 300 μm is generated. A vertical axis is used to position the laser beam focus in the *z*-direction. LDED built Hast-X bulk are cut into small samples of 10 mm × 10 mm dimension using wire electric discharge machining for laser polishing experiment. Laser polishing system uses .dxf files as input and laser track displacement or hatch spacing in the .dxf file is directly related with the laser line overlapping according to relation, hatch spacing = (1-line overlapping) × focus spot diameter.

The process parameters and its levels under investigation are laser power, scanning speed, percentage overlap and stand-off distance as presented in Table 1. Design of experiments is used to systematically study the effect of process parameters on the surface roughness. Taguchi’s L9 orthogonal array as presented in Table 2 is used for the experiment and the parameters considered for the study are laser power, scanning speed and percentage spot overlap at three levels each. In the present experiment,

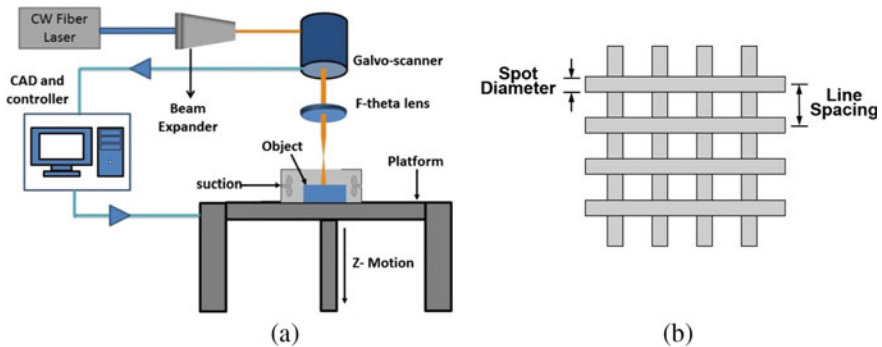


Fig. 1 Laser polishing of LDED Hast-X a schematic of laser polishing system b typical drawing

**Table 1** Laser polishing process parameters and their values

Sr. No.	Process parameter	Symbol	Unit	Levels		
				01	02	03
1	Laser power	$P$	W	75	100	150
2	Scanning speed	$V$	mm/s	300	500	700
3	Percentage spot overlap	$N$	%	70	80	90

**Table 2** Taguchi's orthogonal array L9 array

Expt. No.	Input parameters			Output characteristics
	$P$	$V$	$N$	Average surface roughness ( $\mu\text{m}$ )
01	75	300	70	8.12
02	75	500	80	6.42
03	75	700	90	6.16
04	100	300	80	7.76
05	100	500	90	6.41
06	100	700	70	7.22
07	150	300	90	5.70
08	150	500	70	7.76
09	150	700	80	6.88

hatch spacing has been varied as 0.03, 0.06 and 0.09 mm for the corresponding overlap percentage of 90, 80 and 70%, respectively.

Each experiment was repeated twice and an average surface roughness value was taken for the analysis. After performing the laser polishing experiments, surface of the sample is analysed using surface profilometer. The topography optimization is characterized by the surface roughness reduction as per Eq. 1.

$$R_{a(\text{reduction})}[\%] = (R_{a(\text{initial})} - R_{a(\text{polished})})/R_{a(\text{initial})} \times 100 \quad (1)$$

### 3 Results and Analysis

Average surface roughness is measured for all the samples and it is presented in Table 2. In order to investigate the effect of each process parameter on the performance characteristics, i.e. average surface roughness  $R_a$ , ANOVA analysis is carried out for each set of parameters. Table 3 presents the analysis of variance results for average surface roughness.

$P$ -value indicates that percentage spot overlap and scanning speed are the most important parameters influencing the surface finish. The percentage contribution of

**Table 3** Analysis of variance for surface roughness

Source	DF	Adj SS	Adj MS	F-value	P-value
Laser power	2	0.1898	0.0949	0.17	0.852
Scanning speed	2	0.3146	0.1573	0.21	0.776
Percentage spot overlap	2	3.9194	1.9597	3.59	0.218
Residual error	2	1.0926	0.54630		
Total	8	5.5164			

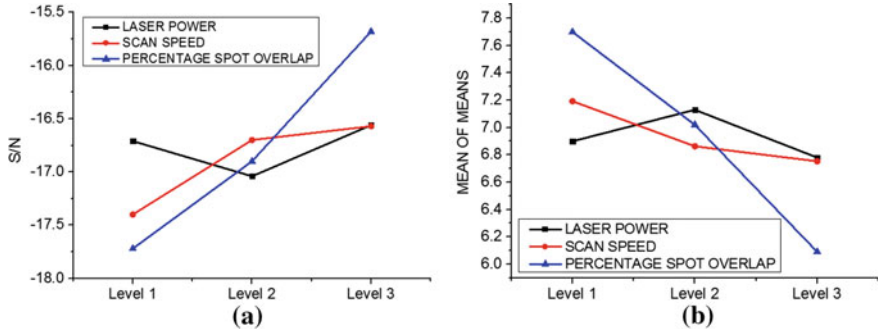


**Fig. 2** Main effect plot for surface roughness

laser power, spot overlap and scanning speed are 3.4%, 5.7% and 71%, respectively. Optimization is carried out by considering “smaller the better” criteria. Figure 2a, b presents the mean of means and signal-to-noise (S/N) ratio, respectively. Thus, level 3 of laser power, level 3 of scanning speed and level 3 of spot overlap are the optimum values for minimum surface finish for the present experimental condition. The effect of different process parameters on the surface finish is explained as follows:

*Effect of laser power:* The ANOVA analysis shows that laser power has only 3.4% percentage contribution indicating it as a non-significant parameter. This is primarily because the range of laser power selected is above the threshold value to initiate the laser melting. The laser power is sufficient to melt surface topography peaks of the LDED built Hast-X samples. With the surface tension, the molten material flow is reallocated into micro cavities of the surface abolishing initial topography yielding reduction in surface roughness. The resulting surface solidifies after laser melting without any significant cracks, pores or hidden defects out of the molten material. However, slightly higher value of surface roughness is observed when laser power is raised to 100 W. This might be attributed to experimental error or non-homogeneity in as-built sample.

*Effect of scanning speed:* At lower scan speeds, dwell time is high, because of which thermal ablation dominates over the surface melting. Thus, surface finish deteriorates considerably at lower scan speeds. However, with increasing scanning speed, surface



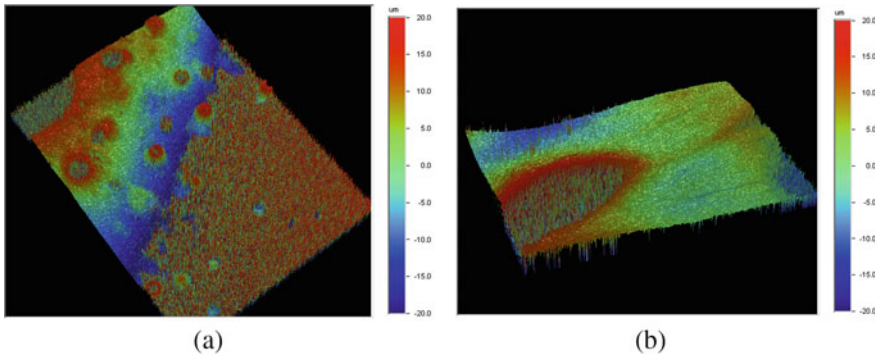


**Fig. 3** Surface profilometer images **a** as-built sample **b** laser polished sample

finish allows melt pool flow and redistribution of the material from peaks to valley. This can lead to reduction in the surface roughness of LDED built samples.

*Effect of percentage spot overlapping:* At lower values of spot overlap, the amount of overlap between the adjacent scans is not enough for providing sufficient energy to assist proper melting of peaks and redistribution of material. Thus, higher surface roughness is observed at level 1 and level 2 of spot overlap. However, very high value of spot overlap results in more amount of energy, which results in higher melt-pool flow. This allows for better redistribution of material during laser polishing and results in higher surface finish.

Figure 3a shows the surface topography and surface roughness value of as-built LAM sample before laser polishing. It is observed that initial average surface roughness is  $8.46 \mu\text{m}$ . The presence of partially melted powders on the surface of the LDED sample is the major factor governing the surface roughness. Figure 3b presents the surface topography of the sample with minimum surface roughness, i.e.  $5.7 \mu\text{m}$ . Sample No. 7 as shown in Table 2 has very good surface finish as compared to other samples after polishing. The values of CW laser process parameters for this sample are 150 W laser power, 90% line over lapping and 300 mm/s scanning speed.

## 4 Conclusions

Laser polishing of LAM built Hast-X is performed successfully using a CW fibre laser to improve the surface finish of LAM samples by remelting a thin surface layer in a short processing time of  $\sim 100 \text{ s/cm}^2$ . ANOVA analysis shows that the percentage of spot overlapping is the most significant parameter followed by scanning speed and laser power. An improvement in average surface finish by  $\sim 30\%$  (from a value of  $R_a = 8.46 \mu\text{m}$  to  $5.7 \mu\text{m}$ ) is achieved at the optimum process parameters of 90% spot overlapping, 700 mm/s scanning speed and 150 W laser power. The roughness on the surface is reduced significantly and the polished surface appears to be glossy and

smooth as compared to as-built sample. The present work can pave a way towards the popularization and application of laser polishing for LAM built components in biomedical, automobile, aerospace, vacuum, nuclear and cryogenic fields.

## 5 Future Work

The work can be extended towards the laser polishing on components with curved geometries, sharp edges and corners. Thermal simulation of the melt pool and simulation of fluid flow in the melt pool during laser polishing is in progress. The work will be extended towards the characterization of laser polished LAM samples using X-ray diffraction (XRD) technique for phase analysis, secondary ion mass spectroscopy (SIMS) for oxide and carbide detection, Goniometer for evaluating the wettability and electrochemical setup for estimating the corrosion resistance and its comparison with as-built samples.

**Acknowledgements** Authors acknowledge the financial support from Ministry of Human Resource Development, Government of India and Raja Ramanna Centre for Advanced Technology. The author acknowledges the support from Mr. C. H. Premsingh and Mr. U. Kumar of Laser Additive Manufacturing Lab (LAML), RRCAT for help during sample preparation, Mr. S. K. Mishra for laser polishing experiments. Authors thank the support from Mr. Adbol, Mr. Lalit and Mr. Sokhen Tudu for help during sample sectioning. The authors also thank the support from other members of LAML, RRCAT for their support.

## References

1. Jinoop AN, Paul CP, Bindra KS (2019) Laser assisted direct energy deposition of Hastelloy-X. *Opt Laser Technol* 109:14–19
2. Marchese G, Bassini E, Aversa A, Lombardi M, Ugues D, Fino P, Biamino S (2019) Microstructural evolution of post-processed Hastelloy X alloy fabricated by laser powder bed fusion. *Materials* 12:486–499
3. Han Q, Mertens R, Montero-Sistiaga ML, Yang S, Setchi R, Vanmeensel K, Van Hooreweder B, Evans SL, Fan H (2018) Laser powder bed fusion of Hastelloy X: effects of hot isostatic pressing and the hot mechanism. *Mater Sci Eng A* 732:228–239
4. Hyub L, Lim CHJ, Low MJ, Tham N, Murukeshan VM, Kim Y-J (2017) Lasers in additive manufacturing: a review. *Int J Precision Eng Manuf Green Technol* 4:307–322
5. Do-Sik S, Baek G-Y, Seo J-S, Shin G-Y, Kim K-P, Lee K-Y (2016) Effect of layer thickness setting on deposition characteristics in direct energy deposition (DED) process. *Opt Laser Technol* 86:69–78
6. El Khalick MA, Wang D (2016) Electrochemical mechanical polishing technology: recent developments and future research and industrial needs. *Int J Adv Manuf Technol* 86(5):1909–1924
7. Kumbhar NN, Mulay AV (2018) Post processing methods used to improve surface finish of products which are manufactured by additive manufacturing technologies: a review. *J Inst Eng (India) Ser C* 99(4):481–487

8. Benoit R, Mognol P, Jean-Yves H (2015) Laser polishing of additive laser manufacturing surfaces. Laser Institute of America. *J Laser Appl* 27:S2
9. Arun K, Fengzhou F (2019) Review on mechanism and process of surface polishing using lasers. *Front Mech Eng* 14(3):1–21
10. Willenborg E (2019) Polishing with laser radiation. In: Poprawe R (ed) *Tailored light*, 2nd edn. Springer, Berlin, pp 196–203
11. Perry TL, Werschmoeller D, Li X, Pfefferkorn FE, Duffie NA (2007) Micromelting for laser micro polishing of meso/micro metallic components. In: *Proceedings of ASME 2007 international manufacturing science and engineering conference*. ASME, Atlanta, pp 363–369
12. Wang HY, Bourell DL, Beaman J (2003) Laser polishing of silica slotted rods. *Mater Sci Technol* 19(3):382–387

# Elucidating Corrosion Behavior of Hastelloy-X Built Using Laser Directed Energy Deposition-Based Additive Manufacturing in Acidic Environments



P. K. Diljith, A. N. Jinoop, C. P. Paul, P. Krishna, S. Bontha, and K. S. Bindra

**Abstract** This paper reports an investigation on the electrochemical corrosion behavior of laser directed energy deposition (LDED)-based additive manufacturing built Hastelloy-X (Hast-X) bulk samples for the first time in various acidic environments (2M HNO<sub>3</sub>, 2M HCl, and 2M H<sub>2</sub>SO<sub>4</sub>). Open-circuit potential results reveal that corrosion activity is more in HCl than the other two media. The corrosion rate (CR) estimated using the Tafel extrapolation method shows that the corrosion rate (CR) is the most in HCl and least in HNO<sub>3</sub>. Potentiodynamic studies reveal active-passive behavior of Hast-X in all the media and it is seen that the material stays in passivation for a longer potential range in HCl. Further, pitting potential is observed to be comparable in all three media. The cyclic polarization curve shows no loops, which points out the absence of pitting in the samples immersed in any of the media. The estimated CR for Hast-X in all the acidic environments under investigation comes within the acceptable CR for nickel-based alloys (4 mpy). The morphology of the corroded surface is analyzed using stereo microscope and it confirms the absence of pitting in all the three samples. These observations confirm the suitability of LDED built Hast-X components for applications in investigated acidic environments.

**Keywords** Laser additive manufacturing · Laser directed energy deposition · Hastelloy-X · Corrosion

---

P. K. Diljith · P. Krishna · S. Bontha

Department of Mechanical Engineering, National Institute of Technology Karnataka, Surathkal, Surathkal, Karnataka 575025, India

A. N. Jinoop · C. P. Paul (✉) · K. S. Bindra

Laser Technology Division, Raja Ramanna Centre for Advanced Technology, Indore, Madhya Pradesh, India

Homi Bhabha National Institute, Anushaktinagar, Mumbai, Maharashtra, India

## 1 Introduction

Laser additive manufacturing (LAM) is one of the advanced manufacturing techniques used for building complex shaped engineering components from digital model data using layer-by-layer build-up methodology. The ability to fabricate components of customized strength-to-weight ratio and composition from a 3D model, quickly and economically, has turned the focus of the manufacturing industry toward LAM. Laser directed energy deposition (LDED) is a LAM process that uses a high-power laser source to create a melt pool on the substrate or previously deposited layers to melt and deposit dynamically fed raw material (powder or wire) as per the required geometry [1]. LDED is widely used to process metallic alloys and it is particularly attractive to process nickel superalloys for various hostile conditions. The self-hardening nature and excellent high-temperature mechanical properties of nickel superalloys cause serious tool wear, low material removal rate, etc., during traditional machining and limits the deployment of traditional machining to manufacture nickel superalloy components in its entirety [2]. Hastelloy-X (Hast-X) is one of the nickel-based superalloys widely used in aero-engines, gas turbines, etc., owing to its good weldability, high corrosion resistance, hot oxidation resistance, and superior mechanical properties at elevated temperatures [3]. Hast-X components can be potentially used for the fabrication of compact heat exchangers, gas turbine blades, fuel nozzles, heat shields, using LDED, which were earlier built by conventional manufacturing methods [3]. Piping components, pressure vessels, and boiler parts made of Hast-X are extensively used in petrochemical industries [4]. These components are exposed to an aggressive corrosive environment during operation [4].

Quang et al. investigated the effect of chemical composition and temperature on the passivation of nickel-based alloys, like Hast-X, Hast-C276, Inconel 625, etc., in  $H_2SO_4$  medium [5]. The authors observed that the variation in chromium and molybdenum significantly affects the corrosion resistance of the alloy. In addition, the increase in temperature leads to the faster dissolution of the passivation layer. Johnson et al. compared the corrosion resistance of Hast-X, Inconel 718, and Inconel 625 fabricated using metal injection molding and compared the behavior with their cast and wrought counterparts using  $HNO_3$ ,  $H_2SO_4$  and HCl solutions [6]. The study revealed that Hast-X is resistant to both oxidizing and reducing the acidic environment. Leonard compared the corrosion behavior of conventionally built Hast-X, in various heat-treated conditions in boiling  $HNO_3$ ,  $H_2SO_4$ , and HCl and discussed the effect of temperature and constituent elements on the corrosion rate of the alloy [7]. An increase in corrosion rate due to the sensitization of Hast-X, due to grain boundary precipitation in HCl was investigated. The increased corrosion resistance in Hast-X exposed to  $H_2SO_4$  with the addition of copper and the increased corrosion resistance with the addition of oxidizers in the solution was also revealed in the paper. Even though the electrochemical behavior of conventionally built Hast-X is available in acidic media, there is no literature available in the public domain on the electrochemical behavior of LDED built-in acidic media.

Recently, LAM of Hast-X became a hotspot for researchers, as there are many publications on LAM of Hast-X both in laser powder bed fusion (LPBF) and LDED [8–11]. Kong et al. compared the corrosion behavior of LPBF built Hast-X with wrought one in sodium borate buffer solution and observed that the corrosion depth of LPBF samples is three times that of wrought ones [12]. In one of our previous work, process parameters were optimized for LDED of Hast-X [3]. Since LAM of Hast-X is becoming popular, it can be anticipated that many engineering components especially those working under high-temperature and highly corrosive media, can be potentially built by LAM. Thus, the understanding of the corrosion behavior of LAM built Hast-X can guide the material designers regarding the reliability of using the same in various applications.

This paper is focused on the electrochemical behavior of LDED built Hast-X in various acidic media. Since HCl, H<sub>2</sub>SO<sub>4</sub>, HNO<sub>3</sub>, and their compounds are commonly found in the service environments of Hast-X, electrochemical tests are conducted in their aggressive solutions (two molar solutions). Various electrochemical tests including open-circuit potential test, potentiodynamic and cyclic potentiodynamic tests are conducted on LDED built Hast-X exposed to the above-mentioned media. Passivation behavior of Hast-X is studied and the occurrence of pitting phenomenon is checked. In addition, the electrochemical behavior of Hast-X in the above-said rigorous corrosive environments is compared.

## 2 Materials and Methods

The Hast-X powder manufactured by gas atomization with particle size 45–106 μm and spherical morphology, conforming to AMS standard, is deposited using LDED. An indigenously developed LDED system is deployed (refer Fig. 1a) to deposit bulk Hast-X structures (refer Fig. 1b) on the SS304L substrate. The parameters used for LDED of Hast-X are laser power—1600 W, scan speed—0.5 m/min, powder feed rate—8 g/min, and laser spot diameter—2.5 mm. More details about the system and process parameter selection are reported in one of our earlier works [3]. Subsequent to LDED, the samples are cut, mounted, polished using silicon carbide papers in the sequence of grit size of 400, 600, 800, and 1000. For microstructural analysis of the as-built sample, cloth polishing is performed and samples are etched using the oxalic acid solution prepared by adding 10 g of oxalic acid to 100 ml of distilled water. The microstructure is analyzed using an optical microscope (Make: OMNITECH, Model: Metagraph). For electrochemical studies, the samples are cleaned with acetone and rinsed with distilled water to obtain a clean surface. Aqueous solutions of 2M H<sub>2</sub>SO<sub>4</sub>, HCl, and HNO<sub>3</sub> are prepared for electrochemical studies. An open-circuit potential test is performed to evaluate the equilibrium potential of the system. The potential is varied in negative and positive directions and the corresponding current density values are used to obtain the Tafel plot for estimating the corrosion rate of the material. The potentiodynamic plot and cyclic potentiodynamic plot are also obtained by applying

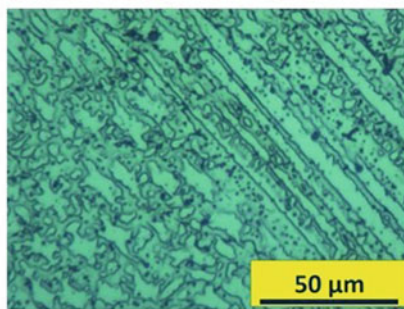
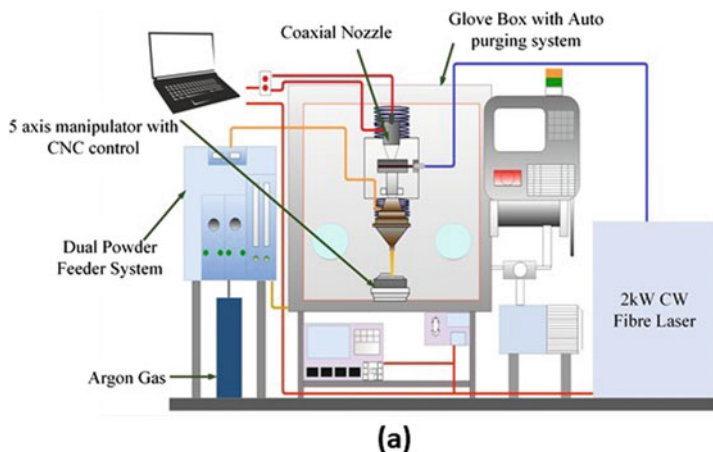


**Fig. 1** LDED of Hast-X **a** setup; photographic view of **b** bulk deposit and **c** cross-sectional microstructure

the potential in a longer range. The recorded values of current density are used to evaluate the material behavior in the three different media.

The tests are performed on an electrochemical workstation (Make: Ametek, Model: PARSTAT 3000A) with an exposed area of  $1 \text{ cm}^2$ , using a potentiostat with a scan rate of  $0.1667 \text{ mV/s}$ , as prescribed by ASTM. Platinized platinum mesh and  $\text{Ag/AgCl}$  electrode are used as the counter and reference electrodes, respectively. Subsequently, the surface morphology of the corroded surface is examined using stereo microscope (Make: Leica, Model: SAPO).

### 3 Results and Discussion

The cross section of the as-built Hast-X structure is examined using optical microscopy and the microstructure reveals defect-free deposition (without cracks, voids, etc.) with fine columnar dendritic growth. In the bottom layers of the component, the contact with the substrate provides a larger thermal gradient and facilitates faster cooling of the deposited layers. As a result, columnar dendritic growth without secondary dendritic arms is found in the bottom layers. In the succeeding layers, the preheating from previous layers lowers the thermal gradient, resulting in the formation of secondary dendritic arms.

The open-circuit potential (OCP) of the samples in the three media is monitored until the OCP stabilizes. As presented in Fig. 2a, OCP of Hast-X in HCl stabilizes faster, whereas in HNO<sub>3</sub> took more time for stabilization. The OCP curve of Hast-X in HCl shows a reducing nature with the curve saturating at an OCP of -434.52 mV. The OCP curves of the sample in H<sub>2</sub>SO<sub>4</sub> and HNO<sub>3</sub> show an oxidizing character, as the potential keeps on increasing with the time and steadies up at -237.66 mV and 160.23 mV, respectively. This positive potential shift in H<sub>2</sub>SO<sub>4</sub> and HNO<sub>3</sub> shows

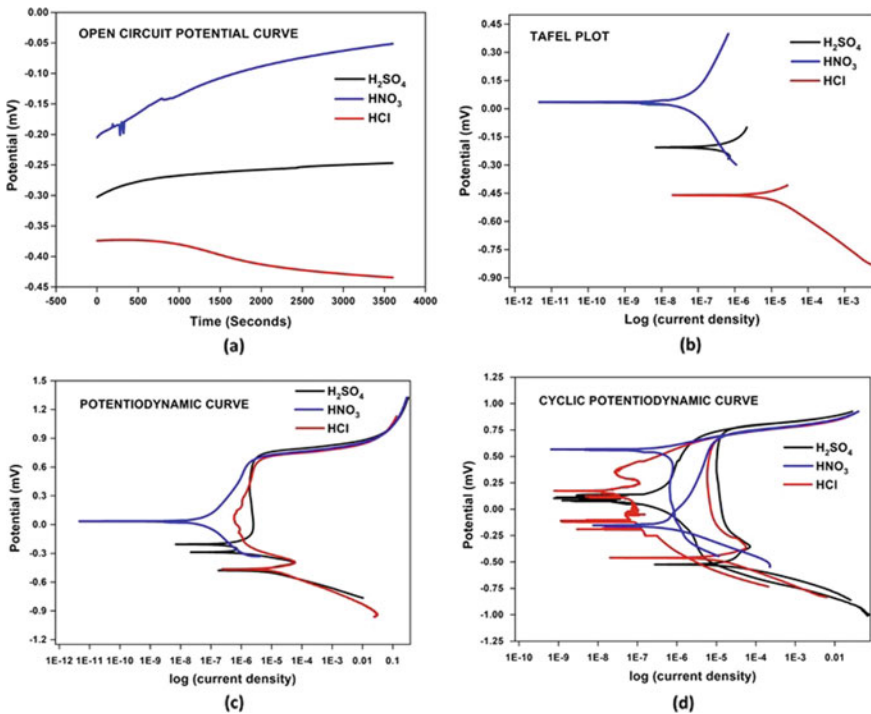


**Fig. 2** Electrochemical analysis of LDED built Hast-X **a** OCP **b** Tafel **c** potentiodynamic **d** cyclic polarization



**Table 1** Electrochemical parameters from Tafel polarization and potentiodynamic test

Solution	OCP (mV)	$E_{CORR}$ (mV)	$I_{CORR}$ ( $\mu A/Cm^2$ )	CR (mpy)	$E_{PIT}$ (mV)	$E_{PIT} - E_{CORR}$ (mV)
H <sub>2</sub> SO <sub>4</sub>	-237.66	-205.71	73.26E-3	0.03	718.83	924.54
HCl	-434.52	-465.38	1.64	0.65	626.08	1091.46
HNO <sub>3</sub>	160.23	32.56	3.50E-3	0.001	666.20	505.97

passivation behavior [13], while the negative shift in HCl indicates activation behaviors. Thus, the corrosion activity is descending in the order of HCl followed by H<sub>2</sub>SO<sub>4</sub> and HNO<sub>3</sub>. It is primarily due to the dissolution of the sample in HCl due to the presence of Cl<sup>-</sup>, which makes it a very severe corrosive agent [14], whereas HNO<sub>3</sub> being a strong oxidizing agent, creates a passive layer which leads to a higher OCP value.

Figure 2b presents the variation in cathodic and anodic reaction kinetics of LDED built Hast-X through Tafel polarization measurements. The cathodic branches of all the three curves show typical Tafel behavior, whereas the anodic branches in HNO<sub>3</sub> and H<sub>2</sub>SO<sub>4</sub> show a higher slope indicating passivation behavior. In the case of HCl, there is a continuous increase in anodic current with an increase in potential representing active corrosion due to the dissolution of Hast-X in HCl. Further, the corrosion current ( $I_{CORR}$ ) and corrosion rate (CR) are estimated using the Tafel extrapolation method and presented in Table 1. The CR values show slow corrosion in HNO<sub>3</sub> and H<sub>2</sub>SO<sub>4</sub>, whereas relatively fast corrosion is observed in HCl. The estimated CR values in all media are lower than the acceptable CR (4 mpy) for nickel-based alloys as per the ASM standard [15].

Potentiodynamic curves presented in Fig. 2c present the corrosion characteristics in the passivated state of the samples in each of the solutions. The value of current at the passivated state (passive current density) of the samples is similar in all the media. As opposed to the active state, the potentiodynamic curve shows that more corrosion occurs in H<sub>2</sub>SO<sub>4</sub> in the passivated state, followed by HCl and then HNO<sub>3</sub>. The range in which the metal lies passivated is maximum in HCl and it is found out to be 1091.46 mV. Hast-X remains passivated in H<sub>2</sub>SO<sub>4</sub> and HNO<sub>3</sub> for a potential range of 924.54 mV and 505.97 mV, respectively. In this sense, the Hast-X sample resists corrosion in HCl for a greater range of potential in the passive state, even though other acids passivate the metal faster being oxidizing in nature. The pitting potential of the three curves lies closer to each other. Once the potential reaches the pitting potential, the passive layer is damaged by the acids and the corrosion in the samples shoots up uncontrollably.

The cyclic potentiodynamic polarization technique is employed to understand the pitting corrosion behavior of the samples in the acidic solutions (refer to Fig. 2d). During the cyclic potentiodynamic polarization test, the potential is applied in the positive direction and taken to a considerable potential above the pitting potential of the sample. Then the potential is reversed and the current response is recorded. At a certain potential, if the value of the current density of the descending curve is greater

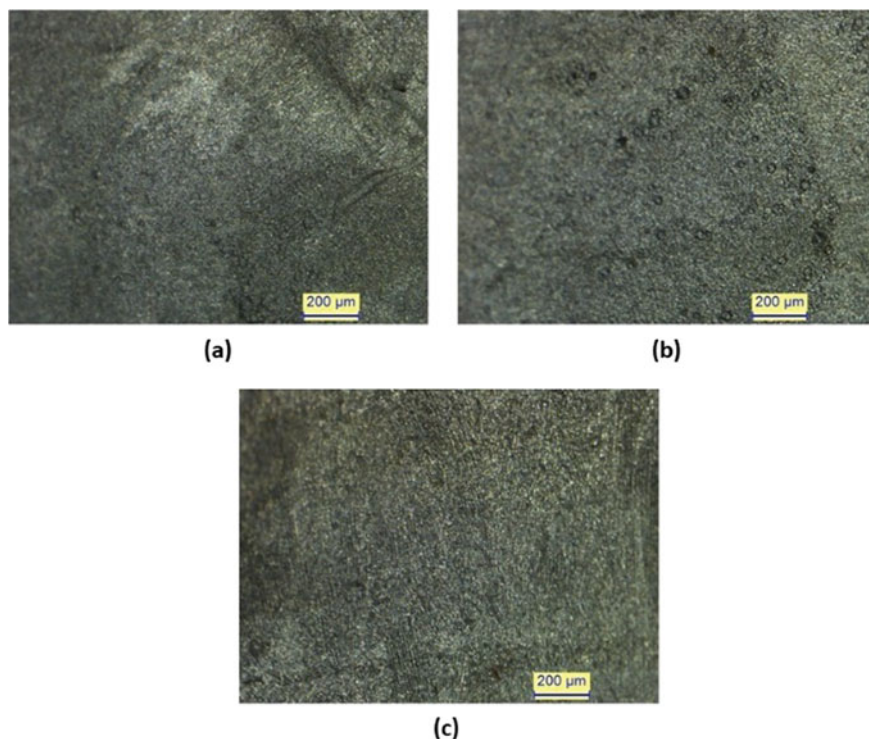


**Fig. 3** Stereo micrographs of Hast-X sampled in **a**  $\text{H}_2\text{SO}_4$  **b**  $\text{HCl}$  **c**  $\text{HNO}_3$

than that of the ascending curve, it shows the corrosion of the sample is more in the descending state, due to the occurrence of localized corrosion. This can be observed in the cyclic potentiodynamic curve as loops. In the present case, none of the cyclic potentiodynamic curves associated with the three acidic media shows signs of pitting corrosion [16].

The stereo micrographs of the corroded samples, which underwent the potentiodynamic test, are shown in Fig. 3. Pits are not observed on the Hast-X samples with any of the solutions. This confirms the absence of pitting behavior obtained from the cyclic potentiodynamic curve.

## 4 Conclusions

Corrosion behavior of LDED built Hast-X is investigated in various acidic environments (2M  $\text{HNO}_3$ ,  $\text{HCl}$ , and  $\text{H}_2\text{SO}_4$ ). Three distinct OCP values indicate that Hast-X shows different tendencies to lose atoms in different acidic media, which is analogous to the corrosion activity. Here, corrosion is active in descending order

under HCl, H<sub>2</sub>SO<sub>4</sub> and HNO<sub>3</sub> environments. Tafel curves show typical behavior for cathodic branches, while for anodic branches, HNO<sub>3</sub> and H<sub>2</sub>SO<sub>4</sub> show passivation behavior faster than HCl. HCl being a reducing media do not promote early passivation. Hast-X sample in HCl remains in the passivated state for a longer time than the other acids. Cyclic potentiodynamic curves and microscopic examination show the absence of pitting in the samples immersed at all solutions. The estimated CR in all solutions is lower than the acceptable maximum CR (4 mpy) for nickel-based alloys as per ASM standards. The study concludes that LDED built Hast-X can be potentially used in acidic environments. This study will be further extended to the corrosion behavior of heat-treated LDED built Hast-X.

## 5 Future Scope

The work will be further extended to the evaluation of the corrosion behavior of LDED built Hast-X in post-heat-treated conditions. Further, the corrosion rate of LDED built samples will be compared with conventionally built Hast-X.

**Acknowledgements** P. K. Diljith and A. N. Jinoop acknowledge the financial support from the Ministry of Human Resources Development and the Department of Atomic Energy, Government of India, respectively. The authors thank Mr. G. K. Mishra, Mr. U. Kumar, Mr. A. Adbol, Mr. S. Tudu, and Mr. Lalit of LAM Lab, RRCAT for their help during the study.

## References

1. Li W, Soshi M (2019) Modeling analysis of grain morphologies in directed energy deposition (DED) coating with different laser scanning patterns. *Mater Lett* 251:8–12
2. Sofuoğlu MA, Çakır FH, Gürgeç S, Orak S, Kuşhan MC (2017) Experimental investigation of machining characteristics and chatter stability for Hastelloy-X with ultrasonic and hot turning. *Int J Adv Manuf Technol* 95:1–4
3. Jinoop AN, Paul CP, Bindra KS (2019) Laser assisted direct energy deposition of Hastelloy-X. *Opt Laser Technol* 109:14–19
4. <https://www.titanmf.com/alloys/applications-of-hastelloy/>. Last accessed 14 Mar 2020
5. Quang KV, Traisnel M, Damie P, Bavay J-C (1980) Influence of chemical composition and temperature on the passivation of some stainless steels and nickel-based alloys in sulphuric acid. *J Appl Electrochem* 10(6):703–708
6. Johnson JL, Tan LK, Suri P, German RM (2004) Mechanical properties and corrosion resistance of MIM Ni-based superalloys. In: *Proceedings of the 2004 international conference on powder metallurgy and particulate materials*, Princeton, USA, vol 4, pp 89–101
7. Leonard RB (1968) The electrochemical behavior of some nickel base and cobalt base alloys. *Corrosion* 24(9):301–311
8. Esmaeilzadeh R, Keshavarzkermani A, Ali U, Mahmoodkhani Y, Behravesh B, Jahed H, Toyserkani E (2020) Customizing mechanical properties of additively manufactured Hast-X parts by adjusting laser scanning speed. *J Alloy Compd* 812

9. Keshavarzkermani A, Esmaeilzadeh R, Ali U, Enrique PD, Mahmoodkhani Y, Zhou NY, Toyserkani E (2019) Controlling mechanical properties of additively manufactured Hast-X by altering solidification pattern during laser powder-bed fusion. *Mater Sci Eng* 762
10. Han Q, Mertens R, Montero-Sistiaga ML, Yang S, Setchi R, Vanmeensel K, Fan H (2018) Laser powder bed fusion of Hast-X: effects of hot isostatic pressing and the hot cracking mechanism. *Mater Sci Eng* 732:228–239
11. Montero-Sistiaga ML, Pourbabak S, Van Humbeeck J, Schryvers D, Vanmeensel K (2019) Microstructure and mechanical properties of Hast-X produced by HP-SLM (high power selective laser melting). *Mater Des* 165
12. Kong D, Ni X, Dong C, Zhang L, Yao J, Man C, Li X (2019) Anisotropic response in mechanical and corrosion properties of Hast-X fabricated by selective laser melting. *Constr Build Mater* 221:720–729
13. Li D, Liang Y, Liu X, Zhou Y (2010) Corrosion behavior of  $Ti_3AlC_2$  in NaOH and  $H_2SO_4$ . *J Eur Ceram Soc* 30(15):3227–3234
14. [https://www.parrinst.com/wp-content/uploads/downloads/2011/07/Parr\\_Inconel-Incoloy-Monel-Nickel-Corrosion-Info.pdf](https://www.parrinst.com/wp-content/uploads/downloads/2011/07/Parr_Inconel-Incoloy-Monel-Nickel-Corrosion-Info.pdf). Last accessed 14 Mar 2020
15. (2003) ASM Handbook. Corrosion: fundamentals, testing, and protection, vol 13A. ASM International, OH
16. Durtewitz CB, Calderón FA (2016) Electrochemical corrosion of ferritic 409 and 439 stainless steels 409 and 439 in NaCl and  $H_2SO_4$  solutions. *Int J Electrochem Sci* 11:1080–1091

# 3-D Printing Technology: Inclusive Study and Applicability in Different Sectors



Mohd. Yunus Khan, P. Sudhakar Rao, and B. S. Pabla

**Abstract** This paper presents an insight of state of the art of 3-D printing (3-DP) technology. 3-DP technique develops three-dimensional products that have been designed using computer software by settling down material layer by layer. In the past years, the many studies have been carried out on 3-DP. This paper reviews the current research trends and recent developments in 3-DP technologies. 3-DP has a wide range of application in automobile, aircraft, medical, fashion design, food industry, jewelry making, etc. A detailed description of applications of 3-DP in various fields is presented. Stepwise procedure of 3-DP along with its advantages and limitations is also given. It is hoped that the information provided in this study will be useful in understanding basic fundamentals of 3-DP printing technology. The review work relies on academic publications and recent conference proceedings.

**Keywords** Additive manufacturing · 3-D printing · Printing layers

## 1 Introduction

3-DP or additive manufacturing is a technique of developing 3-D products by laying down material layer by layer. 3-DP technique is basically computer controlled additive manufacturing process. Physical items are developed by utilizing computerized model information from 3-D model [1–3]. By employing 3-DP, it is conceivable to create products of practically any shape and structure. 3-DP has attracted lot of attention in the course of recent years because of its inherent advantages, for example, unmatched ease in designing and customization [4]. As of late, 3-D printers are available for industries and even for home users. With progress of technology, characteristics of the product enhanced and first application in tool inserts with conformal

---

Mohd. Y. Khan (✉) · P. S. Rao · B. S. Pabla  
National Institute of Technical Teachers' Training and Research (NITTTR), Chandigarh 160019,  
India  
e-mail: [yunus.mech19@nitttrchd.ac.in](mailto:yunus.mech19@nitttrchd.ac.in)

cooling developed [5]. It was in mid-1980s, Chuck Hull designed the first three-dimensional printing process and called it stereolithography (SLA). He characterized SLA as a process and equipment for creating solid products by sequentially printing of slender layers of the UV-curable material one over another [6–8]. With this, foundation of 3-DP was laid.

The term additive manufacturing picked up prominence in the 2000s. As the different additive processes developed, it turned out to be certain that shortly metal evacuation would now not be the only metalworking process. However, at the time, 3-DP still alluded distinctly to the polymer technologies in many minds while the term additive manufacturing was more likely to be employed in metalworking. In the beginning of 2010, it was realized that 3-DP and additive manufacturing are substitute terms for same technology [2, 9].

3-DP helps the industry think faster, initiate higher, and broaden up the horizons of manufacturing. It is a case of technology and manufacturing operating along to become more flexible and scalable, ensuring improved productivity and quality. There are various types of 3-DP technologies. Most commonly used selective laser sintering, fused deposition modeling and stereolithography [1, 10]. The chief disparity is how layers are laid down to develop product. Various materials can be used in this technology such as acrylonitrile butadiene styrene [11, 12], polylactide [11, 12], photopolymers [12, 13], polypropylene (PP) or polyethylene (PE) [14], composite [12, 13], ceramics [15–17], polyamide [18], titanium and its alloy [19–21], nickel-based alloys [19, 20], stainless steel [1–20], cobalt-based alloys [22], aluminum alloys [19, 20], alumide (polyamide/aluminum powder) [21, 23], glass [21], silver [21], gold [21], brass [21], and wax [24]. Figure 1 depicts shapes produced in the laboratory of NITTTR, Chandigarh by 3-DP technology.



**Fig. 1** Shapes produced by 3-D printing

The purpose of this paper is to bring out an inclusive review of the emerging technology known as 3-D printing. Numerous applications of 3-DP process are discussed. Necessary steps involved in 3-DP along with its advantages and limitations are presented.

## 2 Applications of 3-DP

3-DP finds application in almost all industries. Few of the applications are discussed here. Using 3-DP, surgeons can develop specific 3-D printed models of patient's body parts. These models are utilized to plan and execute surgeries. This technology is also finds wide utility in dentistry and prosthetics [25–31]. 3-D printers are used to develop parts of jet engines like fuel nozzles [25, 28, 32]. Racing cars use 3-DP for prototyping, testing, and developing customized parts [25, 28, 32]. Customized jewelry can be developed using this technology [25]. 3-DP can be used in fashion field for making dresses, high heels, handbags, and other items [26, 28]. 3-DP is also used in food industry. Chocolates and cheese are being printed using this technology. Bakery products like cookies, cakes, and pastries are created by 3-DP process [27, 28]. 3-DP is widely used in architecture field. Architects can conveniently and rapidly develop 3-D model from design model which can be further used to develop blueprint [28, 32]. 3-DP finds wide application in construction. Experimentations related to construction technology have been carried out to explore potential of 3-DP in construction industry [33, 34]. Artists and designers use 3-DP for creating various art works. It opens up entirely new dimensions of creativity that go past the points of confinement of conventional methods. This process can also be used to replicate ancient artifacts [35, 36].

## 3 Procedure of 3-DP

Stepwise procedure of 3-DP is described below:

1. First step in 3-DP is generating a digital model of the item to be created. CAD software is employed for this. Reverse engineering can also be used to create a digital model by using scanning techniques.
2. CAD model is transformed into a STL (stereolithography) file that is acceptable by 3-D printers.
3. STL model is analyzed and repaired, if required. Errors can include missing surfaces or unconnected edges. There are software for STL model manipulations and repair.
4. After that device is ready for printing. This process requires proper printer setup and control, cleaning from earlier build and loading print material. Once hardware is ready, build file could be uploaded to the printer.

5. The whole printing procedure is totally automatic. Depending upon the dimensions of the part, printer and material employed, the procedure might take several hours or even days.
6. The developed part is then removed from the printer.
7. Post-processing the product may include removing of supports, high pressure air cleaning, polishing, coloring, and other actions to prepare for final use [37–42].

## 4 Research Progress Conducted on 3-D Printing Technology

Technological advances reported in 3-DP technology that shows the state of the art in industrial research and applications are briefly scrutinized.

3-DP technique finds wide applicability in medical, dental, and prosthesis research. Wu et al. [10] used selective laser sintering to develop wax pattern for a partial nasal prosthesis. They concluded that 3-DP technique can conveniently produce nasal pattern and save lengthy procedures. Taylor et al. [43] investigated 3-DP technology to print models for analyzing representation of eye trauma and presented a preventive model for analysis of various anatomical and anthropological features. Torres et al. [44] studied different rapid prototyping techniques (RPT) for various medical applications. They suggested RPT to be an effective tool for improving anatomical education. Peng et al. [25] presented an exhaustive review of RPT for maxillofacial reconstruction covering all facets of the technology. Torres et al. [45] reviewed all the features of 3-DP for bone tissue engineering. They studied various applications of 3-DP and identified its five significant advancements.

Aerospace and automobile industries are employing 3-DP methods for development of various components. Matta et al. [46] investigated applicability of 3-DP to design light weight unmanned aerial vehicle wing structures. They proposed three lattice designs which were fabricated by 3-D printer using polypropylene-like photopolymer. Joshi and Sheikh [47] studied materials developed particularly for aerospace applications. They also presented ongoing research work in applicability of 3-DP in aerospace and outlined challenges related to 3-DP in microgravity. Various demerits of printed components along with future prospective of aero-spatial industry with 3-D printing were also depicted. Kumar and Nair [48] explored the feasibility of additive manufacturing in aircraft industry. Moon et al. [49] reviewed metal prototyping as applied to automotive industry. They studied various areas of metal prototyping which includes re-engineering model generation, mathematical and software simulation, 3-D printing, metal prototyping through 3-D or 4-D printing and prototype testing.

Fashion industry which includes garment, shoe, jewelry industries is effectively utilizing technology of 3-D printing for create important products. Wang and Chen [50] explored the possibility of 3-DP in fashion industry and investigated the attributes of 3-D clothing. The influence of 3-DP on the clothing design with limitations was presented. It was suggested that 3-DP method applied in the clothing can



result in significant changes to this industry. Yap and Yeong [51] summated various additive manufacturing processes employed in fashion and jewelry industry. They described technique of data capturing and modeling tools, and necessary designing methods for development of 3-D printed fashion products. White et al. [52] employed electro-spinning technique for producing customized 3-D fabrics and textiles. They synopsis important facets of this technique along with its merits over conventional textile manufacturing process. Cooper [53] implied concept of 3-DP to jewelry manufacturing. They discussed various features of 3-DP technology as applied to jewelry designing and development. Valtas and Sun [54] explored the utility of 3-D printing in garment production. They investigated the expenditure and time requirement for creating 3-D printed garment. Vanderploeg et al. [55] discussed various types of 3-DP processes that display immense potential for application in fashion industry. Merits and demerits of all processes were also presented. Further, they provided recommendations for designers about the use, merits, and issues in 3-DP technology applied to fashion industry. Sun and Valtasa [56] discussed utility of 3-DP technique for fashion garment production which included designing and modeling tools, printers, and related raw material choice.

One of the most prominent applications of 3-DP is in food industry. Hao et al. [57] printed Cadbury chocolate in various shapes using additive manufacturing technology. Process resulted in the increase in viscosity of chocolate. Important attributes like rheological behavior of chocolate, nozzle height, and nozzle aperture size were analyzed. Lipton et al. [58] applied additive manufacturing technology in food industry. Food printings development was shown by the reproduction of traditional foods like pizza by 3-D printers. Sun et al. [59] applied 3-DP technique in food industry. They concluded an exhaustive review of researches available to give in-depth insight in the direction of its future development. Godoi et al. [60] reviewed 3-DP technology for designing food products. They provided detailed insight in the food material properties and their behavior during 3-DP. They suggested key parameters on which the rational design of 3-D food constructs depends. Izdebska and Zolek-Tryznowska [61] summarized the major food products that can be printed using 3-DP technology. Pallottino et al. [62] produced an updated analysis of the recent advancement of 3-DP technology in food printing. Derossi et al. [63] and Severini et al. [64] applied 3-DP technology in printing of customized fruits and vegetables. Liu et al. [65] have used wheat flour, freeze dried mango powder, water and olive oil as a material. Experimentations were conducted on dough with other materials one by one and in their combination.

3-DP can be effectively used in art and museum. Short [35] used this technology for replication and restoration of artifacts. Using 3-DP technology, museums can easily reconstruct artifacts. Mathur [66] discussed use of 3-DP technique as an alternate method of construction. He present details of the 3-D printing, its applications, and merits. Mohammed [67] summarized various 3-DP methods that are utilized to oceanography. He discussed wide range of 3-DP applicability in oceanography. Kang and Ma [68] conducted in-depth review of application of 3-DP in the foundry sector. They suggested that this emerging technology has a good potential in casting

attributes which includes printing of wax pattern, ceramic shell, sand core, sand mold, etc.

## 5 Merits of 3-DP

Following are some of the merits of 3-DP:

1. 3-DP technique takes into account customization. Object can be customized without extra expenses. Change in design of product, if required, can be easily carried out in digital design itself.
2. 3-DP technique develops interlocked parts and hence, no assembly is required.
3. Conventional manufacturing techniques require great deal of expertise for producing any product. On the other hand, 3-DP technique requires zero skill manufacturing as printer is guided by digital design file [2].
4. Complex shapes and parts that can be developed easily just by uploading CAD model.
5. 3-DP is a single-step manufacturing process. Production time is short hence 3-DP is used for quick verification and development of design ideas.
6. This technique generally does not require any new tool to develop model.
7. 3-DP is an additive process. Thus, this process just uses the amount of material needed to create that particular object. This process produces very little waste [69].

## 6 Limitations of 3-DP

Following are some of the limitations of 3-DP:

1. 3-D printers and raw materials are costly however, in not so distant future these cost will in general reduce.
2. The ease with which replicas can be created using 3-DP process raises issues over IPR.
3. Majority of 3-D printers are restricted by scale and size.
4. Presently, 3-D printer can work with only limited raw material. There are still a few constraint contrasted with conventional product materials, colors, and finishes [2].
5. Restricted strength and endurance. The strength of object printed is non-uniform due to the layer-by-layer production [70].
6. 3-D printing typically has lower production speed than traditional manufacturing techniques [71].

Despite all short coming, 3-D printers are developing very quickly and cost of printing is reducing, therefore use of this technology is becoming more and more widespread.

## 7 Conclusions

3-DP is a transformative manufacturing process which develops three-dimensional parts from digital file by using laying down material layer by layer. 3-DP technology can revolutionize and reshape the world. Advancement in 3-DP technology can significantly improve the way of manufacturing products. 3-DP can print customized products of complex design in short time with high precision, zero manufacturing skill with no tool. 3-DP finds applicability in nearly all the classes of human requirements like medical, aerospace, automobile, fashion design, food industry, etc. Several materials can be processed to full dense parts. The range of currently available materials is already very large, like Ti alloys, Ni alloys, stainless steel, ABS, PP, PE, etc., to high-grade stainless steels and is increasing rapidly.

In this paper, an overview of 3-DP technology, its applications along with merits and limitations is presented. 3-DP technology is opening up new frontiers for developing complete parts through a single-step process.

## References

1. Sahasrabudhe H, Bose S, Bandyopadhyay A (2018) Laser-based additive manufacturing processes. In: *Advances in laser materials processing*. Elsevier Ltd., Amsterdam, pp 507–539
2. Singh A (2016) 3D printing technology: its principles and processes. *Int J Res Adv Eng Technol* 2(4):53–65
3. Srisairam V, Kumar CDM (2015) Rapid prototyping–additive/solid free form manufacturing in automobile engineering. *Int J Eng Dev Res* 3(4):799–802
4. Kranz J, Herzog D, Emmelmann C (2015) Design guidelines for laser additive manufacturing of lightweight structures in TiAl<sub>6</sub>V<sub>4</sub>. *J Laser Appl* 27(S1):S14001–S14016
5. Rännar LE, Glad A, Gustafson CG (2007) Efficient cooling with tool inserts manufactured by electron beam melting. *Rapid Prototyping J* 13(3):128–135
6. Hull C (1986) Apparatus for production of three-dimensional object by stereolithography. U. S. Patent 4,575,330
7. Gibson I, David R, Brent S (2015) Vat photopolymerization processes. In: *Additive manufacturing technologies*. Springer, New York, NY, pp 63–106
8. Neckers DC (1992) Architecture with photopolymerization. *Polym Eng Sci* 32(20):1481–1489
9. Srivastava M, Mishra M (2016) 3D printing: additive manufacturing. *Int J Eng Sci Adv Res* 2(2):1–4
10. Wu G, Zhou B, Bi Y, Zhao Y (2008) Selective laser sintering technology for customized fabrication of facial prostheses. *J Prosthet Dent* 100(1):56–60
11. Vujaklija I, Farina D (2018) 3D printed upper limb prosthetics. *Expert Rev Med Devices* 15(7):505–512
12. Maroti P, Varga P, Abraham H, Falk G, Zsebe T, Meiszterics Z, Mano S, Csernatony Z, Rendeki S, Nyitrai M (2018) Printing orientation defines anisotropic mechanical properties in additive manufacturing of upper limb prosthetics. *Mater Res Express* 6(3):035403
13. Vorndran E, Moseke C, Gbureck U (2015) 3D printing of ceramic implants. *MRS Bull* 40(2):127–136
14. Moraru E, Besnea D, Dontu O, Gheorghe GI, Constantin V (2018) Applications of additive technologies in realization of customized dental prostheses. *Int J Mechatron Appl Mech* 3:66–71

15. Zocca A, Lima P, Günster J (2017) LSD-based 3D printing of alumina ceramics. *J Ceram Sci Technol* 8(1):141–148
16. Gmeiner R, Deisinger U, Schönherr J, Lechner B, Detsch R, Boccaccini AR, Stampfl J (2015) Additive manufacturing of bioactive glasses and silicate bioceramics. *J Ceram Sci Technol* 6(2):75–86
17. Ianko T, Panov S, Sushchyn'sky O, Pylypenko M, Dmytrenko O (2018) Zirconium alloy powders for manufacture of 3D printed particles used in nuclear power industry. *Prob At Sci Technol* 1(113):148–153
18. Caminero MA, Chacón JM, García-Moreno I, Rodríguez GP (2018) Impact damage resistance of 3D printed continuous fibre reinforced thermoplastic composites using fused deposition modelling. *Compos B Eng* 148:93–103
19. Ngo TD, Kashani A, Imbalzano G, Nguyen KT, Hui D (2018) Additive manufacturing (3D printing): a review of materials, methods, applications and challenges. *Compos Part B Eng* 143:172–196
20. Herzog D, Seyda V, Wycisk E, Emmelmann C (2016) Additive manufacturing of metals. *Acta Mater* 117:371–392
21. Povilus AP, Wurden CJ, Vendeiro Z, Baquero-Ruiz M, Fajans J (2014) Vacuum compatibility of 3D-printed materials. *J Vac Sci Technol A Vac Surf Films* 32(3):033001
22. Hitzler L, Alifui-Segbaya F, Williams P, Heine B, Heitzmann M, Hall W, Merkel M, Öchsner A (2018) Additive manufacturing of cobalt-based dental alloys: analysis of microstructure and physicochemical properties. *Adv Mater Sci Eng* 1–12
23. Unver E, Swann D, Bailey R, Govindarajan I, Dollan F (2013) The art of 3D aculpted printing: royal coat of arms case study
24. Yang J, Li K, Zhu L, Tang W (2017) Fabrication of PDMS microfluidic devices with 3D wax jetting. *RSC Adv* 7(6):3313–3320
25. Peng Q, Tang Z, Liu O, Peng Z (2015) Rapid prototyping-assisted maxillofacial reconstruction. *Ann Med* 47(3):186–208
26. Mpofo TP, Mawere C, Mukosera M (2014) The impact and application of 3D printing technology. *Int J Sci Res* 3(6):2148–2152
27. Dunham S, Mosadegh B, Romito EA, Zgaren M (2018) Applications of 3D printing. In: *3D Printing applications in cardiovascular medicine*. Academic Press, Cambridge, pp 61–78
28. Shahrubudin N, Lee TC, Ramlan R (2019) An overview on 3D printing technology: technological, materials, and applications. *Procedia Manuf* 35:1286–1296
29. Pandey M, Rao PS, Pandey VR (2018) Application of RPT in medical science: a review. *J Basic Appl Eng Res* 5(5):445–451
30. Sriharsha B, Rao PS (2018) Rapid prototyping technology: applications, advantages and limits—A review. *Int J Tech Innov Mod Eng Sci* 4(12):568–572
31. Singh AA, Rao PS, Bansal R (2019) Advantage on biomaterial implants: a review. *Int J Tech Innov Mod Eng Sci* 5(5):1073–1077
32. Marijnissen M, Van Der Zee A (2017) 3D Concrete printing in architecture. A research on the potential benefits of 3D concrete printing in architecture. *Mater Stud Methodol* 2:299–308
33. Wu P, Wang J, Wang X (2016) A critical review of the use of 3-D printing in the construction industry. *Autom Constr* 68:21–31
34. Kreiger MA, MacAllister BA, Wilhoit JM, Case MP (2015) The current state of 3D printing for use in construction. In: White DJ, Alhasan A, Vennapusa P (eds) *The proceedings of the 2015 conference on autonomous and robotic construction of infrastructure*, Ames, Iowa, pp 149–158
35. Short DB (2015) Use of 3D printing by museums: Educational exhibits, artifact education, and artifact restoration. *3D Printing Add Manuf* 2(4):209–215
36. Schwandt H, Weinhold J (2014) 3D technologies for museums in Berlin. In: *Electronic visualisation and the arts (EVA 2014)*, pp 255–261
37. Yao AWL (2005) Applications of 3D scanning and reverse engineering techniques for quality control of quick response products. *Int J Adv Manuf Technol* 26(11–12):1284–1288

38. Tut V, Tulcan A, Cosma C, Serban I (2010) Application of CAD/CAM/FEA, reverse engineering and rapid prototyping in manufacturing industry. *Int J Mech* 4(4):79–86
39. Mueller B (2012) Additive manufacturing technologies—rapid prototyping to direct digital manufacturing. *Assembly Autom* 32(2)
40. Prince JD (2014) 3D printing: an industrial revolution. *J Electron Resour Med Libr* 11(1):39–45
41. Geng Z, Bidanda B (2017) Review of reverse engineering systems—current state of the art. *Virtual Phys Prototyping* 12(2):161–172
42. How 3-D printing works homepage. <https://computer.howstuffworks.com/3-d-printing.htm>. Last accessed on 2020/03/08
43. Taylor LA, Danelson KA, Gayzik FS, Loftis KL, Stitzel JD (2009) Physical model reproduction from ct scans classified according to gender, ethnicity, and age—biomed 2009. *Biomed Sci Instrum* 45:370–375
44. Torres K, Staśkiewicz G, Śnieżyński M, Drop A, Maciejewski R (2011) Application of rapid prototyping techniques for modelling of anatomical structures in medical training and education. *Folia Morphol* 70(1):1–4
45. Halem A, Javaid M, Khan RH, Suman R (2020) 3D printing applications in bone tissue engineering. *J Clin Orthop Trauma* 11:S118–S124
46. Matta AK, Kodali SP, Ivvala J, Kumar PJ (2018) Metal prototyping the future of automobile industry: a review. *Mater Today Proc* 5(9):17597–17601
47. Joshi SC, Sheikh AA (2015) 3D printing in aerospace and its long-term sustainability. *Virtual Phys Prototyping* 10(4):175–185
48. Kumar LJ, Nair CK (2017) Current trends of additive manufacturing in the aerospace industry. In: *Advances in 3D printing & additive manufacturing technologies*. Springer, Singapore, pp 39–54
49. Moon SK, Tan YE, Hwang J, Yoon YJ (2014) Application of 3D printing technology for designing light-weight unmanned aerial vehicle wing structures. *Int J Precision Eng Manuf Green Technol* 1(3):223–228
50. Wang BZ, Chen Y (2014) The effect of 3D printing technology on the future fashion design and manufacturing. *Appl Mech Mater* 496:2687–2691
51. Yap YL, Yeong WY (2014) Additive manufacture of fashion and jewellery products: a mini review: this paper provides an insight into the future of 3D printing industries for fashion and jewellery products. *Virtual Phys Prototyping* 9(3):195–201
52. White J, Foley M, Rowley A (2015) A novel approach to 3D-printed fabrics and garments. *3D Printing Add Manuf* 2(3):1045–149
53. Cooper F (2016) Sintering and additive manufacturing: additive manufacturing and the new paradigm for the jewellery manufacturer. *Prog Add Manuf* 1(1–2):29–43
54. Valtas A, Sun D (2016) 3D printing for garments production: an exploratory study. *J Fashion Technol Text Eng* 4(3):1–4
55. Vanderploeg A, Lee SE, Mamp M (2017) The application of 3D printing technology in the fashion industry. *Int J Fashion Des Technol Educ* 10(2):170–179
56. Sun D, Valtasa A (2019) 3D printing in modern fashion industry. *J Text Sci Fashion Technol* 2(2):1–4
57. Hao L, Mellor S, Seaman O, Henderson J, Sewell N, Sloan M (2010) Material characterisation and process development for chocolate additive layer manufacturing. *Virtual Phys Prototyping* 5(2):57–64
58. Lipton JI, Cutler M, Nigl F, Cohen D, Lipson H (2015) Additive manufacturing for the food industry. *Trends Food Sci Technol* 43(1):114–123
59. Sun J, Zhou W, Huang D, Fuh JY, Hong GS (2015) An overview of 3D printing technologies for food fabrication. *Food Bioprocess Technol* 8(8):1605–1615
60. Godoi FC, Prakash S, Bhandari BR (2016) 3D printing technologies applied for food design: status and prospects. *J Food Eng* 179:44–54
61. Izdebska J, Zolek-Tryznowska Z (2016) 3D food printing—facts and future. *Agro Food Ind Hi Tech* 27(2):33–37

62. Pallottino F, Hakola L, Costa C, Antonucci F, Figorilli S, Seisto A, Menesatti P (2016) Printing on food or food printing: a review. *Food Bioprocess Technol* 9(5):725–733
63. Derossi A, Caporizzi R, Azzollini D, Severini C (2018) Application of 3D printing for customized food. A case on the development of a fruit-based snack for children. *J Food Eng* 220:65–75
64. Severini C, Derossi A, Ricci I, Caporizzi R, Fiore A (2018) Printing a blend of fruit and vegetables. New advances on critical variables and shelf life of 3D edible objects. *J Food Eng* 220:89–100
65. Liu Y, Liang X, Saeed A, Lan W, Qin W (2019) Properties of 3D printed dough and optimization of printing parameters. *Innov Food Sci Emerg Technol* 54:9–18
66. Mathur R (2016) 3D printing in architecture. *Int J Innov Sci Eng Technol* 3(7)
67. Mohammed JS (2016) Applications of 3D printing technologies in oceanography. *Methods Oceanogr* 17:97–117
68. Kang JW, Ma QX (2017) The role and impact of 3D printing technologies in casting. *China Foundry* 14(3):157–168
69. 3dhubs homepage. <https://www.3dhubs.com/knowledge-base/advantages-3d-printing/>. Last accessed on 2020/03/08
70. Orentlicher GP (2012) Digital technologies in oral and maxillofacial surgery, an issue of atlas of the oral and maxillofacial surgery clinics-e-book, 20(1). Elsevier Health Sciences
71. Arbabian ME, Wagner MR (2020) The impact of 3D printing on manufacturer-retailer supply chains. *Eur J Oper Res*

# Advanced Finishing Processes for External Cylindrical Surfaces—A Review



Manpreet Singh , Gagandeep Singh , and Maninder Singh 

**Abstract** External cylindrical surface components are the core of machinery and automotive industry. The sliding and rotational motions are the main working motions provided to the cylindrical components. During these motions, the surface contact with fine finish defines the process performance of the machine or process. This fine finish is obtained through advanced finishing processes like magnetic abrasive finishing (MAF), vibration MAF, and magnetorheological finishing. In this work, advanced finishing processes are introduced and the advantages of these processes are explained. This paper also represents the overview of the MR fluid and its importance in the finishing of external cylindrical surfaces which play an important role in the manufacturing industries.

**Keywords** Cylindrical surfaces · Magnetic abrasive finishing · Magnetorheological finishing · Surface roughness

## 1 Introduction

Nowadays, the surface finishing of components is required in industries for their precise operative functionality [1]. This is because the fine finished surface of industrial components tends to decrease power losses, friction losses, and also enhances the machine working performance. Finishing is a value addition method that leads to an enhancement in cost as well as processing time [2]. Because of this, the efficiency of the finishing processes requires continuous enhancement to minimize time and expense. The ruggedness of the surface is greatly compromised by friction-based

---

M. Singh (✉)

Department of Mechanical Engineering, Baba Farid College of Engineering Technology, Bathinda 151001, Punjab, India  
e-mail: [manpreetsingh@thapar.edu](mailto:manpreetsingh@thapar.edu)

G. Singh · M. Singh

Department of Mechanical Engineering, Sant Longowal Institute of Engineering and Technology, Longowal 148106, Punjab, India

problems such as wear and strength depletion [3]. Finishing processes must also be able to obtain accurate surface finish over the external surface of the work-parts [4].

The finely polished cylindrical exterior parts are the essence of the manufacturing machinery. In various industries like automobile, machine tool manufacturing, aerospace and die manufacturing, etc., the uniform finishing is in great demand for cylindrical components [5]. The finished exterior surface of cylindrical parts has numerous advantages such as reduced vibration, lower noise, decreases wear, improves lifetime, increases load capability, and increases the machine's effectiveness. Finishing processes for external surfaces are mainly divided in two groups, namely commercial and advanced finishing methods [6]. In the industries, the external surface of the components is mainly finished with the traditional finishing processes such as grinding and lapping. Micro-cracks, heat-affected zone, changes in microstructural, etc., are the surface defects which are generated during the commercial finishing methods [7]. The finishing forces are not controlled during the traditional finishing operation and are also responsible for the low grade of finishing [8].

To fulfill the necessities like improvement in surface features and minimize the surface roughness after the traditional finishing process, various advanced finishing processes are developed [9]. Magnetic-aided finishing processes are more favored by the evolved advanced finishing processes, because these methods have stronger influence on the forces of finishing. This leads to better working-piece surface properties with minimal surface imperfections [8]. Magnetic-aided finishing processes [10] are used to precise finishing of 3D and flat surfaces. The magnetorheological (MR) finishing by the ball end MR process is more favored to finish the three-dimensional external surfaces than the other processes [11]. MR polishing fluid in which the carrier fluid suspends the iron particles and abrasives are used in the magnetorheological (MR) finishing processes [12]. Base suspension fluid is a mixture of water or oil, and additives. These components are used in the base fluid with various sizes of CIPs and abrasive particles as needed by the form the chains and finished the work-part surface [2]. The MR polishing fluid's versatility and controllability in the occurrence of the magnetic field make it effective for both hard and soft material finishing [13]. Carbonyl iron particles (CIPs) form stiffened CIP chains in finishing medium, in the occurrence of a magnetic flux. The abrasive particles are closely retained by such chains, which help shear off the roughness peaks from the metal or non-metal surface to obtain the optimal surface finish [14, 15].

## 2 Advanced Finishing Processes

The development of materials results in high strength, high-temperature resistant materials which make it difficult to machine by traditional methods [16]. To use these materials and machining to desire shape and size, the non-traditional processes have been used [3]. High precision on the surface of the workpieces is needed in the manufacturing world, which is attained by the advanced finishing methods [8]. In



traditional finishing processes, the limitation of shape and size has been overcome by the use of the flexible-controlled finishing medium which can be assessable on the different shapes and sizes of the workpiece surfaces. The magnetic field controls finishing forces that are acting over the surface of work-part during the finishing process. The strength of the gripped abrasives by the magnetic iron particles in the finishing medium changes in the occurrence of a magnetic field.

### 2.1 Magnetic Abrasive Finishing (MAF)

Magnetic abrasive finishing (MAF) is an advanced finishing method that is utilized to fine finish the external and internal surface finishing of the cylindrical work-parts. In this method, either bonded or non-bonded abrasive particles are used to finish the workpiece surface [17]. When the cylindrical work-part is rotated at high speed, the abrasive particles in the non-bonded powder tend to separate from the iron particles due to the effect of centrifugal force.

Thus, to overcome this problem, bonded abrasive particles are used. Bonded abrasive particles are nothing but the sintered ferromagnetic and abrasive particles [8]. The brush of the abrasives and sintered ferromagnetic iron particles is utilized (finishing medium) in this process. The magnetic field controls the strength of the dry brush of finishing medium. These abrasives clip off the roughness peaks from the rotating cylindrical work-part as depicted in Fig. 1. The two-dimensional magnetic forces act on the abrasive particles. The  $F_x$  component of the magnetic processing

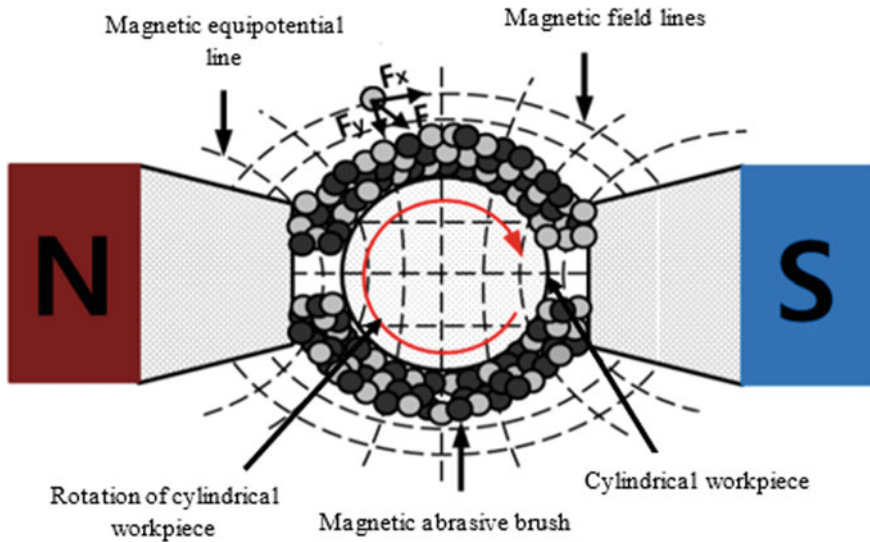
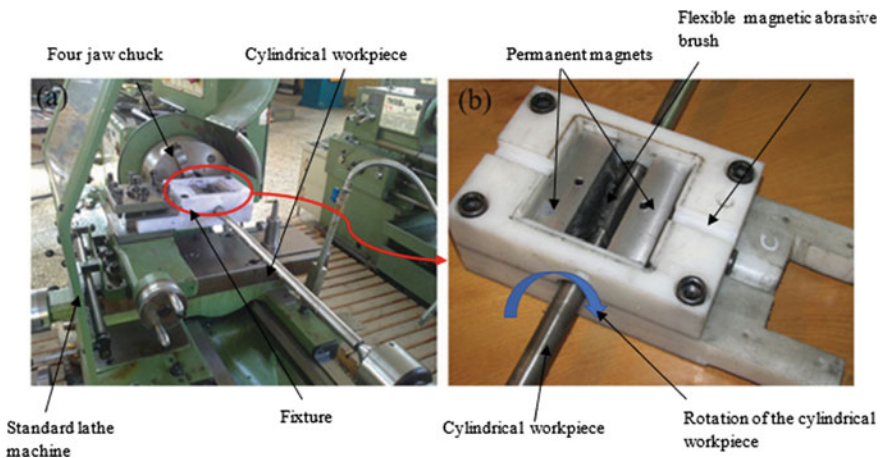


Fig. 1 Mechanism of magnetic abrasive finishing [17]

force ( $F$ ) acts on the direction of magnetic field lines and the  $F_y$  component act on the direction of magnetic equipotential lines depicted in Fig. 1. The  $F_x$  and  $F_y$  act on the cylindrical workpiece and result in the resultant processing force ( $F$ ). This process has been more effective and gives a good surface finish as compared to the traditional finishing processes (cylindrical grinding, belt grinding, and lapping) [18].

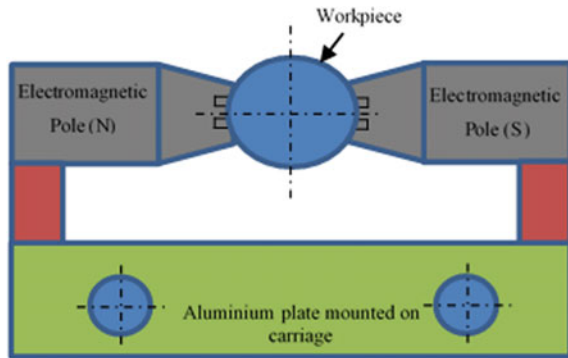
MAF process is found appropriate for various applications because of the micro-chip size material removal and self-refine the cutting edges of the abrasive's capability [19]. The roughness value was decreased from 335 to 68 nm using the optimum parametric conditions (150 rpm rotary speed, 1 mm working gap, 7% concentration of  $H_2O_2$  weight of abrasives 20%) [19]. Due to these advantages, this process helps to produce a fine-level surface finish. With the aid of conventional finishing processes, that is very difficult to accomplish. The advantage of this MAF process is that the materials which are difficult to machine and high hardness are possible to finish.

This process achieves the fine surface finishing and close tolerances for the workpieces made with hard materials [20]. In the MAF process, various types of magnetic abrasives are utilized to finish the different types of work-part materials. MAF is used to finish the internal and external surfaces of the cylindrical work-parts, flat surfaces, etc. In Fig. 2, the MAF process is utilized to finish the AISI321 stainless steel cylindrical work-part. In this MAF setup, the standard lathe is used with the holding fixture for the permanent magnets and cylindrical workpiece. The rotary speed is supplied to the cylindrical work-part with the help of a standard lathe machine and reciprocation motion is given to the work-part fixture for finishing the whole cylindrical work-part.



**Fig. 2** a Magnetic abrasive finishing (MAF) setup for finishing the cylindrical workpiece (AISI321 stainless steel) and b holding fixture of the cylindrical workpiece and permanent magnets during the finishing operation [20]

**Fig. 3** Experimental setup for vibration assisted magnetic finishing process [21]



## 2.2 Vibration Assisted Cylindrical Magnetic Abrasive Finishing

This process is also developed to finish the outer cylindrical work-part of high hardness. The cylindrical work-part is placed between the two electromagnetic poles in this process [21].

The electromagnetic poles are excited by supplying the current through the coil of the electromagnet. In the working space between the tool and work-part, the magnetic flux gradient was created. The abrasives are supplied in the working space that takes the form of the brush to perform the finishing operation and also vibration is supplied to the electromagnetic poles to enhance the process performance. In this process, the normal force acting on magnetic abrasive brush tends to indentation the abrasives in the surface roughness peaks, and rotational and vibration motion of the cylindrical workpiece trim off the asperities over the work-part surface. The vibration system attached to the lathe carriage with the help of the 25 mm diameters shafts as depicted in Fig. 3. The roughness value was decreased from 460 to 180 nm using the optimum parametric conditions [20]. In MAF, the finishing medium is used that generates the greater frictional forces between the work-part surface and abrasives [18]. This results in a high temperature in the working gap. This may lower the finishing process performance. This limitation can be further minimized by the magnetorheological fluid-based finishing processes.

## 2.3 Magnetorheological (MR) Fluid Finishing Processes

The MR polishing fluid (finishing medium) is used in this MR fluid finishing methods. The MR polishing has the advantage that the rheological effect of this finishing medium can be controlled by varying the magnetic flux density. Due to this, these methods are utilized to finish the hard and soft material workpieces. This fluid also

gives the flexibility to the processes to finish the different shapes and sizes of work-pieces. This happens because the carrier fluid gives the space to the magnetic iron particles and abrasive particles to reform as per the shape of the components. This is beneficial for finishing the complex shaped workpiece surface. These processes finish the ferromagnetic as well as non-ferromagnetic workpiece surfaces.

### **Magnetorheological Finishing (MRF)**

The finishing of precise lenses is very difficult because they are made of brittle material. Commonly the grinding and lapping is used in the lens manufacturing industries. The profile required for the lens was obtained by grinding [3]. The cracks and surface defects are generated after the grinding operation [8].

In the lapping, the non-uniformity of pressure and non-uniform distribution of the abrasive are the main limitations. Due to this, the lesser uniform finishing is achieved over the flat work-part surface. To achieve the fine surface finishing, the MR finishing (MRF) process was established in 1996 at the center of optics manufacturing at Rochester [22]. This process uses the magnetorheological (MR) fluid which is known as smart fluid. MR polishing fluid consists of magnetic iron particles and abrasive particles mixed in a fluid such as silicone oil and paraffin oil. The rheological effect of polishing medium gets changed by changing the magnitude of the magnetic field. When there is no magnetic field, the carbonyl iron particles (CIPs) of MR fluid are unevenly distributed. The iron particles converge in the occurrence of magnetic flux along the surface of the magnetic field creating a columnar structure. The CIP chains grip abrasives over the work-part and remove the roughness peaks from the surface of the work-part as shown in Fig. 4. In the magnetorheological finishing process, MR polishing fluid is supplied by the nozzle over the rotating wheel rim as depicted in Fig. 5. It demonstrates that the abrasives interact to the work-part surface while MR polishing fluid is closer to the rotating wheel rim. Indentation force transfers to the work material through the active abrasives and penetrates the surface of the workpiece. When the wheel rotates over the workpiece surface, then because of the relative motion between the gripped active abrasive and work-part surface, the material gets eroded out from the workpiece surface and produces fine finishing.

This process finishes the surface of the optical glass as well as crystals and produces surface accuracy in the order of 10 nm roughness value [3]. The magnetorheological polishing fluid brings heat and debris away from finishing region and does not lose its shape as it is self-deformable.

*Turning-type magnetorheological (MR) finishing process:* This process was established to finish the external surface of both the cylindrical ferromagnetic as well as non-ferromagnetic components [18]. This process overcomes the problems of in-process controlling of forces which give rise to surface defects associated with traditional finishing processes for cylindrical surfaces.

Figure 6 shows the material removal mechanism of the magnetorheological finishing process. The solid tool core was magnetized by the help of an electromagnetic coil and holds the active abrasives which approach the cylindrical workpiece as depicted in Fig. 6a. These active abrasives indent into the roughness asperities

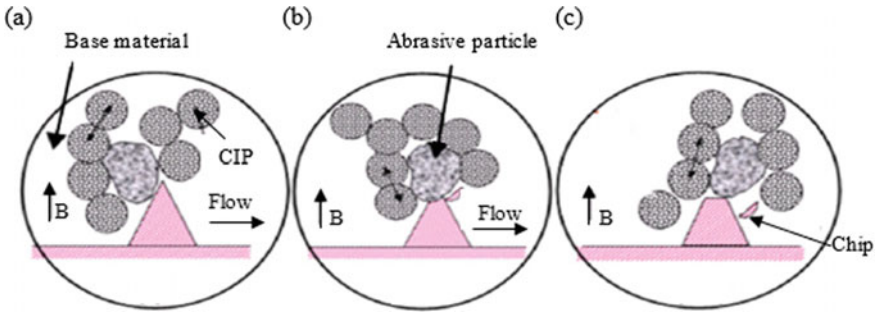


**Fig. 4** Three stages of material elimination from the roughness peaks in MRF process **a** active abrasive approaches the roughness peaks, **b** active abrasive removes the roughness peak, and **c** roughness peak removed in the form of tiny chips [8]

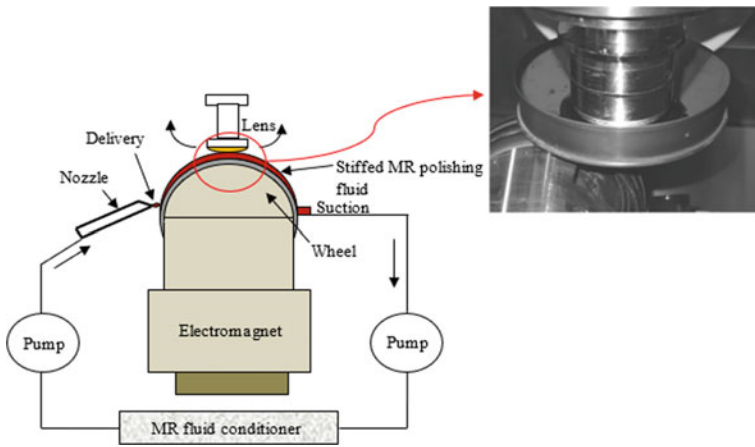


**Fig. 5** Schematic diagram of MRF [14]

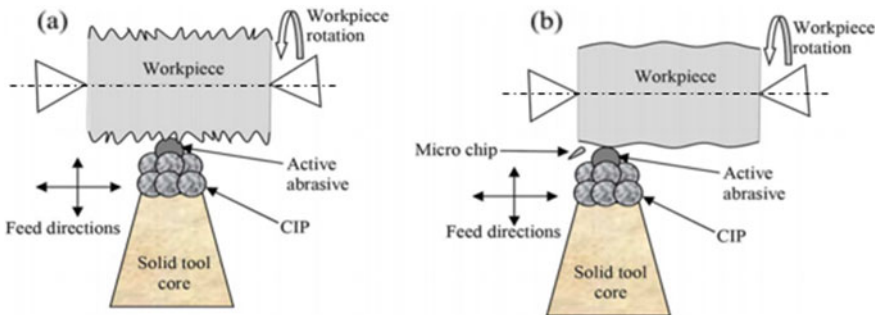


**Fig. 6** Material removal mechanism of MR finishing of the cylindrical workpiece surface [18]

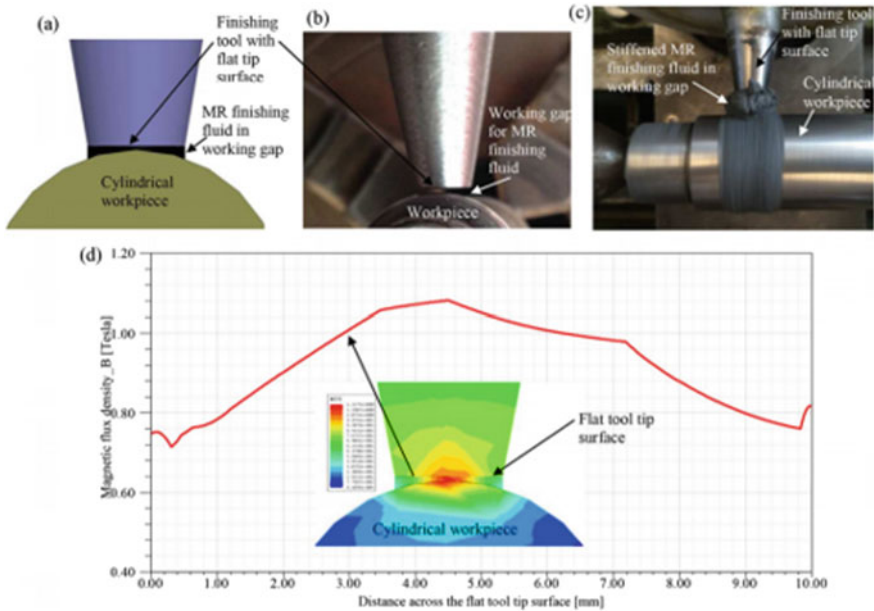


**Fig. 7** Flat solid stationary tool core tip surface **a** finite element analysis (FEA) model, **b** enlarge view with cylindrical workpiece, **c** finishing process, and **d** 2D plot of flux density distribution along tip surface [18]

and because of the rotary speed of the work-part and feed given to the tool core, the surface asperities get sheared off in micro-chips as revealed in Fig. 6b. Further, the performance of solid core surface with a flat and the curved surface is compared with each other on the same operational conditions. The finite element analysis (FEA) is performed on both tool cores as shown in Figs. 7 and 8, respectively. The FEA findings concluded that the surface of the curved shaped tool tip has a uniform flux density distribution over the flat-formed surface of the tool tip as seen in Fig. 8. The FEA analysis confirmed that the MR finishing tool with the curved tip more suited than the flat tip surface in the MR finishing.

The U-shaped aluminum clamp is used to hold the electromagnetic tool with a base plate that is settled on the lathe machine’s tool post. The electromagnetic tool was fixed on the tool post with the help of nut bolt assembly [23]. This turning-type MR finishing process can make its way in automobile, aerospace, and machine-tool industries for utilizing the fine finished cylindrical workpieces. The turning-type MR experimental setup is designed to finish the cylindrical work-parts surface as shown in Fig. 9a. The finishing medium is given in the working space, as seen in Fig. 9b. Owing to a uniform magnitude flux, the efficiency of this method has been tested with the flat tool tip and curved tool tip, and found better with the curved tool tip [18].

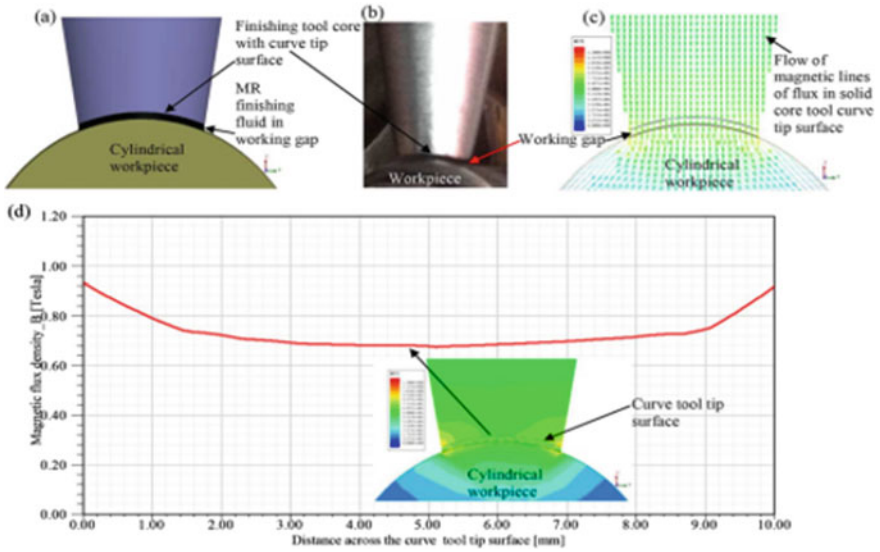


**Fig. 8** Curved solid stationary tool core tip surface **a** finite element analysis (FEA) model, **b** enlarge view with cylindrical work-part, **c** spreading of magnetic field lines, and **d** flux density variation plot along the tool core surface [18]

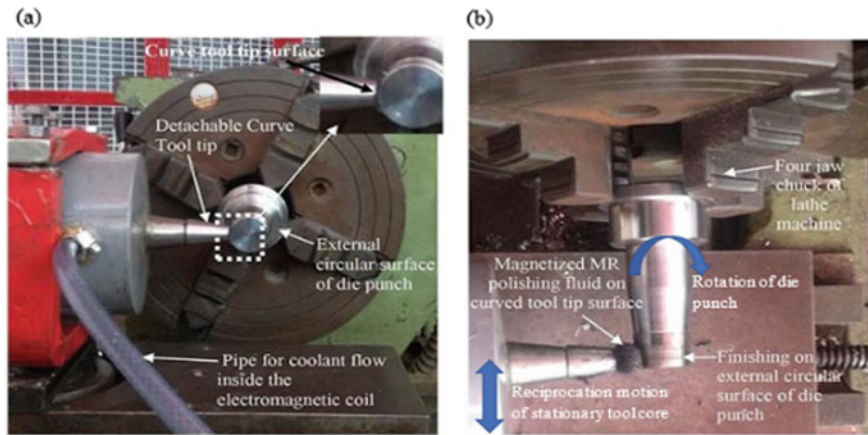


**Fig. 9** Magnetorheological finishing **a** experimental setup for the external cylindrical surface workpiece and **b** during finishing with magnetized MR polishing fluid [23]

*A rotating core-based MR finishing process:* The limitation of this process is that there was no precise and controlled system for the feed rate and not for rotary motion of work-part and the tool. This happens because in the standard lathe, the feed rate was not precise and a fixed ratio of feed was provided in the standard lathe which was also a drawback for this process. Also, the tool core tip was made stationary with only

feed rate while finishing performed on the rotating cylindrical workpiece surface. Due to this arrangement, the lesser relative motion can be provided to the active abrasives which may lower the process performance. Also, this process has no such arrangement for finishing the taper cylindrical surfaces because the electromagnetic tool was settled on the lathe machine's tool post. Also, the curved tool tip surface has fixed curvature to finish a fixed diameter workpiece. This curved tool tip has not finished the tapered and stepped cylindrical workpieces because the curvature is not constant at every point. Due to this, only straight cylindrical surfaces can be finished using the curved tool tip MR finishing process. To fulfill the above requirements of precise finishing, a rotary core MR finishing method is established with the following modifications to further improve the effectiveness of the existing turning-type MR finishing process. The stationary curved core tool tip surface is first transformed into the flat surface and then the core tool tip surface allows the rotational speed to improve relative motion of the active abrasive of MR polishing liquid over the exterior surface of the cylindrical work-part as depicted in Fig. 10.

The tool core rotates freely inside the stationary electromagnetic coil similar to the concept of the ball end MR finishing tool. The electromagnetic coiling was done on a separate hollow part instead of tool core itself as done in the existing turning type MR finishing tool. This separate hollow part is called bobbin and copper wire coiling has been wounded over the bobbin external surface. This bobbin allows the tool core to freely rotate in it by the assistance of bearing support as shown in Fig. 10. The tool core also rotates so that the active abrasive particles are still rotating with the magnetized central surface rotation on the rotating outer surface of the cylindrical workpieces. The value of  $R_a$  was decreased from 740 to 210 nm in the MR turning process with a fixed curved tool. A second hand with the same finishing time, the  $R_a$  value was decreased from 740 to 40 nm by means of the flat rotating tool core

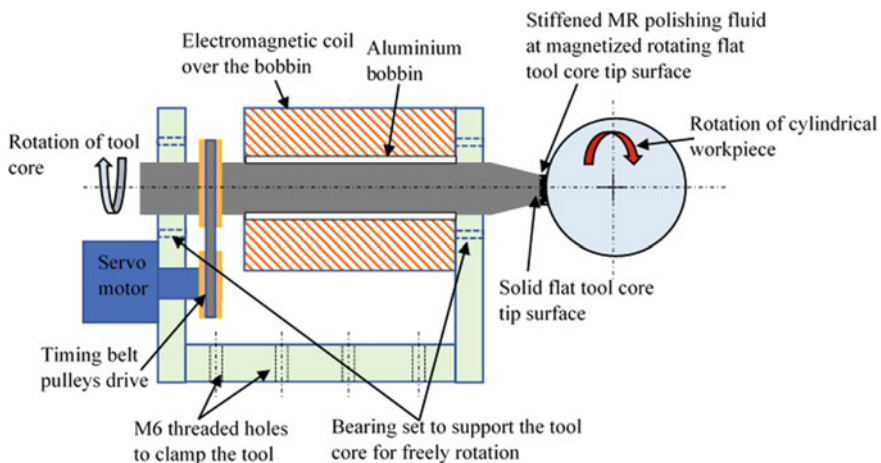


**Fig. 10** Improved magnetorheological (MR) finishing method to fine finish the cylindrical work-parts



surface [24]. This tool adjustment increases the abrasive particle's relative mobility across the cylindrical work-part and can increase its process efficiency. Owing to the rotary acceleration of the tool core, the tangential strength of abrasive particles is strengthened by the magnetized finishing medium over the surface of the work-part. The increase in tangential force helps to trim off the roughness peaks with less time. This results in an increase in the process performance to uniform finish of work-parts. After the development of process, it was realized that the configuration of tool for the best shape tip surface, based on the uniform and maximum magnitude of the magnetic flux on the tool core [6]. Therefore, the design of the previous tool has been improved. Because the circular tip surface was provided the non-uniform magnetic flux density which reduces the process performance. The distribution of the magnetic flux density using the finite element approach was thus planned and analyzed for the various types of tool core. Owing to the strongest tool edge, a uniform and higher magnetic density of flux was discovered on the rectangular core tool surface [6]. This process used for MR finishing of several industrial applications like cylindrical mild steel bar [24], micropunches [25], and H13 rolling rolls [26].

### 3 Conclusions

MRF process is used in various engineering applications and provides the best finishing and improves on the total product quality. The improved technology of the MRF is making it the smart technology of the future. The external cylindrical finishing processes are great importance in manufacturing industries. These processes are fulfilling the finishing requirement of the cylindrical components which enhance the efficiency of the machines and automobile industries. These processes are great need in the mechanical industries. There are various applications of the external cylindrical components which have required nanolevel finishing improving the geometrical properties and functional properties of the components.

**Declaration** I/We hereby certify that all the data collected during the study is presented in this manuscript and no data from the study has been or will be published separately.

The author declares that he has no known competing interests or personal relationships that could have appeared to influence the work reported in this paper.

### References

1. Al-Samaria RA, Haftirman, Ahmed KR, Al-Douri Y (2012) The influence of roughness on the wear and friction coefficient under dry and lubricated sliding. *Int J Sci Eng Res* 3:1–6
2. Cheng H, Yeung Y, Tong H (2008) Viscosity behavior of magnetic suspensions in fluid assisted finishing. *Prog Nat Sci* 18:91–96
3. Jain VK (2008) Abrasive-based nano-finishing techniques. *Mach Sci Technol* 12:257–294

4. Bedi TS, Singh AK (2016) Magnetorheological methods for nanofinishing—a review. *Part Sci Technol* 34(4):412–422
5. Jain RK, Jain VK, Dixit PM (1999) Modeling of material removal and surface roughness in abrasive flow machining process. *Int J Mach Tools Manuf* 39(12):1903–1923
6. Singh M, Singh AK (2019) Improved magnetorheological finishing process with rectangular core tip for external cylindrical surfaces. *Mater Manuf Process* 34(9):1049–1061
7. Singh M, Singh AK (2019) Performance investigation of magnetorheological finishing of rolls in cold rolling process. *J Manuf Process* 41:315–329
8. Jain VK (2009) Magnetic field assisted abrasive based micro-/nano-finishing. *J Mater Process Technol* 209:6022–6038
9. Hashimoto F, Chaudhari RG, Melkote SN (2016) Characteristics and performance of surfaces created by various finishing methods. *Procida CIRP* 45:1–6
10. Sadiq A, Shunmugam MS (2010) A novel method to improve finish on non-magnetic surfaces in magnetorheological abrasive honing process. *Tribol Int* 43:1122–1126
11. Singh AK, Jha S, Pandey PM (2011) Design and development of nanofinishing process for 3D surfaces using ball end MR finishing tool. *Int J Mach Tools Manuf* 51(2):142–151
12. Harris DC (2011) History of magnetorheological finishing. In: *Proceedings of SPIE 8016, Window and Dome technologies and materials XII*, 80160N
13. Niranjan M, Jha S, Kotnala RK (2014) Ball end magnetorheological finishing using bidisperse magnetorheological polishing fluid. *Mater Manuf Process* 29:487–492
14. Shorey AB, Tracy JP, Kordonski WI (2004) Application of magnetorheological jet (MR jet) in precision finishing. *ASME Int Mech Eng Congr* 43:25–39
15. Sidpara A, Jain VK (2014) Rheological properties and their correlation with surface quality in MR fluid-based finishing process. *Mach Sci Technol* 18(3):367–385
16. Kumar A, Mahapatra MM, Jha PK (2014) Effect of machining parameters on cutting force and surface roughness of in situ Al–4.5%Cu/TiC metal matrix composites. *Measurement* 48:325–332
17. Wang R, Lim P, Heng L, Mun SD (2017) Magnetic abrasive machining of difficult-to-cut materials for ultra-high-speed machining of AISI 304 bars. *Materials* 10(9):1029
18. Singh GS, Singh AK, Garg P (2016) Development of magnetorheological finishing process for external cylindrical surfaces. *Mater Manuf Process* 32(5):581–588
19. Sihag N, Kala P, Pandey PM (2015) Chemo assisted magnetic abrasive finishing: experimental investigations. *Procedia CIRP* 26:539–543
20. Saraeian P, Soleimani Mehr H, Moradi B, Tavakoli H, Khalil Alrahmani O (2016) Study of magnetic abrasive finishing for AISI321 stainless steel. *Mater Manuf Process* 31(15):2023–2029
21. Judal KB, Yadava V, Pathak D (2013) Experimental investigation of vibration assisted cylindrical–magnetic abrasive finishing of aluminum workpiece. *Mater Manuf Process* 28(11):1196–1202
22. Kordonski WI (1996) Magnetorheological finishing. *Int J Mod Phys B* 10(23–24):2837–2849
23. Mann S, Singh G, Singh AK (2016) Nano surface finishing of permanent mould punch using MR fluid based finishing processes. *Mater Manuf Process* 32(9):1004–1010
24. Singh M, Singh A, Singh AK (2018) A rotating core-based magnetorheological nanofinishing process for external cylindrical surfaces. *Mater Manuf Process* 33(11):1160–1168
25. Singh M, Singh AK (2019) Magnetorheological finishing of micro-punches for enhanced performance of micro-extrusion process. *Mater Manuf Process* 34(14):1646–1657
26. Singh M, Singh AK (2019) Performance investigation of magnetorheological finishing of rolls surface in cold rolling process. *J Manuf Process* 41:315–329

# A Study of Ceramic Core for Investment Casting



Ganesh Vidyarthee, Nandita Gupta, and Himanshu Khandelwal

**Abstract** In the recent time, the demand of complex castings is continuously increasing, particularly in the field of aerospace, automobile, medical, food processing, and machine tool industry. Investment casting being the oldest manufacturing process is always considered as the most preferred route for producing intricate near-net shape parts. Making undercuts, channels, or passage are the most critical and challenging activity in producing complex shape geometry. For making such castings, cores are used along with the investment molds. In practice cores, in foundries are made from different material such as sand, soluble wax, urea, salt, and ceramic. Among these, the ceramic material-based cores possess better properties compared to any other core materials. Presently, varieties of ceramic cores are used in investment casting foundries. The properties of final cast part significantly affected by the properties of ceramic core, which directly depend on the various core composition. Many researchers have made and tested cores with various ceramic compositions; however, no published research was found which summarizes them in scientifically. This paper presents a study on ceramic core material and core manufacturing process being used in investment casting. The article will be helpful for foundrymen in selecting the appropriate composition of ceramic core material and its manufacturing process based on the part-specific requirements.

**Keywords** Foundry · Investment casting · Core · Ceramic · Near-net · Manufacturing

## 1 Introduction

Investment casting process is commercially used for producing the casting with high degree of surface finish and good dimensional accuracy. The process uses single-piece ceramic shell mold without any parting line. In recent time, the process is being frequently used to produce the complex hollow shape parts with thin passages,

---

G. Vidyarthee (✉) · N. Gupta · H. Khandelwal  
NIFFT, Hatia, Ranchi 834003, India

© The Author(s), under exclusive license to Springer Nature Singapore Pte Ltd. 2021  
C. Pandey et al. (eds.), *Advances in Materials and Mechanical Engineering*,  
Lecture Notes in Mechanical Engineering,  
[https://doi.org/10.1007/978-981-16-0673-1\\_31](https://doi.org/10.1007/978-981-16-0673-1_31)

379

channels, and undercuts, without lowering the properties of castings [1]. Such hollow shapes are molded by positioning a separately prepared core in the investment casting mold. In practice, core for investment casting is fabricated by sand, soluble wax, urea, salt, and ceramic materials. Among these, the ceramic-based cores are the most suitable for producing thin and small sections, because of the ease in shelling process. In terms of strength, high temperature stability, surface finish, and dimensional accuracy, the ceramic material-based core appears to be more suitable than any other core materials [2–5]. However, in order to produce the quality casting, the appropriate ceramic composition needs to be selected. There would be many factors which may be considered while selecting of the core material, i.e., size of the core, complexity of the geometry, shrink rate of ceramic mix, tooling, and materials to be cast. Ceramic core can be used for different types of metal and alloys casting like high melting materials titanium-, nickel-, and cobalt-based alloys, steels, and aluminum. These cores are extensively used for producing vanes and blades castings of a gas turbine engine blocks, cylinder heads, and many more for automobile application. Gas turbine engines are widely used in electric power generation, aircraft propulsion, and ship propulsion.

The primary steps for producing a hollow shape cavity are to place a core between two halves of the die, followed by the wax injection around the core. Methoding components including sprue, in-gates, and down-poles are also prepared separately and assembled together with the cored patterns of the part. Thereafter, the pattern and the core assemblies are dipped in ceramic slurry and dried. These steps are repeated several times to produce a required multilayer shell thickness around the pattern. After the desired thicknesses of shell have been formed, the mold is thoroughly dried and the wax is removed by application of heat. The most commonly used methods for dewaxing are autoclave dewaxing and flash firing dewaxing. After removal of the wax pattern from the ceramic mold, the position of ceramic cores remains same as the required final shape of casting to be cast with hollow passage. After firing and cleaning, the mold is ready to use in metal casting. The molten metal or alloy is used to pour into a ceramic mold containing a core. After the solidification of metal, the ceramic core and shell mold are removed to free the casting with hollow shape. The ceramic core is removed by various means, i.e., chemical process, thermal process, mechanical process, and many more.

For producing a quality casting, the ceramics core should satisfy the following requirements [6, 7]:

1. Chemical stability with the molten metal, absence of reactivity, good dimensional stability, low creep, and resistance to high temperature.
2. High porosity (>20%) and should be leached easily from the cast piece to avoid undue production cost.
3. Having high strength and low shrinkage characteristics, to get the precise shape and size of the casting component and good mechanical characteristics.

In this paper, an attempt is made to delineate the manufacturing process of ceramic core; starts from selection of raw materials, manufacturing method, drying, and firing to leaching process of ceramic core.

## 2 Process of Making Ceramic Core

Ceramic cores are made with excellent bending strength and dimensional stability which offer easy handling at room temperature and avoid easy deformation during the casting process. The process flowchart in accordance with the manufacturing method of ceramic core is shown in Fig. 1. The steps involved in this process are reported next.

### 2.1 Core Raw Materials

Ceramic cores are produced using silica, alumina, zircon, zirconia, chromia, mullite, hafnia, or other suitable materials and their mixtures. There are many factors which may be considered while selecting a suitable core material. Few important factors are the size of the core, complexity of the geometry, core shrinking rate, tooling, and the cost considerations of the core. For different casting materials, different compositions of ceramic core are using as summarized in Table 1. The selection of compositions for the conventional core making for investment casting is discussed in US 7,287,573. The lesser reactive ceramic compositions for geometrically complex articles are discussed in US 7,413,001. US 2014/0182809 disclosed the compositions of ceramic materials to closely match the coefficient of thermal expansion of the metal or alloys to be cast.

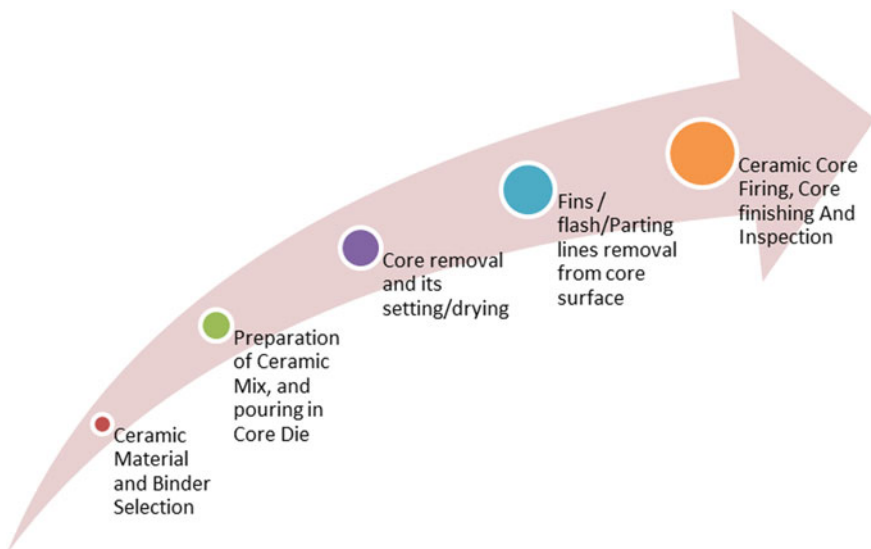


Fig. 1 Ceramic core making process

**Table 1** Summary of literatures available for ceramic core composition

Major compositions	Minor compositions	Casting materials	Comments
Alumina floor	Zircon floor	Aluminum alloy	Binder; sodium hydrogen phosphate and cane sugar [13]
Fused silica	Zircon, zirconia, and alumina	Nickel- and cobalt-based super alloys	Application—turbine blades, compressor blades, parts of jet engine and other precision parts [14]
Silica powder, alumina, mullite, and zircon	Yttria (Y <sub>2</sub> O <sub>3</sub> )	Nickel- and cobalt-based super alloys	Ceramic core is made by additive manufacturing process [15]
Fused silica	Zircon, alumina	Nickel- and cobalt-based super alloys	Binder—paraffin wax and mineral wax. Plasticizer—bee wax. Coupling agent—silane [16]
Fused silica	Zircon, alumina, and cristobalite	Titanium, zirconium, and super alloys	Application—missile power plants, turbine drives, aircraft engine, and other components of structural parts for withstanding extremely high temperature [17]
Alumina, Yttria	MgO, Cr <sub>2</sub> O <sub>3</sub> and carbon bearing fugitive material	Super alloys	Grain growth inhibiting agent. Binder—wax-based materials, ethylene vinyl acetate copolymer, and oleic acid [18]

*Silica*—Silica (SiO<sub>2</sub>) is a most using core material in investment casting, the reason may be of dimensional stability at high temperature, low thermal expansion coefficient, easily removal from the casting and abundant availability [8–10]. In some instances, a few metal or metal alloys may react with the silica-based core during the casting process like Ti- and Ni-based super alloys [11]. The cristobalite percentage in silica core could enhance the core properties and it could be also used for superalloy casting [12].

*Alumina*—The use of silica-based cores is limited in precision casting and casting with internal passage. For these application, alumina-based cores are desirable since alumina is more robust, as it possess excellent thermal shock resistance, thermal expansion, strength, leachability, and remains chemically and dimensionally stable at casting temperatures [12, 19]. However, the process used for dissolving alumina-based cores is less efficient when compare to silica cores. This is because the leaching

rate for alumina cores is longer which makes it uneconomical and less preferred for manufacturing operations. Alumina core compositions are also useful in casting of reactive alloys. US 4,837,187, US 5,409,871, and US 5,580,837 considered alumina and other additives as a thermoplastic organic polymer binder. These binders are used at elevated temperatures in liquid form because at room temperature, it remains in soiled form.

*Zircon*—Zircon is usually used as a main additive to silica- and alumina-based ceramic core, in order to improve their high temperature properties. Zircon or zirconium silicate ( $ZrSiO_4$ ) has low coefficient of thermal expansion which possesses high thermal and chemically stability [20–23]. Other additives that can be used in small amounts in the ceramic core are aluminum, yttrium aluminate, rare earth aluminates, yttrium, hafnium, colloidal alumina, oxides of aluminum, yttrium, hafnium, magnesium, zirconium, etc. Additionally, dispersants like stearic or oleic acid may be added in core composition [24]. In order to further enhance the leaching time, the core material may include calcium carbonate and/or starch [25].

*Binder*—The binders used for making cores mainly depends on type of molding method. Binder can be organic or inorganic compound materials. Organic binders that are used in ceramic core are thermosetting, thermoplastic or cross-linking thermoplastic binder material, and mixtures thereof like gum, wax, ethyl cellulose, polystyrene, polyvinyl, acetate, polymerized resin, polyterpene resins, linseed oil, gilsonite, shellac, ethyl silicate etc. Inorganic binder that used in ceramic core are calcium borate, a preferred binder for most core systems although other borates such as magnesium borate could be used as a substitute. Generally, calcium carbonate is used as a preferred porogen in the core due to solubility in mild acid solution.

## 2.2 *Manufacturing Method of Ceramic Core*

Ceramic cores are preferably made by injection molding or transfer molding. It can be manufactured by other methods also, i.e., pouring method, extruded method, form ground method, or any other conventional methods. The core is extracted from the mold, and in each of the manufacture method, it is then either cured or fired before application. In recent time, additive manufacturing process is also in use for ceramic core making process [15].

*Injection molding*—Injection molding method is generally used for making intricate and thin sections castings for mass production. U.S. Patent 3,222,435 and U.S. Patent 4,737,237 give details of injection molding techniques for making ceramic cores for use in casting process [26]. In this process, cores are produced by injecting ceramic slurry with pressure into a specially made die and allowed to cure or harden therein to form a green core body. Ceramic slurries are prepared by carefully mixing of ceramic mixtures and binder, avoiding any turbulence. The suitable temperatures of the slurry (core mix), injection rate, and injection time are selected for better control

in the process. Vacuum centrifugal equipment can be adopted to give pressurized centrifugal molding of slurries in an enclosed vacuum. The cores are then removed from the mold and to protect any deformation ceramic slumpers can be used. Then, controlled firing cycles are adopted to retain control of shrinkage and dimensional accuracy [27]. Injection molding is relatively costly to practice and economically suitable when mass production of the cast component requires. The application of injection molding cores are like in the manufacturing of cooling systems of Formula 1 motor racing car, oil feeds, turbo inlet ducts, brake ducts, exhausts valve, inlets valves, wing mirrors, fire bottles, turbine components, commercial aerospace, industrial gas turbines, medical, and sports equipment [28].

*Poured cores*—Poured cores are generally used for making simple sections casting. US patent no. 3,60,931 describes the process of making pouring core [29]. The preparations of ceramic slurry are made by careful mixing of ceramic materials, for example, ceramic mix and binders. Thereafter, the uniform mixtures of ceramic slurry are poured in the core cavity. After a complete curing, the core is removed from the cavity. The solidified (green unfired) core is then visually inspected before its further processing. At this stage, the defective cores can be discarded. The inspected cores are then fired to retain the shrinkage and dimensional accuracy. The fired ceramic cores are used in a die cavity to inject the wax pattern [29]. The applications of cores are for hand rails, handles, catch tanks, water header tanks, hollow reinforcing for hatches, cycle frames and parts, canoe paddles, and many others [30].

*Extruded ceramic core*—Extruded ceramic cores are prepared by advanced ceramic materials to form ceramic tubes and ceramic rods [31]. This type of ceramic cores is used in temperature measurement instrumentation in oil and gas trade and many of the alternative applications of business heating. They are employed in some specialist part applications also. The composition of extruded ceramic tubes and rods is made up of varied grades of alumina, magnesia, hafnia, and silicon dioxide. Such composition offers smart thermal conduction and insulating properties. Extrusion sizes may vary from 0.060 in. to two 0.550 in. (1.5–65 mm) in diameter with lengths of up to 24 in. (600 mm) [31].

*Form ground ceramic core*—These cores are made of extruded shapes that are used for features like a second diameter, tapers, notches, flats, and different routine options. Centerless grinding, turning, drilling, and machining are used to turn out these a lot of complicated shapes. Tolerances for these ceramic cores can be maintained up to  $\pm 0.001$  in. (0.04 mm) at diameters [31].

*Slip casting core*—In this method, ceramic-mix is poured into a mold of plaster absorbers liquid. When, most of the solution has been absorbed and ceramic-mix dried. During drying process, the ceramic-mix undergoes the shrinkage and thus help in easy removal from the mold. After proper inspection, ceramic part is left for drying. At last, the part is fired at a high temperature to remove the volatile binding agent and hardened the core.



*Additive manufacturing process*—This is the most recent development in ceramic core manufacturing. The cores are directly built with successive layers of ceramic-mix material to form a 3D object. A 3D CAD model designed by any modeling software can be processed to a slicing software which determine the sequence and pattern of layer formation. US2015/0306657A1 describes a method of making ceramic core using additive manufacturing process [15]. Technology for additive manufacturing processes are 3D printing, direct deposition, stereolithography (SLA), selective laser sintering, direct write (micro pen deposition), etc. [15].

### **2.3 Core Drying**

In core drying process, unfired (green) ceramic core is placing on a setter. The setter, made of ceramic, consists of a top half and a bottom half between which the core is positioned and acts as a support for the core. The setter placing on a conveyor or core carrier, conveying the setter and the green core through the heating oven to heat the setter and the unfired ceramic core. Compositions plates can also be used for carrying and baking of the cores [32]. Mainly, batch- and continuous-type core drying furnaces are using for core drying that depend upon the size of core built and production requirements. Typically, all core drying furnaces are air-circulated type, which uniformly distributes the warmth around the core surfaces and removes the moisture saturated air from the cores [33].

### **2.4 Cores Firing**

All ceramic cores might be given a controlled heat to minimize the thermal shock that gives an adverse effect on core properties. Appropriate firing is required for the better performance of the core. Less heat-treated core might release more gases during the casting process while a more heat-treated core might be hard and brittle that may collapse due to the force of molten metal before solidification or during solidification [34]. Thus, the time and extent of firing entirely depend on the core composition, binders, and size of the core. The binder undergoes chemical and molecular changes as it transforms from liquid to solid with oxygen absorption and polymerization [34].

Heating of the ceramic core with the flexible weight bags on the surface of the setter reduces distortion of the core and it also improves the yield of cores within dimensional tolerances [35]. There are several ceramic layers in the ceramic core and its shrinkage rate can be controlled during firing [36].

## **2.5 Core Finishing and Inspection**

Core finishing and inspection are performed after firing operations to improve the quality of the ceramic core and find out any defective items. Many measuring devices are used for core inspection processes, for example, X-ray diffraction, surface finish, and dimensional gauge [37]. After a proper inspection and finishing operations, all cores are sent to the molding floor or core storage. The finished and inspected cores are sent in core storage for further use for core setting process; it should be smooth, free of flash or projections and without any defects [30].

## **2.6 Core Assembly**

There are numbers of ceramic cores, i.e., single-piece core, two-piece core, or more than two-piece cores. Single-piece core maybe used directly into the mold after proper sizing and cleaning. Other cores which are two or more pieces can be assembled by pasting and bolting. Generally, pasting is suitable for small cores. The adhesives materials are applied to the surfaces of the core to be joined, for example, mixture of talc, dextrin, flour, molasses, water, or other ingredients [37]. If pasting does not produce a sufficiently strong assembly, then cores may bolt together. For larger core assembly bolting is useful like manufacturing of gas turbine engines, for example, turbine blade or vane castings.

## **2.7 Core Setting**

Cores are placed in the mold. The core must be accurate in size and positioned correctly into the mold cavity. Ceramic cores are positioned in the mold by using core prints and other means. Many types of pins or locators are also used for large solid or tubular cores [30]. During the pouring of metal, cores may change position unless they are securely sited. Proper arrangement is required to position the core accurately and held firmly when metal is poured. Many cores may also be assembled and set in the mold specially for making a complex shape of casting. U.S. Pat. No. 2,084,247 describes the well-known core setting techniques.

## **3 Leaching Process for Ceramic Core**

The cleaning method to completely remove the ceramic core from the cast part is an important part of the overall casting process. Assuming the core is not removed completely from the casting before assembling in the part, the residue part of the core

can interfere in the performance of the service, which may lead to premature failure of the part. To address such a problem and ensure that the residue core is completely removed, the cast components are carefully checked after leaching.

By various procedures, the ceramic cores can be removed from the casting, and they are as follows:

- By chemical action
- By application of water
- By thermal stresses
- By dynamic action
- By wave action
- By mechanical action.

With chemical processing of the ceramic core, the strength of the core reduces due to chemical reactions between acting reagents and core materials. Depending on the core compositions, the cores are removed in solutions or melts of alkali, salt, and different solutions or melts of solvents and acids. Ceramic cores can be removed in caustic solutions, often under conditions of elevated temperatures and pressures in an autoclave. Fused silica cores may be removed by leaching with molten caustic soda or aqueous hydrofluoric acid [38]. Several ceramic cores used in the modern foundry industries are water soluble. The ceramic cores used for aluminum alloy castings can be leached by the use of water as the alkali solution is not suitable for aluminum alloys castings [13]. The ceramic cores can also be removed by the dynamic action like the jet of water, shot of quartz, abrasive jet with high pressure. In wave action, the various methods for removing the ceramic cores are used. For high strength ceramic core, using ultrasonic with the combination of chemical methods is more efficient [39]. Additionally, the cores removal may be performed with the use of vibration and electric hydraulic systems.

## 4 Conclusion

Ceramic cores provide better surface finish and accuracy in the casting of complex parts at a low cost and shorter lead time. Depending on the specific application in any industrial process, wide range of compositions of a ceramic core can be used. Specific binders and additives can be added to improve the strength, setting time, and other properties of the core. These cores show sufficient strength to withstand molten metal pressure and temperature. Ceramic cores of the range of compositions can be easily leached using diluted acids or other suitable processes. Nevertheless, ceramic cores can be manufactured by many methods which have enough merits for its scaling to use it commercially.

## References

1. Jiang W, Dong J, Lou L, Liu M, Hu Z (2010) Preparation and properties of a novel water soluble core. *J Mater Sci Technol* 26(3):270–275
2. Qin Y, Pan W (2009) Effect of silica sol on the properties of alumina-based ceramic core composites. *Mater Sci Eng A* 508:71–75
3. Kazemi A, Faghihi-Sani MA, Alizadeh HR (2013) Investigation on cristobalite crystallization in silica-based ceramic cores for investment casting. *J Eur Ceram Soc* 33(15–16):3397–3402
4. Wang LY, Hon MH (1995) The effect of cristobalite seed on the crystallization of fused-silica based ceramic core—a kinetic-study. *Ceram Int* 21(3):187–193
5. Pan JY, Liu XF, He LM, Guo XL, Liu DH, Li CC (2012) *Foundry* 61, pp 174–178
6. Steven K (1995) Ceramic core for investment casting and method for preparation of the same. U. S. Pat. No. 5468285
7. Shaw C (1946) Silica-based ceramic cores. *Foundry Trade J* 78(31):1534
8. Li K, Jiang W, Wang S, Jiuhan X, Lou L (2018) Effect of specimen thickness on the creep deformation of a silica-based ceramic core material. *J Alloy Compd* 763:781–790
9. Park JS, Yeo J-G, Yang SC, Chob C-H (2018) Mechanical properties and crystallization behavior of silica-based ceramic cores with different particle morphologies. *J Ceram Process Res* 19(1):20–24
10. Xu ZL, Zhong JW, Su XL, Xu QY, Liu BC (2018) Experimental study on mechanical properties of silica-based ceramic core for directional solidification of single crystal superalloy. *Ceram Int* 44 394–401
11. Huseby IC, Borom MP (1979) High temperature characterization of silica-base cores for superalloys. *Am Ceram Soc Bull* 58(4):448–452
12. Kato K, Nozaki Y (1991) Ceramic core for precision castings manufactured by injection molding. *Imono* 63:155–160
13. Lee Y-W, Hsien K, Taiwan (2000) Water soluble ceramic core for use in die casting, gravity and investment casting of aluminum alloys. US Patent No. US006024787A
14. Miller JJ, Eppink DL (1978) Cores for investment casting process. US Patent No. 4,093,017
15. Frank GR (2015) Ceramic casting core made by additive manufacturing. US Patent No. 0306657 A1
16. Gibson OE, Gleeson WJ, Burkholder LD, Benton BK (1991) Core molding composition. US patent No. 4998664
17. Robb RR, Yaker C, Burd L (1980) Ceramic cores for manufacturing hollow metal castings. US Patent No. 4,190,450
18. Frank GR, Canfield KA, Wright TR (1989) Alumina-based core containing yttria. US Patent No. 4,837,187
19. Greskovich CD, DeVries RC (1977) Alumina-based ceramic for core materials. U. S. Pat. No. 4156614
20. Chao CH, Lu HY (2002) Optimal composition of zircon–fused silica ceramic cores for casting superalloys. *J Am Ceram Soc* 85(4):773–779
21. Siarampi E, Kontonasaki E, Papadopoulou L, Kantiranis N, Zorba T, Paraskevopoulos KM, Koidis P (2012) Flexural strength and the probability of failure of cold isostatic pressed zirconia core ceramics. *J Prosthet Dent* 108:84–95
22. Wilson PJ, Blackburn S, Greenwood RW, Prajapti B, Smalley K (2011) The role of zircon particle size distribution, surface area and contamination on the properties of silica–zircon ceramic materials. *J Eur Ceram Soc* 31:1849–1855
23. Wereszczak AA, Breder K, Kirkland TP, Payzant EA, Rawn CJ, Krug E, Larocco CL, Pietras RA, Karakus M (2002) Dimensional changes and creep of silica core ceramics used in investment casting of superalloys. *J Mater Sci* 37(19):4235–4245
24. Yang X, Leman JT, Yu-Chung Ku A, Li T, Pollinger JP (2017) Compositions for cores used in investment casting. US Patent No. 0144216 A1
25. Kennerknecht S (1995) Ceramic core for investment casting and method for preparation of the same. US Patent No. 5468285

26. Mellen EJ, Webb JM, Robert J, Dudek JA (1965) Injection molding of ceramic cores. US Patent No. 3,222,435
27. Keller RJ, Haaland RS, Faison JA (2002) Ceramic core and method of making. US Patent No. US2002/0117601A1
28. Brown J (2000) Foseco ferrous foundry-man's handbook, 11th edn. Elsevier, Amsterdam
29. Leach EM, Fiji B (1964) Core casting methods. US Patent-3,60,931
30. Mills D (1980) Properties of ceramic cores. The British Investment Casters Technical Association fifteenth annual conference
31. <https://core-tech-inc.com/our-products>. Last accessed 2020/05/23
32. Brown J (2000) Ferrous foundry-man's handbook. Elsevier, Amsterdam, pp 18–20
33. Jain PL (1996) Principles of foundry technology, 2nd edn. Tata McGraw-Hill, New York
34. Greenwood RE (1985) Ceramic core; nucleus for precision internal section. Mod Technol 29–31
35. Altoonian MA, Runions RD (2002) Method for firing ceramic cores. US Patent No. USOO640302OB1
36. Greskovich CD (1977) Alumina-based ceramics for core materials. US Patent No. 4156614
37. Uram S (1987) Injection molding of ceramic components provides flexibility in metal casting and forming. Ind Heating 42–43
38. Frank GR, Canfield KA, Wright TR (1989) Alumina-based core containing yttria. U. S. Pat. No. 4837187
39. Kruglov EP, Kochetova GK (2007) Improvement of a technological process for ceramic core removal out of internal cavities of aircraft GTE turbine blade castings. Russ Aeronaut 50(2):227–229. ISSN 1068-7998

# Resilient and Robust Strategies for Process-Line Supply Chain in Textile Industry



Dhairya Vora, Jash Patel, Omkar Chandhere, and Satish Takalikar

**Abstract** A textile supply chain is through-and-through susceptible to threats. A thorough study leads the authors to find that solutions found to mitigate risks were only restricted to the end process of retail and distribution. The authors felt the need to shed light on the supply chain threats and risks during the processing phase of the chain. A comparative study was conducted to find the best-suited and feasible strategies among robust and resilient; further, comparison with the risk acceptance strategy was done to find out the most optimum solution for each particular threat/risk. A few of the major risks were considered and strategies to mitigate the most important and commonly occurring risks were analyzed. The authors reached a conclusion to adopt a mix of both, robust and resilient strategies to disperse risks involved in the supply chain. If the threats are only tackled with either would make the supply chain very rigid or very flexible, thus incurring heavy costs.

**Keywords** Resilience · Robust · Supply chain · Risks

## 1 Introduction

Supply chain risk management has fascinated significant attention for several reasons over the past two decades [1]. Firstly, globalization has increased supply chains' magnitude and purview, and therefore, their visibility and susceptibility to risks. Secondly, the theory of lean management has been extensively accepted in the supply chains. This theory has made supply chains more fragile due to the elimination/reduction of redundancies under adverse events. In the era of globalization, many apparel retailers having strong supply chains are going to have an upper hand over their competitors by offering their customers the best value. Supply chain management (SCM) has become very critical when it comes to managing risks of global

---

D. Vora · J. Patel · S. Takalikar  
Department of Mechanical Engineering, DJSCE, Mumbai, India

O. Chandhere (✉)  
Department of Production Engineering, DJSCE, Mumbai, India

sourcing, dynamism and its complexities. For the company to get the most benefits, a completely integrated supply chain is required [2–4].

To create the most efficient supply chain, it is necessary to understand the objective of the supply chain and the output metrics. Performance measures provide a basis for assessing the success and potential of SCM strategies. Usually, SCM is regarded as standing between completely vertically integrated organizations and those where each channel component functions independently. The solution to its effective management is coordination between the different entities in the chain. Broadly speaking, approaches to manage risk can be classified as either robust or resilient. A robust supply chain is capable of thwarting disruptions withholding its original structure and staying efficient under uncertainties; while a resilient supply chain may expeditiously return to its original state or move to a new more favorable state if disturbed [5–7].

In this paper, the authors attempt to propose a model on the integration of robust and resilient strategies to withstand the potential risk or threat in the textile supply chain.

Out of the existing strategies in SCM, the study is focused on two types of supply chain strategies, viz. robust SCM and resilient SCM.

### ***1.1 Robust SCM***

Robustness is the ability of the supply chain to maintain its functions against internal and external disruptions and disturbances.

Example: Multiple suppliers are a robust SCM strategy that reduces the possibility of interruption by widening the supply base to include additional suppliers in the case where a production node is broken, remaining vendors could still at least moderately satisfy the market demand [5].

### ***1.2 Resilient SCM***

Resilience is the capability of the supply chain to react after a disruption or shock has taken place.

Example: Backup supply is a resilient SCM strategy that provides versatility to access supplies from one or more substitute sources in the event of harvest time or interruption in yield. The backup supplies are only activated in the case of an interruption to the supply.

Elaborate studies have been conducted in supply chain risk management, although very few have been conducted in the processing phase supply chain of the textile industry. The authors got their hands on a lot of retail segment supply chain papers and methods to mitigate risks in retail [8] but failed to find any literature in the manufacturing segments and risk associated with them.

The risks encountered were present throughout the process line. The authors looked into the operations of the process line to identify the risks and threats that a textile supply chain faces. In supply, major risks faced were yield quantity, natural calamity, transportation, production, and supply spot price. In demand, risks faced were cultural shift, inventory management, processing, and transportation.

Following flowchart explains the process line of the textile industry and the threats associated with it (Fig. 1).

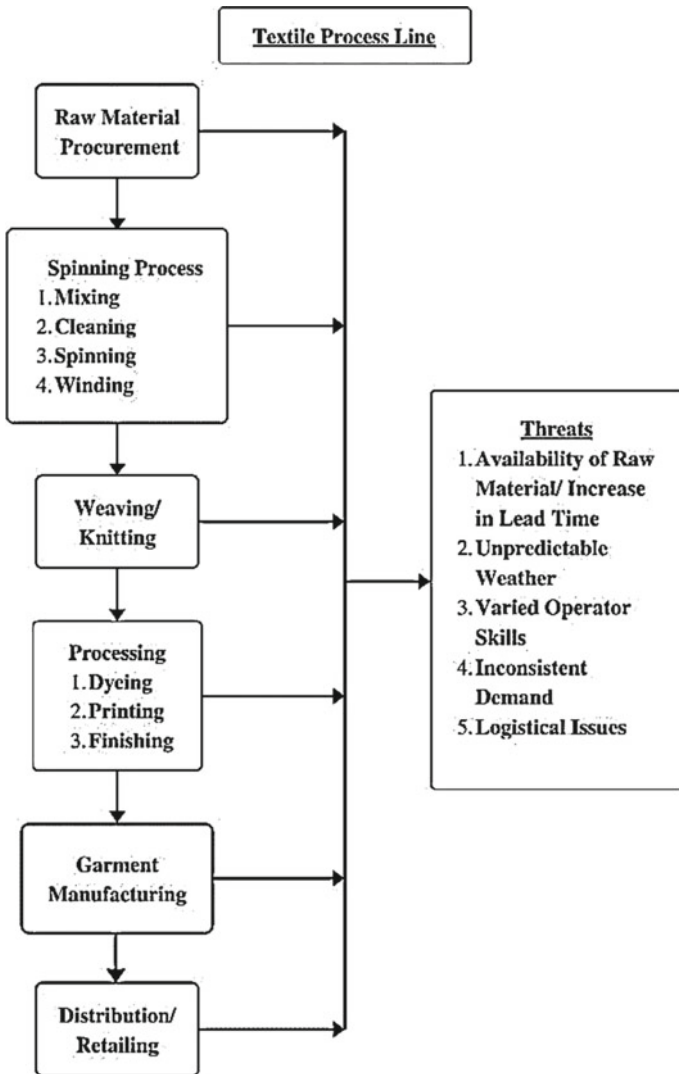


Fig. 1 Process line of textile industry and threats associated to it



To sum up, the supply chain focus in recent times has always been on the B2C supply chain and not on the process line of the business part. In this paper, the focus is on the process-line supply chain of cotton-to-cloth and cloth-to-garments.

Considering that supply chains operate under different forms of risks, a diverse set of robust and resilient strategies with each type of risk should be considered.

## 2 Case Study

The authors sorted out the risks and found out methods to mitigate them using robust and resilient strategies. In this paper, a risk acceptance strategy was adopted which does not do anything to mitigate disruption risks and simply accepts the risk ramification for comparison with the considered robust and resilient strategies.

The limitations in the research are that the size of the textile industry isn't considered in this case study (i.e., neither MSMEs nor large-scale enterprises were considered), and hence, the author's approach was to keep it generalized for the process line for textile industry and not differentiate among the size of the industry.

The study has been focused on the major six processes from the process line having a major impact of risks/threats before the semi-finished product reaches the distribution phase.

Some of the important risks/threats are:

1. Availability of raw material, increase in lead time
2. Unpredictable weather conditions
3. Varied operator skills
4. Inconsistent demand
5. Logistical issues.

Risks were given as follows:

**Table 1** Analysis and selection of best strategies for risks

S. No.	Risks/threats	Reasons of risks/threats	Suggested remedies	Best strategy
1	Availability of raw material/increase in lead time	A supplier's product may or may not meet the quality requirements of a demand. Therefore, a befitting solution is required to tackle this risk. The best efforts put forward can be: Self generation or multiple sourcing	<p><b>Back-up supply:</b> This is a resilient strategy that supplies the ability to gather resources from one or more suppliers in the mishap of harvest or production These additional suppliers are approached only when there is a mishap</p> <p><b>Multiple sourcing:</b> Multiple sourcing is a robust strategy that makes all suppliers competitive as the producer would only buy from the supplier with the best quality</p>	Robust
2	Unpredictable weather conditions	Unavoidable natural circumstances may lead to delays in transportation or deterioration in quality	<p><b>Keeping abundant stock:</b> (Robust strategy) A delay in transportation or destruction of material leads to a shortage, and hence, stocking is adopted</p> <p><b>International outsourcing:</b> (Resilient strategy) The weather may be bad in one region off the world but has to be better in some other region and hence taking geographical and meteorological data into consideration, if the material is outsourced internationally, the threat can be adjusted</p>	Robust

(continued)

**Table 1** (continued)

S. No.	Risks/threats	Reasons of risks/threats	Suggested remedies	Best strategy
3	Varied operator skills	When a new machine is inevitably incorporated in the process line, it becomes necessary for the workers to have the knowledge of that machine. This can be done by either training the current employees or by employing a skilled operator	<p><b>Skilled operator recruitment:</b> This is a robust strategy</p> <p><b>Training employed operator:</b> This is a resilient strategy as the cost to train per operators is lower than the cost to the company while employing a skilled operator</p>	Resilient
4	Inconsistent demand	Depending on the requirement of the market, the demand can be inconsistent. This inconsistent demand can be tackled by proper forecasting and inventory control methods or capacity buffering	<p><b>Proper forecasting and inventory control methods:</b> (Robust strategy) A yearly graph can be forecasted by analyzing data of previous years and managing inventory by producing early on</p> <p><b>Capacity buffer:</b> (Resilient strategy) Capacity buffer are all the efficient means to optimize capacity for a cost</p>	Robust
5	Logistical issues	Transportation logistics is very dicey based on weather, political and geographical conditions	<p><b>In-house logistics facilities:</b> (Robust strategy) The availability concern is deduced by this at an additional investment cost of buying the vehicle</p> <p><b>Third-party logistics (3PL):</b> (Resilient strategy) Transportation is outsourced by multiple logistician service providers</p>	Robust

### **3 Methodology for the Suggested Remedies**

#### ***3.1 Risk: Unavailability of Raw Material/Increase in Lead Time, Selected Remedy: Multiple Sourcing***

While buying from a single manufacturer would cause a business to cut costs (lower cost of stock control, lower cost of products due to volume discount, etc.), it may generate challenges to handle inevitable volatility in demand or significant disruptions. Billington and Johnson [9] elaborated how Hewlett Packard (a renowned name in the world of PCs and Laptops) used its plants in Washington and Singapore as a supply base for manufacturing inkjet printers to mitigate the risk involved with sole-sourcing. HP used the Singapore plant for base volume production to accommodate daily fluctuations in demand seamlessly and used the Washington plant to produce base volume surplus. Not only does a versatile customer base allow an organization to manage changes in the regulatory market, but it may also be used to ensure consistent commodity delivery when there is a significant interruption. Li and Fung's (international supply chain giants) network of 4000 suppliers, for example, gives Li and Fung great versatility to rapidly move output from suppliers in various countries when a disturbance arises in a given nation [10].

Similarly, in the textile industry opting for multiple sourcing is beneficial.

#### ***3.2 Risk: Unpredictable Weather Conditions, Selected Remedy: Keeping Abundant Stock***

In the "pre-JIT" era, supplementary "just in case" safety stock inventories of specific critical components may be considered for ensuring that the supply chain can continue to function smoothly when faced with a supply disruption. But the warehouse keeping and obsolescence effects of these new inventories in protection products may be exorbitant as the product lifecycle shortens and product variety increases. As an alternative of carrying more security stocks, a company could consider sharing inventories with multiple supply chain partners at certain "strategic" locations (warehouse and logistics hubs, and distribution centers). For example, Toyota (famous automobile manufacturer) and Sears (an American Departmental Store Chain) store their inventories of cars and appliances at various places and distribute certain inventories with other stores in the surrounding area. In doing that, Toyota and Sears may reach a greater quality of consumer satisfaction without incurring heavy product prices while faced with daily market variations [10].

Rather than opting for international sourcing and increasing expenditures, keeping abundant stock in the strategically selected places is a good strategy to adopt, to counter the threat of unpredictable weather conditions.

### ***3.3 Risk: Varied Operator Skills, Selected Remedy: Training Employed Operator***

Additional operators are required in an instance of a new machine or method implementation, increasing output or expanding capital investments. The skills of the operator might vary as being skilled, semi-skilled, or unskilled. The cost of employment of skilled operators exceeds the cost of semi-skilled and unskilled operators, and hence, the resilient strategy of “training the operators” was adopted.

As stated in Marc Blatter et al. [11], “Firm-sponsored training” is an alternative hiring strategy, as opposed to hiring skilled workers solely from the external labor market. A turnover augmenting firm will offer internal training and in the due course preserve some workers if the corresponding costs are lower than the external hiring costs. So thus the adopting the strategy of “training the operators” is feasible.

While a number of experts deduced the inference as to which of the two has the better approach, while both having their respective pros and cons. In the context of textile industry, the benefits obtained from training the operators outweigh the benefits obtained from skilled operators’ recruitment.

### ***3.4 Risk: Inconsistent Demand, Selected Remedy: Proper Forecasting and Inventory Control Methods***

Preparing assortments involve making the correct commodity choices and buying the correct quantities to satisfy market demand. Both distributors and supplier producers are littered with such decisions. Such problems within the textile market are even tougher thanks to the tiny product cycles. Brick and mortar store used range marketing to regulate individual commodity preference and customer demand (the collection of things on sale, the position of every commodity on the shelf and therefore the amount off aching are for every category). A study conducted by Chong et al. [12] at five major supermarkets within the USA discovered that a store executive or store manager may be able to influence the merchandise selection of consumers and therefore the demand of shoppers by reconfiguring the merchandise attack display and also the location of every product on the shelves and also the quantity of facings per product [10].

Their observations recommend that assortment planning may be implemented to draw in customers to shop for products which are available in large numbers when some products face strong supply disruptions. Assortment planning are often allotted with the assistance of proper forecasting and appropriate internal control methods.

### **3.5 Risk: Transportation/Logistical Issues, Selected Remedy: *In-house Logistics Facilities***

Transportation could be one of the weakest points in supply chain management which could make a supply chain snap. One should consider a proactive way of adding more flexibility. The availability of in-house logistics facilities helps in mitigating additional expenditure on transportation. The advantage of that is in the textile industry is that it gives more flexibility and less dependency on others to transport the finished goods and earn more profit.

## **4 Results**

All the possible risks/threats which commonly occur in the process line of the textile industry were considered and given in Table 1. The reasons for the development of these risks/threats are mentioned; also remedies to mitigate such risks/threats are suggested. By comparing the remedies through robust and resilient strategies, the best strategy to adopt for a particular risk is also suggested in Table 1. By a thorough literature review, the authors have suggested methodologies, about how the selected strategy has been applied by firms in different industries and proved to be useful. In the similar manner, the authors have tried to implicate that these strategies would also be beneficial in the textile industry.

## **5 Conclusion**

In this paper, a thorough comparative study has been made on the commonly occurring threats/risks in the process-line supply chain of the textile industry with respect to robust and resilient strategies. The study suggests that an integration of robust and resilient strategies is suitable for a supply chain as it is observed that some threats/risks are better solved using robust strategies while some are better resolved with resilient strategies. This study will be beneficial for the textile industry to improve their current supply chain practices and mitigate their risks in the supply chain by referring to the above table and adopt a combination of resilient and robust strategies for an effective process-line supply chain.

## **References**

1. Fahimnia B, Tang CS, Davarzani H, Sarkis J (2015) Quantitative models for managing supply chain risks: a review. *Eur J Oper Res* 247(1):1–15

2. Behzadi G, O'Sullivan MJ, Olsen TL, Scrimgeour F, Zhang A (2017) Robust and resilient strategies for managing supply disruptions in an agribusiness supply chain. *Int J Prod Econ* 191:207–220. <https://doi.org/10.1016/j.ijpe.2017.06.018>
3. Tang CS (2006) Perspectives in supply chain risk management. *Int J Prod Econ* 103(2):451–488
4. Tang O, Musa SN (2011) Identifying risk issues and research advancements in supply chain risk management. *Int J Prod Econ* 133(1):25–34
5. Dong M (2006) Development of supply chain network robustness index. *Int J Serv Oper Inf* 1(1–2):54–66
6. Ferdows K, Lewis MA, Machuca JA (2004) Rapid-fire fulfillment. *Harv Bus Rev* 82(11):104–117
7. Klibi W, Martel A (2012) Modeling approaches for the design of resilient supply networks under disruptions. *Int J Prod Econ* 135(2):882–898
8. Lummus RR, Krumwiede DW, Vokurka RJ (2001) The relationship of logistics to supply chain management: developing a common industry definition. *Ind Manag Data Syst* 101(8):426–432
9. Billington C, Johnson B (2002) A real options perspective on supply chain management in high technology. *J Appl Corp Finance* 15:20–28
10. Christopher S, Tang (2006) Robust strategies for mitigating supply chain disruptions. *Int J Logistics Res Appl Lead J Supply Chain Manage* 9(1):33–45
11. Blatter M, Mühlemann S, Schenker S, Wolter SC (2016) Hiring costs of skilled workers and the supply of firm-provided training. *Oxf Econ Pap* 68(1):238–325
12. Chong JK, Ho T, Tang CS (2001) A modeling framework for category assortment planning. *Manuf Serv Oper Manage* 3:191–210

# Assessing Cognitive Behavior of Subjects Using Learning Effect and NASA-TLX in a Manual Pen Assembly



M. P. Giridhar  and Vinay V. Panicker 

**Abstract** This study investigates various ways to present material and information at workstations, using various assembly scenarios. The experiment is conducted with fifteen participants and six types of pen. The material presentation factors considered are the use of intermixed parts, grouped parts, separated parts in different boxes, and part numbered box. The information presentation factors include text instructions and photographs. From the results, it can be concluded that by using part numbered box as material presentation and instructions as information presentation provides the highest number of parts assembled with least errors. Similarly, using intermixed parts with instructions resulted in a decreased number of assembled pens. The design and preparation of workstations can be performed based on the cognitive abilities of the subjects. The different material and knowledge presentation factors can be designed according to their abilities.

**Keywords** Information presentation · Material presentation · Pen · NASA-TLX · Learning effect

## 1 Introduction

Ergonomics at work is the study of developing the work environment, considering the laborer's abilities and shortcomings. Awful workplace configuration prompts to worker fatigued, irritated, and suffering, which reduces worker productivity. Participatory ergonomics initiatives have been suggested as the most successful way of removing, or redesigning, manual activities in order to reduce the occurrence of musculoskeletal disorders in the workplace. This analysis reviews the evidence base for this claim; describes the range of approaches taken under the umbrella of participatory ergonomics in a variety of industries; and brings together the lessons learned in implementing these programs [1]. The journey toward Industry 4.0 and the growing

---

M. P. Giridhar · V. V. Panicker (✉)

Industrial Engineering Laboratory, Department of Mechanical Engineering, National Institute of Technology Calicut, Kozhikode, Kerala, India

e-mail: [vinay@nitc.ac.in](mailto:vinay@nitc.ac.in)

© The Author(s), under exclusive license to Springer Nature Singapore Pte Ltd. 2021

401

C. Pandey et al. (eds.), *Advances in Materials and Mechanical Engineering*,

Lecture Notes in Mechanical Engineering,

[https://doi.org/10.1007/978-981-16-0673-1\\_33](https://doi.org/10.1007/978-981-16-0673-1_33)



introduction of Cyber Physical Systems provoke improvements in the organization of human life and employment, generating new challenges, and opportunities. To take advantage of these opportunities and address the obstacles, new human-centered solutions and digital technology have to be incorporated [2].

Ergonomic practitioners in general did not expand the usage of conventional direct assessment tools for risk factors. Certified ergonomics professionals tend to have expanded use of some of the formal observational-based evaluation approaches [3]. A reliable tool for assessment of visual work environments, especially for complex tasks. However, efficiency could be further improved by increasing the standard of assessor training. Such results also support further evaluation of new longitudinal studies evaluating its responsiveness to visual environment changes [4]. Modern manufacturing systems vary significantly depending on size of the business and plant, and the quality of the product. Complex manual assembly environment is not just one factor at a time which affects the assembler but several combined factors. The expected workload analysis is also conducted using the NASA Task Load Index (NASA-TLX) workload measurement tool [5]. The assembly work environment places tremendous pressure on the assembler from a cognitive viewpoint that varies from one factor level to other. The purpose of this experimental study is therefore to examine the variables previously identified in a small pen assembly station influencing the cognitive aspects of human performance.

## 2 Background

A subject doing assembly work is often subject to circumstances of increasing cognitive demands. A virtual-engineering approach is to assess the structural complexity of digitally engineered component-based industrial automation systems [6]. Product complexity and the manufacturing process by which a product is produced affect operational efficiency, which is to be considered by manufacturers seeking to understand the effect of expanding product lines on their production systems [7]. The downside from an ergonomic point of view is that the assembler must concentrate solely on the assembly process, i.e., how to assemble, and do not care about which parts to assemble which can eventually contribute to a high level of product quality [8]. Learning curves (LCs) are considered to be effective tools for measuring worker productivity and providing a statistical explanation of the learning process that occurs when the job is repeated. Using technology or other approaches to improve worker learning will reduce the negative impacts of large pools of employees and missing employees [9]. The translation and first assessment of the psychometric property (NASA-TLX), a multidimensional tool for calculating workload in general practice, is a widely used, subjective, multidimensional measuring method that scores perceived workload to evaluate the effectiveness of a task, plan, or team, or other performance aspects [10].

### 3 Experimentation

This section presents an experimental study showing the presentation of the data, the presentation of material, and the effects of using various varieties of pens with different parts. The purpose of the analysis is to analyze assembly task performance, primarily the number of assembled parts and the number of errors in each level combination. This segment describes an experimental study showing the presentation of data, the presentation of knowledge, and the effects of using various varieties of pens with different sections. In this study, there are six varieties of pens as shown in Fig. 1, with varying number of parts are to be assembled in eight different combinations of material and information presentation. Fifteen people volunteered for the trial, mostly engineering graduates, except a few from humanities background. The experiment is conducted at a laboratory premises where the entire setup is designed to identify the subject's cognitive abilities. The subjects perform the task of constructing a pen within the time of ten minutes.

In addition to the subjects which conducted the assembly process, there are two researchers present. One manually controlled the assembly using a stopwatch, and the other disassembled the pieces of pen to measure the quality of the assembled pen. Table 1 shows the steps of the experiment, including the level of factors.

**Fig. 1** Exploded view of six varieties of pen



**Table 1** Factorial experiment design

S. No.	Material presentation	Information presentation
1	Intermixed parts	Instructions
2	Grouped parts	Instructions
3	Intermixed parts	Photograph
4	Grouped parts	Photograph
5	Separated parts in different boxes	Instructions
6	Part numbered box	Instructions
7	Separated parts in different boxes	Photograph
8	Part numbered box	Photograph

### 4 Results

The main aim of the experiment is to identify the number of pens that are correctly assembled and the quality of the assembled parts. The last scenario has the highest number of assembled pens which is due to the experience, the subjects have gained by assembling the pens from the first seven cases. The lowest assembled was in the first scenario as the subjects are not exposed to the assembling task and they only can use the previous knowledge about a pen to assemble.

As per Fig. 2 the number of errors is more in the scenario 7 as the individuals has photograph of the exploded view but as the parts look similar in some cases such as the refill, spring which is misplaced. There are certain parts which are exclusively for certain type of pens; they are inappropriately assembled even with the exploded views. The least number of errors happened in case 6, in which part numbers are given. It can be seen that the part number category has less errors than any other scenarios

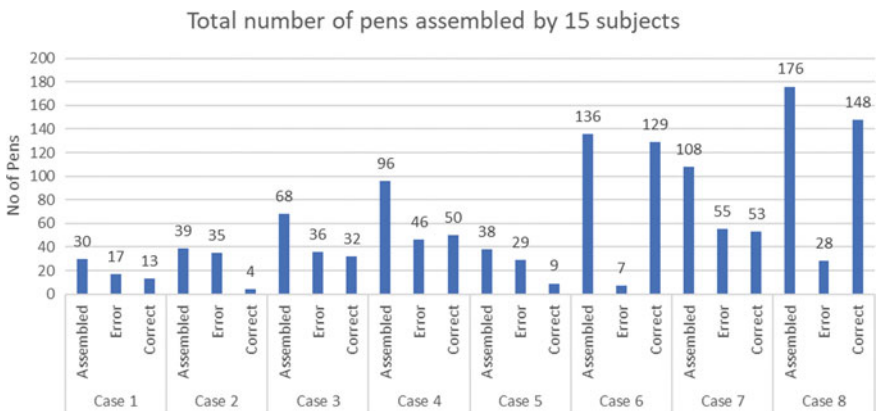


**Fig. 2** Total number of pens assembled by subjects in eight level of factors

which suggests the important of giving part number variations for assembling the product.

### 4.1 Learning Effect Considering the Number of Pens Assembled

A learning curve is a graphical portrayal of how an improvement in learning results from greater experience. The idea of learning curves is translated into pen assembly task as a “difficulty curve”, which described how hard it was for the subject to assemble the pen in different scenarios. The subject become more proficient with the further tasks, gain better understanding of the pen parts, and the error factor is decreased. As with learning curves in industrial aspect, difficulty curves can have multitudes of shapes, and tasks may frequently provide various levels of difficulty that change the shape of this curve relative to subject and effectively find the best person for the task.

The subjects are divided into three clusters for easy identification of the best and worst assembler. From Fig. 3, it is evident that subject 5 is a good learner compared to others in the cluster. Subject 10 can also be considered as a better learner as the number of pens assembled could be higher. Subject 2 showed a better learning experience but in the seventh scenario, there is a decrease in the number of assembled pens.

From Fig. 4, subject 10 can be considered as the best learner and subject 7 as the worst. Subject 6, 9, and 8 showed an increased learning effect but the number of assembled pens was less comparatively. This is critical as it affects the whole amount required for production in a certain time and the error factor can also be considered.

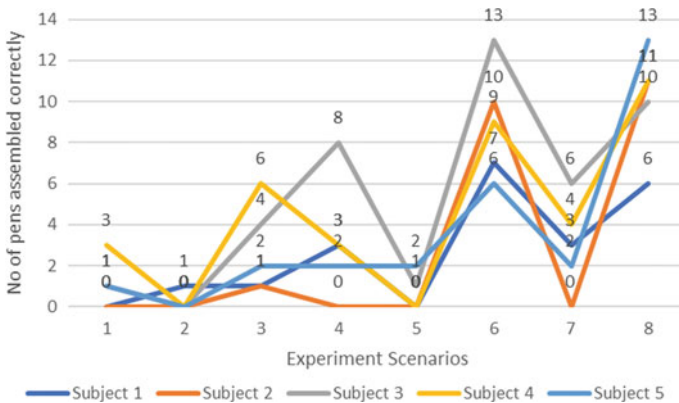


Fig. 3 Number of pens assembled correctly and scenarios by different subjects

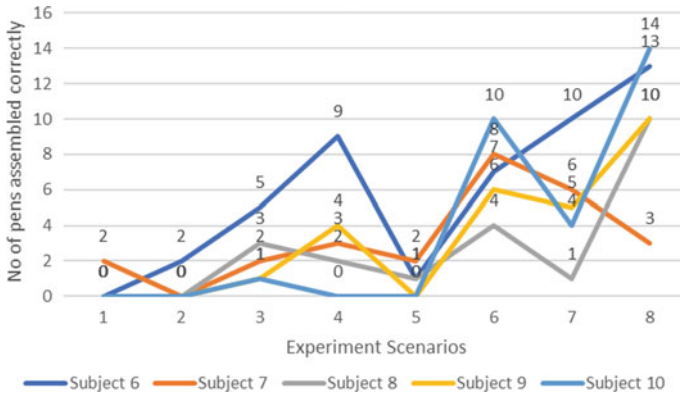


Fig. 4 Number of pens assembled correctly and scenarios by different subjects

From Fig. 5, subject 12 has the best learning curve and subject 14, the worst in terms of learning effect. Subject 15 and 13 had a decrease in the learning effect. Subject 11 had a gradual dip in the seventh scenario.

To summarize the results, it was considered that the end scenario must have a greater number of assembled pens without errors. According to this, subject 12 was the best learner and subjects 14 and 7 were the worst. The skill set of the workers can be identified and thus the allocation of a worker to a specific task according to his capabilities can be assigned.

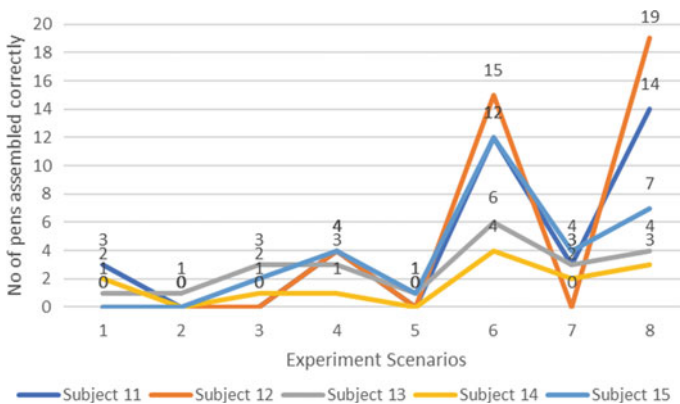


Fig. 5 Number of pens assembled correctly and scenarios by different subjects

### 4.2 NASA-TLX and Number of Pens Assembled

Therefore, study of the expected workload is also carried out using the workload evaluation tool NASA-TLX. In this analysis, after assembling pen in all scenarios, fifteen subjects are asked to rate their perceived workload on six different scales: mental, physical, temporal, performance, effort, and frustration. They set the scales from 0 to 100 and is depicted in Fig. 6. The factors are weighted in relation to each other to illustrate the most important aspects of the workload, where tension and mental workload are the primary focus; physical and performance are weighted as of lesser importance.

The NASA-TLX scores of various subjects are converted to various class intervals of four and is depicted in Table 2.

The comparison of these scores with the number of pens assembled correctly is to be considered so the rating of class intervals is considered as per Table 3.

The actual values of pens assembled can be compared with that of the NASA-TLX scores. The cognitive abilities will be different for different subjects and their rating on the different scenarios will be different from that of the experimental values.

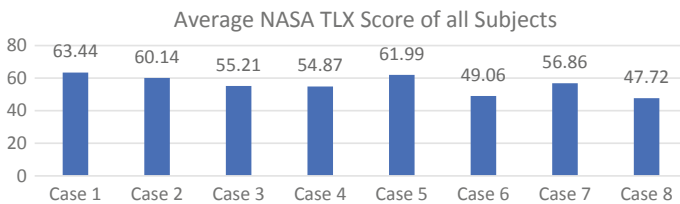


Fig. 6 NASA-TLX scores

Table 2 Rating for NASA-TLX scores

Interval	Number code	NASA-TLX rating
Below 29	1	Very easy
29–46	2	Easy
47–63	3	Medium
64–80	4	Tough

Table 3 Rating for number of pens assembled

Interval (Number of pens assembled)	Number code	Pens assembled rating
0–5	1	Bad
6–10	2	Medium
11–15	3	Good
16–20	4	Very good

**Table 4** Rating for NASA-TLX as per class intervals

Subject/scenario	1	2	3	4	5	6	7	8
1	4	4	3	3	3	3	2	2
2	4	3	3	2	4	3	3	3
3	4	3	3	3	3	3	3	3
4	4	3	3	3	3	3	3	3
5	4	4	3	3	3	2	3	2
6	3	3	3	2	3	2	3	2
7	4	4	3	3	4	3	3	3
8	4	4	4	4	4	4	4	4
9	3	3	3	3	2	2	2	2
10	3	4	4	4	4	4	4	4
11	3	2	3	3	3	2	3	2
12	2	3	2	3	4	2	4	2
13	4	4	3	2	4	3	3	3
14	2	2	2	2	3	3	3	3
15	4	4	3	3	4	2	3	3

The ratings of the scores give an idea about the difficulty level of the tasks and is given in Table 4. Out of the total ratings, the subjects have experienced a medium level of difficulty, considering all the scenarios. Only twenty percentage of subjects in various scenarios claimed that the tasks are easy. The easier ratings are obtained in scenario six and difficult in scenario one. The number of pens assembled are also rated according to the class intervals and they are listed in Table 5.

Subject 12 is the only person with a very good record of the number of pens assembled. Most of the subjects had done only a smaller number of assemblies in each scenario, which is considered as bad. This may be because, the quality of products assembled is the deciding factor in an assembly line. A good number of pens assembled is not observed in scenario six, as per the requirements or the highest value. The number of pens assembled in scenario 1 is bad but only five persons reported that scenario as difficult. In scenario 2, seven subjects rated the task as difficult and that is reflected in the number of pens correctly assembled. In scenario 6, two subjects genuinely rated as difficult but at the end there is no very good rating obtained. The learning effect for the final scenario must show a very good number of pens assembled, but only one subject could effectively achieve it and the rating was not given easy as per the learning experience.

**Table 5** Rating for number of pens assembled as per class intervals

Subject/scenario	1	2	3	4	5	6	7	8
1	1	1	1	1	1	2	1	2
2	1	1	1	1	1	2	1	3
3	1	1	1	2	1	3	2	2
4	1	1	2	1	1	2	1	3
5	1	1	1	1	1	2	1	3
6	1	1	1	2	1	2	2	3
7	1	1	1	1	1	2	2	1
8	1	1	1	1	1	1	1	2
9	1	1	1	1	1	2	1	2
10	1	1	1	1	1	2	1	3
11	1	1	1	1	1	3	1	3
12	1	1	1	1	1	3	1	4
13	1	1	1	1	1	2	1	1
14	1	1	1	1	1	1	1	1
15	1	1	1	1	1	3	1	2

## 5 Conclusion

This study provides an outline of the behavior of various subjects when they perform a specific assembly task for the first time and also how the productivity and quality of the assembled parts eventually increase. In response to manufacturers trying to understand the impact of increasing product lines on their production processes, the product complexity and the number of parts from which product is produced affect operating performance. The subjects show different trends of assembling products and even with the variety of products being increased, factor levels with proper instructions gained more quality and productivity in the assembly. The ability to think and differentiate the parts, learn with a particular phase, and recall the flaws happened concluded that using intermixed parts and grouped parts takes longer time and generates higher workload compared to separate parts in different boxes part numbered boxes. When using part numbered box and separated parts in different boxes, the task is made easier compared to intermixed parts and grouped parts. This is probably due to the difference in cognitive abilities of the subjects such as think, learn, remember, and pay attention. These skills can be further analyzed so that rotations in workstations among the subjects can be done according to their skills. One of the major cognitive ability of the subject must be their learning effect, which is also identified by giving various factor levels and the number of pens which each of them assembled had different trends.

The NASA-TLX values are not supporting the fact that part numbers with instructions are easier to do. The same is applicable for the number of pens assembled.



This suggests that the subjective rating can be deviated from the exact experimental outputs. The errors made in assembly units are a huge loss to the manufacturing units, so assigning proper subjects in their order of their cognitive skills will be the best way to improve productivity especially in manual assembly lines. The assessment of cognitive skills can be verified using electroencephalogram (EEG) and galvanic skin response, but as the person is continuously moving from the position the signals are not accurate to support the assessment which is the major drawback of this experiment.

## References

1. Burgess-Limerick R (2018) Participatory ergonomics: evidence and implementation lessons. *Appl Ergon* 68:289–293
2. Kadir BA, Broberg O, da Conceição CS (2019) Current research and future perspectives on human factors and ergonomics in industry 4.0. *Comput Ind Eng* 3:106004
3. Lowe BD, Dempsey PG, Jones EM (2019) Ergonomics assessment methods used by ergonomics professionals. *Appl Ergon* 81:102882
4. Zetterberg C, Heiden M, Lindberg P, Nylén P, Hemphälä H (2019) Reliability of a new risk assessment method for visual ergonomics. *Int J Ind Ergon* 72:71–79
5. Brodin A, Thorvald P, Case K (2017) Experimental study of cognitive aspects affecting human performance in manual assembly. *Prod Manuf Res* 5(1):141–163
6. Alkan B, Harrison R (2019) A virtual engineering-based approach to verify structural complexity of component-based automation systems in early design phase. *J Manuf Syst* 53:18–31
7. Trattner A, Hvam L, Forza C, Herbert-Hansen ZN (2019) Product complexity and operational performance: a systematic literature review. *CIRP J Manuf Sci Technol* 25:69–83
8. Gewohn M, Beyerer J, Usländer T, Sutschet G (2018) Smart information visualization for first-time quality within the automobile production assembly line. *IFAC-PapersOnLine* 51(11):423–428
9. Glock CH, Grosse EH, Jaber MY, Smunt TL (2019) Applications of learning curves in production and operations management: a systematic literature review. *Comput Ind Eng* 131:422–441
10. Flägel K, Galler B, Steinhäuser J, Götz K (2019) The “national aeronautics and space administration-task load index” (NASA-TLX)—an instrument for measuring consultation workload within general practice: evaluation of psychometric properties. *Zeitschrift für Evidenz, Fortbildung und Qualität im Gesundheitswesen* 147:90–96

# Ranking of Lean Critical Success Factors in Manufacturing Industry: AHP Approach



Virender Chahal, M. S. Narwal, and Sachin Kumar

**Abstract** Lean is an efficient and effective system but there are so many barriers during implementation. In paper, we study the different types of factors which are responsible for waste, after that lean barriers and these barrier solutions as lean implementation critical success factors (CSFs). Proper implementation of lean (CSFs) is very important to identify so that waste can be reduce and overall growth will reach much near to high productivity and profit. AHP technique is used to achieve this goal. It is the current issue that some industries goes for high production but does not focus on that how much waste comes out from industry. So, this paper focused on these factors which are very important and barriers with their solution lean implementation success factor. We can minimize or can remove all barriers which are responsible for improper implementation of lean system. As result, motivational approach (MA), upgrade job environment and satisfaction (UJS), leadership and responsibility (L&R), and develop new behavior pattern/strictly implementation of lean tools and methods (BP/SI) are the rank 1st, 2nd, 3rd, and at 4th, respectively. This calculation will help industry to identify suitable lean implementation success factor.

**Keywords** Lean tools · Lean barriers · Lean solutions · Lean implementation success factor

---

V. Chahal (✉)

Department of Mechanical Engineering, Chandigarh Engineering College, Landran, Mohali, Punjab, India

M. S. Narwal

Department of Mechanical Engineering, Deenbandhu Chhotu Ram University of Science and Technology, Murthal, India

S. Kumar

Department of Mechanical Engineering, Jagannath University, Bahadurgarh, Haryana, India

## 1 Introduction

Lean manufacturing is a disparity on the idea of efficiency based on defect free flow; it is today example of the recurring idea in human effort toward increasing efficiency, minimization of waste, and using pragmatic methods to come to a decision. Lean manufacturing is frequently seen as a more refined description of earlier effectiveness efforts, building ahead the work of previous leaders such as Ford or Taylor, and learning on or after their faults. Japanese manufacturers, mainly in automotive industry, were in problem of shortage of finance, materials, and human resources. Eijitoyoda and Taiichiohno in Toyota motors in Japan found the concept of—Toyota Production System (TPS), and now a day's known as—Lean manufacturing. The vital idea behind the structure is to eradicate the wastage. The primary goal of lean manufacturing is to support the manufacturers who have a wish to recover the company activities and become more aggressive through the achievement of different lean manufacturing methods and techniques. As per Womack and Jones [7], Lean Manufacturing signifies a structure that employ less, makes the same productivity as of conventional mass production system, while increase the varieties for the end buyer. The completion of lean gets better quality and decreases the problems of deprived production system. The waste decrease naturally happens as a result. The benefit of lean production is extremely good as to evaluate traditional processes. The lean system was imaginary for Toyota motor company but now it is used everywhere.

## 2 Literature Lean Manufacturing Working Cycle

Womack and Jones in—Machine that changed the world focused on the deep of lean move toward that was that—lean can change almost everything in every industry, the work style, offer the advantages to industry and good customer happiness. The lean advance focuses on special goals, which aim to get better efficiency, quality, and customers' happiness. Lean manufacturing is a variant on efficiency based on controlled flow; it is a present day example of the recurring topic in human history on the way to increasing effectiveness, decreasing waste, and using experimental methods to come to a decision what matters, relatively than uncritically accepting pre-existing ideas. The core idea behind lean is to minimize wastages in industry and maximize customer [1]. In simple words, leans system is creating a high customer satisfaction with fewer resources. A lean organization can stand as a benchmark for other companies. In lean system, the paper focuses on lean implementation, their problem, and also their solutions with continuously improvement. The overall implementation and aim are to supply perfect value and happiness to the customer through a perfect value construction process that has zero waste. Lean system is a team work, not a responsibility for a single person. Every person must be perfect in their work. Every little change with lean can provide a better change with higher productivity and minimum waste.

### 2.1 Lean Critical Success Factors (CSFs)

Netland [2] discussed the critical success factors and implementing these in lean production. This paper also highlights the effect of CSFs during implementation. According to Dora et al. [3] discuss the CSFs of lean manufacturing on operational performance. The authors also discuss the enablers of CSFs to improve the performance of industry. Belhadi et al. [4] also evaluate the 28 CSFs with AHP technique. The main goal of this paper was to select most suitable success factor. So as per the literature review, some CSFs are adopted which are as follows:

1. Motivational approach (MA)
2. Upgrade job environment and satisfaction (UJS)
3. Leadership and responsibility (L&R)
4. Develop new behavior pattern/strictly implementation of lean tools and methods (BP/SI).

### 3 Methodology to Achieve Objective

The proposed methodology to achieve the objective is shown in Fig. 1 and the detailed procedure of individual steps are as follows:

#### Step 1: Lean Process Cycle

The ten substeps for lean are given below:

- Substep 1:** Reengineering in manufacturing system.
- Substep 2:** Integrate suppliers.
- Substep 3:** Integrate quality control into manufacturing.
- Substep 4:** Level, balance, sequence, and synchronize.
- Substep 5:** Integrate preventive maintenance into manufacturing.

**Fig. 1** Proposed methodology to achieve the objectives



**Substep 6:** Computer-integrated manufacturing.

**Substep 7:** Reduce work-in-process (WIP).

**Substep 8:** Setup reduction and elimination.

**Substep 9:** Automation.

**Substep 10:** Integrate production control into manufacturing.

These ten actions are taken as the defaulting methodology for lean implementation.

### *Step 2: Lean Goals*

*Elimination of Waste:* The main reason of lean system is to diminish costs of the product and also removal of waste. The waste is defined as anything that does not have any value.

*Continuous Improvement:* By removal of waste is the belief of lean system, then incessant improvement. The creation system is being incessantly improved the processes and system.

*Multifunctional Teams:* The most effectual and salient characteristic of lean system is the widespread use of multifunctional groups. These organizations very much make possible task revolving and flexibility to lodge changes in production levels.

*Just-in-Time:* JIT idea implies the delivery of any element in the necessary amount and at right time. This perform is widely adopted amongst the suppliers in the automotive manufacturing.

*Integration of Suppliers:* In manufacturing industries there is activist impact of quicker working link with suppliers on product excellence. It is turn into a more and more popular form of commerce relationship within building over the last decade.

*Flexible Information System:* It is very significant to make system elastic; the principle entails devolution responsibilities to the manufacture line workers and a decline of the hierarchical levels of the corporation. The lean system requires the dispersal of in order to all.

These are the aims by which our manufacture system will be better but some factors influence these goals. After the learning, we find out various barriers which are liable for it.

### *Step 3: Barriers in Lean Manufacturing*

There are some major barriers for lean implementation and that are as follows:

- Cultural (Human/workers related) barriers.
- Technical barriers.
- Organizational barriers.
- Economical barriers.

*Cultural Factors:* Culture of an industry is a perfect image of doing work and rules followed. The lean system makes an industry advance and profitable. Every little lean change provides more powerful and effective system. When we will implement the lean manufacturing system, there is possibility that our culture will be disturbed for a little time. It is our understanding and responsibly to understood that what our goal

is. It is a thing to listen but big when implemented. Every industry starts initially from inside then outside, so it is practical to change.

*Technical Factors:* Technical factors are highly important for any industry. If any industry is technically sound it can take challenges of volatile market otherwise it will fall. If we ignore the technical factors the implementation of lean manufacturing will be suffered.

*Organizational Factors:* In every industry, there is an environment and own organizational chart, It is possible for the very same chart to serve as a barrier to the implementation of lean system. Some authors focused on factors through their papers, i.e., lean is the system where every little activity will be measured, so for this purpose we have to change for better.

*Economic Factors:* The cost is main issue for industry and also for customers. The absence of financial rules, the scope of the internal market and international market will be so difficult. It is a big problem for costumers and also for industry. Because these are inter-related concept, soothe economic barriers important. These are the common factors which are responsible for weak implementation. Every little factor creates a big problem, for example, excess waste, time delay, and money waste (Table 1).

**Table 1** Lean implementation barriers

Barriers	Stefan Andersson [8]	Nordin et al. [9]	Bakas et al. [10]	Darabi et al. [11]	Milita and Ramune [12]
Lack of recourses availability		*		*	
Cultural difference	*	*	*	*	*
Understanding difference		*			*
Lack of management support		*	*		*
Lack of interest in lean and about lean commitment		*			
Technological unawareness		*	*	*	*
Lack of team work	*				*
Economical factor			*	*	

*Step 4: Critical Success Factors (CSFs)/Barriers in Lean Manufacturing Implementation*

After study of the barriers, there are some solutions which will be effective in lean system implementation:

- Motivational approach (MA)
- Upgrade job environment and satisfaction (UJS)
- Leadership and responsibility (L&R)
- Develop new behavior pattern/strictly implementation of lean tools and methods (BP/SI).

*Motivational Approach:* Motivation is an important factor which provides an excitation to do new research frequently and industries employ motivation as strength to boost their productivity. When we are able to understand how people can motivate, you can move forward your workforce to provide you the best outputs in terms of quality and quantity. In lean manufacturing, sometimes, we have to change the environment and rules for better but people does not want to change. When people are highly motivated, our work will be world class.

*Upgrade Job Environment and Satisfaction:* For better implementation, we have to plan for new system and then upgrade. Lean is an advance and more critical theory so it required more work on it. And the term satisfaction comes out from effective and correct system. More satisfied people work more with quality.

*Leadership and Responsibility:* Leadership creates internal confidence for better work. This term is important to achieve goals. Another term is responsibility, and it is also much important. Until all people are not responsible, no system will be followed properly.

*Develop New Behavior Pattern/Strictly Implementation of Lean Tools and Methods:* Many times, number of delay and accidents occur. If we look for a cultural alter based on various behaviors and consideration patterns, then a clear plan must be followed. Knowledge and successes of the history are based on consideration and behavior patterns you strength want to change. Lean is a tool which provides a lot of benefits in production and reduces waste. But it is not implemented properly. Reason behind that is lack of awareness and not implementation of tools and methods properly. So, we have to implement these methods seriously for industrial benefit.

*Step 5: Decision Support System for Selection of Most Useful Success Factor:*

The decision support system (DSS) is introduced for selection of most useful success factor for providing most accurate result. The AHP multi-decision technique is used to make suitable decision making [5]. This DSS will produce based on selected critical success factors (CSFs), i.e., MA, UJS, L&R, and BP/SI with lean barriers which are: Cultural (Human/workers related) barriers, technical barriers, organizational barriers, and economical barriers. After fruition of these barriers industry experts can provide a better decision. For the decision on most useful barriers, the different industrial decision experts and obtained mutual matrices.

AHP decision matrices for MA, UJS, L&R, and BP/SI by dissimilar decision makers (DM) are:

$$DM1 = \begin{matrix} 1 & 6 & 4 & 6 \\ \frac{1}{7} & 1 & 3 & 6 \\ \frac{1}{3} & \frac{1}{2} & 1 & 7 \\ \frac{1}{6} & \frac{1}{7} & \frac{1}{7} & 1 \end{matrix}$$

Eigenvector ( $E1$ ) = (0.577, 0.204, 0.173, 0.044)

Consistency index (CI) = 0.181, Consistency ratio (CR) = 0.203

Similarly, for DM2:

Eigenvector ( $E2$ ) = (0.610, 0.215, 0.134, 0.037),

Consistency index (CI) = 0.190, Consistency ratio (CR) = 0.211

Similarly, for DM3:

Eigenvector ( $E3$ ) = (0.605, 0.182, 0.164, 0.044),

Consistency index (CI) = 0.15

Consistency ratio (CR) = 0.184 (Best consistency ratio among all)

Similarly, for DM4:

Eigenvector ( $E4$ ) = (0.620, 0.213, 0.131, 0.034),

Consistency index (CI) = 1.25, Consistency ratio (CR) = 1.412

The result shows that all matrices reveal a similar level of consistency ratio with an exemption of the common matrix  $D4$ , whose consistency ratio is higher than for the rest of the matrices. The corresponding eigenvectors are given as following:

$E1 = (0.577, 0.204, 0.173, 0.044)$

$E2 = (0.610, 0.215, 0.134, 0.037)$

$E3 = (0.605, 0.182, 0.164, 0.044)$

$E4 = (0.620, 0.213, 0.131, 0.034)$

And average value of Eigenvector ( $Ea$ ) is:

$Ea = (0.603, 0.203, 0.150, 0.039)$

As per decision result, lean critical success factors (CSFs), i.e., MA, UJS, L&R, and BP/SI. The average values of Eigenvector ( $Ea$ ); MA has upper importance



**Table 2** Ranking for lean strategies (LS)

Adopted lean success factor	Ranking based on decision makers
Motivational approach (MA)	1
Upgrade job environment and satisfaction (UJS)	2
Leadership and responsibility (L&R)	3
Develop new behavior pattern/strictly implementation of lean tools and methods (BP/SI)	4

(0.603), UJS (0.203) is less significant. L&R (0.150) and BP/SI (0.039) stand on third and fourth place in consequence, respectively.

After identifying all performance of LS, decision criteria, and relative weight by industrial experts, the result will be in form of ranking with adopted lean strategies (LS). This result is shown in Table 2.

## 4 Result and Discussion

The aim of this research is to find the appropriate lean implementation critical success factors (CSFs). Literature has very less ways obtainable for measuring these critical success factors (CSFs). As results, this research identified the lean implementation barriers and lean implementation (CSFs). A DSS has been generated with MA, UJS, L&R, and BP/SI with lean barriers which are as follows: Cultural (Human/workers related) barriers, technical barriers, organizational barriers, and economical barriers to identify and ranking for suitable lean success factor with help of AHP technique which is more suitable in this situation and is a good decision [6]. So, an industrial study and performance calculation can be conducted. In the future research, decision support system (DSS) can be improved with MATLAB, visual basic and C\*\* programming.

## References

1. Jasti NVK, Kodali R (2015) Lean production: literature review and trends. *Int J Prod Res* 53(3):867–885
2. Netland TH (2016) Critical success factors for implementing lean production: the effect of contingencies. *Int J Prod Res* 54(8):2433–2448
3. Dora M, Kumar M, Van Goubergen D, Molnar A, Gellynck X (2013) Operational performance and critical success factors of lean manufacturing in European food processing SMEs. *Trends Food Sci Technol* 31(2):156–164
4. Belhadi A, Touriki FE, Elfezazi S (2019) Evaluation of critical success factors (CSFs) to lean implementation in SMEs using AHP: A case study. *International Journal of Lean Six Sigma* 10(3):803–829. <https://doi.org/10.1108/IJLSS-12-2016-0078>

5. Pudi R, Martha TR, Roy P, Kumar KV, Rao PR (2019) Regional liquefaction susceptibility mapping in the Himalayas using geospatial data and AHP technique. *Curr Sci* 116(11):1868
6. Singh A, Prasher A (2019) Measuring healthcare service quality from patients' perspective: using fuzzy AHP application. *Total Qual Manag Bus Excellence* 30(3–4):284–300
7. Womack JP, Jones DT (1994) From lean production to the lean enterprise. *Harvard Bus Rev* 72(2):93–103
8. Andersson S (2007) Implement Lean Production in small companies (Master's thesis)
9. Nordin N, Othman SN, Che Mat R (2008) Technology implementation barriers in the Malaysian herbal industry: A case study. *Malaysian Manage J* 12(1 & 2):79–88
10. Bakas O, Govaert T, Van Landeghem H (2011) Challenges and success factors for implementation of lean manufacturing in European SMES. In 13th International conference on the modern information technology in the innovation processes of the industrial enterprise (MITIP 2011) (Vol. 1). Tapir Academic Press
11. Darabi R, Moradi R, Toomari U (2012) Barriers to implementation of lean accounting in manufacturing companies. *Int J Bus Comm* 1(9):38–51
12. Milita V, Ramune C (2013) Lean Manufacturing implementation and progress measurement. *Econ Manage* 18(2):366–373

# Evaluation of the Barriers in the Adoption of Automated Technology by the Manufacturing Sector: A Case from India



Koppiahraj Karuppiah, Bathrinath Sankaranarayanan,  
and Saravanasankar Subramaniam

**Abstract** The advent of Industry 4.0, i.e., automated manufacturing, has shifted the paradigm of the manufacturing process. With the assistance of computers, the automated manufacturing technique increases the production capability along with improved precision. Enhancement of production capability with industrial automation technology has provided a competitive edge for the manufacturing firm. With such automation, it becomes easy for a manufacturing firm to meet the dynamic market demand. However, automated production is not affordable for many industries, as it requires a huge upfront investment. The shift toward automated manufacturing began in developed countries a decade ago; however, the developing countries are still relying on conventional manufacturing. To cope with the global manufacturing trend, it becomes necessary for the manufacturing sectors in developing countries to adopt automated manufacturing techniques. However, many challenges hamper the industrial shift toward automated manufacturing. Considering the challenges, this study intends to identify, evaluate, and prioritize the challenges in adopting automation technology in the Indian context. With the assistance of a literature survey and expert interaction, nine critical challenges the Indian industries face in the adoption of automated technology are identified. Then, using the best–worst method (BWM), these challenges are prioritized based on their weight. An increase in unemployment, less versatility and unpredictable cost are identified as the three most prominent challenges Indian industries face in the implementation of automation. From the outcomes, the study suggests some implications for managers, which may make the automation feasible.

**Keywords** Automation · Best–worst method (BWM) · Globalization

---

K. Karuppiah · B. Sankaranarayanan (✉) · S. Subramaniam  
Department of Mechanical Engineering, Kalasalingam Academy of Research and Education,  
Krishnankoil, Tamilnadu 626126, India

© The Author(s), under exclusive license to Springer Nature Singapore Pte Ltd. 2021  
C. Pandey et al. (eds.), *Advances in Materials and Mechanical Engineering*,  
Lecture Notes in Mechanical Engineering,  
[https://doi.org/10.1007/978-981-16-0673-1\\_35](https://doi.org/10.1007/978-981-16-0673-1_35)

421

## 1 Introduction

The leather industry, located worldwide, has been known to contribute significantly to the countries' economic development. In particular, this industry is generally considered as the economic lifeline for the economically weaker section. As this industry does not require any special skills, most of the semiskilled people rely on this industry for income. However, as the leather products' demand is continuously rising, it necessitates the leather industrial community to increase the production capacity [1]. In meeting the rising demand, the leather sector is in a situation to adopt automation technology. The case industry considered in this study is a leather shoe manufacturing industry, which involves a certain tedious process like maintaining accuracy in the shoe size. Besides maintaining accuracy in size, the industry has to increase its production capacity in meeting demands. In this perspective, the leather shoe manufacturing industry aims to implement automation technology with the perception that automation may yield a better production rate than human workers.

In general, automation is defined as a process progressively transferring, regulating, and controlling systems based on mechanical, electrical, and computer-based systems [2]. Automation's primary task is to execute a great number of functions automatically, but in a reasonably controlled manner referring to safety and rational use of resources. Such automation level requires high standards and is not the most appropriate for making decisions to crises where a high level of unpredictability can appear [3]. By integrating several processes in an industry with automated machinery, it is possible to minimize cycle times and effort, reducing the need for human labor. With industrial automation, investment in workers will be saved.

As automation minimizes human involvement, the possibility of human error is also eliminated. With automation, consistent and reliable product quality can be maintained with greater automation compliance by controlling and monitoring industrial processes at all stages.

The rest of the paper is organized as follows. Section 2 provides a detailed report on relevant literature. Section 3 presents the solution methodology used for evaluating the barriers in automation. A real-world application demonstrating the applicability of the solution methodology is given in Sect. 4. In Sect. 5, the results obtained using the solution methodology are discussed. Finally, Sect. 6 concludes the research work.

## 2 Literature Review

### 2.1 Overview of the Indian Leather Industry

The leather industry, one of India's major export-oriented industries, has a strong bearing on the country's economy with an annual turnover of US \$12 billion [4]. The leather industry occupies a prominent place in the Indian economy due to its substantial export earnings [5]. Besides being a generous revenue generator, the

leather industries provide large-scale employment opportunities to the rural population, especially the semiskilled population. The Indian leather sector meets 10% of the global finished leather requirement. With the introduction of globalization, most small- and medium-sized enterprises (SMEs) got an opportunity to create a niche market for themselves in the global market. The leather product from India is known for its surface finish and texture [6]. However, most of India's leather industries were SMEs that they have to strive hard to withstand in this competitive business environment [7]. As most of the leather industries are SMEs, affording the advanced technology has remained an uphill task. Being unable to adopt advanced technology largely affects the leather industries' production capability. One of the features that distinguish leather from other sectors is the large presence of manual labor and low level of automation. To meet the increasing global demand for leather products, most of the leather industries are willing to adapt to automation technology in the production line to improve its productivity. Attempts to improve productivity were made by some labor-intensive leather SMEs.

The role of government is very crucial in improving the performance of the manufacturing. As most of India's industries are SMEs, they are facing a financial burden [8, 9]. At the same time, leather industries with sufficient financial assistance are capable of upgrading the manufacturing system. Besides, financial burden, factors like a poor commitment from top-level management, management's reluctance to adopt advanced technology and low level of technological knowledge hinders the transformation of leather industries toward automated technology [10, 11]. The production of leather products moved from developed countries to developing countries to keep the production cost low. However, with limited technological advancement, productions in developing countries are still labor-intensive [12, 13].

## ***2.2 Barriers in Automation***

Being labor-intensive, transformation to an automated industry will lead to job loss for many people. Such an attempt may bring an imbalance in the social sustainability of the industry [14]. For a country like India, the increase in unemployment may bring in numerous problems. Loss of jobs may aggregate poverty [15]. A study by Kim et al. [16] indicates that automation in an industry may lead to gender parity. India's leather industry is set to grow exponentially over the next five years, with a growth target of 50% in exports from 2016 to 20. In meeting this predicted growth, the Indian leather industry has to switch for automated technology. However, such a leather industry transition is often jeopardized by several barriers in the Indian context. Among these barriers, financial assistance for the leather industries occupies a prominent place [17]. Other than this, devoid of technological support and lack of skilled resource has been cited as the reason for delay in the leather industries' transition toward automation. Besides these primary challenges, secondary challenges like technical assistance and the need for expertise faced by the leather industries are related to

tariffs [18]. Even if the industries upgrade for automation, additional costs like maintenance costs and installation costs will bring in more problems. Additionally, the requirement of skilled labor will also remain as barriers in automation. So, for the adoption of automation technology, the leather industries have to overcome many barriers. Hence, there is an imminent need to address the issues faced by the leather industries.

From the literature review, it is apparent that the leather sectors contribute immensely to the Indian economy while facing many barriers to automation technology. The leather industries are in a situation to adopt automation technology for competing in the global market. In this connection, this study investigates the barriers faced by the leather industries in the implementation of automation technology.

### 3 Solution Methodology

In this study, the best–worst method (BWM) developed by Rezaei [19] is used to prioritize the leather industry’s barriers in the automation implementation. The steps involved in the best–worst method are as follows:

**Step 1:** The decision-makers (DM) select the set of barriers  $\{C_1, C_2, \dots, C_n\}$ .

In this step, the factors to be evaluated are identified.

**Step 2:** Classify the factors under the best and worst category.

In this step, the decision-maker categorizes the criteria as the best and the worst categories.

**Step 3:** Determine the best criterion’s preference over all the other criteria using a number from 1 to 9 (1—equally important, 9—extremely more important).

$$X_B = (x_{B1}, x_{B2}, \dots, x_{Bn}), \tag{1}$$

where  $x_{Bj}$  indicates the preference of the best criterion  $B$  over criterion  $j$ .

**Step 4:** Determine the preference of all the criteria over the worst criterion using a number between 1 and 9.

$$X_W = (x_{1W}, x_{2W}, \dots, x_{nW})^T, \tag{2}$$

where  $X_{jW}$  indicates the preference of the criterion  $j$  over the worst criterion  $W$ .

**Step 5:** Estimate the optimal weights  $(W_1^*, W_2^*, \dots, W_n^*)$ .

For each pair of  $\frac{x_B}{x_j}$  and  $\frac{x_j}{x_w}$ , the optimal weight should meet the condition  $\frac{x_B}{x_j} = x_{Bj}$  and  $\frac{x_j}{x_w} = x_{jw}$ .

## 4 A Real-World Application

In this section, a real-world application of the proposed methodology is illustrated. For this purpose, we consider the problems faced by the leather industry in implementing automation. The case leather industry considered in this study has created a niche for itself across the globe. However, the major challenge faced by this industry in recent years is in meeting customer demand. In this aspect, the leather industry is in a situation to implement automation. Yet this automation implementation by the industry is hindered by many barriers. To identify the critical barriers in the implementation of automation, we formed an expert panel comprising six experts. The expert panel includes three from industrial management, two from an academic background, and one from automation industry. The average experience of the expert panel is six years. Upon interaction with the expert panel, we identified ten barriers, namely less versatility (*B1*), large initial investment (*B2*), unpredictable cost (*B3*), increase in unemployment (*B4*), increase in maintenance cost (*B5*), skill resource (*B6*), lack of understanding of autonomous technology (*B7*), poor manageability (*B8*), difficulty in the integration of the organizational structure (*B9*). In evaluating these barriers, this study uses the BWM technique. As a first step of BWM, based on experts' opinion, the best and the worst barriers are identified. Next, the best barrier to the other barriers is rated by the experts. The experts' average rating against each barrier is provided in Table 1. Table 2 shows the average of experts rating of worst-to-others. The final weights of the barriers obtained using the BWM are shown in Table 3.

**Table 1** Best-to-other barriers

Best-to-others	<i>B1</i>	<i>B2</i>	<i>B3</i>	<i>B4</i>	<i>B5</i>	<i>B6</i>	<i>B7</i>	<i>B8</i>	<i>B9</i>
<i>B4</i>	3	8	6	1	6	6	6	7	7

**Table 2** Others-to-worst barriers

Others-to-worst	<i>B9</i>
<i>B1</i>	5
<i>B2</i>	6
<i>B3</i>	3
<i>B4</i>	4
<i>B5</i>	5
<i>B6</i>	4
<i>B7</i>	5
<i>B8</i>	5
<i>B9</i>	1

**Table 3** Weights of the barriers obtained by BWM

	B1	B2	B3	B4	B5	B6	B7	B8	B9
Weights	0.17	0.06	0.08	0.33	0.08	0.08	0.08	0.07	0.04

## 5 Results and Discussion

From the results displayed in Fig. 1, it is understood that the increase in unemployment (B4) will be a major challenge for the leather industry while implementing automation technology. By implementing automation, the industry may do injustice to its social sustainability. Loss of job may expose the workers to poverty [20]. Next, less versatility (B1) is the major challenge in automation. In the leather industry, multiple operations have to be performed. In such a case, implementing automation for a selective operation may bring in economical expense only. So, automation may bring in only economic expense and will not provide versatility. Then, unpredictable cost (B3), increase in maintenance cost (B5), skill resource (B6), lack of understanding of autonomous technology (B7) are the other challenges in automation. Unpredictable costs include costs that may exceed the actual cost saved by the automation itself. These costs include research and development costs of automation, maintenance, and employee training costs. For a small- and medium-sized industry, such costs will be an additional burden with automation cost. Hence, automation will only remain a challenge for medium-sized industries. Further, automation implementation demands frequent maintenance costs. The maintenance cost in automation comprises maintenance of sensors, solenoids, and the various equipments. This

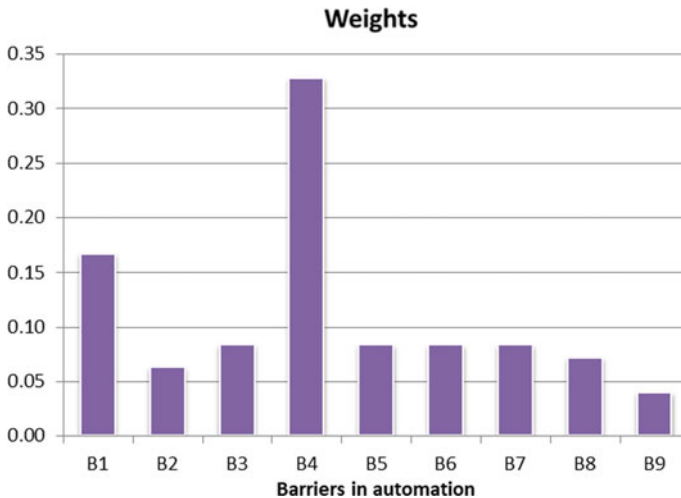


**Fig. 1** Ranking of the automation barriers



equipment involved in the automation technology needs frequent replacement of electronic devices. Wang et al. [21] highlighted that electronic devices used in automation are subject to various types of uncertain information in electronic equipment, frequent degenerative faults, complex relationships of modules, and multiple fault modes.

Most of the leather industry workers are semiskilled and are not adequately educated to operate the equipment of the automation system. In such a situation, the workers are needed to be trained and educated on operating the automation system. For preparing the workers, the industry has to spent additional cost. Hence, the financial burden of the industry may increase. Finally, most of the workers' and industrial management are not well-aware and well-versed with the autonomous technology revolution. Such a poor understanding of autonomous technology will only remain a problem for industrial management.

## 6 Conclusion

With the view of increasing the production rate, most industries are adopting autonomous technology in their production line. The adoption of autonomous technology has become easy for large-scale industries as they can afford the cost of such technology and maintenance. However, when small- and medium-scaled industries make such attempts, the attempt becomes a disaster. In this aspect, this study analyzed various barriers that are hampering the adoption of autonomous technology using the BWM technique. Our study findings reveal that increase in the number of unemployment and less versatility of the autonomous technology restricts the industry from adopting autonomous technology. In addition to this, the lack of skilled resources and increased maintenance costs hamper the adoption.

This study has some significant contribution to the literature on automation technology. For instance, this work is one of the first kinds of exploring the barriers of adopting automation technology in the leather industries. This study sheds light on the importance of automation in developing countries' contexts. Next, this study considered and evaluated the organizational structure problem, which the earlier studies have not considered.

Though the study contributes immensely to the literature, the study has some limitations. Only a limited number of barriers were considered in this study. The study visited only one leather industry. Hence, a multiple case study is necessary to capture a clear picture of barriers in automation. As a future direction of the research work, more barriers in adopting autonomous technology could be analyzed using fuzzy DEMATEL technique, which will reveal their interrelationship among the barriers.

## References

1. Murthy V, Jaganth G (2020) Making of an entrepreneur: a journey with leather—MVR leathers. *Emerald Emerg Mark Case Stud* 10:1–20. <https://doi.org/10.1108/EEMCS-05-2019-0141>
2. Hubka V, Eder WE (1988) *Theory of technical systems*. Springer, Berlin. <https://doi.org/10.1007/978-3-642-52121-8>
3. Mrugalska B, Wyrwicka M, Zasada B (2016) Human-automation manufacturing industry system: current trends and practice. [https://doi.org/10.1007/978-3-319-41983-1\\_13](https://doi.org/10.1007/978-3-319-41983-1_13)
4. Hasan M, Javed MY, Farooq A (2020) Understanding survival challenges of Tamil Nadu leather industry through content analysis and AHP. *J Inf Optim Sci* 41:411–419. <https://doi.org/10.1080/02522667.2020.1723937>
5. Singh S (2018) An analysis of major challenges that an Indian leather industry is facing and their impact on leather export performance in recent years. Available at SSRN: <https://ssrn.com/abstract=3125545>
6. Gupta SK, Gupta S, Dharnija P (2019) An empirical study on productivity analysis of Indian leather industry. *Benchmarking Int J* 26:815–835. <https://doi.org/10.1108/BIJ-06-2018-0156>
7. Faisal AM (2016) Case studies on the implementation of TQM in the Indian leather SMEs. *Int J Qual Innov* 3:17. <https://doi.org/10.1504/IJQI.2016.079911>
8. Bhavani MT, Dhivya S (2019) Export performance of leather products in India. *ZENITH Int J Multidiscip Res* 9:487–495
9. Karuppiyah K, Sankaranarayanan B, Ali SM, Chowdhury P, Paul SK (2020) An integrated approach to modeling the barriers in implementing green manufacturing practices in SMEs. *J Clean Prod* 265. <https://doi.org/10.1016/j.jclepro.2020.121737>
10. Uddin S, Ali SM, Kabir G, Suhi SA, Enayet R, Haque T (2019) An AHP-ELECTRE framework to evaluate barriers to green supply chain management in the leather industry. *Int J Sustain Dev World Ecol* 26:732–751. <https://doi.org/10.1080/13504509.2019.1661044>
11. Karuppiyah K, Sankaranarayanan B, Ali SM (2020) A fuzzy ANP-DEMATEL model on faulty behavior risks: implications for improving safety at the workplace. *Int J Occup Saf Ergon* 1–42. <https://doi.org/10.1080/10803548.2020.1847486>
12. Nayak R, Padhye R (2018) Introduction to automation in garment manufacturing. In: *Automation in garment manufacturing*. Elsevier, pp 1–27. <https://doi.org/10.1016/B978-0-08-101211-6.00001-X>
13. Karuppiyah K, Sankaranarayanan B, Ali SM, Kabir G (2020) Role of ergonomic factors affecting production of leather garment-based SMEs of India: implications for social sustainability. *Symmetry (Basel)* 12. <https://doi.org/10.3390/SYM12091414>
14. Anantharaman L, Sridharan MR (2018) Evolving an industrial digital ecosystem: a transformative case of leather industry. [https://doi.org/10.1007/978-981-10-7515-5\\_18](https://doi.org/10.1007/978-981-10-7515-5_18)
15. Parschau C, Hauge J (2020) Is automation stealing manufacturing jobs? Evidence from South Africa's apparel industry. *Geoforum* 115:120–131. <https://doi.org/10.1016/j.geoforum.2020.07.002>
16. Kim T, Sharma A, Gausdal AH, Chae C (2019) Impact of automation technology on gender parity in maritime industry. *WMU J Marit Aff* 18:579–593. <https://doi.org/10.1007/s13437-019-00176-w>
17. Niyaz AA (2018) Determinants of entrepreneur's competencies at Vellore District in Tamil Nadu-with special reference to the leather industry. *Int J Manag IT Eng* 8:224–231
18. Tripathy IG, Kumar P (2019) Challenges of Indian MSME exporters: a review. *SEDME Small Enterp Dev Manag Ext J* 46:189–195. <https://doi.org/10.1177/0970846419871113>
19. Rezaei J (2015) Best-worst multi-criteria decision-making method. *Omega (United Kingdom)* 53:49–57. <https://doi.org/10.1016/j.omega.2014.11.009>
20. Schönborn G, Berlin C, Pinzone M, Hanisch C, Georgoulis K, Lanz M (2019) Why social sustainability counts: the impact of corporate social sustainability culture on financial success. *Sustain Prod Consum* 17:1–10. <https://doi.org/10.1016/j.spc.2018.08.008>

21. Wang L, Zhou D, Zhang H, Tian H, Zou C, Wang X (2019) Fault inference of electronic equipment based on multi-state fuzzy bayesian network. Appl Sci 9:4248. <https://doi.org/10.3390/app9204248>